fluids

Special Issue Reprint

Recent Advances in Fluid Mechanics

Feature Papers, 2022

Edited by
Mehrdad Massoudi

mdpi.com/journal/fluids

MDPI

Recent Advances in Fluid Mechanics: Feature Papers, 2022

Recent Advances in Fluid Mechanics: Feature Papers, 2022

Editor

Mehrdad Massoudi

MDPI

Basel • Beijing • Wuhan • Barcelona • Belgrade • Novi Sad • Cluj • Manchester

Editor
Mehrdad Massoudi
National Energy Technology Laboratory (NETL)
Pittsburgh, PA
USA

Editorial Office
MDPI
St. Alban-Anlage 66
4052 Basel, Switzerland

This is a reprint of articles from the Special Issue published online in the open access journal *Fluids* (ISSN 2311-5521) (available at: https://www.mdpi.com/journal/fluids/special_issues/019004EM82).

For citation purposes, cite each article independently as indicated on the article page online and as indicated below:

Lastname, A.A.; Lastname, B.B. Article Title. *Journal Name* **Year**, *Volume Number*, Page Range.

ISBN 978-3-7258-1291-2 (Hbk)
ISBN 978-3-7258-1292-9 (PDF)
doi.org/10.3390/books978-3-7258-1292-9

Contents

About the Editor

Mehrdad Massoudi

Mehrdad Massoudi is an Adjunct Professor from the Department of Biomedical Engineering, Carnegie Mellon University, Pittsburgh, PA 15213, USA. Dr. Massoudi received his BS, MS, and PhD in 1979, 1982, and 1986, respectively, from the University of Pittsburgh. His research interests are in the areas of mathematical modeling of non-linear materials, non-Newtonian fluid mechanics, multiphase flows, and granular materials. He is an ASME Fellow and the former Editor-in-Chief of *Fluids*.

fluids

MDPI

Editorial

Recent Advances in Fluid Mechanics: Feature Papers, 2022

Mehrdad Massoudi

U. S. Department of Energy, National Energy Technology Laboratory (NETL), Pittsburgh, PA 15236, USA; mehrdad.massoudi@netl.doe.gov

This Special Issue is a collection of papers from some of the leading researchers discussing new findings or cutting-edge developments relating to all aspects of fluid mechanics.

Amongst the various forces acting on particles in a fluid, the Basset force, related to the fluid inertial effects, is one of the most difficult to study. Procopio and Giona [1] developed a modal expansion of the force acting on a micrometric particle. They show that the viscoelastic effects of the fluids studied induce the regularization of inertial memory, stemming from the finite propagation velocity. They derive an analytical expression for the fluid inertial kernel for a Maxwell fluid, and they also propose a general method to provide accurate approximations of this expression for complex fluids.

Hydropower plants have a high storage capacity and are capable of quick responses; as a result, they are increasingly being used to facilitate and integrate the intermittent energy from other renewable sources of energy, for example, wind and solar energy. At times, the operation of hydro turbines is limited by the formation of a Rotating Vortex Rope (RVR) in the draft tube. Arabnejad et al. [2] studied this phenomenon by using scale-resolving methods, namely, SST-SAS, wall-modeled LES (WMLES), and zonal WMLES. Their numerical simulations consider the effects of different scale-resolving methods on capturing flow, and the results indicate that for a small amount of vapor, cavitation induces broadband high-frequency fluctuations, and as the amount of cavitation increases, these fluctuations tend to have a dominant frequency different from that of the RVR.

There has been a tremendous increase in the applications of fractional calculus as a new and efficient mathematical tool for analyzing the properties of non-linear materials and relating the parameters in the models to experimental results. Lenzi et al. [3] studied the solutions of a generalized diffusion-like equation using a spatial and time-fractional derivative; in their equations, the presence of the non-local terms, related to reaction or adsorption–desorption processes, are also accounted for. They used the Green function approach to obtain solutions. Their study can help us to understand the different scenarios that can occur in connection with diffusion and anomalous diffusion processes.

The study of oscillating airfoils at moderate Reynolds numbers is a suitable candidate for testing the transition and modification needed in the standard Reynolds-Averaged Navier–Stokes (RANS) equations. Alberti et al. [4] used a high-order discontinuous Galerkin solver to study two-dimensional flapping foils at moderate Reynolds numbers when subject to different prescribed harmonic motions. Their simulations show an increase in the effectiveness in predicting loads, which is the case at low Strouhal numbers. Furthermore, their transition model seems to accurately predict wake topology, which is directly related to thrust/drag generation.

Methane pyrolysis appears to be among the new benign technologies for producing hydrogen with zero greenhouse gas emissions, and it is especially suitable for solar energy applications with high-temperature process heat. Msheik et al. [5] examined the possibility of using solar methane pyrolysis as a decarbonization process, producing both hydrogen gas and solid carbon with zero CO_2 emissions. They designed a novel hybrid solar/electric reactor at the PROMES-CNRS laboratory to handle the difficulties associated with direct normal irradiance (DNI). They also used Computational Fluid Dynamics (CFD)

Citation: Massoudi, M. Recent Advances in Fluid Mechanics: Feature Papers, 2022. *Fluids* **2023**, *8*, 262. https://doi.org/10.3390/fluids8100262

Received: 19 September 2023
Accepted: 22 September 2023
Published: 26 September 2023

simulations and investigated the performance of this reactor under different operating conditions. The results of their numerical simulations agree with their experimental results, indicating the applicability of the proposed solar hybrid reactor design for efficient methane decomposition performance.

Vortex stretching and bursting are among the main causes of turbulence and the interactions at different scales of energy transfer; these are generally related to some of the terms in equations of motion, inertia, compression, diffusion, and dissipation. The vortex filament is also noticed in the Taylor–Green vortex, which is different from the simulation results based on the Navier–Stokes equations. Caltagirone [6] studied this problem using spectral analysis and by allowing the decay of kinetic energy to be a function of the wave number.

Waris and Lappa [7] studied the mixed buoyancy–Marangoni convection of a fluid over an inclined layer heated from below and unbounded from above. They used a thermographic visualization technique and took multiple temperature measurements at different points. Using a computer-based reconstruction of the spatial distribution of wavelengths, they show that this flow arrangement can develop interesting patterns, such as spatially localized cells, longitudinal wavy rolls, and finger-like structures.

Flow over rough surfaces occurs in many engineering applications and in nature (for example, flow inside pipes, around turbine blades, atmospheric boundary layers, etc.). The effects of roughness and its impact on flow have been studied extensively. Salomone et al. [8] studied flow over strips placed regularly along the mean stream. They used wall-modeled large-eddy simulations (WMLES) and improved delayed detached-eddy simulations (IDDES) (a hybrid method solving the Reynolds-averaged Navier–Stokes (RANS)) equations near the wall, while the large-eddy simulations (LES) were used in the core of the flow. They noticed that the modifications due to roughness can produce certain non-equilibrium effects, and memory of the upstream conditions also seem to be an important factor in the computational modeling of this flow.

Peristaltic flow occurs in many biological processes, such as digestion, which is an important component of any in silico model of the stomach. Obtaining an analytical solution that can be used for model verification is highly desirable. Liu et al. [9] used a smooth particle hydrodynamics (SPH) code (from CSIRO) and developed a model for use in the stomach wherein wall motion, buoyancy, acid secretion, and food breakdown are included. They used two different numerical methods, namely, the Finite Volume Method (FVM) and the SPH, to study this problem. The simulations show that both methods provide very good agreement with the analytical model.

Studies on synthetic jet actuators (SJAs) have shown a potential to delay flow separation over surfaces, offering applications in aerodynamics, where flow control can be achieved via injection through the external excitation of an enclosed cavity volume. In general, SJAs are smaller than an aircraft's wingspan, and as a result, they are used in an array form. Arafa et al. [10] experimentally studied the effect of the excitation frequency of SJAs on the mean jet velocity issuing from an array of circular orifices. They focused on the acoustic excitation characteristics of the actuator's cavity. They noticed that a large-aspect-ratio-cavity volume with multiple peaks can correspond to the standing-wave-mode shapes of the cavity.

The rheological responses of complex materials such as suspensions, dispersion, slurries, etc., are generally different from those of Newtonian fluids; some of these fluids exhibit non-linear effects such as yield stress, and among the most-used models with yield stress are the Bingham, Herschel–Bulkley, and Casson models. Calus et al. [11] studied the two-dimensional linear stability of a regularized Casson fluid flowing down an incline. Their results, which were obtained using the long-wave approximation method, indicate that the critical Reynolds number at which instability arises depends on the material parameters, the angle of inclination, and the prescribed inlet discharge. They also show that the flow of a Casson-type material over an inclined plane becomes increasingly stable as yield stress increases. This behavior, interestingly, is the opposite of that for a Bingham fluid.

Double-diffusive convection in a porous medium is a challenging topic of study due to the non-linearity inherent in the problem, where, in addition, the Darcy law can cause large-scale damping. Liu and Knobloch [12] studied thermal convection with salinity as a passive scalar; they used direct numerical simulations (DNS), and through the single-mode solutions, they reproduced the root-mean-square and mean temperature profiles of time-dependent states at high Rayleigh numbers. Their results show the potential for this single-mode approach to be applied to other flow configurations where coherent structures are dominant due to the presence of large-scale damping.

With the further requirement and demand for the use of renewable energy to produce electricity, steam turbine power plants are being operated at a low load, where it is possible for the steam turbine rear stages to absorb power from the turbine shaft; this can lead to the so-called "ventilation phenomenon". Mambro et al. [13] correlated the state of the steam within the rotor channel to the measurements obtained downstream of the blades for different ventilation regimes. In their case, the ventilation power was related to the drag force that acts on the moving blades. Their results indicate that the drag coefficient is highly correlated with the Reynolds number based on the reverse blade height.

Computational studies related to membrane system design have shown the effectiveness of performance measures, where, for example, fouling and flow unsteadiness can be induced via different spacer configurations. Heinz et al. [14] numerically studied the local mass distributions in membrane systems and showed that the collective interaction of operation conditions (OCs) can provide further insight into understanding the related problems in the advection–diffusion equation. Using a Fourier series model (FSM), they obtained the exact solutions of an advection–diffusion equation for a wide range of OCs.

Amongst the promising approaches to turbulence modeling, one can mention the two-equation turbulence models in the framework of Reynolds-averaged Navier–Stokes (RANS) equations. As pointed out by Heinz [15], the existing hybrid RANS-LES methods suffer from some inherent problems, which can be alleviated by using a generalization of the continuous eddy simulation (CES) methods. It is also shown that the minimal error methods associated with flows of incompressible fluids can be extended to stratified and compressible flows; this can provide valuable input for the design of consistent turbulence models for cases with significant modeling uncertainties.

The measurement of mass transfer intensity in bubbly flows is an important challenge in innovative bioreactor design. To acquire a better understanding of these multiphase flows, Computational Fluid Dynamics (CFD) approaches can be used to describe flows in the bioreactor loop. Starodumov et al. [16] presented the results they obtained when using a developed thermometry method to evaluate the key performance in a bioreactor, for example, the volumetric mass transfer coefficient, which is an important parameter in the design, operation, scaling-up, and optimization of bioreactors. They designed a mass-transfer apparatus for growing different microorganisms to study a jet bioreactor with the recirculation of liquid and gas phases of a given rheology system.

Bubble dynamics, including bubble formation and dissolution, significantly impact industrial applications, ranging from the production of beverages to foam-manufacturing processes; the rate of bubble expansion or contraction is one of the most important parameters affecting these processes. Maloth et al. [17] studied the motion and expansion of an isolated bubble due to mass transfer in a pool of a supersaturated gas–liquid solution. They numerically solved the advection–diffusion equation and examined the effects of gas–liquid solution parameters, such as the inertia, viscosity, surface tension, diffusion coefficient, system pressure, and solubility of the gas, on the solution. They noticed that surface tension and inertia do not significantly influence bubble expansion, whereas viscosity, pressure, diffusion, and solubility have a noticeable impact on bubble growth.

Recent experimental results indicate that rising gas columns can produce interesting oscillations. Gergely and Néda [18] numerically studied the convective flows of heated fluid columns in a gravitational field using a simplified 2D geometry. They used the FEniCS package to solve the coupled Navier–Stokes and heat equations. In their study,

they examined a hydrodynamics computer simulation where, for simplicity, heated fluid columns are used instead of ascending Helium columns; this way, they were able to reproduce the experimentally observed data.

The flow of a bubble through a confining pore can be affected by the surface roughness and the geometry of the pore. Studies have shown that pore-scale interactions, in addition to the entrance critical pressure and a strong interaction of an isolated dispersed phase and pore geometry, can lead to additional pressure at the exit of the pore geometry. Ansari and Nobes [19] investigate the motion of an isolated bubble through different pore geometries; their simulations indicate that pore shape and surface roughness have a significant effect on the passage of the isolated phase. They were also able to detect the phase-pinning pressure, which can cause a delayed response in multiphase flows in the pore structures.

Dilute flows of gas–solid particles occur in various aspects of industry, such as pneumatic transport, fluidized beds, vertical risers, cyclones, flow-mixing devices, etc. To understand the interaction between a fluid and particles, it is important to know the forces acting on the particles. In the numerical simulation of such flows, the Lagrangian Particle-Tracking method is often used, where packets of individual particles are tracked, recognizing that the main forces acting on the particles are those of gravity and drag. Dodds et al. [20] performed a CFD analysis to study the effects of particles situated both perpendicular and parallel to the flow direction; their results show that the neighboring particles perpendicular to the flow seem to increase the drag force at close separation distances, whereas when entrained particles are co-aligned with the flow, the drag force seems to be reduced for close separation distances and increases as the distance increases.

The main role of the mitral valve (MV), which has an elliptical shape and is composed of an annulus and two leaflets, is to enable and regulate the appropriate flow of blood into the left ventricle (LV). Valve asymmetry presents a special challenge for modern cardiac surgery. Collia and Pedrizzetti [21] performed a systematic numerical study using a healthy ventricle and an ideal valve with varying degrees of valve asymmetry. As they indicate, their computational model should not be confused with an FSI model, since, in their approach, they do not include the elastic properties of the tissues. Their results can provide some important pre-surgical information as to which type of valve asymmetry can be used for correct valve repair/replacement.

Fluid/fluid interfaces and interfacial rheology are important areas of research for rheologists and modelers. These types of processes can occur in flows of foam and emulsion-based applications along with certain chemical processes such as liquid–liquid extraction, froth flotation, wastewater treatment, or tertiary oil recovery. Guzmán et al. [22] provide a review of this topic, focusing on the study of the fluid/fluid interfaces with dilatational stresses. The authors examine the available experimental and theoretical models for the dilatational rheology of fluid/fluid interfaces and discuss the effect of the non-linear character of dilatational deformation on the rheological response of these interfaces.

Finally, I would like to thank all the authors who contributed to this Special Issue. Without their contributions and without the help of qualified reviewers, it would not have been possible to organize this Special Issue. I am also grateful to all the anonymous reviewers for their help. I would like to extend a personal note of appreciation and gratitude to Ms. Wing Wang and the Editorial staff of the *Fluids* Office; without their help and assistance, *Fluids* could not publish high-quality papers in a short period of time.

Conflicts of Interest: The author declares no conflict of interest.

References

1. Procopio, G.; Giona, M. Modal Representation of Inertial Effects in Fluid–Particle Interactions and the Regularity of the Memory Kernels. *Fluids* **2023**, *8*, 84. [CrossRef]
2. Arabnejad, M.H.; Nilsson, H.; Bensow, R.E. Investigation of Flow-Induced Instabilities in a Francis Turbine Operating in Non-Cavitating and Cavitating Part-Load Conditions. *Fluids* **2023**, *8*, 61. [CrossRef]
3. Lenzi, E.K.; Somer, A.; Zola, R.S.; da Silva, L.R.; Lenzi, M.K. A Generalized Diffusion Equation: Solutions and Anomalous Diffusion. *Fluids* **2023**, *8*, 34. [CrossRef]

4. Alberti, L.; Carnevali, E.; Crivellini, A. Assessment of a RANS Transition Model with Flapping Foils at Moderate Reynolds Numbers. *Fluids* **2023**, *8*, 23. [CrossRef]
5. Msheik, M.; Rodat, S.; Abanades, S. CFD Simulation of a Hybrid Solar/Electric Reactor for Hydrogen and Carbon Production from Methane Cracking. *Fluids* **2023**, *8*, 18. [CrossRef]
6. Caltagirone, J.-P. The Role of Inertia in the Onset of Turbulence in a Vortex Filament. *Fluids* **2023**, *8*, 16. [CrossRef]
7. Waris, W.; Lappa, M. Patterning Behavior of Hybrid Buoyancy-Marangoni Convection in Inclined Layers Heated from Below. *Fluids* **2023**, *8*, 12. [CrossRef]
8. Salomone, T.; Piomelli, U.; De Stefano, G. Wall-Modeled and Hybrid Large-Eddy Simulations of the Flow over Roughness Strips. *Fluids* **2023**, *8*, 10. [CrossRef]
9. Liu, X.; Harrison, S.M.; Cleary, P.W.; Fletcher, D.F. Evaluation of SPH and FVM Models of Kinematically Prescribed Peristalsis-like Flow in a Tube. *Fluids* **2023**, *8*, 6. [CrossRef]
10. Arafa, N.; Sullivan, P.E.; Ekmekci, A. Jet Velocity and Acoustic Excitation Characteristics of a Synthetic Jet Actuator. *Fluids* **2022**, *7*, 387. [CrossRef]
11. Calusi, B.; Farina, A.; Fusi, L.; Palade, L.I. Stability of a Regularized Casson Flow down an Incline: Comparison with the Bingham Case. *Fluids* **2022**, *7*, 380. [CrossRef]
12. Liu, C.; Knobloch, E. Single-Mode Solutions for Convection and Double-Diffusive Convection in Porous Media. *Fluids* **2022**, *7*, 373. [CrossRef]
13. Mambro, A.; Congiu, F.; Galloni, E.; Lanni, D. Blade Drag Resistance in Windage Operating of Low Pressure Steam Turbines. *Fluids* **2022**, *7*, 372. [CrossRef]
14. Heinz, S.; Heinz, J.; Brant, J.A. Mass Transport in Membrane Systems: Flow Regime Identification by Fourier Analysis. *Fluids* **2022**, *7*, 369. [CrossRef]
15. Heinz, S. From Two-Equation Turbulence Models to Minimal Error Resolving Simulation Methods for Complex Turbulent Flows. *Fluids* **2022**, *7*, 368. [CrossRef]
16. Starodumov, I.; Nizovtseva, I.; Lezhnin, S.; Vikharev, S.; Svitich, V.; Mikushin, P.; Alexandrov, D.; Kuznetsov, N.; Chernushkin, D. Measurement of Mass Transfer Intensity in Gas–Liquid Medium of Bioreactor Circuit Using the Thermometry Method. *Fluids* **2022**, *7*, 366. [CrossRef]
17. Maloth, R.K.N.; Khayat, R.E.; DeGroot, C.T. Bubble Growth in Supersaturated Liquids. *Fluids* **2022**, *7*, 365. [CrossRef]
18. Gergely, A.; Néda, Z. Computational Fluid Dynamics Approach for Oscillating and Interacting Convective Flows. *Fluids* **2022**, *7*, 339. [CrossRef]
19. Ansari, S.; Nobes, D.S. Effect of the Pore Geometry on the Driving Pressure across a Bubble Penetrating a Single Pore. *Fluids* **2022**, *7*, 333. [CrossRef]
20. Dodds, D.; Sarhan, A.A.R.; Naser, J. CFD Investigation into the Effects of Surrounding Particle Location on the Drag Coefficient. *Fluids* **2022**, *7*, 331. [CrossRef]
21. Collia, D.; Pedrizzetti, G. The Influence of Mitral Valve Asymmetry for an Improved Choice of Valve Repair or Replacement. *Fluids* **2022**, *7*, 293. [CrossRef]
22. Guzmán, E.; Maestro, A.; Carbone, C.; Ortega, F.; Rubio, R.G. Dilational Rheology of Fluid/Fluid Interfaces: Foundations and Tools. *Fluids* **2022**, *7*, 335. [CrossRef]

fluids

MDPI

Article

Modal Representation of Inertial Effects in Fluid–Particle Interactions and the Regularity of the Memory Kernels

Giuseppe Procopio and Massimiliano Giona *

DICMA, Sapienza Università di Roma, via Eudossiana 18, 00184 Rome, Italy
* Correspondence: massimiliano.giona@uniroma1.it

Abstract: This article develops a modal expansion (in terms of functions exponentially decaying with time) of the force acting on a micrometric particle and stemming from fluid inertial effects (usually referred to as the Basset force) deriving from the application of the time-dependent Stokes equation to model fluid–particle interactions. One of the main results is that viscoelastic effects induce the regularization of the inertial memory kernels at $t = 0$, eliminating the $1/\sqrt{t}$-singularity characterizing Newtonian fluids. The physical origin of this regularization stems from the finite propagation velocity of the internal shear stresses characterizing viscoelastic constitutive equations. The analytical expression for the fluid inertial kernel is derived for a Maxwell fluid, and a general method is proposed to obtain accurate approximations of it for generic complex viscoelastic fluids, characterized by a spectrum of relaxation times.

Keywords: microparticle dynamics; complex viscoelastic fluids; fluid inertial effects; time-dependent Stokes equations; modal expansion

Citation: Procopio, G.; Giona, M. Modal Representation of Inertial Effects in Fluid–Particle Interactions and the Regularity of the Memory Kernels. *Fluids* **2023**, *8*, 84. https://doi.org/10.3390/fluids8030084

Academic Editor: Mehrdad Massoudi

Received: 31 December 2022
Revised: 10 February 2023
Accepted: 17 February 2023
Published: 28 February 2023

1. Introduction

Microfluidics and the study of fluid–particle interactions at a microscale represent not only a vast area of practical engineering applications [1,2] as they provide the opportunity of addressing fundamental physical questions in fluid dynamics [3–5], such as the relevance of acoustic propagation in liquid hydrodynamics [6–8], the nature of the boundary conditions and the occurrence of slip effects [9–11], as well as the role of the finite propagation velocity in the evolution of internal stresses [8,12].

A significant role in this research is played by the study, both theoretical and experimental, of Brownian motion, i.e., of the motion of micrometric particles in a quiescent fluid. This is due to the fact that Brownian motion is a central problem in statistical physics, from the early age of Einstein, Langevin, Smoluchowski, Perrin, [13–16] up to now [17,18], providing a direct way of quantifying the influence of thermal fluctuations and of studying the interactions between a fluid and a particle, thus permitting the investigation of the role and the relative relevance of different hydrodynamic effects. In this sense, Brownian motion represents an invaluable probe to verify experimentally fundamental fluid dynamic properties at short time and length scales [11,19].

The last two decades have seen an increasing attention on the experimental analysis of Brownian motion at short time scales in different fluids (gases and liquids) [20–24], with different rheological properties (Newtonian, viscoelastic) [25]. The experimental results have confirmed many predictions of the hydrodynamic theory of Brownian motion [26–28], and in some cases have raised fundamental questions involving basic principles of statistical mechanics [29].

The analysis of the velocity autocorrelation function of a micrometric particle in a liquid phase has shown the importance of fluid inertial contributions, expressed by the occurrence of the Basset force and of the added-mass term [30] in the expression of the force exerted by a fluid on a rigid object [22,23]. These terms arise in the low-Reynolds number

hydrodynamics, using the time-dependent Stokes equations, and provide a power-law decay of the particle velocity autocorrelation function [25], to be compared with the exponential decay occurring if solely the Stokesian drag is considered [31,32]. Indeed, the use of the time-dependent Stokes equation, instead of the instantaneous Stokes formulation, is well justified and appropriate when addressing micrometric particle motion in liquids at short time scale, due to the high frequencies characterizing thermal fluctuations. Consequently, while the Reynolds number is extremely small in these systems, the product of the Reynolds number times the Strouhal numbers is order of unity, justifying the inclusion of the inertial contribution expressed as the time derivative of the velocity in the hydrodynamic equations. In the case of viscoelastic fluids, characterized by time-dependent constitutive equations, this statement is a fortiori valid.

The rheological modeling of complex viscoelastic fluids is well consolidated as regards the quantitative description of viscoelastic properties [33]. As regards the dynamics of a microparticle, this corresponds to the formulation of a generalized Langevin equation with a dissipative memory kernel [34–36]. This class of equations has been introduced by Zwanzig in connection with the interaction of a physical system with a heat bath, and the fluctuation–dissipation theorem for this class of systems has been obtained by Kubo [37]. On the other hand, the hydrodynamic analysis of Brownian motion and the numerical simulation experiments by Alder and Wainwright [38] have clearly indicated that fluid inertial contributions are of paramount importance in order to correctly predict particle dynamics.

The current approach to particle motion in complex fluids is essentially based on the direct hydrodynamic simulation of particle motion [39,40]. What is missing is a physically consistent and computationally tractable formulation of particle dynamics in viscoelastic fluids, analogous to the corresponding equation of motion (which includes Stokes friction, the Basset force and the added mass effect) that apply for Newtonian ones. These equations can be derived into two steps: (i) via the detailed characterization of the fluid inertial contribution to particle motion in a complex fluid, expressing it in a computationally effective representation, and (ii) by generalizing the Kubo fluctuation–dissipation theory in order to include fluid-inertial contributions. In this article, we focus essentially on the first issue, leaving the second one to a forthcoming work.

Albeit the present analysis is focused on the hydrodynamic theory of particle motion, its application to microfluidic engineering for particle separation and nanoparticle production and optimization is significant. Indeed, the obtained result could be directly applied to the design of microfluidic systems enforcing the rheological properties of complex fluids in the limit of Stokesian hydrodynamics. In point of fact, the importance of inertial effects and rheological properties in separation devices is well known, e.g., in connection with the Segré-Silberberg effect [40,41], although this effect involves flows at non-vanishing Reynolds numbers [4,42].

The aim of this article is two-fold. A first goal involves the development of the modal representation of the fluid inertial contributions in the expression of the particle equation of motion in a fluid phase. This naturally leads to a simple field-theoretical representation of these effects. The second goal involves the mathematical structure of the inertial memory kernels entering the convolutional representation of the Basset forces, and their basic qualitative properties derived from fundamental physical principles. Specifically, it is shown that for any viscoelastic fluid (and all the liquids fall in this category, even if their characteristic relaxation times could be extremely small), the inertial memory kernel accounting for the generalized Basset contribution is bounded and non-singular near time $t = 0$.

The article is organized as follows. Section 2 introduces the hydrodynamic problem, the representation of fluid inertial effects and their implications in microparticle dynamics. Section 3 analyzes the modal representation of the Basset force, and its compact description in terms of a simple field equation. Moreover, it is shown in Section 3.2 that the modal representation also provides an efficient computational tool to study inertial particle motion.

This is an important topic that recently emerged in the fluid-dynamic literature [43–45] in connection with the numerical solution of the Maxey–Riley equation [46] (see also [47] and references therein). Specifically, the modal expansion transforms the integro-differential equations of motion into a system of ordinary differential equations. Section 4 addresses the boundedness of the resulting memory kernels in the presence of viscoelastic constitutive equations, outlining the physical and computational relevance of this result. For a simple Maxwell fluid, the expression of this kernel is obtained in closed form, and a general method for approximating it for generic complex viscoelastic fluids is proposed. Finally, Section 4.3 describes the connection between the present theory and the generalization of the Kubo fluctuation–dissipation theory to include fluid inertial effects in the stochastic equations of motion for a microparticle in a heat bath at constant temperature.

2. Fluid–Particle Interactions and Inertial Effects

Consider the motion of a micrometric rigid spherical particle of radius R in a unbounded incompressible fluid. Assume that the fluid is Newtonian, and ρ and μ represent its density and viscosity, respectively. Without loss of generality, assume neutrally buoyant particles (i.e., possessing the same density as the liquid), as the inclusion of Archimedean forces is immaterial in the present analysis. Let B_R be the domain representing the space occupied by the particle, ∂B_R its boundary and $\mathbf{V}_p(t)$ its translational velocity. Since we are considering the motion of a Brownian particle in a still liquid (the liquid is referred to be still if its velocity field originates exclusively from thermal motion of the immersed Brownian particle), the momentum balance equation for the particle reads

$$m\,\frac{d\mathbf{V}_p(t)}{dt} = \mathbf{F}_{f\to p}[\mathbf{V}_p(t)] + \mathbf{S}(t) \tag{1}$$

where $\mathbf{F}_{f\to p}[\mathbf{V}_p(t)]$ represents the force exerted by the fluid on the particle, and is a functional of the particle velocity, expressed by the surface integral over ∂B_R,

$$\mathbf{F}_{f\to p}[\mathbf{V}_p(t)] = -\int_{\partial B_R} (\boldsymbol{\tau} + p\,\mathbf{I})\cdot\mathbf{e}_r\,dS \tag{2}$$

where $\boldsymbol{\tau}$ is the shear stress tensor, p the pressure, $\mathbf{I}$ the identity matrix and $\mathbf{e}_r$ is the unit radial vector (we consider a reference system with the origin at the center of the spherical particle) and $\mathbf{S}(t)$ is a stochastic contribution describing the thermal force fluctuation.

Indicating with $\mathbf{v}(\mathbf{x},t)$ the fluid velocity field, in the low-Reynolds number regime it is the solution of the time-dependent Stokes equations

$$\rho\,\frac{\partial\mathbf{v}}{\partial t} = -\nabla\cdot\boldsymbol{\tau} - \nabla p\,, \quad \nabla\cdot\mathbf{v} = 0\,, \;\; \mathbf{x}\in\mathbb{R}^3/B_R \tag{3}$$

equipped with the boundary and initial conditions,

$$\mathbf{v}(\mathbf{x},t)|_{\mathbf{x}\in\partial B_R} = \mathbf{V}_p(t)\,, \qquad \mathbf{v}(\mathbf{x},t)|_{t=0} = 0 \tag{4}$$

Equation (4) corresponds to the no-slip assumption. For an incompressible Newtonian fluid,

$$\boldsymbol{\tau} = -\mu\left(\nabla\mathbf{v} + \nabla\mathbf{v}^T\right) \tag{5}$$

where the superscript "T" indicates transpose, so that Equation (3) is a linear partial differential equation for $\mathbf{v}(\mathbf{x},t)$ (the time-dependent Stokes equation)

$$\rho\,\frac{\partial\mathbf{v}}{\partial t} = \mu\,\nabla^2\mathbf{v} - \nabla p \tag{6}$$

where, from Equation (3), the velocity field $\mathbf{v}(\mathbf{x},t)$ is incompressible. Owing to the linearity of Equations (5) and (6), the functional $\mathbf{F}_{f\to p}[\mathbf{V}_p]$ is a linear and causal functional of the

particle velocity $\mathbf{V}_p(t)$. Causality means that $\mathbf{F}_{f\to p}[\mathbf{V}_p(t)]$ depends solely on the velocity history in the interval $[0, t)$.

Under these conditions, the force exerted by the fluid onto the rigid spherical particle can be expressed analytically. Let us indicate with $\widehat{\mathbf{F}}_{f\to p}(s)$ the Laplace transform of $\mathbf{F}_{f\to p}[\mathbf{V}_p]$ (henceforth, we will indicate with $\widehat{f}(s) = \int_0^\infty e^{-s\,t} f(t)\,dt$ the Laplace transform of any function $f(t)$ of time t, and with s the complex-valued Laplace variable), $\widehat{\mathbf{F}}_{f\to p}(s)$ attains the expression [48,49]

$$-\widehat{\mathbf{F}}_{f\to p}(s) = 6\,\pi\,\mu\,R\,\widehat{\mathbf{V}}_p(s) + 6\,\pi\sqrt{\frac{\rho\,\mu}{s}}\,R^2\Big(s\,\widehat{\mathbf{V}}_p(s)\Big) + \frac{2}{3}\,\rho\,\pi\,R^3\Big(s\,\widehat{\mathbf{V}}_p(s)\Big) \tag{7}$$

Transforming Equation (7) back into the time domain, one obtains

$$\begin{aligned}&\mathbf{F}_{f\to p}[\mathbf{V}_p(t)] = -6\,\pi\,\mu\,R\,\mathbf{V}_p(t)\\ &-6\sqrt{\pi\,\rho\,\mu}\,R_p^2\int_0^t \frac{1}{\sqrt{t-\tau}}\left(\frac{d\mathbf{V}_p(\tau)}{d\tau} + \mathbf{V}_p(0)\,\delta(\tau)\right)d\tau - \frac{2}{3}\,\rho\,\pi\,R^3\,\frac{d\mathbf{V}_p(t)}{dt}\end{aligned} \tag{8}$$

where $\mathbf{V}_p(0)$ is the initial condition for the particle velocity at $t = 0$. The first term at the r.h.s. of Equation (8) is the Stokesian friction, with the factor $\eta = 6\,\pi\,\mu\,R$, corresponding to the only dissipative term occurring also in the case of the instantaneous Stokes regime. The two other contributions at the r.h.s. stem from fluid inertial effects, and depend on the history of particle acceleration up to time t. The first of these terms is the convolutional integral of $d\mathbf{V}_p(t)/dt$ with the kernel $k(t)$ given by

$$k(t) = \frac{6\sqrt{\pi\,\rho\,\mu}\,R^2}{\sqrt{t}} \tag{9}$$

and it is usually referred to as the Basset force. Let us observe that kernel $k(t)$ is singular at $t = 0$. This property will be thoroughly analyzed in Section 4. The last term at the r.h.s. of Equation (8) is an instantaneous inertial contribution proportional to the actual value (i.e., at time t) of the acceleration $d\mathbf{V}_p(t)/dt$ of the particle, and it defines the hydrodynamic added mass $m_a = 2\rho\,\pi\,R^3/3$, equal to half of the mass of the fluid displaced by the particle [31]. Let us observe within the Basset term the occurrence of a contribution proportional to $\mathbf{V}_p(0)\delta(\tau)$, in the case $\mathbf{V}_p(0) \neq 0$. Equation (8) can be compactly written as

$$m_e\,\frac{d\mathbf{V}_p(t)}{dt} = -\eta\,\mathbf{V}_p(t) - k(t) * \left(\frac{dV_p(t)}{dt} + V_p(0)\,\delta(t)\right) + \mathbf{S}(t) \tag{10}$$

where $m_e = m + m_a$ is the extended mass and "$*$" indicates convolution. The physical importance of the Basset contribution can be appreciated by considering the velocity autocorrelation tensor of a Brownian particle, $\mathbf{C}_v(t) = \langle \mathbf{V}_p(t) \otimes \mathbf{V}_p(0)\rangle$, where "$\otimes$" indicates the dyadic tensor product and "$\langle\cdot\rangle$" the ensemble average over the probability measure of the thermal fluctuations. Since $\langle \mathbf{S}(t) \otimes \mathbf{V}_p(0)\rangle = 0$, as it is physically reasonable to assume that the thermal fluctuations $\mathbf{S}(t)$ at time $t \geq 0$, are independent of (uncorrelated to) the velocity fluctuations at any previous time instant $t = 0$ [32,37] (this principle is by some authors referred to as the principle of causality [50], and it essentially states the non-anticipativity of the action of thermal fluctuations as regards its effects on the particle velocity), by taking the tensorial product of both members of Equation (10) and averaging over the statistics of thermal fluctuations (the operations of time derivative and convolution commute with $\langle\cdot\rangle$), we obtain the evolution equation for $\mathbf{C}_v(t)$,

$$m^*\,\frac{d\mathbf{C}_v(t)}{dt} = -\eta\,\mathbf{C}_v(t) - k(t) * \left(\frac{d\mathbf{C}_v(t)}{dt} + \mathbf{C}_v(0)\right) \tag{11}$$

equipped with the isotropic initial condition

$$\mathbf{C}_v(0) = \langle V^2 \rangle \, \mathbf{I} \tag{12}$$

where $\langle V^2 \rangle$ is the squared variance of any entry $V_{p,h}(t)$, $h = 1, 2, 3$ of the particle velocity vector (proportional at thermal equilibrium to the temperature of the fluid). Therefore, due to this symmetry, the velocity autocorrelation function can be expressed as $\mathbf{C}_v(t) = \langle V^2 \rangle \, c_v(t) \, \mathbf{I}$, where the scalar function $c_v(t)$ satisfies Equation (11) with $c_v(0) = 1$. The occurrence of the Basset contribution determines a qualitative change in the long-term scaling of $c_v(t)$ with respect to the purely dissipative case (corresponding to considering the fluid motion in an instantaneous Stokes flow). In the latter case, the long-term decay is exponential, i.e., $c_v(t) = e^{-\eta \, t/m}$ while inertial effects induce an asymptotic power-law scaling $c_v(t) \sim t^{-\gamma}$, with $\gamma = 3/2$ in the free space [25,37].

The application of Equation (10) in the Lagrangian analysis of particle motion, in the case the kernel $k(t)$ attains the Basset form expressed by Equation (9), raises three main issues:

- A computational issue, as the presence of a convolution in the equations of motion implies that the entire history of $\mathbf{V}_p(t)$ over the time interval $[0, t)$ should be stored in order to evaluate it;
- An analytical issue, associated with the singularity of the Basset kernel $k(t)$ at $t = 0$;
- A physical issue, related to the determination of the stochastic force $\mathbf{S}(t)$, in the case that inertial effects are accounted for.

The first problem is analyzed in the next section, in terms of modal representations. The second one is treated on physical grounds in Section 4. The last point, related to the determination of $\mathbf{S}(t)$, is one of the main issues of fluctuation–dissipation theories [32,37]. To the best of our knowledge, a computationally valid approach to the determination of $\mathbf{S}(t)$ in the presence of the Basset term is lacking, although formal results have been proposed [51]. This point will be addressed in forthcoming works, as it pertains mostly to statistical physics than to strict hydrodynamic theory.

3. Modal Representation

The idea behind modal representations lies in the expression of the fluid inertial memory term entering the particle equation of motion as a linear superposition of elementary stochastic modes, susceptible of a simple evolution. We use the diction "stochastic" in this context, to pinpoint the fact that since $\mathbf{S}(t) \neq 0$, the velocity $\mathbf{V}_p(t)$ is itself a stochastic process, as well as any other process functionally dependent on $\mathbf{V}_p(t)$.

Let us consider Equation (10), and without loss of generality let us set $\mathbf{V}_p(0) = 0$. Since the problem of Brownian motion in the free space is isotropic, we can exclusively consider a scalar formulation of it, setting $V_p(t)$ instead of $\mathbf{V}_p(t)$. Let us assume in the remainder that the stochastic representation of $S(t)$ (replacing $\mathbf{S}(t)$ as a scalar formulation is considered) is known.

Consider a family of stochastic processes $y(t; \lambda)$ parameterized with respect to $\lambda \in [0, \infty)$ and fulfilling the equations

$$\frac{dy(t;\lambda)}{dt} = -\lambda \, y(t, \lambda) + q \, \frac{dV_p(t)}{dt} \tag{13}$$

where q is a constant to be determined. Let us suppose $y(t = 0; \lambda) = 0$ so that

$$y(t;\lambda) = q \int_0^t e^{-\lambda \, (t-\tau)} \, \frac{dV_p(\tau)}{d\tau} \, d\tau \tag{14}$$

The inertial memory kernel can be expressed as a linear superposition of these processes. To this end, let $p(\lambda)$ the probability density of occurrence of $y(t; \lambda)$, so that $p(\lambda) \, d\lambda$

represents the infinitesimal weight factor in the representation of the memory inertial contribution. Thus, the particle equation of motion can be expressed as

$$m^* \frac{dV_p(t)}{dt} = -\eta\, V_p(t) - \underbrace{q \int_0^\infty p(\lambda)\, y(t;\lambda)\, d\lambda}_{I} + S(t) \tag{15}$$

The integral I entering Equation (15) can be rewritten in convolutional form as

$$I = \int_0^t \left[q \int_0^\infty p(\lambda)\, e^{-\lambda(t-\tau)}\, d\lambda \right] \frac{dV_p(\tau)}{d\tau}\, d\tau = k_p(t) * \frac{dV_p(t)}{dt} \tag{16}$$

thus defining the kernel $k_p(t)$.

Let us assume for $p(\lambda)$ the following expression

$$p(\lambda) = \begin{cases} A\, \lambda^{-1/2} & \lambda < \lambda_c \\ 0 & \text{otherwise} \end{cases} \tag{17}$$

where $\lambda_c > 0$, and A is the normalization constant such that $\int_0^\infty p(\lambda)\, d\lambda = 1$. In this case, setting $z = \lambda_c\, t$,

$$k_p(t) = \frac{q\, A}{\sqrt{t}} \int_0^{\lambda_c\, t} \frac{e^{-z}}{\sqrt{z}}\, dz \tag{18}$$

Let us observe that $k_p(0) = q$, while for $t > 0$, and for large λ_c, $\lambda_c t$ can be approximated by an infinite value, and thus

$$k_p(t) = \frac{q\, A}{\sqrt{t}} \int_0^\infty \frac{e^{-z}}{\sqrt{z}}\, dz = \frac{q\, A\, \pi}{\sqrt{t}} \tag{19}$$

The constant q can be always defined in order to match the asymptotics of the Basset kernel Equation (9). Therefore, the modal expansion Equation (15) provides an inertial kernel that does not match the singular behavior of the Basset kernel near $t = 0$, but still represents an excellent approximation of it for t large enough. The regularity of the inertial kernel will be questioned in the next section starting from physical arguments.

If one is interested in obtaining exactly the modal expansion for the Basset kernel, a slightly different parameterization can be chosen by considering the modes $y(t;k)$, $k \in [0, \infty)$, still satisfying the linear relaxation dynamics Equation (13), with the relaxation rates $\lambda = \lambda(k)$ depending quadratically on the parameter k, i.e.,

$$\lambda(k) = \lambda_0\, k^2 \tag{20}$$

with $\lambda_0 > 0$, consequently,

$$y(t;k) = q \int_0^t e^{-k^2(t-\tau)}\, \frac{dV_p(\tau)}{d\tau}\, d\tau \tag{21}$$

Assuming that all the modes at different ks concur uniformly in the expansion of the inertial force, i.e., that the weight function does not have a probabilistic meaning, the integral I in the k-representation becomes

$$I = \int_0^\infty y(t;k)\, dk = k_k(t) * \frac{dV_p(t)}{dt}, \qquad k_k(t) = q \int_0^\infty e^{-\lambda_0\, k^2 t}\, dk \tag{22}$$

providing

$$k_k(t) = \frac{q}{2} \sqrt{\frac{\pi}{\lambda_0\, t}} \tag{23}$$

and thus the parameters q and λ_0 can be always determined in order to exactly match the Basset kernel Equation (9).

3.1. Diffusional Field Representation

The quadratic spectral representation based on the dispersion relation Equation (20) suggests the Basset inertial term could be viewed as the consequence of the interaction of diffusional models associated with a scalar field with the particle. It is therefore interesting to further develop this field approach.

Let $u(x,t)$ be a scalar field of fluctuations, evolving according to a pure diffusion equation over the real line, perturbed by an impulsive forcing term $F(x,t)$

$$\frac{\partial u(x,t)}{\partial t} = \alpha \, \frac{\partial^2 u(x,t)}{\partial x^2} + F(x,t) \tag{24}$$

with $\alpha > 0$ and

$$F(x,t) = \delta(x - x_c) \, f(t) \tag{25}$$

where $f(t)$ is a generic function of time. The forcing $F(x,t)$ represents the action of the particle onto the field (corresponding to the fluid continuum) while the scalar field $u(x,t)$ represents the fluid flow. Set $u(x, t=0) = 0$, the solution of Equations (24) and (25) can be expressed in terms of the diffusional Green function as

$$\begin{aligned} u(x,t) &= \int_0^t d\tau \int_{-\infty}^{\infty} \frac{1}{\sqrt{4\,\pi\,\alpha\,(t-\tau)}} e^{-(x-x')^2/4\,\alpha\,(t-\tau)} F(x',\tau)\, d\tau \\ &= \int_0^t \frac{1}{\sqrt{4\,\pi\,\alpha\,(t-\tau)}} e^{-(x-x_c)^2/4\,\alpha\,(t-\tau)} \, f(\tau)\, d\tau \end{aligned} \tag{26}$$

Let $u_c(t) = u(x = x_c, t)$. From Equation (26) it follows that

$$u_c(t) = \frac{1}{\sqrt{4\,\pi\,\alpha}} \int_0^t \frac{f(\tau)}{\sqrt{t-\tau}}\, d\tau \tag{27}$$

which admits the same functional form of the Basset memory integral. This formal result has also been obtained in [45] (see also [47]), with a different approach, and with a purely computational motivation. Below we are interested in going beyond the pure mathematical formalism, providing a physical interpretation of the field representation of the Basset force.

Let us consider a one-dimensional approximation of the momentum exchange between the fluid, with velocity $v(x,t)$, and the particle, with velocity $V_p(t)$. This can be modeled by considering a one-dimensional moment balance equations in the fluid of purely diffusional nature

$$\rho \, \frac{\partial v(x,t)}{\partial t} = \mu \, \frac{\partial^2 v(x,t)}{\partial x^2} + f(x,t) \tag{28}$$

where $f(x,t)$ is the force density exerted by the particle onto the fluid which can be written as an impulsive contribution centered at the particle center of mass x_c,

$$f(x,t) = \rho \, L_c \, \delta(x - x_c) \, \frac{dV_p(t)}{dt} \tag{29}$$

where, from dimensional analysis, the parameter L_c has the dimension of a length, and corresponds to length scale of inertial influence, in the fluid, due to the perturbation induced by the motion of the particle. From physical reasons, L_c is of the order of magnitude of the particle radius, and the choice

$$L_c = D = 2R \tag{30}$$

where D is the particle diameter, provides, as shown below, the correct value of L_c matching the Basset force. The inertial force exerted by the fluid onto the particle $F^{(i)}_{f\to p}$ can be viewed as a dissipative Stokesian contribution evaluated at the fluid velocity $v_c(t)$,

$$F^{(i)}_{f\to p} = -6\,\pi\,\mu\,R\,v_c(t) \tag{31}$$

Comparing Equations (24) and (25) with Equations (28)–(30), and making use of Equation (27), it follows that

$$v_c(t) = \sqrt{\frac{\rho}{4\,\pi\,\mu}}\,D\int_0^t \frac{1}{\sqrt{t-\tau}}\,\frac{dV_p(\tau)}{d\tau}\,d\tau \tag{32}$$

and from Equation (31) one finally obtains

$$F^{(i)}_{f\to p} = -6\,\pi\,\mu\sqrt{\frac{\rho}{4\,\pi}}\,D\,R\,\frac{1}{\sqrt{t}} * \frac{dV_p(t)}{dt} = -6\,\sqrt{\pi\,\rho\,\mu}\,R^2\,\frac{1}{\sqrt{t}} * \frac{dV_p(t)}{dt} \tag{33}$$

that is exactly the Basset force. This result is physically interesting and requires some interpretation. It indicates that the inertial Basset contribution can be viewed as the inertial dissipation of the fluid elements nearby the solid particle, due to the perturbation exerted by the particle onto the fluid itself. This physical interpretation bears some analogies with Darwin's description of fluid inertial effects [30]. The fact that a scalar model correctly describes the fluid inertial effects onto particle dynamics is a remarkable property, as the fluid hydrodynamics involves vectorial entities, the velocity field $\mathbf{v}(\mathbf{x},t)$, subjected to constraints, in the present case the solenoidal nature of $\mathbf{v}(\mathbf{x},t)$, stemming from the incompressibility of a liquid phase, corresponding to the case of principal theoretical and engineering interest. Whether this would be a purely mathematical result, or a deeper physical property is a matter that we leave open to future investigation. Interpreted on physical grounds, this result indicates that the fluid inertial contributions to the dynamics of immersed bodies are completely independent of the compressibility of the fluid. If this observation would be correct, it follows that in any isotropic problems, as the particle motion is in a unbounded fluid phase, a scalar field model would correctly describe the physics of a fluid–particle inertial interaction. This situation is altogether similar to the properties of the other inertial contribution, namely the added-mass term, which is independent of the constitutive equations in the fluid, and for this reason it can be estimated from the inviscid (Eulerian) approximation of the flow [31].

3.2. A Numerical Case Study

Let us consider the modal expansion in Equations (20)–(22) and its discretization with respect to k. Let $k_{\max}$ be the maximum value of k considered, and Δk the step size in the discretization. Assuming $q = 2/\sqrt{\pi}$, for the sake of normalization, the expression for $k_k(t)$ becomes

$$k_k(t) = \frac{2\,\Delta k}{\sqrt{\pi}}\sum_{i=1}^{N} e^{-(i\,\Delta k)^2\,t} \tag{34}$$

where $N = [k_{\max}/\Delta k]$ and $[x]$ represents the closest integer to the real-valued x. In the limit for $\Delta k \to 0$, and $k_{\max} \to \infty$, $k_k(t)$ defined by Equation (34) converges to $k_\infty(t) = 1/\sqrt{t}$. Figure 1a depicts the behavior of the discretized $k_k(t)$ at $k_{\max} = 10$ for decreasing values of Δk. As expected, as Δk decreases to zero, the deviations of $k_k(t)$ from $k_\infty(t)$ become negligible for $t > 1/k^2_{\max}$.

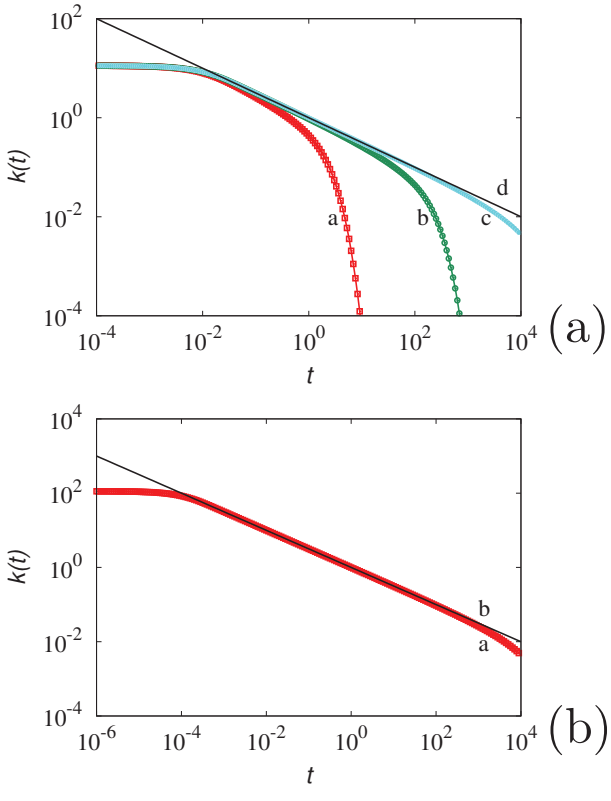

Figure 1. Behavior of the discretized $k_k(t)$ defined by Equation (34) for different discretizations. Panel (**a**) refers to $k_{\max} = 10$, lines and symbols (a) to (c) correspond to $\Delta k = 1$, 0.1, 0.01, respectively. Line (d) represents $k_\infty(t) = 1/\sqrt{t}$. Panel (**b**) $k_{\max} = 100$, $\Delta k = 0.01$ (line a), while line (b) depicts $k_\infty(t)$.

Similarly, the value of $k_{\max}$ controls the convergence to $k_\infty(t)$ at short time scales. Figure 1b depicts the behavior of $k_k(t)$ at $k_{\max} = 100$, $\Delta k = 0.01$. An accurate representation for $k_\infty(t)$ is achieved for $t > 10^{-4}$. The analysis of these data indicates that $k_{\max}$ controls the behavior of $k_k(t)$ near $t = 0$, which reaches a finite limiting value $k(0) \simeq k_{\text{kmax}}$. This property seems to be a basic limitation of any discretization of the Basset force. In point of fact, as shown in the next section, the occurrence of a bounded value of $k_k(0)$ is a physical constraint derived from the viscoelastic nature of a liquid phase. And all the fluid, including water at room temperature, possesses a characteristic non vanishing relaxation time.

Consider Equation (10) for a macroscopic particle (radius greater than a millimeter or higher), for which the stochastic fluctuations could be neglected. Substituting on it the modal expansion Equation (34), we have

$$\begin{aligned} m_e \frac{d\mathbf{V}_p(t)}{dt} &= -\eta\, \mathbf{V}_p(t) - \frac{2\,\beta\,\Delta k}{\sqrt{\pi}} \sum_{i=1}^{N} e^{-(i\,\Delta k)^2\, t} * \left(\frac{d\mathbf{V}_p(t)}{dt} + V_p(0)\,\delta(t) \right) \\ &= -\eta\, \mathbf{V}_p(t) - \frac{2\,\beta\,\Delta k}{\sqrt{\pi}} \sum_{i=1}^{N} \mathbf{z}_i(t) \end{aligned} \tag{35}$$

where $\beta = 6\sqrt{\pi\,\rho\,\mu}\,R^2$, as it stems from Equation (9), and $\mathbf{z}_i(t)$, $i = 1, \ldots, N$ is a system of N auxiliary degrees of freedom accounting for fluid inertial effects, the equations for which read

$$\begin{aligned} \frac{d\mathbf{z}_i(t)}{dt} &= -\mu_i\,\mathbf{z}_i(t) + \frac{d\mathbf{V}_p(t)}{dt} \\ &= -(\mu_i + \eta)\,\mathbf{z}_i(t) - \frac{2\,\beta\,\Delta k}{\sqrt{\pi}}\sum_{i=1}^{N}\mathbf{z}_i(t) \end{aligned} \tag{36}$$

where $\mu_i = (i\,\Delta k)^2$, and the impulsive initial contribution has been included into the initial condition for $\mathbf{z}_i(0) = \mathbf{V}_p(0)$.

Equation (35) represents a major advantage of the model expansion compared to the more recent computational approaches for addressing inertial particle motion [47], as it reduces the integro-differential particle equations of motion to a system of ordinary differential equations that can be solved using standard numerical routines. The analysis here presented for a quiescent fluid can be straightforwardly extended to the presence of a macroscopic (e.g., pressure-driven) velocity field in the fluid phase.

4. Regularity of Inertial Kernels

The second main issue addressed in this article concerns the regularity of the inertial memory kernels $k(t)$, once basic physical requirements (such as the bounded propagation of any physical phenomenon, limited by the speed of light vacuo, as a consequence of relativity theory) are taken into account. We have seen in Section 2 that the Basset kernel diverges at $t = 0$, as seen in Equation (9). As explained below, this is a consequence of the infinite propagation velocity of the internal stresses that characterize the Newtonian constitutive Equation (5). This phenomenon is altogether analogous to the divergence of interfacial fluxes in heat/mass transfer parabolic problems in the presence of a discontinuity between the initial and the boundary conditions at a boundary. This problem can be resolved by removing the paradox of infinite propagation velocity intrinsic to any Fickian/Fourier constitutive equation, simply considering the hyperbolic extension of the transport problem [52].

In the hydrodynamic case, the corresponding hyperbolic generalization merely consists in accounting for fluid viscoelasticity, which is a generic property of any liquid phases. In point of fact, even water at ambient conditions (temperature $T = 300$ K, pressure $p = 10^5$ Pa) behaves as a viscoelastic fluid, but its characteristic relaxation time, $\theta^c \simeq 1$ ps [53,54], is so small that it can be neglected in the overwhelming majority of hydrodynamic problems, since the observation time scales in most of the practical cases of interest are widely larger than θ^c.

To begin with, let us consider the case of a viscoelastic fluid characterized by a single relaxation time θ^c (Maxwell fluid). Neglecting the nonlinear terms in the objective definition of the viscoelastic constitutive equation involving the Oldroyd upper convective derivative [33] (which are small for the typical conditions of Brownian and micrometric particles in microchannels), Equation (5) is replaced by the following viscoelastic constitutive equation:

$$\theta^c\,\frac{\partial\boldsymbol{\tau}}{\partial t} + \boldsymbol{\tau} = -\mu\left(\nabla\mathbf{v} + \nabla\mathbf{v}^T\right) \tag{37}$$

that in the Laplace domain takes the following simple expression:

$$\widehat{\boldsymbol{\tau}}(\mathbf{x}, s) = -\widehat{\mu}_e(s)\left[\nabla\widehat{\mathbf{v}}(\mathbf{x}, s) + \nabla\widehat{\mathbf{v}}(\mathbf{x}, s)^T\right] \tag{38}$$

where

$$\widehat{\mu}_e(s) = \frac{\mu}{\theta^c\,(s + 1/\theta^c)} \tag{39}$$

Consequently, the Laplace transform of $\widehat{\mathbf{F}}_{f\to p}(s)$ of the force subjected by the particle is still given by Equation (7), with the constant viscosity μ replaced by the function $\widehat{\mu}_e(s)$. As well known, this modifies the instantaneous dissipative Stokesian friction $\mathbf{F}^{(d)}_{f\to p}[\mathbf{V}_p(t)] = -\eta\,\mathbf{V}_p(t)$ into a memory term

$$\mathbf{F}^{(d)}_{f\to p}[\mathbf{V}_p(t)] = -\eta\,\frac{1}{\theta^c}\int_0^t e^{-(t-\tau)/\theta^c}\,\mathbf{V}_p(\tau)\,d\tau \tag{40}$$

while the inertial Basset term attains in the Laplace domain the form $-\widehat{k}(s)\,s\widehat{\mathbf{V}}_p(s)$ with

$$\widehat{k}(s) = \frac{\beta}{\sqrt{\theta^c}}\,\frac{1}{\sqrt{s\,(s+1/\theta^c)}} \tag{41}$$

where $\beta = 6\,\pi\sqrt{\rho\,\mu}\,R^2$. It is easy to see that the presence of a non-vanishing relaxation time $\theta^c > 0$ determines a finite value of $k(t)$ for $t = 0$. Enforcing the initial value theorem of Laplace transforms, we have from Equation (41)

$$\lim_{t\to 0} k(t) = \lim_{s\to\infty} s\,\widehat{k}(s) = \frac{\beta}{\sqrt{\theta^c}} \tag{42}$$

In point of fact, the inverse Laplace transform of $\widehat{k}(s)$ is given by

$$k(t) = \frac{\beta}{\sqrt{\theta^c}}\,e^{-t/2\theta^c}\,I_0\left(\frac{t}{2\,\theta^c}\right) \tag{43}$$

where $I_0(\xi)$ is the modified Bessel function of the first kind, which possesses the following asymptotic behaviors:

$$I_0(0) = 1\,, \qquad I_0(\xi) = \frac{e^{\xi}}{\sqrt{2\,\pi\,\xi}}\left[1 + O\left(\frac{1}{\xi}\right)\right] \tag{44}$$

From Equation (44), the asymptotics of the Newtonian Basset kernel is recovered for $t \gg \theta^c$. This phenomenon is depicted in Figure 2 for several values of θ^c. The viscoelastic kernel practically coincides with the Basset counterpart of a Newtonian fluid for $t > 5\,\theta_c$.

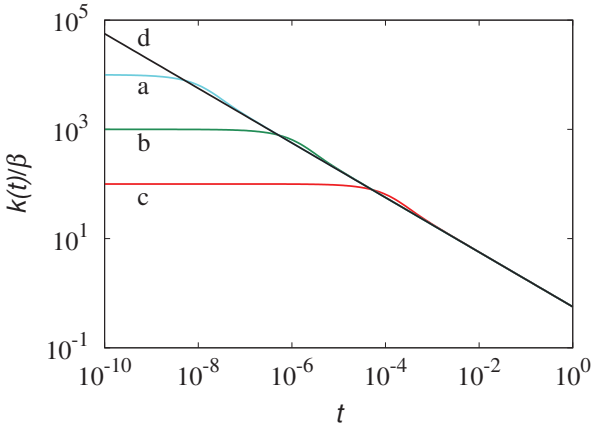

Figure 2. Rescaled inertial kernel $k(t)/\beta$, Equation (41) vs t for a simple Maxwell fluid, characterized by the relaxation time θ^c. Lines (a) to (c) refer to $\theta^c = 10^{-4}$, 10^{-6}, 10^{-8}, respectively. Line (d) depicts the asymptotic nondimensional Basset curve, $k(t)/\beta = 1/\sqrt{\pi\,t}$.

The occurrence of a finite value for $k(0)$ has been observed in Newtonian fluids once slip boundary conditions are enforced at the surface of the solid particle [55–57]. The physical reason for this occurrence, and the eventual analogy with the viscoelastic case, is still an open question.

4.1. Field-Theoretical Analysis

The result expressed by Equation (43) can be recovered from the field approach addressed in the previous section. The presence of viscoelastic effects characterized by a single relaxation time θ^c implies to substitute the parabolic diffusion model Equation (28) with the hyperbolic Cattaneo equation

$$\rho\,\theta^c \frac{\partial^2 v(x,t)}{\partial t^2} + \rho\,\frac{\partial v(x,t)}{\partial t} = \mu\,\frac{\partial^2 v(x,t)}{\partial x^2} + f(x,t) \tag{45}$$

while $f(x,t)$ is identical to Equation (29). The solution of this impulsive model, with $v(x,0) = \partial v(x,t)/\partial t|_{t=0} = 0$, takes the following form (see [58], p. 320):

$$v(x,t) = \frac{1}{2}\sqrt{\frac{\rho\,\theta^c}{\mu}}\,\frac{D}{\theta_c}\int_0^t e^{-(t-\tau)/2\,\theta^c}\,I_0\left(\frac{1}{2\,\theta^c}\sqrt{(t-\tau)^2-(x-x_c)^2\,\rho\,\theta^c/\mu}\right)\frac{dV_p(\tau)}{d\tau}\,d\tau \tag{46}$$

that for $x = x_c$, and $t \geq \tau$ reduces to

$$v_c(t) = \frac{1}{2}\sqrt{\frac{\rho}{\mu\,\theta^c}}\,D\int_0^t e^{-(t-\tau)/2\,\theta^c}\,I_0\left(\frac{t-\tau}{2\,\theta^c}\right)\frac{dV_p(\tau)}{d\tau}\,d\tau \tag{47}$$

providing the same expression for $k(t)$ derived above, as seen in Equation (43).

4.2. Extension to Complex Fluids

The analysis developed above for a viscoelastic fluid possessing a single relaxation time can be generalized to more complex and real fluids. The problem can be stated as follows. Consider a real fluid and suppose to have obtained from rheological experiments the functional form of the dissipation memory kernel $G(t)$ entering the expression of the dissipative contribution to the force exerted by the fluid on a spherical particle

$$\mathbf{F}^{(d)}_{f\to p}[\mathbf{V}_p(t)] = -6\,\pi\,R\int_0^t G(t-\tau)\,\mathbf{V}_p(\tau)\,d\tau \tag{48}$$

Does this information provide a way to quantify the inertial contribution, and specifically the expression for the generalized Basset force in this fluid?

This problem can be tackled as follows. The convolutional nature of Equation (48) suggests that the constitutive equation for the shear stresses is of the form

$$L_t[\boldsymbol{\tau}] = -\mu\left(\nabla\mathbf{v} + \nabla\mathbf{v}^T\right) \tag{49}$$

where L_t is a linear operator acting on the stress tensor $\boldsymbol{\tau}$, and containing its derivatives of any order n, $n = 0, 1, \ldots$, with respect to time, and eventually also its fractional time derivatives (Riemann–Liouville operators) [59]. In the Laplace domain, Equation (49) becomes

$$\widehat{\ell}(s)\,\widehat{\boldsymbol{\tau}}(\mathbf{x},s) = -\mu\left[\nabla\widehat{\mathbf{v}}(\mathbf{x},s) + \nabla\widehat{\mathbf{v}}(\mathbf{x},s)^T\right] \tag{50}$$

where $\widehat{\ell}(s)$ is a function of the Laplace variable s. Equation (50) coincides with Equation (38), and $\widehat{\mu}_e(s)$, coinciding with $\widehat{G}(s)$, is now expressed by

$$\widehat{\mu}_e(s) = \frac{\mu}{\widehat{\ell}(s)} = \widehat{G}(s) \tag{51}$$

The analysis developed above for a Maxwell fluid can be applied to this more general problem, providing for the Laplace transform of the inertial memory kernel the following expression:

$$\widehat{k}(s) = 6\,\sqrt{\rho}\,R^2\,\sqrt{\frac{\widehat{G}(s)}{s}} \tag{52}$$

The inverse Laplace transform $k(t)$ of $\widehat{k}(s)$ defined by Equation (52) cannot be obtained analytically for generic $\widehat{G}(s)$. Nevertheless, it is always possible to derive accurate representations for $k(t)$ enforcing Equation (52).

In order to make a practical example, consider the rheological data for polydimethilsiloxane at $T = 25\ ^\circ\mathrm{C}$ reported in [33], for which an accurate representation involves the occurrence of $N = 5$ relaxation rates λ_h, $h = 1, \ldots, N$,

$$G(t) = \sum_{h=1}^{N} a_h\, e^{-\lambda_h\, t} \tag{53}$$

where $\lambda_h = 1/\theta_h^c$, $h = 1, \ldots, N$ are the relaxation rates i.e., the reciprocal of the relaxation times θ_h^c. The values for λ_h and for the expansion coefficients a_h can be found in [33] (p. 114), and the graph of the resulting $G(t)$ is depicted in Figure 3a. Applying Equation (52) to this case we obtain

$$\widehat{k}(s) = \alpha\,\sqrt{\frac{1}{s}\sum_{h=1}^{N}\frac{a_h}{s+\lambda_h}}\,, \qquad \alpha = 6\,\pi\,\sqrt{\rho}\,R^2 \tag{54}$$

The graph of $k^*(s) = \widehat{k}(s)/\alpha$ is depicted in Figure 3b (symbols). The data can be accurately approximated over the time scales of interest by a linear combination of the inertial contributions obtained for the simple Maxwell fluid Equation (41), each of which is characterized by a different relaxation time

$$k^*(s) = \sum_{h=1}^{N_i}\frac{c_h}{\sqrt{s\,(s+b_h)}} \tag{55}$$

Making use of Equation (43), the memory inertial kernel $k(t)$ is given in this case by the expression

$$k(t) = \alpha\sum_{h=1}^{N_i} c_h\, e^{-b_h\, t/2}\, I_0\left(\frac{b_h\, t}{2}\right) \tag{56}$$

For the use made above of the solutions obtained for the simple Maxwell fluid, each term of the form (41) in the Laplace domain, and (43) in the time domain, can be referred to as a "prototypical visco-inertial mode". In the present case, it is sufficient to consider the combination of $N_i = 2$ prototypical visco-inertial modes, and the resulting approximation is depicted in Figure 3b. The values of the parameters are $c_1 = 125$ a.u., $b_1 = 1.52\ \mathrm{s}^{-1}$, $c_2 = 420$ a.u., $b_2 = 65\ \mathrm{s}^{-1}$. The corresponding inertial memory kernel $k(t)$, i.e., the graph of Equation (56), is depicted in Figure 4.

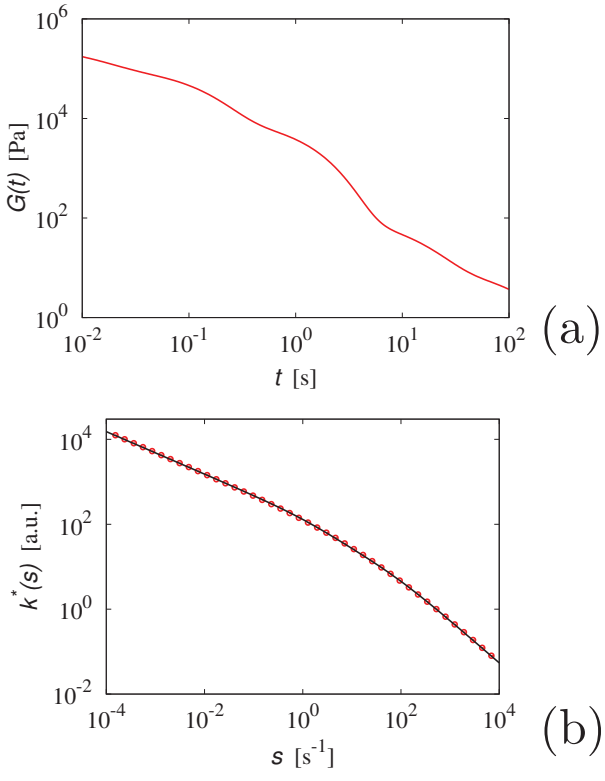

Figure 3. Panel (**a**) $G(t)$ vs t for polydimethilsiloxane at $T = 25\,^{\circ}$C. Panel (**b**) (symbols) $k^*(s) = \widehat{k}(s)/\alpha$ vs s for the same fluid, obtained from Equation (54). The solid line is the approximation of these data using $N_i = 2$, prototypical visco-inertial modes, as discussed in the main text.

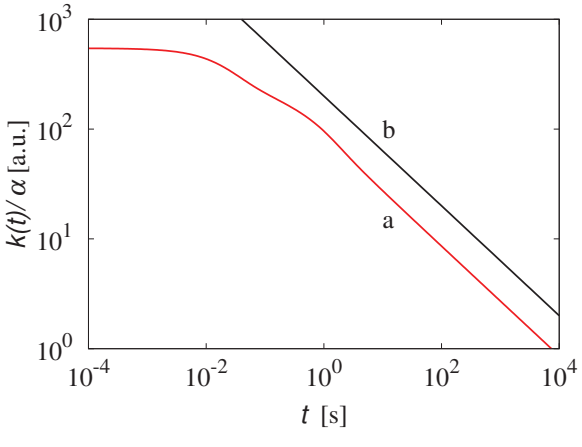

Figure 4. $k(t)/\alpha$ (line a) obtained from Equation (56) with $N_i = 2$ modes. Line (b) corresponds to the long-term scaling $k(t)/\alpha \sim 1/\sqrt{t}$.

From this practical example, we can draw the following conclusions:

1. Enforcing the constitutive model Equation (49), corresponding to the rheological description of a complex viscoelastic fluid, it is possible to derive the functional form of the fluid inertial kernel $k(t)$ from rheological data, i.e., from the functional form of $G(t)$;
2. The fluid inertial kernel $k(t)$ can be expressed as linear combination of a few prototypical visco-inertial modes;
3. The number N_i of modes required to provide an accurate representation of $k(t)$ does not necessarily coincide with the number N of dissipative (exponential) modes adopted for reconstructing $G(t)$.

Of course, it is possible to provide alternative representations of $k(t)$, e.g., adopting the modal decomposition discussed in Section 3. While for an accurate representation of the classical Basset kernel, a uncountable system of exponentially decaying modes is required, the physical constraint of bounded $k(t)$ permits to achieve accurate approximation for $k(t)$ using a finite (and relatively small) number of exponentially decaying modes.

4.3. Toward a Comprehensive Theory of Brownian Motion

To conclude, we can frame another central issue that takes advantage of the present theory. For a microparticle in a quiescent fluid (Brownian particle), the equations of motions in a real complex fluid, accounting for viscoelastic dissipation, fluid inertial effects and thermal fluctuations can be expressed in the form

$$m_e \frac{d\mathbf{V}_p(t)}{dt} = -h(t) * \mathbf{V}_p(t) - k(t) * \left(\frac{d\mathbf{V}_p(t)}{dt} + \mathbf{V}_p(0)\,\delta(t) \right) + \mathbf{S}(t) \tag{57}$$

where $h(t)$ is the viscoelastic kernel proportional to $G(t)$ defined by the linear functional form Equation (53), and $k(t)$ is the corresponding fluid inertial kernel, the properties of which have been addressed in the previous section. From rheological data, the viscoelastic kernel can be expressed as a linear combination of N modes, where usually $N < 10$ for most of the fluids [33], i.e., $h(t) = \sum_{j=1}^{N} h_j\, e^{-\lambda_j t}$. In a similar way, the fluid inertial kernel $k(t)$ analyzed in the previous section can also be accurately approximated by means of a system of exponentially decaying modes,

$$k(t) \simeq \sum_{i=1}^{N_i} k_i\, e^{-\mu_i t} \tag{58}$$

where the rates $\mu_i > 0$, $i = 1, \ldots, N_i$, are in general not related to the relaxation rates λ_j, $j = 1, \ldots, N$ and $N_i \gg N$. The property that $k(0)$ is bounded ensures, as discussed in the previous section, that the approximation Equation (58) can be arbitrarily accurate in the metrics of continuous functions. This means that for any $\varepsilon > 0$, there exist a finite N_i, and finite rates $\mu_i > 0$, $i = 1, \ldots, N_i$, such that $\left| k(t) - \sum_{i=1}^{N_i} k_i\, e^{-\mu_i t} \right| < \varepsilon$ for any $t \geq 0$. Consequently, Equations (57) reduce to the form

$$m_e \frac{d\mathbf{V}_p(t)}{dt} = -\sum_{j=1}^{N} h_j\, e^{-\lambda_j t} * \mathbf{V}_p(t) - \sum_{i=1}^{N_i} k_i\, e^{-\mu_i t} * \left(\frac{d\mathbf{V}_p(t)}{dt} + \mathbf{V}_p(0)\,\delta(t) \right) + \mathbf{S}(t) \tag{59}$$

In order to solve these stochastic differential equations, the expression for $\mathbf{S}(t)$ should be determined, and it would constitute the generalization of the celebrated Kubo fluctuation–dissipation theorem of the second kind [32,37], of which the original formulation is restricted to the pure dissipative case (i.e., to $k(t) = 0$). The analysis of this problem is beyond the scope of this article and it will be addressed in a forthcoming work [60]. It can however be anticipated that the occurrence of a finite value of $k(0)$, coupled with

the modal expansion of the memory kernels ($h(t)$ and $k(t)$) provide the key physical and formal ingredients toward an elegant solution of this problem.

5. Concluding Remarks

This article has presented a comprehensive description of the mathematical properties of the fluid inertial kernel entering the particle equation of motion in a complex viscoelastic fluid. Two main conclusions can be drawn from the present analysis and results. The modal expansion addressed in Section 3 naturally leads to a simplified field-theoretical representation of the fluid inertial effects. The latter has been successfully applied to non-trivial cases, such as a Maxwell fluid, in order to relate the disappearance of the $k(t)$-singularity at $t = 0$ with the physics of stress propagation. It is noteworthy that a simple one-dimensional field-theoretical description could capture the inertial fluid–particle interactions in isotropic conditions (free space). This point deserves further investigation.

The boundedness of $k(0)$ is indeed a consequence of the finite propagation velocity of the internal shear stresses, and this is in agreement with fundamental physical principles (special relativity theory). The importance of this result is that the regularity of the fluid inertial kernel has been derived from physical principles, and not as the result of ad hoc mathematical regularization/mollification techniques. In rheological modeling, this simply corresponds to the occurrence of a viscoelastic constitutive model with non-vanishing relaxation times. For the sake of clarity, the inclusion of viscoelasticity does not ensure either that the corresponding hydrodynamic model is Lorentz covariant [61] nor that all the hydrodynamic perturbations (for instance, density and pressure waves) would propagate at finite speed. In order to match the latter condition, the occurrence of acoustic modes should be included in the description of hydromechanical phenomena as discussed in [8].

The case of a Maxwell fluid, characterized by a single relaxation time, not only provides an analytic expression for the fluid inertial kernel $k(t)$, but it represents the prototypical model for expressing the fluid inertial effects of more complex fluids. The representation of $\widehat{k}(s)$ starting from rheological data on the dissipation kernel $G(t)$ is a simple but relevant result, which applies to any complex fluids.

We have considered in this article spherical micrometric particles, but the obtained results are independent of the geometry of the particles and of the flow domain. Consequently, these results can be extended to particles of arbitrary shape, and to confined geometries of flow devices, provided that the parameters controlling the expression for the force acting on the particle (attaining a tensorial character [5,49]) are known in the case of a Newtonian fluid.

The results obtained in this article are also propedeutical for addressing and solving the other crucial problem associated with micrometric particle motion mentioned in Sections 2 and 4.3, namely the determination of an analytical representation for the stochastic force $\mathbf{S}(t)$ at thermal equilibrium in the presence of fluid inertial effects. This represents, in the terminology introduced by Kubo [32,37], the fluctuation–dissipation relation of the second kind (see [32], p. 37 and the discussion therein), in the presence of fluid inertial effects. This topic is outside the scope of the present article and it will be addressed elsewhere [60]. Nevertheless, it is important to mention that the key ingredient for an elegant solution of this problem is represented by the boundedness of the fluid inertial kernel $k(t)$, proved in the present work for viscoelastic fluids. This could lead to an entropic characterization of the dissipation effects deriving from rheological/inertial properties of complex fluids into which a diffusing Brownian particle is immersed and moves under constant temperature conditions.

Author Contributions: The two authors have contributed to the ideation, formulation, simulation and writing on equal footing. All authors have read and agreed to the published version of the manuscript.

Funding: This research received financial support from ICSC—Centro Nazionale di Ricerca in High Performance Computing, Big Data and Quantum Computing, funded by European Union—NextGenerationEU.

Data Availability Statement: The data are available upon request to the corresponding author.

Conflicts of Interest: The authors declare no conflict of interest.

References

1. Sackmann, E.K.; Fulton, A.L.; Beebe, D.J. The present and future role of microfluidics in biomedical research. *Nature* **2014**, *507*, 181–189. [CrossRef] [PubMed]
2. Guazzelli, E.; Morris, J.F. *A Physical Introduction to Suspension Dynamics*; Cambridge University Press: Cambridge, UK, 2012.
3. Brenner, H.; Ganesan, V. Molecular wall effects: Are conditions at a boundary "boundary conditions"? *Phys. Rev. E* **2000**, *61*, 6879. [CrossRef] [PubMed]
4. Ho, B.P.; Leal, L. Inertial migration of rigid spheres in two-dimensional unidirectional flows. *J. Fluid Mech.* **1974**, *65*, 365–400. [CrossRef]
5. Procopio, G.; Giona, M. Stochastic Modeling of Particle Transport in Confined Geometries: Problems and Peculiarities. *Fluids* **2022**, *7*, 105. [CrossRef]
6. Zwanzig, R.; Bixon, M. Compressibility effects in the hydrodynamic theory of Brownian motion. *J. Fluid Mech.* **1975**, *69*, 21–25. [CrossRef]
7. Chow, T.S.; Hermans, J.J. Brownian motion of a spherical particle in a compressible fluid. *Physica* **1973**, *65*, 156–162. [CrossRef]
8. Giona, M.; Procopio, G.; Adrover, A.; Mauri, R. New formulation of the Navier–Stokes equations for liquid flows. *J. Non-Equilib. Thermodyn.* **2022**. [CrossRef]
9. Lauga, E.; Brenner, M.; Stone, H. Microfluidics: The No-Slip Boundary Condition. In *Springer Handbook of Experimental Fluid Mechanics*; Tropea, C., Yarin, A.L., Foss, J.F., Eds.; Springer: Berlin/Heidelberg, Germany, 2007; pp. 1219–1240.
10. Lauga, E.; Squires, T.M. Brownian motion near a partial-slip boundary: A local probe of the no-slip condition. *Phys. Fluids* **2005**, *17*, 103102. [CrossRef]
11. Mo, J.; Simha, A.; Raizen, M.G. Brownian motion as a new probe of wettability. *J. Chem. Phys.* **2017**, *146*, 134707. [CrossRef]
12. Giona, M.; Brasiello, A.; Crescitelli, S. Stochastic foundations of undulatory transport phenomena: Generalized Poisson–Kac processes—Part III extensions and applications to kinetic theory and transport. *J. Phys. A* **2017**, *50*, 335004. [CrossRef]
13. Einstein, A. *Investigations on the Theory of Brownian Movement*; Dover Publ.: Mineola, NY, USA, 1956.
14. Langevin, P. Sur la theorie du mouvement brownien. *C. R. Acad. Sci.* **1908**, *146*, 530–533.
15. Cichocki, B. (Ed.) *Marian Smoluchowski—Selected Scientific Works*; WUW: Warsaw, Poland, 2017.
16. Chandrasekhar, S. Stochastic problems in physics and astrophysics. *Rev. Mod. Phys.* **1943**, *15*, 1–89. [CrossRef]
17. Frey, E.; Kroy, K. Brownian motion: A paradigm of soft matter and biological physics. *Ann. Der Phys.* **2005**, *517*, 20–50. [CrossRef]
18. Bian, X.; Kim, C.; Karniadakis, G.E. 111 years of Brownian motion. *Soft Matter* **2016**, *12*, 6331–6346. [CrossRef]
19. Mo, J.; Raizen, M.G. Highly resolved Brownian motion in space and in time. *Annu. Rev. Fluid Mech.* **2019**, *51*, 403–428. [CrossRef]
20. Raizen, M.G.; Li, T. The measurement Einstein deemed impossible. *Phys. Today* **2016**, *68*, 56–57. [CrossRef]
21. Huang, R.; Chavez, I.; Taute, K.M.; Lukic, B.; Jeney, S.; Raizen, M.G.; Florin, E.L. Direct observation of the full transition from ballistic to diffusive Brownian motion in a liquid. *Nat. Phys.* **2011**, *7*, 576–580. [CrossRef]
22. Franosch, T.; Grimm, M.; Belushkin, M.; Mor, F.M.; Foffi, G.; Forró, L.; Jeney, S. Resonances arising from hydrodynamic memory in Brownian motion. *Nature* **2011**, *478*, 85–88. [CrossRef]
23. Pusey, P.N. Brownian motion goes ballistic. *Science* **2011**, *332*, 802–803. [CrossRef]
24. Kheifets, S.; Simha, A.; Melin, K.; Li, T.; Raizen, M.G. Observation of Brownian motion in liquids at short times: instantaneous velocity and memory loss. *Science* **2014**, *343*, 1493–1496. [CrossRef]
25. Grimm, M.; Jeney, S.; Franosch, T. Brownian motion in a Maxwell fluid. *Soft Matter* **2011**, *7*, 2076–2084. [CrossRef]
26. Zwanzig, R.; Bixon, M. Hydrodynamic theory of the velocity correlation function. *Phys. Rev. A* **1970**, *2*, 2005. [CrossRef]
27. Widom, A. Velocity fluctuations of a hard-core Brownian particle. *Phys. Rev. A* **1971**, *3*, 1394. [CrossRef]
28. Burgess, R.E. Brownian motion and the equipartition theorem. *Phys. Lett. A* **1973**, *42*, 395–396. [CrossRef]
29. Mo, J.; Simha, A.; Kheifets, S.; Raizen, M.G. Testing the Maxwell-Boltzmann distribution using Brownian particles. *Opt. Express* **2015**, *23*, 1888–1893. [CrossRef] [PubMed]
30. Darwin, C. Note on hydrodynamics. *Math. Proc. Camb. Phil. Soc.* **1953**, *49*, 342–354. [CrossRef]
31. Landau, L.D.; Lifshitz, E.M. *Fluid Mechanics*; Pergamon Press: Oxford, UK, 1993.
32. Kubo, R.; Toda, M.; Hashitsume, N. *Statistical Physics II—Nonequilibrium Statistical Mechanics*; Springer: Berlin, Germany, 1991.
33. Makosko, C.W. *Rheology—Principles, Measurements, and Applications*; Wiley-VCH: New York, NY, USA, 1994.
34. Zwanzig, R. Memory Effects in Irreversible Thermodynamics. *Phys. Rev.* **1961**, *124*, 983–992. [CrossRef]
35. Mori, H. Transport, Collective Motion, and Brownian Motion. *Prog. Theor. Phys.* **1965**, *33*, 423–455. [CrossRef]
36. Zwanzig, R. Nonlinear Generalized Langevin Equations. *J. Stat. Phys.* **1973**, *9*, 215–220. [CrossRef]
37. Kubo, R. The fluctuation-dissipation theorem. *Rep. Prog. Phys.* **1966**, *29*, 255–284. [CrossRef]
38. Alder, B.J.; Wainwright, T.E. Decay of the Velocity Autocorrelation Function. *Phys. Rev. A* **1970**, *1*, 18–21. [CrossRef]

39. D'Avino, G.; Maffettone, P.L. Particle dynamics in viscoelastic liquids. *Non-Newton. Fluid Mech.* **2015**, *215*, 80–104. [CrossRef]
40. D'Avino, G.; Greco, F.; Maffettone, P.L. Particle Migration due to Viscoelasticity of the Suspending Liquid and Its Relevance in Microfluidic Devices. *Annu. Rev. Fluid Mech.* **2017**, *49*, 341–360. [CrossRef]
41. Segré, S.; Silberberg, A. Radial particle displacements in Poiseuille flow of suspensions. *Nature* **1961**, *189*, 209–220. [CrossRef]
42. Ho, B.P.; Leal, L.G. Migration of rigid spheres in a two-dimensional unidirectional shear flow of a second-order fluid. *J. Fluid Mech.* **1976**, *76*, 783–799. [CrossRef]
43. Provencher-Langlois, G.; Farazmand, M.; Haller, G. Asymptotic dynamics of inertial particles with memory. *J. Nonlinear Sci.* **2015**, *25*, 1225–1255. [CrossRef]
44. Parmar, M.; Annamalai, S.; Balachandar, S.; Prosperetti, A. Differential formulation of the viscous history force on a particle for efficient and accurate computation. *J. Fluid Mech.* **2018**, *844*, 970–993. [CrossRef]
45. Prasath, S.G.; Vasan, V.; Govindarajan, R. Accurate solution method for the Maxey–Riley equation, and the effects of Basset history. *J. Fluid Mech.* **2019**, *868*, 428–460. [CrossRef]
46. Maxey, M. R.; Riley, J.J. Equation of motion for a small rigid sphere in a nonuniform flow. *Phys. Fluids* **1983**, *26*, 883–889. [CrossRef]
47. Haller, G. Solving the inertial particle equation with memory. *J. Fluid Mech.* **2019**, *874*, 1–4. [CrossRef]
48. Kim, S.; Karrila, S.J. *Microhydrodynamics—Principles and Selected Applications*; Dover Publ.: Mineola, NY, USA, 2005.
49. Happel, J.; Brenner, H. *Low Reynolds Number Hydrodynamics: With Special Applications to Particulate Media*; Martinus Nijhoff: The Hague, The Netherlands, 1983.
50. Mazur, P.; Bedeaux, D. Causality, time-reversal invariance and the Langevin equation. *Phys. A* **1991**, *173*, 155–174. [CrossRef]
51. Bedeaux, D.; Mazur, P. Brownian motion and fluctuating hydrodynamics. *Physica* **1974**, *76*, 247–258. [CrossRef]
52. Giona, M. Generalized Poisson-Kac Processes and the regularity of laws of nature. *Acta Phys. Pol. B* **2019**, *49*, 827–857. [CrossRef]
53. Cunsolo, A.; Ruocco, G.; Sette, F.; Masciovecchio, C.; Mermet, A.; Monaco, G.; Sampoli, M.; Verbeni, R. Experimental Determination of the Structural Relaxation in Liquid Water. *Phys. Rev. Lett.* **1999**, *82*, 775–778. [CrossRef]
54. O'Sullivan, T.J.; Kannam, S.K.; Chakraborty, D.; Todd, B.D.; Sader, J.E. Viscoelasticity of liquid water investigated using molecular dynamics simulations. *Phys. Rev. Fluids* **2019**, *4*, 123302. [CrossRef]
55. Gatignol, R. On the history term of Boussinesq–Basset when the viscous fluid slips on the particle. *Comptes Rendus Mec.* **2007**, *335*, 606–616. [CrossRef]
56. Premlata, A.R.; Wei, H.-H. The Basset problem with dynamic slip: Slip-induced memory effect and slip–stick transition. *J. Fluid Mech.* **2019**, *866*, 431–449. [CrossRef]
57. Premlata, A.R.; Wei, H.-H. Atypical non-Basset particle dynamics due to hydrodynamic slip. *Phys. Fluids* **2020**, *32*, 097109. [CrossRef]
58. Polyanin, A.D. *Handbook of Linear Partial Differential Equations for Engineers and Scientists*; Chapman & Hall/CRC: Boca Raton, FL, USA, 2002.
59. Oldham, K.J.; Spanier, J. *The Fractional Calculus*; Dover Publ.: Mineola, NY, USA, 2006.
60. Giona, M.; Procopio, G.; Klages, R. *Relativistic Hydrodynamics*; La Sapienza University: Roma, Italy, 2023. (manuscript in preparation).
61. Rezzola, O.; Zanotti, O. *Relativistic Hydrodynamics*; Oxford University Press: Oxford, UK, 2013.

fluids

MDPI

Article

Investigation of Flow-Induced Instabilities in a Francis Turbine Operating in Non-Cavitating and Cavitating Part-Load Conditions

Mohammad Hossein Arabnejad, Håkan Nilsson and Rickard E. Bensow *

Mechanics and Maritime Sciences, Chalmers University of Technology, 412 96 Gothenburg, Sweden
* Correspondence: rickard.bensow@chalmers.se

Abstract: The integration of intermittent renewable energy resources to the grid system requires that hydro turbines regularly operate at part-load conditions. Reliable operation of hydro turbines at these conditions is typically limited by the formation of a Rotating Vortex Rope (RVR) in the draft tube. In this paper, we investigate the formation of this vortex using the scale-resolving methods SST-SAS, wall-modeled LES (WMLES), and zonal WMLES. The numerical results are first validated against the available experimental data, and then analyzed to explain the effect of using different scale-resolving methods in detail. It is revealed that although all methods can capture the main features of the RVRs, the WMLES method provides the best quantitative agreement between the simulation results and experiment. Furthermore, cavitating simulations are performed using WMLES method to study the effect of cavitation on the flow in the turbine. These effects of cavitation are shown to be highly dependent on the amount of vapor in the RVR. If the amount of vapor is small, cavitation induces broadband high-frequency fluctuations in the pressure and forces exerted on the turbine. As the amount of cavitation increases, these fluctuations tend to have a distinct dominant frequency which is different from the frequency of the RVR.

Keywords: cavitating simulations; rotating vortex rope; scale-resolving simulations; synchronous pressure fluctuations

Citation: Arabnejad, M.H.; Nilsson, H.; Bensow, R.E. Investigation of Flow-Induced Instabilities in a Francis Turbine Operating in Non-Cavitating and Cavitating Part-Load Conditions. *Fluids* **2023**, *8*, 61. https://doi.org/10.3390/fluids8020061

Academic Editor: Mehrdad Massoudi

Received: 13 January 2023
Revised: 31 January 2023
Accepted: 4 February 2023
Published: 10 February 2023

1. Introduction

Due to their large storage capacity and quick response, hydro power plants are more and more being used to facilitate the integration of intermittent energy produced by other renewable sources of energy such as wind and solar to the grid system. This requires that hydro power plants expand their range of operation and also operate frequently at off-design conditions. In such off-design operation, the flow in different components of a hydro power plant is prone to complex behaviors and instabilities. One example is the formation of a Rotating Vortex Rope (RVR) in the draft tube which is associated with a high level of pressure fluctuations in the system. These pressure fluctuations can cause oscillation in the mechanical loading of the runner, causing a significant swing in the power produced by the hydro power plant [1,2]. Furthermore, the pressure drop in the core of the RVR can lead to the formation of vapor pockets in the water flow, known as cavitation. The presence of cavitation in hydro turbines is known to have several undesirable effects, such as cavitation erosion [3], performance degradation [4], and increased level of pressure fluctuations and vibration [5].

The detrimental effects of the RVR for hydro turbines operating at off-design conditions have motivated several experimental studies with the aim to investigate the formation of the RVR and its associated cavitating structures. Nishi et al. [6] experimentally examined non-cavitating and cavitating RVRs at different flow conditions. They observed that the pressure fluctuations induced by the RVR can be decomposed into synchronous and convective components. Iliescu et al. [7] studied the dynamics of non-cavitating and cavitating RVRs

using High-Speed Visualization (HSV) and Particle Image Velocimetry (PIV) measurements. They concluded that the formation of vapor pockets in an RVR can lead to fluctuations in its geometrical features. Favrel et al. [8] and Arpe et al. [9] studied the effect of cavitation on the pressure fluctuations induced by the RVR. They both concluded that cavitation formation in the RVR can influence both the amplitude and the frequency of the pressure fluctuations. Further, Landry et al. [10] showed that the presence of cavitation in the RVR can alter the eigenfrequency of the hydraulic system by changing the sound propagation speed in the liquid. This can lead to severe vibrations and power swing if there is a match between this eigenfrequency and the frequency of induced pressure fluctuations by the RVR [1,2].

In addition to experimental investigations, CFD simulations have been used to investigate this flow. In the majority of these simulations, Reynolds-averaged Navier–Stokes (RANS) approaches are used as they have lower computational cost compared to scale-resolving methods. These RANS simulations have been shown to have deficiencies in capturing the correct behavior of RVRs. Ciocan et al. [11] studied the dynamics of the RVR using unsteady RANS and showed that their results under-predicted the level of swirl in the flow entering the draft tube and differed by 13% in RVR frequency compared to the experimental data. Similar deficiency has been observed by Liu et al. [12] who performed unsteady RANS simulations of the RVR in a draft tube and compared the level of pressure fluctuations with the experimental data. Furthermore, the simulations by Ruprecht et al. [13] have shown that using a RANS approach over-estimates the decay of the swirling flow around the RVR, which results in the under-prediction of the pressure fluctuations caused by the RVR. Despite these deficiencies, a few studies have used the RANS approach to study the effect of cavitation on the behavior of RVRs. Yu et al. [14] performed RANS simulations of a cavitating RVR and revealed that the presence of cavitation affects the vorticity production around the RVR as well as the pressure fluctuations generated in the draft tube. Jošt et al. [15] performed simulations of cavitating and non-cavitating flows in a Francis turbine and compared the results with experimental data. They showed that it is necessary to consider cavitation in the simulation to correctly reproduce the RVR-induced pressure fluctuations in the experiment.

To avoid the limitation of RANS approaches in capturing the correct behavior of RVRs, several numerical studies have used scale-resolving approaches to examine non-cavitating and cavitating RVRs. Salehi et al. [16] and Salehi and Nilsson [17] investigated the formation of RVRs during the startup and shutdown in a Francis turbine using a scale-resolving approach. By analyzing the results, they were able to explain the complex flow behavior leading to the formation of RVRs in the draft tube. Foroutan and Yavuzkurt [18] studied the RVR using DES and found a good agreement between their numerical results and experimental data. By analyzing the DES results, they postulated that the RVR is created in the shear layer between the region of low axial velocity in the center of the draft tube cone and the flow outside of this region, due to Kelvin–Helmholtz instability. Minakov et al. [19] used DES to study the RVR in the draft tube at different guide vane openings, and found that changing the guide vane opening leads to a different swirl number and discharge coefficient, which leads to different behavior of the RVR. Rajan and Cimbala [20] studied the flow in a simplified draft tube using the DES approach for different discharge coefficients. It was shown that the level of pressure fluctuations increases substantially when the RVR is formed in the draft tube. Guo et al. [21] used the LES approach to simulate cavitating flows in the draft tube. They highlighted the importance of including the runner to predict the low-pressure region in the center of the RVR. Pacot et al. [22] performed LES simulations for cavitating RVRs and showed that a large amount of cavitation in the RVR can prevent its precession motion, leading to a reduction of the RVR-induced pressure fluctuations.

Although the numerical studies reviewed above have highlighted the importance of using scale-resolving methods to capture the correct behavior of the RVR, only a few of them have performed a detailed comparison between the performance of different

scale-resolving approaches. Furthermore, detailed analyses of how cavitation affects the flow features of the RVR are also scarce in the literature. To address this knowledge gap, in the present paper, the formation of non-cavitating and cavitating RVRs in the Francis-99 turbine is investigated using three scale-resolving methods. The simulation results are compared with the experimental data provided through the Francis-99 workshop, and the differences between the results obtained by different scale-resolving methods are highlighted. Then, cavitating simulations are performed for three cavitating conditions, covering the condition near the inception of cavitation in the RVR to the fully cavitating RVR. Using these simulations, the effect of cavitation on the behavior of the RVR, the generated pressure fluctuations and the forces exerted on different component of the turbine are discussed in detail. This paper is organized into five sections. After this introduction, the next section briefly summarizes the employed numerical set-up. Then, the studied turbine and flow conditions are described in the following section. The results are presented in the fourth section, where first the effects of different scale-resolving methods on capturing the flow features are discussed, and then, the effects of cavitation on the flow features of the RVR are explained in detail.

2. Numerical Set-Up

In this paper, the modified interPhaseChangeFoam solver [23–25] from the OpenFOAM-2.2.x framework [26] is used to perform the simulations. The governing equations in this solver are the incompressible Navier–Stokes equations for two-phase (liquid-vapor) isothermal flows. Using the homogeneous mixture approach, only one set of equations is solved for the two-phase mixture. Similar to turbulent single-phase flows, turbulent two-phase mixture flows include a wide range of scales. For engineering flow, RANS, LES, or zonal hybrid RANS/LES approaches can be employed, where the governing equations of a two-phase mixture with homogeneous assumption read

$$\frac{\partial}{\partial t}(\rho) + \nabla \cdot (\rho \tilde{\mathbf{u}}) = 0, \tag{1}$$

$$\frac{\partial}{\partial t}(\rho \tilde{\mathbf{u}}) + \nabla \cdot (\rho \tilde{\mathbf{u}} \otimes \tilde{\mathbf{u}}) + \nabla \cdot ([p\mathbf{I} - \tau]) + \nabla \cdot (\tau_{unres}) = 0, \tag{2}$$

where ρ is the mixture density, $\mathbf{u}$ is the velocity vector, p is the pressure, $\mathbf{I}$ is the identity tensor, τ is the viscous stress tensor, and τ_{unres} is the stress tensor due to unresolved turbulence in the flow. The tilde operation on the velocity vector in the above equations, $\tilde{\mathbf{u}}$, represents a time-averaging operation in the RANS approach or spatial filtering in the LES approach. Assuming that the mixture of liquid and vapor is homogeneous and that the dynamic viscosity and the density in each phase are constant, the mixture viscous stress tensor, τ, and the mixture density ρ can be obtained from

$$\tau = (\alpha^l \mu^l + \alpha^v \mu^v) S, \tag{3}$$

$$\rho = \alpha^l \rho^l + \alpha^v \rho^v, \tag{4}$$

where S is the mixture strain tensor, and α^l, α^v, ρ^l, and ρ^v are, respectively, the liquid volume fraction, the vapor volume fraction, the density of the liquid and the density of the vapor. In order to close the governing equations, α^l, α^v and τ_{unres} should be determined. In non-cavitating simulations, the liquid volume fraction, α^l, is equal to 1 while the volume fraction of the vapor phase, α^v, is equal to zero in the entire domain. For two-phase cavitating flows, α^l is obtained using a transport equation, reading

$$\frac{\partial}{\partial t}(\alpha^l \rho^l) + \nabla \cdot (\alpha^l \rho^l \tilde{\mathbf{u}}) = \dot{m}, \tag{5}$$

where $\dot{m}$ is the mass transfer term due to vaporization and condensation. The vapor volume fraction, α^v, is then determined using $\alpha^v + \alpha^l = 1$. To model the mass transfer term, $\dot{m}$, the Schnerr–Sauer model [27] is used in this paper. This term can written as

$$\dot{m} = \alpha^l \left(\dot{m}_{\alpha_v^l} - \dot{m}_{\alpha_c^l} \right) + \dot{m}_{\alpha_c^l}, \tag{6}$$

where $\dot{m}_{\alpha_c^l}$ and $\dot{m}_{\alpha_v^l}$ are, respectively, condensation and vaporization terms and can be defined as

$$\dot{m}_{\alpha_c^l} = C_c \alpha^l \frac{3\rho^l \rho^v}{\rho R_B} \sqrt{\frac{2}{3\rho^l}} \sqrt{\frac{1}{|p - p_v|}} \max(p - p_v, 0), \tag{7}$$

$$\dot{m}_{\alpha_v^l} = C_v \left(1 + \alpha_{Nuc} - \alpha^l \right) \frac{3\rho^l \rho^v}{\rho R_B} \sqrt{\frac{2}{3\,\rho^l}} \sqrt{\frac{1}{|p - p_v|}} \min(p - p_v, 0). \tag{8}$$

In the above equations, C_c and C_v, the condensation and vaporization constants, are 1, p_v is the vapor pressure, α_{Nuc} is the initial volume fraction of nuclei, and R_B is the radius of the nuclei which is obtained from

$$R_B = \sqrt[3]{\frac{3}{4\pi n_0} \frac{1 + \alpha_{Nuc} - \alpha^l}{\alpha^l}}. \tag{9}$$

The initial volume fraction of nuclei is calculated from

$$\alpha_{Nuc} = \frac{\frac{\pi n_0 d_{Nuc}^3}{6}}{1 + \frac{\pi n_0 d_{Nuc}^3}{6}}, \tag{10}$$

where the average number of nuclei per cubic meter of liquid volume, n_0, and the initial nuclei diameter, d_{Nuc}, are assumed to be 10^{11} and 10^{-5}, respectively.

To model the τ_{unres} term, the eddy-viscosity hypothesis is used as

$$\tau_{unres} = -2\mu_{unres}\bar{S} + \frac{2}{3} k_{unres} \mathbf{I}, \tag{11}$$

where μ_{unres} is the eddy viscosity and k_{unres} is the unresolved turbulent kinetic energy. In this paper, we use three models to approximate μ_{unres} and k_{unres} which are explained in the following.

2.1. SST-SAS RANS Approach

The eddy viscosity, μ_{unres}, and unresolved turbulent kinetic energy, k_{unres}, represent, respectively, the turbulent viscosity, μ_t, and the turbulent kinetic energy, k_t within the context of the RANS approach. Here, these terms are modeled using the Shear Stress Transport-based Scale-Adaptive Simulation model (SST-SAS) [28,29]. In this turbulence model, the turbulent kinetic energy, k_t, and the turbulent specific rate of dissipation, ω_t, are calculated using transport equations. These two terms are then used to calculate μ_t as

$$\mu_t = \rho a_1 \frac{k_t}{\max(a_1 \omega_t, b_1 F_{23} S)}, \tag{12}$$

where S is the invariant measure of the strain rate, a_1 and b_1 are constants, and F_{23} is a blending function. The transport equation for k_t in SST-SAS is the same as the equation in the k-ω SST turbulence model [30], and can be written as

$$\frac{\partial k_t}{\partial t} + \nabla \cdot (\bar{u} k_t) = P_k + \nabla^2 \left[\frac{1}{\rho} (\mu + \mu_t) k_t \right] - \beta^* \omega_t k_t, \tag{13}$$

where P_k and β^* are, respectively, the production term and a constant. The transport equation for ω_t can be read as

$$\frac{\partial \omega_t}{\partial t} + \nabla \cdot (\tilde{u}\omega_t) = \alpha \frac{P_k}{\mu_t} - \nabla^2 \left[\frac{1}{\rho}(\mu + \mu_t)\omega_t \right] - \beta \omega_t^2 - 2(F_1 - 1)\rho\sigma_{w2}\frac{1}{\omega}\nabla k_t \nabla \omega_t + Q_{SAS}, \quad (14)$$

where α, β, and σ_{w2} are constants, F_1 is a blending function, and Q_{SAS} is an extra term compared to the equation in the k-ω SST turbulence model. This extra term can be obtained as

$$Q_{SAS} = \max\left[\rho\zeta_2\kappa S^2 \left(\frac{L}{L_{vK}} \right)^2 - C\frac{2\rho k_t}{\sigma_\Phi} \max\left(\frac{|\nabla\omega_t|^2}{\omega_t^2}, \frac{|\nabla k_t|^2}{k_t^2} \right), 0 \right], \quad (15)$$

where ζ_2, κ, σ_Φ, and C are constants. In Equation (15), L and L_{vK} are the modeled turbulence length scale and the von Karman length scale, respectively, which are defined as

$$L = \frac{\sqrt{k}}{c_\mu^{1/4}\omega}, \; L_{vK} = \max\left(\frac{\kappa S}{|\nabla^2 \tilde{\mathbf{u}}|}, C_s \sqrt{\frac{\kappa\zeta_2}{\beta/c_\mu - \alpha}} \right), \quad (16)$$

where c_μ, β, C_s and α are constants.

2.2. WALE LES Approach

Within the LES context, μ_{unres} and k_{unres} are the sub-grid scale viscosity, μ_{sgs}, and the sub-grid turbulent kinetic energy, k_{sgs}, respectively. Here, the wall-adapting local eddy-viscosity (WALE) LES model proposed by Nicoud and Ducros [31] is used to model these terms as

$$\mu_{sgs} = C_k \Delta \sqrt{k_{sgs}}, \quad (17)$$

$$k_{sgs} = \left(\frac{C_w^2 \Delta}{C_k} \right)^2 \frac{(\tilde{S}^d \tilde{S}^d)^3}{\left((\tilde{S}\tilde{S})^{5/2} + (\tilde{S}^d \tilde{S}^d)^{5/4} \right)^2}, \quad (18)$$

where Δ is the cell length scale calculated based on the cubic root of the cell volume and $C_k = 1.6$ and $C_w = 0.325$ are the model constants. $\tilde{S}$ and $\tilde{S}^d$ are also, respectively, the resolved-scale strain rate tensor and traceless symmetric part of the square of the velocity gradient tensor.

2.3. Zonal RANS/LES Approach

In the zonal approach, the SST-SAS RANS and WALE LES approaches are used in predefined regions of the domain. To mark these predefined regions, a scalar field r_{LES} is set to 1 in the LES regions and zero in the RANS regions. Using this scalar field, the μ_{unres} and k_{unres} can be obtained as

$$\mu_{unres} = r_{LES}\mu_{sgs} + (1 - r_{LES})\mu_t, \quad (19)$$

$$k_{unres} = r_{LES}k_{sgs} + (1 - r_{LES})k_t, \quad (20)$$

where μ_{sgs} and k_{sgs} are obtained using the WALE LES approach from Equations (17) and (18), while μ_t and k_t are determined using the SST-SAS RANS approach from Equations (12) and (13).

2.4. Discretization Schemes and Solution Algorithm

To discretize convective terms in the momentum equations, the Linear-Upwind Stabilized Transport (LUST) convection scheme is used. This scheme blends 2nd order upwind (25%) and central differencing (75%) schemes [32]. The discretization of diffusion terms in

the momentum equations are done using the linear scheme. For the convective term in the liquid volume fraction transport equation, the first-order upwind scheme is used. Using this scheme is consistent with the mixture assumption and is recommended in the original publication [33] for the Schnerr–Sauer model. A second-order backward implicit scheme is used for time discretization and a pressure-based PIMPLE approach, a combination of SIMPLE and PISO algorithms, is employed to solve the discretized equations. To ensure the convergence of the algorithm, the residual target for the pressure and velocities are set to 10^{-13} for the simulations with cavitation and 10^{-7} for the simulations without cavitation. For more details about the solution procedure, the reader can refer to Asnaghi et al. [24] and Bensow and Bark [23].

3. The Francis-99 Turbine and Computational Mesh

In this paper, the Francis-99 turbine model is used. This turbine is a scaled-down model of the prototype Francis turbine installed at the Tokke power plant in Norway [34]. The computational domain shown in Figure 1 includes the spiral casing, the stay vanes, the guide vanes, the runner, and the draft tube. There are 14 stay vanes and 28 guide vanes. The runner includes 15 splitter blades and 15 full-length blades. The inlet and outlet diameters of the runner are 0.63 m and 0.347 m, respectively. The mesh in different components of the turbine are produced using the Pointwise V18.3 mesh generation software. The mesh specifications for each component are shown in Table 1. The mesh has 20.88 M cells, which according to the mesh dependency studies performed for simulations of the Francis-99 turbine found in the literature [35–39] is enough for mesh-independent results of the flow in the draft tube. The table also shows that the average y^+ value is larger than 1 for all components; therefore, the wall function based on Spalding's law is used at the walls [25,40,41]. It should be mentioned that using the wall function for the simulations of the flow in the draft tube of Francis turbines is justified as the work by Wilhelm et al. [42] showed that resolving near-wall regions instead of using the wall function has insignificant effects on the captured flow in the draft tube.

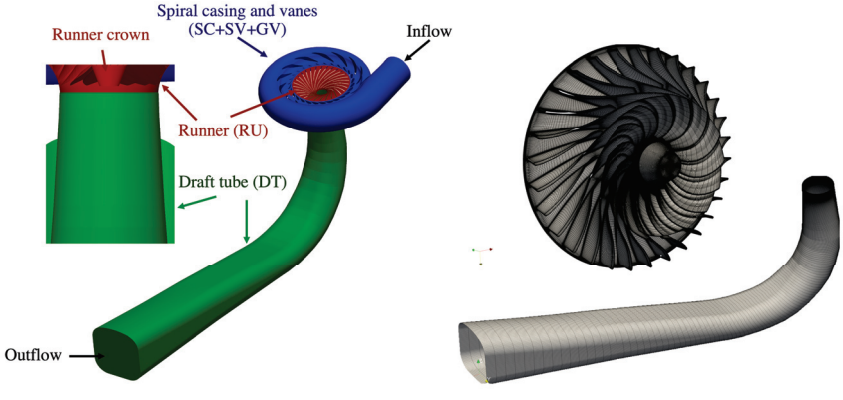

Figure 1. Computational domain and mesh in the runner and draft tube.

Table 1. Mesh resolution.

Components	# of Cells	Average y^+
SC+SV+GV	10.12 M	20
RU	5.13 M	12
DT	5.63 M	14
Total	20.88 M	17

As mentioned in Section 2, we use a zonal WMLES approach where the RANS and WMLES approaches are used in different regions of the domain. Since the focus of the paper is to investigate the RVR in the draft tube, we use the WMLES approach in the draft tube (region labeled by DT in Figure 1) and in the rest of the domain (regions labeled by RU, SC, SV, and GV in Figure 1), the SST-SAS RANS approach is employed.

The experimental data used for validation in the present study are from the second Francis-99 workshop. These data include both pressure and velocity measurements at different locations. The velocity measurements includes the axial and horizontal components over three lines in the draft tube, Line 1, Line 2, and Line 3 in Figure 2a. The data also include the static pressure fluctuations at two probes in the draft tube, Probe 2 and Probe 3 in Figure 2a and the static pressure in the vaneless region between the guide vane blades and runner blades, is marked by Probe 1 in Figure 2b.

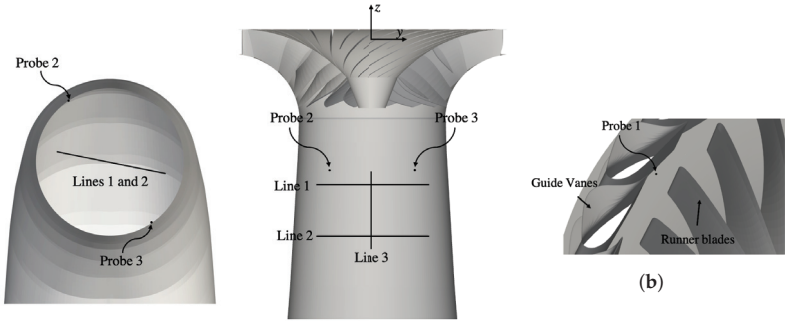

(**a**)

Figure 2. Measurement probes and lines in the experimental data provided by the second Francis-99 workshop. (**a**) Measurement probes and lines in the draft tube, (**b**) probe between guide vanes and runner.

3.1. Studied Flow Conditions

In this paper, the part-load (PL) condition in the second Francis-99 workshop is studied. In this condition, the guide vane opening is $\alpha = 6.72^\circ$, the runner angular speed is $n = 332.84\,\mathrm{r/min}$, and the discharge is $Q = 0.13962\,\mathrm{m^3/s}$. In order to study the effect of cavitation in this PL condition, the simulations are performed for both non-cavitating and cavitating conditions. The cavitation number, σ, in these simulations is defined as

$$\sigma = \frac{(p_2 - p_v)/\rho_l + \frac{1}{2}(Q/A_2)^2}{gH}, \tag{21}$$

where p_2 and A_2 are, respectively, the pressure and the cross-section area at the draft tube outlet, p_v is the vapour pressure, ρ_l is liquid density, and H is the turbine head. Here, we study the flows at $\sigma = \{0.07, 0.06, 0.05\}$ which includes the near-inception cavitation in the RVR ($\sigma = 0.07$) as well as the condition corresponding to the fully cavitating RVR ($\sigma = 0.05$).

4. Results

The results are divided into two parts. The first part presents the effect of turbulence modeling on capturing the global quantities, the velocity profiles and the pressure fluctuations in the draft tube. The second part is devoted to studying the effects of cavitation on the same flow features.

4.1. Effect of Turbulence Modeling

In Table 2, the global quantities captured with different turbulence modeling techniques are compared with the experimental values. The relative errors in this table are obtained by dividing the difference between the experimental and numerical values by the experimental values. This comparison shows that all of the turbulence modeling techniques can capture these global quantities with a relatively small error, although a slightly lower relative error can be seen in the WMLES results. According to Čelič and Ondráčka [43], this error can be due to neglecting the labyrinth seal and disk friction losses.

Table 2. Effect of turbulence modeling technique on predicted global quantities, torque, M_z, head, H, and efficiency η.

Quantities	SAS	Zonal WMLES	WMLES	Exp.
M_z (Nm)	440.57	440.51	439.68	420.79
Relative error for M_z	4.7%	4.7%	4.5%	-
H (m)	12.71	12.70	12.48	11.87
Relative error for H	7.1%	7.0%	5.1%	-
η	88.14	88.19	89.58	90.13
Relative error for η	2.2%	2.2%	0.6%	-

Figure 3 compares the time-averaged experimental and numerical velocity profiles along the three lines shown in Figure 2a. The experimental profiles are taken from the data provided by the second Francis-99 workshop [44]. The experimental axial velocity over Line 1 and Line 2 indicates that a region with low values of absolute axial velocity exists near the center of the draft tube. The comparison between the numerical results in Figure 3a,c indicates that this region is captured by all simulations, although there are some quantitative differences between the different results. As it can be seen in the axial velocity profiles on Lines 1 and 2 (Figure 3a), the regions with low values of absolute axial velocity in the SAS and zonal WMLES results are more confined to the center of the draft tube cone compared to the WMLES results and the experimental data. The axial velocity along the centerline (Figure 3c) shows that while the WMLES simulation predicts a negative averaged axial velocity along the entire Line 3, similar to the experimental data, positive values for the time-averaged axial velocity can be seen in the SAS and zonal WMLES results. Considering the definition of the axial direction (z), shown in Figure 2a, this positive axial velocity means that there is a reversed flow along the centerline of the draft tube cone in these two simulations. The cause of this difference is explained later in this paper. The horizontal velocity profiles (Figure 3b,c) show that the simulations can capture the trends similar to the experiment. However, the values of horizontal velocity in these simulations are shifted compared with the experimental values. It should be noted that the absolute value of the horizontal velocity is very close to zero over the measurement lines, the relative uncertainty for these velocities is higher compared with that for the axial velocities according to Salehi and Nilsson [45]. This higher uncertainty can be one reason for the difference between the results for these velocity profiles.

It is well-established that the region with low values of absolute axial velocity shown in Figure 3 is caused by the formation of the RVR in the draft tube at part-load condition. Figure 4 shows snapshots of the RVRs of the different numerical results. In this figure, the RVRs are visualized using an iso-surface of Q, which is the second invariant of the velocity gradient tensor. The level of the iso-surface is $5000\,s^{-2}$, which is chosen for an optimal visualization of the RVRs. In the zoom-in view, it can be seen that the RVR consists of many vortices wrapping around each other. At the location of these vorticies, the positive value of axial velocity (red color in the figure) indicates the presence of a reversed flow. The figure also presents the time history of the axial velocity on Line 1 for one period of

the RVR rotation. The time instance corresponding to the snapshot of the iso-surfaces is shown by black dashed lines. These time histories show that as the RVR passes Line 1, the axial velocity on these lines becomes positive (red regions). The sweeping motion of the vortices causes the tilted streaks seen in the time history. A comparison between the results from the different simulations indicates that the number and size of the vortices in the RVR are strongly influenced by the selection of the turbulence modeling technique. In the SAS simulation, the RVR consists of a small number of large vortices, as shown in the zoom-in views, and this leads to fewer and large streaks in the time history of the axial velocity. In the zonal WMLES and WMLES simulations, however, the RVR has a large number of smaller vortices, which creates thinner streaks in the time history.

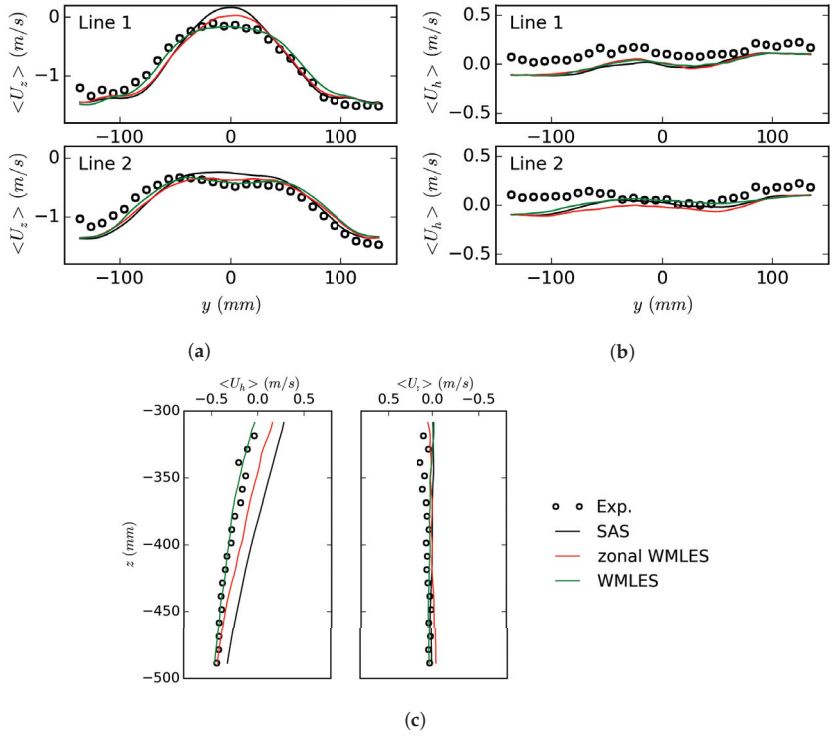

Figure 3. Comparison between the averaged velocities along the measurement lines in Figure 2a in the experiment [44] and the simulations. (**a**) Axial velocity, Lines 1 (upper) and 2 (lower). (**b**) Horizontal velocity, Lines 1 (upper) and 2 (lower). (**c**) Axial (right) and horizontal (left) velocities, Line 3.

As mentioned earlier and shown in Figure 3, the region with a low value of absolute axial velocity in the center of the draft tube cone is affected by the selection of the turbulence modeling. To provide a reason for this effect, the phase-averaged axial velocity over Lines 1 and 2 in the experiment and simulations is shown in Figure 5. To obtain the phase-averaged values in this paper, the data signal corresponding to one cycle of the RVR rotation, T_{RVR}, is divided into 30 windows. The data corresponding to each window are averaged together. Two instances A and B are marked in these figures. At instance A, the axial velocity has a high positive value which is due to the passage of the RVR over the measurement lines. At instance B, the RVR has rotated further and left the measurement lines, which leads to the observed decrease in the axial velocity toward the negative values. The comparison in Figure 5 shows that when the vortex passes the measurement lines at instance A, all simulations predict a distribution of axial velocity which is quite similar to the experimental data. However, this is not case for the instance when the RVR leaves the measurement lines

(instance B). At this instance, the axial velocity over Line 1 near the center of the draft tube ($y = 0$ mm) has positive values in the SAS and zonal WMLES simulations while the values in the experiment and the WMLES simulations are negative. The reason for this difference is that the RVR in the SAS and zonal WMLES simulations rotates on a path which is closer to the center of draft tube as compared with the experiment and the WMLES simulation. To clearly show this, the figure shows vertical black lines passing through the maximum values of axial velocity when the RVR is on the measurement line. The distance between these lines is also shown. It can be seen that distance between these lines is larger in the experiment and the WMLES results as compared with the other two simulations. This difference means that a portion of the RVR in the SAS and zonal WMLES simulations has overlaps with Line 1 near the center of the draft tube all through the rotational cycle of the RVR. Since the axial velocity in the RVR is positive according to Figure 4, this overlap would lead to the positive values of axial velocity over Line 1 at instance B in the SAS and zonal WMLES simulations. It also leads to the positive values of the averaged axial velocity in these two simulations which is shown in Figure 3.

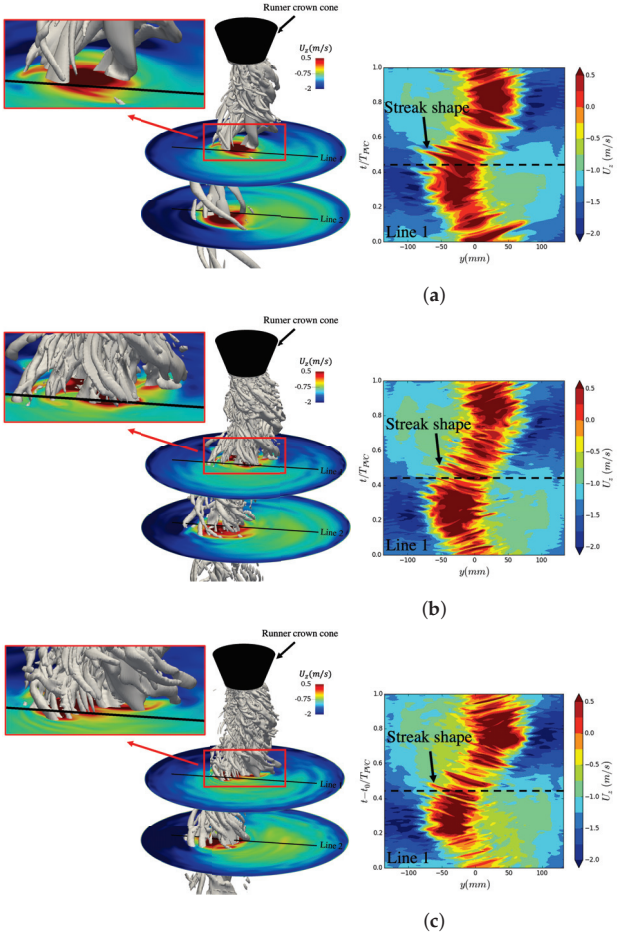

Figure 4. RVR (left figures) and its effect on the axial velocity at Line 1 during one RVR cycle (right figures), (**a**) SAS, (**b**) zonal WMLES, (**c**) WMLES. The vortices are shown by the iso-surface $Q = 5000\,\mathrm{s}^{-2}$.

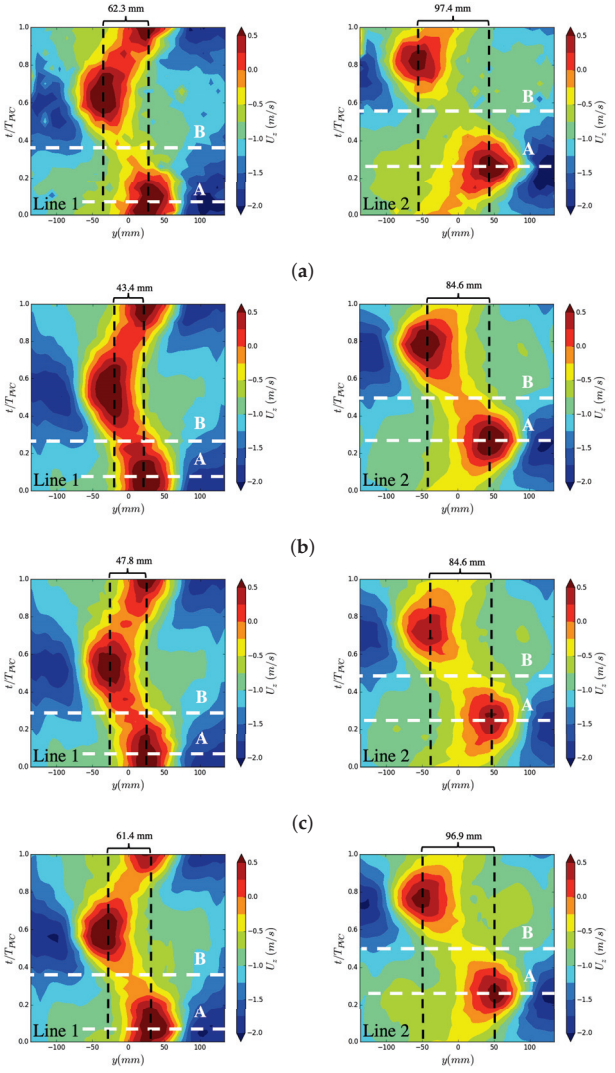

Figure 5. Phase-averaged axial velocity over Lines 1 and 2 in the experiment and simulations, instance A corresponds to RVRs being on the line and instance B corresponds to RVRs leaving the lines. (**a**) Exp., (**b**) SAS, (**c**) zonal WMLES, (**d**) WMLES .

The RVR in the draft tube creates a large amount of pressure fluctuations which can lead to vibrations. To evaluate how well these pressure fluctuations can be captured by the different turbulence modeling techniques, Figure 6 compares the experimental and numerical pressure fluctuation signals in Probe 2 in the draft tube. For each signal, the Root Mean Square (RMS) of the fluctuations is noted in the plot. It can be seen that in all of the numerical results, the RMS values are lower compared with the values in the experiment. The numerical RMS values however increase towards the experimental one as the resolution of the turbulence modeling technique increases. It can be seen that, as expected, it is mainly the smaller scales of the fluctuations that differ between the results from the different turbulence modeling techniques, while the amplitude and frequency of the large-scale RVR motion are similar.

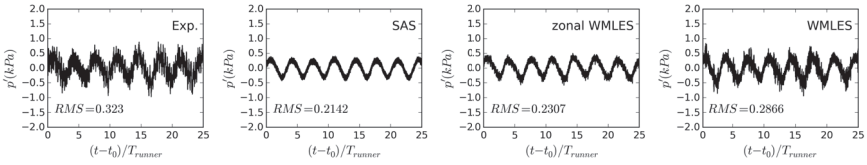

Figure 6. The signal of pressure fluctuations at Probe 2 shown in Figure 2a in the experiment and simulations.

To investigate the reasons why the RMS values of the pressure fluctuations are lower in the simulations compared with the experiment, Figure 7 shows a frequency analysis of the pressure fluctuations. For the experiment, the analysis (Figure 7a) includes the power spectrum analysis of the pressure signal from Probe 2 (left plot), the coherence (middle plot), and the phase difference (right plot) between the pressure signals from Probes 2 and 3. The coherence and phase difference between the two signals are calculated from the cross-spectral density, P_{xy}, which is obtained using Welch's method [46]. The frequency analysis of the experimental pressure signal (left plot) indicates the existence of two dominant frequencies, f_1 and f_2. For these dominant frequencies, the coherence between the signals at Probes 2 and 3 (middle plot) is almost one, which means that these dominant frequencies also exist in the signal from Probe 3. The phase difference between the two signals (right plot) is π for the dominant frequency f_1 and its harmonic $2f_1$. Considering that the locations of Probes 2 and 3 are exactly at opposite sides of the cone region in the draft tube, this phase difference suggests that the dominant frequency, f_1, is due to the precession of the RVR in the draft tube cone. It should be mentioned that the precession frequency $0.29f_{runner}$ is in the range 0.2–0.4 f_{runner}, which has been found in previous studies [7,47]. For the dominant frequency f_2, the phase difference is almost zero indicating that the corresponding pressure fluctuations are synchronous meaning that they have the same phase and amplitude for the pressure sensors located in the same cross section of the draft tube. The frequency analyses of the pressure signals in the simulations with different turbulence modeling techniques show that the dominant frequency of the RVR, f_1, and its harmonic, $2f_1$, is captured by all turbulence modeling techniques. The experimental dominant frequency f_2 can however not be seen in any of the numerical results, which causes a reduced RMS value.

To investigate the origin of the dominant frequency f_2 in the experiment, Figure 8 shows a spectral analysis of the pressure fluctuations in the draft tube at the Best Efficiency Point (BEP) and High Load (HL) conditions for which there is no RVR. Similar to the PL condition, a dominant frequency at f_2 can be seen also for BEP and HL (left plots). As for the PL condition, the coherence (middle plots) is close to one and the phase difference (right plots) is zero for this frequency. This indicates a synchronous nature of these pressure fluctuations, at a frequency that is rather independent of the operating condition. Based on this observation, we can conclude that the synchronous pressure fluctuations seen in the experimental results is related to a component in the system rather than the flow features in the components studied here. It should be mentioned that similar synchronous pressure fluctuations have been observed by Favrel et al. [8], Arpe et al. [9], with frequencies in the range of 2–4 f_{runner}. These studies, however, have shown that this type of pressure fluctuations occurs in cavitating conditions and can be attributed to the interaction between the cavitating RVR and the elbow in the draft tube.

To further analyze the high-frequency content of the signals and its effects on the RMS values, the fluctuations are decomposed into two components as

$$p' = p'_{RVR} + p'_{Other}, \tag{22}$$

where p'_{RVR} denotes the pressure fluctuations due to the precession of the RVR and p'_{Other} denotes the pressure fluctuations due to other sources. To perform this decomposition, we assume that the pressure fluctuations due to RVR at Probe 2 have a phase difference of π with the corresponding fluctuations at Probe 3. This assumption is shown to be true in

Figure 7a. Based on this assumption, the frequencies of pressure fluctuations due to RVR are determined. These frequencies are then filtered from the signal of pressure fluctuations to obtain the pressure fluctuations due to other sources, p'_{Other}. The fluctuations due to RVR, p'_{RVR}, then can be obtained by subtracting p'_{Other} from the original pressure fluctuation signal according to Equation (22).

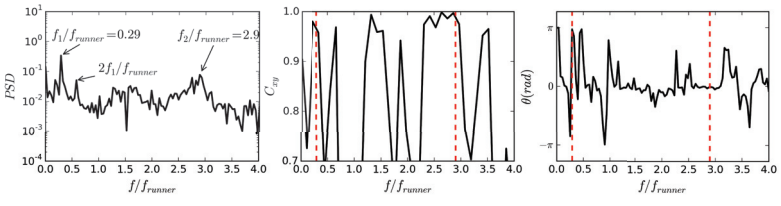

(**a**)

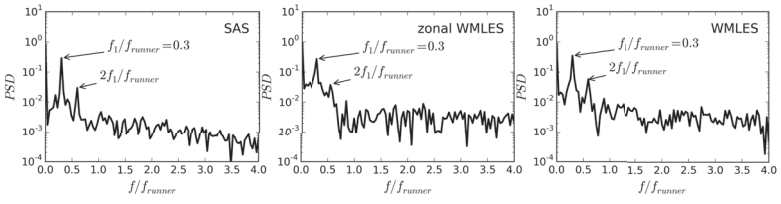

(**b**)

Figure 7. Spectral analysis of pressure signals from Probes 2 and 3 in the draft tube in the experiment and simulations. (**a**) Frequency analysis of pressure signal from Probe 2 (left plot), the coherence (middle plot) and the phase difference (right plot) between the pressure signals from Probes 2 and 3 in the experiment. (**b**) Frequency analysis of the pressure signals from Probe 2 in the draft tube in the simulations with different turbulence modeling techniques.

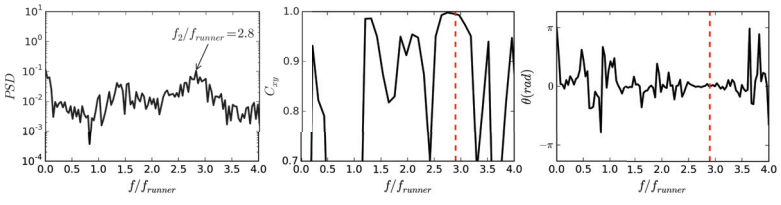

(**a**)

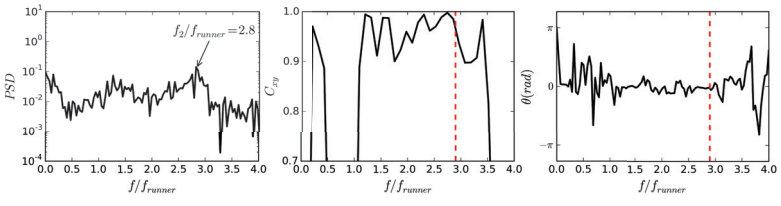

(**b**)

Figure 8. Spectral analysis of pressure signal from Probes 2 and 3 in the draft tube in the experiment at (**a**) Best Efficiency Point (BEP), and (**b**) High Load (HL), frequency analysis of pressure signal from Probe 2 (left plot), the coherence (middle plot) and the phase difference (right plot) between the pressure signals from Probes 2 and 3 in the experiment.

Figure 9 shows the different components of the pressure fluctuations at Probe 2 according to Equation (22) and their corresponding RMS values from the results of the simulations and experiment. For the pressure fluctuations due to the RVR, the difference

between the predicted RMS values and the experimental RMS value correspond to 16%, 14% and 4% for the SAS, zonal WMLES and WMLES simulations, respectively. The reason for these differences will be explained later. The corresponding differences for the pressure fluctuations due to other sources are 77%, 59%, and 39%. The reason for these large differences is mainly that (as shown before) the numerical fluctuations do not include the synchronous pressure fluctuations with the experimental dominant frequency of f_2 shown in Figure 7a. The comparison between the results of the different simulations also shows that the RMS values of p'_{Other} are very sensitive to the selected turbulence modeling technique. This type of pressure fluctuations includes the pressure fluctuations due to wakes of the guide vanes, runner blades, and runner crown which are captured to a larger extent in the WMLES simulation compared with the zonal WMLES and SAS simulations, for which the region upstream the draft tube is resolved using a RANS approach.

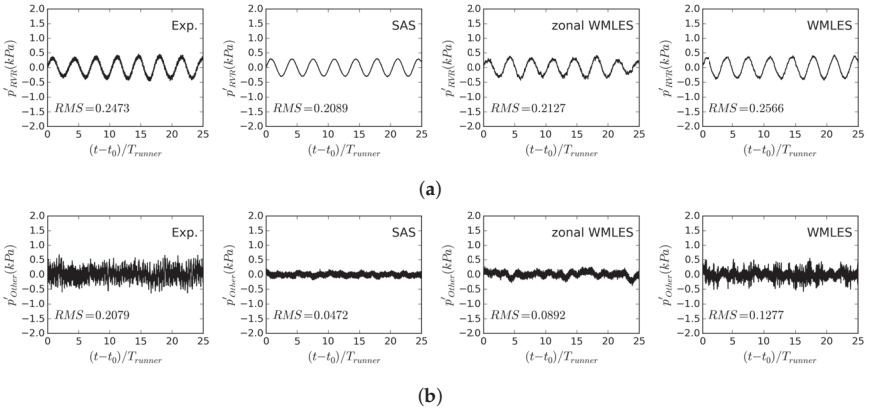

Figure 9. Different components of pressure fluctuations at Probe 2 (shown in Figure 2a), (**a**) due to the rotation of RVR, (**b**) due to other sources than RVR.

The comparison between the RMS values of the pressure fluctuations due to the RVR in Figure 9a showed that the predicted value from the WMLES simulation is closer to the experimental value than the values using the other turbulence modeling techniques. In order to investigate the reason for this and also study the effect of turbulence modeling on the pressure field in the draft tube, Figure 10 shows the phase-averaged pressure over Line 1 with the different turbulence modeling techniques. The core of the RVR, where the pressure is low, passes Line 1 at instances A and B. It can be seen that the RVR core pressure drops more in the WMLES results compared with the results of the other turbulence modeling techniques. A more quantitative comparison is shown in Figure 10d, at time instance B only. It can be seen that the pressure field far from the vortex core ($y > 50$ mm) is almost the same in all simulations. However, the pressure in the near-field of the RVR ($y < 0$ mm) is affected by the choice of turbulence modeling technique. In the WMLES results, the minimum pressure in the near-field is lower and the extent of the low pressure region is larger and slightly closer to the nearest wall compared with the other two results. This can explain the higher RMS level of the pressure fluctuations due to the RVR in the WMLES simulation as shown in Figure 9a. It should particularly be stressed that capturing the correct pressure drop in the RVR is very important for cavitating simulations as this pressure drop is the driving force of the cavitation formation. In WMLES simulations, where a larger pressure drop can be captured, a larger volume of cavitation should be expected in cavitating simulations.

To explain the reason for the larger pressure drop in the RVR of the WMLES simulation, Figure 11 shows the phase-averaged normal velocity over Line 1 at time instance B that was shown in Figure 10. The center of the RVR approximately corresponds to $U_n = 0$ due to the rotating flow around the center of the RVR. The comparison between the numerical

results shows that the gradient of the normal velocity $\frac{\partial U_n}{\partial y}$ is larger around the center of the RVR in the WMLES result than with the other turbulence model techniques. This indicates that the swirling motion around the RVR in the WMLES simulation is stronger, which leads to the larger pressure drop shown in Figure 10.

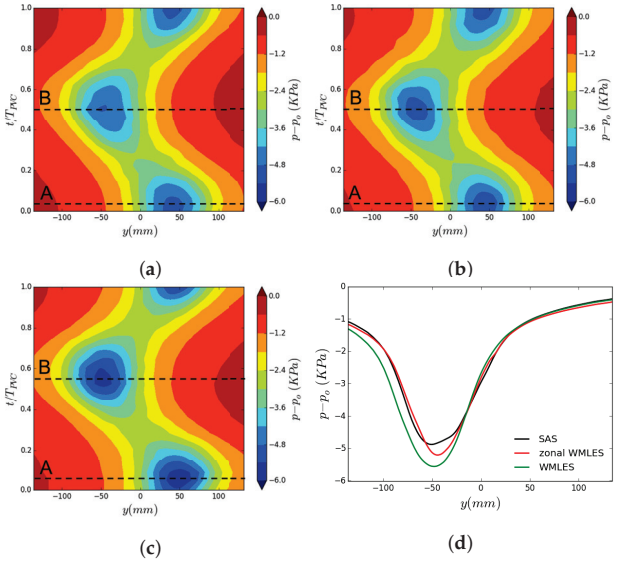

Figure 10. Phase-averaged pressure over Line 1 with different turbulence modeling techniques, (**a**) SAS, (**b**) zonal WMLES , (**c**) WMLES, (**d**) comparison over line at instance B. Instances A and B correspond to RVR passing Line 1.

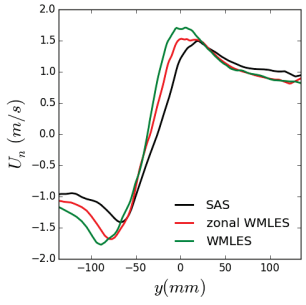

Figure 11. Phase-averaged distribution of the normal velocity over Line 1, for time instance B in Figure 10.

4.2. Effect of Cavitation

As mentioned in Section 3.1, cavitation simulations using WMLES are performed for three different cavitation numbers to study the effect of cavitation on the global quantities, the velocity profiles and the pressure fluctuations in the draft tube. It should be mentioned that since there are no experimental data for cavitating conditions in a Francis-99 turbine, no comparison is made between the simulation results and experimental ones. To show the extent of the cavitating region in these simulations, Figure 12 presents the cavitating part of the RVR using a blue iso-surface of $\alpha_v = 0.99$. This figure also shows the variation of the total volume of vapor in the RVR as well as a spectral analysis of this variation. It can be seen that the cavitation inception at $\sigma = 0.07$ happens at the root of the RVR near the runner crown. The total vapor content at this condition exhibits significant fluctuations,

indicating that the cavitation is highly unstable. The spectral analysis of the vapor volume variation shows that this instability in the cavity volume does not have any dominant frequency. By decreasing the cavitation number to $\sigma = 0.06$, the cavitation starts to incept in the small vortices further downstream the runner exit. Similar to the previous condition, the cavitation is unstable, although with a lower frequency. The spectral analysis indicates that although there is an increase in the PSD level of frequencies lower than $f = 3f_{runner}$, this increase does not lead to a dominant peak in the PSD level. By further decreasing the cavitation number to $\sigma = 0.05$, the cavitating region covers almost the entire root of the RVR near the runner exit. The variation of vapor volume indicates that there are fluctuations in the size of the cavitating region of the vortex. Unlike the other two cavitating conditions, the spectral analysis shows that these fluctuations have a dominant frequency at $f_3/f_{runner} = 0.43$.

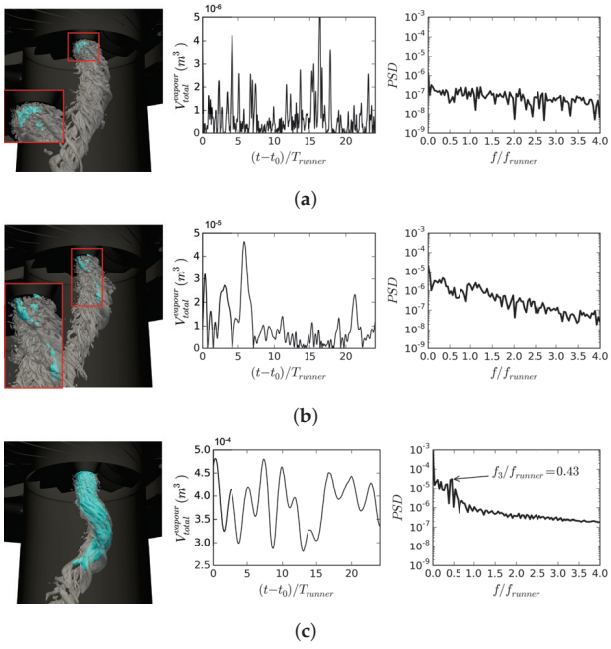

Figure 12. Cavitating regions in the RVR, shown by the blue iso-surface of $\alpha_v = 0.99$, for different cavitation numbers, (**a**) $\sigma = 0.07$, (**b**) $\sigma = 0.06$, (**c**) $\sigma = 0.05$, The RVR is shown by a transparent gray iso-surface of $Q = 5000\,s^{-2}$. Plots show variation of total volume of vapor (with different scales on y-axis for different cavitation numbers) in the RVR as well as spectral analysis of this variation.

Table 3 presents the global quantities in the form of torque, M_z, head, H, and efficiency η, for the different cavitation numbers and for the non-cavitating condition ($\sigma = \infty$). It can be seen that the cavitation number does not have any significant effect on these quantities, as the maximum variation in these quantities with respect to the cavitation number is less than 0.2 percent. This is expected, as the studied cavitation numbers are far from the cavitation breakdown for the studied turbine [48].

Table 3. Effect of cavitation number on the torque, M_z, head, H, and efficiency η.

σ	∞	**0.07**	**0.06**	**0.05**
M_z (Nm)	439.68	439.02	439.00	438.99
H (m)	12.48	12.46	12.46	12.46
η	89.58	89.61	89.60	89.60

To study the effect of cavitation on the velocity field, Figure 13 shows the time-averaged velocity profiles on Lines 1–3 (shown in Figure 2) for different cavitation numbers. It can be seen that cavitation does not have any effect on these velocity profiles for $\sigma = 0.06$ and $\sigma = 0.07$. For these conditions, the size of the region with low values of absolute axial velocity is almost identical to the size of this region in the non-cavitating condition. In the fully cavitating RVR in the simulation with $\sigma = 0.05$, however, the velocity profiles are slightly affected by the presence of cavitation. This effect is more dominant in the profiles for Line 1 as this line is closer to the cavitating part of the RVR.

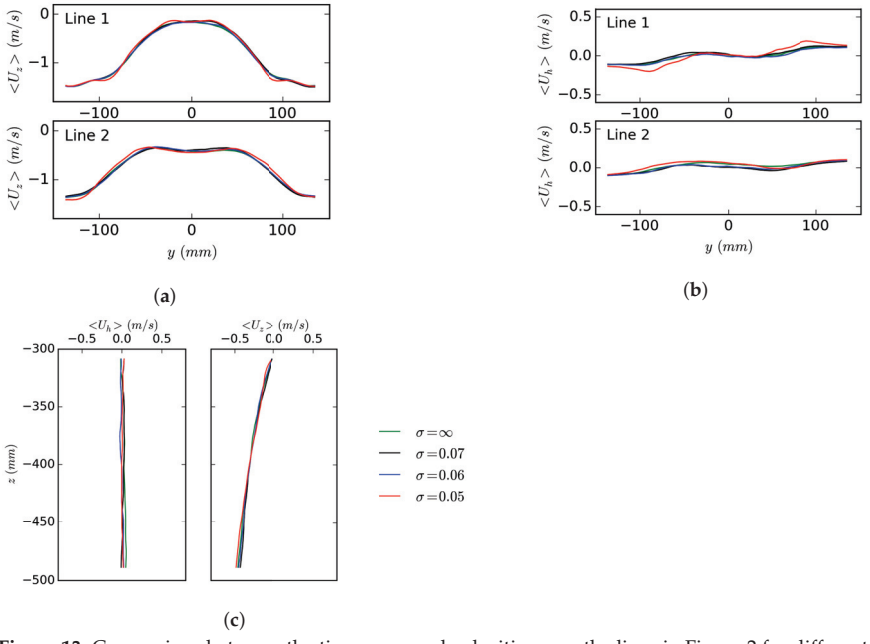

Figure 13. Comparison between the time-averaged velocities over the lines in Figure 2 for different cavitation numbers. (**a**) Averaged axial velocity over Lines 1 and 2. (**b**) Averaged horizontal velocity over Lines 1 an 2. (**c**) Averaged horizontal (left) and axial (right) velocities over Line 3.

In order to investigate the effects of cavitation on the structure of the RVR and the instantaneous velocity field, Figure 14 presents the iso-surface of the Q criterion (left plots) and the history of the axial velocity over Line 1 for one period of vortex rotation (right plots) for different cavitation numbers. The iso-surface of the Q-criterion shows that similar to the non-cavitating condition, shown in Figure 4c, the RVR of the cavitating conditions consists of small vortices and there is a reverse flow at the location of these small vortices. The plots of history of the axial velocity on Line 1 show that streaks are formed as these vorticies and their reverse flows pass Line 1. A comparison between the results for the different cavitation numbers shows that the reversed flow in these streaks is highly affected by the presence of cavitation. At $\sigma = 0.07$, for which the amount of cavitation in the RVR is small, the reverse flow in the streaks is quite similar to the non-cavitating condition (see Figure 4c). As the amount of cavitation increases, for $\sigma = 0.06$ and $\sigma = 0.05$, the reverse flow in the streaks becomes weaker.

Figure 15a shows the pressure fluctuations at Probe 2 for different cavitation numbers, including their RMS values. It can be seen that the inception of cavitation (at $\sigma = 0.07$) leads to spikes in the pressure fluctuations, which is due to the collapse of the cavitation region. This can be seen in Figure 15b, where the total vapor volume decreases to near-zero values at the time of the pressure spikes. Due to these spikes, the RMS of the pressure fluctuations increases by 54% compared to the non-cavitating case. It should be noted that the spikes

are truncated in the plot in order to keep a scale that still shows the variations due to the RVR. By slightly increasing the amount of cavitation (for $\sigma = 0.06$), the spikes are not as frequent as those at $\sigma = 0.07$, which indicates that the cavitation region is less frequently entirely collapsing. This is confirmed in Figure 12b, where the total volume fraction goes to zero less frequently than in Figure 12a. There is however a further increase in the RMS value as the cavitation number is decreased from $\sigma = 0.07$ to $\sigma = 0.06$, indicating that the collapses of the larger cavitation regions give higher pressure pulses. Again, it should be noted that the spikes are truncated in the plot. In the case of the fully cavitating RVR, at $\sigma = 0.05$, most of the spikes are gone. This indicates that the cavitation region never collapses entirely (confirmed in Figure 12c), and that the collapses of smaller cavitation regions in the freestream give much smaller pressure spikes. This leads to smaller RMS values. On the other hand, it can clearly be seen that the variations due to the RVR is much less periodic at $\sigma = 0.05$ than for the other cavitation numbers, indicating that the general flow features are influenced to a larger extent. In accordance with the increase in the RMS value compared to the non-cavitating condition, the cavitation increases the amplitude of the variations due to the RVR as a major contributor to the RMS value.

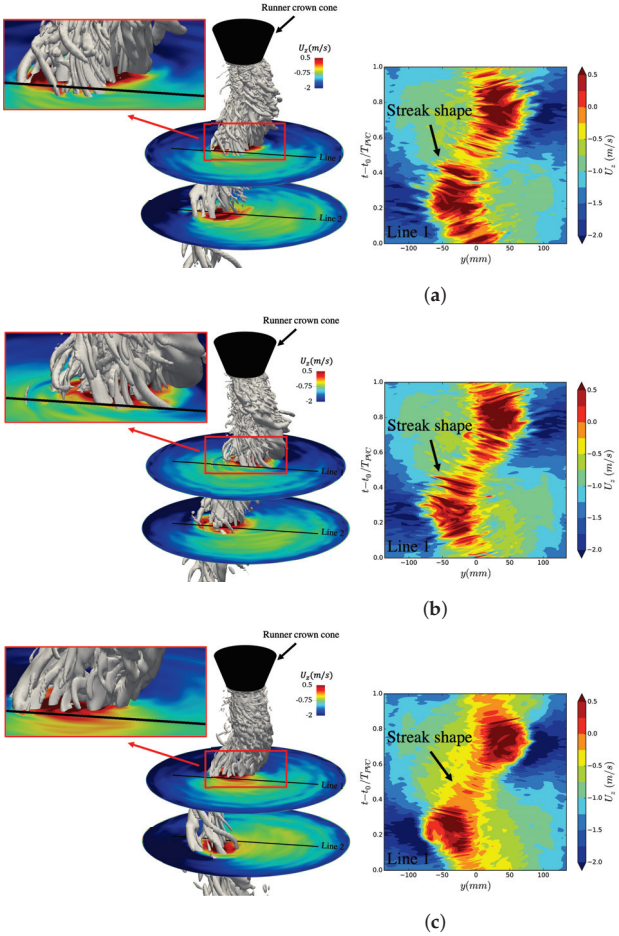

Figure 14. RVR, visualized by $Q = 5000\,\mathrm{s}^{-2}$ (left), and its effects on the velocity at Line 1 during one cycle (right) for different cavitation numbers, (**a**) $\sigma = 0.07$, (**b**) $\sigma = 0.06$, (**c**) $\sigma = 0.05$.

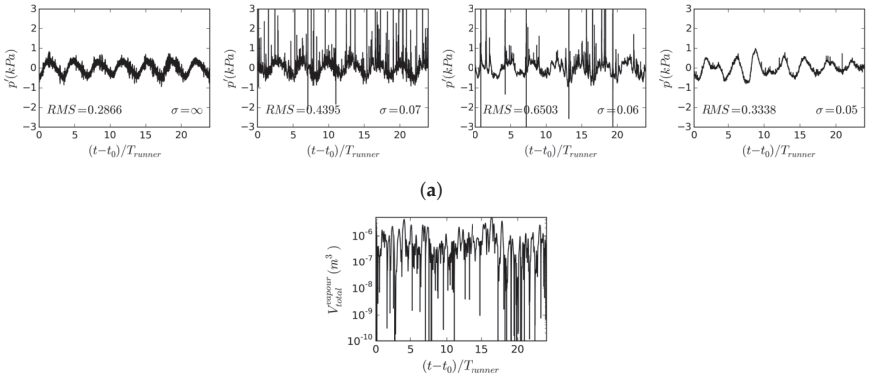

(**a**)

(**b**)

Figure 15. Pressure fluctuations and total volume of vapor in the cavitating simulations, (**a**) pressure fluctuations at Probe 2 (shown in Figure 2a) for different cavitation numbers, (**b**) total volume of vapor for $\sigma = 0.07$.

Figure 16 shows spectral analyses of the pressure fluctuations at Probe 2 for the different cavitation numbers, as well as the phase difference between the pressure fluctuations at Probes 2 and 3. The spectral analyses show that the dominant frequency, $f_1/f_{runner} = 0.3$, is not affected by the presence of cavitation. As mentioned earlier, this frequency is related to the frequency of the RVR rotation. A comparison between the non-cavitating and cavitating conditions indicates that cavitation mostly affects the PSD level of the higher frequencies rather than that of the relatively low RVR frequency. For $\sigma = 0.07$, at cavitation inception, an increase can be seen in the PSD level of frequencies larger than $2.0f_{runner}$. By further increasing the amount of cavitation, at $\sigma = 0.06$, the increase in the PSD level of the pressure fluctuations happens already at $f > f_{runner}$. At $\sigma = 0.05$, the increase in the PSD level approaches the f_1 frequency, with a local peak at $f_3/f_{runner} = 0.43$, and the PSD level of the higher frequencies again decreases. The frequency of the additional peak is the same as the dominant frequency of the vapor volume fluctuations for this cavitation number, as shown in Figure 12c. The phase difference between the pressure fluctuations at Probes 2 and 3, shown in Figure 16b, shows that for the frequencies where there is an increase in the PSD level due to cavitation, the phase difference is highly reduced (approaching zero). This means that the increased pressure fluctuations in these frequencies are synchronous.

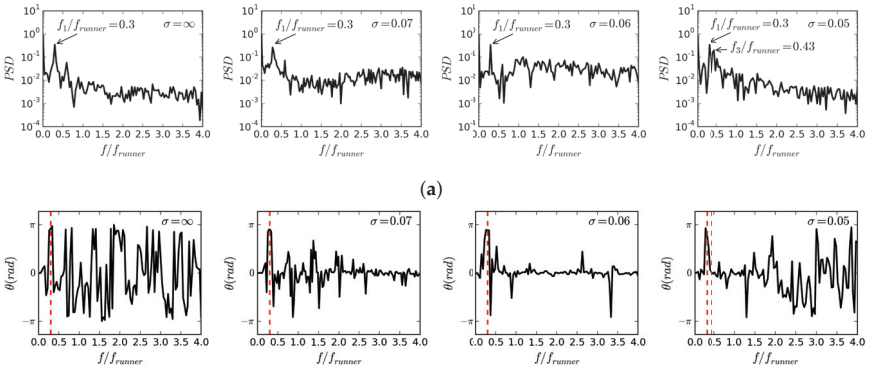

(**a**)

(**b**)

Figure 16. Spectral analysis of the pressure fluctuations in draft tube for different cavitation numbers. (**a**) Frequency analysis of the pressure fluctuations at Probe 2. (**b**) Phase difference between the pressure fluctuations at Probes 2 and 3.

Figure 17 shows the effects of cavitation on the different components of the pressure fluctuations and their RMS values, decomposed according to Equation (22). It can be seen that the cavitation has insignificant effects on the RMS values of the pressure fluctuations due to the RVR, as the maximum difference between the RMS values for the different cavitation numbers is around 7%. However, the RMS values of the other sources are highly affected by the presence of cavitation. Similar to the trends shown in Figure 15a, the RMS of the synchronous pressure fluctuations first increases as the amount of cavitation increases ($\sigma = 0.07$ and $\sigma = 0.06$), and then decreases when the RVR is fully cavitating ($\sigma = 0.05$).

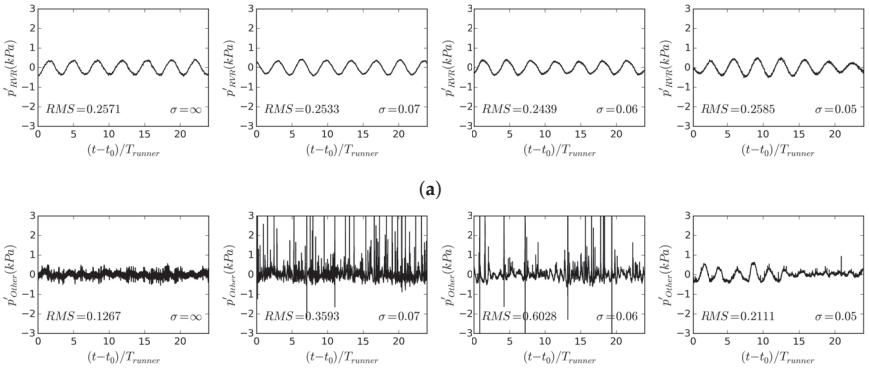

Figure 17. Different components of pressure fluctuations at Probe 2 shown in Figure 2a in the simulations with different cavitation numbers, (**a**) the pressure fluctuations due the rotation of RVR, (**b**) the pressure fluctuations due to other sources than RVR.

Figure 18 shows the effects of cavitation on the forces exerted on the runner and draft tube in the frequency domain. For the runner, only the z-component of the force (the blue curve) is affected by the cavitation, while for the draft tube, both the x- and z-components of the forces (red and blue curves, respectively) are affected by the cavitation. The trends of the changes due to cavitation, however, are the same for these affected force components, and they are quite similar to the trends for the pressure fluctuations shown in Figure 16a. At $\sigma = 0.07$, where the amount of cavitation is small, there is an increase in the PSD level of the high-frequency fluctuations of the affected force components. The same increase can be seen for $\sigma = 0.06$, although the increase in the PSD level starts to appear already at lower frequencies. At $\sigma = 0.05$, this increase in PSD level leads to the dominant frequency $f_3/f_{runner} = 0.43$, which is the same as the dominant frequency of the vapor volume fluctuations as shown in Figure 12c. It should be mentioned that the changes in the forces discussed here are caused by cavitation-induced pressure fluctuations, which are shown to be synchronous in Figure 16. Due to the synchronous nature of these pressure fluctuations, they affect only the forces in the directions where the geometry is asymmetrical. In the symmetrical directions, the changes in the forces due to these pressure fluctuations cancel each other out. For the runner, the geometry is almost symmetrical with respect to the x- and y-directions, and therefore, the cavitation-induced pressure fluctuations can affect only the forces in the z-direction. In the draft tube, however, the geometry is symmetric only with respect to the y-direction, and the effects of cavitation can be seen both in the x- and z-components of the forces.

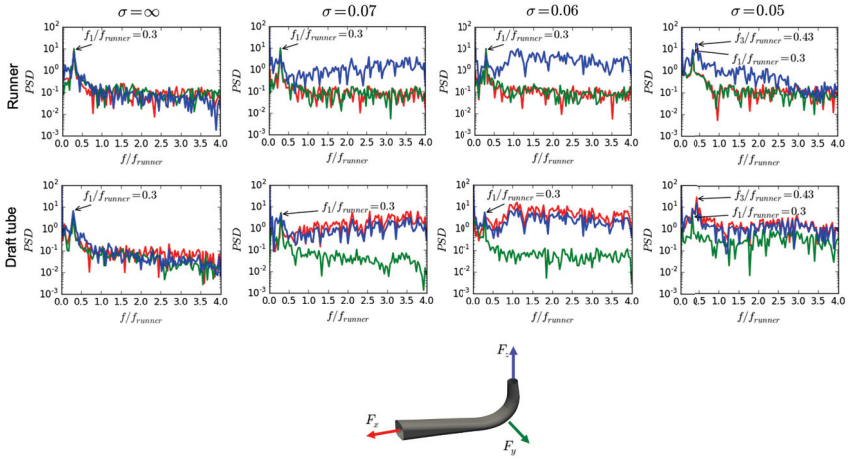

Figure 18. Effect of cavitation on the forces exerted on the runner and draft tube. Curve colors correspond to colors of coordinate directions.

5. Conclusions

In this work, we examine non-cavitating and cavitating RVR (Rotating Vortex Rope) in the Francis-99 turbine model using scale-resolving approaches. The non-cavitating simulations are performed using the SST-SAS, zonal wall-modeled LES and wall-modeled LES (WM) approaches, and the results are compared with the experimental data made available by the Francis-99 workshop. Furthermore, cavitating simulations are conducted for three cavitation numbers using the WMLES approach. The results from these simulations are used to study the effects of cavitation on the flow features, such as the velocity distribution and pressure fluctuations in the draft tube, and the forces acting on the draft tube and the runner.

The comparison between the results of the non-cavitating simulations and the experimental data reveals that the averaged velocity profiles and the pressure fluctuations predicted by the WMLES approach are in better agreement with the experimental data compared with the SST-SAS and zonal WMLES approaches. It is shown for the first time that the better velocity prediction is related to a correctly predicted rotating path of the RVR in the WMLES simulation. In the SST-SAS and zonal WMLES simulations, the RVR rotates on a path which is closer to the center of the draft tube as compared to the WMLES simulation and experiment. This yields an over-prediction of the influence of the RVR on the time-averaged velocity profile near the center of the draft tube. The comparison between the numerical results and the experimental data also shows that all methods under-predict the RMS values of the pressure fluctuations in the experiment, although the predicted RMS of the pressure fluctuations using the WMLES approach is closest to the experimental value. Using a detailed analysis of the pressure fluctuations in the simulations and experiment, the reason for the difference between the numerical and experimental values is shown to be related to a synchronous type of fluctuations only appearing in the experimental data, with a dominant frequency of around 2.8 times the frequency of the runner. An analysis of the pressure fluctuations in the experimental data shows that this synchronous pressure fluctuations can be seen also at the BEP and HL conditions, which suggests that these synchronous pressure fluctuations are created by a component in the system rather than the RVR. Such a finding has not been reported in the previous studies on the Francis-99 turbine. It is also shown that the WMLES simulation can capture a larger pressure drop in the center of the RVR compared to the other two approaches, which is shown to be due to the larger swirling velocity around the RVR in the WMLES simulation.

The results from the cavitating simulations reveal that cavitation slightly affects the average velocity profiles in the draft only if there is a large amount of cavitation in the RVR.

They also show that the presence of cavitation damps out the instantaneous reverse flow in the small vortices in the RVR. The pressure fluctuations are also shown to be significantly affected by the presence of cavitation. Cavitation induces synchronous pressure fluctuations with a frequency larger than the frequency of the RVR. Capturing these synchronous pressure fluctuations in simulations has previously not been reported in the literature. When the amount of cavitation in the RVR is small, these fluctuations have a broadband high-frequency spectrum, while in the case of a fully cavitating RVR, they have a dominant frequency close to the dominant frequency of the RVR. The analysis of the forces reveals that the cavitation-induced pressure fluctuations have different effects on the forces exerted on the runner and draft tube. In the runner, the presence of cavitation induces significant force fluctuations only in the direction aligned with the rotational axis of the runner, while the force fluctuations in the draft tube are additionally affected in the direction of the bend. This finding can be used to design a method to detect cavitation in the turbine based on the direction of the vibrations in the draft tube and runner.

Author Contributions: Conceptualization, M.H.A., R.E.B. and H.N.; methodology, M.H.A.; validation, M.H.A.; Analysis, M.H.A.; investigation, M.H.A.; writing—original draft preparation, M.H.A.; writing—review and editing, R.E.B. and H.N.; supervision, R.E.B. and H.N.; project administration, R.E.B. and H.N.; funding acquisition, R.E.B. and H.N. All authors have read and agreed to the published version of the manuscript.

Funding: The work was funded by Chalmers Energy Area of Advance and was carried out as a part of the "Swedish Hydropower Centre - SVC". SVC is established by the Swedish Energy Agency, EnergiForsk and Svenska Kraftnät together with Luleå University of Technology, The Royal Institute of Technology, Chalmers University of Technology, and Uppsala University. The computations were enabled by resources provided by the Swedish National Infrastructure for Computing (SNIC) at NSC and C3SE partially funded by the Swedish Research Council through grant agreement no. 2018e05973. The investigated test case is provided by NTNU, Norwegian University of Science and Technology, under the Francis-99 workshop series.

Data Availability Statement: The data that support the findings of this study can be available from the corresponding author upon reasonable request.

Conflicts of Interest: The authors declare no conflict of interest.

References

1. Rheingans, W. Power swings in hydroelectric powerplants. *Trans. ASME* **1940**, *62*, 171–184.
2. Valentín, D.; Presas, A.; Egusquiza, E.; Valero, C.; Egusquiza, M.; Bossio, M. Power swing generated in Francis turbines by part load and overload instabilities. *Energies* **2017**, *10*, 2124.
3. Arndt, R.E.; Voigt, R.L., Jr.; Sinclair, J.P.; Rodrique, P.; Ferreira, A. Cavitation erosion in hydroturbines. *J. Hydraul. Eng.* **1989**, *115*, 1297–1315. [CrossRef]
4. Avellan, F. *Introduction to Cavitation in Hydraulic Machinery*; Technical Report; Politehnica University of Timişoara: Timişoara, Romania, 2004. [CrossRef]
5. Brennen, C. *Cavitation and Bubble Dynamics*; Cambridge University Press: Cambridge, UK, 2014.
6. Nishi, M.; Kubota, T.; Matsunaga, S.; Senoo, Y. Study on swirl flow and surge in an elbow type draft tube. In Proceedings of the 10th IAHR Symposium on Hydraulic Machinery and Cavitation, Tokyo, Japan, 28 September–2 October 1980; Volume 1, pp. 557–568.
7. Iliescu, M.; Ciocan, G.; Avellan, F. Analysis of the cavitating draft tube vortex in a Francis turbine using particle image velocimetry measurements in two-phase flow. *J. Fluids Eng.* **2008**, *130*, 021105.
8. Favrel, A.; Müller, A.; Landry, C.; Yamamoto, K.; Avellan, F. LDV survey of cavitation and resonance effect on the precessing vortex rope dynamics in the draft tube of Francis turbines. *Exp. Fluids* **2016**, *57*, 1–16. [CrossRef]
9. Arpe, J.; Nicolet, C.; Avellan, F. Experimental evidence of hydroacoustic pressure waves in a Francis turbine elbow draft tube for low discharge conditions. *J. Fluids Eng.* **2009**, *131*, 081102. [CrossRef]
10. Landry, C.; Favrel, A.; Müller, A.; Nicolet, C.; Avellan, F. Local wave speed and bulk flow viscosity in Francis turbines at part load operation. *J. Hydraul. Res.* **2016**, *54*, 185–196. [CrossRef]
11. Ciocan, G.; Iliescu, M.S.; Vu, T.C.; Nennemann, B.; Avellan, F. Experimental study and numerical simulation of the FLINDT draft tube rotating vortex. *J. Fluids Eng.* **2007**, *12*, 146–158. [CrossRef]
12. Liu, S.; Zhang, L.; Nishi, M.; Wu, Y. Cavitating turbulent flow simulation in a Francis turbine based on mixture model. *J. Fluids Eng.* **2009**, *131*, 051302 . [CrossRef]

13. Ruprecht, A.; Helmrich, T.; Aschenbrenner, T.; Scherer, T. Simulation of vortex rope in a turbine draft tube. In Proceedings of the 21st IAHR Symposium on Hydraulic Machinery and Systems, Lausanne, Switzerland, 9–12 September 2002; Volume 1, pp. 259–266. [CrossRef]
14. Yu, A.; Zou, Z.; Zhou, D.; Zheng, Y.; Luo, X. Investigation of the correlation mechanism between cavitation rope behavior and pressure fluctuations in a hydraulic turbine. *Renew. Energy* **2020**, *147*, 1199–1208.
15. Jošt, D.; Škerlavaj, A.; Morgut, M.; Nobile, E. Numerical prediction of cavitating vortex rope in a draft tube of a Francis turbine with standard and calibrated cavitation model. *J. Phys. Conf. Ser.* **2017**, *813*, 012045. [CrossRef]
16. Salehi, S.; Nilsson, H.; Lillberg, E.; Edh, N. An in-depth numerical analysis of transient flow field in a Francis turbine during shutdown. *Renew. Energy* **2021**, *179*, 2322–2347. [CrossRef]
17. Salehi, S.; Nilsson, H. Flow-induced pulsations in Francis turbines during startup-A consequence of an intermittent energy system. *Renew. Energy* **2022**, *188*, 1166–1183. [CrossRef]
18. Foroutan, H.; Yavuzkurt, S. Flow in the Simplified Draft Tube of a Francis Turbine Operating at Partial Load—Part I: Simulation of the Vortex Rope. *J. Appl. Mech.* **2014**, *81*, 061010. [CrossRef]
19. Minakov, A.; Platonov, D.; Dekterev, A.; Sentyabov, A.; Zakharov, A. The analysis of unsteady flow structure and low frequency pressure pulsations in the high-head Francis turbines. *Int. J. Heat Fluid Flow* **2015**, *53*, 183–194. [CrossRef]
20. Rajan, G.; Cimbala, J. Computational and theoretical analyses of the precessing vortex rope in a simplified draft tube of a scaled model of a francis turbine. *J. Fluids Eng.* **2017**, *139*, 021102. [CrossRef]
21. Guo, Y.; Kato, C.; Miyagawa, K. Large-eddy simulation of non-cavitating and cavitating flows in the draft tube of a Francis turbine. *Seisan Kenkyu* **2007**, *59*, 83–88. [CrossRef]
22. Pacot, O.; Matsui, J.; Suzuki, T.; Tani, K.; Kato, C. LES Computation of the Cavitating Vortex Rope in the Draft Tube of a Francis Turbine. In Proceedings of the 13th Asian International Conference on Fluid Machinery, Tokyo, Japan, 7–10 September 2015.
23. Bensow, R.; Bark, G. Implicit LES predictions of the cavitating flow on a propeller. *J. Fluids Eng.* **2010**, *132*, 041302.
24. Asnaghi, A.; Feymark, A.; Bensow, R. Improvement of cavitation mass transfer modeling based on local flow properties. *Int. J. Multiph. Flow* **2017**, *93*, 142–157. [CrossRef]
25. Asnaghi, A. Developing Computational Methods for Detailed Assessment of Cavitation on Marine Propellers. Licentiate Thesis, Chalmers University of Technology, Goteborg, Sweden, 2015. [CrossRef]
26. Weller, H.; Tabor, G.; Jasak, H.; Fureby, C. A tensorial approach to computational continuum mechanics using object-oriented techniques. *Comput. Phys.* **1998**, *12*, 620–631.
27. Sauer, J. Instationär Kavitierende strömungen-Ein Neues Modell, Basierend auf front Capturing (VoF) und Blasendynamik. Ph.D. Thesis, Karlsruhe Institute of Technology, Karlsruhe, Germany, 2000. [CrossRef]
28. Menter, F.; Egorov, Y. A scale adaptive simulation model using two-equation models. In Proceedings of the 43rd AIAA Aerospace Sciences Meeting and Exhibit, Reno, NV, USA, 10–13 January 2005; p. 1095.
29. Egorov, Y.; Menter, F. Development and application of SST-SAS turbulence model in the DESIDER project. In *Advances in Hybrid RANS-LES Modelling*; Springer: Berlin/Heidelberg, Germany, 2008; pp. 261–270.
30. Menter, F. Zonal two equation kw turbulence models for aerodynamic flows. In Proceedings of the 23rd Fluid Dynamics, Plasmadynamics, and Lasers Conference, Orlando, FL, USA, 6–9 July 1993; p. 2906.
31. Nicoud, F.; Ducros, F. Subgrid-scale stress modelling based on the square of the velocity gradient tensor. *Flow Turbul. Combust.* **1999**, *62*, 183–200.
32. Weller, H. Controlling the computational modes of the arbitrarily structured C grid. *Mon. Weather. Rev.* **2012**, *140*, 3220–3234. [CrossRef]
33. Schnerr, G.H.; Sauer, J. Physical and numerical modeling of unsteady cavitation dynamics. In Proceedings of the Fourth International Conference on Multiphase Flow, New Orleans, LA, USA, 27 May–1 June 2001; Volume 1. [CrossRef]
34. Trivedi, C.; Cervantes, M.; Gandhi, B.; Dahlhaug, O. Experimental and numerical studies for a high head Francis turbine at several operating points. *J. Fluids Eng.* **2013**, *135*, 111102.
35. Wallimann, H.; Neubauer, R. Numerical study of a high head Francis turbine with measurements from the Francis-99 project. *J. Phys. Conf. Ser.* **2015**, *579*, 012003. [CrossRef]
36. Mössinger, P.; Jester-Zürker, R.; Jung, A. Investigation of different simulation approaches on a high-head Francis turbine and comparison with model test data: Francis-99. *J. Phys. Conf. Ser.* **2015**, *579*, 012005. [CrossRef]
37. Jošt, D.; Škerlavaj, A.; Morgut, M.and Mežnar, P.; Nobile, E. Numerical simulation of flow in a high head Francis turbine with prediction of efficiency, rotor stator interaction and vortex structures in the draft tube. *J. Phys. Conf. Ser.* **2015**, *579*, 012006. [CrossRef]
38. Aakti, B.; Amstutz, O.; Casartelli, E.; Romanelli, G.; Mangani, L. On the performance of a high head Francis turbine at design and off-design conditions. *J. Phys. Conf. Ser.* **2015**, *579*, 012010. [CrossRef]
39. Yaping, Z.; Weili, L.; Hui, R.; Xingqi, L. Performance study for Francis-99 by using different turbulence models. *J. Phys. Conf. Ser.* **2015**, *579*, 012012. [CrossRef]
40. Huuva, T. Large Eddy Simulation of Cavitating and Non-Cavitating Flow. Ph.D. Thesis, Chalmers University of Technology, Göteborg, Sweden, 2008. [CrossRef]
41. Lu, N.; Bensow, R.E.; Bark, G. LES of unsteady cavitation on the delft twisted foil. *J. Hydrodyn. Ser. B* **2010**, *22*, 784–791.

42. Wilhelm, S.; Balarac, G.; Métais, O.; Ségoufin, C. Analysis of head losses in a turbine draft tube by means of 3D unsteady simulations. *Flow Turbul. Combust.* **2016**, *97*, 1255–1280. [CrossRef]
43. Čelič, D.; Ondráčka, H. The influence of disc friction losses and labyrinth losses on efficiency of high head Francis turbine. *J. Phys. Conf. Ser.* **2015**, *579*, 012007. [CrossRef]
44. Cervantes, M.; Trivedi, C.; Dahlhaug, O.; Nielsen, T. Francis-99 Workshop 2: Transient operation of Francis turbines. *J. Phys. Conf. Ser.* **2017**, *782*, 011001. [CrossRef]
45. Salehi, S.; Nilsson, H. Effects of uncertainties in positioning of PIV plane on validation of CFD results of a high-head Francis turbine model. *Renew. Energy* **2022**, *193*, 57–75.
46. Welch, P. The use of fast Fourier transform for the estimation of power spectra: A method based on time averaging over short, modified periodograms. *IEEE Trans. Audio Electroacoust.* **1967**, *15*, 70–73. [CrossRef]
47. Favrel, A.; Müller, A.; Landry, C.; Yamamoto, K.; Avellan, F. Study of the vortex-induced pressure excitation source in a Francis turbine draft tube by particle image velocimetry. *Exp. Fluids* **2015**, *56*, 1–15. [CrossRef]
48. Trivedi, C. (Waterpower Laboratory, Norwegian University of Science and Technology, Trondheim, Norway). Personal communication, 2020. [CrossRef]

fluids

MDPI

Article

A Generalized Diffusion Equation: Solutions and Anomalous Diffusion

Ervin K. Lenzi [1,2,*], Aloisi Somer [1], Rafael S. Zola [3], Luciano R. da Silva [2,4] and Marcelo K. Lenzi [5]

[1] Departamento de Física, Universidade Estadual de Ponta Grossa, Av. Gen. Carlos Cavalcanti 4748, Ponta Grossa 84030-900, PR, Brazil
[2] National Institute of Science and Technology for Complex Systems, Centro Brasileiro de Pesquisas Físicas, Rio de Janeiro 22290-180, RJ, Brazil
[3] Departamento de Física, Universidade Tecnológica Federal do Paraná, R. Marcílio Dias, 635, Apucarana 86812-460, PR, Brazil
[4] Departamento de Física, Universidade Federal do Rio Grande do Norte, Natal 59078-900, RN, Brazil
[5] Departamento de Engenharia Química, Universidade Federal do Paraná, Curitiba 80060-000, PR, Brazil
* Correspondence: eklenzi@uepg.br

Abstract: We investigate the solutions of a generalized diffusion-like equation by considering a spatial and time fractional derivative and the presence of non-local terms, which can be related to reaction or adsorption–desorption processes. We use the Green function approach to obtain solutions and evaluate the spreading of the system to show a rich class of behaviors. We also connect the results obtained with the anomalous diffusion processes.

Keywords: fractional dynamics; heterogeneity; unusual spreading; diffusion process; flow

Citation: Lenzi, E.K.; Somer, A.; Zola, R.S.; da Silva, R.S.; Lenzi, M.K. A Generalized Diffusion Equation: Solutions and Anomalous Diffusion. *Fluids* **2023**, *8*, 34. https://doi.org/10.3390/fluids8020034

Academic Editor: Mehrdad Massoudi

Received: 30 November 2022
Revised: 7 January 2023
Accepted: 10 January 2023
Published: 17 January 2023

1. Introduction

Fractional calculus has quickly become a new efficient mathematical tool to analyze different properties of a given system and connect them with experimental results. A simple extension of the differential operators incorporating non-integer indexes has serious consequences, connecting the formalism with memory effects, long-range correlations, and many other features characterizing complex systems. In this manner, it has brought great insights into many fields of science [1–6]. One of them occurs for the diffusion processes, which have been found through fractional calculus a suitable approach to incorporate several effects which are not suitably described in terms of the classical integer order calculus. For instance, infiltration in porous building materials [7], the electrical response of electrolytic cells [6,8], amorphous semiconductors [9], and micellar solutions [10]. In these situations, there is a nonlinear time dependence exhibited by the mean-square displacement, which, in general, is characterized by $\langle (x - \langle x \rangle)^2 \rangle \sim t^{\alpha}$, where α characterized the diffusion, e.g., $\alpha < 1$, $\alpha = 1$, and $\alpha > 1$ correspond to the sub-, usual, and superdiffusion, respectively. This behavior of the mean square displacement and effects related, e.g., non-Markovian processes and fractal structure has motivated the analysis of different approaches, which extend the usual approach, such as fractional diffusion equations [11–13], master equation [14,15], generalized Langevin equations [16], and random walks [17]. One noticeable point regarding these extensions is that the behavior of the solutions is characterized by power laws and stretched exponential for fractional differential operators. In particular, the previous scenarios concerning the diffusion on fractals have indicated that the asymptotic form of the propagator, such as the Sierpinski gasket, is essentially in this form [11,18]. A similar situation is also found in fluid flow through porous media [19–21]. Other applications can be found in transport in the porous pellet [22], transport of chloride in concrete [23], and oxidation behaviors of needle-punched carbon/carbon composites [24].

Here, we consider the following extension of the diffusion equation:

$$\frac{\partial}{\partial t}\rho(x,t) = {}_0\mathcal{D}_t^{\gamma}\int_0^{\mu} d\overline{\mu}\, p(\overline{\mu}) D_x^{\overline{\mu},\eta}\rho(x,t) + \int_0^t dt' \Lambda(t-t')\rho(x,t') \,, \tag{1}$$

with $1 \leq \mu \leq 2$, $-1 < \eta$, $p(\overline{\mu})$ is a distribution, ${}_0\mathcal{D}_t^{\gamma}(\cdots)$ is a fractional time operator, and $D_x^{\overline{\mu},\eta}(\cdots)$ is a spatial fractional operator [12,25]. The last term can be related to different processes, such as absorption and adsorption–desorption, depending on the choice of the kernel $\Lambda(t)$. It can also be related to reaction processes of the first order, i.e., irreversible reaction processes or reversible processes depending on the choice of $\Lambda(t)$. The fractional time operator ${}_0\mathcal{D}_t^{\gamma}(\cdots)$ is defined in terms of a generalized kernel $\mathcal{K}_{\gamma}(t)$ as follows:

$${}_0\mathcal{D}_t^{\gamma}\rho(x,t) = \frac{\partial}{\partial t}\int_0^t dt' \mathcal{K}_{\gamma}(t-t')\rho(x,t') \,. \tag{2}$$

Note that depending on the choice of $\mathcal{K}_{\gamma}(t)$ in the previous equation, we may connect it to different integrodifferential operators with singular or non-singular kernels. One of them is the Riemann–Liouville fractional operator, i.e., $\mathcal{K}_{\bar{\gamma}}(t) = t^{-\bar{\gamma}}/\Gamma(1-\bar{\gamma})$ [26], which implies

$$\frac{\partial^{\bar{\gamma}}}{\partial t^{\bar{\gamma}}}\rho(x,t) = \frac{1}{\Gamma(1-\bar{\gamma})}\frac{\partial}{\partial t}\int_0^t dt' \frac{1}{(t-t')^{\bar{\gamma}}}\rho(x,t'), \tag{3}$$

another one is the Fabrizio–Caputo fractional operator, for $\mathcal{K}_{\bar{\gamma}}(t) = \mathcal{N}_{\bar{\gamma}} e^{-\frac{\bar{\gamma}}{1-\bar{\gamma}}t}/(1-\bar{\gamma})$, i.e.,

$$\frac{\partial^{\bar{\gamma}}}{\partial t^{\bar{\gamma}}}\rho(x,t) = \frac{\mathcal{N}_{\bar{\gamma}}}{1-\bar{\gamma}}\frac{\partial}{\partial t}\int_0^t dt' e^{-\frac{\bar{\gamma}}{1-\bar{\gamma}}(t-t')}\rho(x,t') \,, \tag{4}$$

or the Atangana–Baleanu fractional operator, for $\mathcal{K}_{\bar{\gamma}}(t) = \mathcal{N}_{\bar{\gamma}} E_{\bar{\gamma}}(-\bar{\gamma}t^{\bar{\gamma}}/(1-\bar{\gamma}))/(1-\bar{\gamma})$, given by

$$\frac{\partial^{\bar{\gamma}}}{\partial t^{\bar{\gamma}}}\rho(x,t) = \frac{\mathcal{N}_{\bar{\gamma}}}{1-\bar{\gamma}}\frac{\partial}{\partial t}\int_0^t dt' E_{\bar{\gamma}}\left(-\frac{\bar{\gamma}}{1-\bar{\gamma}}(t-t')^{\bar{\gamma}}\right)\rho(x,t'), \tag{5}$$

where $\mathcal{N}_{\bar{\gamma}}$ is a normalization constant [27–29]. These operators may be related to different scenarios in connection with anomalous diffusion, which implies memory effects, long-range correlation, and fractal structures, among others. In particular, these fractional operators have been used in many contexts such as boundary value problems [30,31], electric circuits [32,33], and electrical impedance [34,35] (see also Refs. [36–38]). It is also possible to consider other kernels for Equation (2), with different implications for the relaxation processes (see, e.g., Refs. [39,40]).

Following the developments performed in Ref [12,25], the spatial operator is defined as follows:

$$\frac{1}{2}\int_{-\infty}^{\infty} dx \psi_{\pm,\eta}(x,k)\left(D_x^{\mu,\eta}\rho(x,t)\right) \equiv -|k|^{\mu+\eta}\widetilde{\rho}_{\pm}(k,t), \tag{6}$$

with the integral transform given by:

$$\frac{1}{2}\int_{-\infty}^{\infty} dx \psi_{\pm,\eta}(x,k)\rho(x,t) = \widetilde{\rho}_{\pm}(k,t) \,, \tag{7}$$

$$\frac{1}{2}\int_{-\infty}^{\infty} dk \psi_{\pm,\eta}(x,k)\widetilde{\rho}_{\pm}(k,t) = \rho(x,t), \tag{8}$$

where

$$\psi_{+,\eta}(x,k) = (|k||x|)^{\frac{1}{2}(1+\eta)} \mathrm{J}_{-\nu}\Big(2(|k||x|)^{\frac{1}{2}(2+\eta)}/(2+\eta)\Big) \quad \text{and} \tag{9}$$

$$\psi_{-,\eta}(x,k) = xk(|k||x|)^{\frac{1}{2}(1+\eta)-1} \mathrm{J}_{\nu}\Big(2(|k||x|)^{\frac{1}{2}(2+\eta)}/(2+\eta)\Big) \,, \tag{10}$$

where $\psi_{+,\eta}(x,k)$ and $\psi_{-,\eta}(x,k)$ refer to the odd and even functions, $\nu = (1+\eta)/(2+\eta)$, and $\mathrm{J}_{\nu}(x)$ is the Bessel function [6]. Equations (7) and (8) may be related to a generalized Hankel transform [41–44] and for $\mu = 2$, we can directly relate the fractional operator present in Equation (6) with standard differential operators as follows:

$$D_x^{2,\eta}(\cdots) \equiv \frac{\partial}{\partial x}\left\{ |x|^{-\eta} \frac{\partial}{\partial x}(\cdots) \right\} . \tag{11}$$

This case allows us to relate Equation (6) with a diffusion process in heterogeneous media. Such behaviors are also exhibited by diffusion-related problems, such as diffusion on fractals [45,46], turbulence [47,48], diffusion and reaction on fractals [49], and solute transport in fractal porous media [50], where the properties of the media promote an anomalous diffusion. In these scenarios, we have non-Gaussian distributions related to these processes and nonlinear behavior of the mean square displacement. Equation (11) also allows us to connect Equation (1), for $p(\mu) = \delta(\mu - 2)$, directly with the continuity equation with an additional term as follows:

$$\frac{\partial}{\partial t}\rho(x,t) + \frac{\partial}{\partial x}\mathcal{J}(x,t) = \int_0^t dt' \Lambda(t-t')\rho(x,t') \,, \tag{12}$$

with the current density given by

$$\mathcal{J}(x,t) = -\,{}_0\mathcal{D}_t^{\gamma}\left\{ |x|^{-\eta} \frac{\partial}{\partial x}\rho(x,t) \right\} . \tag{13}$$

Notice that $|x|^{-\eta}\partial_x(\cdots) \equiv (1+\eta)\partial_{|x|^{1+\eta}}(\cdots)$, i.e., it corresponds to a fractal derivative [51–53], respectively. Thus, the spatial fractional operator defined above by Equation (6) can be considered a mixing between the Riesz–Wely operator [11] and fractal operators [54]. This feature implies that the solutions of Equation (6) can be related to Lévy distributions and/or distributions with characteristics of stretched exponential. From the above discussion, Equation (1) has a particular case of several situations analyzed in different scenarios and allows analyzing the mixing between different effects on the diffusion process connected to these fractional operators. Further, the reaction term may be connected to different processes, particularly the stochastic resetting [55,56].

We aim to analyze Equation (1) by considering different scenarios. The first considers the absence of the non-local term, i.e., $\Lambda(t) = 0$. For this case, we obtain solutions by considering different spatial and time fractional operator choices. In particular, we also consider the case $p(\overline{\mu}) = \chi_{\mu}\delta(\overline{\mu} - \mu) + \chi_2\delta(\overline{\mu} - 2)$, where χ_{μ} and χ_2 are constants. After we incorporate the non-local term, i.e., $\Lambda(t) \neq 0$, in our analysis. We obtain exact solutions in the framework of Green's function approach for all cases. These formal developments are shown in Section 2. Section 3 discusses the main results and concludes with some remarks.

2. Fractional Dynamics and Diffusion

Let us start our discussion about Equation (1) by establishing the boundary conditions, which are $\lim_{x\to\pm\infty}\rho(x,t) = 0$. An arbitrary function represents the initial condition, i.e., $\rho(x,0) = \varphi(x)$. After establishing the boundary and the initial condition, Equation (1) in the absence of the non-local term is given by

$$\frac{\partial}{\partial t}\rho(x,t) = \,{}_0\mathcal{D}_t^{\gamma}\int_0^{\mu} d\overline{\mu}\, p(\overline{\mu}) D_x^{\overline{\mu},\eta}\rho(x,t) \,. \tag{14}$$

Formally, we can write the solution for this equation as follows:

$$\rho(x,t) = \int_{-\infty}^{\infty} dx' \mathcal{G}(x,x',t)\varphi(x') \,, \tag{15}$$

where the Green's function [57], $\mathcal{G}(x,x',t)$, satisfies the following equation:

$$\frac{\partial}{\partial t}\mathcal{G}(x,x',t) - {}_0\mathcal{D}_t^{\gamma} \int_0^{\mu} d\overline{\mu} p(\overline{\mu}) D_x^{\overline{\mu},\eta} \mathcal{G}(x,x',t) = \delta(x-x')\delta(t) \,. \tag{16}$$

The Green's function is subjected to the following conditions: $\lim_{x\to\pm\infty} \mathcal{G}(x,x',t) = 0$ and $\mathcal{G}(x,x',t) = 0$ for $t < 0$. In terms of the Equations (9) and (10), it is possible to write Green's function as

$$\mathcal{G}(x,x',t) = \frac{1}{2}\int_{-\infty}^{\infty} dk \Big[\psi_{+,\eta}(x,k)\widetilde{\mathcal{G}}_+(k,x',t) + \psi_{-,\eta}(x,k)\widetilde{\mathcal{G}}_-(k,x',t) \Big]. \tag{17}$$

Equation (16) can be simplified by using the integral transform defined by Equations (7) and (8), yielding

$$\frac{\partial}{\partial t}\widetilde{\mathcal{G}}_{\pm}(k,x',t) + {}_0\mathcal{D}_t^{\gamma} \int_0^{\mu} d\overline{\mu} p(\overline{\mu}) |k|^{\mu+\eta} \widetilde{\mathcal{G}}_{\pm}(k,x',t) = \frac{1}{2}\psi_{\pm,\eta}(x',k)\delta(t) \,, \tag{18}$$

which, after applying the Laplace transform, has the solution given by

$$\widehat{\widetilde{\mathcal{G}}}_{\pm}(k,x',s) = \frac{\psi_{\pm,\eta}(x',k)}{2s\big(1+\mathcal{K}_{\gamma}(s)\int_0^{\mu} d\overline{\mu} p(\overline{\mu})|k|^{\overline{\mu}+\eta}\big)} \,. \tag{19}$$

The inverse Laplace transform of Equation (18) depends on the choice of the fractional time operator, i.e., the option performed to $\mathcal{K}_{\gamma}(t)$.

Let us start with the case $\mathcal{K}_{\gamma}(s) = 1/s$ ($\mathcal{K}_{\gamma}(t) = const$) with $p(\overline{\mu}) = \chi_{\mu}\delta(\overline{\mu}-\mu)$. Applying these conditions in Equation (19) , we have that

$$\widetilde{\mathcal{G}}_{\pm}(k,x',t) = \frac{1}{2}\psi_{\pm,\eta}(x',k)e^{-\chi_{\mu}|k|^{\mu+\eta}t} \,. \tag{20}$$

By applying the inverse of the integral transform, it is possible to show that

$$\mathcal{G}(x,x',t) = \mathcal{G}_+(x,x',t) + \frac{xx'}{|x||x'|}\mathcal{G}_-(x,x',t), \tag{21}$$

with

$$\begin{aligned}
\mathcal{G}_{\pm}(x,x',t) &= \frac{(2+\eta)^2}{2(\mu+\eta)|x|^{2+\eta}} \big(|x||x'|\big)^{\frac{1}{2}(1+\eta)} \\
&\times \mathrm{H}^{1,0,1,1,1}_{2,[0:1],0,[0:2]} \left[\begin{array}{c|c} \left(\frac{|x'|}{|x|}\right)^{2+\eta} & \left(\frac{2\mp\nu}{2},1\right);\left(\frac{2\pm\nu}{2},1\right) \\ \frac{\overline{\mathrm{Y}}_{\mu,\eta}t^{\frac{2+\eta}{\mu+\eta}}}{|x|^{2+\eta}} & --;(0,\frac{2+\eta}{\mu+\eta}) \\ & --;-- \\ & (\mp\frac{\nu}{2},1);(\pm\frac{\nu}{2},1);(0,\frac{2+\eta}{\mu+\eta}),(0,\frac{2+\eta}{\mu+\eta}) \end{array} \right],
\end{aligned} \tag{22}$$

where $\overline{\mathrm{Y}}_{\mu,\eta} = (2+\eta)^2\chi_{\mu}^{\frac{2+\eta}{\mu+\eta}}$ and

$$\mathrm{H}^{L,M,M_1,N,N_1}_{E,[A:C],F,[B,D]} \left[\begin{array}{c|c} x & (\varepsilon_1,\omega_1),\cdots,(\varepsilon_E,\omega_E) \\ y & (a_1,\alpha_1),\cdots,(a_A,\alpha_A);(c_1,\beta_1),\cdots,(c_C,\beta_C) \\ & (\xi_1,\varpi_1),\cdots,(\xi_F,\varpi_F) \\ & (b_1,\beta_1),\cdots,(b_B,\beta_B);(d_1,\delta_1),\cdots,(d_C,\delta_D) \end{array} \right] \tag{23}$$

is the generalized H−function of Fox [58–60].

For the particular case $\mu = 2$, it is possible to simplify Equation (22) and to show that

$$\begin{aligned}\mathcal{G}(x,x',t) &= \frac{1}{(2+\eta)\chi_\mu t}\left(|x||x'|\right)^{\frac{1}{2}(1+\eta)} e^{-\frac{1}{(2+\eta)^2\chi_\mu t}\left(|x|^{2+\eta}+|x'|^{2+\eta}\right)} \\ &\times \left\{ I_{-\nu}\left(\frac{2(|x||x'|)^{\frac{1}{2}(2+\eta)}}{(2+\eta)^2\chi_\mu t}\right) + \mathrm{sgn}(xx') I_\nu\left(\frac{2(|x||x'|)^{\frac{1}{2}(2+\eta)}}{(2+\eta)^2\chi_\mu t}\right)\right\}, \quad (24)\end{aligned}$$

where $I_\nu(x)$ is the Bessel function of order ν of modified argument [57]. Note that the mean square displacement for this particular case is given by $\sigma_x^2 = \left\langle (x - \langle x \rangle)^2 \right\rangle \sim t^{2/(2+\eta)}$ evidencing the anomalous behavior of the system with the time evolution.

Now, we extend the previous case for $\mathcal{K}_\gamma(s) = 1/s^\gamma$, which corresponds to considering the Riemann–Liouville fractional time derivative. For this case, with $p(\overline{\mu}) = \chi_\mu \delta(\overline{\mu} - \mu)$, we have that

$$\widetilde{\mathcal{G}}_\pm(k,x',t) = \frac{1}{2}\psi_{\pm,\eta}(x',k) E_\gamma\left(-\chi_\mu |k|^{\mu+\eta} t^\gamma\right), \quad (25)$$

where $E_\gamma(x)$ is the Mittag–Leffler function, defined as follows:

$$E_\gamma(x) = \sum_{n=0}^{\infty} \frac{x^n}{\Gamma(1+\gamma n)}. \quad (26)$$

An interesting point concerning the Mittag–Leffler function is the asymptotic behavior governed by a power law instead of an exponential. This feature has implications for the random process connected to these functions, characterized by waiting time distributions with long-tailed behavior. This point can be verified by using the continuous time random walk approach, for example, in Ref. [11], which connects the fractional diffusion equations with a random process. The solution for this case is also given by Equation (21) with

$$\begin{aligned}\mathcal{G}_\pm(x,x',t) &= \frac{(2+\eta)^2}{2(\mu+\eta)|x|^{2+\eta}}\left(|x||x'|\right)^{\frac{1}{2}(1+\eta)} \\ &\times \mathrm{H}^{1,0,1,1,1}_{2,[0:1],0,[0:2]}\left[\begin{array}{c|c} \left(\frac{|x'|}{|x|}\right)^{2+\eta} & \left(\frac{2\mp\nu}{2},1\right);\left(\frac{2\pm\nu}{2},1\right) \\ \frac{\overline{\mathrm{Y}}_{\mu,\eta} t^\gamma \frac{2+\eta}{\mu+\eta}}{|x|^{2+\eta}} & --;(0,\frac{2+\eta}{\mu+\eta}) \\ & --;-- \\ & (\mp\frac{\nu}{2},1);(\pm\frac{\nu}{2},1);(0,\frac{2+\eta}{\mu+\eta}),(0,\gamma\frac{2+\eta}{\mu+\eta}) \end{array}\right] \quad (27)\end{aligned}$$

Equation (27) mixing three different parameters, which in connection with a random walk, can be connected to the waiting time and jumping distributions. The parameter γ related to the fractional time derivative is connected to the waiting time distribution, and the other parameters η and μ are connected to the jumping probability. We can have a short or a long-tailed behavior for the spatial distribution depending on the choice of the parameter η and μ. Figures 1 and 2 show the behavior of $\mathcal{G}_+(x,x',t)$ and $\mathcal{G}_-(x,x',t)$ for different values of the parameters γ, η, and μ. In particular, it is possible to observe that depending on the choice of the parameters, the previous Green functions can exhibit a unimodal or a bimodal behavior. Figure 3 shows the behavior of the Green function $\mathcal{G}(x,x',t)$ given by Equations (21) and (27). It is worth mentioning that different choices for the parameters imply different behaviors obtained with the mixing of different behaviors.

In addition, by using the scaling arguments [13], it is possible to show that the solution can be written as $\rho(x,t) = \rho(\xi)/t^{\gamma/(\mu+\eta)}$ with $\xi = |x|/t^{\gamma/(\mu+\eta)}$ and, consequently, $\sigma_x^2 \sim t^{2\gamma/(\mu+\eta)}$ for $\int_{-\infty}^{\infty} d\xi \xi^2 \rho(\xi)$ finite. This result implies that for $2\gamma/(\mu+\eta)$ less, equal, or greater than one, we have subdiffusion, usual diffusion, or superdiffusion, respectively (see Figure 4).

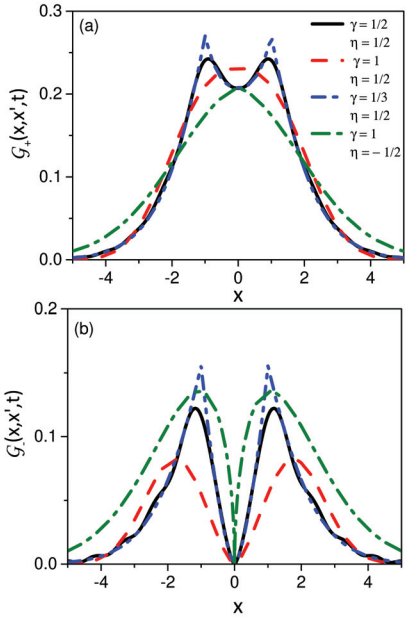

Figure 1. Trend of $\mathcal{G}_+(x,x',t)$ and $\mathcal{G}_-(x,x',t)$ obtained from Equation (22) for $\mu = 2$ and different values of γ and η. We consider, for illustrative purposes, $\chi_2 = 1$, $x' = 1$, and $t = 1$. Note that in (**a**,**b**) show that $\mathcal{G}_+(x,x',t)$ and $\mathcal{G}_-(x,x',t)$ have different behavior, in particular, near the origin.

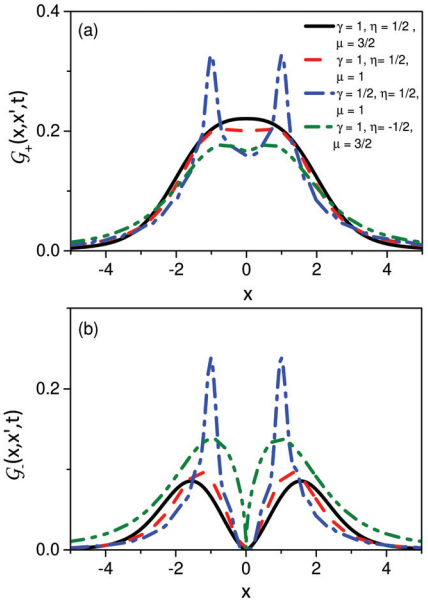

Figure 2. Trend of $\mathcal{G}_+(x,x',t)$ and $\mathcal{G}_-(x,x',t)$ obtained from Equation (27) for different values of μ, γ and η, with $p(\overline{\mu}) = \chi_\mu \delta(\overline{\mu} - \mu) + \chi_2 \delta(\overline{\mu} - 2)$. We consider, for illustrative purposes, $\chi_2 = 1$, $x' = 1$, and $t = 1$. Note that in (**a**,**b**) show that $\mathcal{G}_+(x,x',t)$ and $\mathcal{G}_-(x,x',t)$ have different behavior, in particular, near the origin.

Now, we consider the case $p(\overline{\mu}) = \chi_2\delta(\overline{\mu}-2)+\chi_\mu\delta(\overline{\mu}-\mu)$. This case can be connected to the mixing of two different behaviors. For this case, we have that Equation (19) can be written as follows:

$$\widehat{\widetilde{\mathcal{G}}}_{\pm}(k,x',s) = \frac{1}{2}\frac{\psi_{\pm,\eta}(x',k)}{s+s^{1-\gamma}\left(\chi_2|k|^{2+\eta}+\chi_u|k|^{\overline{\mu}+\eta}\right)}\,. \tag{28}$$

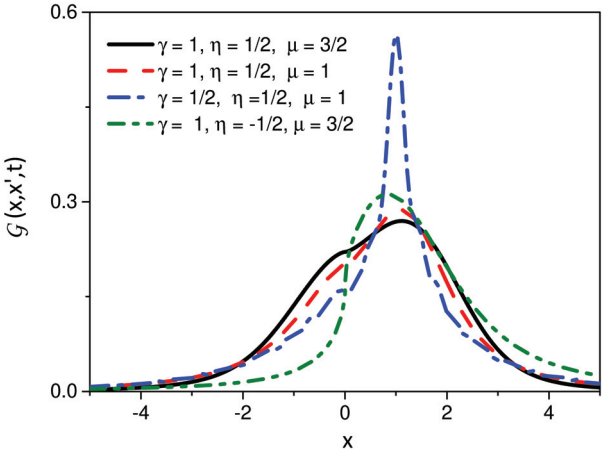

Figure 3. Trend of $\mathcal{G}(x,x',t)$ obtained from Equations (21) and (22) for different values of μ, γ and η, with $p(\overline{\mu}) = \chi_\mu\delta(\overline{\mu}-\mu)$. We consider, for illustrative purposes, $\chi_\mu = 1$, $x' = 1$, and $t = 1$.

Applying the inverse of the Laplace transform, we obtain that

$$\begin{aligned}\widetilde{\mathcal{G}}_{\pm}(k,x',t) &= \sum_{n=0}^{\infty}\frac{(-1)^n}{\Gamma(1+n)}\left(\chi_\mu|k|^{\mu+\eta}t^\gamma\right)^n E_\gamma^{(n)}\left(\chi_2|k|^{2+\eta}t^\gamma\right)\\ &= \sum_{n=0}^{\infty}\frac{(-1)^n}{\Gamma(1+n)}\left(\chi_\mu|k|^{\mu+\eta}t^\gamma\right)^n \mathrm{H}_{1,2}^{1,1}\left[\chi_2|k|^{2+\eta}t^\gamma\Big|_{(0,1),(-\gamma n,\gamma)}^{(0,1)}\right]\,.\end{aligned} \tag{29}$$

Performing the inverse of the integral transform, we obtain that

$$\begin{aligned}\mathcal{G}_{\pm}(x,x',t) &= \frac{2+\eta}{2|x|^{2+\eta}}\left(|x||x'|\right)^{\frac{1}{2}(1+\eta)}\sum_{n=0}^{\infty}\frac{(-1)^n}{\Gamma(1+n)}\left(\overline{\chi}_{2,\mu}t^{\frac{2-\mu}{\mu+\eta}\gamma}\right)^n\\ &\times\ \mathrm{H}_{2,[0:1],0,[0:2]}^{1,0,1,1,1}\left[\begin{matrix}\left(\frac{|x'|}{|x|}\right)^{2+\eta}\\ \frac{\overline{\chi}_2 t^\gamma}{|x|^{2+\eta}}\end{matrix}\middle|\begin{matrix}\left(\frac{2\mp\nu}{2},1\right);\left(\frac{2\pm\nu}{2},1\right)\\ --;\left(\frac{2+\eta}{\mu+\eta}n,1\right)\\ --;--\\ \left(\mp\frac{\nu}{2},1\right);\left(\pm\frac{\nu}{2},1\right);\left(\frac{2+\eta}{\mu+\eta}n,1\right),\left(-\frac{2-\mu}{2+\eta}n\gamma,\gamma\right)\end{matrix}\right],\end{aligned} \tag{30}$$

where $\overline{\chi}_{2,\mu} = \chi_\mu/\chi_2^{(\mu+\eta)/(2+\eta)}$ and $\overline{\chi}_2 = (2+\eta)^2\chi_2$.

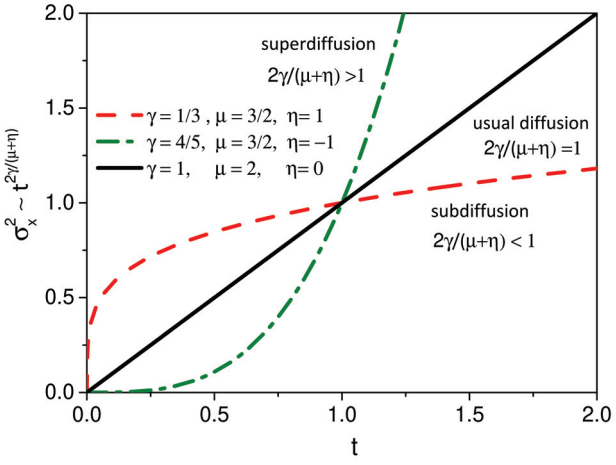

Figure 4. Trend of the mean square displacement σ_x^2 versus t for different values of γ, μ, and η. Note that depending on the value of the parameter, different behaviors can be obtained.

Figure 5 shows the behavior of the Green function for the previous case, which

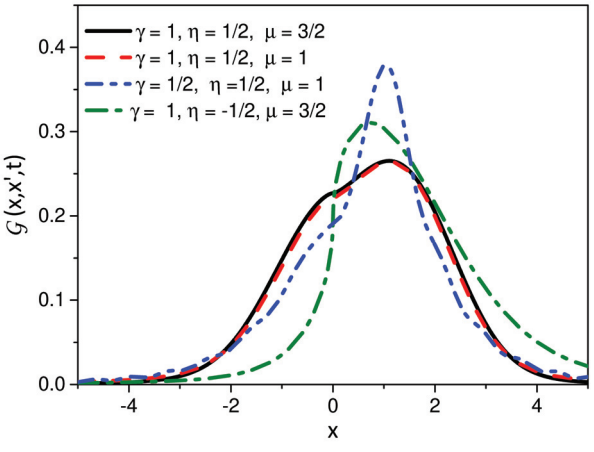

Figure 5. Trend of $\mathcal{G}(x, x', t)$ obtained from Equations (21) and (22) for different values of μ, γ and η, with $p(\overline{\mu}) = \chi_\mu \delta(\overline{\mu} - \mu) + \chi_2 \delta(\overline{\mu} - 2)$. We consider, for illustrative purposes, $\chi_\mu = 1$, $\chi_2 = 0.6$, $x' = 1$, and $t = 1$.

For the initial condition given by $\rho(x, 0) = \delta(x)$, the solution is illustrated in Figure 6 for different values of the parameters γ, μ, and η. We also illustrate the behavior of $1/[\rho(0, t)]^2$, which is connected to the mean square displacement related to this case. In particular, from Figure 6b, it is possible to observe the presence of different diffusion regimes depending on the choice of the parameters.

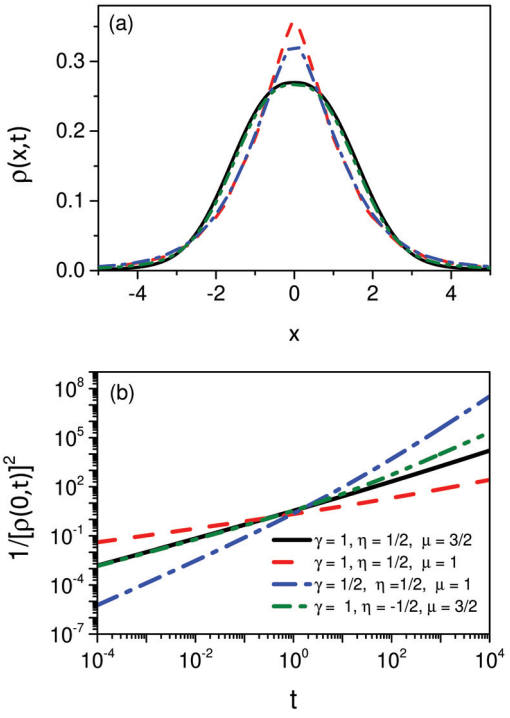

Figure 6. (**a**) shows the profile of $\rho(x,t)$ obtained from Equations (15), (21) and (22) for different values of μ, γ and η, with $p(\overline{\mu}) = \chi_\mu \delta(\overline{\mu} - \mu)$, $t = 1$, and $\rho(x,0) = \delta(x)$. (**b**) shows the behavior of $1/[\rho(0,t)]^2$ to illustrate the spreading of the system. We consider, for illustrative purposes, $\chi_\mu = 1$ and $t = 1$.

We can consider a different fractional time operator for the previous scenarios defined by Equation (14). One of them is the Caputo–Fabrizio fractional operator [28]. In this case, Equation (14) can be written as follows:

$$\frac{\partial}{\partial t}\rho(x,t) = \int_0^\mu d\overline{\mu} p(\overline{\mu}) D_x^{\overline{\mu},\eta} \rho(x,t) + r\big(\delta(x-x') - \rho(x,t)\big)\,, \tag{31}$$

with $r = \gamma/(1-\gamma)$, for the initial condition $\rho(x,0) = \delta(x-x')$. It is worth mentioning that Equation (31) corresponds to a system subjected to a stochastic resetting [61]. In particular, it extends the processes described in Ref. [56]. By using the previous approach, it is possible to show that the solution for this case is given by

$$\rho(x,t) = e^{-rt}\mathcal{G}(x,x',t) + r\int_0^t dt' e^{-rt'}\mathcal{G}(x,x',t') \tag{32}$$

with the Green function given by Equations (21) and (27). For the particular case, $p(\overline{\mu}) = \chi_\mu \delta(\overline{\mu} - \mu)$ with $x' = 0$, we have that the Green function is given by

$$\mathcal{G}(x,0,t) = \frac{2+\eta}{2(\mu+\eta)|x|\Gamma\left(\frac{3+\eta}{2+\eta}\right)}\, \mathrm{H}_{2,3}^{2,1}\left[\frac{|x|^{2+\eta}}{(2+\eta)^2\left(\chi_\mu t^\gamma\right)^{\frac{2+\mu}{2+\eta}}}\middle| \begin{matrix}\left(1,\frac{2+\eta}{\mu+\eta}\right),\left(1,\frac{2+\eta}{\mu+\eta}\right)\\ \left(\frac{1}{2+\eta},1\right),\left(1,\frac{2+\eta}{\mu+\eta}\right),(1,1)\end{matrix}\right]. \tag{33}$$

Figure 7a shows the behavior of Equation (32) and Figure 7b shows the behavior of $1/[\rho(0,t)]^2$ to illustrate the spreading of the system for different values of the parameters

η and μ with $\gamma = 1/2$. From this figure, we observe that the system has long been stationary. It is also interesting to mention that Equation (32) with the Green function given by Equation (33) allows us to investigate a diffusive process in heterogeneous media with stochastic resetting.

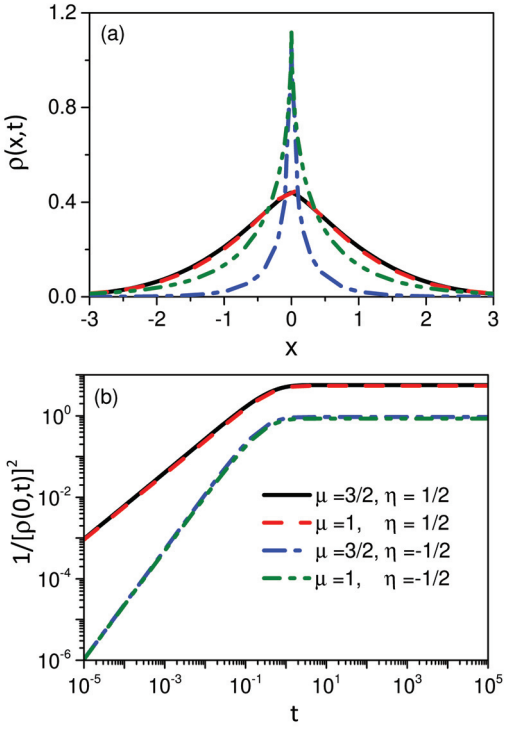

Figure 7. (**a**) shows the profile of $\rho(x,t)$ obtained from Equations (31) and (33) for different values of μ, γ and η, with $p(\overline{\mu}) = \chi_\mu \delta(\overline{\mu} - \mu)$, $t = 1$, and $\rho(x,0) = \delta(x)$. (**b**) shows the behavior of $1/[\rho(0,t)]^2$ to illustrate the spreading of the system. We consider, for illustrative purposes, $\chi_\mu = 1$ and $r = 1$.

Now, we consider the presence of a non-local term in the diffusion equation. We also consider, for simplicity, the initial condition $\rho(x,0) = \delta(x)$, $p(\overline{\mu}) = \chi_\mu \delta(\overline{\mu} - \mu)$, and the Riemann–Liouville fractional time operator. For this case, we can apply the previous procedure based on integral transforms, yielding

$$\widehat{\widetilde{\rho}}_+(k,s) = \frac{1}{2}\frac{\psi_+(0,k)}{s + s^{1-\gamma}\chi_\mu |k|^\mu + \Lambda(s)} \,. \tag{34}$$

After performing a series of expansions, we have that

$$\widehat{\widetilde{\rho}}_+(k,s) = \frac{1}{2}\frac{\psi_+(0,k)}{s + s^{1-\gamma}\chi_\mu |k|^\mu} \sum_{n=0}^{\infty} (-1)^n \left[\frac{\Lambda(s)}{s + s^{1-\gamma}\chi_\mu |k|^\mu}\right]^n , \tag{35}$$

which, after performing the inverse integral transforms, yields

$$\begin{aligned} \rho(x,t) &= \mathcal{G}_+(x,0,t) + \sum_{n=1}^{\infty}\left(-\frac{1}{2}\right)^n \int_0^t dt_n \int_{-\infty}^{\infty} dx_n \Upsilon(x,x_n,t-t_n)\cdots \\ &\times \int_0^{t_2} dt_1 \int_{-\infty}^{\infty} d_{x_2}\Upsilon(x_2,x_1,t_2-t_1)\Upsilon(x_1,0,t_1) \end{aligned} \tag{36}$$

where $\Upsilon(x,\xi,t) = \int_0^t dt' \mathcal{G}_+(x,\xi,t-t')\Lambda(t')$.

3. Discussion and Conclusions

We have investigated a generalized diffusion equation which has, in particular cases, several situations. We have started our analysis by considering the fractional spatial operator and analyzed the influence of the fractional time operators on the solutions. In this scenario, we have obtained the time behavior of the mean square displacement by using scaling arguments when fractional space and time derivatives are present in the diffusion equation. In this case, we consider a singular kernel for the fractional time derivative that allows a connection with the Riemann–Liouville fractional time derivative. For the spatial fractional operator, we have also considered an operator of distributed order. In particular, we analyzed the mixing between two cases, i.e., $p(\overline{\mu}) = \chi_\mu \delta(\overline{\mu} - \mu) + \chi_2 \delta(\mu - 2)$. In each case, the solutions can be directly connected to the stretched exponential or power laws, depending on the choice of the parameters characterizing the spatial fractional operator. We have also considered Fabrizio–Caputo fractional time operator. For this case, we have related this case with a stochastic resetting process following the approach presented in Ref. [28] and analyzed the behavior of the solutions. For each case, the solutions were obtained using the Green function approach. In addition, we have also considered the solutions for an arbitrary non-local term in the generalized diffusion equation. Finally, we hope that the results found here can be helpful in the discussion of different scenarios in connection with diffusion and anomalous diffusion processes.

Author Contributions: Conceptualization, E.K.L., A.S., R.S.Z., L.R.d.S. and M.K.L.; methodology, E.K.L., A.S., R.S.Z., L.R.d.S. and M.K.L.; formal analysis, E.K.L., A.S., R.S.Z., L.R.d.S. and M.K.L.; investigation, E.K.L., A.S., R.S.Z., L.R.d.S. and M.K.L.; writing—original draft preparation, E.K.L., A.S., R.S.Z., L.R.d.S. and M.K.L.; writing—review and editing, E.K.L., A.S., R.S.Z., L.R.d.S. and M.K.L. All authors have read and agreed to the published version of the manuscript.

Funding: E.K.L. acknowledges the support of the CNPq (Grant No. 302983/2018-0) and the National Institute of Science and Technology of Complex Systems-INCT-SC. R.S.Z thanks CNPq (304634/2020-4) and the National Institute of Science and Technology of Complex Fluids-INCT-FCx. Research developed with the support of LAMAP-UTFPR.

Institutional Review Board Statement: Not applicable.

Informed Consent Statement: Not applicable.

Data Availability Statement: Not applicable.

Acknowledgments: We acknowledge the support given by CNPq.

Conflicts of Interest: The authors declare no conflicts of interest.

References

1. Hilfer, R. *Applications of Fractional Calculus in Physics*; World Scientific: Singapore, 2000.
2. Meerschaert, M.M.; Sikorskii, A. *Stochastic Models for Fractional Calculus*; de Gruyter: Berlin, Germany, 2019.
3. Tarasov, V.E. *Fractional Dynamics: Applications of Fractional Calculus to Dynamics of Particles, Fields and Media*; Springer Science & Business Media: Berlin, Germany, 2011.
4. Magin, R. Fractional calculus in bioengineering, part 1. *Crit. Rev. Biomed. Eng.* **2004**, *32*, 1–104 [CrossRef] [PubMed]
5. Herrmann, R. *Fractional Calculus: An Introduction for Physicists*; World Scientific: Singapore, 2011.
6. Evangelista, L.R.; Lenzi, E.K. *Fractional Diffusion Equations and Anomalous Diffusion*; Cambridge University Press: Cambridge, UK, 2018.
7. Kuntz, M.; Lavallée, P. Experimental evidence and theoretical analysis of anomalous diffusion during water infiltration in porous building materials. *J. Phys. D Appl. Phys.* **2001**, *34*, 2547. [CrossRef]
8. Rosseto, M.P.; Evangelista, L.R.; Lenzi, E.K.; Zola, R.S.; Ribeiro de Almeida, R.R. Frequency-Dependent Dielectric Permittivity in Poisson–Nernst–Planck Model. *J. Phys. Chem. B* **2022**, *126*, 6446–6453. [CrossRef]
9. Scher, H.; Montroll, E.W. Anomalous transit-time dispersion in amorphous solids. *Phys. Rev. B* **1975**, *12*, 2455. [CrossRef]
10. Jeon, J.H.; Leijnse, N.; Oddershede, L.B.; Metzler, R. Anomalous diffusion and power-law relaxation of the time averaged mean squared displacement in worm-like micellar solutions. *New J. Phys.* **2013**, *15*, 045011. [CrossRef]
11. Metzler, R.; Klafter, J. The random walk's guide to anomalous diffusion: A fractional dynamics approach. *Phys. Rep.* **2000**, *339*, 1–77. [CrossRef]

12. Lenzi, E.K.; Evangelista, L.; Zola, R.; Scarfone, A. Fractional Schrödinger equation for heterogeneous media and Lévy-like distributions. *Chaos Solitons Fractals* **2022**, *163*, 112564. [CrossRef]
13. Magin, R.L.; Lenzi, E.K. Slices of the Anomalous Phase Cube Depict Regions of Sub-and Super-Diffusion in the Fractional Diffusion Equation. *Mathematics* **2021**, *9*, 1481. [CrossRef]
14. Kenkre, V.; Montroll, E.; Shlesinger, M. Generalized master equations for continuous-time random walks. *J. Stat. Phys.* **1973**, *9*, 45–50. [CrossRef]
15. Swenson, R.J. Derivation of generalized master equations. *J. Math. Phys.* **1962**, *3*, 1017–1022. [CrossRef]
16. Cortes, E.; West, B.J.; Lindenberg, K. On the generalized Langevin equation: Classical and quantum mechanicala. *J. Chem. Phys.* **1985**, *82*, 2708–2717. [CrossRef]
17. Klafter, J.; Sokolov, I.M. *First Steps in Random Walks: From Tools to Applications*; OUP Oxford: Oxford, UK, 2011.
18. Giona, M.; Roman, H.E. Fractional diffusion equation on fractals: One-dimensional case and asymptotic behaviour. *J. Phys. A Math. Gen.* **1992**, *25*, 2093. [CrossRef]
19. Hashan, M.; Jahan, L.N.; Imtiaz, S.; Hossain, M.E. Modelling of fluid flow through porous media using memory approach: A review. *Math. Comput. Simul.* **2020**, *177*, 643–673. [CrossRef]
20. Razminia, K.; Razminia, A.; Baleanu, D. Fractal-fractional modelling of partially penetrating wells. *Chaos Solitons Fractals* **2019**, *119*, 135–142. [CrossRef]
21. Raghavan, R.; Chen, C. The Theis solution for subdiffusive flow in rocks. *Oil Gas Sci. Technol. Rev. D'Ifp Energies Nouv.* **2019**, *74*, 6. [CrossRef]
22. Zhokh, A.; Strizhak, P. Macroscale modeling the methanol anomalous transport in the porous pellet using the time-fractional diffusion and fractional Brownian motion: A model comparison. *Commun. Nonlinear Sci. Numer. Simul.* **2019**, *79*, 104922. [CrossRef]
23. Feng, C.; Si, X.; Li, B.; Cao, L.; Zhu, J. An inverse problem to simulate the transport of chloride in concrete by time–space fractional diffusion model. *Inverse Probl. Sci. Eng.* **2021**, *29*, 2429–2445. [CrossRef]
24. Han, M.; Zhou, C.; Silberschmidt, V.V.; Bi, Q. Multiscale heat conduction and fractal oxidation behaviors of needle-punched carbon/carbon composites. *Sci. Eng. Compos. Mater.* **2022**, *29*, 508–515. [CrossRef]
25. Lenzi, E.K.; Evangelista, L. Space–time fractional diffusion equations in d-dimensions. *J. Math. Phys.* **2021**, *62*, 083304. [CrossRef]
26. Podlubny, I. *Fractional Differential Equations*; Academic Press: Cambridge, MA, USA, 1999.
27. Atangana, A.; Baleanu, D. New Fractional Derivatives with non-local and non-singular kernel. *Therm. Sci.* **2016**, *20*, 763–769. [CrossRef]
28. Tateishi, A.A.; Ribeiro, H.V.; Lenzi, E.K. The role of fractional time-derivative operators on anomalous diffusion. *Front. Phys.* **2017**, *5*, 52. [CrossRef]
29. Fernandez, A.; Baleanu, D. Classes of operators in fractional calculus: A case study. *Math. Methods Appl. Sci.* **2021**, *44*, 9143–9162. [CrossRef]
30. Singh, H. Chebyshev spectral method for solving a class of local and nonlocal elliptic boundary value problems. *Int. J. Nonlinear Sci. Numer. Simul.* **2021**. [CrossRef]
31. Singh, H. Solving a class of local and nonlocal elliptic boundary value problems arising in heat transfer. *Heat Transf.* **2022**, *51*, 1524–1542. [CrossRef]
32. Singh, H. An efficient computational method for non-linear fractional Lienard equation arising in oscillating circuits. In *Methods of Mathematical Modelling*; CRC Press: Boca Raton, FL, USA, 2019; pp. 39–50.
33. Singh, H.; Srivastava, H. Numerical investigation of the fractional-order Liénard and Duffing equations arising in oscillating circuit theory. *Front. Phys.* **2020**, *8*, 120. [CrossRef]
34. Scarfone, A.M.; Barbero, G.; Evangelista, L.R.; Lenzi, E.K. Anomalous Diffusion and Surface Effects on the Electric Response of Electrolytic Cells. *Physchem* **2022**, *2*, 163–178. [CrossRef]
35. Barbero, G.; Evangelista, L.; Lenzi, E.K. Time-fractional approach to the electrochemical impedance: The Displacement current. *J. Electroanal. Chem.* **2022**, *920*, 116588. [CrossRef]
36. Singh, H.; Srivastava, H.; Nieto, J.J. *Handbook of Fractional Calculus for Engineering and Science*; CRC Press: Boca Raton, FL, USA, 2022.
37. Singh, H.; Kumar, D.; Baleanu, D. *Methods of Mathematical Modelling: Fractional Differential Equations*; CRC Press: Boca Raton, FL, USA, 2019.
38. Singh, H.; Kumar, D.; Baleanu, D. *Methods of Mathematical Modelling: Infectious Disease*; Elsevier Science: Amsterdam, The Netherlands, 2022.
39. Gómez-Aguilar, J.; Atangana, A. Fractional Hunter-Saxton equation involving partial operators with bi-order in Riemann–Liouville and Liouville–Caputo sense. *Eur. Phys. J. Plus* **2017**, *132*, 100. [CrossRef]
40. Evangelista, L.R.; Lenzi, E.K. *An Introduction to Anomalous Diffusion and Relaxation*; Springer Nature: Berlin, Germany, 2023.
41. Ali, I.; Kalla, S. A generalized Hankel transform and its use for solving certain partial differential equations. *Anziam J.* **1999**, *41*, 105–117. [CrossRef]
42. Garg, M.; Rao, A.; Kalla, S.L. On a generalized finite Hankel transform. *Appl. Math. Comput.* **2007**, *190*, 705–711. [CrossRef]
43. Nakhi, Y.B.; Kalla, S.L. Some boundary value problems of temperature fields in oil strata. *Appl. Math. Comput.* **2003**, *146*, 105–119. [CrossRef]

44. Xie, K.; Wang, Y.; Wang, K.; Cai, X. Application of Hankel transforms to boundary value problems of water flow due to a circular source. *Appl. Math. Comput.* **2010**, *216*, 1469–1477. [CrossRef]
45. O'Shaughnessy, B.; Procaccia, I. Diffusion on fractals. *Phys. Rev. A* **1985**, *32*, 3073–3083. [CrossRef]
46. O'Shaughnessy, B.; Procaccia, I. Analytical Solutions for Diffusion on Fractal Objects. *Phys. Rev. Lett.* **1985**, *54*, 455–458. [CrossRef]
47. Richardson, L.F. Atmospheric diffusion shown on a distance-neighbour graph. *Proc. Math. Phys. Eng. Sci.* **1926**, *110*, 709–737.
48. Boffetta, G.; Sokolov, I.M. Relative Dispersion in Fully Developed Turbulence: The Richardson's Law and Intermittency Corrections. *Phys. Rev. Lett.* **2002**, *88*, 094501. [CrossRef]
49. Ben Avraham, D.; Havlin, S. *Diffusion and Reactions in Fractals and Disordered Systems*; CUP: Cambridge, UK, 2000.
50. Su, N.; Sander, G.; Liu, F.; Anh, V.; Barry, D. Similarity solutions for solute transport in fractal porous media using a time- and scale-dependent dispersivity. *App. Math. Model.* **2005**, *29*, 852–870. [CrossRef]
51. He, J.H. Fractal calculus and its geometrical explanation. *Results Phys.* **2018**, *10*, 272–276. [CrossRef]
52. Cai, W.; Chen, W.; Xu, W. The fractal derivative wave equation: Application to clinical amplitude/velocity reconstruction imaging. *J. Acoust. Soc. Am.* **2018**, *143*, 1559–1566. [CrossRef]
53. Chen, W.; Liang, Y. New methodologies in fractional and fractal derivatives modeling. *Chaos Solitons Fractals* **2017**, *102*, 72–77. [CrossRef]
54. Liang, Y.; Chen, W.; Cai, W. *Hausdorff Calculus: Applications to Fractal Systems*; Walter de Gruyter GmbH & Co KG: Berlin, Germany, 2019; Volume 6.
55. Evans, M.R.; Majumdar, S.N. Diffusion with stochastic resetting. *Phys. Rev. Lett.* **2011**, *106*, 160601. [CrossRef] [PubMed]
56. Lenzi, M.K.; Lenzi, E.K.; Guilherme, L.; Evangelista, L.R.; Ribeiro, H.V. Transient anomalous diffusion in heterogeneous media with stochastic resetting. *Phys. A Stat. Mech. Appl.* **2022**, *588*, 126560. [CrossRef]
57. Wyld, H.W.; Powell, G. *Mathematical Methods for Physics*; CRC Press: Boca Raton, FL, USA, 2020.
58. Mathai, A.M.; Saxena, R.K.; Haubold, H.J. *The H-Function: Theory and Applications*; Springer Science & Business Media: Berlin, Germany, 2009.
59. Lenzi, E.K.; Evangelista, L.; Lenzi, M.K.; Ribeiro, H.V.; de Oliveira, E.C. Solutions for a non-Markovian diffusion equation. *Phys. Lett. A* **2010**, *374*, 4193–4198. [CrossRef]
60. Jiang, X.; Xu, M. The time fractional heat conduction equation in the general orthogonal curvilinear coordinate and the cylindrical coordinate systems. *Phys. A Stat. Mech. Appl.* **2010**, *389*, 3368–3374. [CrossRef]
61. Evans, M.R.; Majumdar, S.N.; Schehr, G. Stochastic resetting and applications. *J. Phys. A* **2020**, *53*, 193001. [CrossRef]

fluids

MDPI

Article

Assessment of a RANS Transition Model with Flapping Foils at Moderate Reynolds Numbers

Luca Alberti, Emanuele Carnevali and Andrea Crivellini *

Department of Industrial Engineering and Mathematical Sciences, Polytechnic Marche University, 60131 Ancona, Italy
* Correspondence: a.crivellini@staff.univpm.it

Abstract: Numerical simulations based on a high-order discontinuous Galerkin solver were performed to investigate two-dimensional flapping foils at moderate Reynolds numbers, moving with different prescribed harmonic motion laws. A Spalart–Allmaras RANS model with and without an algebraic local transition modification was employed for the resolution of multiple kinematic configurations, considering both moderate-frequency large-amplitude flapping and high-frequency small-amplitude pure heaving. The propulsive performance of the airfoils with the two modelling approaches were tested by referring to experimental and (scale-resolving) numerical data available in the literature. The results show an increase in effectiveness in predicting loads when applying the transition model. This is particularly true at low Strouhal numbers when, after laminar separation at the leading edge, vorticity dynamics appears to have a strong effect on the forces exerted on the profile. Specifically, the transition model more accurately predicts the wake topology emerging in the flow field, which is the primary influence on thrust/drag generation.

Keywords: discontinuous Galerkin; oscillating foil; thrust efficiency; reduced frequency; NACA0012; SD7003; algebraic transition model; Spalart–Allmaras; moderate Reynolds number

Citation: Alberti, L.; Carnevali, E.; Crivellini, A. Assessment of a RANS Transition Model with Flapping Foils at Moderate Reynolds Numbers. *Fluids* **2023**, *8*, 23. https://doi.org/10.3390/fluids8010023

Academic Editors: Mehrdad Massoudi and Pier Marzocca

Received: 22 November 2022
Revised: 29 December 2022
Accepted: 6 January 2023
Published: 8 January 2023

1. Introduction

Starting from the pioneering work of Knoller [1] and Betz [2], the fluid dynamics aspects of oscillating foils have drawn the attention of researchers such as Burgers and von Kármán [3], Lighthill [**?**], and many others, whose endeavours have been extensively reported in a recent review by Wu et al. [5].

In particular, several experimental and numerical studies [6–12] have been carried out at moderate Reynolds numbers, for which transitional effects can be relevant. In this circumstance, the use of the standard, fully turbulent, Reynolds-averaged Navier–Stokes equations (RANS) approach can be erratic, while scale-resolving simulations, namely large eddy simulations (LES) and direct numerical simulations (DNS), are still prohibitively expensive, particularly when a large-scale investigation is required. Hybrid LES-RANS approaches [13–16] allowed the reduction in the computational cost while retaining large-scale solution accuracy through a mesh size relaxation at solid boundaries ; despite this, the required computational resources remain closer to a LES rather than a RANS. A viable alternative consists of using RANS equipped with a transition model [17–19], which may require the solution of additional partial differential equations (PDE). Among all the possibilities, the local algebraic approach is well suited for unstructured solvers, because it does not increase the computational effort and, at the same time, significantly improves the prediction capabilities. For instance, when the Reynolds number is of the order of 10^4 or 10^5, employing a transition model enables capture of phenomena such as formation of a laminar separation bubble over an airfoil and more accurate prediction of the onset of the stall. Despite the availability of results involving transition models applied to airfoils at moderate Reynolds number, even recently [20], the authors are not aware of studies that

specifically consider the oscillating motion of airfoils using RANS and a local transition algebraic model. This is the main subject of this work. Note that in the literature it is possible to find flapping foils at moderate Reynolds number simulated solving both the two-dimensional Navier–Stokes (Ashraf et al. [21] at $Re = 20{,}000$ and Li et al. [22] at $Re = 40{,}000$) and the fully turbulent RANS governing equations (Young and Lay [23] at $Re = 10{,}000$–$80{,}000$ and Wang et al. [24] at $Re = 13{,}800$), so the purpose of this article is also to establish the limits of applicability of the latter approach.

In particular, the analysis proposed here is focused on performance evaluation concerning the prediction of loads, efficiency, and flow structure emerging from the dynamics of two-dimensional oscillating airfoils given by a Spalart–Allmaras (SA) RANS approach with and without the contribution of a local algebraic transition model referred to as SA-BCM. The choice of the SA model relies on its extensive use in aerodynamic applications and its suitability to simulate turbulent flows past an airfoil, all while having a low computational expense. Within the subject of oscillating foils, the same model has been adopted in [10] for comparing numerical results with experimental particle image velocimetry (PIV) data. Therein, the model performance are considered satisfactory; however, in Section 3 we will show how the approach presented here can further increase the agreement between simulations and experimental visualizations for moderate Reynolds numbers. As far as the transition model is concerned, the implementation considered in this work follows the mathematical description sketched in [25], which will be explored in more detail in the dedicated section (Section 2.2). The appeal for algebraic models stems from the absence of any additional transport equation for the intermittency field, which is instead modelled through a suitable empirical correlation with local flow quantities and embedded within the transport equation for an eddy viscosity-like variable. Its effect consists of determining the activation of the eddy viscosity-like production term corresponding to the regions exhibiting turbulent features. This algebraic transition approach proved to increase the accuracy of the solution considerably over a wide range of Reynolds numbers without significant variation in the computational cost [25–27].

Both models are implemented on top of a discontinuous Galerkin (DG) solver. This method preserves high-order accuracy independently from the grid characteristics, and it has been exploited here to ensure the resolution independence of the solutions through p-refinement. Moreover, as a side result, it is shown that the transition-modified SA model does not compromise the scheme robustness, despite the well-known stability issues due to the implementation of RANS equations within high-order frameworks.

As far as the airfoil motion is concerned, two oscillatory configurations have been considered: (1) a two-dimensional flapping motion, composed of a vertical translation with a superimposed rotation around a pivotal point and (2) a two-dimensional, high-frequency small-amplitude vertical oscillation with a constant angle of attack. These two prescribed motions allowed testing of the models with kinematic configurations producing rather different effects. Specifically, the flapping motion may be assimilated to the tail movement of oscillatory swimmers, such as tuna and sharks, and it has been thoroughly investigated as a propulsive mechanism, whereas high-frequency heaving has been proposed as a motion strategy aimed at drag reduction and flight stability improvement of air vehicles.

To validate the derived results, enabling the capture of consistent conclusions over the performance of the two models, suitable reference works have been used as a foundation. Concerning the flapping motion, the work of Schouveiler, Hover and Triantafyllou [8] has been taken as a benchmark for the evaluation of hydrodynamic forces and propulsive efficiency. In order to be able to make comparisons with their experimental results, the simulations were performed by changing the motion parameters in such a way to simulate Strouhal numbers in the range $0.1 < St < 0.45$ for two different values of maximum angles of attack, i.e., $\alpha_{max} = 15^\circ, 30^\circ$. A more detailed description of the parameters will be outlined in the dedicated section (Section 3.1). For the second motion condition, namely high-frequency plunging, the work of Visbal [11] and Krais et al. [12] have instead been used as a reference. In [11], a three-dimensional LES analysis was provided for a plunging

SD7003 airfoil, considering different values of Reynolds number and motion parameters, together with validation of the experimental results [10]. The comparison between SA and SA-BCM models was carried out using the previously reported configurations with a frequency $k = 3.93$ at $Re = 40{,}000$ and $k = 10$ at $Re = 60{,}000$. A more detailed description will be given in Section 3.2. The work of Krais et al. [12] provides additional data, once again derived from scale-resolving simulations (ILES) employing a nodal DG solver adopting the plunging configuration characterized by $k = 3.93$ and $Re = 40{,}000$ defined in [11] as a test case.

The overall organization of the manuscript is as follows: in Section 2.1 the parametrization of the profile motion is reported. This is followed in Section 2.2 by an outline of the high-order DG method and the implemented turbulence models. In Section 3, the results obtained from simulating both NACA0012 (Section 3.1) and SD7003 (Section 3.2) are provided. Finally, in Section 4, the main findings are summarized and discussed.

2. Simulation Setup

2.1. Kinematic Framework

The airfoil motion is fully defined by the following periodic kinematic functions:

$$\begin{aligned} \theta(t) &= \alpha_0 + \theta_0 \sin(2\pi f t) \\ h(t) &= h_0 \sin(2\pi f t + \psi) \, , \end{aligned} \tag{1}$$

where α_0 is the mean angle of attack; h_0 and θ_0 are the vertical and angular displacement, respectively; f is the frequency of oscillation; and ψ is the phase shift between the heaving and pitching sinusoidal waves. In terms of velocity, the vertical oscillation reads as

$$u_2^t(t) = 2\pi f h_0 \, \cos(2\pi f t + \psi) = U_0 \cos(2\pi f t + \psi) \tag{2}$$

where $U_0 = 2\pi f h_0$ is the maximum vertical velocity associated with the oscillating motion. Similarly, the angular pitching velocity is

$$\omega_3^t(t) = 2\pi f \theta_0 \, \cos(2\pi f t) \, . \tag{3}$$

The effective angle of attack α, according to our sign convention, is related to the other kinematic quantities through

$$\alpha(t) = \theta(t) + \arctan\left(\frac{u_2^t(t)}{U_\infty}\right) . \tag{4}$$

The maximum value assumed by α during the oscillating cycle is denoted with α_{max}. An illustration of the various kinematic variables is given in Figure 1.

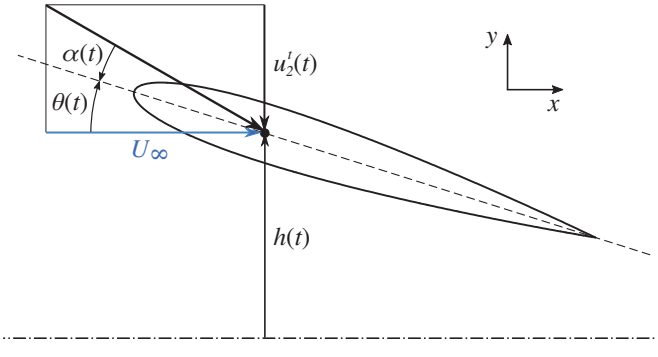

Figure 1. Scheme of the NACA0012 airfoil.

The amplitude-based Strouhal number of the oscillation (St) and/or the reduced frequency (k),

$$St = \frac{U_0}{\pi U_\infty}\,, \quad k = \pi \frac{cSt}{2h_0}\,, \tag{5}$$

are the non-dimensional numbers used to characterize the foil motion. In particular, St represents the ratio between the maximum heave velocity U_0 and the free-stream speed U_∞, except for an additional π in the denominator. Finally, the Reynolds number is, as usual, defined as $Re = U_\infty c/\nu$, where c is the foil chord and ν is the kinematic viscosity. Note that c and U_∞ are hereafter used as reference scales of length and velocity.

In order to identify the position of the profile during its motion for the different cases explored, the notation adopted in [10,11] is followed. According to that, the instantaneous vertical position of the foil is expressed in terms of a parameter Φ, called the motion phase, which expresses the vertical coordinate as a percentage of the oscillating period. In this way, the vertical positions of interest will be denoted in the following way: $\Phi = 0$ indicates the maximum upward displacement, $\Phi = 0.25$ the neutral position during downstroke, $\Phi = 0.5$ the maximum downward displacement, and $\Phi = 0.75$ the neutral position during upstroke.

2.2. Numerical Framework

The numerical simulations were performed using a DG solver (see [28–31]). The advantage of using such a class of methods is related to the ability to provide accurate high-order solutions on stretched, curved, and unstructured computational grids. In this work, we consider a two-dimensional incompressible DG code, which is able to deal with a non-inertial reference frame to account for the foil oscillations. Note that the results here reported are not DG specific and the high-order accuracy, up to the seventh order, was only exploited in order to reach the numerical resolution independence. The governing equations are expressed in terms of the absolute velocity u_i, a vector in the inertial frame observed by the non-inertial frame attached to the foil (see, for example, [32,33]). Consequently, the inter-frame velocity components are $U_i = u_i^t(t) + \varepsilon_{ijk}\omega_j^t(t)(x_k - x_{0,k})$, where $x_{0,k}$ is the centre of rotation. Note that, for the sake of convenience, in the U_i identity we adopted the same $u_i^t(t)$ notation already used in Equation (2); however, here the heaving velocity should be interpreted as defined in the rotating frame and not in the inertial one. The resulting PDE system reads as

$$\begin{aligned}
&\frac{\partial u_i}{\partial x_i} = 0\,,\\
&\frac{\partial u_i}{\partial t} + \frac{\partial u_i u_j}{\partial x_j} = -\frac{\partial p}{\partial x_i} + \frac{\partial}{\partial x_j}\left((\nu + \nu_t)\frac{\partial u_i}{\partial x_j}\right) - \varepsilon_{ijk}\omega_j^t u_k + U_j\frac{\partial u_i}{\partial x_j}\,,\\
&\frac{\partial \tilde{\nu}}{\partial t} + \frac{\partial \tilde{\nu} u_j}{\partial x_j} = \gamma_{BC} C_{b1}\tilde{S}\tilde{\nu} + \frac{C_{b2}}{\sigma}\frac{\partial \tilde{\nu}}{\partial x_j}\frac{\partial \tilde{\nu}}{\partial x_j} - C_{w1} f_w\left(\frac{\tilde{\nu}}{d}\right)^2 + \frac{1}{\sigma}\frac{\partial}{\partial x_j}\left((\nu + \nu_t)\frac{\partial \tilde{\nu}}{\partial x_j}\right) + U_j\frac{\partial \tilde{\nu}}{\partial x_j}\,,
\end{aligned} \tag{6}$$

where p is the pressure divided by the density, ν_t is the kinematic eddy viscosity, d is the minimum distance from the wall, and ε_{ijk} is the Levi-Civita tensor. Note that in Equation (6), taking advantage of the identity $\partial U_i/\partial x_i = 0$ and deviating from the process that is usually performed in the literature, the divergence of the convective fluxes does not contain the relative velocity, and all the non-inertial terms are moved to the right-hand side.

Following the standard RANS approach and Boussinesq's hypothesis, the flow-governing equations are combined with a closure model for the turbulent Reynolds stresses. More precisely, the Spalart–Allmaras one-equation model has been used, with the eddy viscosity-like variable identified by $\tilde{\nu}$. The eddy viscosity is computed according to the equation $\nu_t = f_{v1}\tilde{\nu}$, where $f_{v1} = \chi^3/(\chi^3 + C_{v1}^3)$ and $\chi = \tilde{\nu}/\nu$.

In order to fully define the SA model, the following functions should be also specified:

$$\tilde{S} = S + \frac{\tilde{\nu}}{k^2 d^2}, \quad r = \frac{\tilde{\nu}}{\tilde{S} k^2 d^2}, \quad g = r + c_{w2}\Big(r^6 - r\Big), \quad f_w = g\left(\frac{1 + c_{w3}^6}{g^6 + c_{w3}^6}\right)^{1/6}, \tag{7}$$

where $k = 0.41$ is the Von Kármán constant and $S = (2\Omega_{ij}\Omega_{ij})^{1/2}$ is the magnitude of the vorticity tensor, $\Omega_{ij} = 1/2(\partial u_i/\partial x_j - \partial u_j/\partial x_i)$. As performed in several SA implementations, the trip term is ignored in Equation (6). Thus, the base model is fully turbulent.

For the sake of compactness, the model constants, such as C_{b1}, C_{b2}, etc., will not be given in this paper. Interested readers can refer to the original work of Spalart and Allmaras [34]. In the following, the algebraic transition model proposed in [26] and more recently modified in [25,27] will be introduced. The latter version solves an issue regarding the Galilean invariance of the prior version, which is obviously crucial for the type of application handled here.

For the SA standard, fully turbulent model, the intermittency function γ_{BC} is set to 1 in Equation (6), and for the transition model, it is evaluated as

$$\gamma_{BC} = 1 - e^{-\sqrt{T_1} - \sqrt{T_2}}, \quad T_1 = \max\left(\frac{Re_\theta - Re_{\theta c}}{\chi_1 Re_{\theta c}}, 0\right), \quad T_2 = \max\left(\frac{\nu_t}{\chi_2 \nu}, 0\right), \tag{8}$$

where $\chi_{1,2} = 0.002, 50$ are calibration constants of the model. Thanks to the observation (see [35]) that the momentum thickness Reynolds number, Re_θ, is proportional to the vorticity Reynolds number, $Re_v = d^2/\nu S$, the former is evaluated as $Re_\theta = Re_v/2.193$. Finally, the critical momentum thickness Reynolds number, $Re_{\theta c}$, is computed according to the empirical correlation $Re_{\theta c} = 803.73(Tu_\infty + 0.6067)^{-1.027}$. Note that the value of Tu_∞ is not assigned to the inflow/far-field boundary conditions, because the SA model does not consider the turbulent kinetic energy. As explained in [26], the term T_1 establishes the onset of transition, whereas the term T_2 propagates high levels of the intermittency function γ_{BC} within the boundary layer.

Moreover, we decided to complement the model with the recent low Reynolds correction of Spalart and Garbaruk [34], which seems very well suited to deal with transitional flows. Following the latter approach, the model constant $c_{w2} = 0.3$ in Equation (7) is changed to the function

$$c_{w2,LRe} = c_{w4} + \frac{c_{w5}}{(\chi/40 + 1)^2}, \tag{9}$$

with $c_{w4} = 0.21$ and $c_{w5} = 1.5$.

The DG discretization can be obtained by expressing the system of Equation (6) in variational form, decomposing the domain by elements, and defining an appropriate polynomial space of order q within each element. In this work, the convective numerical fluxes that are used to couple the solution at the interior faces of the mesh are computed through the artificial compressibility flux method of [36]. On the other hand, the second form of the Bassi and Rebay scheme (see [28]) has been used for the viscous terms. The DG discretized system can be written in the following compact form

$$M^0 \frac{dW}{dt} = R(W, t), \tag{10}$$

where W is the global vector of the degrees of freedom (DOF), M^0 is a modified mass matrix with null entries corresponding to the pressure DOF, and R is the vector of residuals. This system of differential algebraic non-linear equations is integrated in time through a linearly implicit Rosenbrock-type Runge–Kutta scheme named ROS3P by [37]. The advantage of this class of schemes is that the non-linear solution process is completely avoided and the Jacobian matrix $\partial R/\partial W$ has to be computed only once for each time step. The resulting time-discretized equations can be stated as

$$
\begin{aligned}
W^{n+1} &= W^n + \sum_{j=1}^{s} m_j Y_j \,, \\
\left(\frac{M^0}{\gamma_{ii}\Delta t} - \frac{\partial R}{\partial W}(W^n, t^n)\right) Y_i &= R\left(W^n + \sum_{j=1}^{i-1} a_{ij} Y_j,\ t^n + \alpha_i \Delta t\right) + \\
&\quad + M^0 \sum_{j=1}^{i-1} \frac{c_{ij}}{\Delta t} Y_j + \gamma_i \Delta t \frac{\partial R}{\partial t}(W^n, t^n) \,, \quad i = 1, \ldots, s
\end{aligned}
\tag{11}
$$

where the superscript n refers to the marching time step, $s = 3$ is the number of stages and $m_j, \gamma_i, \gamma_{ii}, a_{ij}, \alpha_i$ are the coefficients of the scheme, which can be found in [37]. The last term of Equation (11) considers that the system is non-autonomous. In fact, due to the non-inertial frame, the absolute velocity vector u_i changes at the non-slip, wall, and free-stream boundary conditions to follow the airfoil motion. Moreover, in Equation (6), U_j and ω_j^t are not constant in time. At the wall, $\tilde{\nu}$ is set to zero, and the free-stream value depends on the choice of the model. Fully turbulent standard computations are performed with $\tilde{\nu}_\infty = 3\nu$, and for the transitional simulations this value is set to 0.02ν. These data are consistent with the recommendations found in the current literature (see, for example, [27,38]). The requirement to use smaller $\tilde{\nu}_\infty$ boundary data highlights the need of a strategy to prevent negative (spurious and non-physical) values of $\tilde{\nu}$, which may result in the blow up of the simulations. This stability issue is exacerbated when a high-order scheme is adopted. Our approach is described in [30], where the details of our SA implementation are given.

The solution of the linear systems arising from Equation (11) were handled using a flexible generalized minimal residual (GMRES) solver preconditioned by a highly parallel efficient p-multigrid algorithm, described by [39].

3. Results

In the following section, we present the results obtained for two test cases that include a symmetric (NACA0012) and an asymmetric (SD7003) airfoil. The numerical grids, generated using the open-source software GMSH [40], are unstructured, as illustrated in Figure 2. In both cases, the outer boundary is a circle with a radius equal to $25c$. The boundary layer region is discretized using structured-like quadrangular elements suitably curved to accurately represent the foil's curvature. To this end, a piece-wise third-order polynomial approximation of the faces of the elements is employed. The height of the first cell, expressed in wall friction units, is at most of the order of $y^+ = 1$ for all the computations here reported. The NACA0012 grid was significantly refined behind the airfoil because we paid particular attention (see the following section) to the wake topology. For this reason, the NACA0012 mesh consists of more elements: 7416 instead of 2875. We did not perform a classical grid refinement study, but rather we verified the numerical resolution by raising the polynomial order q of the solution. See Sections 3.1 and 3.2.2 for examples of the solution convergence analysis. If not otherwise stated, the results here reported are obtained with $q = 6$, ensuring a seventh-order space accuracy for the velocity components and the eddy viscosity and sixth-order accuracy for pressure. The time step size was also carefully verified, and in this work it ranges between $10^{-3}c/U_\infty$ and $10^{-2}c/U_\infty$. In regard to the choice of the value of Tu_∞ in the transition model, we did not find any clear statement in the references available for NACA0012 (e.g., [8]), thus we arbitrarily decided to use a small value such as 0.2%. For the SD7003 computations, instead, we used $Tu_\infty = 0.1\%$, in agreement with the experimental data reported in [10]. However, multiple tests showed that the results are quite insensitive to small changes of Tu_∞.

The forces F_i acting on the airfoil expressed in the inertial frame and the momentum M_3 are non-dimensionalized using the chord c and the free-stream velocity U_∞, obtaining the following drag, lift, and moment coefficients:

$$C_D = \frac{F_1}{1/2\,\rho\, S\, U_\infty^2}\,, \quad C_L = \frac{F_2}{1/2\,\rho\, S\, U_\infty^2}\,, \quad C_M = \frac{M_3}{1/2\rho\, cS\, U_\infty^2}\,, \tag{12}$$

where ρ is the fluid density and S is the reference area, which is the chord c times a unit's span-wise length.

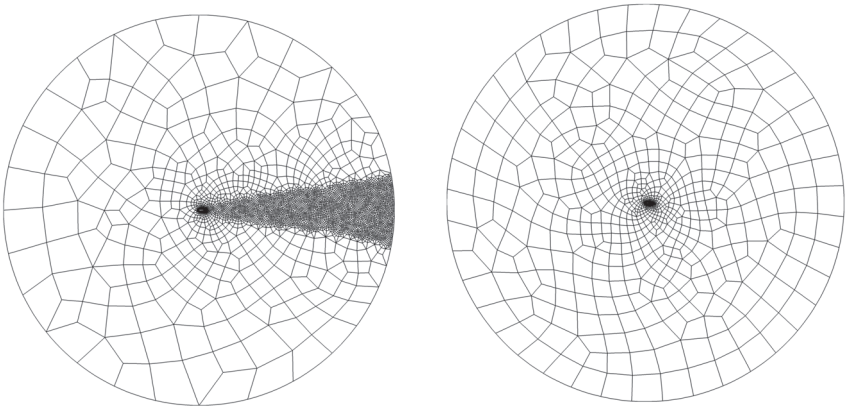

(**a**) (**b**)

Figure 2. Mesh of NACA0012 (**a**) and SD7003 (**b**).

3.1. NACA0012

The first analysis focused on a sinusoidal pitching/plunging, two-dimensional NACA0012 airfoil at $Re = 40{,}000$. The motion laws are given by Equation (1), with $\alpha_0 = 0$. The heaving amplitude was fixed at $h_0 = 0.75c$. Meanwhile, the axis of rotation was positioned at a distance of 1/3 chords from the leading edge. The heaving signal led the pitching harmonic by a quarter period, so $\psi = 90°$, which is known to be the optimal value in terms of efficiency ([7–9]).

Analysis was conducted through the comparison of propulsive performance and flow structure for several kinematic configurations. Specifically, we studied propulsive attributes at $\alpha_{max} = 15°$ and $\alpha_{max} = 30°$ while ranging St from 0.1 to 0.45 with an interval of 0.05. On the other hand, flow fields were inspected for cases at $\alpha_{max} = 20°$ and $\alpha_{max} = 30°$, both with $St = 0.45$. The polynomial degree was adapted to the value of the frequency, with a minimum of $q = 3$ for low St and a maximum of $q = 6$ for high St, because as the Strouhal number increases, the vortical structures become smaller, requiring a greater spatial resolution. Results were then compared with the experiments of Schouveiler et al. [8] for validation, although the experimental data available in the literature appear to be scattered.

The series of surveys, aiming to perform a direct comparison to the models, are focused on the examination of propulsive performance sensitivity to St, as heaving/pitching amplitude and frequency are the main factors influencing the wake topology [41–44]. The shape of the wake is in fact directly correlated with the thrust that the airfoil is able to create, as explained in [3]. This means that simulating a broad spectrum of combinations of θ_0 and f constitutes a solid benchmark to test the goodness of the numerical models.

Propulsive performance was assessed in terms of the thrust coefficient $C_T = -C_D$ and propulsive efficiency η_p, defined as

$$\eta_p = \frac{\overline{C}_T}{\overline{C}_P}\,. \tag{13}$$

The terms $\overline{C}_T$ and $\overline{C}_P$ are, respectively, the mean thrust and mean power coefficient, computed as

$$\overline{C}_T = \frac{1}{n_c T}\int_0^{n_c T} C_T\, dt\,, \quad \overline{C}_P = -\frac{1}{n_c T}\int_0^{n_c T}\left[C_L \frac{u_2^t}{U_\infty} + C_M \frac{c\omega_3^t}{U_\infty}\right] dt\,, \tag{14}$$

where u_2^t and ω_3^t are defined in Equations (2) and (3), respectively; n_c indicates the number of cycles considered for the average; and T represents the motion period.

Note that the definition of Equation (13) admits negative values of η_p when the flapping foil experiences drag, whereas it is positive when thrust is generated.

The results are collected in Figure 3.

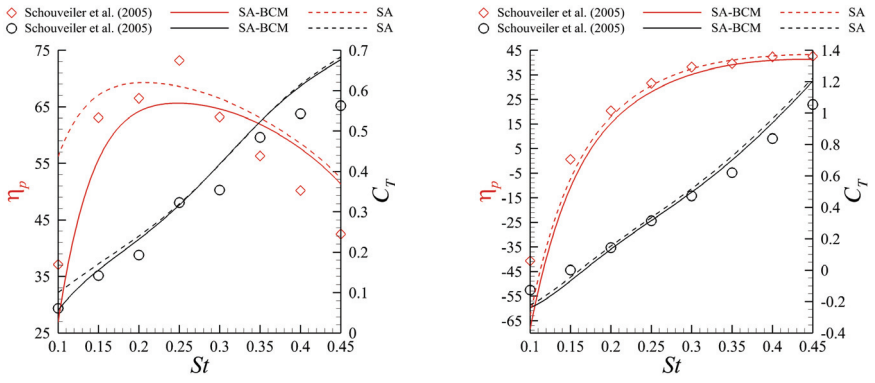

Figure 3. Propulsive efficiency and mean thrust coefficient as a function of the Strouhal number for $\alpha_{max} = 15°$ (**a**) and $\alpha_{max} = 30°$ (**b**). Experimental data digitized from [8].

At a high angle of attack, both models seem to perform in a quite similar fashion, retracing well the experimental data points at medium/high frequencies, especially if we consider η_p. As f decreases, the gap between simulations and experiments starts to widen. Indeed, at $St = 0.1$ we have that $\eta_{p_{exp}} \approx -40.7\%$. Instead, the transition and fully turbulent models predict efficiencies of -68.3% and -63.0%, respectively. Nonetheless, throughout the frequency spectrum analysed, SA always provides a moderately higher thrust than SA-BCM, which translates into a greater efficiency. This is probably attributed to the more diffusive nature of the fully turbulent model, which postpones separation and contributes positively to thrust generation. At a small angle of attack, the situation changes drastically, as the transition and fully turbulent models largely differ at low frequencies. For example, at $St = 0.1$, SA estimates a mean thrust coefficient of 0.100, whereas SA-BCM provides a value of $\overline{C}_T = 0.056$, which is very close to the experimental value of 0.061. In addition to this, the efficiency of SA is characterized by $\eta_p = 56.2\%$, whereas SA-BCM shows a value of $\eta_p = 26.9\%$, much closer to the value of 37.1 obtained from the experiments. This seems to imply a better performance of the transition model, as it is also able to replicate the drop of the η_p curve at small values of f, unlike the fully turbulent model.

In order to gain insight on this diverse behaviour at a small angle of attack, it is useful to exploit the phase space (C_L, C_D) representation composed of the instantaneous lift and drag coefficient curves, as proposed in [45], coupled with a visualization of the flow fields.

Figure 4 depicts (C_L, C_D) phase maps at the extremes of our frequency range for the case $\alpha_{max} = 15°$. As expected, when $St = 0.1$, the two models trace a completely different orbit. Instead, when $St = 0.45$, the curves are more or less overlapped. At high frequencies, the transition model moves between larger negative and positive values of the lift coefficient than the fully turbulent model and it is capable of revealing 'richer'

dynamics as the airfoils generate resistance ($C_D > 0$), but the overall paths are coincident. Furthermore, SA-BCM does not hold a perfectly periodic trajectory due to the unsystematic activation/deactivation of γ_{BC} within multiple periods. At small frequencies, the models follow their own trajectory, with SA-BCM featuring an imperfectly symmetric curve with respect to $C_L = 0$ and a much longer portion in drag conditions ($C_D > 0$). The reason why this happens can be sensed by examination of the vorticity fields in Figure 5. It is evident how the transition model captures flow separation. Meanwhile, the classic Spalart–Allmaras model only causes a thickening of the boundary layer. At high frequencies, where just a trailing-edge vortex (TEV) detaches from the profile, this approximation is sufficient for replication of the wake pattern. At low frequencies, separation is anticipated, and there is the creation of a LEV that travels along the suction surface, eventually interacting with the TEV. The lack of this interaction when using SA causes little to no separation and leads to a streamlined wake. This supports the thesis of Guglielmini et al. [46], which states that in order to accurately evaluate performances of oscillating foils, flow separation must be modelled at the leading and trailing edges. Animations showing the physical mechanisms involved in the arise of flow instabilities are provided as Supplementary Material, although we will not focus on those aspects as it is beyond the purpose of this work.

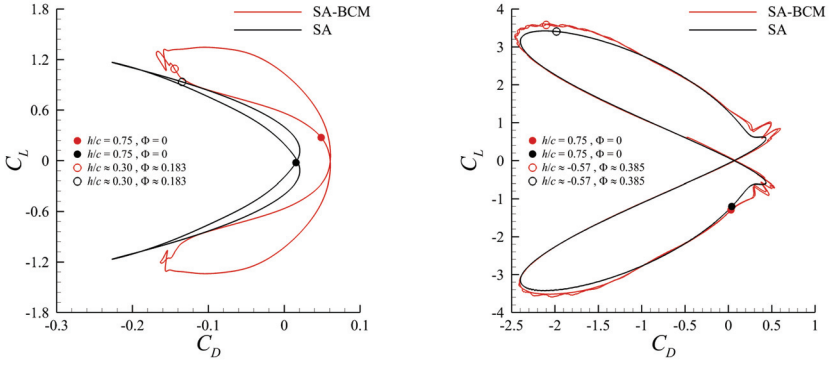

(**a**) (**b**)

Figure 4. (C_L, C_D) phase diagram for $\alpha_{max} = 15°$ using transition and fully turbulent model with $St = 0.1$ (**a**) and $St = 0.45$ (**b**). The curves cover a total of two time periods; solid circles (●) identify the starting point of the oscillating cycle and empty circles (○) indicate the point where vorticity fields in Figure 5 are depicted.

(**a**) (**b**)

Figure 5. *Cont.*

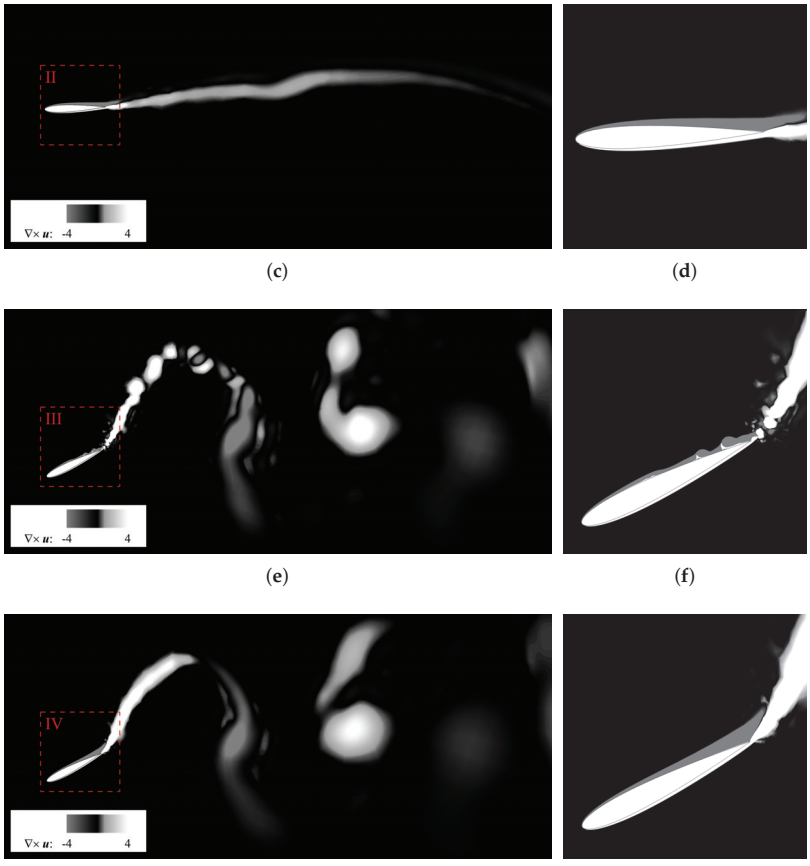

(**c**) (**d**)

(**e**) (**f**)

(**g**) (**h**)

Figure 5. Contour plot of the instantaneous vorticity field for $\alpha_{max} = 15^{\circ}$ using the transition and fully turbulent models. The snapshots are taken at $\Phi \approx 0.183$ for $St = 0.1$ and at $\Phi \approx 0.385$ for $St = 0.45$. (**a**) $St = 0.1$, SA-BCM; (**b**) detail I; (**c**) $St = 0.1$, SA; (**d**) detail II; (**e**) $St = 0.45$, SA-BCM; (**f**) detail III; (**g**) $St = 0.45$, SA; (**h**) detail IV.

The inability of the fully turbulent model to capture flow detachment is confirmed by Figure 6. At $\alpha_{max} = 20^{\circ}$ and $St = 0.45$, the transition model displays swirling structures forming at the leading edge, as portrayed in Figure 6f, instead in the fully turbulent model the flow remains attached (see Figure 6h). Despite this clear contrast, the fast dynamics appears to uniform the flow field at the trailing edge, yielding a good similarity in the wake topology, which also finds a good agreement with the visual recordings in [8]. This seems to imply that, for $\alpha_{max} \leq 20^{\circ}$, both models perform well if St is high enough, but as soon as St decreases, SA-BCM becomes much more accurate than SA. That said, Figure 6e,g still exhibit some minor differences. In particular, adopting the designation introduced by Williamson and Roshko [41], we have that SA-BCM draws a 2P + 2S wake, with a pair of corotating vortices (denoted by the letter 'P') plus a single vortex (denoted by the letter 'S') formed during each half cycle, whereas the wake resulting from SA falls into the 2P category, because the single vortex becomes embedded into the tail of the paired eddies. The only configuration where SA also reveals a separated flow upstream the trailing edge is at a high angle of attack and high frequency ($\alpha_{max} = 30^{\circ}$, $St = 0.45$), due to the fact that the turbulence level is so high that even a standard RANS model is suitable. Indeed, SA-BCM

and SA both induce a 2P + 2S wake, as shown in Figure 6a,c, which once again manifest a good resemblance to the visualizations obtained experimentally by Schouveiler et al. [8]. We point out that each wake in Figure 6 evolves in a 2S reverse von Kármán vortex street after $\approx 10c$ for $\alpha_{max} = 20^\circ$ and $\approx 7c$ for $\alpha_{max} = 30^\circ$; hence, they all generate thrust.

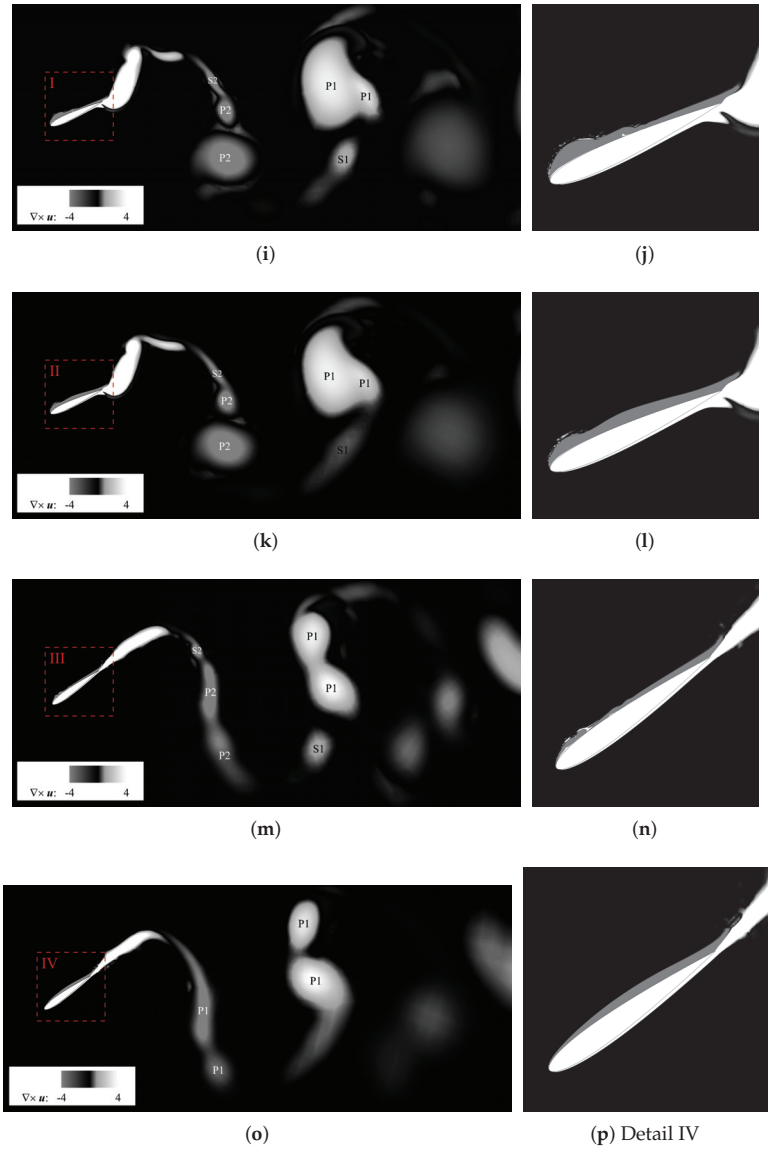

Figure 6. Contour plot of the instantaneous vorticity field using transition and fully turbulent model for $St = 0.45$. All snapshots are taken at $\Phi = 0.25$. (**a**) $\alpha_{max} = 30^\circ$, SA-BCM; (**b**) Detail I; (**c**) $\alpha_{max} = 30^\circ$, SA; (**d**) Detail II; (**e**) $\alpha_{max} = 20^\circ$, SA-BCM; (**f**) Detail III; (**g**) $\alpha_{max} = 20^\circ$, SA; (**h**) Detail IV.

For completeness, it is worth finally providing an example of the convergence study of the solutions here reported. Space and time resolution-independence have been guaranteed through a polynomial refinement of the space discretization q and the choice of the time step size Δt. It should be noted that by raising the degree of the polynomial approxima-

tion, the order of accuracy of the solution increases, although this also corresponds to a significant growth in the number of degrees of freedom. For instance, moving from $q = 3$ to $q = 6$, the total number of variables goes from 296,640 to 830,592. An increase by a factor almost equal to 3 in the dimension of the numerical problem may be observed as a result of such a raise in the polynomial-order approximation. The solutions' accuracy was verified by examining the behaviour of both the average performance coefficients and the (C_L, C_D) phase diagrams. For the sake of conciseness, in the following we only report the convergence results referring to the particular case with $\alpha_{max} = 20^\circ$ and $St = 0.45$. Its stringent requirement for high spatial and temporal resolutions due to the large St makes it indeed a most challenging scenario. Considering the SA-BCM model, which presents relatively stricter accuracy constraints compared to the standard SA due to its algebraic modification, the average drag coefficient and efficiency have been observed to remain substantially unchanged throughout the performed space–time refinement: moving from $q = 3$ and $\Delta t = 10^{-2} c/U_\infty$ up to $q = 6$ and $\Delta t = 2.5 \times 10^{-3} c/U_\infty$, we have that $\overline{C}_D$ ranges between -1.016 and -1.017, whereas η_p spans between $= 0.548$ and 0.551. In Figure 7, the (C_L, C_D) phase diagrams for different polynomial approximations are reported over one cycle. It is easy to notice that for $q \geq 3$ the results are almost indistinguishable. When only adopting SA-BCM, very small differences arise; however, as previously mentioned, with this model an imperfectly periodic behaviour of the solution is often observed, and small differences can be seen even between consecutive cycles performed at the same polynomial order, as will be further shown in Section 3.2.2. Note that another detailed space convergence study is also presented for the SD7003 profile in Section 3.2.2.

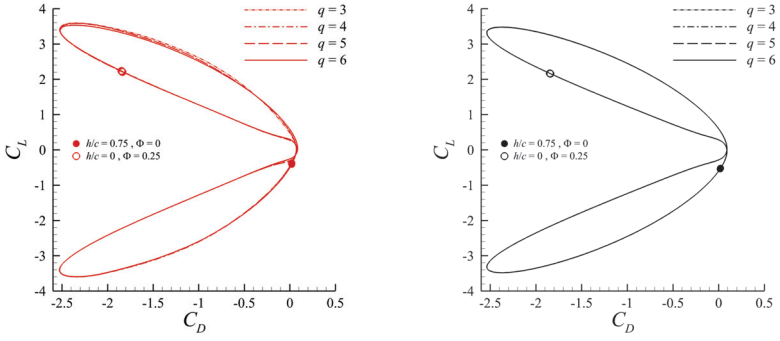

Figure 7. Single−period (C_L, C_D) phase diagram at increasing polynomial degree q for the case with $\alpha_{max} = 20^\circ$ and $St = 0.45$, using transition (**a**) and fully turbulent model (**b**). (i) $q = 3$, $\Delta t = 10^{-2} c/U_\infty$; (ii) $q = 4$, $\Delta t = 5 \cdot 10^{-3} c/U_\infty$; (iii) $q = 5$, $\Delta t = 2.5 \cdot 10^{-3} c/U_\infty$; (iv) $q = 6$, $\Delta t = 2.5 \cdot 10^{-3} c/U_\infty$. Solid circles (●) identify the starting point of the oscillating cycle, empty circles (○) indicate the point where vorticity fields in Figure 6e–h are depicted.

3.2. SD7003

For the SD7003 airfoil, the turbulence models were investigated by considering a high-frequency plunging at a constant angle of attack. Two different kinematic parametrizations have been explored; in both cases, the pitch angle of the profile was kept constant by switching off its time dependence in Equation (1), placing $\theta_0 = 0$.

3.2.1. Case 1

In this configuration, the airfoil was set to describe a plunging motion with reduced frequency $k = 3.93$, amplitude $h_0 = 0.05c$, and a constant angle of attack $\alpha_0 = 4^\circ$ at $Re = 40{,}000$. The corresponding Strouhal number can be easily derived by inserting the values of k and h_0 in Equation (5), giving $St = 0.125$.

During the downward motion, the effective angle of attack increases as a consequence of the vertical velocity of the profile. In particular, substituting u_2^t into Equation (4) leads to $\alpha > 20°$. This high value determines a boundary layer separation at the leading edge resulting in the formation of several LEVs trailing downstream.

Even though an accurate capture of the LEV dynamics, and thus an overall accurate flow description, is thought to be fundamental for precise computation of the forces exerted on the profile, the simulated configuration revealed to be solely dominated by the dynamics of the profile motion rather than the flow structure itself. Such an observation seems to be justified by the small difference in the forces predicted by the two models, even though SA-BCM allowed the derivation of a much more accurate representation of the relevant flow features with respect to the standard SA, especially when compared with the three-dimensional results in [11,12]. To demonstrate this, in Table 1 the thrust coefficients derived from the two models are reported as averages realized over five motion periods together with the aforementioned experimental and numerical reference values. It is possible to note that the models employed in the two-dimensional computations present no significant difference in terms of mean drag coefficient, placing both at a similar distance from the three-dimensional results.

Table 1. Comparison of the mean drag coefficient $\overline{C}_D$ between the different models, together with experimental and numerical reference data.

SA	SA-BCM	Visbal [11]	Krais et al. [12]
−0.072	−0.073	−0.083	−0.082

This is further supported by examining the instantaneous behaviour of the hydrodynamic forces given in Figure 8, where the variations occurring in the phase plane (C_L, C_D) are jointly reported with the associated time dynamics over two periods. In these figures, it is possible to note that the curves related to the two models overlap almost entirely, aside from a minor offset in the trajectories drawn in the phase plane. Moreover, in Figure 8a, there is also a fairly good agreement between the C_D signal of both models and the scale-resolving data from [11]. This suggests a substantial model independence in terms of instantaneous and mean force computations.

On the other hand, significant differences can be found by examining the details of the vorticity dynamics at the solid surface and the associated vortex development as a result of boundary-layer instabilities. From the instantaneous contours of the span-wise vorticity reported in Figures 9 and 10, it can be noted that while the results of the two models in the aft portion of the profile are fairly congruent, a quite significant deviation is observed at the fore region close to the leading edge.

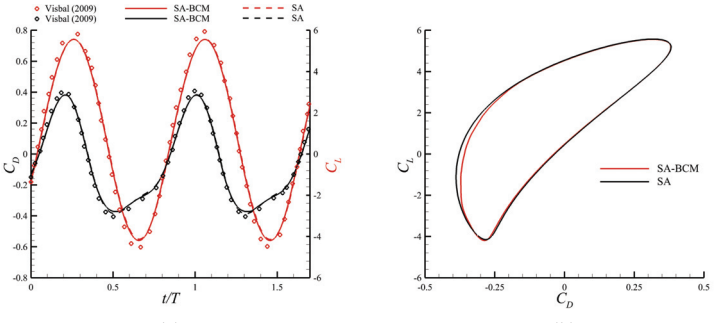

(**a**) (**b**)

Figure 8. (**a**) Time behaviour of drag and lift coefficients for SA, SA−BCM, and scale−resolving 3D model obtained via image digitization of data in [11]. (**b**) Phase plane representation of drag and lift coefficients for SA and SA−BCM model.

Considering the transition model computations, it is possible to see that when the profile reaches the top position $\Phi = 0$, (Figure 9a,b), two vortices develop over the lower surface of the profile due to boundary-layer separation, discernible by the regions of strongly negative vorticity generated by the wall-enforced no-slip condition. On the upper surface, the boundary layer appears to be fully attached on a relatively large zone past the leading edge, but a strongly diffused vorticity structure, a remnant of the previous cycle, travels downstream. Three-dimensional reference data in [11] clearly highlight the span-wise homogeneous character of the laminar boundary-layer instabilities at the onset corresponding to the front part of the airfoil. As a consequence, this region exhibits a local physical behaviour that is purely two-dimensional and is fully captured by the transition model. Conversely, the standard SA model at the same position presents a much smoother vorticity distribution over the profile surface (Figure 10a,b). Even though separation at the lower surface is still visible in the small layer of negative vorticity produced at the wall, the enhanced diffusivity here induces a coalescence of the two vortices into a single vortex. Furthermore, a single core of vorticity is again visible on the upper surface, which seems, however, to remain more closely attached to the solid surface.

As the position $\Phi = 0.25$ is reached, the profile assumes its maximum downward velocity. By examination of the vorticity contour of the SA-BCM model in Figure 9c,d, it is possible to note a separation with the subsequent incipient roll-up of the boundary layer in the region close to the leading edge at the upper surface, resulting in a thinning of the layer in the immediate vicinity. The two formed vortices, upon their interaction with the solid surface, generate two visible regions of positive-sign vorticity arising from the boundary. This region is found to exhibit striking similarities with the field predicted by the three-dimensional simulation (see [11]), once again justified by the two-dimensional character of the instabilities at their onset. On the contrary, by examination of Figure 10c,d referring to the SA model, it is evident that all the aforementioned details of boundary-layer instability are not adequately captured due to the absence of any modifications accounting for the transition. In particular, the characteristic ripples of the boundary layer edge are completely absent, implying that the local flow acceleration toward the solid surfaces resulting from boundary roll-up is completely sheared out, and the flow almost immediately reattaches at the boundary without any flow organization in a coherent structure. Similar observations are also true for the dynamics of the lower surface boundary layer; although the SA-BCM model predicts the presence of three clockwise-rotating structures, the use of a fully turbulent SA closure does not seem to be able to capture any vorticity ejection into the fluid domain. The higher accuracy resulting from the application of a transition model is made evident upon inspection of the three-dimensional results in [11,12]. The early transition state at the upper surface, with the presence of span-wise homogeneous vortices, seems to be exactly captured by the SA-BCM model. In contrast, the scale-resolving results show that the lower vortex trailing downstream exhibits a significant non-homogeneous spanwise character, suggesting a less accurate description given by the two-dimensional simulation due to the absence of three-dimensional mechanisms of vorticity redistribution.

At $\Phi = 0.5$, the profile reached the maximum downward displacement. Considering again the referenced three-dimensional results [11,12], the presence of two distinct turbulent regions over the upper surface of the profile separated by a laminar, spanwise homogeneous zone can be seen. By examination of Figure 9e, it can be seen that, corresponding to those regions, the SA-BCM model predicts the presence of two large, highly diffused vorticity regions. The vortex close to the leading edge (see Figure 9f), in particular, arises as a result of the diffusion-induced coalescence of the previously formed vortex into a single structure, attributed to the activation of the source term in the model. Behind this single core region, the boundary layer reattaches laminarly—with the intermittency function (not displayed for this phase) locally assuming a value of zero—before separating again. This second separated region, as can be seen by the presence of the positive sign of the vorticity below the rippled boundary layer edge, gives rise to three spanwise-homogeneous distinct vortices that have also been observed in [11,12]. By examining the corresponding

field reported by the SA model in Figure 10e,f, the upper surface single vortex is again observable. However, in this case, it emerges as a single structure after boundary-layer separation at the leading edge. Further downstream to such structure, the boundary layer reattaches and then simply increases its thickness along the downstream direction; no significant instability phenomena nor further separation region can be appreciated in the boundary layer by adopting the SA model.

Finally, at $\Phi = 0.75$ the profile reaches the maximum velocity in its upstroke motion. The three-dimensional results [11,12] show the formation of complex vorticity organization over a large portion of the upper surface as a consequence of interactions between the profile and the previously formed vortex structures. In the SA-BCM model, such interactions seem to be captured in a more adequate manner with respect to the SA model, even though not exactly due to the two-dimensional nature of the simulation. By examination of Figure 9g,h, it is possible to observe the single leading-edge vortex being pushed towards the solid surface by the vertical, motion-induced velocity as it becomes advected downstream. As a consequence of this wall–vortex interaction, a region of positive-sign vorticity is formed and subsequently ejected into the fluid domain. The two-dimensional instantaneous vorticity contours derived via implementation of SA-BCM model appear to be in fairly good agreement with the planar vorticity distribution reported in [11,12]. On the contrary, in the SA case, Figure 10g,h, the situation is significantly different: the vorticity distribution is much smoother with respect to the three-dimensional findings. Moreover, the leading-edge vortex appears to be much more heavily diffused and stretched in the streamwise direction with only a small, positive vorticity region confined close to the solid wall. Further downstream, no visible sign of boundary-layer instability can be identified over the upper surface. The overall effect of the upward motion in the SA case is a compression of the boundary layer towards its bounding solid wall without generation of any clearly detectable instability.

To further demonstrate the improvement brought on by the application of a transition model over the common RANS approach, another detail of vortex generation due to leading-edge separation corresponding to the position $\Phi = 0.35$ is reported in Figure 11, and comparison is drawn again from the spanwise vorticity distribution provided in [11,12] at the same position. Once again, striking similarities can be seen between the two-dimensional SA-BCM results and the fields computed in the three-dimensional simulations reported in the previously mentioned works. In more detail, at this stage of the motion the profile is decelerating towards its maximum downward displacement position; three coherent, clockwise-rotating structures are clearly detectable close to the leading edge, separated by regions of positive-valued vorticity. The last of these formed at previous stages of motion become further stretched and are transported away from the solid boundary upon interaction with the upward-moving fluid of the negative vorticity cores. The interactions between these counter-clockwise-rotating regions then trigger instability mechanisms involving the spanwise direction, as clearly highlighted in [11], inducing a transition to a fully turbulent regime characterized by the collapse of the generated structures into smaller scales. Obviously, such mechanisms cannot be captured by two-dimensional simulations; however, the implementation of a transition model enables description with a sufficient degree of accuracy of the onset and the initial evolution of the boundary-layer spanwise instabilities that eventually evolve into the turbulent structures that are resolved in the three-dimensional problems.

Figure 11b provides the instantaneous value of the intermittency factor γ_{BC} modulating the activation of the eddy viscosity-like production. As the parameter reaches unitary value according to the local flow features, it induces a local increase in diffusivity exactly corresponding to the regions that also appear to develop a fully turbulent behaviour based on the three-dimensional results. In more detail, the model activates, triggering a local enhancement of momentum diffusivity corresponding to the region occupied by the three clockwise-rotating structures close to the leading edge and both on the lower and upper surface extending from the trailing edge up to half-profile length. It could be speculated

that the localized increase in diffusivity in the fore region determines the coalescence of the three structures therein present, in turn determining the emergence of the single vortex core observed in Figure 9f.

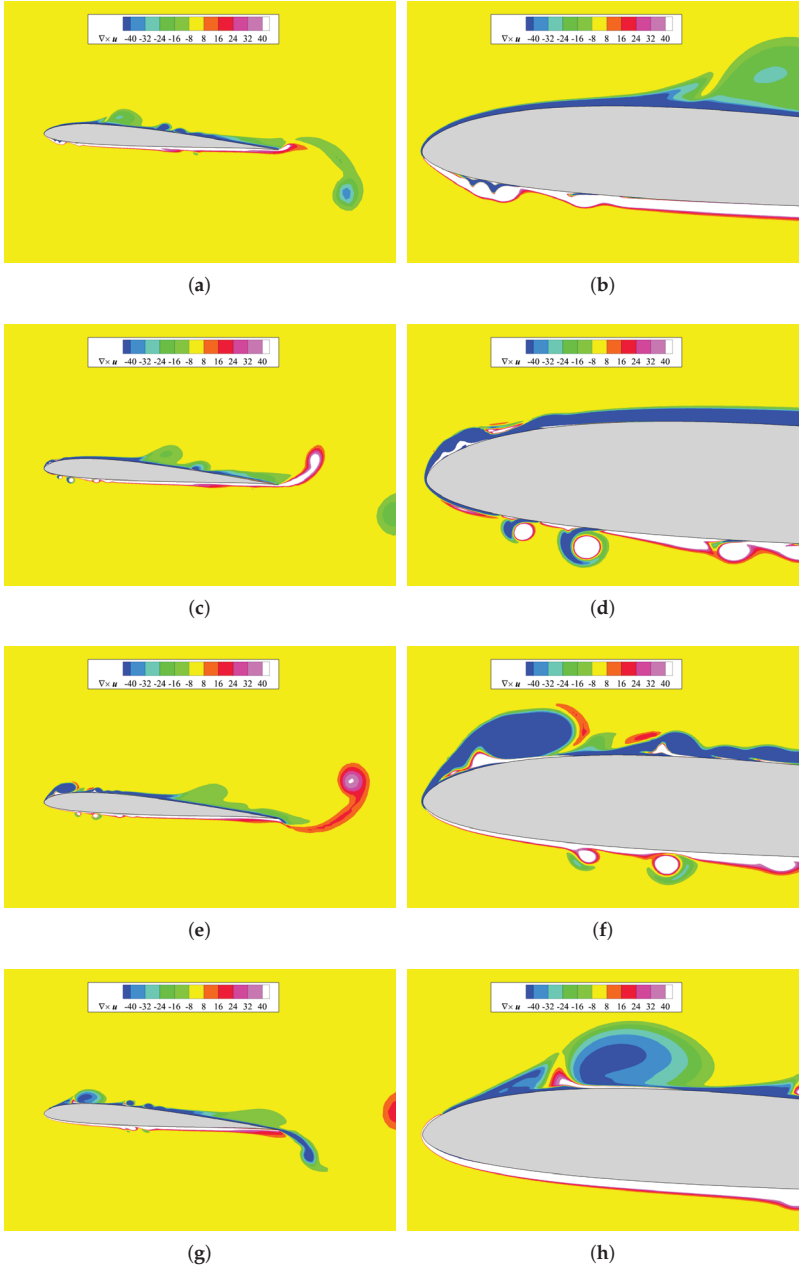

Figure 9. SA−BCM model. Contour of instantaneous spanwise vorticity. From top to bottom, the vertical positions are presented in the sequence: (**a**,**b**) $\Phi = 0$; (**c**,**d**) $\Phi = 0.25$; (**e**,**f**) $\Phi = 0.5$; (**g**,**h**) $\Phi = 0.75$. The right column reports the details of the instability developing at leading edge.

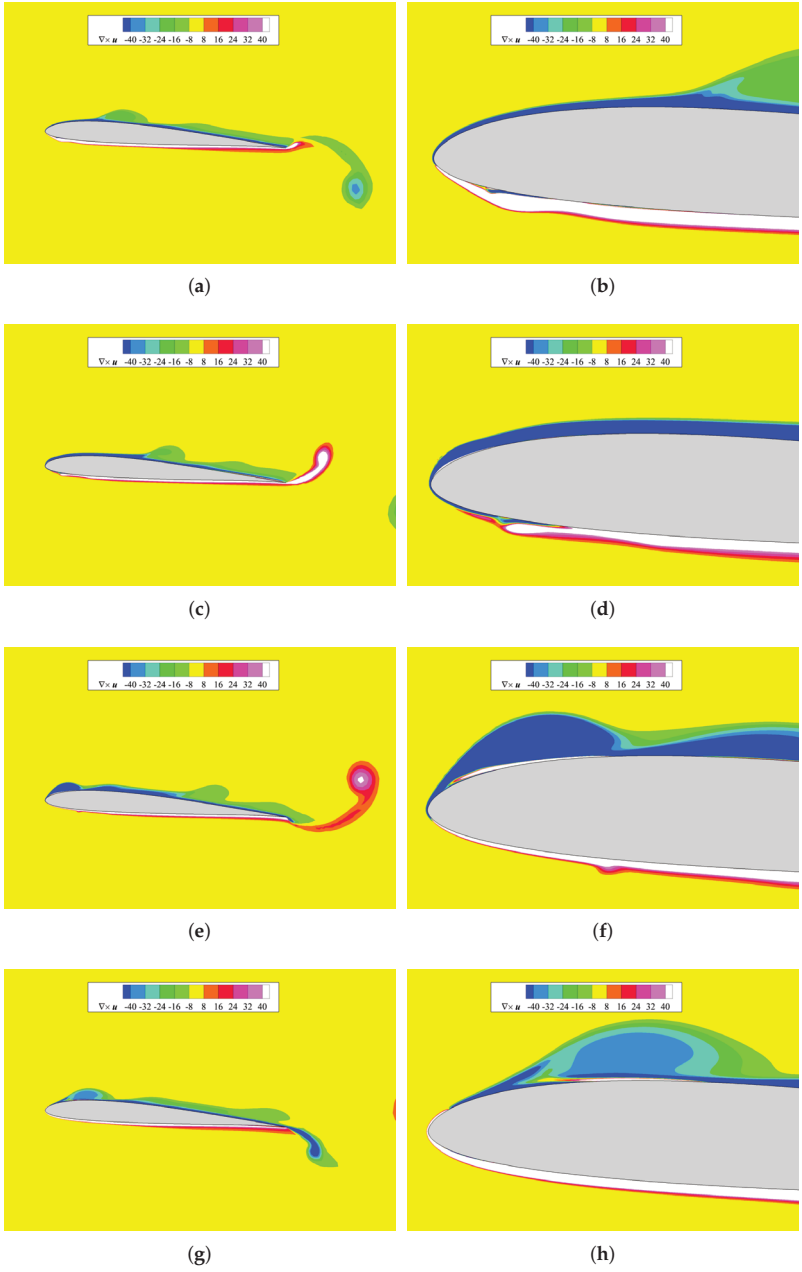

Figure 10. SA model. Contour of instantaneous spanwise vorticity. From top to bottom, the vertical positions are presented in the sequence: (**a**,**b**) $\Phi = 0$; (**c**,**d**) $\Phi = 0.25$; (**e**,**f**) $\Phi = 0.5$; (**g**,**h**) $\Phi = 0.75$. The right column reports the details of the instability developing at leading edge.

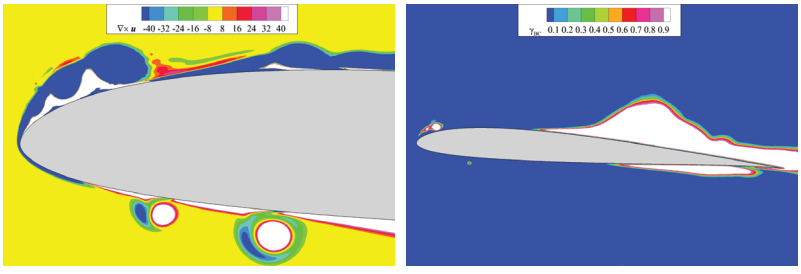

(**a**) (**b**)

Figure 11. SA−BCM model. Vertical position $\Phi = 0.35$. Contour of instantaneous spanwise vorticity (**a**) and intermittency function γ_{BC} (**b**).

The implementation of the transition SA-BCM model for this case of the plunging airfoil at a moderate Reynolds number is found to provide an overall improved flow structure prediction when compared to the three-dimensional results with respect to the more commonly used Spalart–Allmaras RANS approach. It should be noted that this comes without any variation in terms of the magnitude of neither the mean nor instantaneous force computations.

3.2.2. Case 2

The second explored case for the asymmetric SD7003 profile has been proposed as a mechanism for stall suppression based on high-frequency small-amplitude oscillations. The mean angle of attack was increased to $\alpha_0 = 14°$, the Reynolds number to $Re = 60{,}000$, and the reduced frequency assumed a value of $k = 10$. The vertical amplitude of the oscillations has been set to a value equal to 0.5% of the chord length , i.e., $h_0 = 0.005c$. Analogously to the previous case, the corresponding Strouhal number may be derived upon substitution of the above parameters into Equation (5), resulting in $St = 0.03$.

For this configuration, the two models have been firstly tested by considering stationary simulations in a static stall condition, fixing the profile at the constant angle of attack reported above. Table 2 collects the values of C_D resulting from different polynomial approximations to provide an example, relative to the steady case, of the space convergence study. The presence of a plateau in the drag coefficient value suggests that an independence of the solution with respect to the adopted space discretization is achieved.

Table 2. Steady case. Space convergence shown by means of the trend of the drag coefficient C_D at increasing polynomial degree q.

q	SA	SA-BCM
1	0.210	0.215
2	0.196	0.204
3	0.194	0.204
4	0.194	0.205
5	0.194	0.205
6	0.194	0.205

Moving to the steady case results, no noticeable difference could be appreciated between the two models, neither in terms of flow structures nor from the viewpoint of mean drag coefficient. Such a situation is depicted in Figure 12: due to the large separated region, the intermittency function of the SA-BCM model is active over a major portion of the domain such that both cases adopt the same eddy diffusivity equation over a critically large region, providing a justification for the essentially overlapping results.

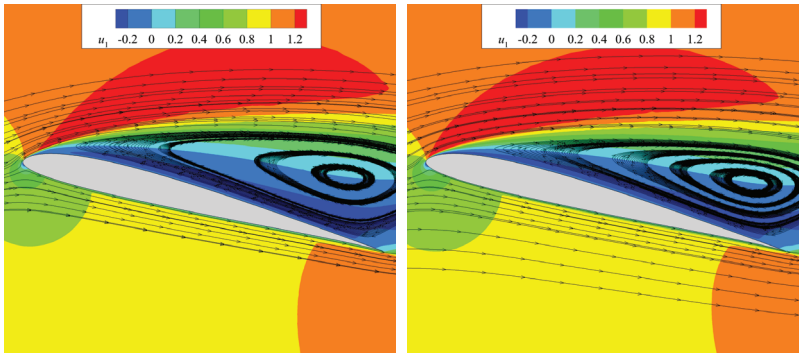

(**a**) (**b**)

Figure 12. Stationary case. Contour of streamwise velocity u_1. SA−BCM model (**a**) and SA model (**b**).

As far as the time-dependent analysis is concerned, the motion prescribed according to the parametrization given above has been observed to exhibit a significant reduction in the average dimension of the separated region with a parallel diminishing of the drag coefficient up to 40% in three-dimensional, scale-resolving simulations [11].

Figure 13 reports the mean streamwise velocity field of the two-dimensional case for both the SA and the SA-BCM models. The SA-BCM (Figure 13a) shows a significantly larger reduction in the size of the recirculation region behind the profile when compared with the corresponding effect given by the SA model in Figure 13b. Indeed, the local flow reattachment is a result of the interactions between the stall vortex detaching from the leading edge and the moving surface, so an adequate resolution of such structures appears to be fundamental for capture of an effective stall reduction. When adopting a fully turbulent SA model, instabilities are immediately sheared out by the turbulent stresses so that the mean flow strongly accelerates past the leading edge as a result, exhibiting a neat separation.

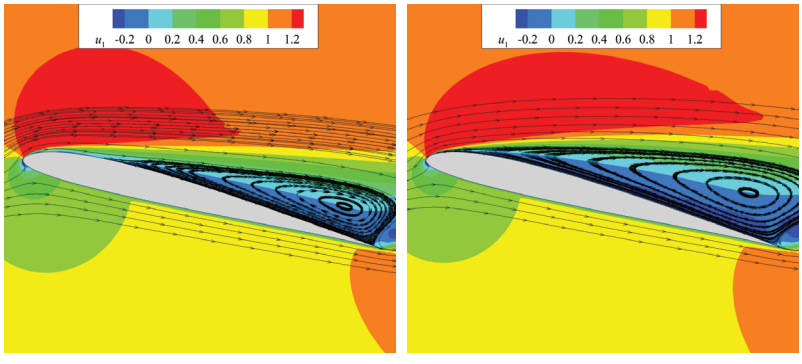

(**a**) (**b**)

Figure 13. Time−dependent case. Contour of the mean streamwise velocity u_1. SA−BCM model (**a**) and SA model (**b**).

Conversely to the case previously explored in Section 3.2.1, an adequate capture of stall reduction phenomena seems to be intimately dependent upon an accurate resolution of the flow structures emerging from leading-edge separation, which is in turn better guaranteed by the application of a transition modification rather than a standard, globally diffusive RANS.

By examining the behaviour of the hydrodynamic forces over multiple cycles in the (C_L, C_D) plane (see Figure 14), it is possible to note that whilst the SA curve exhibits a substantial periodicity, the orbit drawn by the transition model moves within a bounded area in the phase plane.

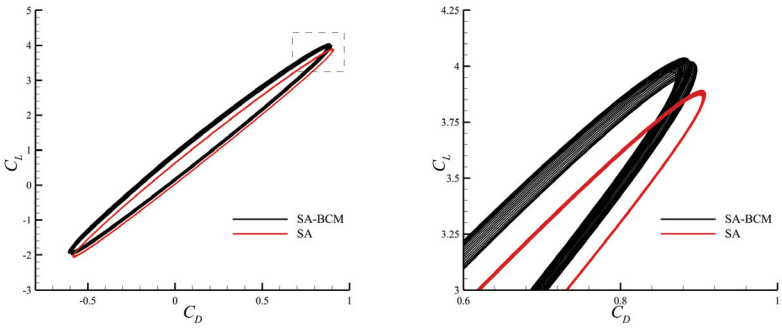

Figure 14. Time−dependent case. Instantaneous phase space representation of hydrodynamic forces over multiple motion cycles (**a**) and relative enlargement (**b**).

In particular, the non-periodic SA-BCM solution is characterized by a low-frequency variation in the single-period average drag coefficient between two finite values, both of which are reported in Table 3. Furthermore, it is worth noting that the two $\overline{C}_D$ limits provided by SA-BCM are significantly smaller than the value predicted by SA and is closer to the three-dimensional reference data in [11].

Table 3. Comparison of $\overline{C}_D$ between the different models and experiments for the steady (first row) and high-frequency plunge (second row) cases. The values reported for SA−BCM in the plunging configuration are the minimum and maximum value of the single-period average drag coefficient.

Case	SA	SA-BCM	Visbal [11]
$k = 0, h_0/c = 0$	0.193	0.205	0.225
$k = 10, h_0/c = 0.005$	0.158	0.133–0.148	0.133

4. Conclusions

In the present work, two-dimensional high-order DG methods have been applied to the problem of oscillating airfoils at moderate Reynolds numbers, adopting both a standard SA-RANS approach and its algebra-based, transition modification SA-BCM as closure models. Two different profiles, namely NACA0012 and SD7003, have been used under different Strouhal regime and motion conditions to explore the relevant differences between the two models in terms of flow structure and force prediction capabilities.

As far as NACA0012 is concerned, for which a composed flapping motion was considered, the transition model seemed to behave adequately in the entire range of kinematic configurations explored. Moreover, at a low Strouhal number, an overall improved agreement with the experimental results has been observed upon the application of SA-BCM. The latter, in particular, proved to be able to capture flow separation more accurately on the surface of the airfoil for low-frequency oscillations. In contrast, the SA succeeded in this task only when separation was very intense, i.e., for high angles of attack and/or fast dynamics. Similar considerations can be made for the SD7003 profile. The high-frequency plunging configurations showed, upon confrontation with the scale-resolving studies [11,12], that the embedding of a transition model into the standard SA equations guarantees a significant increase in the accuracy of the flow field close to the solid boundary. In particular, at $k = 10$ the reattachment of the mean flow was captured only by the SA-BCM model, whose

prediction of the mean drag was significantly closer to the three-dimensional references with respect to the standard SA.

In conclusion, the distinct transitional aspects of the flow induced by oscillating airfoils at moderate Reynolds numbers, featured by laminar separation followed by turbulent reattachment, make them suitable candidates to test transition modification of standard RANS models. The embedding of an intermittency function γ_{BC} locally modulating the magnitude of the production term within the closure eddy viscosity-like equation allows for an exact resolution of the spanwise-homogeneous region at the leading edge during the early transition state. This, in turn, enables more accurate assessment of the dynamics of the coherent structures arising from such instabilities in comparison to the standard SA. For motion configurations characterized by very low Strouhal numbers, where the interactions of the LEV with the TEV are crucial for correct evaluation of the hydrodynamic forces, the application of the SA-BCM provided results more in line with the experimental data. Contrarily, model performances were found to be almost identical when the dynamics were characterized by combinations of high frequency and large amplitude, where an abrupt separation of the boundary layer occurs. In such cases, γ_{BC} reaches the unit value in a considerably large zone, so SA-BCM and SA basically solve an identical set of equations.

Supplementary Materials: The following supporting information can be downloaded at: https://www.mdpi.com/article/10.3390/fluids8010023/s1, Video S1: Time evolution of the vorticity field in Figure 5a. Video S2: Time evolution of the vorticity field in Figure 5b. Video S3: Time evolution of the vorticity field in Figure 5c. Video S4: Time evolution of the vorticity field in Figure 5d. Video S5: Time evolution of the vorticity field in Figure 5e. Video S6: Time evolution of the vorticity field in Figure 5f. Video S7: Time evolution of the vorticity field in Figure 5g. Video S8: Time evolution of the vorticity field in Figure 5h. Video S9: Time evolution of the vorticity field for Case 1, SA-BCM model (Figure 9). Video S10: Time evolution of the vorticity field for Case 1, SA model (Figure 10). Video S11: Time evolution of the intermittency function field for Case 1 (Figure 11b).

Author Contributions: Conceptualization, A.C.; methodology, A.C.; software, A.C., E.C. and L.A.; validation, A.C., E.C. and L.A.; formal analysis, A.C., E.C. and L.A.; investigation, A.C., E.C. and L.A.; resources, A.C.; data curation, A.C., E.C. and L.A.; writing—original draft preparation, A.C., E.C. and L.A.; writing—review and editing, A.C., E.C. and L.A.; visualization, A.C., E.C. and L.A.; supervision, A.C. All authors have read and agreed to the published version of the manuscript.

Funding: This research received no external funding.

Data Availability Statement: The data presented in this study are available on request from the corresponding author.

Conflicts of Interest: The authors declare no conflicts of interest.

Abbreviations

The following abbreviations are used in this manuscript:

DG	Discontinuous Galerkin
DNS	Direct numerical simulation
DOF	Degrees of freedom
GMRES	Generalized minimal residual method
ILES	Implicit large eddy simulation
LES	Large eddy simulation
LEV	Leading-edge vortex
PDE	Partial differential equation
PIV	Particle image velocimetry
RANS	Reynolds-averaged Navier–Stokes
SA	Spalart–Allmaras
SA-BCM	Spalart–Allmaras—Bas-Cakmakcioglu-Mura
TEV	Trailing-edge vortex

References

1. Knoller, A. Die gesetzedes luftwiderstandes. *Flug Und Mot.* **1909**, *3*, 1–7.
2. Betz, A. Ein beitrag zur erklaerung segelfluges. *Z. Flugtech Mot.* **1912**, *3*, 269–272.
3. Von Kármán, T.; Burgers, J. General Aerodynamic Theory-Perfect Fluids. *Aerodyn. Theory* **1943**, *2*, 346–349.
4. Lighthill, S.J. *Mathematical Biofluiddynamics*; Society for Industrial and Applied Mathematics: Philadelphia, PA, USA, 1975. [CrossRef]
5. Wu, X.; Zhang, X.; Tian, X.; Li, X.; Lu, W. A review on fluid dynamics of flapping foils. *Ocean. Eng.* **2020**, *195*, 106712. [CrossRef]
6. Triantafyllou, M.; Triantafyllou, G.; Gopalkrishnan, R. Wake mechanics for thrust generation in oscillating foils. *Phys. Fluids Fluid Dyn.* **1991**, *3*, 2835–2837. [CrossRef]
7. Read, D.; Hover, F.; Triantafyllou, M. Forces on oscillating foils for propulsion and maneuvering. *J. Fluids Struct.* **2003**, *17*, 163–183. [CrossRef]
8. Schouveiler, L.; Hover, F.; Triantafyllou, M. Performance of flapping foil propulsion. *J. Fluids Struct.* **2005**, *20*, 949–959. [CrossRef]
9. Anderson, J.M.; Streitlien, K.; Barrett, D.; Triantafyllou, M.S. Oscillating foils of high propulsive efficiency. *J. Fluid Mech.* **1998**, *360*, 41–72. [CrossRef]
10. Ol, M.V.; Reeder, M.; Fredberg, D.; McGowan, G.Z.; Gopalarathnam, A.; Edwards, J.R. Computation vs. Experiment for High-Frequency Low-Reynolds Number Airfoil Plunge. *Int. J. Micro Air Veh.* **2009**, *1*, 99–119. [CrossRef]
11. Visbal, M. High-fidelity simulation of transitional flows past a plunging airfoil. *AIAA J.* **2009**, *47*, 2685–2697. [CrossRef]
12. Krais, N.; Schnücke, G.; Bolemann, T.; Gassner, G.J. Split form ALE discontinuous Galerkin methods with applications to under-resolved turbulent low-Mach number flows. *J. Comput. Phys.* **2020**, *421*, 109726. [CrossRef]
13. Fröhlich, J.; Von Terzi, D. Hybrid LES/RANS methods for the simulation of turbulent flows. *Prog. Aerosp. Sci.* **2008**, *44*, 349–377. [CrossRef]
14. Chaouat, B. The state of the art of hybrid RANS/LES modeling for the simulation of turbulent flows. *Flow Turbul. Combust.* **2017**, *99*, 279–327. [CrossRef]
15. Yang, W.; Fan, Z.; Deng, X.; Zhao, X. RANS/LES Simulation of Low-Frequency Flow Oscillations on a NACA0012 Airfoil Near Stall. In Proceedings of the 2021 International Symposium on Electrical, Electronics and Information Engineering, Seoul, Republic of Korea, 19–21 February 2021; pp. 62–65.
16. Sanchez-Rocha, M.; Kirtas, M.; Menon, S. Zonal hybrid RANS-LES method for static and oscillating airfoils and wings. In Proceedings of the 44th AIAA Aerospace Sciences Meeting and Exhibit, Reno, Nevada, 9–12 January 2006; p. 1256.
17. Menter, F.R.; Langtry, R.B.; Likki, S.R.; Suzen, Y.B.; Huang, P.G.; Völker, S. A Correlation-Based Transition Model Using Local Variables—Part I: Model Formulation. *J. Turbomach.* **2004**, *128*, 413–422. [CrossRef]
18. Langtry, R.B.; Menter, F.R.; Likki, S.R.; Suzen, Y.B.; Huang, P.G.; Völker, S. A Correlation-Based Transition Model Using Local Variables—Part II: Test Cases and Industrial Applications. *J. Turbomach.* **2004**, *128*, 423–434. [CrossRef]
19. Walters, D.K.; Leylek, J.H. A New Model for Boundary Layer Transition Using a Single-Point RANS Approach. *J. Turbomach.* **2004**, *126*, 193–202. [CrossRef]
20. Carreño Ruiz, M.; D'Ambrosio, D. Validation of the $\gamma - Re_\theta$ Transition Model for Airfoils Operating in the Very Low Reynolds Number Regime. *Flow Turbul. Combust.* **2022**, *109*, 279–308. [CrossRef]
21. Ashraf, M.; Young, J.; Lai, J. Oscillation frequency and amplitude effects on plunging airfoil propulsion and flow periodicity. *AIAA J.* **2012**, *50*, 2308–2324. [CrossRef]
22. Li, X.; Liu, Y.; Kou, J.; Zhang, W. Reduced-order thrust modeling for an efficiently flapping airfoil using system identification method. *J. Fluids Struct.* **2017**, *69*, 137–153. [CrossRef]
23. Young, J.; Lai, J.C. Oscillation frequency and amplitude effects on the wake of a plunging airfoil. *AIAA J.* **2004**, *42*, 2042–2052. [CrossRef]
24. Wang, Z.; Du, L.; Zhao, J.; Sun, X. Structural response and energy extraction of a fully passive flapping foil. *J. Fluids Struct.* **2017**, *72*, 96–113. [CrossRef]
25. Cakmakcioglu, S.; Bas, O.; Mura, R.; Kaynak, U. A Revised One-Equation Transitional Model for External Aerodynamics. In Proceedings of the AIAA Aviation 2020 Forum, Virtual Event, 15–19 June 2020. [CrossRef]
26. Cakmakcioglu, S.C.; Bas, O.; Kaynak, U. A correlation-based algebraic transition model. *Proc. Inst. Mech. Eng. Part J. Mech. Eng. Sci.* **2017**, *232*, 3915–3929. [CrossRef]
27. Mura, R.; Cakmakcioglu, S.C. A Revised One-Equation Transitional Model for External Aerodynamics—Part I: Theory, Validation and Base Cases. In Proceedings of the AIAA Aviation 2020 Forum, Virtual Event, 15–19 June 2020. [CrossRef]
28. Bassi, F.; Crivellini, A.; Rebay, S.; Savini, M. Discontinuous Galerkin solution of the Reynolds averaged Navier-Stokes and k-ω turbulence model equations. *Comput. Fluids* **2005**, *34*, 507–540. [CrossRef]
29. Bassi, F.; Crivellini, A.; Di Pietro, D.; Rebay, S. An implicit high-order discontinuous Galerkin method for steady and unsteady incompressible flows. *Comput. Fluids* **2007**, *36*, 1529–1546. [CrossRef]
30. Crivellini, A.; D'Alessandro, V.; Bassi, F. A Spalart-Allmaras turbulence model implementation in a discontinuous Galerkin solver for incompressible flows. *J. Comput. Phys.* **2013**, *241*, 388–415. [CrossRef]
31. Crivellini, A.; D'Alessandro, V.; Bassi, F. High-order discontinuous Galerkin solutions of three-dimensional incompressible RANS equations. *Comput. Fluids* **2013**, *81*, 122–133. [CrossRef]

32. Gledhill, I.M.A.; Roohani, H.; Forsberg, K.; Eliasson, P.; Skews, B.W.; Nordström, J. Theoretical treatment of fluid flow for accelerating bodies. *Theor. Comput. Fluid Dyn.* **2016**, *30*, 449–467. [CrossRef]
33. Bassi, F.; Botti, L.; Colombo, A.; Crivellini, A.; Franchina, N.; Ghidoni, A. Assessment of a high-order accurate Discontinuous Galerkin method for turbomachinery flows. *Int. J. Comput. Fluid Dyn.* **2016**, *30*, 307–328. [CrossRef]
34. Spalart, P.; Allmaras, S. A one-equation turbulence model for aerodynamic flows. In Proceedings of the 30th Aerospace Sciences Meeting and Exhibit, Reno, NV, USA, 6–9 January 1992. [CrossRef]
35. Menter, F.R.; Matyushenko, A.; Lechner, R.; Stabnikov, A.; Garbaruk, A. An Algebraic LCTM Model for Laminar–Turbulent Transition Prediction. *Flow Turbul. Combust.* **2022**, *109*, 841–869. [CrossRef]
36. Bassi, F.; Crivellini, A.; Di Pietro, D.A.; Rebay, S. An artificial compressibility flux for the discontinuous Galerkin solution of the incompressible Navier-Stokes equations. *J. Comput. Phys.* **2006**, *218*, 794–815. [CrossRef]
37. Lang, J.; Verwer, J. ROS3P—An accurate third-order Rosenbrock solver designed for parabolic problems. *BIT* **2001**, *41*, 731–738. [CrossRef]
38. Rumsey, C.L. Apparent transition behavior of widely-used turbulence models. *Int. J. Heat Fluid Flow* **2007**, *28*, 1460–1471. [CrossRef]
39. Franciolini, M.; Botti, L.; Colombo, A.; Crivellini, A. *p*-Multigrid matrix-free discontinuous Galerkin solution strategies for the under-resolved simulation of incompressible turbulent flows. *Comput. Fluids* **2020**, *206*, 104558. [CrossRef]
40. Geuzaine, C.; Remacle, J.F. Gmsh: A 3-D finite element mesh generator with built-in pre-and post-processing facilities. *Int. J. Numer. Methods Eng.* **2009**, *79*, 1309–1331. [CrossRef]
41. Williamson, C.H.; Roshko, A. Vortex formation in the wake of an oscillating cylinder. *J. Fluids Struct.* **1988**, *2*, 355–381. [CrossRef]
42. Koochesfahani, M.M. Vortical patterns in the wake of an oscillating airfoil. *AIAA J.* **1989**, *27*, 1200–1205. [CrossRef]
43. Ol, M. Vortical structures in high frequency pitch and plunge at low Reynolds number. In Proceedings of the 37th AIAA Fluid Dynamics Conference and Exhibit, Miami, FL, USA, 25–28 June 2007; p. 4233.
44. Andersen, A.; Bohr, T.; Schnipper, T.; Walther, J.H. Wake structure and thrust generation of a flapping foil in two-dimensional flow. *J. Fluid Mech.* **2017**, *812*. [CrossRef]
45. Cimarelli, A.; Franciolini, M.; Crivellini, A. On the kinematics and dynamics parameters governing the flow in oscillating foils. *J. Fluids Struct.* **2021**, *101*, 103220. [CrossRef]
46. Guglielmini, L.; Blondeaux, P.; Vittori, G. A simple model of propulsive oscillating foils. *Ocean. Eng.* **2004**, *31*, 883–899. [CrossRef]

fluids

MDPI

Article

CFD Simulation of a Hybrid Solar/Electric Reactor for Hydrogen and Carbon Production from Methane Cracking

Malek Msheik, Sylvain Rodat and Stéphane Abanades *

Processes, Materials and Solar Energy Laboratory, PROMES-CNRS, 7 Rue du Four Solaire, 66120 Font Romeu, France

* Correspondence: stephane.abanades@promes.cnrs.fr; Tel.: +33-04-68-30-77-30

Abstract: Methane pyrolysis is a transitional technology for environmentally benign hydrogen production with zero greenhouse gas emissions, especially when concentrated solar energy is the heating source for supplying high-temperature process heat. This study is focused on solar methane pyrolysis as an attractive decarbonization process to produce both hydrogen gas and solid carbon with zero CO_2 emissions. Direct normal irradiance (DNI) variations arising from inherent solar resource variability (clouds, fog, day-night cycle, etc.) generally hinder continuity and stability of the solar process. Therefore, a novel hybrid solar/electric reactor was designed at PROMES-CNRS laboratory to cope with DNI variations. Such a design features electric heating when the DNI is low and can potentially boost the thermochemical performance of the process when coupled solar/electric heating is applied thanks to an enlarged heated zone. Computational fluid dynamics (CFD) simulations through ANSYS Fluent were performed to investigate the performance of this reactor under different operating conditions. More particularly, the influence of various process parameters including temperature, gas residence time, methane dilution, and hybridization on the methane conversion was assessed. The model combined fluid flow hydrodynamics and heat and mass transfer coupled with gas-phase pyrolysis reactions. Increasing the heating temperature was found to boost methane conversion (91% at 1473 K against ~100% at 1573 K for a coupled solar-electric heating). The increase of inlet gas flow rate Q_0 lowered methane conversion since it affected the gas space-time (91% at Q_0 = 0.42 NL/min vs. 67% at Q_0 = 0.84 NL/min). A coupled heating also resulted in significantly better performance than with only electric heating, because it broadened the hot zone (91% vs. 75% methane conversion for coupled heating and only electric heating, respectively). The model was further validated with experimental results of methane pyrolysis. This study demonstrates the potential of the hybrid reactor for solar-driven methane pyrolysis as a promising route toward clean hydrogen and carbon production and further highlights the role of key parameters to improve the process performance.

Keywords: methane cracking; hydrogen production; hybrid reactor; concentrated solar energy; CFD simulation; gas-phase pyrolysis

Citation: Msheik, M.; Rodat, S.; Abanades, S. CFD Simulation of a Hybrid Solar/Electric Reactor for Hydrogen and Carbon Production from Methane Cracking. *Fluids* **2023**, *8*, 18. https://doi.org/10.3390/fluids8010018

Academic Editor: Mehrdad Massoudi

Received: 26 October 2022
Revised: 23 December 2022
Accepted: 26 December 2022
Published: 2 January 2023

1. Introduction

Most of the hydrogen demand worldwide is mainly produced by steam methane reforming (SMR) [1]. Although this route is still the most economical, the derived greenhouse gas emissions represent a significant concern [2]. Environmental norms involve capture and sequestration of the produced CO_2 (CCS) in underground depositories located in unpopulated areas. Such sequestration techniques are still not efficient enough for safe and long-term storage [3]. Moreover, this obligation implies additional cost to the process [4]. On the other hand, water splitting (electro/thermo/photo-chemical) for hydrogen production has also been investigated because of its green asset. Such a process does not generate any CO_2. Although it could be promising in the future thanks to relative water abundance on earth, the hydrogen production cost is higher than in common routes (1.81 $/kg H_2

and 1.98 \$/kg H_2 from SMR without and with CO_2 sequestration, respectively, against 3.38 \$/kg H_2 from water electrolysis using wind energy) [5,6].

Among the other interesting pathways for potentially clean hydrogen production, methane cracking is especially suitable because it is an endothermic reaction yielding both solid carbon and hydrogen gas (Equation (1)) [7–10]. Therefore, methane pyrolysis is clean if the heating source is derived from a renewable energy such as concentrated solar energy [11–13]. Regardless of the heating means, there are two possibilities to dissociate methane: conventional gas-phase (or solid/gas-phase in case there is a solid catalyst) or molten media methane pyrolysis [6]. Both routes can involve either catalytic or non-catalytic reactions. Pyrolysis in molten media (e.g., liquid metals) is mainly suggested to enhance heat transfer in the reactor and carbon separation at the liquid surface. In conventional pyrolysis, some limitations hinder process stability. A gas phase has generally weaker heat transfer rates than liquids. Moreover, reactor clogging and catalyst coking (if used) are possible locks in conventional pyrolysis [14–16]. Such issues might be overcome by pyrolysis in molten metals/salts. Herein, methane is bubbled, and thus decomposes while rising in a hot liquid bath. The molten medium can be either a molten metal (such as tin [17–19], magnesium [20], tellurium [21], or metallic alloys [22,23]), a molten salt (KCl, KBr, NaCl, NaBr, etc.) [24–26], or a molten metal phase overlaid by a molten salt [27]. Others used catalytic solid metals dispersed in molten media [28]. Thus, heat transfer may be improved, hydrogen is released with outlet gases, and carbon floats on the surface of the bath due to the difference of density [29]. This pathway is still new, quite challenging, and not thoroughly investigated to date [6].

$$CH_{4_{(g)}} \rightarrow 2H_{2(g)} + C_{(s)} \qquad \Delta H_{298\ K} = 74.85\ \text{kJ/mol of } CH_4 \tag{1}$$

Both cracking routes allow operation at high temperatures in a wide range with no CO_2 emissions thanks to solar heating [8,30,31]. High operating temperatures eliminate the need for catalysts, since methane molecules dissociate entirely above 1673 K for long-enough residence time. This phenomenon is known as the thermal decomposition of methane (decomposition under only the effect of temperature) [32]. Alternatively, the use of metal- [33,34] or carbon-based catalysts [35–38] appears as an option to reduce the operation temperature to around 1273 K. However, solar direct normal irradiance (DNI) variations caused by weather changes may hinder the process continuity. A hybrid solar/electric reactor appears as a possible solution for continuous and stable processing under fluctuating solar irradiation conditions [39,40]. Methane pyrolysis in a novel hybrid solar/electric reactor was considered in this work. The reactor was modeled by computational fluids dynamics (CFD) in the case of gas-phase pyrolysis to assess the influence of various process parameters including temperature, gas residence time, methane dilution, and hybridization on the methane conversion. Consequently, the main influencing factors affecting methane pyrolysis were considered in CFD simulations. The model combines fluid flow hydrodynamics and heat and mass transfer coupled with gas-phase pyrolysis reaction. Experimental validation was further considered by comparing simulation results with experimentally measured methane conversions under different conditions. The objective of this study was to demonstrate the potential of the hybrid reactor for solar-driven methane pyrolysis as a promising route toward clean hydrogen and carbon production, and to assess the impact of key operating parameters affecting the process performance.

2. Design of the Hybrid Reactor

Coupling electric and solar heating in the same reactor design allows operation with a variable DNI by compensating solar energy fluctuations with electric heating. In addition, for a non-solar operation, methane pyrolysis should still be possible thanks to electric heating, thus enabling round-the-clock operation. On the other hand, in the case of sufficient DNI, both solar and electric heating can be activated simultaneously. Therefore, the heating is more efficient throughout a larger part of the reactor. Then, the reaction zone (heated zone) also becomes enlarged, thus increasing the effective gas residence time inside the reaction

zone, which may improve the methane conversion. This unique design is applicable for both conventional and molten media methane pyrolysis.

Figure 1a,b shows the hybrid reactor configuration. Two coaxial tubes, the outermost being closed at one end, are centered in an insulated circular layer to reduce conductive heat losses to the environment. The tubes are made of alumina (Al_2O_3) to allow operation at high temperatures (1273–1673 K). Heating is possible using either a solar cavity receiver or an electric heater located a few centimeters below the cavity, or even using both heating modes when DNI is not high enough for a fully on-sun operation. The height of the electric heater set at the bottom of the reactor is 115 mm. The maximal power of the heater is 400 W, which is high enough to reach temperatures in the range of 1273–1673 K. Then, a 25 mm-thick insulation layer is set between the electric heater and the solar cavity. The height of this cavity is 50 mm, with an aperture of 15 mm (Figure 1) for concentrated solar radiation entrance. The cavity absorbs the concentrated solar flux received from a 1.5 kW (thermal) heliostat-parabola solar system (2 m diameter parabolic dish with a peak concentration ratio of about 10,000).

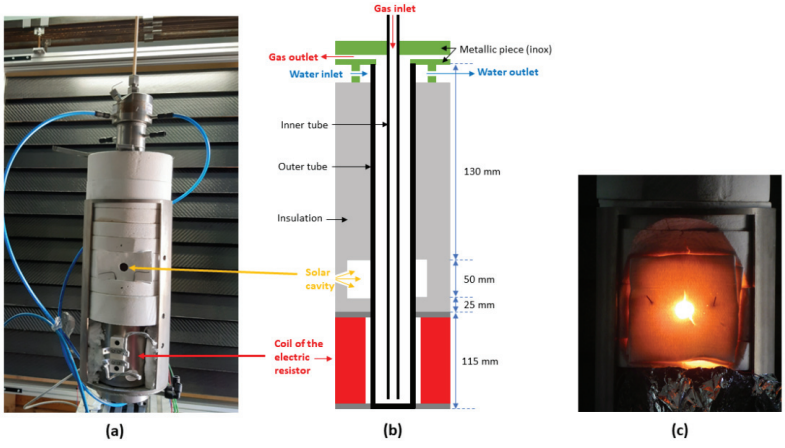

Figure 1. Hybrid solar/electric reactor installed at PROMES-CNRS (Odeillo, France): (**a**) real picture of the implemented reactor, (**b**) representative scheme of the reactor configuration, (**c**) photo of the hot cavity just after a solar run.

For experimental processing, solar and electric heating are both achieved progressively and slowly enough to avoid thermal shocks in the reactor. The average time of reactor heating is almost 30–40 min to reach the operating temperature (1273–1473 K). Solar and electric heating are controlled through an adjustable shutter (input solar power) and a command box with variable current and voltage (input electric power), respectively. It should be noticed that, for the experimental validation part of this work, only electric heating was applied. The reactive gas flows downward in the inner tube and then upward in the annular space between both tubes.

For the reactor design, simulations were performed using computational fluid dynamics (CFD) simulations (using ANSYS Fluent, Canonsburg, WA, USA). Numerical simulation results of the hybrid reactor achieved in the case of gas-phase pyrolysis revealed promising thermochemical performance.

3. Modeling and Simulation Methods

3.1. System Geometry

The model geometry of the hybrid reactor described in Figure 1 was developed and designed to provide a fast-enough convergence of the Fluent solver. Only the tubular reaction zone was simulated. In particular, the solar cavity receiver and the electric heater were not implemented. In place, the wall temperature was set as a boundary condition.

Constant wall temperature was chosen as a first approach because homogeneous temperatures are expected when reaching thermal equilibrium, both in the solar cavity (black-body behavior, heated length corresponding to the cavity height: 50 mm) and in the electric heater (uniform heating along the coil, the effective heated length of the electric resistance was assumed to be 85 mm).

Figure 2 represents the 2D axisymmetric geometry of the reactor designed through Design Modeler software. The inner tube has a thickness of 1.5 mm, an inner diameter of 3 mm, and a length of 310 mm. The outer tube has a thickness of 2.5 mm, an inner diameter of 25 mm, and a length of 320 mm. All faces (solid walls + interior of the tubes) were meshed as quadrilaterals of 0.6 mm size (reference case), as shown in Figure 3. In addition, other finer and coarser quadrilateral meshing of 0.2 mm, 1 mm, 2 mm, 3 mm, and 4 mm mesh sizes were tested to check the independence of the results on the grid, more particularly regarding the chemical conversion of methane (Figure 3). The results of grid independence study are provided in the Results and Discussion section. Insulation layers are perfectly insulated walls with the heat flux boundary condition set to zero in the Fluent solver. In parallel, the top parts of both tubes are water-cooled, and thus a fixed boundary temperature condition of 300 K is assigned to each. The walls standing for the electric heater (85 mm height) and the solar cavity (50 mm height) are defined with a fixed temperature (equal to the desired heating temperature for pyrolysis).

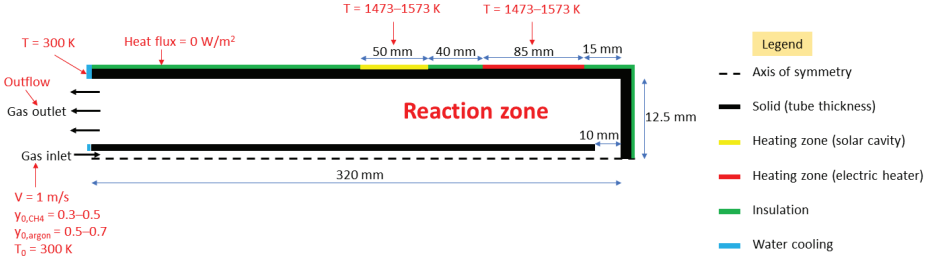

Figure 2. Simplified representative scheme of the 2D hybrid reactor geometry along with boundary conditions.

3.2. Modelling Methods

3.2.1. Species, Models, and Boundary Conditions

Methane, argon, hydrogen, and solid carbon were selected from the FLUENT database. Intermediate products such as acetylene, ethylene, etc., were not considered.

The simulation was converged in steady state and in axisymmetric 2D space. The gravity was enabled and set to 9.81 m/s^2. Reynolds number of the flow varies with the medium temperature because the latter affects the dynamic viscosity of the gas ($\mu = 1.1 \times 10^{-5}$ Pa.s at T = 300 K and $\mu = 2.53 \times 10^{-5}$ Pa.s at T = 1473 K). Reynolds number calculations for the gas flow mixture in both coaxial tubes reveal a laminar flow, thus the laminar model was chosen (Re = 311–135 in the inner tube vs. Re = 2–4 in the outer tube annular space). Concerning the radiation model, discrete ordinates (DO) was adapted to allow for radiative heat transfer between the fluid zone and the inner solid parts of the reactor. Species transport was enabled, and a mixture template was set for the reaction. The methane cracking reaction was considered as a first order reaction, and a finite rate (Arrhenius type) was set with an activation energy of 281 kJ/mol and a pre-exponential factor of 2×10^{10} s^{-1} [32,41]. Behind these models, there are mainly three transport conservation equations solved in CFD: (i) conservation of mass, also known as continuity equation, (ii) conservation of momentum, and (iii) conservation of energy. These equations are expressed as follows [42]:

Continuity equation:

$$\frac{\partial}{\partial t}\left(\rho_f\right) + \nabla\left(\rho_f.\vec{v}_f\right) = 0 \quad (2)$$

where ρ_f is the density of the fluid mixture (kg/m^3) and $\vec{v}_f$ is the flow velocity vector field (m/s). The latter can be calculated through Equation (3):

$$\vec{v}_f = \frac{\sum_{k=1}^{n} \alpha_k \rho_k \vec{v}_k}{\rho_f} \tag{3}$$

where n is the total number of existing species, k is the index for species k, α_k is its volumetric fraction, ρ_k is its relevant density, and $\vec{v}_k$ is its velocity vector field.

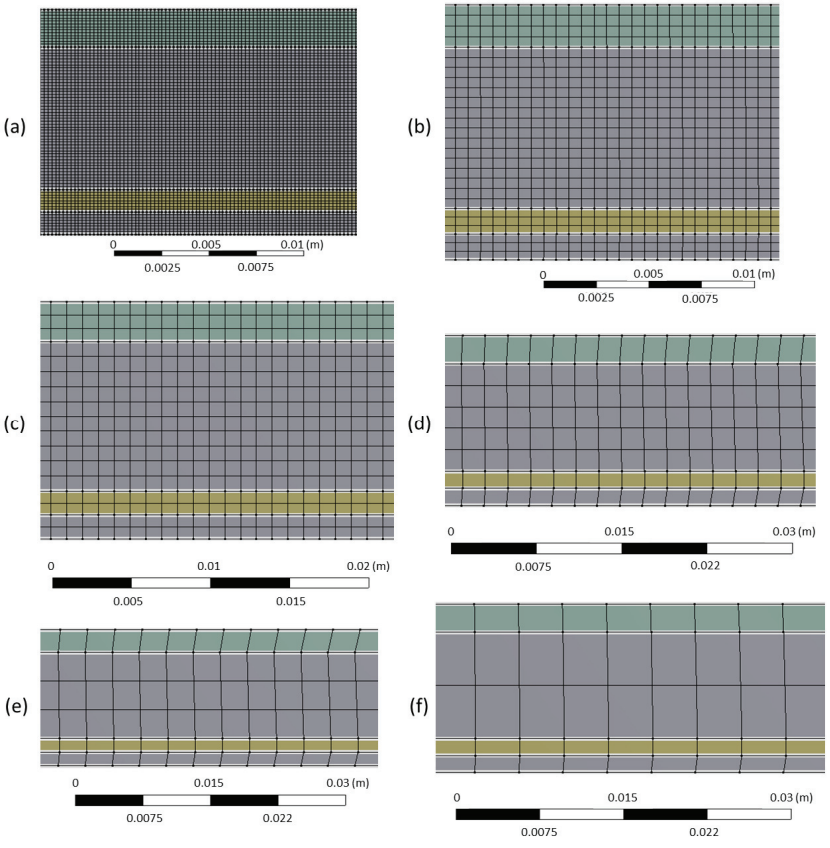

Figure 3. Quadrilateral meshing sizes for the study of independency on meshing: (**a**) mesh size = 0.2 mm; (**b**) mesh size = 0.6 mm; (**c**) mesh size = 1 mm; (**d**) mesh size = 2 mm; (**e**) mesh size = 3 mm; (**f**) mesh size = 4 mm.

The density of the mixture is defined by:

$$\rho_f = \sum_{k=1}^{n} \alpha_k \rho_k \tag{4}$$

Conservation of momentum:

$$\frac{\partial}{\partial t}\left(\rho_f \vec{v}_f\right) + \nabla\left(\rho_f . \vec{v}_f . \vec{v}_f\right) = -\nabla p + \nabla\left(\mu_f\left(\nabla \vec{v}_f + \left(\nabla \vec{v}_f\right)^T\right)\right) + \rho_f \vec{g} + \vec{F} + \nabla(\sum_{k=1}^{n} \alpha_k \rho_k \vec{v}_{dr,k} \vec{v}_{dr,k}) \tag{5}$$

where $\vec{F}$ is an eventual external force (N), p is the static pressure (Pa), $\vec{g}$ is the gravitational acceleration vector (m/s^2), μ_f is the fluid mixture viscosity (kg/m/s), and $\vec{v}_{dr,k}$ is the derivative velocity of species i (m/s). The mixture viscosity is written in Equation (6):

$$\mu_f = \sum_{k=1}^{n} \alpha_k \mu_k \tag{6}$$

Energy conservation equation:

$$\frac{\partial}{\partial t} \sum_{k=1}^{n} (\alpha_k \rho_k E_k) + \nabla \sum_{k=1}^{n} (\alpha_k \vec{v}_k (\rho_k E_k + p)) = \nabla \left(k_{eff} \nabla T \right) + S_E \tag{7}$$

where $\nabla . \left(k_{eff} \nabla T \right)$ represents the conductive heat transfer, while S_E represents every other heating source. k_{eff} is the effective conductivity (W/m/K) and can be defined as follows:

$$k_{eff} = \sum \alpha_k (k_k + k_t) \tag{8}$$

where k_t is the turbulent conductivity, which is actually equal to zero in this study, since the flow is laminar (Re < 2000).

For the ideal incompressible gas model, pressure loss in the reactor is negligible, therefore $E_k = h_k$, where the latter is the sensible enthalpy of species k (J/kg).

The radiative heat transfer was computed based on the discrete ordinates model, whose equation is:

$$\frac{d\left(I\left(\vec{r}, \vec{s} \right) \right)}{ds} + (a + \sigma_s) I\left(\vec{r}, \vec{s} \right) = an^2 \frac{\sigma T^4}{\Pi} + \frac{\sigma_s}{4\Pi} \int_0^{4\Pi} I\left(\vec{r}, \vec{s}' \right) \varphi \left(\vec{s}, \vec{s}' \right) d\Omega' \tag{9}$$

where $\vec{r}$ is the position vector, $\vec{s}$ is the direction vector, $\vec{s}'$ is the diffusion direction vector, s is the path length (m), a is the absorption coefficient (1/m), n is the refraction index, σ_s is the diffusion coefficient (1/m), σ is the Stefan–Boltzmann constant (5.672×10^{-8} W/m^2·K^4), $I\left(\vec{r}, \vec{s} \right)$ is the total luminescence (W/m^2/sr), T is the local temperature (K), φ is the phase function, and Ω' is the solid angle (steradian).

The reaction rate was computed using an Arrhenius expression given in Equation (10) coupled with the conservation equations. The chemistry was thus coupled with the heat and mass transfer via the net rate of production/consumption of each species by chemical reaction [42].

$$r = k \cdot [CH_4]_t = A \cdot e^{-\frac{E_a}{R \cdot T}} \cdot [CH_4]_t \tag{10}$$

where r is the reaction rate, k is the kinetic constant, A is the pre-exponential factor (s^{-1}), E_a is the activation energy (J/mol), R is the universal gas constant (8.314 J/mol·K), and T is the operating temperature (K).

Assuming a plug flow reactor (PFR), k can be calculated as follows:

$$k = \frac{-\beta \cdot (1 + \alpha) \cdot ln\left(1 - X_{CH_4}\right) - \alpha \cdot \beta \cdot X_{CH_4}}{\tau} \tag{11}$$

where α is the chemical expansion factor and τ is the gas (methane + argon) space-time.

The boundary conditions of the model are detailed in Figure 2. Heating wall temperature was set to the desired operating temperature. For the base case, a 1 m/s inlet velocity in the inner tube was defined (equivalent to 0.42 NL/min flow rate). In the species, inlet methane mole fraction was set to 0.5, the rest being argon. The outlet was simulated as an outflow. A value of 10^{-6} was chosen for residuals to warrant satisfactory convergence.

3.2.2. Parametric Study

The effect of reactor hybridization via coupled solar-electric heating, residence time, methane dilution, and temperature was studied. In order to provide insights into the associated trends in the conversion of methane, a reference case was first simulated (Table 1). In this case, referred to as case 1, both heating sources (electric and solar) were enabled with a fixed wall temperature of 1473 K. The initial total inlet volumetric flow rate was 0.42 NL/min (CH_4 + Ar), while the molar fraction of methane was 0.5. Other cases were simulated as described in the following paragraph.

Table 1. Operating conditions simulated through ANSYS Fluent.

	$T_{electric}$ (K)	T_{solar} (K)	Q_0 (NL/min)	$y_{0,CH4}$	Mesh Size (mm)	Parameter Effect
Case 1 (ref)	1473	1473	0.42	0.5	0.6	Reference case: hybridization (coupled heating)
Case 2	1473	Insulated	0.42	0.5	0.6	Electric heating only
Case 3	1473	1473	0.84	0.5	0.6	Residence time
Case 4	1473	1473	0.42	0.3	0.6	Methane dilution
Case 5	1573	1573	0.42	0.5	0.6	Heating temperature

To illustrate the effect of hybridization (case 2), solar heating was turned off (the solar cavity was assumed as an insulated wall), while the total inlet flow rate and the species mole fraction in the reacting flow were kept constant. This approach was used to clearly identify the difference between a reactor with only one heating source and a hybrid one with both solar and electric heating. To investigate the gas residence time effect (case 3), the total inlet flow rate was varied. A different flow rate indeed modifies the gas velocity in the reactor tubes, which implies a different gas residence time (the total flow rate was doubled in case 3). The dilution effect can be examined by changing the inlet methane molar fraction while keeping the inlet total flow rate constant (inlet methane mole fraction was reduced to 0.3 in case 4). Finally, the temperature effect can be readily studied by increasing the heating temperature of both the electric and solar heating zone (this temperature was set to 1573 K in case 5). The effect of meshing quality on methane conversion in the reactor was checked separately in Section 4.1 (grid independence study).

4. Results and Discussion

The first section focuses on the mesh independence study. Once the quality of the mesh was successfully checked, a study on the model sensitivity to the activation energy was achieved in order to confirm the suitability of the considered kinetic rate law of methane decomposition. Then, the numerical model was validated based on a comparison with the results of an experimental work to demonstrate its ability to predict relevant results. Once validated, different operating conditions were simulated to investigate the effect of various parameters. Table 2 recaps the results of the numerical simulations. $T_{electric}$ and T_{solar} are the temperatures of heating in the electric and the solar section, respectively. Q_0 is the total inlet volumetric flow rate, and $y_{0,CH4}$ is the methane mole fraction in the inlet gas mixture. The mesh size is also reported. The effective residence time is the time spent in the reaction zone where operating conditions allow chemical reaction.

The total residence time in a reactor is given by:

$$\tau = \frac{V_r}{Q_{T,P}} = \frac{V_r}{Q_0 \cdot \frac{P_0 . T}{P . T_0}} \quad (12)$$

where V_r is the total tubular reactor volume (150×10^{-6} m^3), $Q_{T,P}$ is the volumetric flow rate at the actual operating conditions (m^3/s), Q_0 is the total inlet flow rate at normal conditions (m^3/s), P_0 is the atmospheric pressure (101,325 Pa), T_0 is the normal temperature (273 K), P is the operating pressure (Pa), and T is the operating temperature (K). The effective

residence time corresponding to electric (τ_e) and solar (τ_s) heating zones can be calculated with the same expression as in Equation (12) by replacing V_r with the relevant heated volume only (the heated volume is relevant to the heated height: $V_{r\text{-electric}} = 42 \times 10^{-6}$ m^3, $V_{r\text{-solar}} = 25 \times 10^{-6}$ m^3). The summation of τ_e and τ_s is the total effective residence time, entitled τ_{total}. It is important to notice that these residence times were only calculated based on physical expansion of the gas (effect of both temperature and pressure). Chemical expansion due to the formation of H_2 was not considered. X_{CH4} and Y_{H2} are methane chemical conversion and hydrogen yield at the outlet, respectively. They can be calculated as follows:

$$X_{CH_4} = \frac{F_{CH_4 in} - F_{CH_{4_{out}}}}{F_{CH_4 in}} \quad (13)$$

$$Y_{H_2} = \frac{F_{H_2 out}}{2F_{CH_{4_{in}}}} \quad (14)$$

where $F_{CH4\text{-}in}$ and $F_{CH4\text{-}out}$ are methane molar flow rates in the inlet and the outlet stream, respectively (mol/s). $F_{H2\text{-}out}$ is the hydrogen molar flow rate in the outlet stream (mol/s).

Table 2. Results of parameter effects on performance metrics of gas-phase methane pyrolysis.

	$T_{electric}$ (K)	T_{solar} (K)	Q_0 (NL/min)	$y_{0,CH4}$	Mesh Size (mm)	τ_e (s)	τ_s (s)	τ_{total} (s)	CH_4 conversion, X_{CH4} (%)	H_2 yield, Y_{H2} (%)
Case 1 (ref)	1473	1473	0.42	0.5	0.6	0.94	0.56	1.5	91	92
Case 2	1473	Insulated	0.42	0.5	0.6	0.94	0	0.94	75	74
Case 3	1473	1473	0.84	0.5	0.6	0.47	0.28	0.75	67	73
Case 4	1473	1473	0.42	0.3	0.6	0.94	0.56	1.5	95	94
Case 5	1573	1573	0.42	0.5	0.6	0.88	0.52	1.4	100	100

4.1. Effect of Mesh Size (Grid Independence Study)

The independence of results (especially temperature, CH_4 conversion, and H_2 yield) on the meshing was checked using different sizes of quadrilateral meshes for both interior and solid walls. Reference mesh was of 0.6 mm size, and the finer one was 0.2 mm, whereas the larger ones were 1 mm, 2 mm, 3 mm, and 4 mm (Table 3). The convergence through Fluent was longer when decreasing the mesh size, as expected. For the largest meshing (with mesh size = 4 mm), the solver diverged, indicating that meshing was not fine enough nor appropriate for a physical convergence (Figure 4). In contrast, meshes of 0.2 mm, 0.6 mm, and 1 mm led to very similar results in terms of output species mole fractions (Table 3). However, coarser meshing was associated with higher errors. Results such as CH_4 and H_2 mole fractions, methane conversion, and temperature profile revealed no noticeable difference between 0.2 mm, 0.6 mm, and 1 mm meshes (Figure 5). For H_2 yield in the outlet stream, calculations showed a slight decrease from 92% to 90% with the finer meshing, which is also insignificant. Consequently, one can say that the selected reference mesh (0.6 mm size) was a fair compromise between fast convergence and reliable results, as it was of good quality and fine enough to let the solver converge with minimal errors.

Table 3. Study of the meshing influence on the CFD numerical results.

	$T_{electric}$ (K)	T_{solar} (K)	Q_0 (NL/min)	$y_{0,CH4}$	Mesh Size (mm)	τ_e (s)	τ_s (s)	τ_{total} (s)	X_{CH4} (%)	Y_{H2} (%)
Mesh 1	1473	1473	0.42	0.5	0.2	0.94	0.56	1.5	91	90
Mesh 2	1473	1473	0.42	0.5	0.6	0.94	0.56	1.5	91	92
Mesh 3	1473	1473	0.42	0.5	1	0.94	0.56	1.5	91	90
Mesh 4	1473	1473	0.42	0.5	2	0.94	0.56	1.5	90	88
Mesh 5	1473	1473	0.42	0.5	3	0.94	0.56	1.5	90	86
Mesh 6	1473	1473	0.42	0.5	4	0.94	0.56	1.5	Divergence	

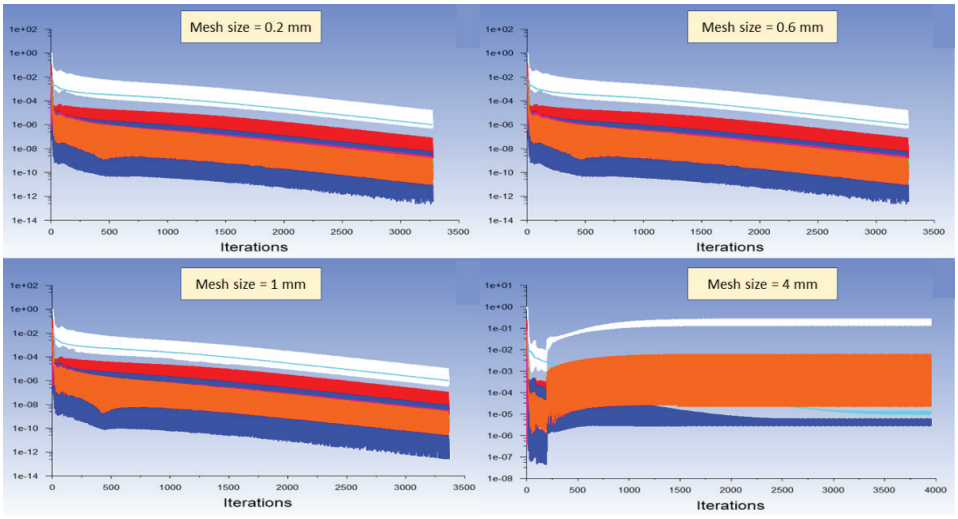

Figure 4. Residuals of the Fluent solver for different meshing sizes. (white: continuity, red: x-velocity, green: y-velocity, dark blue: energy, light blue: density, pink: CH_4 mass balance, yellow: H_2 mass balance, orange: C mass balance).

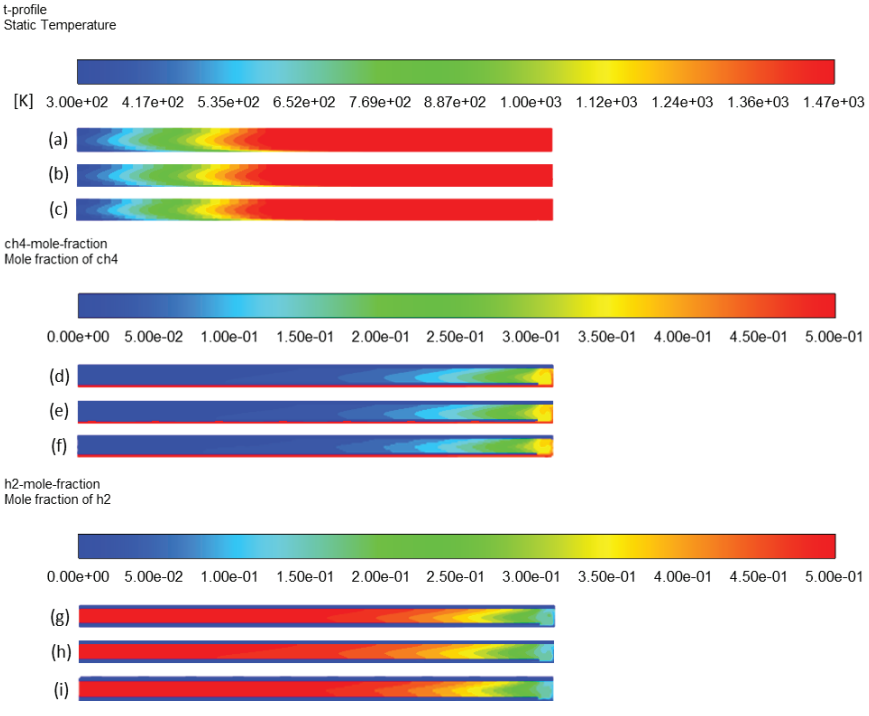

Figure 5. Effect of meshing on temperature profile: (**a**) mesh 1, (**b**) mesh 2, and (**c**) mesh 3; CH_4 mole fraction profile: (**d**) mesh 1, (**e**) mesh 2, and (**f**) mesh 3; H_2 mole fraction profile: (**g**) mesh 1, (**h**) mesh 2, and (**i**) mesh 3.

4.2. Model Sensitivity to Activation Energy

The kinetic model of methane pyrolysis may have a high impact on the simulation results. The activation energy E_a and the pre-exponential factor A used in Arrhenius law (Equation (10)) could indeed change results drastically. However, for simplification, the A value was fixed [32] while E_a was varied in order to get an accurate kinetic model for methane pyrolysis. Different values of E_a were reported (for uncatalyzed methane pyrolysis) in a very broad range (for example, E_a = 281 kJ/mol in [32], while E_a = 422 kJ/mol in [43]). The model sensitivity against E_a was studied to show the importance of choosing a proper kinetic model.

Four different values of E_a were studied (200–281–310–350 kJ/mol) at a fixed temperature (1473.15 K), gas inlet flow rate (0.5 NL/min), and methane inlet mole fraction (0.5). Only electric heating was activated. Results are shown in Figure 6.

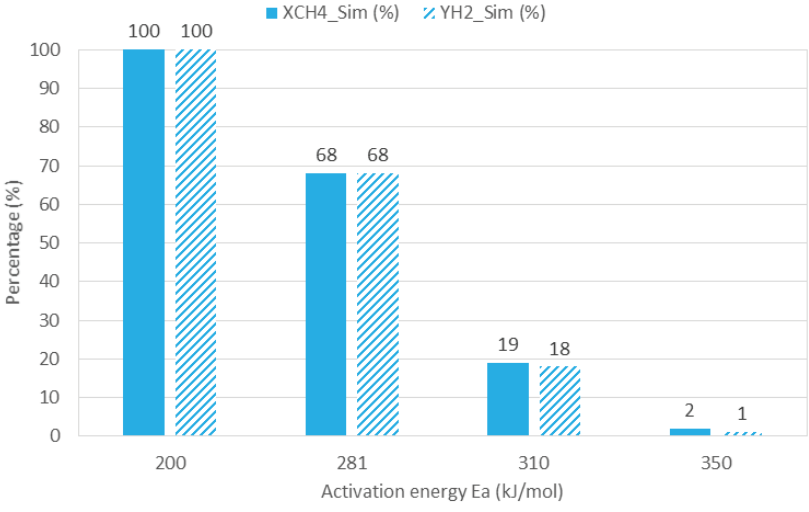

Figure 6. CFD results sensitivity to different values of activation energy.

Based on Arrhenius law, E_a is inversely proportional to the reaction rate of methane decomposition. Increasing E_a decreases the reaction rate and results in lower methane conversion and hydrogen yield. CFD simulation confirmed such a tendency and showed complete methane conversion and hydrogen yield with E_a = 200 kJ/mol and decreasing performance as E_a was increasing. With E_a value of 350 kJ/mol, there was almost no methane decomposition (X_{CH4} = 2% and Y_{H2} = 1%).

The aim of this sensitivity analysis was to validate the value of the activation energy chosen in the kinetic model based on experimental data. Thus, an experimental run was conducted with electric heating under the same operating conditions (i.e., temperature = 1473 K, gas inlet flow rate = 0.5 NL/min, and methane inlet mole fraction = 0.5) and resulted in 71% methane conversion and 65% hydrogen yield. Such a result was obviously very close to the numerical one when E_a was 281 kJ/mol [28] (X_{CH4} = 68% and Y_{H2} = 68%). Therefore, one can consider that the selected kinetic model (with E_a = 281 kJ/mol [28]) is relevant to simulate methane cracking in the reactor.

4.3. Experimental Validation of the Model

The reliability of the model simulations was addressed and validated with an experimental study. The aim was to compare the simulation with experimental results regarding both the effect of heating temperature (1273–1573 K) and inlet gas flow rate (0.5–1 L/min) on methane conversion and hydrogen yield. Methane pyrolysis was experimentally studied in the reactor with an electric heating, as shown in the geometry in Figure 2. No solar heat-

ing was applied. Instead, insulation rings (polycrystalline mullite/alumina wool (PCW) and special inorganic fibers and binders) replaced the solar heating zone. For both studies (numerical and experimental), there was only electric heating (case 2 in Table 1) with a fixed methane inlet fraction ($y_{0,CH4}$ = 0.5). Two different parameters were studied: (i) the temperature (T = 1273–1373–1473–1573 K) at a fixed methane inlet fraction ($y_{0,CH4}$ = 0.5) and gas inlet flow rate (Q_0 = 0.5 NL/min), and (ii) the gas inlet flow rate (Q_0 = 0.5–0.75–1 NL/min) at a fixed temperature (T = 1573 K) and a fixed methane inlet fraction ($y_{0,CH4}$ = 0.3).

Figure 7 shows the comparison of the numerical model with the experimental performance of the reactor. In Figure 7a, a high degree of coherence can be observed between numerical and experimental results in terms of both methane conversion and hydrogen yield at all temperatures. For instance, at 1373 K, numerical and experimental values of methane conversion and hydrogen yield were very close (X_{CH4} = 31% vs. 30% and Y_{H2} = 30% vs. 27%). At the other temperatures, the results were also consistent (for example, at 1573 K: X_{CH4} = 96% vs. 91% and Y_{H2} = 96% vs. 89%). The small gap between simulation and experiments might arise from several factors. In particular, the simulation does not consider partial decomposition of methane, which, in fact, results in some secondary intermediate hydrocarbons (C_2H_2, C_2H_4, and C_2H_6).

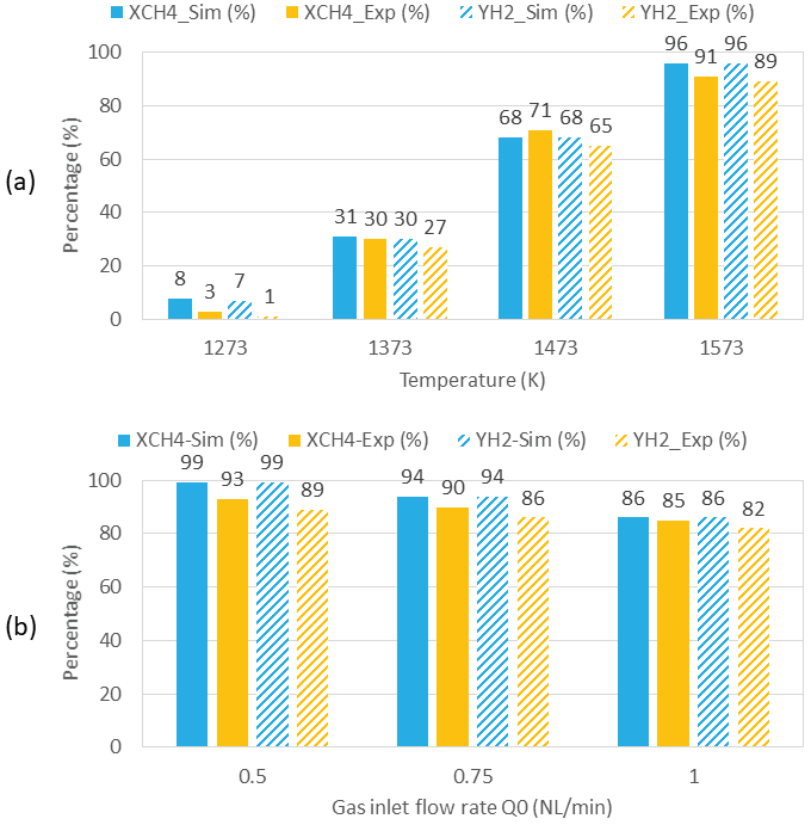

Figure 7. Comparison of numerical and experimental results in terms of methane conversion and hydrogen yield as a function of (**a**) operating temperature and (**b**) gas inlet flow rate.

In Figure 7b, the numerical model still fits the experimental data with higher differences in terms of hydrogen yield, because the simulation does not consider secondary byproducts (such as secondary hydrocarbons C_2H_m). It is thus normal that the experimen-

tally measured values are lower than the simulation values, especially at higher kinetic rates (i.e., at lower flow rates). Thus, the highest difference between numerical and experimental values corresponds to Q_0 = 0.5 NL/min (X_{CH4} = 99% vs. 93% and Y_{H2} = 99% vs. 89%, respectively), while a more accurate fit between numerical and experimental performance is observed at Q_0 = 1 NL/min (X_{CH4} = 86% vs. 85% and Y_{H2} = 86% vs. 82%, respectively).

In summary, the experimental study shows very close results to those predicted by the numerical model. This experimental validation confirmed the suitability of the model to simulate the methane pyrolysis process in the hybrid reactor. Thus, the considered approach can be considered reliable to investigate methane cracking under specific operating conditions. Moreover, this model could be further developed to simulate methane cracking in molten media, which is a novel technology that has not been numerically modelled yet.

4.4. Effect of Hybridization

Figure 8a,b provides the temperature distribution throughout the entire reactor volume (fluid zone) when only electric heating is activated (case 2) compared to the case in which both heating sources are implemented (case 1). The heated length is longer in the latter case, as expected, because the additional heating zone extends the heated part. The reactional zone thus becomes larger, which increases the total effective residence time of methane molecules from 0.94 s (τ_e) to 1.5 s ($\tau_e + \tau_s$). Figure 8c–f shows higher methane conversion and hydrogen production in case 1 than in case 2. Methane conversion significantly increases from 75% (case 2) to 91% (case 1), while hydrogen yield increases from 74% to 92%, as shown in Table 2.

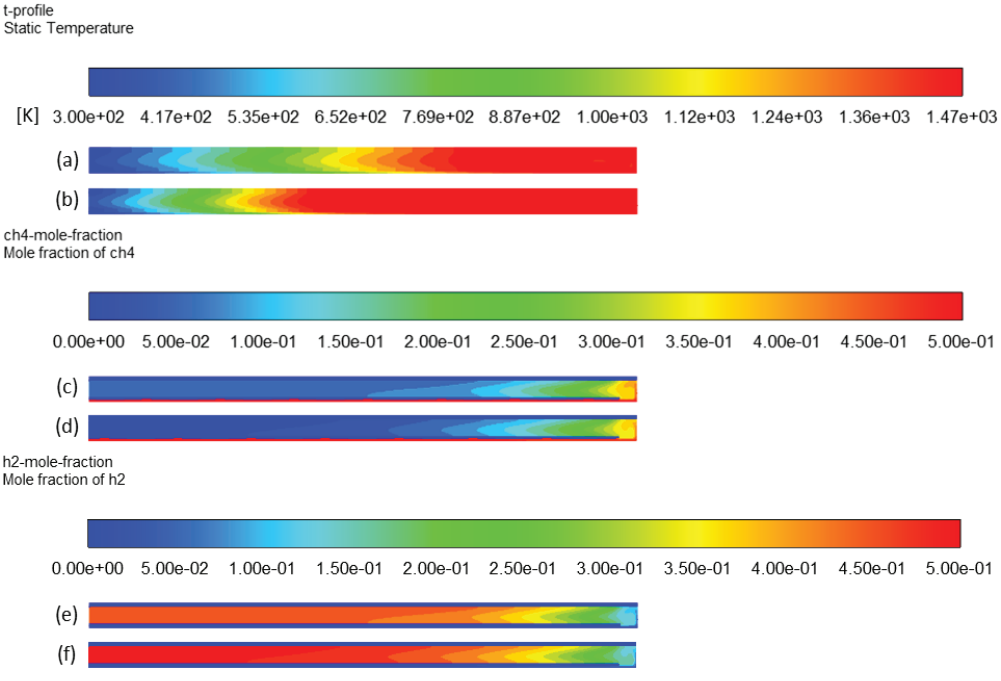

Figure 8. Effect of hybridization on temperature profile: (**a**) case 2 and (**b**) case 1; CH_4 mole fraction profile: (**c**) case 2 and (**d**) case 1; H_2 mole fraction profile: (**e**) case 2 and (**f**) case 1.

The plots of temperature and outlet mole fractions of methane and hydrogen in the annular region of the tube along the *x*-axis are shown in Figure 9. The *x*-axis of the curves is actually the red line shown in Figure 9a. In Figure 9b, temperature plots were overlaid up to x = 0.1 m, which almost represents the end of the electric heating zone. Further from

x = 0.1 m, toward the reactor outlet (x = 0.32 m), the temperature in the hybrid heating case (case 1) was much higher than in case 2. For instance, at x = 0.2 m, the temperature was still 1473 K in case 1, while T was lower than 1000 K in case 2. This was clearly caused by the solar heating in case 1 that enlarged the hot zone throughout the reactor. Such an effect improved the decomposition of methane. Therefore, a clear difference in methane and hydrogen outlet mole fractions is observed after x = 0.1 m (Figure 9c). Methane mole fraction continued to decrease down to 0.025 in case 1 (hybrid heating) vs. 0.075 in case 2 (electric heating only). In parallel, hydrogen mole fraction reached almost 0.47 in case 1 vs. only 0.42 in case 2.

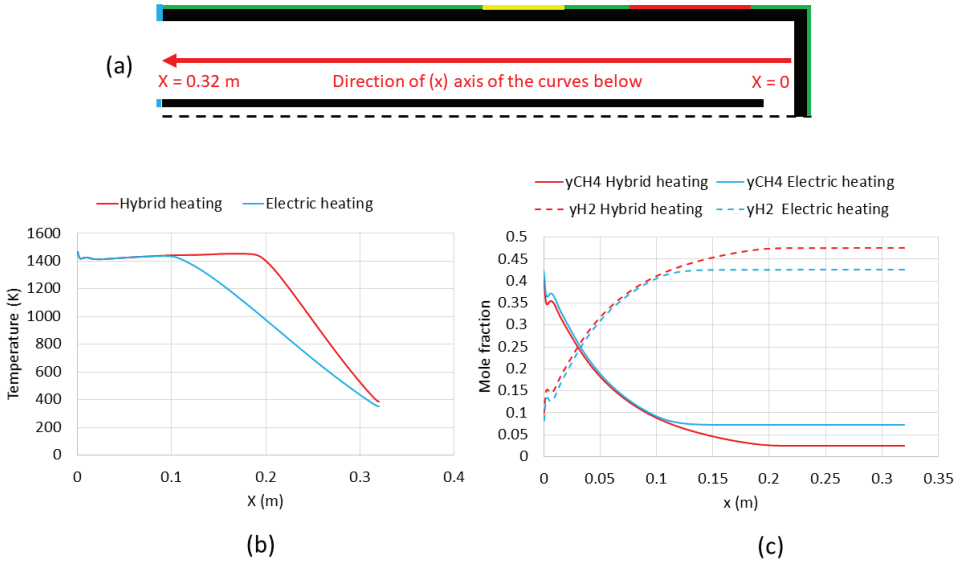

Figure 9. Effect of heating on temperature and outlet mole fractions of methane and hydrogen. (**a**) Scheme of the reactor annular region including the *x*-axis of the curves, (**b**) temperature plot, (**c**) outlet mole fractions plot.

4.5. Effect of Residence Time

The residence time effect was evidenced in the previous section by increasing the heated length, and thus the heated volume V_r. Another approach to study this parameter consists of modifying the total inlet flow rate while fixing the methane mole fraction. Thus, a modification of the total flow rate Q_0 changes the residence time. In case 3, Q_0 was doubled (0.84 NL/min) in comparison to case 1. Thus, based on Equation (12), the resulting effective residence time was divided by two (0.75 s). CH_4 and H_2 mole fraction profiles (Figure 10c–f, respectively) confirm this effect on methane conversion. At a high inlet gas flow rate (0.84 NL/min), CH_4 conversion and H_2 yield drop from 91% to 67% and from 92% to 73%, respectively.

In fact, a higher gas velocity in the reactor decreased the residence time. Figure 11 represents the gas velocity (velocity streamlines) inside the reactor in both cases to emphasize the impact of Q_0 on methane conversion. Regardless of the inlet flow rate (Q_0), the velocity is higher in the inner tube since the cross section is smaller, and the velocity is maximal in the center and null near the walls.

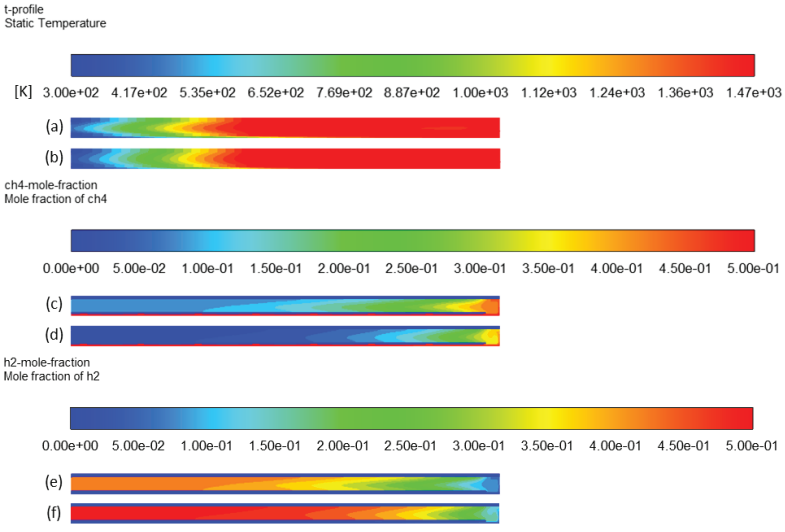

Figure 10. Effect of residence time on temperature profile: (**a**) case 3 and (**b**) case 1; CH_4 mole fraction profile: (**c**) case 3 and (**d**) case 1; H_2 mole fraction profile: (**e**) case 3 and (**f**) case 1.

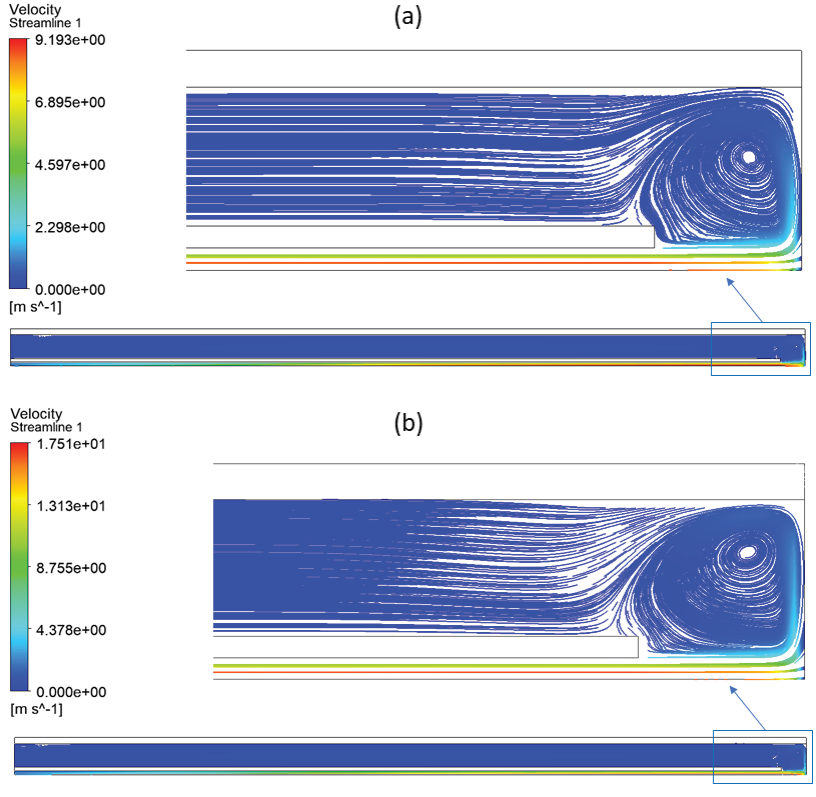

Figure 11. Velocity streamlines in the reactor with a zoom at the bottom part: (**a**) case 1 and (**b**) case 3.

Figure 12 plots the velocity for case 1 and case 3 according to the direction of the y-axis (vertical direction) 20 mm above the bottom of the reactor (i.e., along the green line in the small reactor scheme in Figure 12 that indicates the location where the velocity was plotted). In case 1 (blue curve in Figure 12a), when Q_0 was 0.42 NL/min, the maximal velocity in the inner tube was almost 9 m/s at the axis (in the center of the inner tube). This velocity decreased progressively to zero near the walls (at x = 0.0015 m). In the annular space (blue curve in Figure 12b), the same aspect was observed: the maximal velocity was almost 0.14 m/s (at x = 0.0065 m), and it progressively decreased to zero when approaching the walls (x = 0.003 m and x = 0.0125 m). The velocity in the annular space was much smaller than in the inner tube due to the higher cross section.

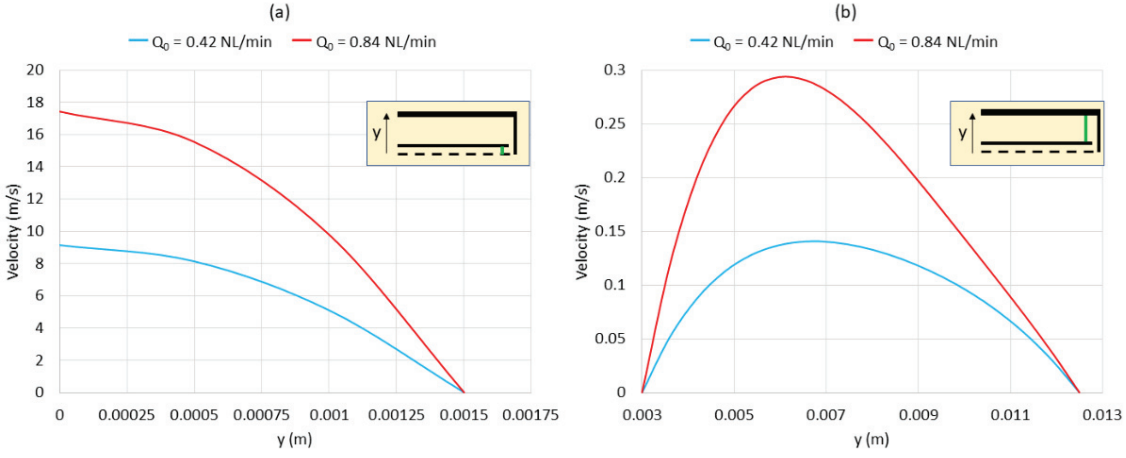

Figure 12. Velocity plots according to the direction of the y-axis 20 mm above the bottom (along the green line): (**a**) velocity in the inner tube and (**b**) velocity in the annular space. Blue curves: case 1; red curves: case 3.

In case 3 (red curve in Figure 12a), when Q_0 was 0.84 NL/min, the maximal velocity in the inner tube was almost 17.5 m/s at the axis (x = 0 m). This velocity decreased progressively to zero near the walls (at x = 0.0015 m). In the annular space (red curve in Figure 12b), the maximal velocity was almost 0.29 m/s (at x = 0.0065 m) and decreased to zero near the walls (x = 0.003 m and x = 0.0125 m). As a comparison, the maximal velocities were higher in case 3 than in case 1 (17.5 m/s vs. 9 m/s in the inner tube and 0.29 m/s vs. 0.14 m/s in the annular space). Such results confirm the high impact of Q_0 on the gas residence time, which is a key parameter in gas-phase methane cracking.

4.6. Effect of Methane Molar Fraction

To study the dilution effect, all parameters were kept constant as the reference case while reducing inlet methane molar fraction from 0.5 to 0.3 (case 1 versus case 4). Temperature and species mole fraction contours are shown in Figure 13. Differences in contours are not noticeable. Some previous works concerning methane cracking reported a slight increase in conversion when the inlet methane mole fraction was increased [13,44]. However, simulation results show that the methane conversion increased from 91% to 95%, accompanied by a hydrogen yield increase from 92% to 94% when the methane mole fraction was reduced from 0.5 to 0.3. Theoretically, methane conversion should rather decrease when dilution increases because the reaction rate is directly proportional to methane concentration (first order reaction). On the other hand, the diluted gas could allow more efficient heating of methane to achieve a higher decomposition extent. In addition, the real residence time of methane is affected by chemical expansion, which is increased when more methane dissociates (2 moles of H_2 formed per mole of CH_4). Thus, a lower methane mole

fraction could slightly increase the residence time, and thus the conversion according to the effect of residence time. Thus, there is a subtle balance between residence time and methane molar fraction effects. This aspect should be further analyzed thanks to real residence time distribution extracted from Fluent.

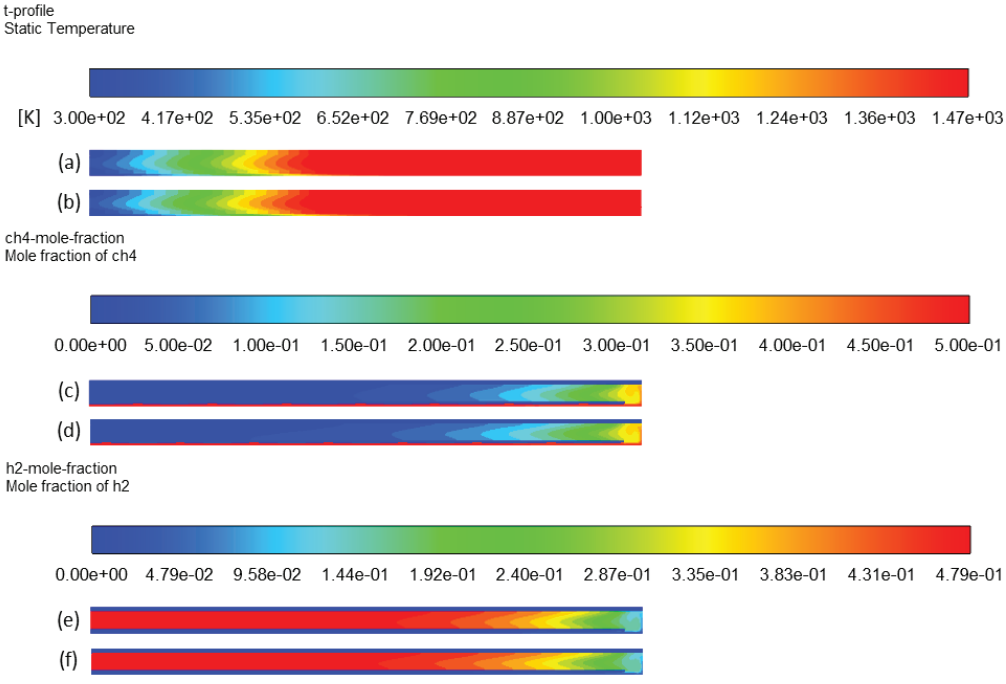

Figure 13. Effect of methane inlet mole fraction on temperature profile: (**a**) case 4 and (**b**) case 1; CH_4 mole fraction profile: (**c**) case 4 and (**d**) case 1; H_2 mole fraction profile: (**e**) case 4 and (**f**) case 1.

4.7. Effect of Heating Temperature

Methane cracking is an endothermic reaction that requires external energy as a process heat source [6]. Thus, an increase in the heating temperature improves the conversion. When the temperature was increased from 1473 K to 1573 K, for both heating sources, the methane concentration in the reactor was reduced (Figure 14c compared to Figure 14d), hence resulting in higher methane decomposition. Hydrogen concentration profiles also reflect a higher hydrogen yield in Figure 14e than in Figure 14f. Simulation results (Table 2) confirm this effect with a complete conversion at 1573 K (case 5). Experimental studies on methane cracking also confirm that complete conversion is reachable above 1673 K [44–47]. However, the residence time is also an important parameter to be considered for explaining this result. In all those experimental works, the gas residence time was in the order of a few milliseconds (<100 ms). In this study, the effective residence time was significantly higher (about 1.4 s), which explains the complete conversion reached at the outlet for a lower temperature.

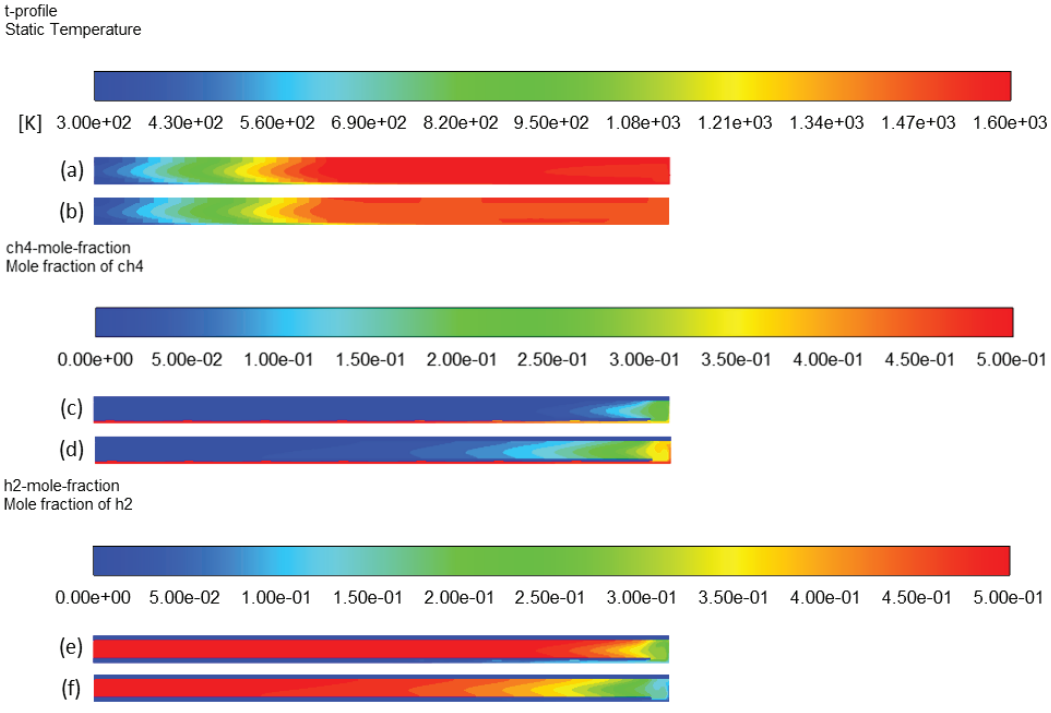

Figure 14. Effect of heating temperature on temperature profile: (**a**) case 5 and (**b**) case 1; CH_4 mole fraction profile: (**c**) case 5 and (**d**) case 1; H_2 mole fraction profile: (**e**) case 5 and (**f**) case 1.

5. Conclusions

Solar methane cracking is worth investigating to develop a sustainable process for clean hydrogen production. Indeed, the methane cracking process is advantageous compared with conventional methane reforming since it produces hydrogen without greenhouse gas emissions, while solid carbon material is formed as a high-value marketable co-product with various potential applications. A hybrid solar/electric reactor was designed and simulated at PROMES-CNRS to overcome solar radiation variability. Such a reactor is proposed for continuous and stable operation when the DNI is low or unstable, thanks to the possibility of additional heating by electric means. Thus, the process continuity is made possible. When the DNI is not high enough for stable on-sun operation, the process can still be maintained by enabling the two heating sources (both electric and solar). The benefits of coupled hybrid heating were illustrated through numerical CFD simulation for methane cracking in gas-phase using ANSYS Fluent. The kinetic model was assessed beforehand to confirm its reliability for the numerical study. A good agreement was shown between experimental and CFD results with an activation energy of 281 kJ/mol. Consequently, the numerical study was achieved and showed that activating both heating sources enlarged the reaction zone inside the reactor. Consequently, the effective residence time increased, improving the methane conversion significantly. However, when solar heating is not possible, reactor operation under only electric heating results in a reasonable methane conversion (75%). The effects of operating parameters on the reactor performance were also numerically studied via simulation. The inlet volumetric flow rate modifies the gas residence time of the reactant molecules in the reactor. A higher inlet volumetric flow rate decreases the residence time and, consequently, the methane conversion. Increasing dilution slightly favors methane conversion. Finally, the temperature is also a key parameter in methane cracking, since the endothermic reaction requires external energy. Increasing

the temperature increased the rate of the reaction and enhanced the methane conversion. In addition, the model was further validated by methane pyrolysis experiments. A good agreement between numerical and experimental results was demonstrated, confirming the reliability of the numerical model. These CFD simulations validated the proposed design of the solar hybrid reactor for efficient methane decomposition performance. Moreover, this numerical model could be extended to simulate methane cracking in molten media as a novel technology that has not been modelled yet.

Author Contributions: Methodology, validation, formal analysis, investigation, and data curation, M.M., S.R. and S.A.; writing—original draft preparation, M.M.; writing—review and editing, M.M., S.R. and S.A.; supervision, S.R. and S.A.; project administration, S.R. and S.A.; funding acquisition, S.R. and S.A. All authors have read and agreed to the published version of the manuscript.

Funding: This work was supported by the French "Investments for the Future" program. managed by the National Agency for Research, under contract ANR-10-LABX-22-01 (Labex SOLSTICE).

Data Availability Statement: Simulation data files are available upon request.

Acknowledgments: The authors thank Roger Garcia (PROMES-CNRS) for his support in the design and installation of the solar reactor, and Régis Rodriguez (PROMES-CNRS) and Emmanuel Guillot (PROMES-CNRS) for their support to set the data acquisition system.

Conflicts of Interest: The authors declare no conflict of interest.

References

1. Kothari, R.; Buddhi, D.; Sawhney, R.L. Comparison of Environmental and Economic Aspects of Various Hydrogen Production Methods. *Renew. Sustain. Energy Rev.* **2008**, *12*, 553–563. [CrossRef]
2. Abánades, A. The Challenge of Hydrogen Production for the Transition to a CO_2-Free Economy. *Agron. Res.* **2012**, *10*, 11–16.
3. Abbas, H.F.; Wan Daud, W.M.A. Hydrogen Production by Methane Decomposition: A Review. *Int. J. Hydrogen Energy* **2010**, *35*, 1160–1190. [CrossRef]
4. Abánades, A.; Ruiz, E.; Ferruelo, E.M.; Hernández, F.; Cabanillas, A.; Martínez-Val, J.M.; Rubio, J.A.; López, C.; Gavela, R.; Barrera, G.; et al. Experimental Analysis of Direct Thermal Methane Cracking. *Int. J. Hydrogen Energy* **2011**, *36*, 12877–12886. [CrossRef]
5. Lemus, R.G.; Martínez Duart, J.M. Updated Hydrogen Production Costs and Parities for Conventional and Renewable Technologies. *Int. J. Hydrogen Energy* **2010**, *35*, 3929–3936. [CrossRef]
6. Msheik, M.; Rodat, S.; Abanades, S. Methane Cracking for Hydrogen Production: A Review of Catalytic and Molten Media Pyrolysis. *Energies* **2021**, *14*, 3107. [CrossRef]
7. Dahl, J. Intrinsic Kinetics for Rapid Decomposition of Methane in an Aerosol Flow Reactor. *Int. J. Hydrogen Energy* **2002**, *27*, 377–386. [CrossRef]
8. Dahl, J.K.; Buechler, K.J.; Weimer, A.W.; Lewandowski, A.; Bingham, C. Solar-Thermal Dissociation of Methane in a Fluid-Wall Aerosol Flow Reactor. *Int. J. Hydrogen Energy* **2004**, *29*, 725–736. [CrossRef]
9. Dahl, J.K.; Buechler, K.J.; Finley, R.; Stanislaus, T.; Weimer, A.W.; Lewandowski, A.; Bingham, C.; Smeets, A.; Schneider, A. Rapid Solar-Thermal Dissociation of Natural Gas in an Aerosol Flow Reactor. *Energy* **2004**, *29*, 715–725. [CrossRef]
10. Dahl, J.K.; Tamburini, J.; Weimer, A.W.; Lewandowski, A.; Pitts, R.; Bingham, C. Solar-Thermal Processing of Methane to Produce Hydrogen and Syngas. *Energy Fuels* **2001**, *15*, 1227–1232. [CrossRef]
11. Rodat, S.; Abanades, S.; Grivei, E.; Patrianakos, G.; Zygogianni, A.; Konstandopoulos, A.G.; Flamant, G. Characterisation of Carbon Blacks Produced by Solar Thermal Dissociation of Methane. *Carbon N. Y.* **2011**, *49*, 3084–3091. [CrossRef]
12. Abanades, S.; Kimura, H.; Otsuka, H. A Drop-Tube Particle-Entrained Flow Solar Reactor Applied to Thermal Methane Splitting for Hydrogen Production. *Fuel* **2015**, *153*, 56–66. [CrossRef]
13. Rodat, S.; Abanades, S.; Flamant, G. Experimental Evaluation of Indirect Heating Tubular Reactors for Solar Methane Pyrolysis. *Int. J. Chem. React. Eng.* **2010**, *8*, A25. [CrossRef]
14. Berndt, F.M.; Perez-Lopez, O.W. Catalytic Decomposition of Methane over Ni/SiO_2: Influence of Cu Addition. *React. Kinet. Mech. Catal.* **2017**, *120*, 181–193. [CrossRef]
15. Rahman, M.S.; Croiset, E.; Hudgins, R.R. Catalytic Decomposition of Methane for Hydrogen Production. *Top. Catal.* **2006**, *37*, 137–145. [CrossRef]
16. Lázaro, M.J.; Pinilla, J.L.; Suelves, I.; Moliner, R. Study of the Deactivation Mechanism of Carbon Blacks Used in Methane Decomposition. *Int. J. Hydrogen Energy* **2008**, *33*, 4104–4111. [CrossRef]
17. Msheik, M.; Rodat, S.; Abanades, S. Experimental Comparison of Solar Methane Pyrolysis in Gas-Phase and Molten-Tin Bubbling Tubular Reactors. *Energy* **2022**, *260*, 124943. [CrossRef]

18. Zaghloul, N.; Kodama, S.; Sekiguchi, H. Hydrogen Production by Methane Pyrolysis in a Molten-Metal Bubble Column. *Chem. Eng. Technol.* **2021**, *44*, 1986–1993. [CrossRef]
19. Geißler, T.; Abánades, A.; Heinzel, A.; Mehravaran, K.; Müller, G.; Rathnam, R.K.; Rubbia, C.; Salmieri, D.; Stoppel, L.; Stückrad, S.; et al. Hydrogen Production via Methane Pyrolysis in a Liquid Metal Bubble Column Reactor with a Packed Bed. *Chem. Eng. J.* **2016**, *299*, 192–200. [CrossRef]
20. Wang, K.; Li, W.S.; Zhou, X.P. Hydrogen Generation by Direct Decomposition of Hydrocarbons over Molten Magnesium. *J. Mol. Catal. A Chem.* **2008**, *283*, 153–157. [CrossRef]
21. Zeng, J.; Tarazkar, M.; Pennebaker, T.; Gordon, M.J.; Metiu, H.; McFarland, E.W. Catalytic Methane Pyrolysis with Liquid and Vapor Phase Tellurium. *ACS Catal.* **2020**, *10*, 8223–8230. [CrossRef]
22. Palmer, C.; Tarazkar, M.; Kristoffersen, H.H.; Gelinas, J.; Gordon, M.J.; McFarland, E.W.; Metiu, H. Methane Pyrolysis with a Molten Cu-Bi Alloy Catalyst. *ACS Catal.* **2019**, *9*, 8337–8345. [CrossRef]
23. Upham, D.C.; Agarwal, V.; Khechfe, A.; Snodgrass, Z.R.; Gordon, M.J.; Metiu, H.; McFarland, E.W. Catalytic Molten Metals for the Direct Conversion of Methane to Hydrogen and Separable Carbon. *Science* **2017**, *358*, 917–921. [CrossRef] [PubMed]
24. Kang, D.; Rahimi, N.; Gordon, M.J.; Metiu, H.; McFarland, E.W. Catalytic Methane Pyrolysis in Molten MnCl2-KCl. *Appl. Catal. B Environ.* **2019**, *254*, 659–666. [CrossRef]
25. Kang, D.; Palmer, C.; Mannini, D.; Rahimi, N.; Gordon, M.J.; Metiu, H.; McFarland, E.W. Catalytic Methane Pyrolysis in Molten Alkali Chloride Salts Containing Iron. *ACS Catal.* **2020**, *10*, 7032–7042. [CrossRef]
26. Parkinson, B.; Patzschke, C.F.; Nikolis, D.; Raman, S.; Dankworth, D.C.; Hellgardt, K. Methane Pyrolysis in Monovalent Alkali Halide Salts: Kinetics and Pyrolytic Carbon Properties. *Int. J. Hydrogen Energy* **2021**, *46*, 6225–6238. [CrossRef]
27. Rahimi, N.; Kang, D.; Gelinas, J.; Menon, A.; Gordon, M.J.; Metiu, H.; McFarland, E.W. Solid Carbon Production and Recovery from High Temperature Methane Pyrolysis in Bubble Columns Containing Molten Metals and Molten Salts. *Carbon N. Y.* **2019**, *151*, 181–191. [CrossRef]
28. Patzschke, C.F.; Parkinson, B.; Willis, J.J.; Nandi, P.; Love, A.M.; Raman, S.; Hellgardt, K. Co-Mn Catalysts for H_2 Production via Methane Pyrolysis in Molten Salts. *Chem. Eng. J.* **2021**, *414*, 128730. [CrossRef]
29. Sánchez-Bastardo, N.; Schlögl, R.; Ruland, H. Methane Pyrolysis for CO_2-Free H_2 Production: A Green Process to Overcome Renewable Energies Unsteadiness. *Chem.-Ing.-Tech.* **2020**, *92*, 1596–1609. [CrossRef]
30. Rodat, S.; Abanades, S.; Sans, J.-L.; Flamant, G. A Pilot-Scale Solar Reactor for the Production of Hydrogen and Carbon Black from Methane Splitting. *Int. J. Hydrogen Energy* **2010**, *35*, 7748–7758. [CrossRef]
31. Maag, G.; Zanganeh, G.; Steinfeld, A. Solar Thermal Cracking of Methane in a Particle-Flow Reactor for the Co-Production of Hydrogen and Carbon. *Int. J. Hydrogen Energy* **2009**, *34*, 7676–7685. [CrossRef]
32. Rodat, S.; Abanades, S.; Sans, J.-L.; Flamant, G. Hydrogen Production from Solar Thermal Dissociation of Natural Gas: Development of a 10 kW Solar Chemical Reactor Prototype. *Sol. Energy* **2009**, *83*, 1599–1610. [CrossRef]
33. Guil-Lopez, R.; Botas, J.A.; Fierro, J.L.G.; Serrano, D.P. Comparison of Metal and Carbon Catalysts for Hydrogen Production by Methane Decomposition. *Appl. Catal. A Gen.* **2011**, *396*, 40–51. [CrossRef]
34. Utrilla, R.; Pinilla, J.L.; Suelves, I.; Lázaro, M.J.; Moliner, R. Catalytic Decomposition of Methane for the Simultaneous Co-Production of CO2-Free Hydrogen and Carbon Nanofibre Based Polymers. *Fuel* **2011**, *90*, 430–432. [CrossRef]
35. Muradov, N.; Smith, F.; T-Raissi, A. Catalytic Activity of Carbons for Methane Decomposition Reaction. *Catal. Today* **2005**, *102–103*, 225–233. [CrossRef]
36. Botas, J.A.; Serrano, D.P.; Guil-López, R.; Pizarro, P.; Gómez, G. Methane Catalytic Decomposition over Ordered Mesoporous Carbons: A Promising Route for Hydrogen Production. *Int. J. Hydrogen Energy* **2010**, *35*, 9788–9794. [CrossRef]
37. Serrano, D.P.; Botas, J.A.; Guil-Lopez, R. H2 Production from Methane Pyrolysis over Commercial Carbon Catalysts: Kinetic and Deactivation Study. *Int. J. Hydrogen Energy* **2009**, *34*, 4488–4494. [CrossRef]
38. Pinilla, J.L.; Torres, D.; Lázaro, M.J.; Suelves, I.; Moliner, R.; Cañadas, I.; Rodríguez, J.; Vidal, A.; Martínez, D. Metallic and Carbonaceous-Based Catalysts Performance in the Solar Catalytic Decomposition of Methane for Hydrogen and Carbon Production. *Int. J. Hydrogen Energy* **2012**, *37*, 9645–9655. [CrossRef]
39. Rodat, S.; Abanades, S. A Hybrid Windowless Dual Tube Solar Reactor for Continuous Volumetric Natural Gas Dissociation. *Front. Energy Res.* **2020**, *8*, 206. [CrossRef]
40. Rodat, S.; Abanades, S.; Boujjat, H.; Chuayboon, S. On the Path toward Day and Night Continuous Solar High Temperature Thermochemical Processes: A Review. *Renew. Sustain. Energy Rev.* **2020**, *132*, 110061. [CrossRef]
41. Abanades, S.; Flamant, G. Experimental Study and Modeling of a High-Temperature Solar Chemical Reactor for Hydrogen Production from Methane Cracking. *Int. J. Hydrogen Energy* **2007**, *32*, 1508–1515. [CrossRef]
42. ANSYS, Inc. *ANSYS Fluent Theory Guide*; ANSYS Inc.: Canonsburg, PA, USA, 2013.
43. Keipi, T.; Tolvanen, K.E.S.; Tolvanen, H.; Konttinen, J. Thermo-Catalytic Decomposition of Methane: The Effect of Reaction Parameters on Process Design and the Utilization Possibilities of the Produced Carbon. *Energy Convers. Manag.* **2016**, *126*, 923–934. [CrossRef]
44. Abanades, S.; Flamant, G. Hydrogen Production from Solar Thermal Dissociation of Methane in a High-Temperature Fluid-Wall Chemical Reactor. *Chem. Eng. Process. Process Intensif.* **2008**, *47*, 490–498. [CrossRef]
45. Rodat, S.; Abanades, S.; Flamant, G. Co-Production of Hydrogen and Carbon Black from Solar Thermal Methane Splitting in a Tubular Reactor Prototype. *Sol. Energy* **2011**, *85*, 645–652. [CrossRef]

46. Yeheskel, J.; Epstein, M. Thermolysis of Methane in a Solar Reactor for Mass-Production of Hydrogen and Carbon Nano-Materials. *Carbon N. Y.* **2011**, *49*, 4695–4703. [CrossRef]
47. Abanades, S.; Tescari, S.; Rodat, S.; Flamant, G. Natural Gas Pyrolysis in Double-Walled Reactor Tubes Using Thermal Plasma or Concentrated Solar Radiation as External Heating Source. *J. Nat. Gas Chem.* **2009**, *18*, 1–8. [CrossRef]

fluids

MDPI

Article

The Role of Inertia in the Onset of Turbulence in a Vortex Filament

Jean-Paul Caltagirone

Bordeaux INP, Arts et Métiers Institute of Technology, University of Bordeaux, CNRS UMR-5295, INRAE, I2M Bordeaux, 33405 Talence, France; calta@ipb.fr

Abstract: The decay of the kinetic energy of a turbulent flow with time is not necessarily monotonic. This is revealed by simulations performed in the framework of discrete mechanics, where the kinetic energy can be transformed into pressure energy or vice versa; this persistent phenomenon is also observed for inviscid fluids. Different types of viscous vortex filaments generated by initial velocity conditions show that vortex stretching phenomena precede an abrupt onset of vortex bursting in high-shear regions. In all cases, the kinetic energy starts to grow by borrowing energy from the pressure before the transfer phase to the small turbulent structures. The result observed on the vortex filament is also found for the Taylor–Green vortex, which significantly differs from the previous results on this same case simulated from the Navier–Stokes equations. This disagreement is attributed to the physical model used, that of discrete mechanics, where the formulation is based on the conservation of acceleration. The reasons for this divergence are analyzed in depth; however, a spectral analysis allows finding the established laws on the decay of kinetic energy as a function of the wave number.

Keywords: turbulence cascade; vortex stretching; vortex bursting; discrete mechanics; conservation of acceleration; Helmholtz–Hodge decomposition; inertial curvature

Citation: Caltagirone, J.-P. The Role of Inertia in the Onset of Turbulence in a Vortex Filament. *Fluids* **2023**, *8*, 16. https://doi.org/10.3390/fluids8010016

Academic Editor: Mehrdad Massoudi

Received: 2 December 2022
Revised: 26 December 2022
Accepted: 28 December 2022
Published: 2 January 2023

1. Introduction

The phenomena of vortex stretching and bursting are the main mechanisms for the appearance of turbulence and interactions between the different scales of energy transfer: [1–4]. From the physical point of view, these phenomena are related to the balance of the different actions associated with the terms of the equations of motion, inertia, compression, diffusion, and dissipation. The production of turbulence, the transfer of energy, and energy decay are described by the different contributions of the law of motion. The progress on the physical understanding of turbulence analyzed on experiments has been corroborated by simulations produced from the Navier–Stokes equation.

An alternative to the Navier–Stokes equation was recently implemented to search for solutions related to fluid flows or two-phase flows. The corresponding equation of motion [5] was also used to represent fluid–structure interactions or heat transfer on small time scales. The solutions of the discrete formulation and the Navier–Stokes equation for fluids or the Navier–Lamé equation for solids are the same despite important differences in the physical models.

The discrete formulation is here implemented in the framework of turbulent vortex flows. Indeed, the discrete formulation includes a different modeling of the physical effects; this is the case, in particular, for the inertia that is formulated in two terms of a Helmholtz–Hodge decomposition [6]. These terms play a very important role in the energy transfer mechanism of vortices on different spatial scales. The form of the equation of motion causes inertial effects to be intertwined with compressive effects. In a turbulent flow, pressure plays a regulating role, allowing local energy storage and energy redistribution in the form of kinetic energy; this phenomenon is present in all turbulent flows, including incompressible ones. The analysis of a rotating flow of a solid body clearly shows that

the discrete formulation satisfies the rotational invariance of the equation of motion. In this sense, it extends the Galilean invariance of translational motion to the rotations of the solid body.

Several cases of inviscid or viscous vortex filament are analyzed in a first step to understand and verify that energy exchanges between turbulent structures are due to both vortex stretching and, occasionally, vortex bursting. The evolution of the mean kinetic energy and pressure fields shows inverse variations even for inviscid flows. The last part is devoted to the simulation of a Taylor–Green vortex at a Reynolds number of $Re = 1600$. The result is consistent with the previous long-term validations but shows a different behavior of the variation in the mean kinetic energy in the first instants of the flow. Contrary to the simulations performed with the Navier–Stokes equation, the kinetic energy increases by transforming the potential energy. As in a vortex filament, the velocity increases in the core at the expense of the pressure energy, while maintaining its angular momentum. A thorough analysis is provided to explain the observations and to give the reasons for the disagreements with the Navier–Stokes equation.

2. Discrete Mechanics Framework

2.1. Physical Principles

The fundamental principles of discrete mechanics have already been described Cal19a, Cal21b. Its presentation is developed here in a more synthetic way by specifying the most essential aspects related to the described phenomena. Some concepts of classical mechanics are abandoned, such as the existence of a global inertial reference frame, which forces us to abandon the principles of one-point derivation, integration, and analysis in general. At the same time, the notion of continuous medium is disregarded, it is the very reason for the creation of a global reference frame. Similarly, mass is an abstraction that is not necessary for the description of the laws of physics, as is momentum; in fact, the physical quantities that are expressed using mass are all of the first order, which allows the same quantities to be defined per unit of mass.

The main concepts introduced by discrete mechanics can be summarized by:

- A primary one-dimensional view of mechanical equilibrium governed by acceleration, thus preserving the notion of relativity of velocity. The one-dimensional geometrical description is fixed by the existence of a rectilinear segment delimited by two extremities and a length dh, called a discrete horizon. The extension of the physical model to several dimensions of space is realized by cause and effect, with the interactions being established through the extremities common to several segments.
- A translation invariance in time that, according to Noether's theorem, ensures the conservation of energy. The discrete equation of motion is therefore the same at all times. With the exception of acceleration, which is an absolute quantity, the other quantities of physics are subject to the principle of invariance, which allows us to evaluate the value of a quantity at time t from its knowledge at an earlier time t^o. This incremental process allows building a continuous memory model where velocity, energy, and other quantities are updated by a time integration.
- A local reference frame linked to a segment, which inhibits any change in reference frame, allows building an equation of motion on a geometrical structure, where the spatial dependencies from one segment to another are ensured by the principle of causality. The dynamics of a material medium or a particle in a one-dimensional space is limited by the velocity of the medium (the propagation of the swell, the acoustic signal, and the light). To use the concept of change in reference frame, the velocity must be constant, which is not guaranteed. Therefore, any interaction is limited by a horizon defined by the velocity of the medium.
- Classical notions of scalar, vector, pseudo-vector, and tensor are replaced by a unique concept of amplitude parameter defining the value of the intensity of the quantity attached to a point, segment, surface, etc. If this parameter is attached to a point, it is a scalar; if it is attached to a segment, it is a vector, etc. For example, kinetic energy is a

scalar when it is defined at a point and becomes a vector when it is associated with a segment.

- Conservation of the total energy per unit of mass: mass and energy are two homologous forms of the equivalence principle of relativity. The laws of classical mechanics require several equations to translate the conservation of mass, momentum, and energy; they are redundant. The conservation of discrete energy also conserves acceleration as well as angular momentum, so it is not necessary to explicitly conserve mass.
- The association to the principles of equivalence and relativity of an additional concept, the Helmholtz–Hodge decomposition, which consists of writing that any acceleration is the sum of a solenoidal contribution and an irrotational one. The intrinsic acceleration of the particle or of the material medium is thus the sum of the gradient of a scalar potential and of the curl of a vector potential. This decomposition gives very valuable properties to the conservation laws written in this form.
- A principle included in Maxwell's analysis to synthesize the laws of electrostatics and magnetism by introducing the time dependence of the fields. Direct and induced unsteady currents are the two possible alternatives for the creation of fields in electromagnetism. These two forms are associated with the two components of the Helmholtz–Hodge decomposition. The extension of these concepts to mechanics leads to consider compressive effects as direct actions and viscous effects as induced actions.

2.2. One-Dimensional Model

Discrete mechanics is developed from a one-dimensional view of dynamic equilibrium. Figure 1 represents a rectilinear segment Γ oriented by the vector $\mathbf{t}$ bounded by the two vertices a and b; its length $dh = [a, b]$ is named a discrete horizon in reference to the maximum distance perceived by an observer located on one of the ends. This distance is related to the wave velocity c (swell, acoustic, and light) and to a duration dt corresponding to the observation time of the phenomenon by the relationship $dh = c\,dt$.

The intrinsic acceleration of the material medium or of a particle on the segment Γ is denoted γ; it is both a scalar γ defined on the oriented segment and a vector $\gamma = \mathbf{t}$, but also the component of the acceleration vector of a space for which knowledge is not necessary. In the same way, the velocity v is the component of a vector of space $\mathbf{V}$ projected on Γ. While the velocity is relative and is given only at a constant, the acceleration γ is considered absolute. The derivation of the equation of motion in discrete mechanics is based on the equality of the accelerations: those due to the external actions $\boldsymbol{h}$ and the intrinsic acceleration γ of the material medium or of a particle. This law expresses the conservation of acceleration, it is written as:

$$\gamma = \boldsymbol{h} \tag{1}$$

where $\boldsymbol{h}$ is the sum of the accelerations: those of the effects of compression and shear but also all the other potential source terms: gravitation, capillary acceleration, etc.

The law (1) does not disagree with the fundamental principle of dynamics $m : \gamma = \mathbf{F}$; in the case where the force is associated with gravity, we have $m : \gamma = m : \mathbf{g}$, where m is the moving mass, or $\gamma = \mathbf{g}$. Galileo's principle of equivalence expresses that the effects of inertia and gravitation are of the same nature. However, the presence of mass poses two problems: (i) its generalization to any acceleration other than gravity; (ii) the association of a necessarily volumetric quantity, mass, and another essentially vectorial one, acceleration. Paradoxically, the force seen as a vector in the context of classical mechanics is the product of two disjoint quantities. The law (1) restricts the principle of equivalence to accelerations only by expressing that the intrinsic acceleration of a medium is equal to the sum of the accelerations applied to it.

Mass is at the center of Copernican and Galilean mechanics, which is attributed to the understanding of planetary motion. This importance continues today even if the theory of special relativity introduces the equivalence between mass and energy; moreover, mass is still present in the expression of energy $e = m\,c^2$. In the same way, the actual law of

fluid mechanics is a conservation of momentum, $\mathbf{q} = m\,v$, the product of mass and velocity. Discrete mechanics abandons the notion of momentum to define an equivalent quantity per unit of mass, the acceleration.

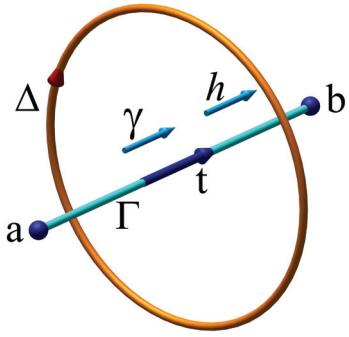

Figure 1. Local frame of reference of discrete mechanics; the rectilinear segment Γ oriented by **t** is the constitutive element of the primal structure and the support of the intrinsic acceleration γ or imposed by the exterior $\boldsymbol{h}$. This segment, limited by its extremities a and b, is of length dh and called the discrete horizon. The dual structure is schematized by the contour Δ, which defines the induced actions then projected on Γ.

The principle of relativity must be respected; the velocity is a relative quantity that has no absolute reference, not even the velocity that is a strictly independent physical quantity. Velocity v at time $t^o + dt$ is calculated from the acceleration in the form $v = v^o + \gamma\,dt$, where v^o is the velocity at time t^o. In the same way, the displacement $\boldsymbol{u}$ is calculated from the velocity in the form $\boldsymbol{u} = \boldsymbol{u}^o + v\,dt$. These two quantities are thus updated from their values at time t^o. Many other quantities are relative, in particular energy, which is defined only to a constant. If we define the total energy per unit mass Φ, then its variation along the segment takes the form:

$$\Phi_b - \Phi_a = \int_a^b \boldsymbol{\gamma} \cdot \mathbf{t}\,dl \tag{2}$$

The intrinsic acceleration γ is that of an isolated particle that follows the trajectory Γ or that of the material medium, and the acceleration $\boldsymbol{h}$ of the law (1) is the sum of the external accelerations on Γ. In one dimension of space, the intrinsic acceleration is written as $\gamma = dv/dt = \partial v/\partial t + \nabla(|v|^2/2)$. The quantity $|v|^2/2$ is the kinetic energy; it is also written as $1/2(v \cdot v)$. It is both a scalar assigned to the oriented segment Γ and the vector $1/2(v \cdot v)\,\mathbf{t}$. This quantity can also be defined on the extremities a and b of the segment, where $\nabla(|v|^2/2)$ represents an acceleration opposing the increase or decrease in the velocity over time. This is the principle of inertia, which tends to establish a uniform motion in the absence of any external acceleration $\boldsymbol{h}$.

2.3. Extension of Physical Model to Other Dimensions

The discrete physical model is one-dimensional, represented by the segment Γ on which all direct and induced accelerations are projected, whether intrinsic or applied. The extension to a higher dimension is immediate; it is realized by assembling the segments by their extremities. These extremities become the vertices of the primal structure formed of planar polygons delimited by the collection Γ^* of the sides of the triangle in Figure 2. This primal structure is thus composed of vertices, segments, and polygonal facets; contrary to other approaches coming from differential geometry, mimetic methods, discrete exterior calculus, or the cell method, discrete mechanics does not address volumes even if the assembly of facets forms polyhedra with planar faces.

The absence of a global reference frame is both a disadvantage and an advantage. It is no longer possible to express the invariance of the system of equations in a change of reference frame, for example, or to project each term on axes in an inertial reference frame to ensure mechanical equilibrium, as in continuum mechanics. The advantage is the ability to extend the principle of inertia to uniform rotational motions. The interactions from one local reference frame to another are realized by cause and effect. The celerity c of the waves is defined locally including for the celerity of light c_0, which can vary according to the medium.

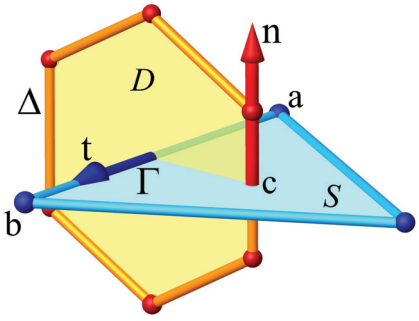

Figure 2. Geometric structures of discrete mechanics: the primal structure (in blue) is composed of a collection of segments Γ oriented by a unit vector **t** bounded by the ends a or b; these segments form a polygonal planar surface $\mathcal{S}$, whose barycenter, denoted c, defines the normal **n** that is positively oriented according to Maxwell's rule. The dual structure (in red) has a flat polygonal surface $\mathcal{D}$ bounded by segments Δ. The unit vectors are orthogonal by construction, $\mathbf{n} \cdot \mathbf{t} = 0$.

Energies per unit volume of compression carried by ϕ^o and of rotation, represented by $\boldsymbol{\psi}^o$, are defined at time t^o and are named the retarded potentials in reference to the electromagnetic potentials of Liénard [7].

$$\phi^o = -\int_0^{t^o} c_l^2 \, \nabla \cdot \boldsymbol{v} \, d\tau; \qquad \boldsymbol{\psi}^o = -\int_0^{t^o} c_t^2 \, \nabla \times \boldsymbol{v} \, d\tau \tag{3}$$

where c_l and c_t are the longitudinal and transverse celerities.

They express the accumulation of the respective energies over time from an initial state, where all quantities $(\boldsymbol{v}, \phi^o, \boldsymbol{\psi}^o)$ satisfy the equation of motion. From this point of view, the discrete equation of motion is a physical model with continuous memory.

2.4. Discrete Equation of Motion

The conservation of the total energy Φ corresponds to the integration of the acceleration on the segment Γ, but $\boldsymbol{\gamma}$ and the velocity $\boldsymbol{v}$ are average values on this segment. It is then possible to derive an equation of motion whose unknowns are the velocities $\boldsymbol{v}$ on the basis of discrete operators, the divergence $\nabla \cdot \boldsymbol{v}$, gradient of a scalar $\nabla\phi$, primal curl $\nabla \times \boldsymbol{v}$, and dual curl $\nabla^d \times \boldsymbol{\psi}$. The law of discrete mechanics (1) expresses that the intrinsic acceleration of an isolated particle or of the material medium is equal to the sum of the accelerations imposed by the exterior, mainly the compressive and rotational accelerations. Intrinsic acceleration is simply the material derivative $\boldsymbol{\gamma} = d\boldsymbol{v}/dt$.

Discrete mechanical equilibrium corresponds to the equality on the accelerations $\boldsymbol{\gamma} = \boldsymbol{h}$, which becomes $\boldsymbol{\gamma} = -\nabla\phi + \nabla^d \times \boldsymbol{\psi}$ in the framework of a Helmholtz–Hodge decomposition where $\phi = \phi^o + d\phi$ is the scalar potential, and $\boldsymbol{\psi} = \boldsymbol{\psi}^o + d\boldsymbol{\psi}$ is the potential vector of the intrinsic acceleration; ϕ^o and $\boldsymbol{\psi}^o$ are named the retarded potentials in reference to the electromagnetic potentials [7,8]. Physical modeling of the increases in potentials, $d\phi$ and $d\boldsymbol{\psi}$, can be found in the references associated with discrete mechanics [9,10]. The relative increase in compression is a function of the divergence of the velocity, and that of the rotation is obtained by the primal curl of the latter. The equation of motion becomes:

$$\begin{cases} \dfrac{d\boldsymbol{v}}{dt} = -\nabla\left(\phi^o - c_l^2\, dt\, \nabla\cdot\boldsymbol{v}\right) + \nabla^d\times\left(\boldsymbol{\psi}^o - c_t^2\, dt\, \nabla\times\boldsymbol{v}\right) + \boldsymbol{h}_s \\ \alpha_l\,\phi^o - c_l^2\, dt\, \nabla\cdot\boldsymbol{v} \longmapsto \phi^o \\ \alpha_t\,\boldsymbol{\psi}^o - c_t^2\, dt\, \nabla\times\boldsymbol{v} \longmapsto \boldsymbol{\psi}^o \end{cases} \tag{4}$$

where $\boldsymbol{h}_s$ represents the acceleration due to sources, gravitation, capillary effects, etc.; α_l and α_t are the attenuation factors for longitudinal and transverse waves, respectively. For a Newtonian fluid, $\alpha_l \approx 1$ and the factor α_t is equal to zero for characteristic times lower than $t \approx 10^{-11}$ s; transverse waves are dissipated very quickly.

The discrete equation of motion is accompanied by two updates of the scalar ϕ^o and vector $\boldsymbol{\psi}^o$ potentials computed from the divergence and the primal curl of the velocity. Symbol $\longmapsto$ means that the potentials are updated from the retarded potentials. The discrete equation is self-contained: it does not require any additional mass conservation law or constitutive laws. The variable is the velocity $\boldsymbol{v}$ on each of the segments of the primal structure. The quantity dt is the time lapse between two observations of the physical system. It is closely related to the physical phenomenon studied, and its value can be very large for the simulation of stationary phenomena, at 10^{-20} s to translate the propagation of light, where $c_0 \approx 10^8$ ms^{-1}. In all unsteady cases, it is necessary to choose a time span $dt << dh/c$. Even if the velocity of the medium is very large, the compression energy is not zero. Indeed, the grouping $d\phi = dt\, c^2\, \nabla\cdot\boldsymbol{v}$ is the energy increase between two observations of the evolution of the physical system; $d\phi$ remains constant because $\nabla\cdot\boldsymbol{v} \approx 1/c^2$. Thus, a medium considered rather incompressible can propagate sound waves, for example, in water. The discrete equation of motion applies to any incompressible or compressible flow.

The system (4) is an alternative to the Navier-Stokes equation and the conservation of mass. It is primarily a law of conservation of total energy per unit mass, i.e., acceleration. As mass is a form of energy, it is not necessary to keep the mass or density in the equation of motion; it would be an overabundant quantity. Moreover, all the quantities of physics that are currently functions of mass make this one appear at the order one, which allows the definition of equivalent quantities per unit of mass. The length dh and time dt are the only two fundamental quantities to define any law of mechanics and, more generally, of physics.

Finally, the acceleration or the material derivative [6] in one or more space dimensions is written as:

$$\gamma = \frac{d\boldsymbol{v}}{dt} = \frac{\partial\boldsymbol{v}}{\partial t} + \nabla\left(\frac{|v|^2}{2}\right) - \nabla^d\times\left(\frac{|v|^2}{2}\,\mathbf{n}\right) \tag{5}$$

This discrete form significantly differs from that of continuum mechanics. In particular, the last term is here a dual curl with zero divergence, whereas the corresponding term in continuum mechanics, the Lamb vector, $\mathcal{L} = -\mathbf{V}\times\nabla\times\mathbf{V}$, is the gradient of another potential. The two terms of inertia or the equivalent form $\mathbf{V}\cdot\nabla\mathbf{V}$ have projections on each of the three axes of a global reference frame. In discrete mechanics, the two terms of inertia (5) have as support the same segment Γ of the local reference frame.

The cornerstone of the discrete model is precisely the formulation of the inertia; Figure 1 well schematizes the competition between the compression term and the rotation term of the relation (5). The first contribution is fixed by the gradient of the inertial potential $|v|^2/2$ defined on the vertices a and b,and the second contribution is represented by the dual curl of the vector potential $|v|^2/2\mathbf{n}$. Within a turbulent flow, the energy exchange between these two forms of inertial acceleration is most likely the force driving the transfer between the different spatial scales.

2.5. Discrete Kinetic Energy Theorem

It is important to specify the differences in the kinetic energy theorem between continuum mechanics and discrete mechanics. These differences are not so much related to the presence or absence of mass as to the fact that we consider the integration on an elementary volume specific to the notion of continuous medium. Let us take the Navier-Stokes equation multiplied by the velocity vector of space $\mathbf{V}$ and, to simplify the matter, let us consider the only contribution of the pressure and an incompressible flow. Let us consider an elementary volume Ω limited by an impermeable surface Σ; the conservation of kinetic energy is written as follows:

$$\int_{\Omega} \rho \, \frac{d|\mathbf{V}|^2}{dt} \, dv = - \int_{\Omega} \mathbf{V} \cdot \nabla p \, dv \tag{6}$$

The term $\mathbf{V} \cdot \nabla p$ can be transformed into the form $\mathbf{V} \cdot \nabla p = \nabla \cdot (p \, \mathbf{V}) - p \, \nabla \cdot \mathbf{V}$; the last term in (6) vanishes when incompressibility is taken into account, and the equation becomes:

$$\int_{\Omega} \rho \, \frac{d|\mathbf{V}|^2}{dt} \, dv = - \int_{\Sigma} p \, \mathbf{V} \cdot \mathbf{n} \, ds \tag{7}$$

and, as the surface is impermeable, $\mathbf{V} \cdot \mathbf{n} = 0$, we obtain:

$$\int_{\Omega} \frac{d|\mathbf{V}|^2}{dt} \, dv = 0 \tag{8}$$

This observation translated by (8) is perfectly legitimate if we stick to the equilibrium on the volume Ω. For a material point $dE_k/dt = 0$, the kinetic energy remains constant when we follow the medium in its motion; this local form is, however, questionable. In the presence of viscous forces, the form adopted by many authors Bra84, Van11, Wan13 only takes into account the latter terms, and the energy decay becomes:

$$-\frac{d|\mathbf{V}|^2}{dt} = \boldsymbol{\varepsilon} \tag{9}$$

considered as the evolution of the only dissipation $\varepsilon = 2 \, \nu \, \mathbf{S} : \mathbf{S}$, where $\mathbf{S}$ denotes the deviating part of the rate-of-strain tensor. The problem remains for compressible flows where the divergence is not zero.

The major objection to this conclusion lies in the notion of the continuous medium itself; the use of a transformation of a weak integral formulation leads to a loss of information: it amounts to asserting that locally one imposes $\mathbf{V} \cdot \nabla p = 0$ but these two vectors are not necessarily orthogonal. In continuum mechanics, the kinetic energy theorem specifies that the sum of the forces applied to a material medium is equal to the variation in its kinetic energy.

Its transposition into discrete mechanics is immediate: the sum of the accelerations applied to a material medium is equal to the variation in the kinetic energy per unit of mass; this is noted $\boldsymbol{e}_k$. It is both a scalar attached to the vertices of the primal structure and a vector related to the Γ segment, $\boldsymbol{e}_k = 1/2 \, (\boldsymbol{v} \cdot \boldsymbol{v}) \, \mathbf{t}$ because the vector $\boldsymbol{v}$ is associated with the segment Γ. This is not a new law; it is deduced from the equation of motion. In discrete mechanics, the equation of motion (4) is multiplied by $\boldsymbol{v}$ and integrated over the length of the segment:

$$\int_{\Gamma} \frac{1}{2} \frac{d|\boldsymbol{v}|^2}{dt} = - \int_{\Gamma} \boldsymbol{v} \cdot \nabla \phi + \int_{\Gamma} \boldsymbol{v} \cdot \nabla^d \times \boldsymbol{\psi} \tag{10}$$

The potential $\phi = \left(\phi^o - c_l^2 \, dt \, \nabla \cdot \boldsymbol{v} \right)$ is the compression or translational kinetic energy and $\boldsymbol{\psi} = \left(\boldsymbol{\psi}^o - c_t^2 \, dt \, \nabla \times \boldsymbol{v} \right)$ is the rotational energy or angular kinetic energy. The form (4) of the equation of motion includes from the start the balance of the sum of the forces but

also the moments. The acceleration γ is not only related to the translational motion but also translates the conservation of angular momentum.

Contrary to classical mechanics, where the vector $\mathbf{V}$ is not necessarily collinear with the pressure gradient vector ∇p and similar to viscous forces, the discrete formulation removes any interpretation on the orientation of the terms in the kinetic energy equation. v is well collinear to $\nabla\phi$ and to $\nabla^d \times \boldsymbol{\psi}$; the results of the scalar product allow us to consider that $-\boldsymbol{v} \cdot \nabla\phi$ and $\boldsymbol{v} \cdot \nabla^d \times \boldsymbol{\psi}$ are, at the same time, scalars on the oriented segment and vectors. With the unknown of the equation of motion being v, the local kinetic energy is simply obtained by a scalar product $e_k = 1/2(v \cdot v) = 1/2|v|^2$. The quantity e_k considered as an average on a segment allows the definition of the discrete theorem of the local kinetic energy:

$$\frac{de_k}{dt} = -\boldsymbol{v} \cdot \nabla\phi + \boldsymbol{v} \cdot \nabla^d \times \boldsymbol{\psi} \tag{11}$$

It is possible to define an average value E_k on the whole physical domain of the kinetic energy per unit of mass from its value on each segment of the primal structure e_k:

$$E_k = \frac{1}{[\Gamma^*]} \int_{\Gamma^*} \frac{1}{2} |\boldsymbol{v}|^2 \, dl \tag{12}$$

where $[\Gamma^*]$ is the length measure of all segments. Similarly, the global compression energy E_c is represented by an integral over the primal volume Ω:

$$E_c = \frac{1}{[\Omega]} \int_{\Omega} \phi^o \, dv \tag{13}$$

Returning to the local form (11), the velocity v is aligned not only with $\nabla\phi$ but also with $\nabla^d \times \boldsymbol{\psi}$. This last term corresponds to the rotation of the medium but only reflects dissipation in the case of a viscous fluid for which the potential vector is of the form $\boldsymbol{\psi} = \nu \, \nabla \times \boldsymbol{v}$. In this situation, the transverse waves are completely attenuated over very small time constants ($\tau \approx 10^{-11} s$). The local variation in the kinetic energy of a material medium during its motion can thus be positive or negative, but the most important aspect is that the integration to the whole volume Ω of the considered flow cannot be limited a priori to a monotonous decay. Indeed, the discrete law of motion (4) expresses the conservation of the total energy $\Phi = E_c + E_r$, where E_c is the compression energy per unit of mass, and E_r is the rotation energy. The kinetic energy E_k is only a part of the total energy. In the absence of viscous friction for a fluid, there remain two energies, E_c and E_k, the sum of which is indefinitely conserved over time from an Eulerian view. For a given flow, the velocity v and the potential ϕ are nonzero and fixed by the initial condition. The evolution in time of the system is governed by only the equation of motion (4). Equation (11) is only a consequence of it. Like any mechanical system, the kinetic energy and the potential energy evolves in such a way as to preserve the total energy. The following form of the equation of motion allows us to be convinced of this:

$$\frac{\partial \boldsymbol{v}}{\partial t} = -\nabla \left(\phi^o + \frac{1}{2} |\boldsymbol{v}|^2 - c_l^2 \, dt \, \nabla \cdot \boldsymbol{v} \right) + \nabla^d \times \left(\boldsymbol{\psi}^o + \frac{1}{2} |\boldsymbol{v}|^2 \, \mathbf{n} - c_t^2 \, dt \, \nabla \times \boldsymbol{v} \right) \tag{14}$$

The two terms of the right-hand side are two Lagrangians associated, respectively, with the conservation of the compression and rotation accelerations. Noether's theorem applied to laws of physics in the form of Lagrangians or Hamiltonians allows us to invoke the invariances of a mechanical system. In particular, the pressure energy defined by ϕ^o and the kinetic energy $1/2 \, |v|^2$ can change over the course of time while keeping the total energy. In particular, the total kinetic energy can increase while the pressure decreases.

In the case of a vortex filament where the angular velocity is v and the potential ϕ depend only on the distance to the axis of rotation, these two quantities are orthogonal and $\boldsymbol{v} \cdot \nabla\phi = 0$, and the flow remains axial. When a modulation of the velocity along

the axial direction is introduced, this condition is no longer met and axial currents are generated to try to re-establish the axisymmetric equilibrium; this is the phenomenon of vortex stretching.

2.6. Conservation of Angular Momentum

The equation of motion (4) is a law of conservation of total energy per unit mass, but it also conserves angular momentum along with momentum. In continuum mechanics, the angular momentum theorem is a separate law from the equation of motion expressing the conservation of the quantity $\mathbf{r} \times \mathbf{p}$, where $\mathbf{p}$ is the momentum, and $\mathbf{r}$ is the distance from the axis of rotation.

Let us consider an incompressible rotational motion without longitudinal effects; in these conditions, the discrete equation of motion becomes:

$$\frac{\partial \boldsymbol{v}}{\partial t} = \nabla^d \times \left(\boldsymbol{\psi}^o + \frac{1}{2} |\boldsymbol{v}|^2 \, \mathbf{n} - c_t^2 \, dt \, \nabla \times \boldsymbol{v} \right) + \boldsymbol{h}_s \tag{15}$$

The first term of the parenthesis is the potential $\boldsymbol{\psi}^o$, which would represent a possible mechanical action that would be associated with a storage of the mechanical energy of rotation, for example, a balance spring of a watch or a pendulum. The second term is a kinetic energy per unit of mass; it is the rotational inertia and $\nabla^d \times \boldsymbol{\psi}_i$ is the inertial acceleration related to the rotation. The term $-c_t^2 \, dt \, \nabla \times \boldsymbol{v}$ is the instantaneous energy that is redistributed to the other components of the equation over time. In an unsteady rotational motion, all these terms are related, but the total rotational energy is conserved. The dual curl of the sum of these is the rotational acceleration, i.e., the angular momentum per unit mass. In the absence of viscous dissipation, the angular momentum is conserved.

For example, the application of Equation (15) to a simple pendulum oscillating under the effect of the acceleration of gravity $\boldsymbol{h}_s = -g \, \sin\theta \, \mathbf{t}$ allows us to find the result of Newtonian or Lagrangian mechanics, including in the nonlinear regime. In the linear domain, the solution is then $\theta(t) = \theta_0 \, \cos(\sqrt{g/r}t)$, and the period $T = 2\,\pi\,\sqrt{r/g}$, where θ_0 is the initial angle of the pendulum, and r is its length.

In the case of a purely viscous flow, the term $dt \, c_t^2$ is replaced by the kinematic viscosity ν, and the attenuation factor α_t is equal to unity, the transverse waves are attenuated in a very short time. The retarded vector potential at time t^o is equal to $\boldsymbol{\psi}^o = -\nu \, \nabla \times \boldsymbol{v}^o$, but the exchanges between the rotational inertia and the other terms of the equation, including pressure terms, persist. In classical mechanics, the formulation of the inertia is not at all the same as in discrete mechanics, and the Navier–Stokes equation does not preserve a priori the angular momentum. In turbulence, this discrepancy can be of the first order in the representation of the interactions between vortices.

3. Turbulent Flows in Vortex Filaments

Examples of vortex filaments for a perfect or viscous fluid are analyzed in order to highlight the phenomena of vortex stretching and bursting in configurations simpler than a developed turbulent flow. The objective is to show that the kinetic energy can increase, even in cases of decreasing turbulence. Finally, the reference case of the Taylor–Green vortex at a Reynolds number of $Re = 1600$ is taken again to highlight these same phenomena and to demonstrate to a disagreement with the previous results and to attribute it to the chosen physical model.

3.1. Inviscid Vortex-Filament

The appearance of turbulence is first analyzed on a cylindrical vortex of an inviscid fluid in the first moments of the flow before the creation of small structures leads to its divergence. The physical domain corresponds to a cylinder of dimensions $[(0, \pi/2), (0, 2\,\pi), (-\pi, \pi)]$. In cylindrical coordinates (r, θ, z), the initial velocity field is given by the vector:

$$\mathbf{V} = [0, \cos r \, (1 + \alpha \, \cos z), 0] \tag{16}$$

where α is a modulation factor of the velocity perturbation along the z direction. The initial scalar potential (pressure) is directly deduced from the equation of motion and the imposed velocity (16).

If $\alpha = 0$, the initial streamlines are circles, $v_\theta = \cos r$, and the potential field $\phi(r)$ is purely radial. Under these conditions, the vector quantities v and $\nabla\phi$ are orthogonal, and the evolution of the kinetic energy per unit mass during its motion given by:

$$\frac{de_k}{dt} = -v \cdot \nabla\phi \tag{17}$$

is zero. We notice that the components v and $\nabla\phi$ are carried by the same segment Γ; they are thus collinear. This is not a paradox because they are components of the velocity $\mathbf{V}$ and not of the velocity vector itself. Moreover, when v and $\nabla\phi$ are oriented along the radius, the velocity component is indeed null and vice versa for the orthoradial direction. The simulation of this case with the system (4) leads to a strictly angular motion with constant velocity and a kinetic energy e_k constant in time. Contrary to a common idea, the nonexistence of a 2D turbulent motion is not due to a 2D restriction of the physical space. By applying the curl operator to the Navier–Stokes equation, we find the form on $\omega = \nabla \times \mathbf{V}$:

$$\frac{\partial\omega}{\partial t} + \mathbf{V} \cdot \nabla\omega - \omega \cdot \nabla\mathbf{V} = \nu\,\nabla^2\omega \tag{18}$$

where $\mathbf{V} \cdot \nabla\omega$ represents the advection of the vortex, and a term $\omega \cdot \nabla\mathbf{V}$, which cancels out in the two dimensions of space because the velocity is defined in this planar surface whereas ω is orthogonal to it. The result obtained in discrete mechanics shows that a vortex without longitudinal modulation leads to an invariance of the kinetic energy, even in three dimensions.

In the case where there is a velocity modulation along the z direction with $\alpha = 0.2$, the problem is different. Indeed, $\mathbf{V}$ and $\nabla\phi$ are no longer orthogonal, and a longitudinal motion is superimposed on the rotational motion of the vortex. As the flow is incompressible and the boundary conditions are such that $\mathbf{V} \cdot \mathbf{n} = 0$, the motion generates positive and negative longitudinal velocities, which in turn generate pressure variations along the axis of the vortex. This phenomenon of stretching and compression of the vortex can be observed in Figure 3 from an initial condition fixed by the velocity field (16). This vortex stretching shows that the axial velocities in the core of the vortex are higher than on the periphery. In the image of the center, we can see that the kinetic energy is more important in the central core.

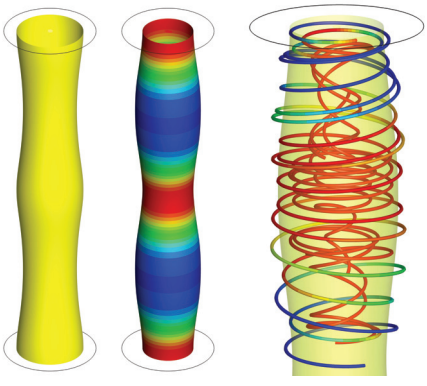

Figure 3. Inviscid vortex filament initiated by the velocity field (16); initial potential field ϕ^o (**left**), potential field at $t = 6$ decorated by the local kinetic energy (**center**), and a snapshot of streamlines (**right**).

Figure 4 shows the evolution over time of the kinetic energy defined by the average over all segments of the local energy on each segment $1/2|v|^2$. We observe that the variations in the kinetic energy E_k and potential are in phase opposition even if the definitions of these quantities are different. They reflect the periodic movements of the vortex stretching phenomenon. To understand these oscillations, we return to the equation of motion for an inviscid flow:

$$\frac{\partial v}{\partial t} = -\nabla\left(\phi^o + \frac{1}{2}\,|v|^2 - c_l^2\,dt\,\nabla\cdot v\right) \tag{19}$$

First, it is necessary to recall that the incompressibility of the flow is not fixed a priori but established by the term $c_l^2\,dt\,\nabla\cdot v$, which becomes constant for a lapse of time dt because the divergence of the velocity is of the order of magnitude of the inverse of c_l^2. This term corresponds to the update of the scalar potential linked to a modification of the equilibrium between the compression energy characterized by the retarded potential ϕ^o and the kinetic energy. Equation (19) is solved for an inviscid flow ($\nu = 0$) for several spatial approximations and the solution well converges, but, in all cases, the numerical solution diverges for a time $t > 15$. It is not possible to obtain a very long-term solution without viscosity. However, a stable flow can be maintained by introducing a very low viscosity in order to find the behavior obtained for $Re = \infty$.

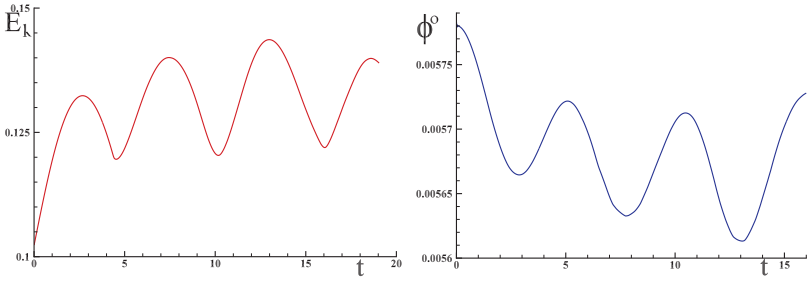

Figure 4. Evolutions of the mean kinetic energy E_k and the scalar potential ϕ^o where E_k and ϕ^o are given in $m^2\,s^{-2}$ and t in s.

The exchange between kinetic energy and pressure energy is a major element for the understanding of turbulent flows, including for incompressible flows. The discrete equation of motion (4) has the essential characteristic of interweaving the compression and rotation accelerations with the two components of inertia within the same law. Any splitting aiming at separating the conservation of the total energy from the conservation of the mass can lead to unpredictable artifacts.

3.2. Vortex Filament at $Re = 1600$

The case treated now is of another nature: the modulation of the initial velocity of the previous problem is replaced by a very important shear generated by the inversion of the direction of rotation of the flow along the longitudinal direction. It is close to the Taylor–Green vortex benchmark discussed later. For a physical domain defined by $L^3 = [(-\pi/2, \pi/2), (-\pi/2, \pi/2), (-\pi, \pi)]$, the initial condition of the vortex is fixed by the velocity in Cartesian coordinates:

$$\begin{cases} u = -\cos x\,\sin y\,\cos z \\ v = \;\;\sin x\,\cos y\,\cos z \\ w = 0 \end{cases} \tag{20}$$

The potential field ϕ, the pressure in the presence of a density $\rho = 1$, is defined unilaterally as the quantity which translates the mechanical equilibrium by the equation of

motion for the velocity field (21). Indeed, in the case of an incompressible flow, it is useless to specify the pressure field corresponding to this equilibrium. From this, simulations were carried out for three configurations representing a vortex filament: (i) a cylinder of radius $\pi/2$ and height $2\,\pi$ tessellated by curvilinear hexahedra in cylindrical coordinates, (ii) a prism circumscribed to the previous cylinder represented by a mesh based on prisms with triangular sections, and (iii) a parallel channel with square section whose meshes are Cartesian hexahedra. The approximations used have approximately the same number of cells, about 220^3, which corresponds to a number of unknowns $n_e = 30 \times 10^6$, the number of edges of geometric structure. The Reynolds number adopted in the three cases is $Re = v_0\, L/\nu = 1600$, where $v_0 = 1$. Details of the numerical methodology are provided in several cited papers including [10]. The objective of this section is to show that although the geometries of the three configurations are different, the turbulence appears in the same way; however, the turbulent structures generated are impacted by the shape of the vortex filament considered.

Figure 5 shows three snapshots corresponding to time $t = 10$ s. The Bernoulli scalar potential field $\phi^o_B = \phi^o + |\boldsymbol{v}|^2/2$ is colored by the local kinetic energy.

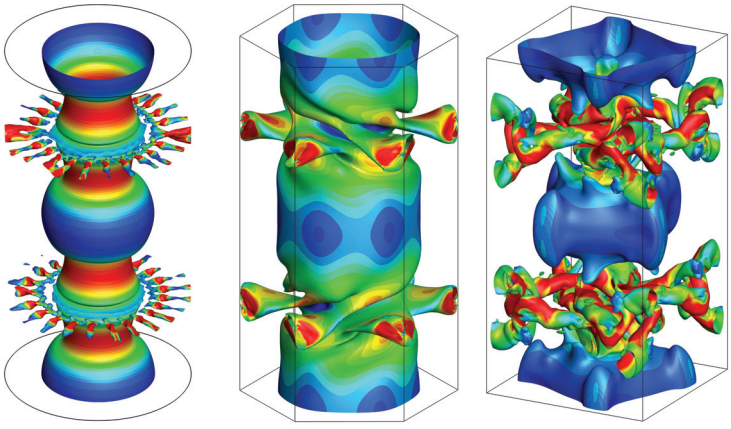

Figure 5. Snapshots of potential fields decorated by kinetic energy for three vortex filaments with circular, hexagonal, and square bases.

In all three cases, we observe that the turbulent structures are animated by an important velocity in the zones of important shear. The number of structures resulting from vortex busting closely depends on the geometry of the chosen physical domain. Figure 6 shows the evolution of the mean kinetic energy E_k over time for the cases of the cylindrical and square-based filaments; the evolution corresponding to the prismatic structure is roughly the same as for the cylinder. In the cases, we observe a rapid increase in the mean kinetic energy over time for a time $t < 4$, which is accompanied, as for the inviscid filament, by a decrease in the scalar potential ϕ^o.

The potential energy characterized by ϕ^o is transformed from the first instants into kinetic energy, while the impact of viscosity is negligible. In the case of the cylinder, we observe the effect of the vortex stretching phenomenon similar to that of inviscid vortex-filament. Beyond a time $t \approx 4$, the vortex bursting creates finer and finer structures, which are then dissipated by viscosity; for the hexahedral geometry, the evolution of the kinetic energy presents three phases: (i) an increase until the appearance of the vortex bursting at $t < 4$, (ii) a decrease characterizing the transfers between the large and small structures, and (iii) a decreasing exponential evolution for $t > 18$ characterizing the viscous dissipation.

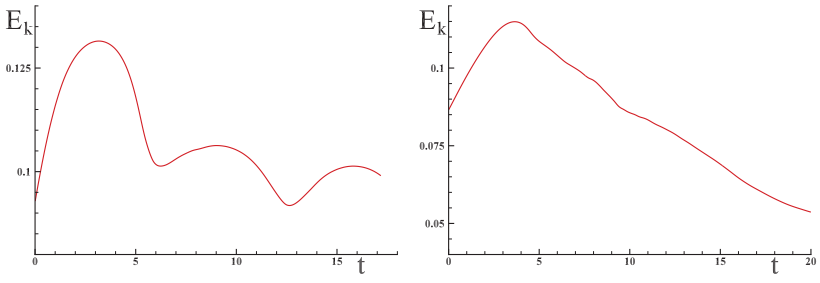

Figure 6. Evolution of the kinetic energy with time in the case of a cylinder (**left**) and for the geometry with square base (**righ**).

The mechanisms leading to the appearance of vortex bursting turbulence in viscous and nonviscous cases having now been described, it is necessary to confront the discrete physical model with a reference case that has been the subject of numerous theoretical studies and numerical simulations: the Taylor–Green vortex at $Re = 1600$.

3.3. Taylor–Green Vortex at $Re = 1600$

The Taylor–Green vortex test case is emblematic of the turbulence decay of a three-dimensional velocity field, initially introduced into a cubic cavity of dimensions $L^3 = [-\pi, \pi]^3$, where the boundary conditions are periodic for velocity and pressure. This test case is widely used to verify the convergence properties of numerical methods; the results are broadly reported in the literature, for example, [11]. The Reynolds number chosen is the one whose results are most often found, namely $Re = 1600$, a value adopted for the benchmark corresponding to [12]. The Reynolds number is defined by $Re = v_0\, L/\nu$, where $L = \pi$, $v_0 = 1$, and $\nu = (v_0 : L)/Re$ is the kinematic viscosity, assumed constant. The initial condition is defined in Cartesian coordinates by the components of the vector $\mathbf{V} = u\,\mathbf{e}_x + v\,\mathbf{e}_y + w\,\mathbf{e}_z$:

$$\begin{cases} u = -\sin x\, \cos y\, \cos z \\ v = \cos x\, \sin y\, \cos z \\ w = 0 \end{cases} \tag{21}$$

The potential field ϕ^o is obtained from the conservation of acceleration Equation (4), consistent with the constraint $\nabla \cdot \boldsymbol{v} = 0$, where $\boldsymbol{v}$ is the discrete velocity. The simulation from this initial condition allows us to obtain at each instant the solution $(\boldsymbol{v}, \phi, \boldsymbol{\psi})$. The associated instantaneous quantities, the kinetic energy per unit of mass E_k, the dissipation ε, and the enstrophy per unit of mass are saved in time. The time evolutions of the global kinetic energy E_k and the compression energy E_c as a function of time are shown in Figure 7.

As for the vortex filament cases, the kinetic energy E_k increases until a time $t \approx 3.5$, where the first turbulent structures appear in the form of vortex bursting, mainly in the shear zones generated by the initial conditions (21).

In correlation with the growth of the kinetic energy, the compression energy E_c decreases; the mechanical equilibrium defined by the invariance of the total energy imposed by the Equation (4) allows the exchanges between the two terms of inertia, pressure, and effect of the limited viscosity in this phase. From a time $t \approx 3.5$ begins the energy cascade phase toward the small structures, which is marked by a quasilinear decrease in the kinetic energy in time and irregular variations in the pressure energy. Beyond a time $t = 18$ begins the dissipation phase, marked by a decay toward zero of the kinetic and compression energies.

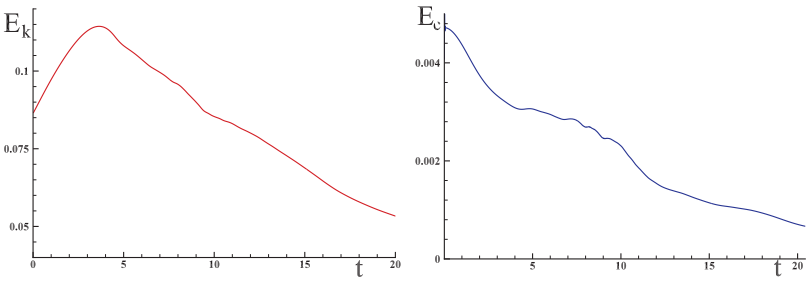

Figure 7. Global kinetic energy E_k and compression energy E_c at Reynolds number $Re = 1600$ for $n_c = 256^3$ cells and $n_e \approx 50 \times 10^6$ unknowns.

The observation of the velocity and pressure fields shows that the energy cascade where the kinetic energy is globally decreasing is due to the phenomena of vortex stretching and vortex bursting at different scales. Instantaneous variations in the fields, in particular of the pressure, reveal very sudden increasing variations of the pressure, which can reach local values several times higher than $v_0^2/2$, the initial maximum kinetic energy. Figure 8 shows the Bernoulli potential field ϕ_B^o decorated by the local kinetic energy for time $t = 20$.

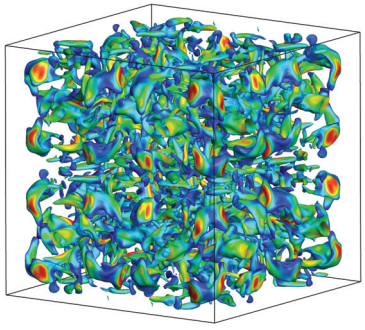

Figure 8. Snapshot of the potential field decorated by the kinetic energy for $t = 20$, $n_c = 256^3$ et $n_e \approx 50 \times 10^6$ unknowns

This representation of the turbulent field is quite consistent with the fields given by the many authors who have simulated this benchmark.

The energy cascade in the inertial zone is very comparable to the evolutions previously obtained by different authors. More precisely, the spectral analysis in wavelengths k for Reynolds number $Re = 1600$ and time $t = 20$ allows us to show the spectrum $E_k(k)$ in Figure 9. The Kolmogorov law $E_k \propto k^{-5/3}$ is approximately satisfied by discrete mechanics.

However, if the energy decay phase in the domain seems to qualitatively be the same, the first phase of increase in E_k presented in Figure 7 is radically different from the results obtained by the many authors who have studied this configuration since 1983. The following section provides an analysis of the underlying reasons for this disagreement.

3.4. Behavior as a Function of Reynolds Number

Like other simulations performed with the proposed model, the numerical solutions obtained are convergent to order two in space and time. The specificity of turbulent flow simulations lies in the ability to capture the smallest spatial and temporal scales of turbulence by using adapted meshes and time steps. The decrease in the scales to capture those related to viscosity is all the more important as the Reynolds number increases; the range of Reynolds numbers studied is therefore necessarily limited. Considering the available means, the Reynolds number of 1600 has been chosen in most of the simulations

on this test case. In order to verify that this value corresponds to a case of developed turbulence, other values of Reynolds number have been used for the numerical simulations: $Re = 100$, $Re = 500$, and a case of flow for an inviscid fluid. For $Re = 100$, the flow is clearly laminar, while the one corresponding to $Re = 500$ is transient but presents strong similarities on the turbulence decay to the $Re = 1600$ case.

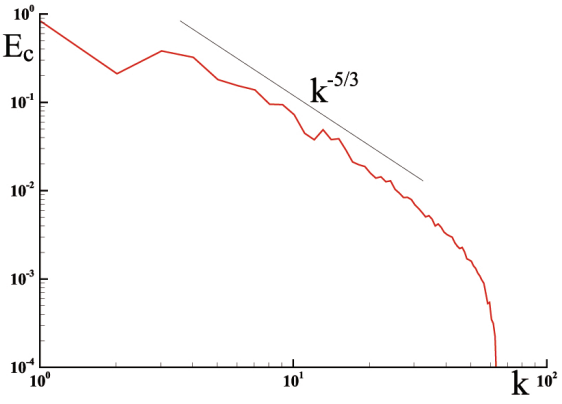

Figure 9. Energy spectrum as a function of the wave number $E_k(k)$ for $t = 20$ on one-quarter of the domain.

Figure 10 presents the evolutions of kinetic energy E_k for these values ($Re = 500, 1600, \infty$) as a function of the time limited to $t = 5$ s; indeed, the solution for the inviscid case explodes beyond this time, whereas it is perfectly represented for the lower times. The structure of the flows is the same in all three cases at this time; the shearing of the fluid filaments generates a vortex bursting similar to those observed on the individual filaments simulated before. These results at different Reynolds numbers show very similar behaviors even though, just after the vortex bursting, the decay shows limited differences.

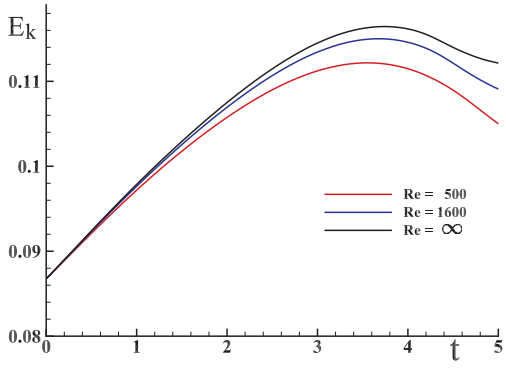

Figure 10. The evolution of the kinetic energy E_k corresponding to the Taylor–Green vortex case shows a similar behavior at Reynolds numbers of $Re = 500, 1600$ and for an inviscid fluid.

4. Analysis

Let us take the incompressible Navier–Stokes equation with constant density used for many decades for the Taylor–Green vortex and especially in reference [12]:

$$\begin{cases} \dfrac{\partial \mathbf{V}}{\partial t} - \mathbf{V} \times \boldsymbol{\omega} = -\nabla \left(p + \dfrac{1}{2} \mathbf{V}^2 \right) + \nu \, \nabla^2 \mathbf{V} \\ \\ \nabla \cdot \mathbf{V} = 0 \end{cases} \tag{22}$$

where $\boldsymbol{\omega} = \nabla \times \mathbf{V}$ is the curl of the velocity vector. The inertia is here split into a part with zero rotation to form the Bernoulli pressure and the Lamb vector $-\mathbf{V} \times \boldsymbol{\omega}$, which is a priori not a curl. The incompressibility constraint $-\nabla \cdot \mathbf{V} = 0$ is taken into account in a different way according to the authors, whereas others have used a compressible formulation at low Mach numbers. In all cases, among which include [12–17], the results obtained with the model (22) are very close. This problem is now considered as a benchmark to present new physical models or innovative numerical methodologies of high accuracy. Direct simulations of the TGV case at Reynolds number $Re = 1600$ can be summarized by the time variations in the kinetic energy and dissipation $\varepsilon = -dE_k/dt$; they are represented in Figure 11,where the values are borrowed from W. van Rees [11].

The kinetic energy E_k on the volume decreases toward zero in a monotonic way over time with a very slight decrease for times lower than $t = 4$ due to the viscosity of the fluid. For times $4 < t < 18$, the inertial zone is characterized by a fast decrease in E_k. The dissipation $\varepsilon = -dE_k/dt$, calculated from the expression $\boldsymbol{\varepsilon} = 2\,\nu\,\mathbf{S} : \mathbf{S}$ or directly from E_k, shows a maximum of this quantity around $t \approx 9.5$.

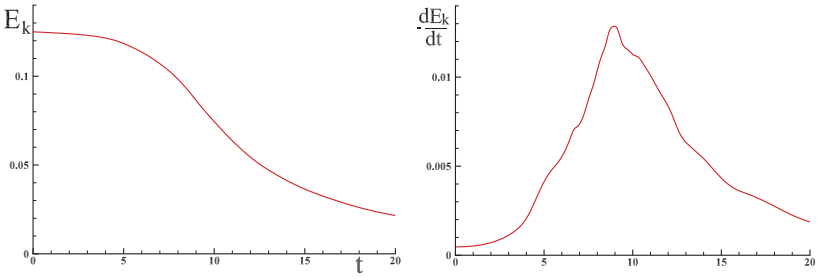

Figure 11. Taylor–Green vortex at $Re = 1600$; the spectral simulation provides the evolution of E_k and dissipation rate $\varepsilon = -dE_k/dt$ for the Navier–Stokes model after W. van Rees [11], file Re-1600-512.gdiag.

The comparison between the discrete kinetic energy in Figure 7 and the Navier–Stokes one (11) reveals profound discrepancies in the behavior of the flow at $t < 5$. These differences are not due to the method of performing the statistics or to the form of the kinetic energy theorem because it is directly derived from the physical model used. The numerous simulation results from discrete mechanics on reference flows all show a very good agreement with those of continuum mechanics [5,6,18,19]. For the first time, for the TGV flow, the results diverge.

In discrete mechanics, the unknowns of the equation of motion are the velocities v on the segment Γ, and the velocity vector $\mathbf{V}$ is not necessary to model the flow. The kinetic energy per unit mass $e_k = 1/2\, v \cdot v$ is a quantity attached to Γ but is also defined on the vertices of the primal structure, a or b, and on the barycenters of the $\mathcal{S}$ facets. The global kinetic energy E_k computed on the segments, on the dual volumes or on the facets has an identical behavior over time; $E_k(t)$ increases in the preinertial phase, whereas it remains almost constant in continuum mechanics.

The growth of the kinetic energy can only be possible at the expense of the potential energy represented by the Bernoulli scalar potential ϕ_B^o. Indeed, in the region $t \in [0, 4]$, the viscous effects are not perceptible. Numerous simulations at different Reynolds numbers all show the same phenomenon, including for an inviscid flow; in this last case, the vortex

bursting phenomenon for $t \approx 4$ logically leads to a divergence in the simulation. The conservation of the total energy given by the discrete Equation (4) associates the two inertia terms, the compression term, and the viscous term. The energy exchanges due to inertia and compression effects are reciprocal because compression does not lead to dissipation of acoustic waves on these spatial scales. Thus, a decrease in compression energy ϕ^o can be transformed into an increase in kinetic energy e_k and vice versa. This is the phenomenon observed in the first phase where the potential pressure energy is converted into kinetic energy. Let's take the inertia term from the Navier-Stokes equation:

$$\mathbf{V} \cdot \nabla \mathbf{V} = \nabla \left(\frac{1}{2} |\mathbf{V}|^2 \right) - \mathbf{V} \times \nabla \times \mathbf{V} \tag{23}$$

The two equivalent formulations are established within the concept of a continuous medium and therefore valid at a point of it. To be able to calculate explicitly each term it becomes necessary to project the equation on a global reference frame.

In discrete mechanics the mechanical equilibrium is realized within a local reference frame. Solving the discrete equation of motion (4) implicitly entangle all the terms of this nonlinear equation over time and it is difficult to predict the behavior of the solution. Observation of the simulation results shows that the roles of the Bernoulli scalar potential $\phi_B^o = \phi^o + \phi_i$ are related to compression and that they correspond to the rotational inertia $\boldsymbol{\psi}_i$. The inertial potentials ϕ_i and $\boldsymbol{\psi}_i$ also exchange their energy; the longitudinal compression generates a modification of the rotation and vice versa. The inertial acceleration, $\boldsymbol{\kappa}_i$, is written as:

$$\boldsymbol{\kappa}_i = \nabla \left(\frac{1}{2} |\boldsymbol{v}|^2 \right) - \nabla^d \times \left(\frac{1}{2} |\boldsymbol{v}|^2 \, \mathbf{n} \right) \tag{24}$$

This quantity, κ_i, is globally conserved in the absence of external accelerations, notably viscous effects. The physical meaning of the inertial vector κ_i is illustrated by the vortex schematized in Figure 12.

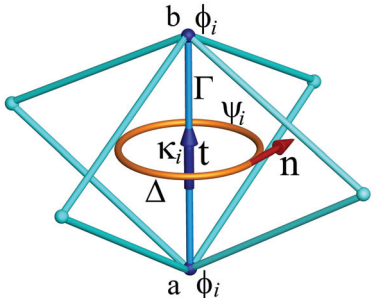

Figure 12. Scheme of the inertia vector $\boldsymbol{\kappa}_i$ on the oriented segment Γ and the respective representations of its two components such that $\boldsymbol{\kappa}_i = \nabla \phi_i - \nabla^d \times \boldsymbol{\psi}_i$.

A change in the compression energy represented by $\nabla \phi_i = (|\boldsymbol{v}_b|^2 - |\boldsymbol{v}_a|^2)/(2\,dh)$ generates a variation in the velocity $\boldsymbol{v}$ on Γ and, consequently, of the velocities on the other segments of the four primal structures. The circulation of the velocities on these lead us to define a potential vector $\boldsymbol{\psi}_i$ carried by the unit vector $\mathbf{n}$. The dual curl of this vector, $\nabla^d \times \boldsymbol{\psi}_i$, is in turn carried by the segment Γ. Thus, the compression energy is compensated by an equivalent variation in the rotational kinetic energy, i.e., a variation in the velocity on the dual contour Δ. More precisely, a stretching in the $\mathbf{t}$ direction associated with a decrease in $\nabla \phi_i$ leads to an increase in the rotational inertial term $\nabla^d \times \boldsymbol{\psi}_i$. The vortex stretching mechanism is closely related to the energy exchange between the two components of the $\boldsymbol{\kappa}_i$ vector; while the angular momentum is conserved in the rotation of a vortex filament, the kinetic energy increases.

This expression of the inertia in the form of a Helmholtz–Hodge decomposition gives the physical model particular properties, for example, when the divergence or curl operators are applied to $\boldsymbol{\kappa}_i$, which allows the suppression of one of its components. Let us consider the velocity field corresponding to a solid body rotation $\mathbf{V}_r = \boldsymbol{\Omega} \times \mathbf{r} = \omega\, r\, \mathbf{e}_\theta$. In the framework of continuum mechanics, the inertia would be written as $\boldsymbol{\kappa}_i = \omega^2\, r\, \mathbf{e}_r + \omega^2\, r\, \mathbf{e}_\theta$, which does not conform to the classical view of a mechanical equilibrium defined by component. In discrete mechanics, each $\boldsymbol{v}$ component has a direct acceleration and an induced acceleration, both associated with the same Γ segment. The assembly of the segments in a geometrical structure such as the one represented in Figure 2 leads to an entanglement of the inertia terms. In turbulence, rotation and inertia play major roles in the production of kinetic energy, in the exchange between vortices, and in the decay of energy at small scales. The classical (23) and discrete (24) forms are very different and lead to divergences in the specific cases of turbulence in rotating flows.

The law of motion of discrete mechanics represents the conservation of total energy per unit mass, i.e., acceleration. It has the particularity of strongly entangling the terms of pressure and inertia; this dynamic entanglement is a strict coupling of the scalar potential and the divergence of the velocity. There is no adjoint equation; mass, or density, is absent from the discrete equation of motion also for flows with variable density [10]. The scalar ϕ^o and vector $\boldsymbol{\psi}^o$ potentials are completely subject to acceleration. There are also no constitutive laws to take into account. Whether the flows are compressible or incompressible, the energy increase associated with compression is always $d\phi = -dt\, c_l^2\, \nabla \cdot \boldsymbol{v}$ and that of rotation at $d\boldsymbol{\psi} = -dt\, c_t^2\, \nabla \times \boldsymbol{v}$; only the velocities c_l and c_t must be known. From a fixed velocity field, we derive the scalar potential field ϕ^o satisfying the initial mechanical equilibrium. Then, all the terms of the equation come into action and exchange energy in the course of time. It is very difficult to predict the behavior of each term, but we know that the energy initially introduced in the form of kinetic and potential energy decreases towards zero through viscous dissipation. Thus, the TGV case solved in discrete mechanics shows an increasing evolution of the kinetic energy in the first instants, in contradiction with the phenomenon observed in continuum mechanics. The dynamic entanglement of inertia and compression effects represents the essence of the creation of turbulence and its evolution in time.

5. Conclusions

The proposed formulation is essentially based on (i) the conservation of the total energy, the sum of the compressive energy, and the rotational energy; and (ii) the form of the inertia, which is decomposed into a curl-free part and a divergence-free part:

- The observation of the solutions on the turbulent vortex filament cases and on the Taylor–Green vortex case shows a nonmonotonic decay in the kinetic energy. This observation is consistent with the principle of conservation of angular momentum for a vortex-like flow for an inviscid fluid where the potential and kinetic energies can be mutually exchanged over time. However, the Taylor–Green vortex at $Re = 1600$, considered as a reference for the study of turbulence decay and as a benchmark for numerical methods, approached with the Navier–Stokes equation, shows a monotonic decay over time of the kinetic energy. The reasons for this disagreement are attributed to the essential discrepancies between discrete and continuum mechanics, and the derivation of the equation of motion on a segment instead of a volume model. Discrete mechanics leads us to consider the conservation of the total energy on the segment as an equality between the intrinsic acceleration of the material medium and the accelerations imposed on it.
- In the particular cases of turbulence in vortices, inertia plays a very important role in the energy exchange; the very different form adopted in discrete mechanics helps to explain the discrepancy in behavior in the inertial zone, even though the decay in the kinetic energy in the transfer zone is very similar to the observations made from the Navier–Stokes equation. The numerous simulations carried out from this equation are not questioned: only the choice of the physical model can explain the

differences observed. Discrete mechanics develops another point of view that remains consistent with the fundamental principles of mechanics; it has particular properties whose effects should be specified in the future.

Funding: This research received no external funding.

Data Availability Statement: Data is contained within the article.

Conflicts of Interest: The author declares no conflict of interest.

References

1. Buaria, D.; Bodenschatz, E.; Pumir, A. Vortex stretching and enstrophy production in high Reynolds number turbulence. *Phys. Rev. Fluids* **2020**, *5*, 104602. [CrossRef]
2. Carbone, M.; Bragg, A.D. Is vortex stretching the main cause of the turbulent energy cascade? *J. Fluid Mech.* **2020**, *883*. [CrossRef]
3. Spalart, P.R. Airplane Trailing Vortices. *Annu. Rev. Fluid Mech.* **1998**, *30*, 107–138. [CrossRef]
4. Moet, H.; Laporte, F.; Chevalier, G.; Poinsot, T. Wave propagation in vortices and vortex bursting. *Phys. Fluids* **2005**, *17*, 054109. [CrossRef]
5. Caltagirone, J.P.; Vincent, S. On primitive formulation in fluid mechanics and fluid-structure interaction with constant piecewise properties in velocity-potentials of acceleration. *Acta Mech.* **2020**, *231*, 2155–2171. [CrossRef]
6. Caltagirone, J.P. On Helmholtz-Hodge decomposition of inertia on a discrete local frame of reference. *Phys. Fluids* **2020**, *32*, 083604. [CrossRef]
7. Liénard, A. *Champ électrique et Magnétique Produit par une Charge électrique Concentrée en un Point et Animée d'un Mouvement Quelconque*; G. Carré et C. Naud: Paris, France, 1898.
8. Heras, R. Alternative routes to the retarded potentials. *Eur. J. Phys.* **2017**, *38*, 055203. [CrossRef]
9. Caltagirone, J.P. *Discrete Mechanics, Concepts and Applications*; ISTE, John Wiley & Sons: London, UK, 2019. [CrossRef]
10. Caltagirone, J.P. Application of discrete mechanics model to jump conditions in two-phase flows. *J. Comput. Phys.* **2021**, *432*, 110151. [CrossRef]
11. van Rees W.M. Vortex bursting. *Phys. Rev. Fluids* **2020**, *5*, 110504. [CrossRef]
12. Brachet, M.E.; Meiron, D.I.; Orszag, S.A.; Nickel, B.G.; Morf, R.H. Small-scale structure of the Taylor-Green vortex. *J. Fluid Mech.* **1983**, *130*, 411–452. [CrossRef]
13. Brachet, M.; Meiron, D.; Orszag, S.; Nickel, B.; Morf, R.; Frish, U. The Taylor-Green vortex and fully developed turbulence. *J. Stat. Phys.* **1984**, *34*, 1049–1063. [CrossRef]
14. van Rees W.M.; Leonard, A.; Pullin, D.; Koumoutsakos, P. A comparison of vortex and pseudo-spectral methods for the simulation of periodic vortical fows at high Reynolds numbers. *J. Comput. Phys.* **2011**, *230*, 2794–2805. [CrossRef]
15. Wang, Z.; Fidkowski, K.; Abgrall, R.; Bassi, F.; Caraeni, D.; Cary, A.; Deconinck, H.; Hartmann, R.; Hillewaert, K.; Huynh, H.; et al. High-Order CFD Methods: Current Status and Perspective. *Int. J. Numer. Methods Fluids* **2013**, *72*, 811–845. [CrossRef]
16. Diosady, L.; Murman, S. Case 3.3: Taylor-Green Vortex Evolution. In Proceedings of the Case Summary for 3rd International Workshop on Higher-Order CFD Methods, Kissimmee, FL, USA, 3–4 January 2015.
17. de la Llave Plata, M.; Lamballais, E.; Naddei, F. On the performance of a high-order multiscale DG approach to LES at increasing Reynolds number. *Comput. Fluids* **2019**, 194, 104306. [CrossRef]
18. Caltagirone, J.P. On a reformulation of Navier-Stokes equations based on Helmholtz-Hodge decomposition. *Phyics Fluids* **2021**, *33*, 063605. [CrossRef]
19. Caltagirone, J.P. An alternative to the concept of continuous medium. *Acta Mech.* **2021**, *232*, 4691–4703. [CrossRef]

fluids

MDPI

Article

Patterning Behavior of Hybrid Buoyancy-Marangoni Convection in Inclined Layers Heated from Below

Wasim Waris and Marcello Lappa *

Department of Mechanical and Aerospace Engineering, University of Strathclyde, James Weir Building, 75 Montrose Street, Glasgow G1 1XJ, UK
* Correspondence: marcello.lappa@strath.ac.uk

Abstract: Alongside classical effects driven by gravity or surface tension in non-isothermal fluids, the present experimental study concentrates on other exotic (poorly known) modes of convection, which are enabled in a fluid layer delimited from below by a hot plate and unbounded from above when its container is inclined to the horizontal direction. By means of a concerted approach based on the application of a thermographic visualization technique, multiple temperature measurements at different points and a posteriori computer-based reconstruction of the spatial distribution of wavelengths, it is shown that this fluid-dynamic system is prone to develop a rich set of patterns. These include (but are not limited to), spatially localized (compact) cells, longitudinal wavy rolls, various defects produced by other instabilities and finger-like structures resulting from an interesting roll pinching mechanism (by which a single longitudinal roll can be split into two neighboring rolls with smaller wavelength). Through parametric variation of the tilt angle, the imposed temperature difference and the volume of liquid employed, it is inferred that the observable dynamics are driven by the ability of gravity-induced shear flow to break the in-plane isotropy of the system, the relative importance of surface-tension-driven and buoyancy effects, and the spatially varying depth of the layer. Some effort is provided to identify universality classes and similarities with other out-of-equilibrium thermal systems, which have attracted significant attention in the literature.

Keywords: Marangoni convection; hydrothermal wave; solid particles; patterning behavior

Citation: Waris, W.; Lappa, M. Patterning Behavior of Hybrid Buoyancy-Marangoni Convection in Inclined Layers Heated from Below. *Fluids* **2023**, *8*, 12. https://doi.org/10.3390/fluids8010012

Academic Editor: Mehrdad Massoudi

Received: 23 November 2022
Revised: 24 December 2022
Accepted: 28 December 2022
Published: 29 December 2022

1. Introduction

In this study, the properties of mixed buoyancy-Marangoni convection are investigated in an inclined layer uniformly heated from below and unbounded from above (in contact with a gaseous ambient at constant temperature). A justification for our interest in this specific subject stems from the paucity of similar results in the literature. Apart from the relevance of this problem to the general kingdom of thermal convection (which naturally makes it a fundamental topic of interest to fluid physicists and other scholars), additional obvious aspects making it a subject worthy of analysis are the various areas of applications it is somehow connected to. A first example is represented by the sector of crystal 'growth from the melt', where crystals of materials of various kinds (e.g., silicon, semiconductors or oxides) to be used for advanced electronic or opto-electronic devices are typically produced through melting and re-solidification 'in well-controlled conditions' of an initially polycrystalline substance; it is known that even tilt angles as small as 0.5° can cause non-axisymmetric growth conditions in such processes and related detrimental effects (see, e.g., Markham and Rosenberger [1]; Bachran et al. [2]; Mizev and Schwabe [3]).

Similar concepts apply to the solidification of metal alloys (e.g., Jones [4]; Coriell et al. [5]; Webb and Viskanta [6]; Forth and Wheeler [7]) where inclination-induced shear flow can lead to serious morphological instabilities. Another relevant case is represented by phase change materials (PCMs), typically used in 'energy-saving' applications. These substances (ideally suited to store energy during melting and release it during solidification) can

support during these repeated cycles of solid/liquid transition the emergence of both buoyancy and surface-tension driven convection (Lappa [8]); moreover, the liquid domain produced accordingly has often a variable depth (see, e.g., Salgado Sanchez et al. [9,10]).

In all these instances, mixed buoyancy-Marangoni convection can be produced by gradients of temperature (Lappa [11]), gradients of concentration (Zhang et al. [12]) or both effects (Boura and Gebhart [13], Qin and Grigoriev [14]). In the present study, we concentrate on the situation where convection is produced by thermal effects only. In particular, the reader is referred to Figure 1 for the required details about the configuration used here to 'mimic' situations such as those occurring in the abovementioned technological applications. The greater proximity of the free surface to the heated bottom in the areas where the depth of the layer is smaller is responsible for the emergence of a temperature inhomogeneity at the interface, thereby giving rise to fluid convection directly driven by the Marangoni effect. This flow is also supported by buoyancy. Indeed, the component of gravity parallel to the bottom plate, causes relatively warm fluid to flow up along this wall (from left to right in Figure 1) and in the opposite direction along the free interface. The magnitude ratio of buoyant and surface-tension-driven effects can be varied by changing the overall amount of fluid, i.e., its average depth. The larger the depth, the higher the relative importance of gravitational effects in comparison to surface tension ones. The most important implication of this observation is that relevant links also exist between this problem and a series of problems of meteorological, oceanographic and geophysical interest (see, e.g., Lipps [15] and Thorpe [16] for the atmosphere; Farrow and Patterson [17] for the hydrosphere and Richter [18] for analogous considerations about the mantle of our planet).

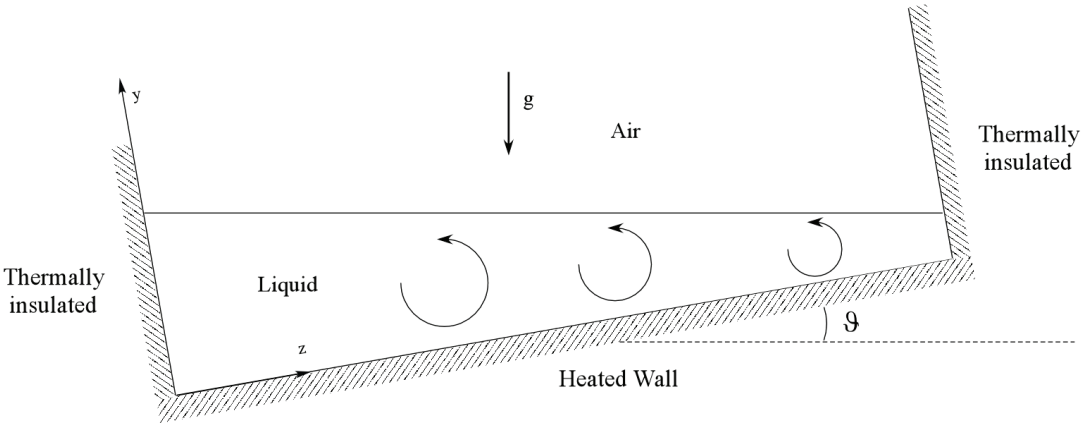

Figure 1. Sketch of the considered problem.

It is also worth noting that, from a purely theoretical standpoint, the considered problem may be regarded as a specific realization of a more general category of phenomena where a 'shear flow' breaks the in-plane isotropy of the system (see, e.g., Weber [19]). This effect can cause a deviation from the known dynamics of out-of-equilibrium systems, which are invariant with respect to translations in a direction parallel to the bottom boundary such as the canonical Rayleigh-Bénard and Marangoni-Bénard flows.

Until now, the former has been explored for fluid domains with "uniform thickness" tilted with respect to the horizontal direction. In these cases, the isotropy is lost due to the mismatch in the symmetry of the boundary conditions in relation to the applied body force (gravity). This condition can make the perfect stationary bifurcation typical of Rayleigh-Bénard (RB) convection structurally "unstable to the tilt" (and "imperfect" even if the tilt angle is as small as $O(10^{-3})$, see Cliffe and Winters [20]; Mizushima and Adachi [21]). Studies conducted in the past two decades have conclusively established that, depending

on the inclination, the considered fluid, the size of the system and the applied temperature difference, many complexities and a rich variety of flow phenomena can take place. Works of relevance to the subject include those by Clever and Busse [22], Weber [23], Chen and Pearlstein [24], Shadid and Goldstein [25], Busse and Clever [26], Fujimura and Kelly [27], Kaloni and Qiao [28].

According to all these studies, the emerging (gravitational) modes of convection in tilted enclosures can be broadly classified/categorized into two groups; namely, transverse rolls and longitudinal rolls. A dichotomy is generally introduced between these because, while the former have essentially a shear driven nature, the latter have a strong thermal (buoyant) origin (Daniels et al. [29,30]; Tao and Busse [31]; Subramanian et al. [32]).

As even a cursory perusal of the existing literature on these subjects would immediately reveal, in comparison to gravitational convection, studies on systems driven by surface-tension-driven effects where the isotropy of the classical heated-from-below configuration is broken, are much more rare and sparse. Some interesting efforts exist for the case where the isotropy-breaking shear flow has been obtained by inclining the temperature gradient with respect to the liquid-gas interface rather than by inclining the layer itself (i.e., a temperature difference resulting from the combination of heating from below and horizontal differential heating). As an example, after the problem's initial popularization by Nepomnyashchy et al. [33] and Ueno et al. [34], additional insights into this specific situation have been provided by Shklyaev and Nepomnyashchy [35], Mizev and Schwabe [3] and Patne et al. [36]. Most interestingly, these efforts have revealed that, despite the shift in the driving force from buoyancy to Marangoni effects, the duality in terms of transverse and longitudinal modes of convection still holds in these case (with the classical compact hexagonal cells typical of Marangoni-Bénard (MB) convection being recovered only in the limit as the horizontal contribution to the overall temperature difference tends to zero).

One may therefore conclude that a line of inquiry dedicated to thermal flows and related instabilities in inclined systems (or systems with an inclined temperature gradient) only exists for the case in which the geometry has a constant thickness along the entire extension of the heated wall, which may be regarded as the main justification or motivation for the present work.

Here, the problem is tackled experimentally (see Section 2) and analyzed from both the traditional coarse-grained macroscopic (i.e., patterning behavior) perspective (see Section 3) and from a fine-grained micromechanical level in which an interpretation for the underlying mechanisms is sought in the light of the existing literature for problems that share a significant degree of similarity (see Section 4).

2. The System

2.1. The Geometry

A sketch of the considered fluid-dynamic system is shown in Figure 1. While the bottom of the cavity has a constant temperature higher than that of the external gaseous environment (air), the lateral walls are thermally insulated.

The inclination of the container causes the liquid to redistribute its volume in such a way that its surface remains perfectly horizontal with respect to an external observer (on tilting the system, the liquid-gas interface adjusts its orientation in order to remain perpendicular to gravity). Since the resulting liquid depth is not independent from the z coordinate, this naturally causes a breakage in the horizontal translational invariance (isotropy) of the system. Notably, given its spatially varying depth, the problem would not be isotropic even by replacing gravity with a force perfectly perpendicular to the bottom wall. Similarly, no isotropy would be recovered by considering a quiescent state, i.e., a condition where the fluid does not move. Obviously, the loss of horizontal translational invariance is reinforced by the presence the shear flow induced by the inclination of the heated bottom wall, which contributes to this effect as it does in classical problems dealing with inclined thermal convection in constant-thickness layers. Remarkably, all these factors

are expected to expand the set of possible solutions with respect to those identified in earlier studies.

2.2. The Liquid

The physical properties of the used fluid (Emkarate RL22H oil) as a function of the temperature are summarized in Figure 2 (these figures also include the related fitting laws in the form of polynomial expressions).

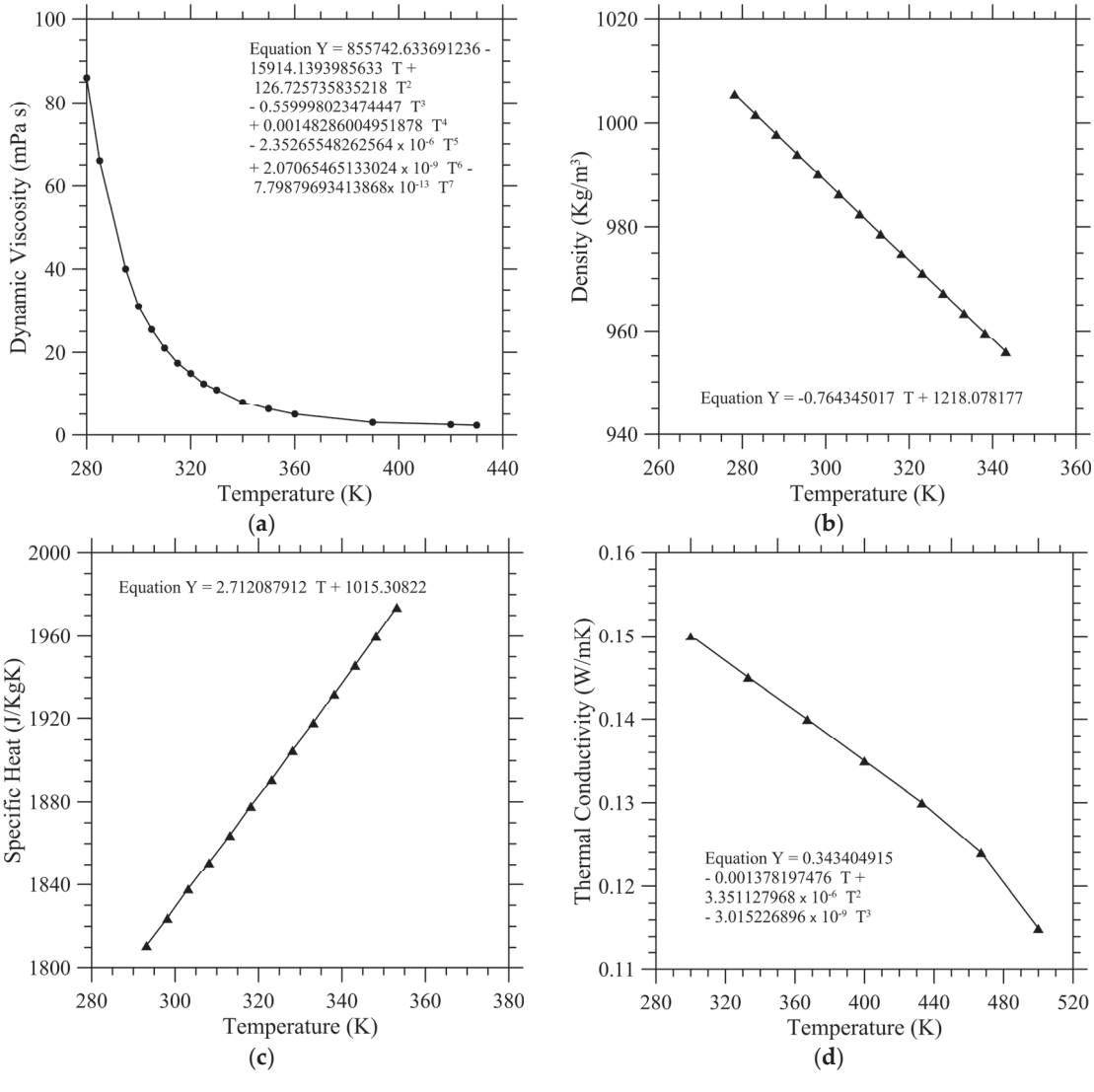

Figure 2. *Cont*.

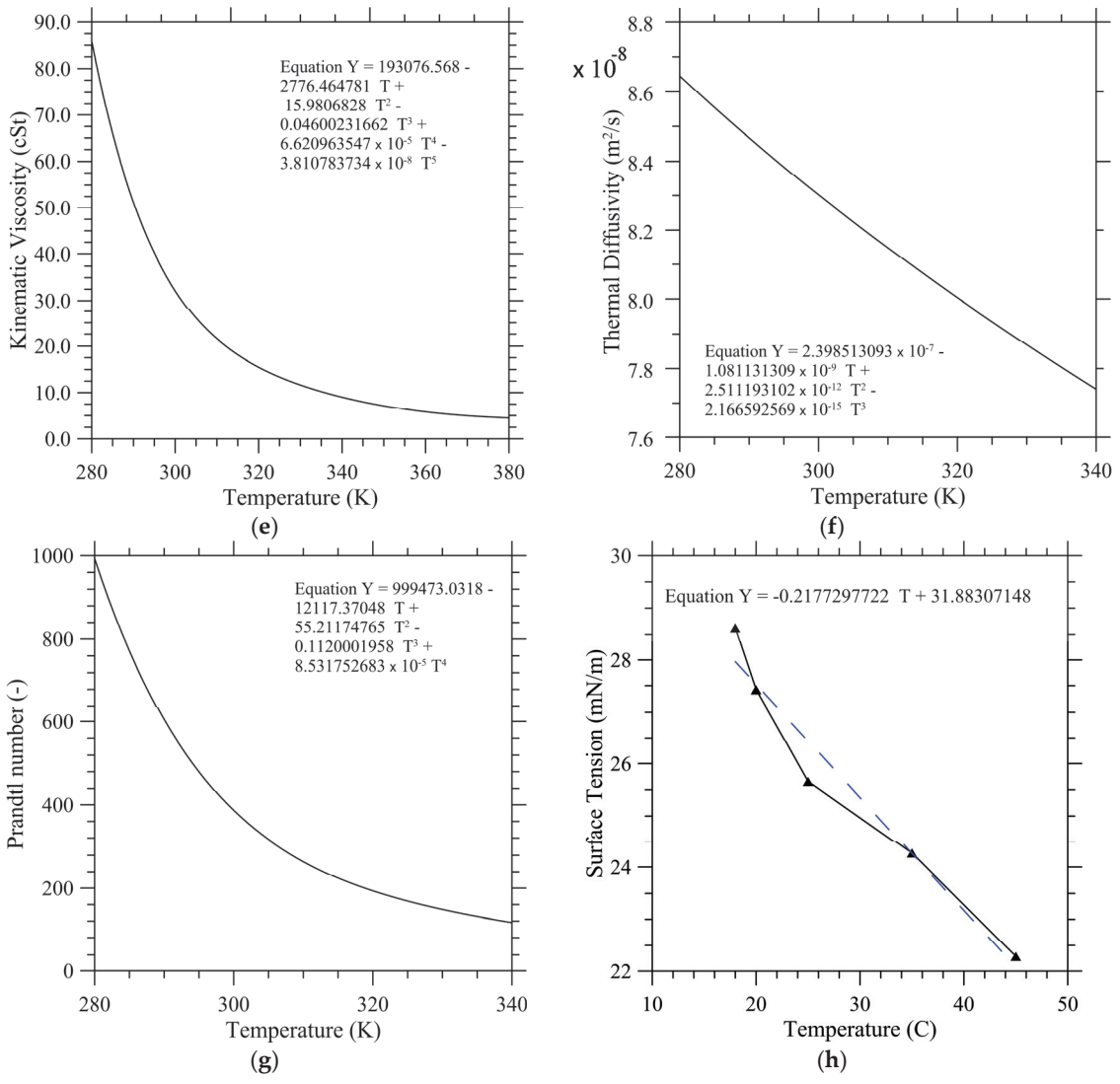

Figure 2. Physical Properties of Emkarate RL22H as a function of temperature as provided by the manufacturer: (**a**) Dynamic viscosity μ (exp. measurements); (**b**) Density ρ (exp. measurements); (**c**) Specific Heat at constant pressure C_p (exp. measurements); (**d**) Thermal conductivity λ (exp. measurements); (**e**) Kinematic viscosity ν (derived quantity, $\nu = \mu/\rho$, 1 cSt = 10^{-6} m^2/s); (**f**) Thermal diffusivity α (derived quantity, $\alpha = \lambda/\rho C_p$); (**g**) Prandtl number (derived quantity, $Pr = \nu/\alpha$), (**h**) Surface tension σ.

These figures are instrumental in showing that the physical properties of the considered fluid display a variable degree of sensitivity to temperature depending on the considered property (density ρ, specific heat C_p, thermal conductivity λ, thermal diffusivity α, dynamic viscosity μ, kinematic viscosity ν). The quantities ρ, C_p, λ and α (Figures 2b, 2c, 2d and 2f, respectively) undergo a 10% percentage variation (or even smaller) over a range of 100 K. Nevertheless, the corresponding change in terms of μ and ν is much more significant (see Figures 2a and 2e, respectively).

The fluid Prandtl number can be introduced following the classical definition as:

$$\mathrm{Pr} = \frac{\nu}{\alpha} \tag{1}$$

The dependence of this parameter on temperature can be gathered from Figure 2g where it is shown that for the considered oil a relatively high increase in the average temperature is equivalent to considering a fluid with a much smaller value of the Prandtl number (e.g., a value of the Prandtl Pr ≅ 520 for $T \cong 20$ °C is reduced to a value as small as Pr ≅ 170 for $T \cong 50$ °C).

2.3. Characteristic Numbers

In order to make the outcomes of the present experimental study more general, following a common practice in the literature, it is convenient to define non-dimensional groups by which the number of influential parameters can be drastically reduced and the related interpretation of the system dynamics strongly simplified. In the considered problem, these are the classical Prandtl number (Equation (1)) and the canonical Rayleigh and Marangoni numbers. Introducing the average (or "equivalent") depth of the layer (d) as ratio between the effective volume (Ω) of liquid present in the container and the area of the container base (corresponding to constant depth of the fluid when no tilt is applied), the last two numbers can be cast in compact form as:

$$Ra = \frac{g\beta_T \Delta T d^3}{\nu_0 \alpha_0} \tag{2}$$

$$\mathrm{Ma} = \frac{\sigma_T \Delta T d}{\mu_0 \alpha_0} \tag{3}$$

where ΔT accounts for a representative temperature difference, namely, the difference between the temperature of the bottom plate (T_{plate}) and that of the ambient (T_{air}), i.e., $\Delta T = T_{plate} - T_{air}$, (this temperature difference, much higher than that effective through the liquid, is used for practical purposes as the temperature of the free liquid-gas interface is not known a priori and behaves as a spatially varying quantity in the presence of convection); moreover, g and β_T are the gravity acceleration and the thermal expansion coefficient, 9.81 ms^{-2} and ≅ 7.7 × 10^{-4} K^{-1} of the considered fluid, respectively; σ_T is the surface tension derivative coefficient (≅0.218 $\mathrm{mNm}^{-1}\mathrm{K}^{-1}$ for the considered fluid, see Figure 2h). The subscript "0" refers to a reference temperature, which in the present work, for simplicity and without loss of generality, is assumed to be the temperature T_0 of the environment (i.e., T_{air}). These two characteristic numbers can be further combined into a third non-dimensional group, generally known as the dynamic Bond number:

$$Bo_{dyn} = \frac{Ra}{\mathrm{Ma}} = \frac{\rho g \beta_T d^2}{\sigma_T} \tag{4}$$

Although this should be regarded as a 'derived' parameter, the convenience in using it stems from its independence from the temperature difference and the immediate information it provides on the relative importance of buoyancy and surface-tension driven effects according to whether it is larger or smaller than 1 (buoyancy effects being more important in the former case).

3. Experimental Apparatus

The containers used for the present experiments are shown in Figure 3. They differ about both shape and size. While one container has a square symmetry and characteristic internal size 8 cm (Figure 3a), the other has the cylindrical symmetry and an internal diameter of 13.3 cm (Figure 3b). Experiments are conducted in these containers for the same conditions (same liquid depth, temperature of the bottom plate and overall system inclination) to distillate out the role played in the considered dynamics (if any) by the solid

lateral wall and the aspect ratio A of the fluid domain (defined as ratio of the container horizontal size and the depth of the liquid).

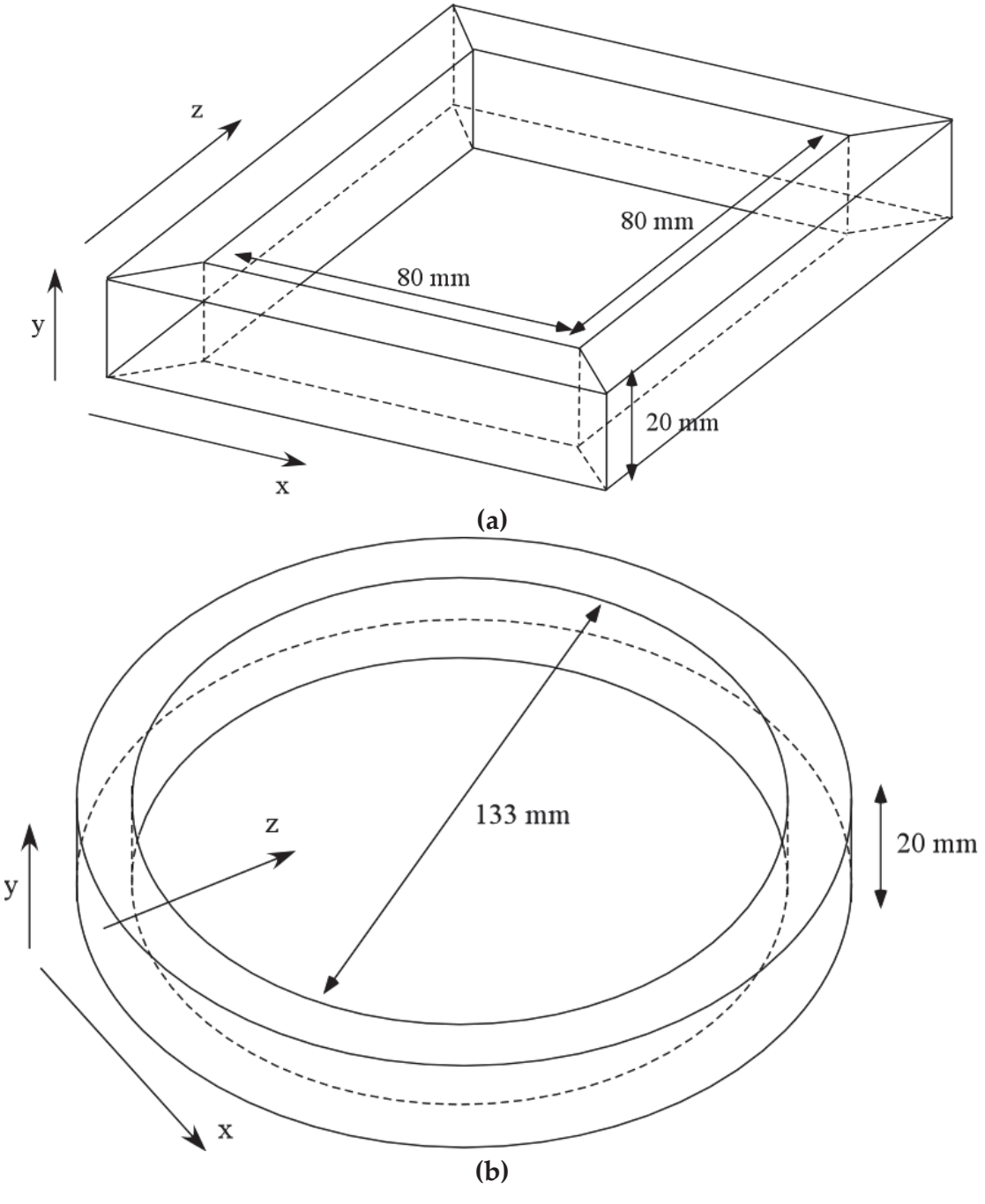

Figure 3. Three-dimensional sketch of the fluid container delimited by sidewalls of Perspex: (**a**) square container, (**b**) cylindrical container.

In order to set a well-defined temperature difference between the bottom of the container and the external environment, we rely on a commercial component, namely, a MS-H280-Pro Round ceramic coated Steel Hotplate/Stirrer, able to produce a uniform temperature T_{plate} with an accuracy of 1 °C up to 280 °C (the reader being referred to Table 1 for other specifications).

Table 1. Specifications of MS-H280-Pro Round ceramic coated Steel Hotplate/Stirrer.

Parameter	Value/Range
Work plate Dimension	Diameter 135 mm
Work plate material	Stainless steel cover with ceramic
Motor type	Brushless DC motor
Motor rating input	5 W
Motor rating output	3 W
Power	515 W
Heating output	500 W
Voltage	100–120/200–240 V 50/60 Hz
Heating temperature range	Room temp.–280, increment 1°C
Control accuracy of work plate	±1 °C (<100°C) ±1%(>100 °C)
External temperature sensor	PT1000 (accuracy ±0.5 °C)
Dimension [W × D × H]	150 × 260 × 80 mm
Weight	1.8 kg

In line with other successful attempts in the literature (see, e.g., Cerisier et al. [37,38]; Ismagilov et al. [39]; Chauvet et al. [40]; Wang et al. [41]; Wu et al. [42]; Sobac et al. [43]; Tönsmann et al. [44]), the distribution of temperature on the free surface of the considered liquid is observed using a FLIR C3-X Compact Thermal Imaging Camera (the related IR sensor has a resolution of 128 × 96 px and thermal sensitivity of 70 mK; moreover, it can detect and measure temperatures between −20 °C and +300 °C to an accuracy of ±3%).

The overall inclination of the system is measured using a digital inclinometer with an accuracy of 0.01° (Neoteck NTK033-V). The following cases are investigated in terms of liquid depth: $0.5 \leq d \leq 0.75$ cm corresponding to $0.86 \leq Bo_{dyn} \leq 1.94$, moreover, $T_{air} \cong 21 \pm 1$ °C.

4. Results

4.1. Canonical States of Thermal Convection in the Horizontal Case

Following a logical approach, we start from the simplest case, i.e., the perfectly horizontal configuration ($\vartheta = 0°$) for which convection is expected to emerge in the form of rolls or hexagonal cells according to whether buoyancy or surface-tension effects are dominant, respectively (Rayleigh-Marangoni-Bénard convection). In this regard the first set of figures, collected in Figure 4 for the case with constant liquid depth 0.5 cm, is instructive as these figures show that the pattern-less state visible in the first panel (Figure 4a) is taken over by a recognizable distribution of rolls and localized convective cells as soon as the critical threshold for the onset of convection is exceeded (Figure 4b–d).

These are made evident by the rising (descending) currents of hot (cold) fluid manifesting themselves as localized spots or strips with temperature higher (smaller) than the surrounding fluid.

On increasing the depth of the layer, as expected the horizontal extension of the convective features grows accordingly (compare, e.g., each panel of Figure 5 with the corresponding one in Figure 4). Another key observation stemming from Figure 5 concerns the complexity of the pattern and the number of convective features, which in qualitative agreement with other results in the literature, keep increasing with the ΔT, i.e., grow with the distance from the critical conditions.

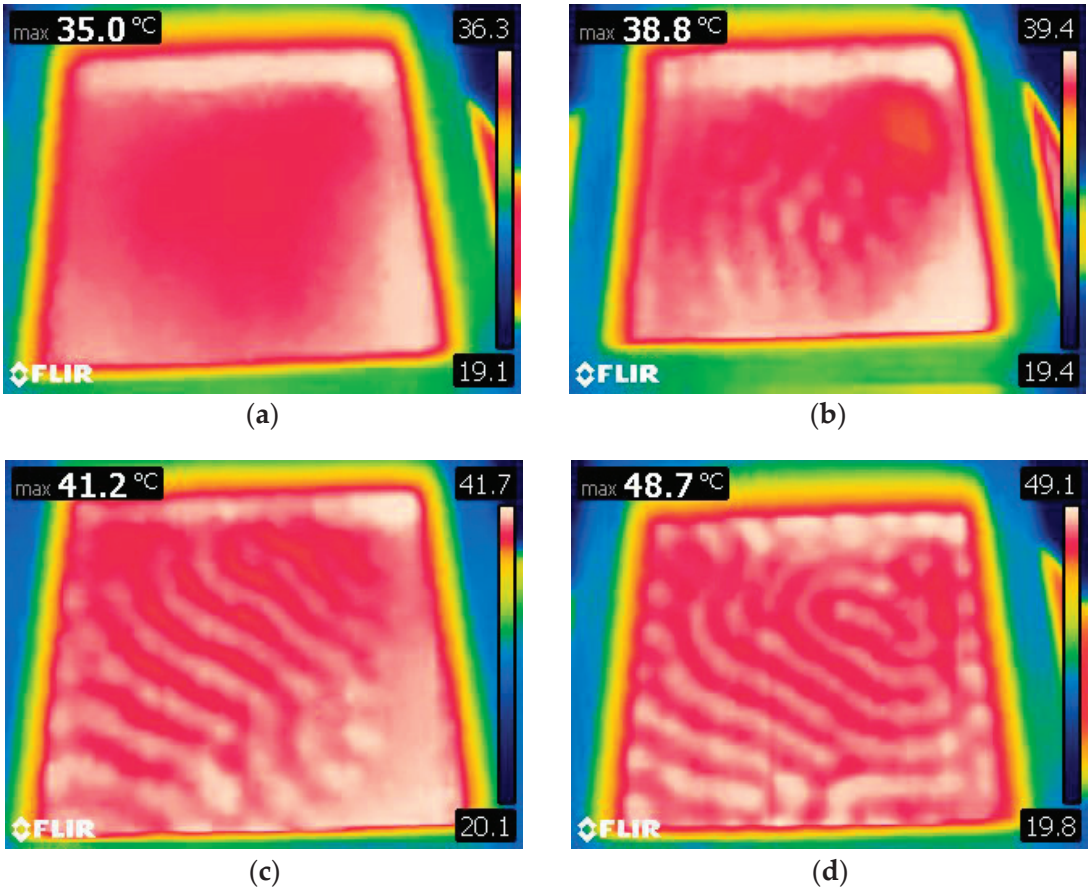

Figure 4. Surface temperature distribution for d = 0.50 cm (Ω = 32 mL) and no inclination (A = 16, $Bo_{dyn} \cong 0.86$, $Ra \cong 2.5 \times 10^2 \times \Delta T$, Ma $\cong 2.94 \times 10^2 \times \Delta T$): (**a**) ΔT = 13 °C, (**b**) ΔT = 18 °C, (**c**) ΔT = 21 °C, (**d**) ΔT = 27 °C.

4.2. Convection in Inclined Square Layer

The simplest way to undertake a discussion of the situation where the layer is inclined to the horizontal is to start from the major remark that, unlike the canonical case considered in Section 4.1, for $\vartheta \neq 0$ the basic state is *not in quiescent conditions*. Rather it consists of a *symmetry-breaking shear flow* induced by the horizontal component of the temperature gradient (see the related discussion in the introduction). Put differently, no critical ΔT has to be exceeded in order to induce fluid flow, i.e., convection is produced as soon as a temperature difference is established.

Following up on the previous point, Figure 6 provides a first glimpse of the patterning behavior in such conditions when $\vartheta \cong 3.5°$.

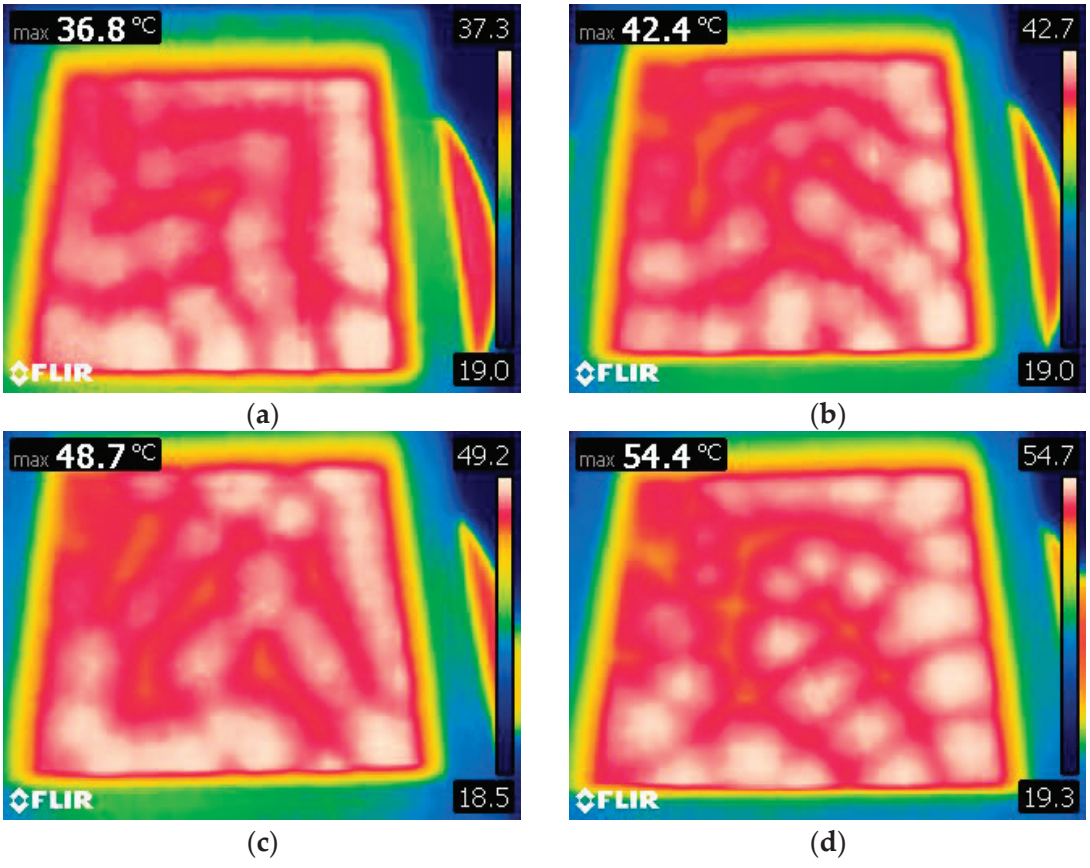

Figure 5. Surface temperature distribution for d = 0.75 cm (Ω = 48 mL) (A = 10.6, $Bo_{dyn} \cong 1.94$, $Ra \cong 8.6 \times 10^2 \times \Delta T$, Ma $\cong 4.4 \times 10^2 \times \Delta T$): (**a**) ΔT = 15 °C, (**b**) ΔT = 21 °C, (**c**) ΔT = 27 °C, (**d**) ΔT = 33 °C.

The significance of this figure primarily resides in its ability to make evident that the inclination leads to two remarkable effects. The first concerns the hybrid (spatial) nature of the visible pattern. In place of the scattered distribution of spots occupying all the available space in Figure 4, the surface temperature exhibits in this case an almost feature-free region localized in the part of the physical domain where the depth of the layer is smaller (Figure 6a). Moreover, the random distribution of rolls (in terms of direction in the xz plane) seen in the constant-depth case is taken over by a much more ordered arrangement where the convective features display a tendency to align with the z axis (the vertical direction in the figures, see, e.g., the black dashed lines in Figure 6c).

Notably, although these may immediately be classified as 'longitudinal rolls' (their axes being parallel to the tilt direction), their specific spatial configuration bares characteristic ingredients, which also need to be pinpointed suitably here. Their cross-extension, i.e., the typical size in a direction perpendicular to the roll axis undergoes remarkable variations along the z (tilt) direction, which indicates that the dimensional wavelength *is not constant* in the physical domain. Here, this quantity is defined as the distance between two consecutive corresponding crests or "points of the same phase" along the x axis for a fixed value of z. The related behaviors are quantitatively substantiated in Figure 7, where the wavelength has been plotted as a function of the z coordinate for a representative ΔT. Interestingly, as the ΔT is increased, some other interesting changes show up. The length of the rolls along

the z direction grows (compare, e.g., Figure 6a,f, the reader being also referred to the data reported in Figure 8).

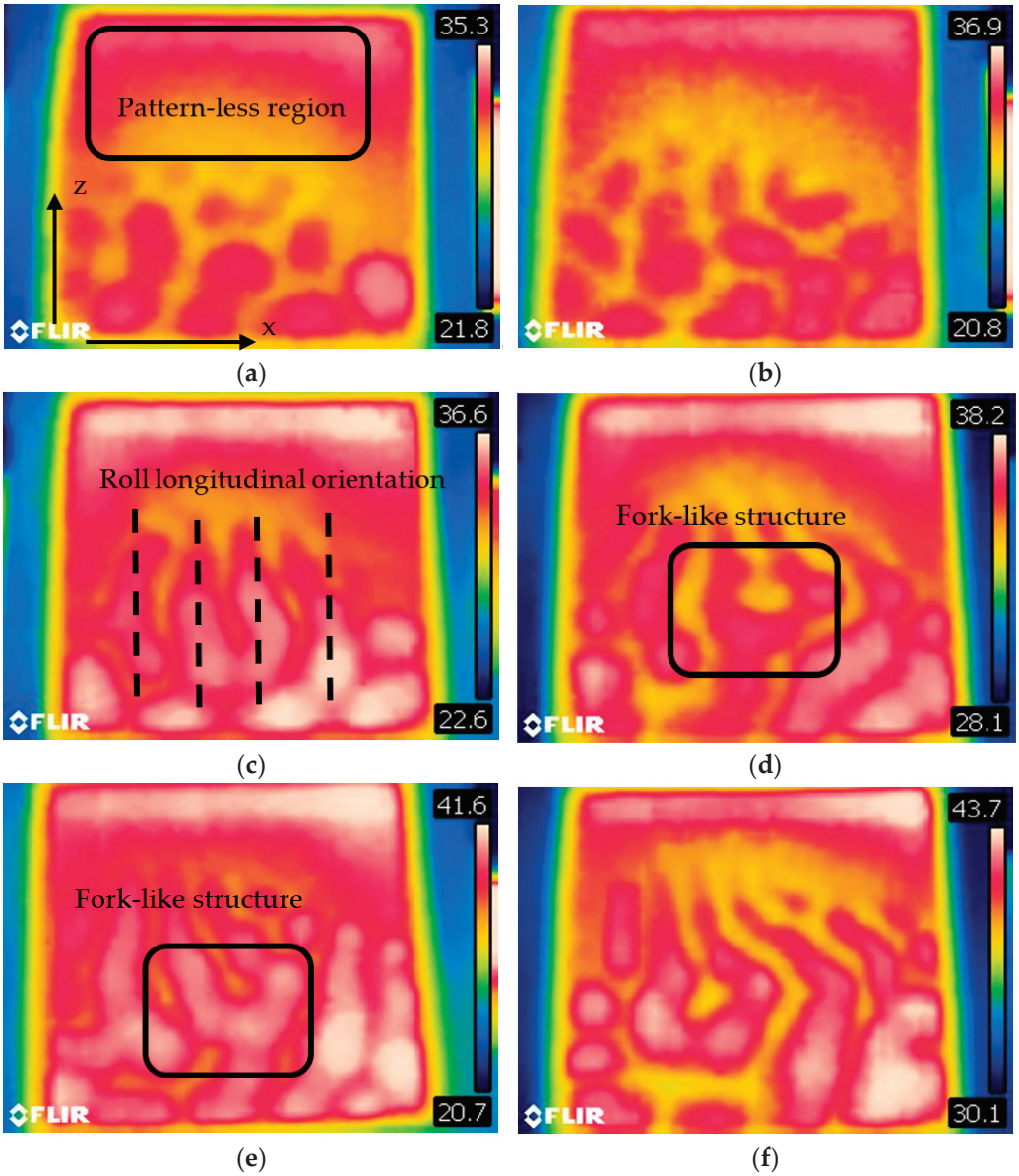

Figure 6. Surface temperature distribution for d = 0.50 cm (Ω = 32 mL) and $\vartheta \cong 3.5°$ (A = 16, $Bo_{dyn} \cong 0.86$, $Ra \cong 2.5 \times 10^2 \times \Delta T$, Ma $\cong 2.94 \times 10^2 \times \Delta T$): (**a**) ΔT = 15 °C, (**b**) ΔT = 18 °C, (**c**) ΔT = 21 °C, (**d**) ΔT = 24 °C, (**e**) ΔT = 27 °C, (**f**) ΔT = 30 °C (the x and z axes correspond to the horizontal and vertical directions in all the panels).

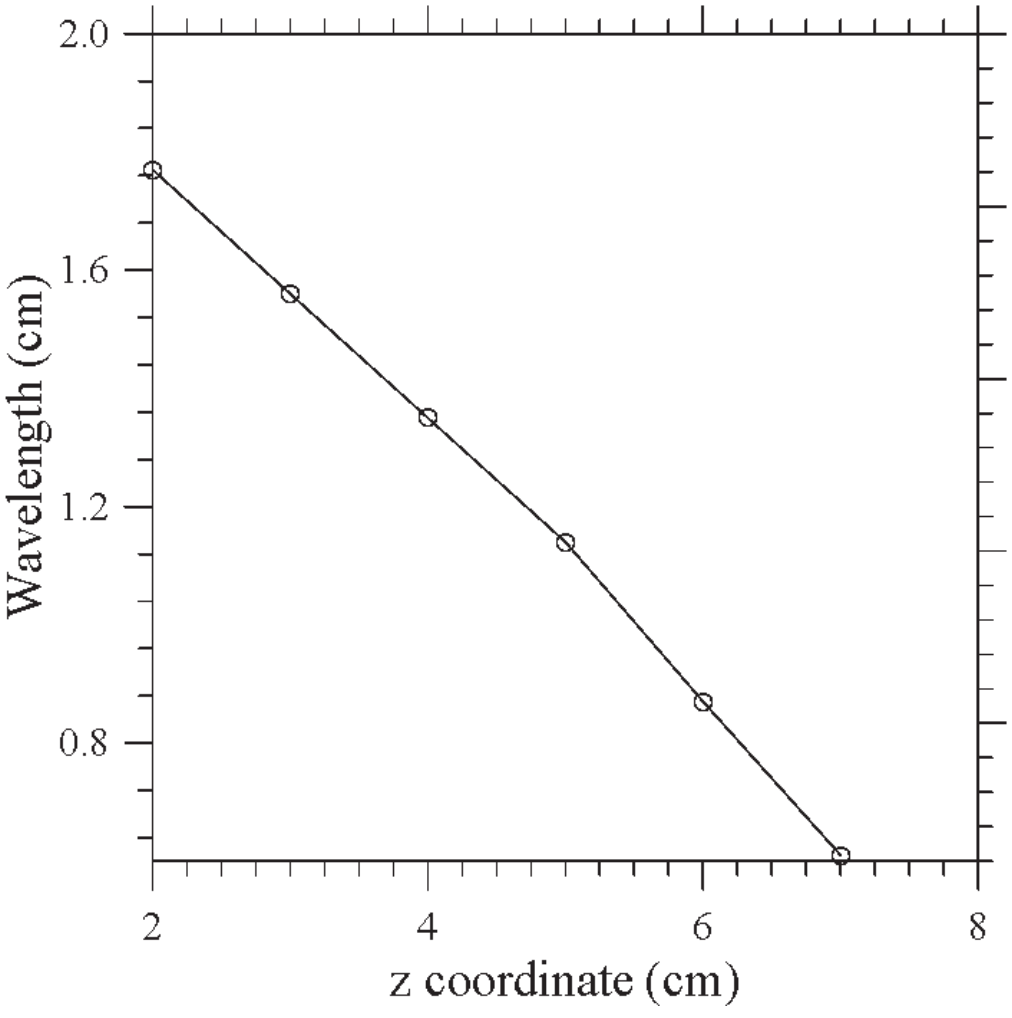

Figure 7. Transverse roll extension as a function of the longitudinal direction z for $\Delta T = 27°C$ (square container, $A = 16$, $d = 0.50$ cm, $Bo_{dyn} \cong 0.86$, $\vartheta \cong 3.5°$).

Superimposed on these trends, most interestingly, in some cases, in place of the striped pattern, which one would expect in the ideal situations of parallel longitudinal rolls, tree-like shapes can be distinguished in the surface temperature distribution. These give an external observed the illusion of a roll with a fork-like structure (two strips originating from a single initial strip, see the black rectangle in Figure 6d,e).

Given the complexity of such phenomena, which seem to escape a possible simple definition or classification within the framework of the past lines of research (still retaining, however, some affinities with the typical features and salient ingredients pertaining to such categories), in the following, we implement a peculiar modeling and analysis hierarchy in order to 'filter out' already known facts and concentrate selectively on new mechanisms. More specifically, this modus operandi is based on the step-by-step variation of the distinct (independent) parameters controlling the various degrees of freedom of the considered system, these being the characteristic temperature ΔT (whose effects have already been outlined before), the tilt angle ϑ, the volume of liquid and the shape and aspect ratio of

the considered container. While the effect of the ΔT has already been outlined before (see gain Figure 8), the overall volume of liquid is expected to influence the dynamics through the related value of the dynamic Bond number based on the average depth of the liquid, which accounts for the relative importance of buoyancy and surface-tension driven effects. Similarly, the shape and aspect ratio of the considered container may influence the pattern selection mechanism through confinement and other geometrical effects.

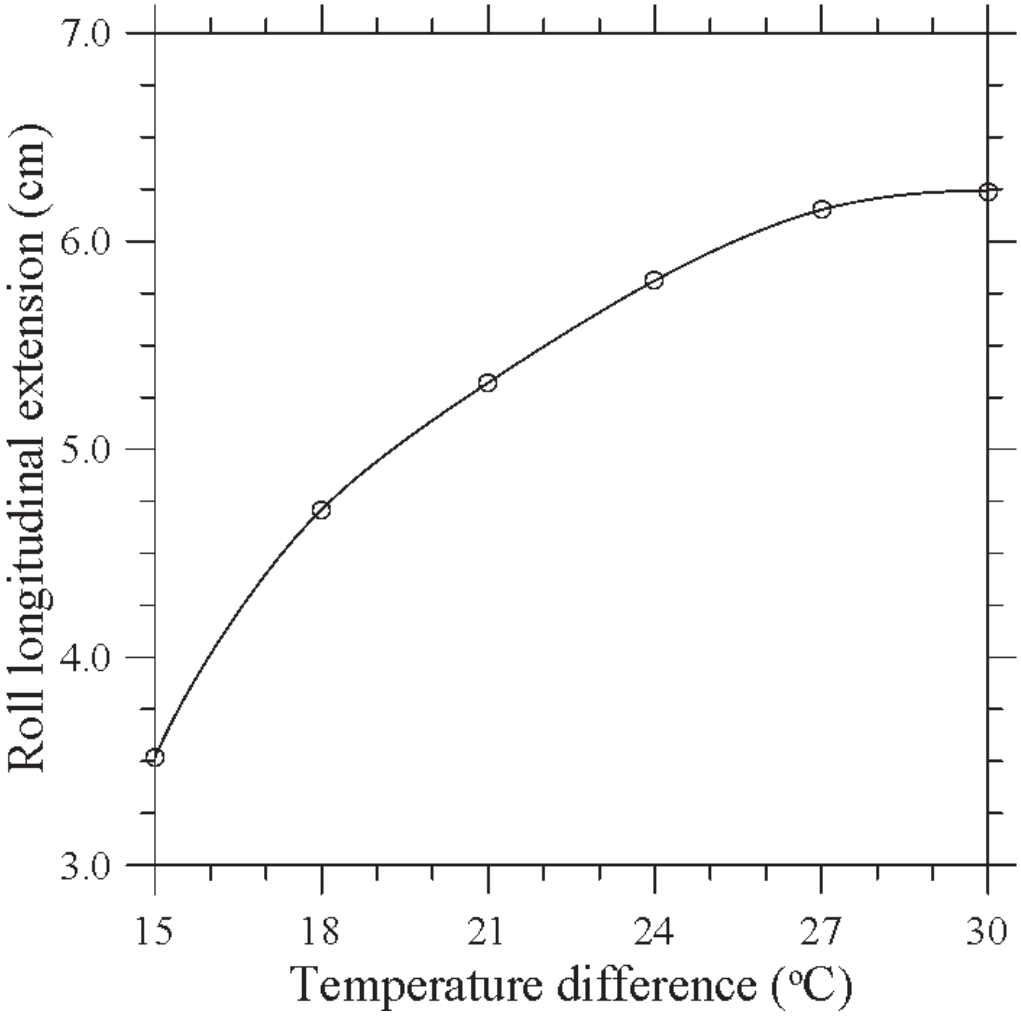

Figure 8. Longitudinal extension of the rolls as a function of ΔT (square container, $A = 16$, $d = 0.50$ cm, $Bo_{dyn} \cong 0.86$, $\vartheta \cong 3.5°$).

As a first step of this analysis hierarchy, we consider a larger value of the inclination angle for the same conditions of Figure 6 (same volume of liquid and set of temperature differences).

As immediately made evident by Figure 9, an increase in ϑ can produce a mitigation of the aforementioned roll pinching mechanism (by which a single longitudinal roll can be split into two neighboring rolls with smaller wavelength). A slightly larger values of ϑ

has also another remarkable consequence; on average, it causes a small (non-negligible) growth of the transverse extension of the rolls (we will return to this effect later).

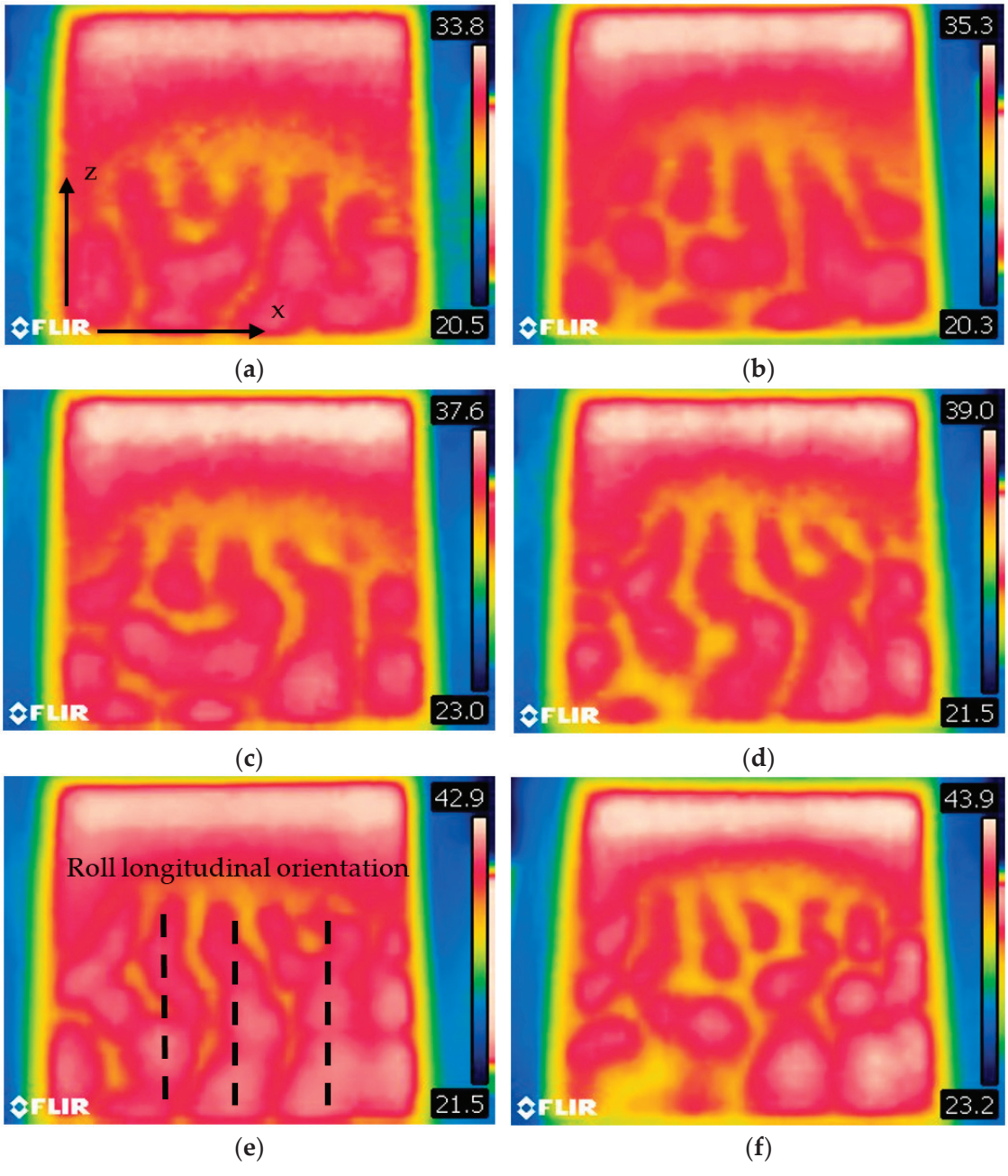

Figure 9. Surface temperature distribution for d = 0.50 cm (Ω = 32 mL) and $\vartheta \cong 5°$ (A = 16, $Bo_{dyn} \cong 0.86$, $Ra \cong 2.5 \times 10^2 \times \Delta T$, Ma $\cong 2.94 \times 10^2 \times \Delta T$): (**a**) ΔT = 15 °C, (**b**) ΔT = 18 °C, (**c**) ΔT = 21 °C, (**d**) ΔT = 24 °C, (**e**) ΔT = 27 °C, (**f**) ΔT = 30 °C (the x and z axes correspond to the horizontal and vertical directions in all the panels).

The reduced tendency of the system to support roll pinching mechanism is qualitatively substantiated in Figure 10. On closer inspection, indeed, this figure reveals that the number of peaks visible at each station z remains almost constant throughout the longitudinal extension of the domain (until no well-defined peaks can be seen as a certain limiting value of z is exceeded, which corresponds to the transition from the patterned to the spot-free region).

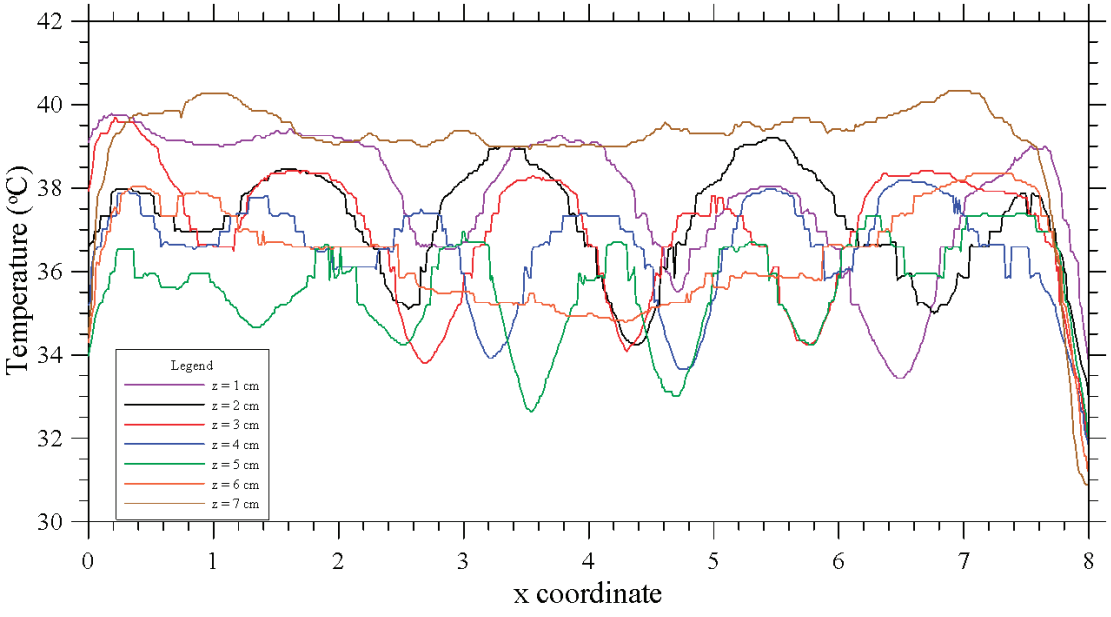

Figure 10. Profiles of temperature at different stations along the longitudinal direction z (square container, $A = 16$, $d = 0.50$ cm, $Bo_{dyn} \cong 0.86$, $\Delta T = 27°C$, $\vartheta \cong 5°$).

Towards the end of getting a better grasp on how all these dynamics are affected by the depth of the layer, the next set of figures refers to the case where the average depth of the liquid is 0.75 cm (see Figure 11, yet for $\vartheta \cong 5°$). Along these lines, taken together Figures 9 and 11 are instrumental in showing that an increase in the relative importance of buoyancy forces with respect to surface-tension driven effects (as witnessed by the related rise in the dynamic Bond number) can help to make the roll-pinching mechanism even less frequent in favor of a more regular (parallel) distribution of longitudinal rolls. As even a fleeting glimpse into Figure 11 would immediately reveal, in fact, the patterned surface now corresponds to the entire free liquid-gas interface of the fluid layer, i.e., no cell-free area can be identified in this case (a kind of "saturated state" is attained in terms of roll extension along the tilt direction z).

Additional insights follow naturally from a cross-comparison of Figures 10 and 12. It can be seen that the number of rolls sitting in the cavity is reduced in the $d = 0.75$ cm case (as clearly demonstrated by the smaller number of recognizable peaks at any given station in comparison to the equivalent ones visible in Figure 10 for $d = 0.5$ cm).

All these trends are finally summarized in Figure 13 in terms of roll extension along x as a function of the longitudinal coordinate z for different values of the layer average depth and inclination.

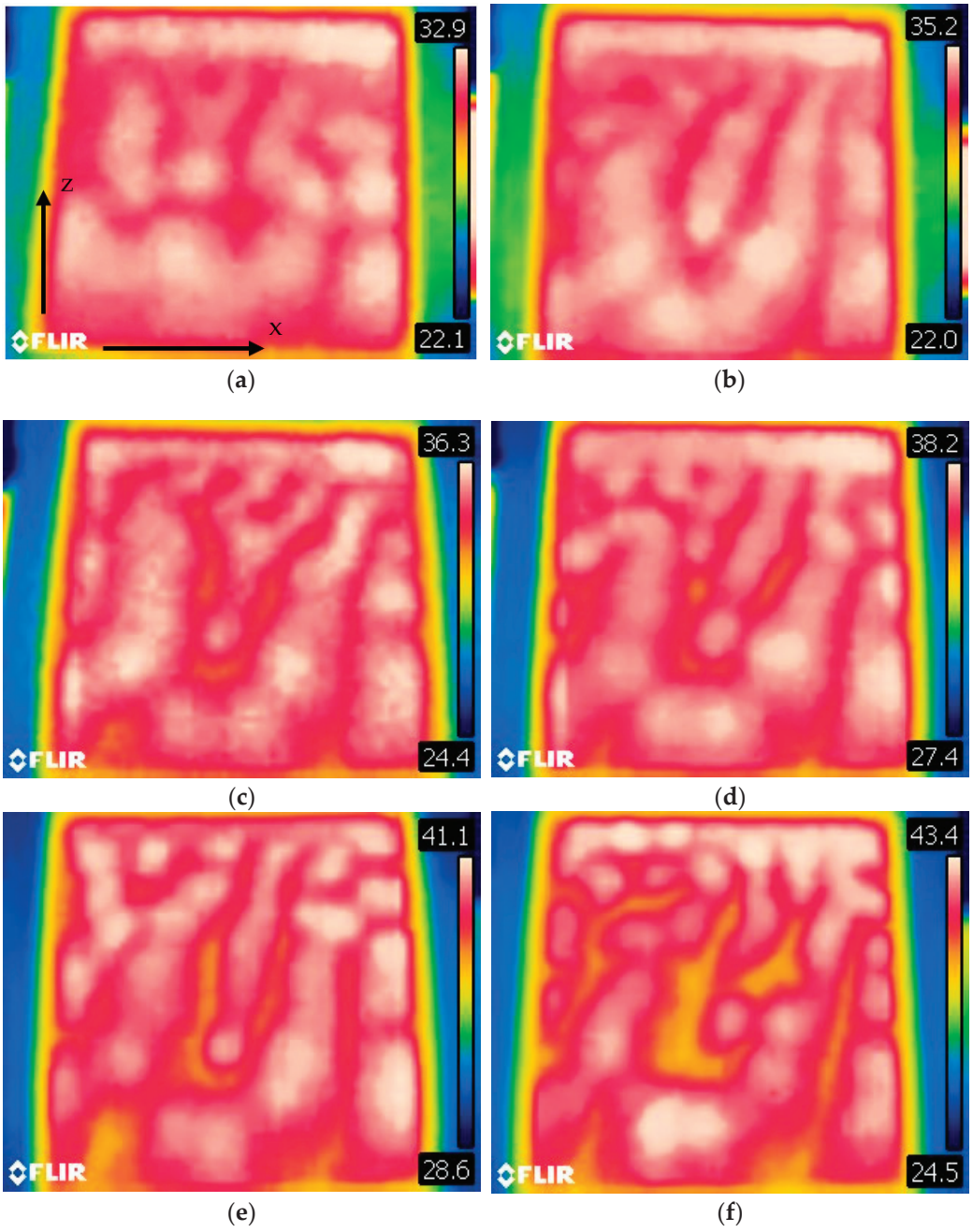

Figure 11. Surface temperature distribution for d = 0.75 cm (Ω = 48 mL) and $\vartheta \cong 5°$ (A = 10.6, $Bo_{dyn} \cong 1.94$, $Ra \cong 8.6 \times 10^2 \times \Delta T$, Ma $\cong 4.4 \times 10^2 \times \Delta T$) (**a**) ΔT = 15 °C, (**b**) ΔT = 18 °C, (**c**) ΔT = 21 °C, (**d**) ΔT = 24 °C, (**e**) ΔT = 27 °C, (**f**) ΔT = 30 °C (the x and z axes correspond to the horizontal and vertical directions in all the panels).

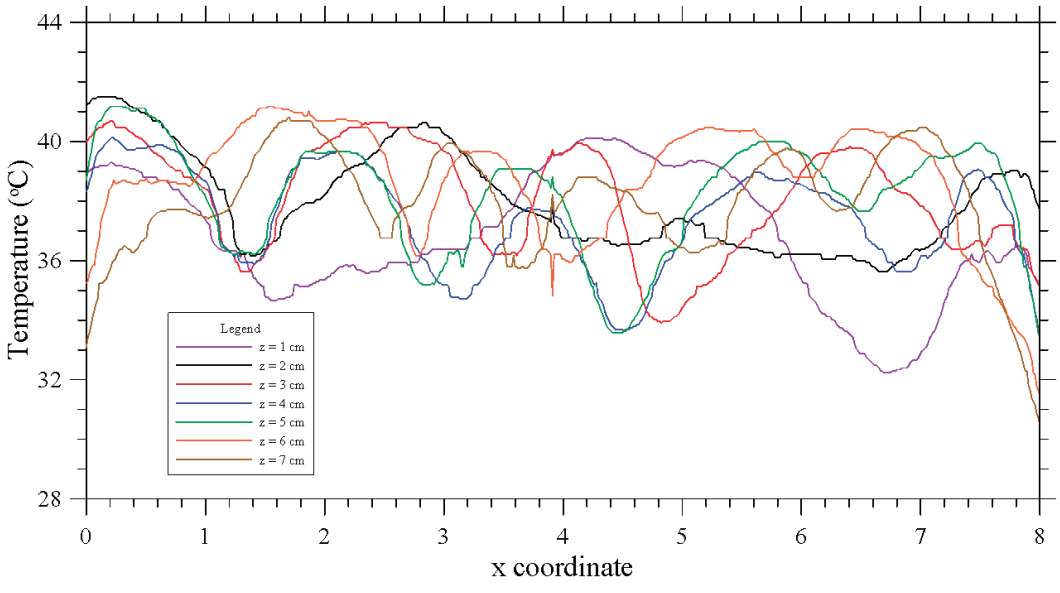

Figure 12. Profiles of temperature at different stations along the longitudinal direction z (square container, $A = 10.6$, $d = 0.75$ cm, $Bo_{dyn} \cong 1.94$, $\Delta T = 27$ °C, $\vartheta \cong 5°$).

Having completed a description of the observed phenomena in the square geometry case, we now turn to considering briefly the equivalent dynamics emerging in the cylindrical container. As already explained to a certain extent before, this practice finds its justification in the two-fold purpose of assessing the role played by the system aspect ratio (ratio of the horizontal and average vertical extension) and the shape of the side boundary.

4.3. Convection in Inclined Cylindrical Layer

As the reader will immediately realize by inspecting Figure 14, moving on from the case with square boundary to that with cylindrical sidewall (compare with Figure 6), no significant or appreciable changes can be discerned in terms of patterning behavior. The flow still displays a set of coexisting rolls, which originate from the side where the fluid depth is larger and protrude into the pattern-less region located at the other end of the container.

Although from a qualitative standpoint, the scenario is essentially the same, however, a discrepancy or departure from the equivalent dynamics shown in Figure 6 can be identified. It is represented by the tendency of the rolls to assume an *oblique configuration* with respect to the tilt direction (North-West/South-East in the different panels of Figure 14, see, e.g., the black dashed lines in Figure 14c,f).

Moreover, as revealed by a closer (quantitative) assessment of the pattern in terms of wavelength, this difference in the prevailing roll orientation occurs in conjunction with an appreciable increase in the roll transverse extension (Figure 15).

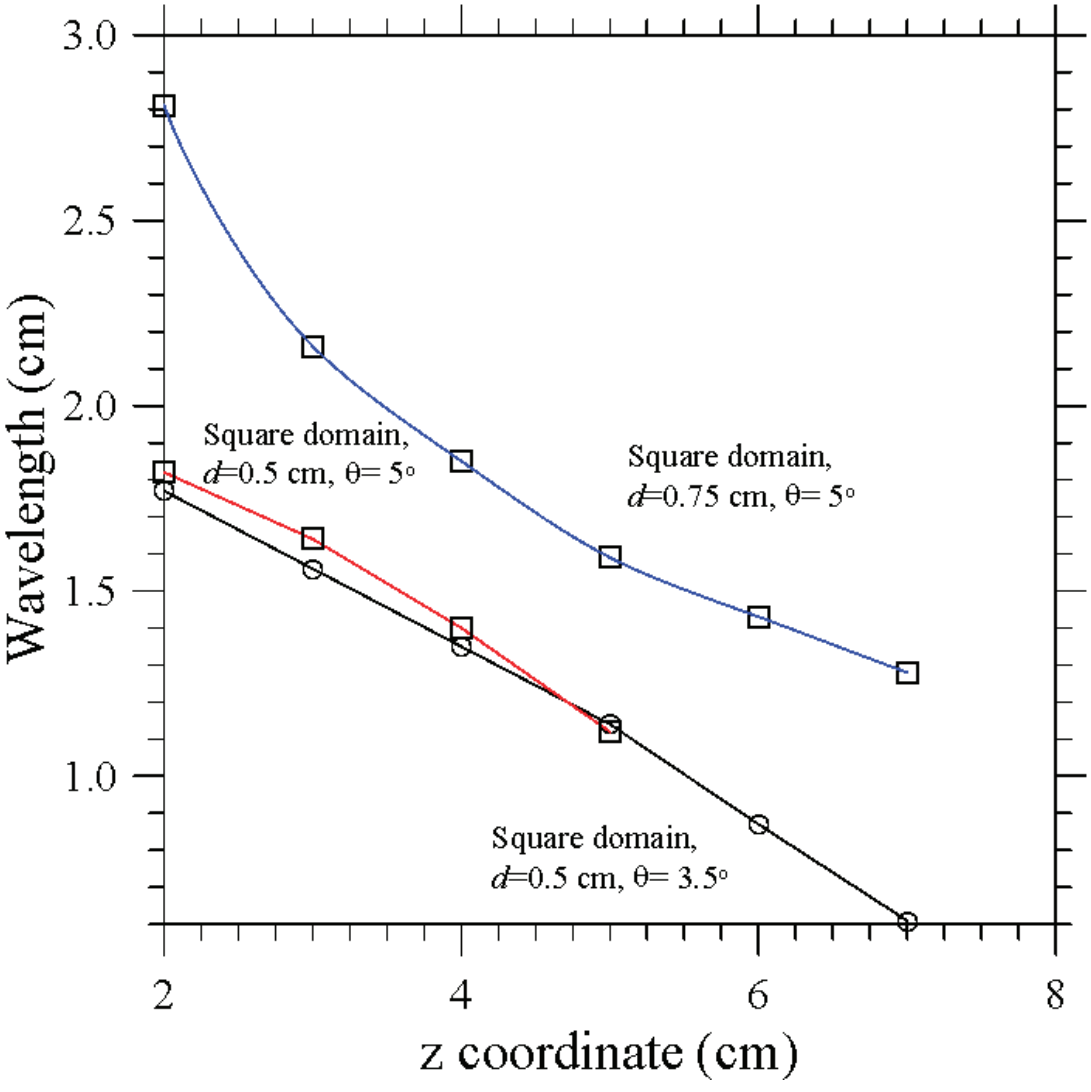

Figure 13. Transverse roll extension as a function of the longitudinal direction z for ΔT = 27 °C for different average fluid depths and inclinations (square container).

On the one hand, these results indicate that the scenario does not depend significantly on the shape of the domain, on the other hand, they provide evidence that, if the geometrical aspect ratio is increased (A = 26.6 as opposed to A = 16), the pattern is allowed to "relax" in the horizontal direction, thereby causing an increase in the dimensional wavelength. Another (more obvious) outcome of the cylindrical nature of the outer solid boundary is the modulation of the longitudinal extension of the rolls along the x axis for any fixed value of ΔT (the rolls closer to left and right side of the container having smaller longitudinal extension than those located in the center).

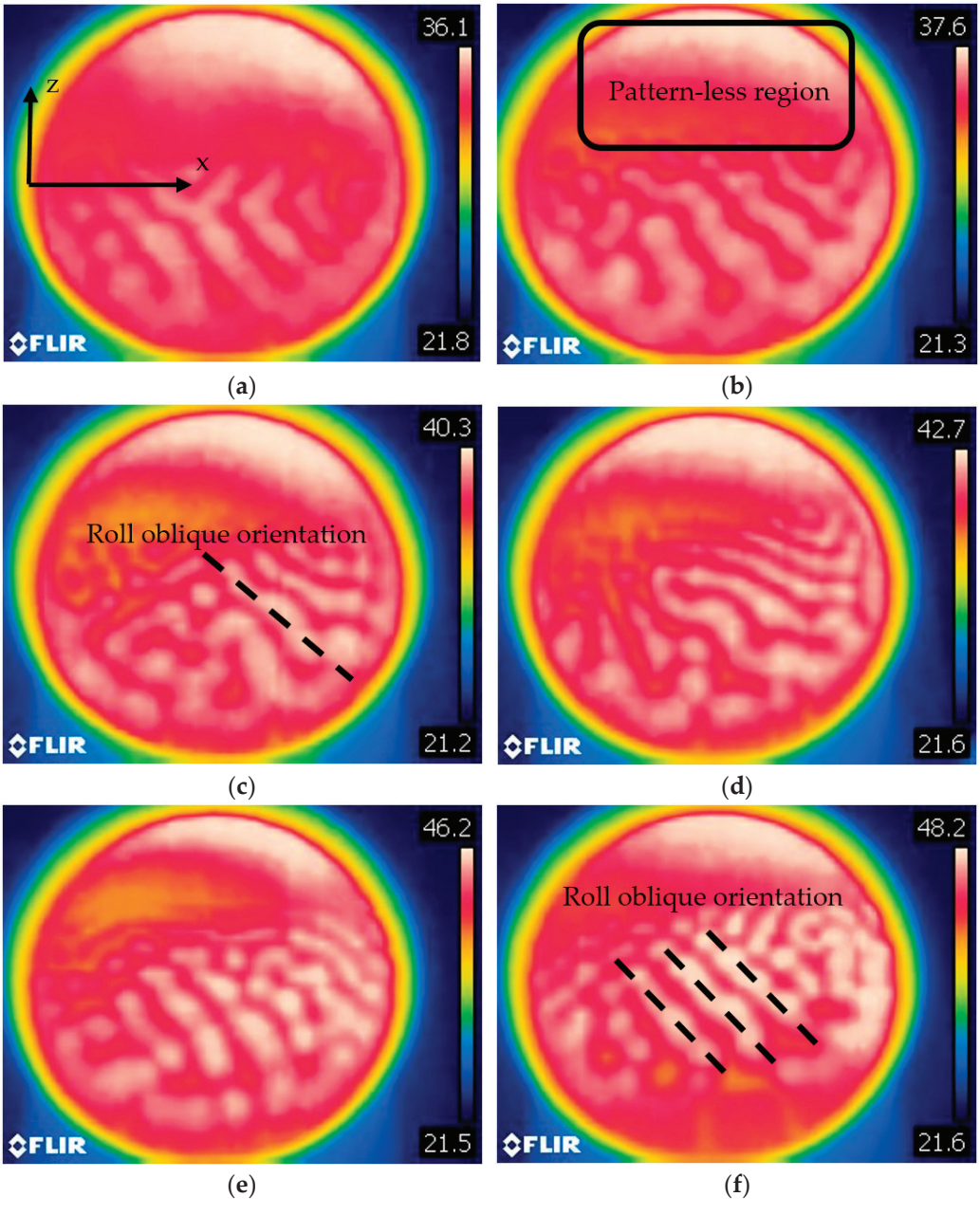

Figure 14. Surface temperature distribution for d = 0.50 cm ($\Omega \cong$ 70 mL) and $\vartheta \cong 3.5°$ (A = 26.6, $Bo_{dyn} \cong 0.86$, $Ra \cong 2.5 \times 10^2 \times \Delta T$, Ma $\cong 2.94 \times 10^2 \times \Delta T$): (**a**) ΔT = 15 °C, (**b**) ΔT = 18 °C, (**c**) ΔT = 21 °C, (**d**) ΔT = 24 °C, (**e**) ΔT = 27 °C, (**f**) ΔT = 30 °C (the x and z axes correspond to the horizontal and vertical directions in all the panels).

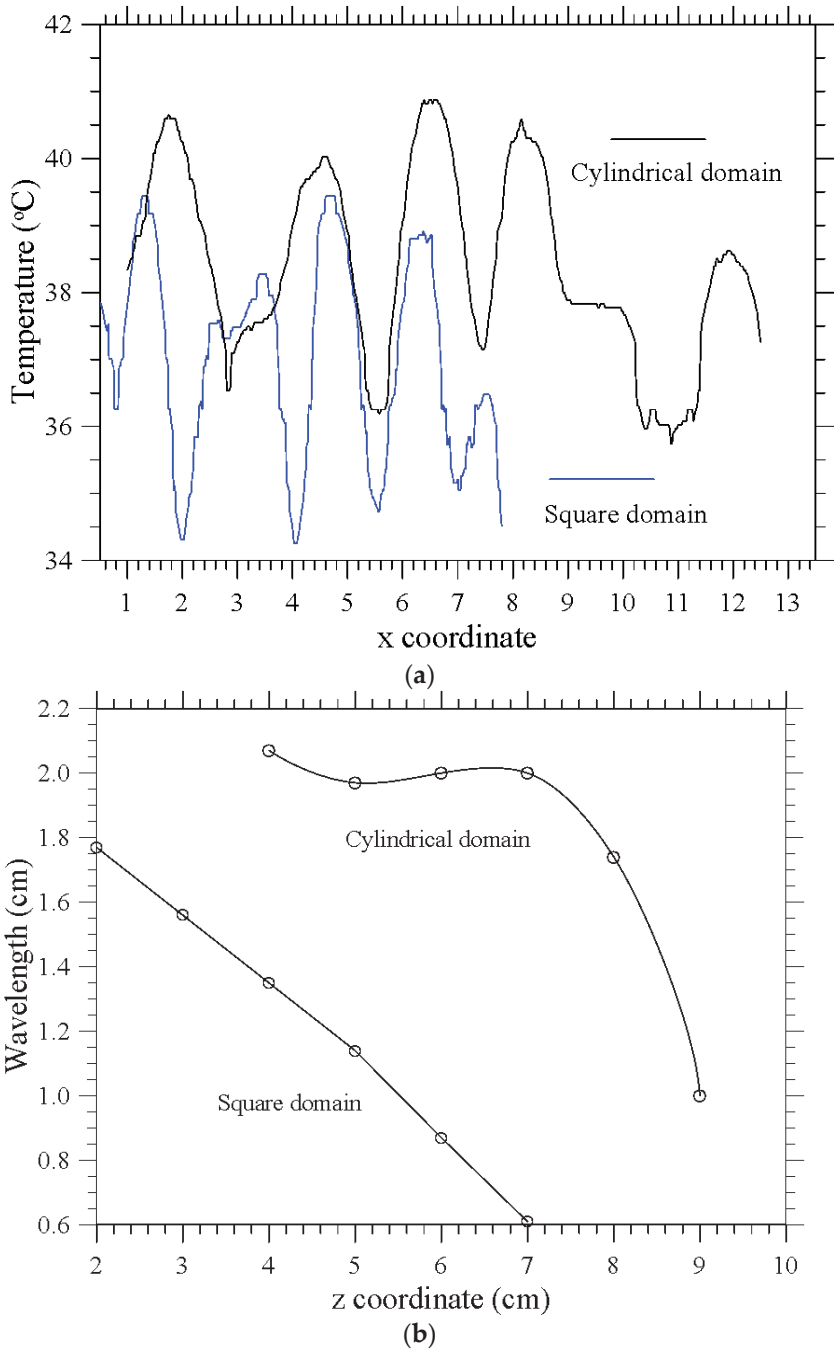

Figure 15. Transverse roll extension analysis (d= 0.50 cm, $Bo_{dyn} \cong 0.86$, ΔT = 27 °C, $\vartheta \cong 3.5°$): (**a**) Temperature as a function of the transverse coordinate x at z= 4 cm, (**b**) Roll extension along x as a function of the longitudinal direction z.

Figure 16 naturally complements Figure 14, where additional evidence is provided that, on increasing the inclination, the transverse wavelength can be made higher (especially for intermediate values of *z*).

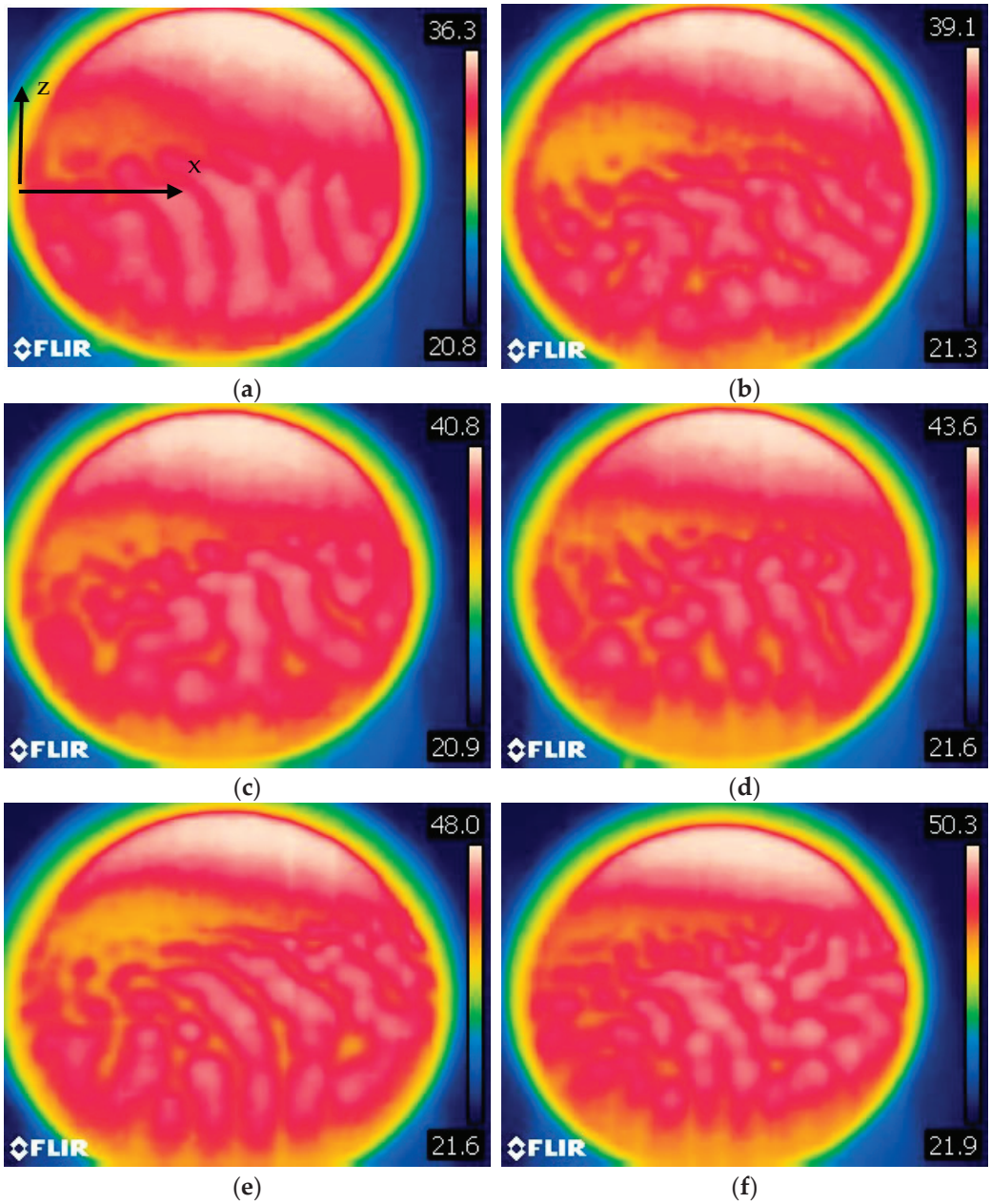

Figure 16. Surface temperature distribution for d = 0.50 cm ($\Omega \cong$ 70 mL) and $\vartheta \cong 5°$ (A = 26.6, $Bo_{dyn} \cong 0.86$, $Ra \cong 2.5 \times 10^2 \times \Delta T$, Ma $\cong 2.94 \times 10^2 \times \Delta T$): (**a**) ΔT = 15 °C, (**b**) ΔT = 18 °C, (**c**) ΔT = 21 °C, (**d**) ΔT = 24 °C, (**e**) ΔT = 27 °C, (**f**) ΔT = 30 °C (the x and z axes correspond to the horizontal and vertical directions in all the panels).

Figures 17 and 18 complete this sequence by illustrating the behavior for larger average depth of the layer (Figure 18 to be compared for analogous cicumstances with the findings about the square layer in Figure 11).

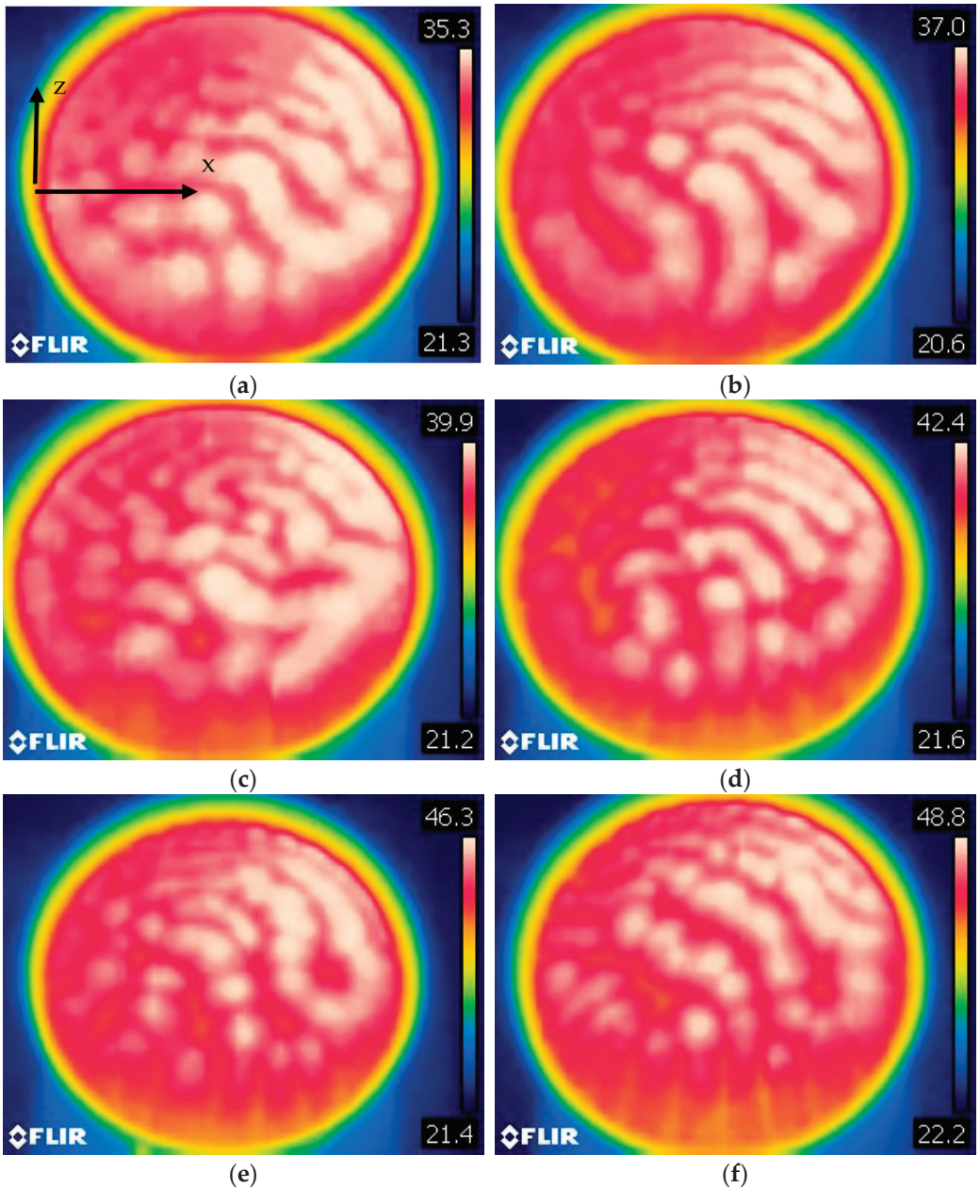

Figure 17. Surface temperature distribution for d = 0.75 cm (Ω = 104 mL) and $\vartheta \cong 3.5°$ (A = 17.7, $Bo_{dyn} \cong 1.94$, $Ra \cong 8.6 \times 10^2 \times \Delta T$, $\mathrm{Ma} \cong 4.4 \times 10^2 \times \Delta T$) (**a**) ΔT = 15 °C, (**b**) ΔT = 18 °C, (**c**) ΔT = 21 °C, (**d**) ΔT = 24 °C, (**e**) ΔT = 27 °C, (**f**) ΔT = 30 °C (the x and z axes correspond to the horizontal and vertical directions in all the panels).

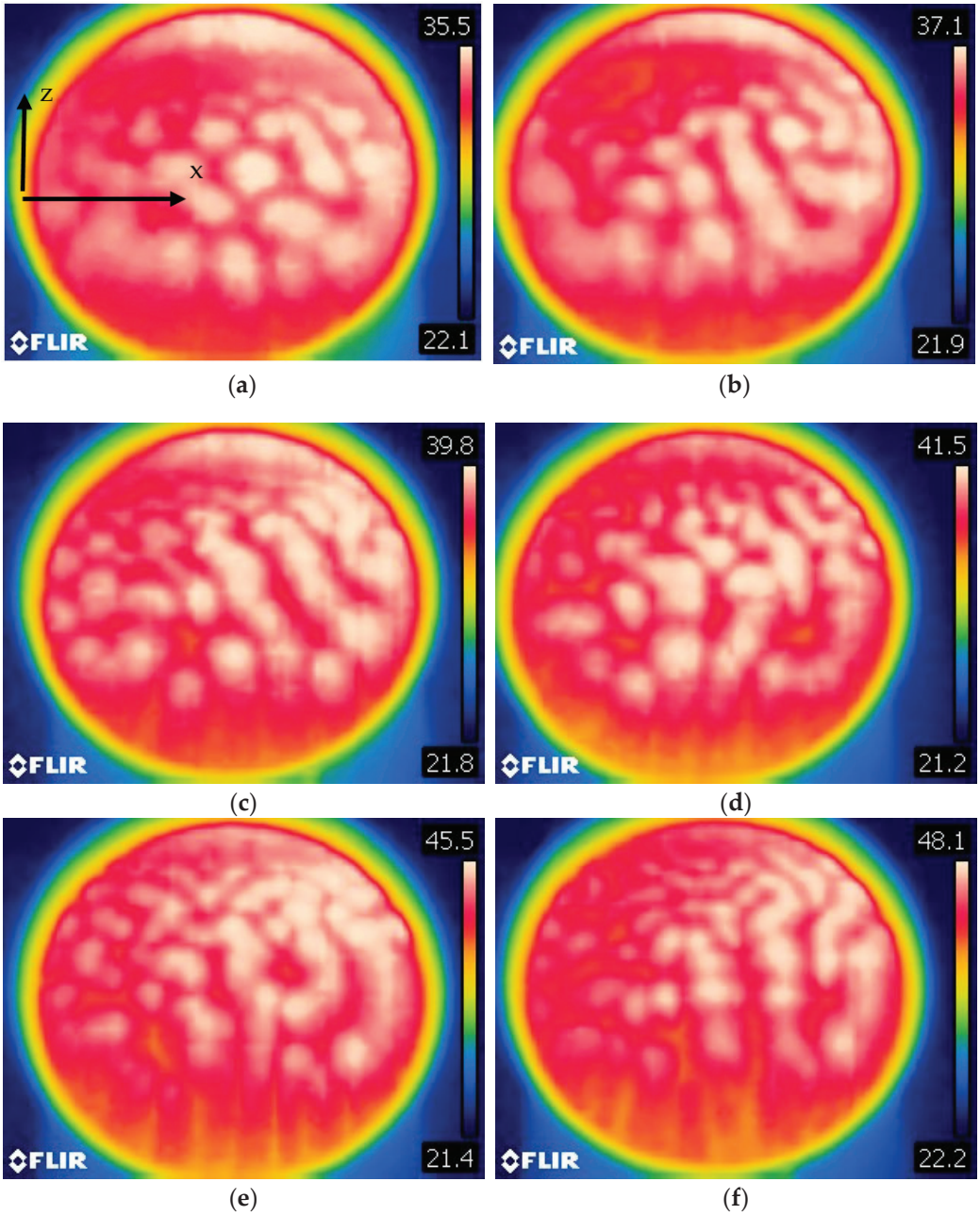

Figure 18. Surface temperature distribution for d = 0.75 cm (Ω = 104 mL) and $\vartheta \cong 5°$ (A = 17.7, $Bo_{dyn} \cong 1.94$, $Ra \cong 8.6 \times 10^2 \times \Delta T$, Ma $\cong 4.4 \times 10^2 \times \Delta T$) (**a**) ΔT = 15 °C, (**b**) ΔT = 18 °C, (**c**) ΔT = 21 °C, (**d**) ΔT = 24 °C, (**e**) ΔT = 27 °C, (**f**) ΔT = 30 °C (the x and z axes correspond to the horizontal and vertical directions in all the panels).

Figure 19 finally provides an ensemble perspective on the system response for all the cases considered in Sections 4.2 and 4.3. A number of interesting functional dependences can be discerned accordingly. In addition to the aforementioned tendency of the transverse wavelength to attain larger values as the inclination and/or the liquid average depth (volume) are increased (with the values for the cylindrical domain being generally located above the corresponding ones for the square container with smaller aspect ratio), some interesting non-monotonic behaviors can be spotted there.

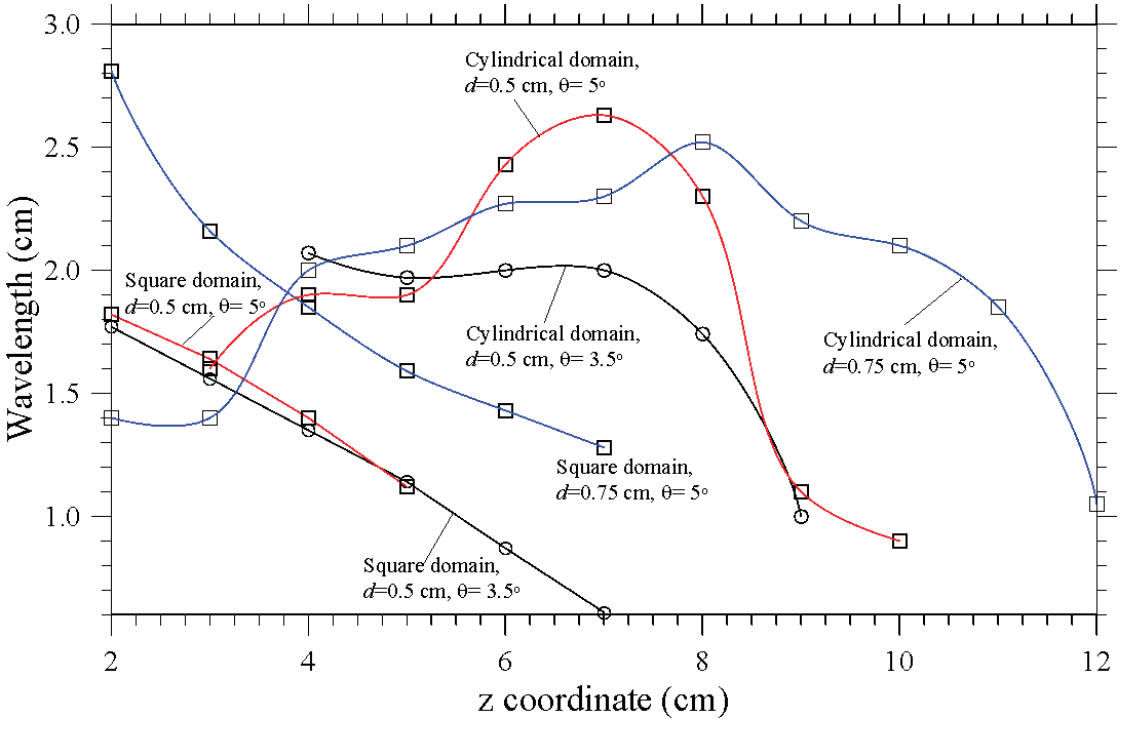

Figure 19. Transverse roll extension as a function of the longitudinal direction z for all the cases considered in the present work (ΔT = 27 °C).

In the cylindrical case, for d = 0.5 cm ($Bo_{dyn} \cong 0.86$) and $\vartheta \cong 5°$ the wavelength curve is entirely located above the corresponding one for the square domain (refer to the red branches in Figure 19). The cylindrical case, however, displays a maximum for z = 7 cm, followed by a branch of decreasing behavior. Notably, an interval of the z coordinate can be identified accordingly where the wavelength for $\vartheta \cong 5°$ is smaller than that attained for the same average liquid depth (d = 0.5 cm) and $\vartheta \cong 3.5°$ (z < 5.2 cm). The same concept applies to the curve for d = 0.75 cm ($Bo_{dyn} \cong 1.94$) and $\vartheta \cong 5°$. Although, the wavelength is larger than the corresponding one for d = 0.5 cm over almost the entire longitudinal extension of the fluid domain, this relationship is inverted in the range 5.7 < z < 7.7 cm. This curve even intersects the corresponding one for the square container for z ≅ 3.8 cm (refer to the blue branches in Figure 19), which indicates that circumstances exist where the wavelength in the cylindrical case can become smaller than the equivalent square-domain value ($Bo_{dyn} \cong 1.94$, $\vartheta \cong 5°$ and z < 3.8 cm).

5. Discussion

It is a well-known concept that, regardless of whether the underpinning processes are different or not, systems that are driven out of equilibrium often display similar behaviors or patterns (Lappa [11]). To put the present work in perspective, therefore, in this section some effort is provided to emphasize on some prior research displaying some potential links with the results described in Section 4. In other words, we sift through existing studies with different foci in order to glean hints and draw inferences about possible affinities in terms of underlying mechanisms with the present phenomena.

In particular, in our endeavor to do so, the discussion is articulated along two different threads. Namely, first, we consider the existing literature on surface-tension driven convection in horizontal layers with inclined temperature gradient and then we review the existing studies on pure gravitational convection in inclined shallow enclosures with constant depth (geometries with a rectangular transverse section).

In the former case, some commonality can be seen the existence of a symmetry breaking shear flow, which can deeply influence the effective patterning behavior. A detailed classification of the fundamental modes of surface-tension-driven convection developed by horizontal layers with an inclined temperature gradient can be found in the linear stability analysis by Nepomnyashchy et al. [33], where these were categorized as stationary longitudinal rolls (LR) essentially driven by the same thermal effects that can produce classical MB convection and transverse rolls for which shear plays a much more important role (manifesting as traveling entities through the layer). Hydrothermal waves (HTW) were also identified in the case for which the horizontal component of the temperature gradient becomes so strong that it can hinder the concurrent mechanisms driven by the vertical component (this being the opposite extreme case with respect to that where the vertical component of the temperature gradient is dominant, thereby producing the classical MB hexagonal cells).

Due to the lack of HTWs in the present case even in the situation for which the depth of the layer is minimal (Figures 6, 9, 14 and 16), we infer that the present conditions are far from those for which these specific modes of convection can be excited. Another possible explanation could be rooted in another class of studies dealing with hybrid Marangoni-buoyancy convection in differentially heated liquid layers (the gradient of temperature being parallel to the free interface in this case). Evidence has been provided in the literature that if buoyancy is sufficiently strong in comparison to surface-tension driven effects, the HTW (which would represent the preferred mode of supercritical Marangoni convection) is taken over by longitudinal rolls with axes parallel to the (horizontal) temperature gradient. Relevant examples of related findings can be found in the experimental studies by Gillon and Homsy [45], Braunsfurth, and Homsy [46], Burguete et al. [47] and Pelacho et al. [48], to which the interested reader is referred for additional details.

In such a context, another work deserving a quote is that by Shklyaev and Nepomnyashchy [35]. These authors shed additional lights on the pure Marangoni-flow case with inclined temperature gradient by gaining relevant information about the effective morphology of the emerging convection structures through non-linear numerical simulations. For a sample liquid with Pr = 7, they could determine the morphological changes undergone by the compact cells typical of MB convection under the effect of a superimposed shear flow (leading to cells that "drift" in the physical domain) and show that between the areas of the existence of the hexagonal patterns and the longitudinal rolls (obtained for a horizontal temperature gradient larger than that needed to produce the drifting cells), there is a stability domain of "oblique rolls", i.e., rolls inclined with respect to the direction of the horizontal temperature gradient. Most interestingly, they also found states with half of the convective pattern consisting of oblique rolls with positive inclination angle and the other half displaying rolls with a negative inclination angle of the same modulus.

Yet, for the case with inclined temperature gradient, Ueno et al. [34] were the first to report on stationary longitudinal rolls and drifting cells by means of experiments with layers of silicone oils with viscosity 2, 5, 10 and 20 cSt (Pr = 27.9, 67.0, 111.9 and 206.8 at room temperature, respectively) up to 2 [mm] in depth. Later, Mizev and Schwabe [3] conducted an experimental campaign to assess the role played in such dynamics by the depth of the layer (10 cSt silicone oil with a thickness d varying from 1.0 to 6.0 mm). These authors found that as the layer thickness increases the Marangoni– Bénard cells elongate along the direction of thermocapillary motion. Finally, when the longitudinal size of the cells reaches the horizontal size of the layer, a new flow structure appears in the form of LRs. More precisely, they observed that for any depth of the layer in the considered range, while an increase in the horizontal component of the temperature gradient for a fixed vertical contribution can cause a transition from drifting cells to LRs, vice versa, an increase in the vertical component of the temperature gradient for a fixed horizontal contribution leads to the opposite transition.

Although several analogies might be identified between these behaviors and the present findings, we should recall at this stage that in the present case, in addition to the inclination of the temperature gradient with respect to the free interface, the depth of the liquid layer is not constant.

Moreover, drawing a parallelism with the existing findings for surface-tension driven convection may not be exhaustive because buoyancy should be expected to play a significant role in the situations considered here for which $Bo_{dyn} > 1$. Along these lines, a critical analysis of the existing literature for pure buoyancy flow in inclined shallow enclosures (no free interface) might also lead to interesting insights.

The simplest way to do so, perhaps, is to start from the simple remark that for inclined systems subjected to buoyancy only and relatively small angles of inclination such as those considered in the present work, these systems tend to develop stationary longitudinal rolls (LR), i.e., rolls of essentially buoyant nature that aligns with the direction of the shear flow are the typical outcome of the primary instability of these systems. Only if the inclination angle is relatively large, the ground is left to transverse rolls (TR), i.e., rolls with axes perpendicular to the shear flow essentially driven by shear (Chen and Pearlstein [23]). Fujimura and Kelly [26] clarified that the transition angle essentially depends on the Prandtl number of the considered fluid and it is less than 90° only if the Prandtl number is smaller than 12.47 (Fujimura and Kelly [26]), which implicitly leads to the conclusion that LR should be regarded as the primary pattern forming process in oils and other fluids with relatively large values of the Prandtl number.

The present findings (see, in particular, Figure 11 for the case in which buoyancy is dominant) confirm that such a trend (i.e., the tendency to favor LRs for small tilt angles) still holds although situations with non-constant depth of the layer have been considered.

Remarkably, Figures 17 and 18 also provide a hint or clue for another interesting connection or affinity with the dynamics described in the studies by Shadid and Goldstein [24] and Busse and Clever [25]. In this regard, it is worth recalling that the former authors could observe experimentally in the case of a fluid with Pr = 90 (reagent grade ethylene glycol) that, for low to moderate angles of inclination and a sufficiently high value of the Rayleigh number, the longitudinal rolls can become unstable against a three-dimensional "wavy" instability (in line with the predictions of the linear stability analysis by Clever and Busse [22]). Two instability mechanisms were revealed accordingly, i.e., an instability of the cross-roll type, by which a disturbance perpendicular to the original roll axis is produced, and a pinching process able cause coalescence of adjacent rolls. Apart from these steady-rolls wavelength-changing mechanism, Shadid and Goldstein [24] also reported on unsteady longitudinal rolls taking over for $Ra > 10^4$ over the interval $5 \leq \theta \leq 25°$. By means

of numerical simulations, Busse and Clever [25] could confirm that a three-dimensional "wavy" instability is the main mechanisms responsible for the emergence of the so-called *undulations patterns*.

As even a cursory comparative assessment of Figures 11 and 18 would immediately confirm, similar phenomena show up in the present circumstances when the lateral confinement is relaxed. Indeed, the latter figure clearly reveals a tendency of the present system to develop oblique rolls characterized by sinusoidal spatial distortions as the aspect ratio is increased from 10.6 to 17.7 and the straight (parallel) sidewalls are replaced by a curved boundary (although at this stage the role played in such a process by surface-tension effects in the present case is not clear).

As a concluding remark for this section, we wish to remark that these arguments should obviously be regarded for what they are, i.e., observations stemming from the quest for universality classes through the observation of companion or somehow related phenomena. Nevertheless, they point to interesting similarities in the underlying physics or mechanisms, which would require additional investigation in the frame of the linear stability analysis approach or other numerical techniques. Some general conclusions stemming from the present experimental work are elaborated accordingly in the next section.

6. Conclusions

Hybrid Marangoni-buoyancy convection in a fluid domain with variable fluid depth and inclined temperature gradient with respect to the horizontal direction has been investigated in the attempt to enrich the current knowledge about the fluid-dynamic behavior of these systems. In particular, the unique examined configuration should be regarded as an intentional attempt to move beyond the models adopted so far by the community of theoretical physicists and engineers, which has essentially been based on the paradigm of a series of different idealized setups and has not yet branched out to heated systems with irregular transversal thickness.

It has been shown that, in analogy with the companion cases represented by Marangoni convection in horizontal layers with temperature gradient inclined to the free liquid-gas interface and buoyancy convection in constant-thickness tilted enclosures, the preferred (or dominant) mode of convection for relatively small tilt angles is represented by longitudinal rolls. These manifest with a wavelength that increases with the layer depth. A relaxation in the lateral confinement can also contribute to increase their transverse extension, which indirectly proves that the sidewalls play role in the wavenumber selection mechanism in the considered range of aspect ratios.

A coherent picture of the richness of possible scenarios in terms of roll transverse size, longitudinal extension and orientation with respect to the tilt direction has been provided by varying parametrically the system influential factors, namely the temperature difference, liquid volume (average layer depth), inclination angle and the aspect ratio of the fluid container.

It has been shown that the hallmark of the considered dynamics is a modulation of the abovementioned transverse wavelength along the longitudinal direction, which should be regarded as an important distinguishing factor with respect to the "similar" behaviors displayed by these modes of convection in systems with a constant depth, regardless of whether the main driving force is represented by thermocapillarity or buoyancy. An increase in the temperature difference generally causes an increase in the longitudinal extension of the rolls.

Future attempts shall be devoted to clarify the nature of the interesting roll pinching mechanism (by which a single longitudinal roll can be split into two neighboring rolls with smaller wavelength), found in the case for which the lateral confinement is significant (small aspect ratio) and the layer depth is relatively small. Critical comparison with the existing literature has revealed that although most of existing results can be organized in well-studied universality classes, the interpretation of some experimental realizations

is not always a relatively simple task. Factors contributing to the inherent complexity of this objective are the essentially counter-intuitive non-linear behavior displayed by these systems and the blending of convective modes (normally operating separately) due to the nature of the specific problem considered here. Another open question relates to the influence of container shape. Although it has been proven here that the patterning behavior does not depend significantly on it (longitudinal rolls being selected over the entire space of parameters) and that the main impact of a variation in the aspect ratio is limited to a modification of the transverse roll extension, additional care shall be put to discern separately the role played by the container aspect ratio and its shape. The latter might indeed be the root cause of the differences observed in terms of monotonic or non-monotonic nature of the curves providing the relationship between the roll wavelength and the longitudinal coordinate.

Author Contributions: Conceptualization, M.L.; methodology W.W.; software, M.L.; formal analysis, M.L. and W.W.; investigation, W.W.; data curation, W.W. and M.L.; writing—original draft preparation, M.L.; writing—review and editing, M.L.; visualization, W.W.; supervision, M.L. All authors have read and agreed to the published version of the manuscript.

Funding: This research received no external funding.

Data Availability Statement: The data presented in this study are available on request from the corresponding author.

Conflicts of Interest: The author declares no conflict of interest.

References

1. Markham, B.L.; Rosenberger, F. Diffusive-convective vapor transport across horizontal and inclined rectangular enclosures. *J. Cryst. Growth* **1984**, *67*, 241–254. [CrossRef]
2. Bachran, A.; Reinshaus, P.; Seifert, W. Influence of Thermal Processing Parameters and Material Properties on Velocity Configurations in Semiconductor Melts during the Vertical Bridgman Growth Technique. *Cryst. Res. Technol.* **1998**, *33*, 27–36. [CrossRef]
3. Mizev, A.I.; Schwabe, D. Convective instabilities in liquid layers with free upper surface under the action of an inclined temperature gradient. *Phys Fluids* **2009**, *21*, 112102. [CrossRef]
4. Jones, A.D.W. Spoke patterns. *J. Cryst. Growth* **1983**, *63*, 70–76. [CrossRef]
5. Coriell, S.R.; McFadden, G.B.; Boisvert, R.F.; Sekerka, R.F. Effect of a forced Couette flow on coupled convective and morphological instabilities during unidirectional solidification. *J. Cryst. Growth* **1984**, *69*, 15–22. [CrossRef]
6. Webb, B.W.; Viskanta, R. Natural-convection-dominated melting heat transfer in an inclined rectangular enclosure. *Int. J. Heat Mass Transf.* **1986**, *29*, 183–192. [CrossRef]
7. Forth, S.A.; Wheeler, A.A. Coupled convective and morphological instability in a simple model of the solidification of a binary alloy, including a shear flow. *J. Fluid Mech.* **1992**, *236*, 61–94. [CrossRef]
8. Lappa, M. On the Formation and Propagation of Hydrothermal waves in Solidifying Liquid Layers. *Comput. Fluids* **2018**, *172*, 741–760. [CrossRef]
9. Salgado Sanchez, P.; Ezquerro, J.M.; Fernandez, J.; Rodriguez, J. Thermocapillary effects during the melting of phase-change materials in microgravity: Steady and oscillatory flow regimes. *J. Fluid Mech.* **2021**, *908*, A20. [CrossRef]
10. Salgado Sanchez, P.; Porter, J.; Ezquerro, J.M.; Tinao, I.; Laverón-Simavilla, A. Pattern selection for thermocapillary flow in rectangular containers in microgravity. *Phys. Rev. Fluids* **2022**, *7*, 053502. [CrossRef]
11. Lappa, M. *Thermal Convection: Patterns, Evolution and Stability*; John Wiley & Sons, Ltd.: Chichester, UK, 2009.
12. Zhang, J.; Sekimoto, A.; Okano, Y.; Dost, S. Numerical simulation of thermal-solutal Marangoni convection in a shallow rectangular cavity with mutually perpendicular temperature and concentration gradients. *Phys. Fluids* **2020**, *32*, 102108. [CrossRef]
13. Boura, A.; Gebhart, B. The stability of a vertical flow which arises from combined buoyancy modes. *AIChE* **1976**, *22*, 94–102. [CrossRef]
14. Qin, T.; Grigoriev, R.O. A numerical study of buoyancy-Marangoni convection of volatile binary fluids in confined geometries. *Int. J. Heat Mass Transf.* **2018**, *127*, 308–320. [CrossRef]
15. Lipps, F.B. Two-dimensional numerical experiments in thermal convention with vertical shear. *J. Atm. Sci.* **1971**, *28*, 3–19. [CrossRef]
16. Thorpe, S.A. Transitional phenomena and the development of turbulence in stratified fluids: A review. *J. Geophys. Res.* **1987**, *92*, 5231–5248. [CrossRef]

17. Farrow, D.E.; Patterson, J.C. On the stability of the near shore waters of a lake when subject to solar heating. *Int. J. Heat Mass Transf.* **1993**, *36*, 89–100. [CrossRef]
18. Richter, F.M. Convection and the large-scale circulation of the mantle. *J. Geophys. Res.* **1973**, *78*, 8735–8745. [CrossRef]
19. Weber, J.E. On the stability of thermally driven shear flow heated from below. *J. Fluid Mech.* **1978**, *87*, 65–84. [CrossRef]
20. Cliffe, K.A.; Winters, K.H. A numerical study of the cusp catastrophe for Bénard convection in tilted cavities. *J. Comput. Phys.* **1984**, *54*, 531–534. [CrossRef]
21. Mizushima, J.; Adachi, T. Structural Stability of the Pitchfork Bifurcation of Thermal Convection in a Rectangular Cavity. *J. Phys. Soc. Jpn.* **1995**, *64*, 4670–4683. [CrossRef]
22. Clever, R.M.; Busse, F.H. Instabilities of longitudinal convection rolls in an inclined layer. *J. Fluid Mech.* **1977**, *81*, 107–125. [CrossRef]
23. Chen, Y.; Pearlstein, A.J. Stability of free-convection flows of variable-viscosity fluids in vertical and inclined slots. *J. Fluid Mech.* **1989**, *198*, 513–541. [CrossRef]
24. Shadid, J.N.; Goldstein, R.J. Visualization of longitudinal convection roll instabilities in an inclined enclosure heated from below. *J. Fluid Mech.* **1990**, *215*, 61–84. [CrossRef]
25. Busse, F.H.; Clever, R.M. Three-dimensional convection in an inclined layer heated from below. *J. Eng. Math.* **1992**, *26*, 1–19. [CrossRef]
26. Fujimura, K.; Kelly, R.E. Mixed mode convection in an inclined slot. *J. Fluid Mech.* **1993**, *246*, 545–568. [CrossRef]
27. Kaloni, P.N.; Qiao, Z. On the nonlinear stability of thermally driven shear flow heated from below. *Phys. Fluids* **1996**, *8*, 639. [CrossRef]
28. Daniels, K.E.; Bodenschatz, E.; Pesch, W.; Brausch, O. Pattern formation in inclined layer convection; Session QC28—Topics in Pattern Formation and Nonlinear Dynamics. In Proceedings of the APS Centennial Meeting, Atlanta, GA, USA, 20–26 March 1999; Available online: https://flux.aps.org/meetings/YR99/CENT99/abs/S6255001.html (accessed on 20 November 2022).
29. Daniels, K.E.; Plapp, B.B.; Bodenschatz, E. Pattern Formation in Inclined Layer Convection. *Phys. Rev. Lett.* **2000**, *84*, 5320–5323. [CrossRef]
30. Daniels, K.E.; Brausch, O.; Pesch, W.; Bodenschatz, E. Competition and bistability of ordered undulations and undulation chaos in inclined layer convection. *J. Fluid Mech.* **2008**, *597*, 261–282. [CrossRef]
31. Tao, J.; Busse, F.H. Oblique roll instability in inclined buoyancy layers. *Eur. J. Mech. B/Fluids* **2009**, *28*, 532–540. [CrossRef]
32. Subramanian, P.; Brausch, O.; Daniels, K.E.; Bodenschatz, E.; Schneider, T.M.; Pesch, W. Spatio-temporal patterns in inclined layer convection. *J. Fluid Mech.* **2016**, *794*, 719–745. [CrossRef]
33. Nepomnyashchy, A.A.; Simanovskii, I.B.; Braverman, L.M. Stability of thermocapillary flows with inclined temperature gradient. *J. Fluid Mech.* **2001**, *442*, 141–155. [CrossRef]
34. Ueno, I.; Kurosawa, T.; Kawamura, H. Thermocapillary Convection in Thin Liquid Layer with Temperature Gradient Inclined to Free Surface. In Proceedings of the IHTC12, Grenoble, France, 18–23 August 2002.
35. Shklyaev, O.E.; Nepomnyashchy, A.A. Thermocapillary flows under an inclined temperature gradient. *J. Fluid Mech.* **2004**, *504*, 99–132. [CrossRef]
36. Patne, R.; Agnon, Y.; Oron, A. Thermocapillary instabilities in a liquid layer subjected to an oblique temperature gradient. *J. Fluid Mech.* **2021**, *906*, A12. [CrossRef]
37. Cerisier, P.; Pantaloni, J.; Finiels, G.; Amalric, R. Thermovision applied to Benard-Marangoni convection. *Appl. Opt.* **1982**, *21*, 2153–2159. [CrossRef]
38. Cerisier, P.; Rahal, S.; Azuma, H. Pattern dynamics of the Bénard-Marangoni instability in a medium aspect ratio container. *J. Phys. Conf. Ser.* **2007**, *64*, 012004. [CrossRef]
39. Ismagilov, R.F.; Rosmarin, D.; Gracias, D.H.; Stroock, A.D.; Whitesides, G.M. Competition of intrinsic and topographically imposed patterns in Bénard–Marangoni convection. *Appl. Phys. Lett.* **2001**, *79*, 439–441. [CrossRef]
40. Chauvet, F.; Dehaeck, S.; Colinet, P. Threshold of Bénard-Marangoni instability in drying liquid films. *EPL Europhys. Lett.* **2012**, *99*, 34001. [CrossRef]
41. Wang, J.M.; Liu, G.H.; Fang, Y.L.; Li, W.K. Marangoni effect in nonequilibrium multiphase system of material processing. *Rev. Chem. Eng.* **2016**, *32*, 551–585. [CrossRef]
42. Wu, D.; Duan, L.; Kang, Q. Wavenumber Selection by Bénard–Marangoni Convection at High Supercritical Number. *Chin. Phys. Lett.* **2017**, *34*, 054702. [CrossRef]
43. Sobac, B.; Colinet, P.; Pauchard, L. Influence of Bénard–Marangoni instability on the morphology of drying colloidal films. *Soft Matter* **2019**, *15*, 2381–2390. [CrossRef]
44. Tönsmann, M.; Scharfer, P.; Schabel, W. Critical Solutal Marangoni Number Correlation for Short-Scale Convective Instabilities in Drying Poly(vinyl acetate)-Methanol Thin Films. *Polymers* **2021**, *13*, 2955. [CrossRef]
45. Gillon, P.; Homsy, G.M. Combined thermocapillary-buoyancy convection in a cavity: An experimental study. *Phys. Fluids* **1996**, *8*, 2953–2963. [CrossRef]
46. Braunsfurth, M.G.; Homsy, G.M. Combined thermocapillary-buoyancy convection in a cavity. Part II. An experimental study. *Phys. Fluids* **1997**, *9*, 1277–1286. [CrossRef]

47. Burguete, J.; Mukolobwiez, N.; Daviaud, N.; Garnier, N.; Chiffaudel, A. Buoyant-thermocapillary instabilities in extended liquid layers subjected to a horizontal temperature gradient. *Phys. Fluids* **2001**, *13*, 2773–2787. [CrossRef]
48. Pelacho, M.A.; Garcimartin, A.; Burguete, J. Travel instabilities in lateral heating. *Int. J. Bifurcat. Chaos* **2001**, *11*, 2881–2886. [CrossRef]

fluids

MDPI

Article

Wall-Modeled and Hybrid Large-Eddy Simulations of the Flow over Roughness Strips

Teresa Salomone [1,2,*], Ugo Piomelli [1] and Giuliano De Stefano [2]

[1] Department of Mechanical and Materials Engineering, Queen's University, Kingston, ON K7L 3N6, Canada
[2] Engineering Department, University of Campania Luigi Vanvitelli, 81031 Aversa, Italy
* Correspondence: teresa.salomone@queensu.ca or teresa.salomone@unicampania.it

Abstract: The flow over alternating roughness strips oriented normally to the mean stream is studied using wall-modeled large-eddy simulations (WMLES) and improved delayed detached-eddy simulations (IDDES) (a hybrid method solving the Reynolds-averaged Navier–Stokes (RANS) equations near the wall and switching to large-eddy simulations (LES) in the core of the flow). The calculations are performed in an open-channel configuration. Various approaches are used to account for roughness by either modifying the wall boundary condition for WMLES or the model itself for IDDES or by adding a drag forcing term to the momentum equations. By comparing the numerical results with the experimental data, both methods with both roughness modifications are shown to reproduce the non-equilibrium effects, but noticeable differences are observed. The WMLES, although affected by the underlying equilibrium assumption, predicts the return to equilibrium of the skin friction in good agreement with the experiments. The velocity predicted by the IDDES does not have memory of the upstream conditions and recovers to the equilibrium conditions faster. Memory of the upstream conditions appears to be a critical factor for the accurate computational modeling of this flow.

Keywords: turbulent flows; large-eddy simulation; Reynolds-averaged Navier–Stokes; wall model; delayed detached-eddy simulation; roughness

Citation: Salomone, T.; Piomelli, U.; De Stefano, G. Wall-Modeled and Hybrid Large-Eddy Simulations of the Flow over Roughness Strips. *Fluids* **2023**, *8*, 10. https://doi.org/10.3390/fluids8010010

Academic Editor: Mehrdad Massoudi

Received: 10 November 2022
Revised: 17 December 2022
Accepted: 20 December 2022
Published: 27 December 2022

1. Introduction

Roughness occurs in many applications in engineering and the natural sciences, such as in pipes, turbine blades, atmospheric boundary layers and plant canopies. Because of its practical importance, the effects of roughness on flow have been studied for many years, starting from the seminal work in [1], which was reviewed in [2,3] and can be summarized as (1) increased drag [1,4], (2) decreased anisotropy of the Reynolds stresses [5], (3) modification of the near-wall region through break-up of the streaky structures and (4) the presence of an additional production mechanism for the turbulent kinetic energy [2,6].

In many cases, roughness is not uniform; rather, regions of varying roughness heights are adjacent to each other. This occurs, for instance, in boundary layers over plant canopies or mixed terrain, where built areas, woods and planted fields can be present. In all these cases, a sudden change in the wall boundary condition (BC) occurs that modifies the flow, and its effects can be significant. The simplest type of heterogeneous roughness is represented by the abrupt transition from a two-dimensional rough patch oriented normally to the flow to a smooth surface or from a smooth to a rough patch. Although very simple, this particular configuration is compelling because it can be found very often, for example, in atmospheric boundary layers [7,8] or in meteorological flows [9]. Downstream of the transition, an internal boundary layer is formed that can be separated into two regions: an equilibrium inner layer, in which the flow has adjusted to the change of the BC, and an outer one, in which the flow still has memory of the different upstream BC.

Several investigators have studied this flow either experimentally [8,10–14] or numerically [15–19]. A common observation is that after the transition, the flow variables return to

equilibrium at different downstream locations. For instance, the skin friction adapts more rapidly to the new conditions than the mean velocity and Reynolds stresses.

Experimentally, it was found that the skin friction measurement is very strongly affected by the technique used. With an indirect method that infers the wall shear stress from outer flow data, two sources of error arise: first, the use of equilibrium relations is not justified (the Clauser plot, for instance), and second, if the data are taken from locations outside the equilibrium region of the internal boundary layer, the effect of the transition might not propagate yet to the measurement location. Additionally, if the measurements are taken very close to the wall, then in the equilibrium region, the viscous component of the drag can be evaluated, but the form drag prediction is unreliable.

Wall-resolved numerical simulations such as direct numerical simulations (DNSs) and large-eddy simulations (LESs) can provide more insights than experiments, since the flow inside the roughness sublayer is known and the contributions of both the form and viscous drags to the skin friction can be evaluated. However, these simulations are limited to low or intermediate Reynolds numbers by their high computational cost, which is particularly significant due to the opposite requirements that the roughness size should be small enough to avoid blockage but large enough to achieve the fully rough regime [3].

The first fully resolved simulation of the flow over a rough-to-smooth transition was performed by Ismail et al. [19], who confirmed the long recovery region required to reach self-similarity. Li et al. [14] complemented their experimental database with a fully resolved simulation, demonstrating that a good estimation of the skin friction recovery in the vicinity of the transition can only be attained by using direct methods.

Unfortunately, the engineering need for the prediction of high Reynolds number flows cannot be met by computationally expensive wall-resolved calculations, while turbulence models for the affordable Reynolds-averaged Navier–Stokes (RANS) simulations have difficulties in predicting flows that are strongly out of equilibrium (such as for heterogeneous roughness). Furthermore, typical corrections used to include the effects of roughness [20–24] were developed using equilibrium assumptions (typically fully rough flow in the absence of pressure gradient) and are therefore not very accurate in non-equilibrium rough wall boundary layers [25].

Methods that combine the LES approach in the outer region of the flow with a simpler methodology near solid surfaces are gaining popularity, due to their ability to capture the outer layer non-equilibrium naturally with much lower computational costs compared with wall-resolved calculations. These savings, of course, are at the expense of additional modeling. The two most common techniques of this type are wall-modeled large-eddy simulation (WMLES) and hybrid RANS/LES methods. In the first case, the outer layer is obtained from the solution of the filtered Navier–Stokes equations that govern LES, and approximate methods (for instance, correlations based on the log law or other shape functions) are used to derive the wall stress from the outer layer data. In hybrid RANS/LES methods, the character of the turbulence model changes in such a way that the RANS approach is used near the wall while switching to LES at some distance from the surface. Corrections for roughness have been developed for both of these approaches. Comprehensive reviews of these methods can be found in [26–29] for WMLES and [30,31] for hybrid RANS/LES. Although they tend to be based on equilibrium arguments, these methods may be more accurate than their RANS analogs, since the inner layer eddies have shorter time scales than the outer layer ones and tend toward equilibrium faster, while the non-equilibrium effects are accounted for by the outer layer LES [28].

Several investigators have performed WMLES of the flow over heterogeneous roughness and strips normal to the flow direction in particular, which are the focus of the present study. Bou-Zeid et al. [15,32] imposed locally the law of the wall to evaluate the wall shear stress from the LES field. They pointed out how surface heterogeneity highly affects the flow, inducing sharp variations in the velocity profiles and discontinuities in the shear stress. Saito and Pullin [17] instead derived an ordinary differential equation for the friction velocity based on filtered quantities supplied by the outer LES. Their work was centered on the

effects of different Reynolds numbers and roughness heights for a smooth-rough-smooth surface arrangement. They concluded that in both smooth-to-rough and rough-to-smooth transitions, a slower initial response in the recovery of the wall shear stress was found when increasing the Reynolds number, whereas the response was faster when increasing the roughness height. Chamorro and Porté-Agel [8] proposed a new model to estimate the velocity profile over a rough-to-smooth transition, using a weighted average between two limiting logarithmic profiles. The first one corresponded to the upstream equilibrium velocity, while the second log law was adjusted to the downstream local flow conditions after recovery. This methodology has the potential to be implemented as a BC for the LES field.

In the investigations described above, only one type of modeling approach for the wall BC was considered, but of crucial importance is understanding how different modeling approaches predict the flow behavior in step changes in surface roughness, particularly identifying the limitations of the different methodologies. The purpose of the present work is to complement the above investigations by assessing the accuracy of two typical techniques, which are WMLES and hybrid RANS/LES, in predicting the sudden transition from a smooth surface to a rough one, and vice versa. In addition to this, roughness is included using two different methods: the modification of either the log law or model equations and the use of a localized drag force [33]. Because of the independence of the drag model from the particular turbulence model used, this technique is particularly attractive, since it does not require ad hoc adjustments when the model for the resolved scales is changed.

In the following, the problem formulation, including model equations and roughness corrections, will be presented first. The numerical method and BCs used will then be described, and the numerical results will be discussed. Our final conclusions and directions for future work will close the paper.

2. Methodology

2.1. Governing Equations

The governing equations for incompressible flow can be formally written the same way for both LES and unsteady RANS approaches:

$$\frac{\partial \overline{u}_i}{\partial x_i} = 0 \tag{1}$$

$$\frac{\partial \overline{u}_i}{\partial t} + \frac{\partial}{\partial x_j}(\overline{u}_i \overline{u}_j) = -\frac{\partial \overline{P}}{\partial x_i} + \nu \frac{\partial^2 \overline{u}_i}{\partial x_j \partial x_j} - \frac{\partial \tau_{ij}}{\partial x_j}\,, \tag{2}$$

where the overbar represents either the LES spatial filtering or the Reynolds-averaging operation. In the above equations, $\overline{u}_i$ stands for the resolved velocity, $\overline{P} = \overline{p}/\rho$ is the (resolved) kinematic pressure, ν is the constant kinematic viscosity and $\tau_{ij} = \overline{u_i u_j} - \overline{u}_i \overline{u}_j$ represents the residual (unresolved) stresses. The latter have to be interpreted as either the subfilter-scale (SFS) stresses in LES or the Reynolds stresses in unsteady RANS simulations and need to be modeled.

2.2. Turbulence Models

The unknown residual stresses are normally approximated using an eddy viscosity assumption for the deviatoric part of the stress tensor:

$$\tau_{ij}^d \equiv \tau_{ij} - \frac{1}{3}\delta_{ij}\tau_{kk} = -2\nu_T \overline{S}_{ij}\,, \tag{3}$$

where

$$\overline{S}_{ij} = \frac{1}{2}\left(\frac{\partial \overline{u}_i}{\partial x_j} + \frac{\partial \overline{u}_j}{\partial x_i}\right) \tag{4}$$

is the resolved strain rate tensor. For incompressible flows, the isotropic part of the stress tensor may be absorbed into an effective resolved pressure field. The present WMLES method uses the eddy viscosity SFS model proposed by Vreman [34], which was constructed in such a way that the modeled dissipation is relatively small in the near-wall regions. The standard value of the model constant was used.

The hybrid RANS/LES method used in this work follows the improved delayed detached-eddy simulation (IDDES) approach [35]. The IDDES in its formulation with the Spalart–Allmaras (SA) turbulence model was used, in which a transport equation for the eddy viscosity ν_T is solved [36]. The RANS and LES fields are coupled by introducing a hybrid turbulent length scale, which is modified as follows. Near the wall, according to the SA model, the distance from the wall is used, whereas in the outer layer, a blending function is formulated that allows shifting from the RANS levels of the eddy viscosity in the near-wall region to the LES levels of the eddy viscosity in the core of the flow. The two regions are separated by a zone where the eddy viscosity is very low to allow the rapid generation of eddies. More details on the IDDES formulation can be found in the original paper [37].

2.3. Numerical Model

The simulations were conducted using the open-channel configuration sketched in Figure 1, where x, y and z represent the streamwise, wall-normal, and spanwise directions, respectively. The domain size was $L_x \times L_y \times L_z = 56\delta \times \delta \times 14\delta$, where δ is the open-channel height and the rough strip, whose length is L_r, occupies 66% of the domain. The present geometry corresponds to the experimental set-up in [14], where a spatially developing boundary-layer flow was examined rather than the periodic open channel used here. The Reynolds number based on the bulk velocity was $Re_b = U_b\delta/\nu = 121{,}000$, which roughly corresponds to the experimental value at the rough-to-smooth interface. Following the notation used in [14], the transition location was indicated by x_o, and $\widehat{x} = x - x_o$ stands for the relative streamwise position.

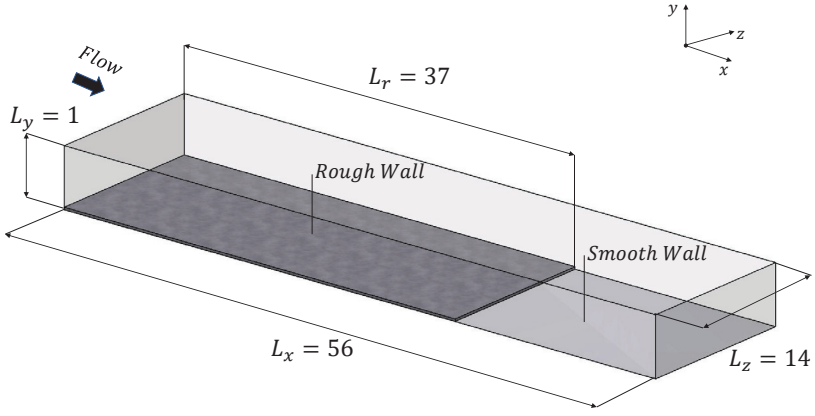

Figure 1. Sketch of the computational domain (not to scale).

A fractional step method was used to advance the governing equations in time. The Crank–Nicolson time advancement was used for the wall-normal diffusion, and a third-order Runge–Kutta scheme was used for the remaining terms. Spatial discretization was performed using conservative second-order finite differences on a staggered grid. In the WMLES, the spatial grid was uniform and isotropic, while for the IDDES, it was suitably stretched in the wall-normal direction, with the first grid point being located at $y^+ < 1$ (where a plus denotes scaling in the inner units).

Periodic BCs were applied in the homogeneous streamwise and spanwise directions, simulating an infinite domain of alternating rough and smooth strips, while a symmetry

condition was imposed at the top boundary. For IDDES, no-slip conditions were applied at the wall. For WMLES, the wall stress was obtained, given the velocity at the interface, by satisfying the log law of the wall. Details will be given in the next subsection.

2.4. Roughness Modeling

Depending on the particular approach followed, different methods were used to incorporate the effect of roughness on the flow. One consisted of modifying either the model for the unresolved scales (for IDDES) or the wall BC (for WMLES). The other was based on the addition of a drag force to the resolved momentum in Equation (2). Aupoix and Spalart [23] proposed two different extensions of the SA model to include the effect of roughness. The so-called "Boeing extension", which is employed here, consists of a change in the BC for the eddy viscosity field, which must satisfy the following relation at the wall:

$$\frac{\partial \tilde{\nu}}{\partial n} = \frac{\tilde{\nu}}{d}\,, \tag{5}$$

instead of $\tilde{\nu} = 0$, where $\tilde{\nu}$ is the modified eddy viscosity used in the SA model (which is proportional to ν_T). In addition, the length-scale d must be modified to account for the fact that $y = 0$ corresponds to a virtual wall where the turbulent quantities are non-zero. They suggested using $d = d_o + y$, where $d_o = 0.03\, k_s$ is the distance between the virtual wall and the bottom of the roughness sublayer and k_s is the equivalent sand grain roughness height. In the WMLES case, as mentioned above, the wall stress is obtained using an approximate integration of the equations of motion between the inner and outer layer interface at $y = y_{if}$ and the wall [26]. We follow the simplest (and most common) approach (i.e., the use of the logarithmic law of the wall) [38]. If the wall is rough, a roughness function $\Delta\mathcal{U}^+ = f(k_s^+)$ is introduced to account for the increased wall stress caused by the form drag on the roughness elements. Therefore, the logarithmic law of the wall takes the following forms for the smooth and the rough strips, respectively:

$$u_{if}^+ = \frac{1}{\kappa}\log y_{if}^+ + B \quad (\text{for } \widehat{x} > 0)\,, \tag{6}$$

$$u_{if}^+ = \frac{1}{\kappa}\log \frac{y_{if}}{k_s} + 8.5 \quad (\text{for } \widehat{x} < 0)\,, \tag{7}$$

where the subscript if denotes quantities evaluated at the inner and outer layer interface, which is located at $y = 0.05\delta$. Note that y_{if} exceeds the location of the first grid point to allow better development of the near-wall eddies [39]. In the above expressions, $\kappa = 0.41$ is the von Kàrmàn constant, and $B = 5.0$. The present roughness height k_s matches the experimental value at the transition location $k_s^+ \simeq 130$ [14], which results in $\Delta\mathcal{U}^+ \simeq 8.2$ for the roughness function.

As an alternative, one can employ the drag model recently proposed in [33]. Roughness effects are included by adding a forcing term to the right-hand side of the Equation (2). The drag force, which is active in a volume region adjacent to the wall, referred to as the "roughness zone", is defined by

$$f_i = \alpha_{ij}|\mathbf{u}_{rz}|u_{rz,j} \tag{8}$$

where $\alpha_{ij} = \mathrm{diag}\{\alpha_t, \alpha_t, \alpha_n\}$ determines the force intensity, with the subscripts t and n denoting the wall-tangential and wall-normal components, respectively. Note that the roughness zone extends in the wall-normal direction up to a distance corresponding to the mean peak height of the rough surface. In this study, the normal component was set to zero, and the tangential component was chosen to give the same roughness function obtained by using the equivalent sand grain roughness height modification. Practically, $\alpha_{ij} = \mathrm{diag}\{\alpha, \alpha, 0\}$ was prescribed.

By combining the two turbulence models and the two roughness models introduced above, four different methods were tested in this work. In the following discussion, WMLES-k_s and IDDES-k_s denote the simulations with roughness model modifications,

whereas WMLES-DM and IDDES-DM are the calculations that use the drag model. In addition, angle brackets will denote quantities averaged over time and in the spanwise direction, with a prime representing the resolved fluctuations.

3. Results

3.1. Grid Convergence Study

A grid convergence study was conducted for the WMLES. Several meshes were used, whose parameters are listed in Table 1. The corresponding mean velocity profiles at the ends of the rough and smooth strips are shown in Figure 2. The medium grid was considered to have converged and was used to generate the results presented in the following section.

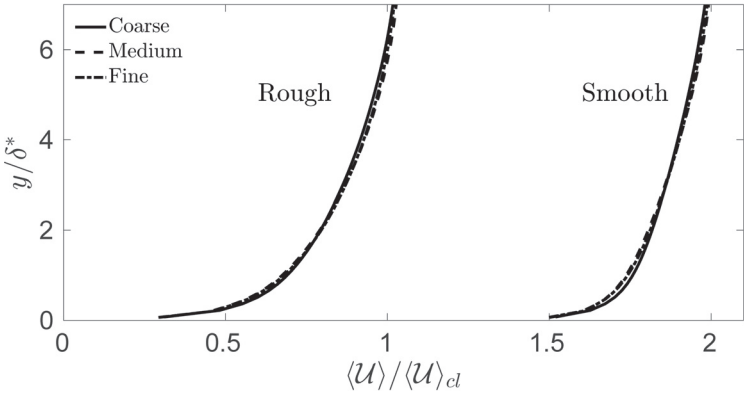

Figure 2. WMLES grid convergence study: mean velocity profiles at 95% of the length of the (**left**) rough and (**right**) smooth strips. Normalization is carried out with the center line velocity $\langle \mathcal{U} \rangle_{cl}$ and the displacement thickness δ^*.

Regarding the IDDES, a rigorous grid convergence study could not be carried out since the character of the solution (in particular at the RANS/LES interface) depended on the grid size. Then, the same resolution as the grid-converged WMLES was used in the wall-parallel directions while increasing the number of points in the wall-normal direction such that $y^+ < 1$ for the first grid point away from the wall. The maximum grid spacing (close to the top boundary) was 0.025 δ, which was slightly larger than that of WMLES but fine enough to resolve the outer layer structures.

Table 1. WMLES grid-convergence study: summary of mesh parameters.

Resolution	Grid Points	$\Delta x = \Delta z$	$\Delta x_r^+ = \Delta z_r^+$ [1]	$\Delta x_s^+ = \Delta z_s^+$ [1]
Coarse	$1024 \times 60 \times 256$	0.055	400	279
Medium	$1792 \times 60 \times 448$	0.031	219	155
Fine	$2240 \times 60 \times 560$	0.025	175	124

[1] The subscripts r and s represent values at the end of rough and smooth strips, respectively.

3.2. Skin Friction

Figure 3 shows the skin friction coefficient predicted by the four models. In all cases, the sudden increase and decrease in C_f at the interface was predicted. However, some discrepancies existed. At the end of the rough strip, the WMLES were in good agreement with each other, reflecting the fact that both the wall BC and the drag model were calibrated using fully developed rough channel data. There was a significant difference between the IDDES results, however, which was probably due to the sensitivity of the drag model constant α to the grid resolution when coupled with IDDES. This parameter was actually calibrated in reference simulations for which coarser resolutions (but sufficient for achieving

grid convergence) were used. Here, the grid was finer in the streamwise direction to resolve the surface discontinuity, and a new calibration appears to be necessary. In IDDES, the grid plays a very important role because of the definition of the model's length scale, whose changes affect not only the eddy viscosity level in the outer layer but also (and more importantly) the location of the RANS/LES interface.

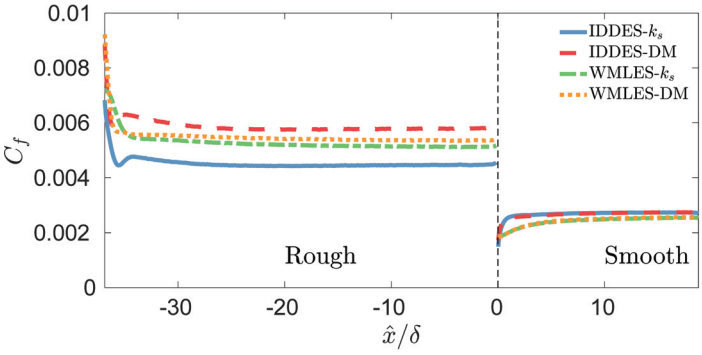

Figure 3. Skin friction coefficient development over rough and smooth strips.

The recovery length on the smooth strip predicted by the IDDES was much shorter than that obtained from the WMLES. This issue will be discussed further momentarily. After the smooth-to-rough interface, the IDDES showed a small dip that was not present in the WMLES. A similar undershoot was found in the WMLES of [17], becoming more prominent when the Reynolds number or the roughness height were increased. This phenomenon was due to the global mass conservation that was enforced in the channel. To explain this behavior, the mean velocity profile with the IDDES-k_s model at four locations around the dip region was compared with that at the reference location on the rough strip, which was close to fully developed rough conditions. Before the dip (Figure 4a), the velocity was higher than the reference throughout the layer, still resembling the smooth strip profile. At the dip itself (Figure 4b), the mean velocity profile in the wall layer matched the reference location, whereas the outer layer, which adapted more slowly to the new surface conditions, was still accelerated. After this location, the outer layer begins to approach a fully developed rough state, as is shown in Figure 4c. The mass flux is maintained to be constant, and thus the velocity decrease in the outer layer must be balanced by a velocity increase elsewhere. Since the wall region has a faster response to disturbances propagating from the outer layer, the velocity increase takes place in the wall region, resulting in a higher velocity gradient at the wall and the subsequent formation of the dip in the skin friction coefficient. After the dip (Figure 4d), the inner and outer layer recovered at the same speed, attaining self-preservation. The aforementioned effects all took place below the WMLES interface ($y/\delta = 0.05$), which explains why with this methodology, the dip was not present.

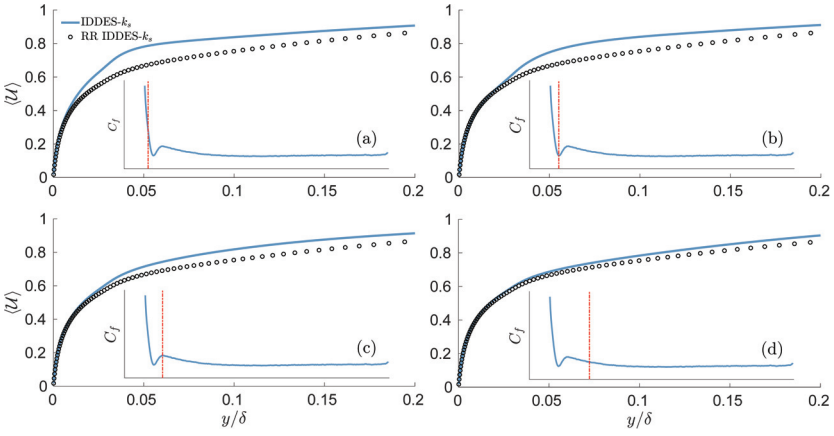

Figure 4. IDDES-k_s model: mean velocity profile at the locations shown in the insets, compared with the mean velocity profile at the rough reference location. The different positions are located: (**a**) before the dip, (**b**) at the dip, (**c**) at the crest, (**d**) after the crest.

Figure 5 compares the skin friction coefficient on the smooth strip with the experimental data [8,14]. Here, the skin friction coefficient was normalized by $C_{f,ref}$ (i.e., the value of C_f at 95% of the smooth strip). The position was normalized by either the open channel height δ in the numerical simulations or the boundary layer thickness δ_{bl} at the transition location in the experiments. It is worth noting a substantial difference in the C_f prediction between the two experimental datasets. The experiments by Chamorro and Porté-Agel [8] were carried out at a higher Reynolds number of $Re_\infty = \mathcal{U}_\infty \delta_{bl}/\nu \simeq 273,000$ (where $\mathcal{U}_\infty$ is the freestream velocity), while the equivalent sand grain roughness height was $k_s^+ \simeq 479$ (evaluated at the end of the rough-to-smooth transition). The experiments by Li et al. [14], on the other hand, were performed at $Re_\infty \simeq 110{,}000$ with $k_s^+ \simeq 130$ at the same location. In addition, the measurement techniques were different, as near-wall hot wire measurements were performed in [8], whereas oil-film interferometry (OFI) was used in [14]. Because both experimental techniques take information within the viscous sublayer, they were expected to give approximately the same results. Therefore, differences may be attributed to the discrepancy in the Reynolds number and equivalent sand grain roughness height, as was also conjectured by Li et al. [14]. In the present simulations, the freestream Reynolds number at the transition location was $Re_\infty = \mathcal{U}_\infty \delta/\nu \simeq 142{,}000$ (where for a channel flow, $\mathcal{U}_\infty$ is the centerline velocity), and as mentioned in the previous section, $k_s^+ = 130$. In this way, since the current flow conditions were much closer to those used in [14], one would expect better agreement with this experimental dataset.

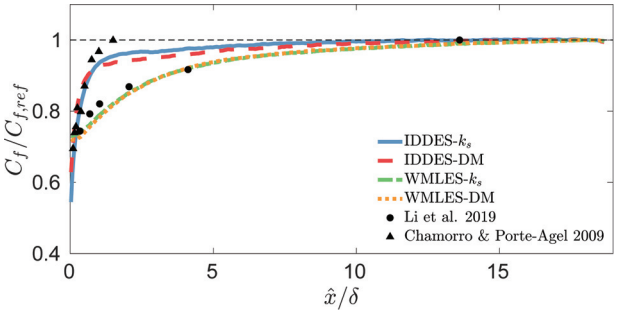

Figure 5. Normalized skin friction coefficient on the smooth strip compared with experimental results [8,14].

The normalization by $C_{f,ref}$ removed the discrepancies due to errors in the prediction of the fully developed roughness, highlighting the response of the models to the change in the BC. The roughness modeling did not affect the recovery length significantly. The WMLES accurately reproduced the recovery of the skin friction coefficient at the flow conditions in [14]. The IDDES predictions, however, agreed better with the higher-*Re* results. The reason for this difference will be discussed later. Another distinction between the IDDES and WMLES is the fact that in the WMLES, the wall stress depended on the velocity at the interface. The BC change did not affect the velocity at the interface immediately but required some downstream distance to penetrate to the height of the interface. In other words, with WMLES, the wall stress has memory of the upstream flow. In the IDDES, on the other hand, the BC transition was immediately felt throughout the layer because of the model modifications. This issue will be discussed in Section 3.4. Furthermore, as will be shown later, the Reynolds shear stress predicted by the IDDES was higher than that obtained by the WMLES, as the enhanced mixing caused the mean velocity profile to be flatter and the wall stress to increase.

3.3. Mean Velocity

The mean velocity profiles are shown in Figures 6 and 7. In the first figure, the velocity is plotted in the outer units (i.e., normalized by the center-line velocity $\langle \mathcal{U} \rangle_{cl}$) as a function of y/δ^*. Four streamwise locations after the transition were considered. The closer prediction of the skin friction coefficient obtained with WMLES was accompanied by better agreement with the experimental data in [14] in terms of the mean velocity profiles as well. The velocity profiles obtained from the IDDES were flatter, reflecting the overpredition of the wall stress due to its faster recovery (observed in Figure 5). In particular, a region of a higher velocity is visible near the wall (Figure 6). Regarding roughness modeling, little difference was observed between the drag force method and the model modifications. The mean velocity profiles in the inner units, i.e., $\langle \mathcal{U} \rangle^+ = \langle \mathcal{U} \rangle / u_\tau$ and $y^+ = y u_\tau / \nu$, where u_τ represents the local friction velocity depending on the x position, are shown in Figure 7. Apparently, in the experiments, the flow preserved some memory of the rough wall condition even after the transition, as evidenced by the presence of a downward displacement of the logarithmic layer (the roughness function) at the first location. The boundary condition in Equation (6), on the other hand, forced the WMLES to match the standard log law at the interface. As a consequence, the reversion to the equilibrium log law was immediate. Above the interface, however, the velocity profile was parallel to the experimental one, reflecting the fact that the error was due to the incorrect wall stress prediction, while the outer flow was captured accurately. The IDDES did not suffer from the same constraint. However, the shift of the log law was not as significant as in the experiments, again indicating a faster recovery toward equilibrium.

3.4. Eddy Viscosity and Reynolds Stresses

To better understand the difference between the two different turbulence modeling approaches, in Figure 8, the contour maps of the normalized eddy viscosity $\langle \nu_T \rangle / \nu$ are shown. It should be pointed out that ν_T represents the subfilter-scale eddies only in the WMLES calculations, while it parameterized the effect of all the eddies in the RANS region of the IDDES, although only the subfilter ones in the outer LES zone. As far as IDDES are concerned, the roughness modifications employed by the IDDES-k_s enhanced the eddy viscosity level close to the wall. At the rough-to-smooth interface, the model changed abruptly as the roughness modifications were removed, resulting in a discontinuous eddy viscosity field. On the contrary, when the drag model was used for the IDDES-DM, the eddy viscosity smoothly varied across the interface. Very close to the wall, ν_T increased slightly because of the near-wall flow acceleration, which was due to the removal of the forcing term outside of the roughness zone. This change, which occurred suddenly, affected the model's length scale, which depended on both the grid size and the solution itself (see the discussion in Section 2 of [37]). Practically, for the IDDES-DM, the sudden change

in roughness modified the eddy viscosity indirectly (affecting the velocity, which in turn changed the length scale and thus ν_T). Therefore, the variation was weaker than that for the IDDES-k_s, where the model modifications directly affected the modeled eddy viscosity.

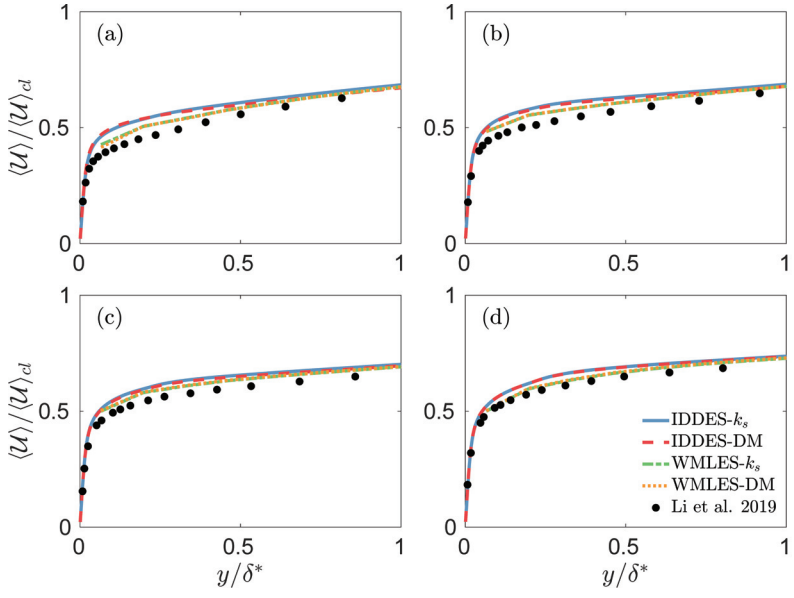

Figure 6. Mean velocity profiles in outer units at (**a**) 3%, (**b**) 10%, (**c**) 19% and (**d**) 63% of the length of the smooth strip compared with experimental results [14].

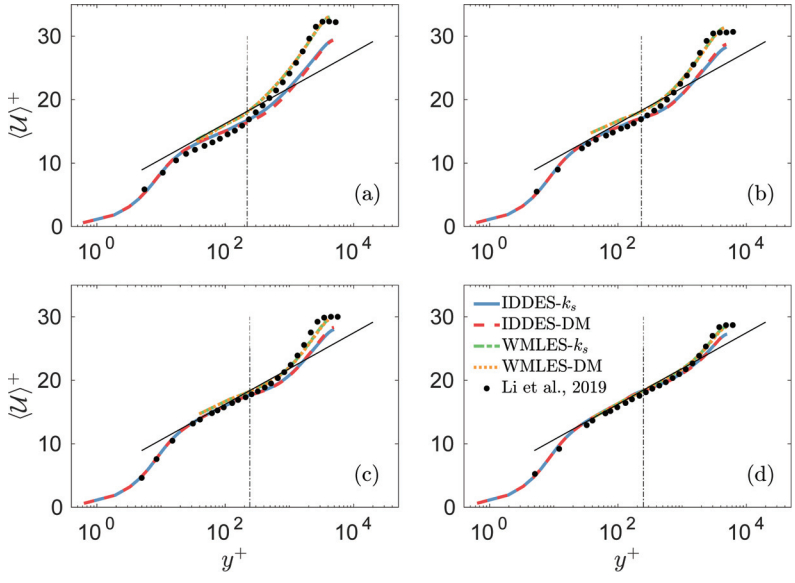

Figure 7. Mean velocity profiles in inner units at (**a**) 3%, (**b**) 10%, (**c**) 19% and (**d**) 63% of the length of the smooth strip. The thin line represents the log law (6), and the vertical dashed line represents the location of the inner/outer layer interface for WMLES [14].

In the WMLES, on the other hand, the eddy viscosity field was continuous, and a decrease was observed at the interface, reflecting the mean velocity changes. Note that the form of the eddy viscosity model did not change at the interface, and ν_T reacted only to the velocity changes. Most of these effects occurred below the inner/outer layer interface.

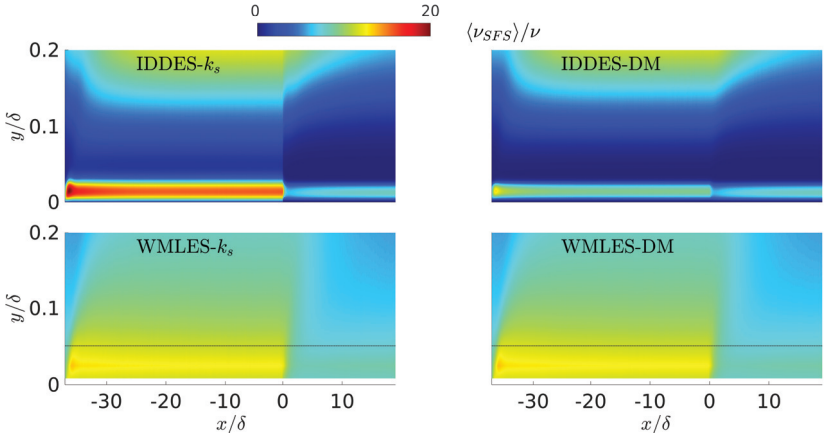

Figure 8. Contours of eddy viscosity normalized by the fluid viscosity. The horizontal dashed line indicates the location of the inner/outer layer interface for WMLES.

Furthermore, Figure 9 shows the eddy viscosity profiles near the rough-to-smooth interface at four different streamwise locations. At the end of the roughness strip, where a quasi-equilibrium rough wall flow condition was reached, the ν_T predicted by the IDDES-k_s was significantly higher than that for the IDDES-DM, as can be seen in Figure 9a. In fact, in the former case, the increased drag due to roughness was entirely accounted for by the wall shear stress definition:

$$\tau_w = (\nu + \nu_T) \frac{\partial \mathcal{U}}{\partial y}\bigg|_{y=0}, \tag{9}$$

where, since $\nu_T > 0$ at the wall, the modeled eddy viscosity leads to increased friction. On the other hand, for the drag-model case where $\nu_T = 0$ at the wall, the additional force (Equation (8)) supplies the drag due to the roughness elements, while the turbulence model is not directly modified. Since both approaches were calibrated using Nikuradze's data [1], they provided the same effective drag and the same velocity profile. Immediately after the interface, in the IDDES-k_s, the eddy viscosity at the wall changed from a finite value to zero, as illustrated in Figure 9b, and took on very low values, especially for $y/\delta \lesssim 0.01$. Since this region was in the RANS zone, a lower ν_T implied decreased total stress, which resulted in the flow acceleration near the wall (and led to the excessively rapid increase in C_f observed in Figure 5). Within a sort distance (less than half the height of a channel), as illustrated in Figure 9d, ν_T fell below the smooth wall value in the RANS region while it was relatively unchanged in the LES zone. This fact also contributed to the higher velocity further from the wall observed in Figure 6. For $\widehat{x}/\delta \gtrsim 1$, the value of ν_T predicted with the two approaches was the same, and the equilibrium smooth wall condition was achieved within 8δ. The WMLES, as observed before, had a much more gradual response to the change in the surface roughness, since the changed BC did not affect the outer flow for some distance. The fact that memory of the upstream conditions was maintained allowed a more accurate prediction of the eddy viscosity and velocity.

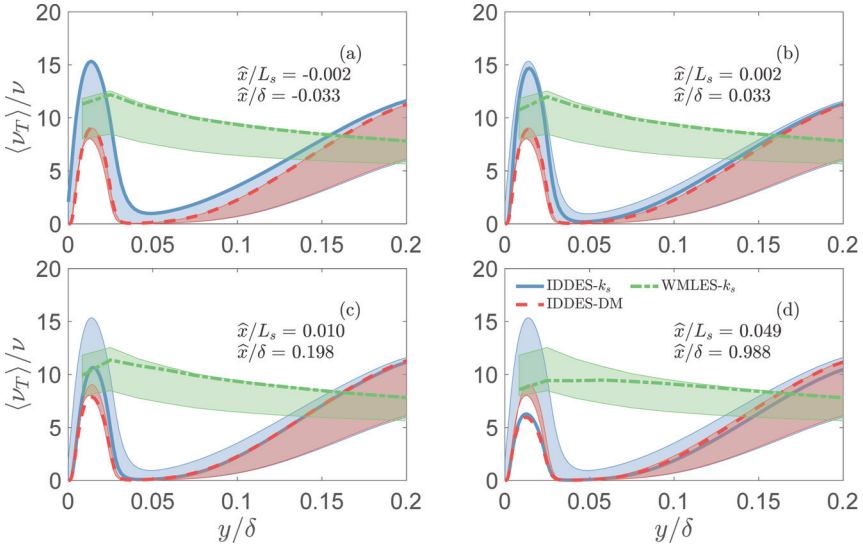

Figure 9. Profiles of the normalized eddy viscosity $\langle\nu_T\rangle/\nu$ near the rough-to-smooth interface at (**a**) -0.2%, (**b**) 0.2%, (**c**) 1% and (**d**) 5% of the smooth strip length. The shaded regions show the eddy viscosity variation between the fully smooth and fully rough limits (corresponding to the lower and upper boundaries, respectively).

Figure 10 shows the streamwise development of various quantities of interest near the rough-to-smooth interface. Two y positions were chosen for the IDDES solutions: one very close to the wall and another one in the outer LES zone. Near the wall, the mean velocity predicted by the IDDES in Figure 10a showed the sudden acceleration discussed in Section 3.3. A smoother behavior only occurred further away from the wall. The eddy viscosity behaviors discussed earlier are perhaps most clearly shown in Figure 10b. Note the jump in ν_T, which becomes less significant away from the wall.

Considering the Reynolds shear stress, in the IDDES-k_s, the discontinuous eddy viscosity led to the jump in the modeled stress. The point closest to the wall was in the RANS region, and the modeled stress was predominant. The increase in resolved shear stress $-\langle u'v'\rangle$ immediately after the interface, which can be observed in Figure 10c, was insufficient to balance it. The total stress reached the values expected for a smooth wall very quickly, as shown in Figure 10d. This decrease, as mentioned above, caused the flow acceleration downstream of the interface. On the other hand, in the WMLES case, the eddy viscosity and thus the total stress were continuous across the interface while decreasing quite slowly downstream, which reflects the decreased turbulence level over the smooth wall. As a consequence, the flow acceleration was milder, as illustrated in Figure 10a.

Similar but reversed behaviors can be observed for the smooth-to-rough transition. The eddy viscosity predicted by the IDDES-k_s had an upward jump that was not balanced by the reduction in resolved shear stress, and the flow decelerated in the near-wall region. This sharp velocity gradient immediately drove the flow toward rough conditions in the near-wall region (Figure 4b), leading to a faster recovery for C_f than what occurred for the WMLES. As explained in Section 3.2, since the outer region is less affected by the rapid changes experienced near the wall in WMLES, the flow requires more time to readjust, forcing the near-wall region to further accelerate and creating the dip shown in Figure 3.

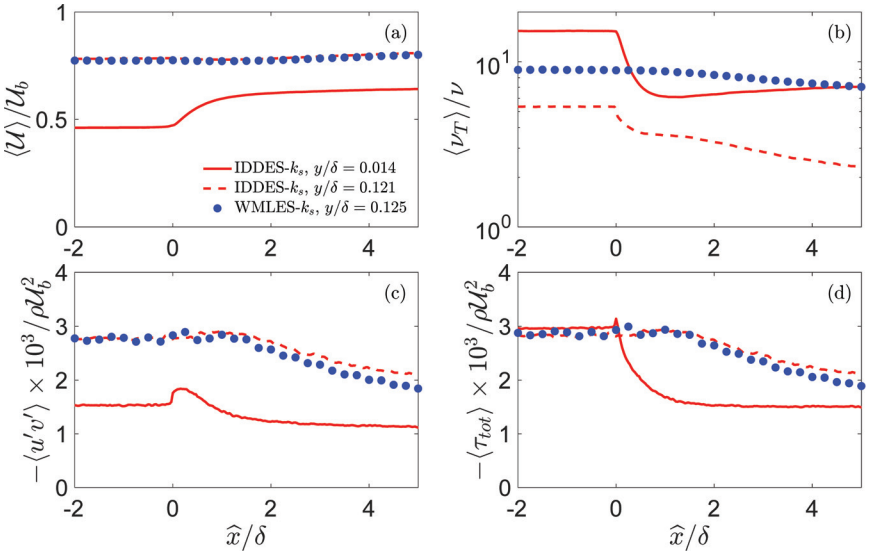

Figure 10. Streamwise development near the rough-to-smooth interface for (**a**) mean velocity, (**b**) eddy viscosity, (**c**) resolved Reynolds shear stress and (**d**) total Reynolds shear stress.

4. Conclusions

Two modeling approaches (i.e., the log law-based wall-modeled large-eddy simulations (WMLES) and the improved delayed detached-eddy simulations (IDDES)), were used to predict the flow over alternating rough and smooth strips oriented normally to the mean stream in an open-channel configuration. Comparisons with experimental data highlighted that the WMLES captured the recovery of the skin friction to equilibrium flow conditions downstream of the rough-to-smooth transition and predicted fairly accurately the mean velocity profile. However, being constrained to match the log law at the inner/outer layer interface, the WMLES were unable to reproduce the variation in the roughness function after the rough-to-smooth transition. The IDDES predicted a much faster recovery for both the mean velocity and the skin friction.

In the IDDES, there was a strong coupling between the boundary conditions and the modeled eddy viscosity, particularly if both the model and boundary conditions were modified to account for the roughness. This coupling resulted in the excessively rapid variation in the Reynolds shear stress and a disproportionate flow acceleration (on the rough-to-smooth interface) or deceleration (on the smooth-to-rough surface), which resulted in too rapid a return to equilibrium. In terms of the mean velocity profile normalized in the inner units, the IDDES were not constrained to match the log law as the WMLES were, and they should be able to predict the recovery of the roughness function to the zero equilibrium value of the smooth strip, as provided by the experiments. However, because of the excessively rapid return to equilibrium, the readjustment of the roughness function was incorrectly predicted with IDDES. In the WMLES, on the other hand, the wall shear stress was calculated based on the outer layer information. Because of this, the perturbation introduced by the change in the boundary condition must propagate away from the wall before the wall model reacts. The WMLES effectively retained memory of the upstream conditions, producing a smooth recovery of the modeled shear-stress and skin friction coefficient.

When comparing the two approaches to roughness modeling, they gave essentially the same results, which largely depends on the fact that both approaches are calibrated to match Nikuradze's data [1]. The drag model, which is much simpler to implement, appears to be very promising, even if additional studies in different configurations are needed to reach more general conclusions.

Finally, in the present arrangement of roughness strips, the WMLES were found to give better prediction of the flow field than IDDES. In addition, IDDES have a much higher computational cost, and the model length scale appears to be extremely sensitive to the flow conditions. However, since log law-based WMLES are not expected to be accurate in other complex flow configurations (in the presence of strong pressure gradients or flow separation, for instance), the development and testing of wall models that have memory of the upstream conditions (such as the one recently proposed by Fowler et al. [40]) is desirable.

Author Contributions: Conceptualization, T.S., U.P. and G.D.; methodology, T.S. and U.P.; software, T.S.; validation, T.S., U.P. and G.D.; formal analysis, T.S., U.P. and G.D.; investigation, T.S., U.P. and G.D.; resources, U.P. and G.D.; data curation, T.S. and U.P.; writing—original draft preparation, T.S. and U.P.; writing—review and editing, U.P. and G.D.; supervision, U.P. and G.D.; project administration, U.P. and G.D.; funding acquisition, G.D. and U.P. All authors have read and agreed to the published version of the manuscript.

Funding: U.P. acknowledges financial support from the Natural Sciences and Engineering Research Council (NSERC) of Canada under the Discovery Grant program.

Data Availability Statement: The data presented in this study are available on request from the corresponding author. The data are not publicly available due to size of data sets.

Acknowledgments: The authors acknowledge the computational support by CINECA under the ISCRA initiative (Project HP10BSBCBZ) and by Alliance-Compute Canada.

Conflicts of Interest: The authors declare no conflict of interest.

Abbreviations

The following abbreviations are used in this manuscript:

BC	boundary condition
DNS	direct numerical simulation
IDDES	improved delayed detached-eddy simulation
LES	large-eddy simulation
RANS	Reynolds-averaged Navier–Stokes
SA	Spalart–Allmaras
SFS	subfilter scale
WMLES	wall-modeled large-eddy simulation
WRLES	wall-resolved large-eddy simulation

References

1. Nikuradse, J. Strömungsgesetze in Rauhen Rohren. *VDI-Forschungsheft* **1933**, *361*, 1–64.
2. Raupach, M.R.; Antonia, R.A.; Rajagopalan, S. Rough-wall boundary layers. *Appl. Mech. Rev.* **1991**, *44*, 1–25. [CrossRef]
3. Jiménez, J. Turbulent flows over rough walls. *Annu. Rev. Fluid Mech.* **2004**, *36*, 173–196. [CrossRef]
4. Colebrook, C.F. Turbulent flow in pipes, with particular reference to the transition region between smooth and rough pipe laws. *J. Inst. Civ. Eng.* **1939**, *11*, 133–156. [CrossRef]
5. Shafi, H.S.; Antonia, R.A. Anisotropy of the Reynolds stresses in a turbulent boundary layer on a rough wall. *Exp. Fluids* **1995**, *18*, 213–215. [CrossRef]
6. Finnigan, J. Turbulence in plant canopies. *Annu. Rev. Fluid Mech.* **2000**, *32*, 519–571. [CrossRef]
7. Cheng, H.; Castro, I.P. Near-wall flow development after a step change in surface roughness. *Bound. Layer Meteorol.* **2002**, *105*, 411–432. [CrossRef]
8. Chamorro, L.P.; Porté-Agel, F. Velocity and surface shear stress distributions behind a rough-to-smooth surface transition: A simple new model. *Bound. Layer Meteorol.* **2009**, *130*, 29–41. [CrossRef]
9. Garratt, J.R. The internal boundary layer—A review. *Bound. Layer Meteorol.* **1990**, *50*, 171–203. [CrossRef]

10. Bradley, E.F. A micrometeorological study of velocity profiles and surface drag in the region modified by a change in surface roughness. *Q. J. R. Meteorol. Soc.* **1968**, *94*, 361–379. [CrossRef]
11. Antonia, R.A.; Luxton, R.E. The response of a turbulent boundary layer to a step change in surface roughness. Part 1. Smooth to rough. *J. Fluid Mech.* **1971**, *48*, 721–761. [CrossRef]
12. Antonia, R.A.; Luxton, R.E. The response of a turbulent boundary layer to a step change in surface roughness. Part 2. Rough to smooth. *J. Fluid Mech.* **1972**, *53*, 737–757. [CrossRef]
13. Hanson, R.E.; Ganapathisubramani, B. Development of turbulent boundary layers past a step change in wall roughness. *J. Fluid Mech.* **2016**, *795*, 494–523. [CrossRef]
14. Li, M.; de Silva, C.M.; Rouhi, A.; Baidya, R.; Chung, D.; Marusic, I.; Hutchins, N. Recovery of wall-shear stress to equilibrium flow conditions after a rough-to-smooth step change in turbulent boundary layers. *J. Fluid Mech.* **2019**, *872*, 472–491. [CrossRef]
15. Bou-Zeid, E.; Meneveau, C.; Parlange, M.B. Large-eddy simulation of neutral atmospheric boundary layer flow over heterogeneous surfaces: Blending height and effective surface roughness. *Water Resour. Res.* **2004**, *40*, W02505. [CrossRef]
16. Abkar, M.; Porté-Agel, F. A new boundary condition for large-eddy simulation of boundary-layer flow over surface roughness transitions. *J. Turbul.* **2012**, *13*, N23. [CrossRef]
17. Saito, N.; Pullin, D.I. Large eddy simulation of smooth–rough–smooth transitions in turbulent channel flows. *Int. J. Heat Mass Trans.* **2014**, *78*, 707–720. [CrossRef]
18. Ismail, U.; Zaki, T.A.; Durbin, P.A. The effect of cube-roughened walls on the response of rough-to-smooth (RTS) turbulent channel flows. *Int. J. Heat Fluid Flow* **2018**, *72*, 174–185. [CrossRef]
19. Ismail, U.; Zaki, T.A.; Durbin, P.A. Simulations of rib-roughened rough-to-smooth turbulent channel flows. *J. Fluid Mech.* **2018**, *843*, 419–449. [CrossRef]
20. Wilcox, D.C. Reassessment of the scale-determining equation for advanced turbulence models. *AIAA J.* **1988**, *26*, 1299–1310. [CrossRef]
21. Hellsten, A.; Laine, S. Extension of the k-omega-SST turbulence model for flows over rough surfaces. In Proceedings of the 22nd AIAA Atmospheric Flight Mechanics Conference, New Orleans, LA, USA, 11–13 August 1997.
22. Knopp, T.; Eisfeld, B.; Calvo, J.B. A new extension for $k-\omega$ turbulence models to account for wall roughness. *Int. J. Heat Fluid Flow* **2009**, *30*, 54–65. [CrossRef]
23. Aupoix, B.; Spalart, P.R. Extensions of the Spalart–Allmaras turbulence model to account for wall roughness. *Int. J. Heat Fluid Flow* **2003**, *24*, 454–462. [CrossRef]
24. Aupoix, B. Roughness corrections for the $k-\omega$ shear stress transport model: Status and proposals. *ASME J. Fluids Eng.* **2015**, *137*, 021202. [CrossRef]
25. Dutta, R.; Nicolle, J.; Giroux, A.M.; Piomelli, U. Evaluation of turbulence models in rough-wall boundary layers for hydroelectric application. *Int. J. Fluid Mach. Sys.* **2017**, *10*, 228–239. [CrossRef]
26. Piomelli, U.; Balaras, E. Wall-layer models for large-eddy simulations. *Annu. Rev. Fluid Mech.* **2002**, *34*, 349–374. [CrossRef]
27. Piomelli, U. Wall-layer models for large-eddy simulations. *Prog. Aerosp. Sci.* **2008**, *44*, 437–446. [CrossRef]
28. Larsson, J.; Kawai, S.; Bodart, J.; Bermejo-Moreno, I. Large eddy simulation with modeled wall-stress: Recent progress and future directions. *Mech. Eng. Rev.* **2016**, *3*, 1–23. [CrossRef]
29. Bose, S.T.; Park, G.I. Wall-modeled large-eddy simulation for complex turbulent flows. *Annu. Rev. Fluid Mech.* **2018**, *50*, 535–561. [CrossRef]
30. Spalart, P.R. Detached-Eddy Simulation. *Annu. Rev. Fluid Mech.* **2009**, *41*, 181–202. [CrossRef]
31. Heinz, S. A review of hybrid RANS-LES methods for turbulent flows: Concepts and applications. *Prog. Aerosp. Sci.* **2020**, *114*, 100597. [CrossRef]
32. Bou-Zeid, E.; Parlange, M.B.; Meneveau, C. On the parameterization of surface roughness at regional scales. *J. Atmos. Sci.* **2007**, *64*, 216–227. [CrossRef]
33. Varghese, J.; Durbin, P.A. Representing surface roughness in eddy resolving simulation. *J. Fluid Mech.* **2020**, *897*, A10. [CrossRef]
34. Vreman, A.W. An eddy-viscosity subgrid-scale model for turbulent shear flow: Algebraic theory and applications. *Phys. Fluids* **2004**, *16*, 3670–3681. [CrossRef]
35. Travin, A.K.; Shur, M.L.; Spalart, P.R.; Strelets, M.K. Improvement of delayed detached-eddy simulation for LES with wall modelling. In Proceedings of the European Conference on Computational Fluid Dynamics ECCOMAS CFD 2006, Bergen, The Netherlands, 5–8 September 2006; Wesseling, P., Oñate, E., Pèriaux, J., Eds.; TU Delft: Delft, The Netherlands, 2006; pp. 410–432.
36. Spalart, P.R.; Allmaras, S.R. A one-equation turbulence model for aerodynamic flows. *Rech. Aerosp.* **1994**, *1*, 5–21.
37. Shur, M.L.; Spalart, P.R.; Strelets, M.K.; Travin, A.K. A hybrid RANS/LES model with delayed DES and wall-modeled LES capabilities. *Int. J. Heat Fluid Flow* **2008**, *29*, 1638–1649. [CrossRef]

38. Schumann, U. Subgrid-scale model for finite difference simulation of turbulent flows in plane channels and annuli. *J. Comput. Phys.* **1975**, *18*, 376–404. [CrossRef]
39. Kawai, S.; Larsson, J. Wall-modeling in large eddy simulation: Length scales, grid resolution, and accuracy. *Phys. Fluids* **2012**, *24*, 015105. [CrossRef]
40. Fowler, M.; Zaki, T.A.; Meneveau, C. A Lagrangian relaxation towards equilibrium wall model for large eddy simulation. *J. Fluid Mech.* **2022**, *934*, 1–37. [CrossRef]

fluids

MDPI

Article

Evaluation of SPH and FVM Models of Kinematically Prescribed Peristalsis-like Flow in a Tube

Xinying Liu [1], Simon M. Harrison [2], Paul W. Cleary [2] and David F. Fletcher [1,*]

[1] School of Chemical and Biomolecular Engineering, University of Sydney, Sydney, NSW 2006, Australia
[2] CSIRO Data61, Clayton South, VIC 2168, Australia
* Correspondence: david.fletcher@sydney.edu.au; Tel.: +61-2-9351-4147

Abstract: Peristaltic flow is important in many biological processes, including digestion, and forms an important component of any in silico model of the stomach. There is a clear need to verify the simulations of such flows. An analytical solution was identified that can be used for model verification, which gives an equation for the net volumetric flow over a cycle for an applied sinusoidal wall motion. Both a smooth particle hydrodynamics (SPH) code (from the CSIRO), which is being used to develop a stomach model that includes wall motion, buoyancy, acid secretion and food breakdown, and the Ansys Fluent Finite Volume Method (FVM) solver, that is widely used in industry for complex engineering flows, are used in this exercise. Both give excellent agreement with the analytic solution for the net flow over a cycle for a range of occlusion ratios of 0.1–0.6. Very similar velocity fields are obtained with the two methods. The impact of parameters affecting solution stability and accuracy are described and investigated. Having validated the moving wall capability of the SPH model it can be used with confidence in stomach simulations that include wall motion.

Keywords: peristaltic flow; CFD; smooth particle hydrodynamics; finite volume method; model verification

Citation: Liu, X.; Harrison, S.M.; Cleary, P.W.; Fletcher, D.F. Evaluation of SPH and FVM Models of Kinematically Prescribed Peristalsis-like Flow in a Tube. *Fluids* **2023**, *8*, 6. https://doi.org/10.3390/fluids8010006

Academic Editor: Mehrdad Massoudi

Received: 5 December 2022
Revised: 18 December 2022
Accepted: 20 December 2022
Published: 23 December 2022

1. Introduction

Peristaltic flow arises when a series of contraction and expansion movements propagate along elastic tube-shaped structures. The fluid and/or solid content inside moves along with the wave as it propagates. In physiology, peristaltic waves are generated by the longitudinal and circular muscular fibers along the wall [1]. This motion is essential in the digestive system for its role in transporting and mixing food/nutrients in the gastrointestinal tract (GIT) [2–6]. The peristaltic motor patterns in the human gut are very complex and governed by multiple mechanisms and factors, including muscle activity, the thickness of the muscularis, and muscle tissue characteristics (elasticity, contractility, extensibility) [7–10].

In vivo studies provide the most relevant insights into the digestion process due to the complexity and inter-person variabilities of the digestion system. Researchers usually use animal models to study digestion because human subjects are not easy to recruit, experiments are hard to perform and to get measurements from, and complex ethical approval is required [11]. Even though animal models are often used as an alternative to humans [12–15], they do not necessarily accurately reflect the human situation and still require strict ethics approval and specific technical skills. Therefore, in vitro models (e.g., test tube-based or similar) are designed to replicate the digestion process. These experimental studies are constructed with an aim to replicate the fluid flow conditions, shear stresses and complex chemistry in the GIT. Detailed reviews of in vitro digestion models are provided by Li et al. [16], Zhong and Langrish [17], Bornhorst and Singh [11], Dupont et al. [18] and Hur et al. [19]. In vitro models allow control of many factors that cannot be controlled in the in vivo system [11], which affords a better systematic understanding of individual factors.

However, these experimental systems can be hard to design to replicate local flow and concentration fields that occur in the body and can be very hard to customize to represent in vivo scenarios. With the massive improvements in numerical methods and computing power over the last few decades, in silico methods have the huge advantage that local data can be obtained for all variables, such as velocity, pressure, and species concentration [3,4,6,20–23]. Therefore, if a suitably accurate computational model of an in vivo system can be constructed, the in silico results can provide insights into the in vivo system behavior. Although the primary aim is to understand in vivo behavior, in silico models can guide in vitro experimental design after being validated by data from the in vitro model. This synergistic approach is important in model developments that utilize in silico models that benefit from the verification work performed here. Ultimately, the in silico and in vitro work will lead to in silico models that can simulate the full digestion process happening in the human stomach.

In the past two decades, many numerical models of this process based on Computational Fluid Dynamics (CFD) methods have been developed. Models have been built for different parts of the GI tract, including the esophagus [24], stomach [4,25,26] and intestine [3,20–23,27,28]. These models provide valuable insights into the flow pattern of the digestion content, which is not easily quantified in both in vivo and in vitro studies. In the early developed models, single-phase fluid was simulated with various densities and viscosities. Recently, multiphase flow simulations (including with free surfaces and particles) have been implemented and improved by Sinnott et al. [3] and Harrison et al. [4]. Some models also include gastric secretion [6] and electrophysiology [27]. The developed models have demonstrated their capability and high potential in simulating this complex system but, to date, lack systematic validation for replicating physical outcomes. It is therefore important to verify and validate the components of established models to demonstrate their accuracy and stability.

An analytical solution [29], described later, can be used to calculate the detailed peristaltic-induced fluid motion for an idealized tube geometry. However, numerical analysis is needed to understand complicated systems, such as the intestine and the stomach, which involve the combination of fluid flow, free surfaces, complex boundary conditions, and solids content. The capability of SPH in simulating the digestion model has been demonstrated in the intestine models developed using the CSIRO SPH code [3,20–23,28] and the stomach model developed by Harrison et al. [4]. Peristaltic flow is a fundamental component of all these models, and it is therefore useful to validate computational models for this process and then to perform additional validation as more physics is added, knowing that the underlying moving wall flow model is well validated.

The main aim of this paper is to validate the accuracy of the smooth particle hydrodynamics (SPH) method when applied to the peristaltic motion of a single-phase Newtonian fluid. Once the model is validated for this simple system, it will provide a high level of confidence for other applications, where peristalsis is involved in more complicated systems. The Finite Volume method (FVM) is also employed in the study and acts as a comparison approach. Compared with the novel mesh-free SPH method, FVM is a traditional mesh-based method that has been well-established for decades [30]. By comparing the performance of both numerical methods, their accuracy and efficiency can be explored.

2. Analytical Solution

Several studies have investigated flow in a tube during simplified peristalsis driven by a moving wall [1,29,31,32]. Under constrained flow conditions the flow field and pressure distribution can be calculated from the amplitudes of the wall deformations only. In this study, the analytical solution of Shapiro et al. [29] is used to validate the numerical models of peristalsis. A continuous sinusoidal wave train moving in one direction along the tube axis with a constant speed is used to determine the instantaneous shape of a moving boundary wall on a tube of uniform initial diameter. The applied motion generates a volumetric flow

which can be compared with analytic results. An illustration of the fluid-filled tube, which has a deforming wall that is one wavelength long, is shown in Figure 1.

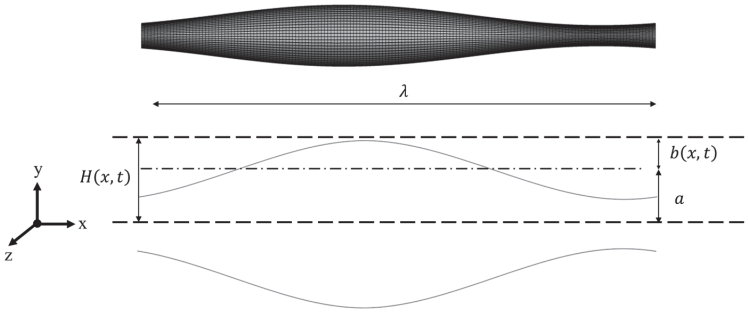

Figure 1. Illustrations of tube geometry used in the peristalsis validation model.

In the simulations, the wavelength λ of the imposed wave is specified, which is related to the wavenumber by:

$$k = \frac{a}{\lambda} \tag{1}$$

where a is the radius of the tube. Using these definitions, a Reynolds number can be formed as

$$Re = \frac{\rho a c}{\mu} \times \frac{a}{\lambda} \tag{2}$$

where c is the speed of the imposed wave, μ is the dynamic viscosity and ρ is the fluid density.

The analytical model assumes a continuous train of waves and inertia-free fluid flow, which requires two criteria to be met. Firstly, the wavenumber (k), which is the ratio of the radius to the wavelength, should be close to zero, as it is assumed to be zero in the analytical solution. Under this condition, the transverse velocities and pressure gradients are negligible compared with their longitudinal counterparts. Secondly, the Reynolds number (Re), which gives the ratio of inertial to viscous forces must be close to zero, as it is again assumed to be zero in the analytical solution.

From Fung and Yih [1], the equation for the imposed peristaltic waves is:

$$b(x,t) = a\phi \sin 2\pi \left(\frac{x - ct}{\lambda} \right) \tag{3}$$

where $b(x,t)$ denotes the wall deformation in the radial direction, x is the longitudinal location, t is time and $\phi = b/a$ is the amplitude ratio, which is set to a range of 0.1 to 0.6, corresponding to occlusions of 10% to 60%, deemed to be sufficient given the purpose of this study.

The effect of changing the amplitude ratio, ϕ, on the fluid flow is investigated. In the analytical solution, the fluid is assumed to be incompressible. The fluid flows through the tube with constant static pressure at the tube boundaries. The dimensionless time-average volumetric flow rate ($\dot{V}$) is a good measure of the flow behaviour and is dependent on the amplitude ratio (ϕ) [29]:

$$\dot{V} = \frac{\phi(4 + \phi)}{2 + 3\phi^2} \tag{4}$$

3. Setup of the Numerical Model

3.1. Physiological Parameters

The physiological data for the human ureter [1] are used in the peristalsis model developed in this work. As shown in Table 1, the input parameters include the tube

dimensions, the characteristics of the imposed motion and the properties of the fluid inside the tube. Both the wavenumber and Reynolds number are close to zero as required.

Table 1. Parameters used in the numerical models.

Geometrical Dimensions		
Radius	a	0.001 m
Length	L	0.05 m
Peristaltic Waves Characteristics		
Wave speed	c	0.03 m/s
Wavelength	λ	0.05 m
Amplitude ratio	ϕ	0.1–0.6
Fluid Properties		
Dynamic viscosity	μ	0.01 Pa·s
Density	ρ	1000 kg/m^3
Conditions		
The ratio of tube radius to wavelength	k	0.02 (close to 0)
Reynolds number	Re	0.06 (close to 0)

The nodes on the boundary are displaced radially according to the profile given by Equation (3) in both the SPH and FVM simulations. The wall location used in the simulation, $H(x,t)$, is determined from the imposed wave motion given by $b(x,t)$ (Equation (3)) with the inclusion of a ramp to start the simulation gradually to prevent mesh distortion:

$$H(x,t) = a\left(1 + \min\left(\frac{t}{t_i},\, 1\right) \times \phi \sin 2\pi\left(\frac{x - ct}{\lambda}\right)\right) \tag{5}$$

where t_i is the ramp time, set to λ/c. Results before time t_i are not included when calculating the averaged flow rate.

The following equations are applied to convert the equations into Cartesian coordinates.

$$\theta = \tan^{-1}\left(\frac{z}{y}\right) \tag{6}$$

$$y = H(x,t)\cos(\theta) \tag{7}$$

$$z = H(x,t)\sin(\theta) \tag{8}$$

where y and z are the transformed coordinates in a Cartesian coordinate system.

The problem described above is next set up and solved using both SPH and FVM so that the results can be compared for the same geometry, boundary conditions and fluid properties.

3.2. SPH Model

In the SPH approach, the Navier–Stokes equations are used to solve fluid dynamics problems, with particles representing discrete "lumps" of fluid, that are tracked in a Lagrangian framework. The formulation of the model results in a set of ordinary differential equations describing the motion of fluid particles [33]. More details of the method can be found in Monaghan [34,35] and Cleary et al. [20,33]. The CSIRO SPH code [36] is used in this study.

To obtain values of quantities such as density and velocity at a given point, data must be obtained from the surrounding region. The interpolated value of a function A at a point $\boldsymbol{r}$, is the sum over all particles within a radius of distance related to h from point $\boldsymbol{r}$ [34]:

$$A(\boldsymbol{r}) = \sum_b m_b \frac{A_b}{\rho_b} W(\boldsymbol{r} - \boldsymbol{r}_b, h) \tag{9}$$

where A_b is the value of A at $\boldsymbol{r}_b$, m_b is the mass of fluid particle b, and W is an interpolation kernel function with a smoothing length of h evaluated at a distance $|\boldsymbol{r} - \boldsymbol{r}_b|$ from the position of interest. In this work, h is set to be 1.2 times the initial particle separation distance, Δx. The concept of a smoothing kernel is shown in Figure 2 below.

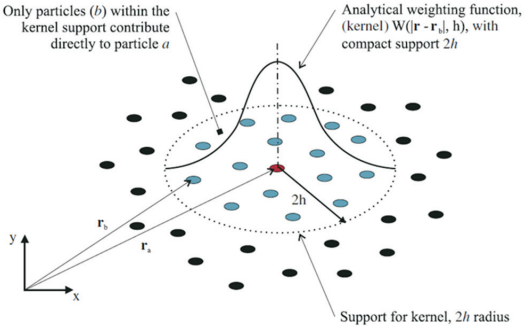

Figure 2. Schematic representation of a typical kernel. Reprinted with permission from Cummins et al. [37]. Copyright 2022 John Wiley and Sons.

The kernel is essential to the entire method as it is used for the calculation of both spatially interpolated values and gradients. The effect of three different kernels is examined in this work for the same smoothing length. The dimensionless distance used in the kernel is defined as

$$\Delta = \frac{\boldsymbol{r}_{ab}}{h} \tag{10}$$

where $\boldsymbol{r}_{ab}$ is the distance between particles b and a.

The quartic spline kernel [37] is used for the base case in this study

$$W(\boldsymbol{r}_{ab}, h) = \frac{1}{20\pi h^3} \begin{cases} (2.5-\Delta)^4 - 5(1.5-\Delta)^4 + 10(0.5-\Delta)^4, \ \Delta \leq 0.5 \\ (2.5-\Delta)^4 - 5(1.5-\Delta)^4, \ 0.5 \leq \Delta \leq 1.5 \\ (2.5-\Delta)^4, \ 1.5 \leq \Delta \leq 2.5 \\ 0, \ \Delta \geq 2.5 \end{cases} \tag{11}$$

The fifth-order Wendland kernel [37,38] is also studied:

$$W(\boldsymbol{r}_{ab}, h) = \frac{7}{85.336\pi h^3} \begin{cases} (2-\Delta)^4 (1+2\Delta), \ 0 \leq \Delta \leq 2 \\ 0, \ \Delta \geq 2 \end{cases} \tag{12}$$

as well as the cubic spline kernel [35,39]:

$$W(\boldsymbol{r}_{ab}, h) = \frac{1}{\pi h^3} \begin{cases} 1 - \frac{3}{2}(\Delta)^2 + \frac{3}{4}(\Delta)^3, \ \Delta \leq 1 \\ \frac{1}{4}(2-\Delta)^3, \ 1 \leq \Delta \leq 2 \\ 0, \ \Delta \geq 2 \end{cases} \tag{13}$$

A comparison of the kernel shapes is shown in Figure 3. To display them the dimensionless kernel $W(\boldsymbol{r}_{ab}, h)h^3$ was plotted as a function of the normalized distance.

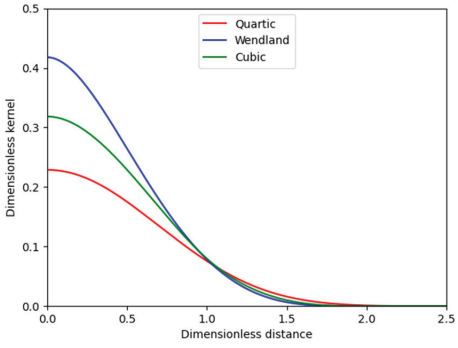

Figure 3. Comparison of the kernels used in this work.

From Figure 3 several important observations can be made:

(1) The value of any variable at a given point depends on all particle values inside a sphere of radius nh centred on that point. In SPH this is usually referred to as a kernel having compact support with radius nh. For the cubic and Wendland kernels $n = 2$, and for the quartic kernel $n = 2.5$. Therefore, for any given particle configuration the quartic kernel involves summation of more particles over a greater spatial extent than the other two.

(2) The kernels give different relative weighting to particles closer to the point of interest. This impacts not only the value but also the gradients of variables.

The gradient of the function A is obtained by differentiating Equation (9):

$$\nabla A(\boldsymbol{r}) = \sum_b m_b \frac{A_b}{\rho_b} \nabla W(\boldsymbol{r} - \boldsymbol{r}_b, h) \tag{14}$$

The conservation equation for mass can then be formulated as [34,40]:

$$\frac{d\rho_a}{dt} = \sum_b m_b \boldsymbol{v}_{ab} \cdot \nabla_a W_{ab} \tag{15}$$

where ρ_a is the density of fluid particle a, t is time, $\boldsymbol{v}_{ab} = \boldsymbol{v}_a - \boldsymbol{v}_b$, is the relative velocity between particles a and b.

The fluid pressure can then be calculated based on the particle density. Although the analytic solution is derived for an incompressible fluid, a weakly compressible approach is adopted here and is configured to have low compressibility. This approach is applied by introducing an equation of state of the form:

$$P = P_0 \left[\left(\frac{\rho}{\rho_0} \right)^{\mathrm{Y}} - 1 \right] + P_{\mathrm{off}} \tag{16}$$

where P is the fluid pressure; P_0 is the pressure scale factor; ρ is the particle density; ρ_0 is the reference density, set to 1000 kg/m^3 for water in this work; P_{off} is a background pressure that is added to avoid negative pressure values.

Weakly compressible SPH is designed for free surface flow prediction [34] with an essential component being the ability of diverging fluid (which has a negative pressure when calculated by Equation (16) when $P_{\mathrm{off}} = 0$) to create new free surface. In a fully enclosed expanding flow this will allow unphysical internal void formation. However, the analytical model assumes that the tube content is a single-phase fluid without internal free surfaces. The equation of state therefore needs to be adapted to ensure that $P > 0$ throughout the tube and for the entirety of the simulation. This is achieved by including a pressure offset, P_{off}, which is sufficiently large to guarantee that the pressure remains

positive. Since the fluid dynamical force only depends on the pressure gradient, the addition of such a constant has no other effect aside from ensuring the positivity of the pressure.

The effect of this offset pressure in the current work is very important, as shown in Figure 4. Without the offset pressure voids are created, which are not present in the single-phase flow being modelled here. A background pressure of 100 Pa is found to be sufficient to ensure $P > 0$ and therefore inhibit this internal free surface generation and is used for all cases.

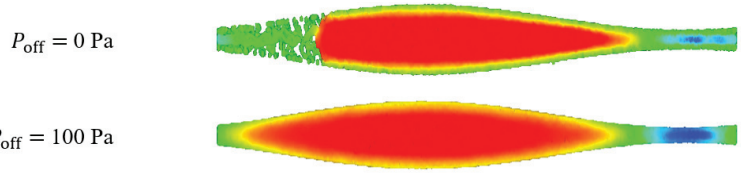

Figure 4. Addition of a background pressure is used to prevent void formation. The contours show velocity, but the key point is the breakup of the fluid in the top picture is avoided when the offset pressure is present.

The pressure scale factor P_0 in Equation (16) is given by

$$\frac{\gamma P_0}{\rho_0} = {c_s}^2 = (10V)^2 \tag{17}$$

where γ is 7, which is a material constant defined for water [41]; c_s is the local speed of sound, which needs to be large enough to make sure the density variations are small and the fluid is close to incompressible, but it also needs to be low enough to avoid the need for unnecessarily small timesteps [41] (see later); c_s needs to be at least 10 times larger than the characteristic fluid velocity in the flow field (V), which corresponds to a Mach number of 0.1 or smaller and gives a density variation of less than 1% [34].

The conservation equation for momentum becomes:

$$\frac{d\boldsymbol{v}_a}{dt} = -\sum_b m_b \left[\left(\frac{P_b}{\rho_b^2} + \frac{P_a}{\rho_a^2} \right) - \frac{\xi}{\rho_a \rho_b} \frac{4\mu_a \mu_b}{(\mu_a + \mu_b)} \frac{\boldsymbol{v}_{ab} \cdot \boldsymbol{r}_{ab}}{(r_{ab}^2 + \eta^2)} \right] \nabla_a W_{ab} + \sum_k \boldsymbol{f}_{ak} \tag{18}$$

where P_a and P_b are the pressure of particles a and b, μ_a is the viscosity of particle a, ξ is a calibration factor associated with the viscous term, which is calculated during the simulation. The calculation of this factor is described in Cleary [42]; η is a small parameter used to regularise the singularity when $\boldsymbol{r}_{ab} = 0$. The term $\boldsymbol{f}_{ak}$ represents the particle–wall force between particle a and wall particle k and is present only near boundary walls (see [20,37] for details).

An explicit integration scheme [34] is used in the simulations. The timestep is governed by the Courant condition modified to account for the viscous term to ensure simulation stability. The details of the modification can be found in Cleary [36] and gives

$$\Delta t = \min_a \left(\frac{0.5h}{c_s + 2\xi \mu_a / h\rho_a} \right) \tag{19}$$

For this application, a constant spatial resolution h and a constant particle size are used. Adaptive resolution can be used to improve accuracy in regions of high wall deformation, but the simpler uniform resolution SPH is sufficient for the deformations of interest (ϕ up to 0.6). For the base case simulation, a particle size of 0.10 mm is used to construct the domain in the SPH model. The tube is filled with 158,000 particles, representing the fluid content, with an initial spacing of 0.10 mm.

The tube wall is represented by 66,000 SPH boundary particles with a particle size of 0.10 mm. The boundary particles are arranged with an equidistant spacing around

the circumference and length of the tube. At each timestep, their position, velocity and normal vector are updated using Equation (5), which are functions of time. Interaction between boundary and fluid particles is calculated using a Lennard Jones penalty force in the direction of the wall normal vector and a no-slip boundary condition in the plane perpendicular to this [34]. The inlet and outlet of the tube are set to be periodic boundaries, meaning that the velocity from the downstream boundary is applied at the upstream boundary, so that $v_{\text{inlet}} = v_{\text{outlet}}$. The average volumetric flow rate is calculated based on the average velocities of the particles at the mid-plane of the tube.

Once the velocity of the particles is known (from Equation (18)) their position can be updated using Equation (20).

$$\frac{d\boldsymbol{r}_a}{dt} = \boldsymbol{v}_a + 0.5 \sum_b \frac{2m_b}{\rho_a + \rho_b}(\boldsymbol{v}_b - \boldsymbol{v}_a)W_{ab} \tag{20}$$

The first term represents the usual dynamical behavior, whilst the second is the XSPH smoothing term which is advantageous for solution stability [43]. Details of the solution process used by the CSIRO SPH code are given elsewhere [36].

3.3. FVM Model

In FVM, the mass and momentum conservation equations employed for incompressible flow with a moving mesh are:

$$\nabla \cdot (\boldsymbol{u} - \boldsymbol{u}_g) = 0 \tag{21}$$

$$\frac{\partial(\rho \boldsymbol{u})}{\partial t} + \nabla \cdot \left(\rho(\boldsymbol{u} - \boldsymbol{u}_g) \otimes \boldsymbol{u}\right) = -\nabla P + \nabla \cdot \left(\mu\left(\nabla \boldsymbol{u} + \nabla \boldsymbol{u}^T\right)\right) \tag{22}$$

where $\boldsymbol{u}$ is the fluid velocity, $\boldsymbol{u}_g$ is the velocity of the moving mesh, ρ is the fluid density, t is time, μ is the dynamic viscosity, and P is the pressure.

The FVM model is developed using Ansys Fluent, 2022R2, a commercial software package that has undergone extensive verification and validation [44]. Using the Ansys SpaceClaim Meshing tools, the geometry is split into 68,000 hexahedral elements. Figure 5 shows the computational mesh generated on the tube in the longitudinal and transverse directions. The mesh is swept between the inlet and outlet faces. Two inflation layers are placed on the boundary. The minimum orthogonal quality of the generated mesh is 0.64, and the maximum skewness is 0.69. The undeformed cell volume varies from 1.2×10^{-12} to 3.9×10^{-12} m^3, which is equivalent to cell sizes of 0.11–0.16 mm.

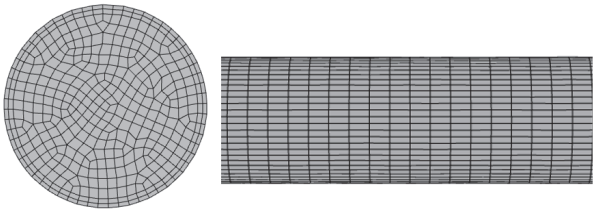

Figure 5. Computational mesh for the undeformed tube in the transverse and the longitudinal directions. (Only a short section of the longitudinal mesh is displayed).

Figure 6 shows the computational mesh in the transverse direction for the deformed tube when $\phi = 0.6$. The original element aspect ratio is 3:1 (Figure 5). The volume of the cell is maintained when deformed and therefore the aspect ratio of the cells changes. When deformed, the aspect ratio is roughly 2:1 at the widest section (Figure 6b) and 6:1 at the narrowest section (Figure 6c), which is well inside the acceptable range for the Ansys Fluent solver.

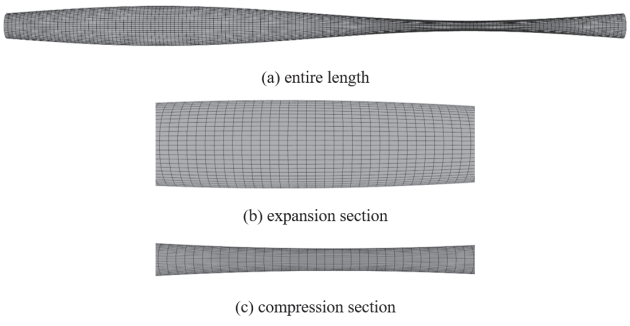

Figure 6. Computational mesh for the deformed tube in the transverse direction.

The tube wall is prescribed to have a no-slip boundary condition. A diffusion-based method is used to distribute the boundary motion uniformly throughout the interior mesh with the number and connectivity of the mesh cells remaining constant. The inlet and outlet of the tube are again set to be periodic boundaries. The initial values for the gauge pressure, x, y and z velocity components are set to zero.

The transient, pressure-based solver is used with the laminar flow assumption. The SIMPLE [45] algorithm is used for pressure–velocity coupling, with the first-order implicit transient scheme. Gradients are determined using the least-squares cell-based method, the pressure is determined using a second-order method, and the bounded second-order upwind scheme is used for the momentum equation. A time step of 0.01 s is chosen after assessing the timestep effect upon results. The simulation is run for 8000 steps for each amplitude ratio. The maximum iteration number for each time step is set to 20, with 5 iterations typically being needed for convergence. Convergence is deemed to have occurred when the locally scaled root-mean-square (RMS) residual values for continuity and the three velocity components are below 10^{-5}.

The mass flow rate passing through the mid-plane of the tube is recorded during the simulations. The mass flow rate is then converted to a volumetric flow rate and integrated over time to retrieve the time–mean volumetric flow rate ($\overline{Q}$). The integration process is conducted using Matlab R2020a.

4. Simulation Results

Figure 7 shows the axial velocity contours on the mid-longitudinal plane for a single wavelength and different amplitude ratios for both models. In the FVM, nodal values are interpolated onto a longitudinal cross-sectional plane and in the SPH model data from adjacent particles (which are disordered) are interpolated onto the plane. As the amplitude of the wave increases, larger deformation results in faster flow through the tube. The data show a larger region of positive flow in the expanded region and a smaller region of negative flow in the contracted region. The positive flow region becomes much larger than the negative region as the occlusion ratio is increased. The flow patterns achieved by both methods show good agreement. Visually the regions of high positive and negative velocity are slightly larger for the FVM results, principally because the gradients are higher so there is a smaller region of the duct occupied by transition values.

The volumetric flow rate at the mid-plane from both models is recorded over time and is shown in Figure 8 for the six levels of contraction. The quartic spline kernel is used for the base case in the SPH model (see later). The overall patterns from both models are very similar. The periodic behavior is established in both models after the ramp time has elapsed and the flow pattern is smooth for all amplitude ratios.

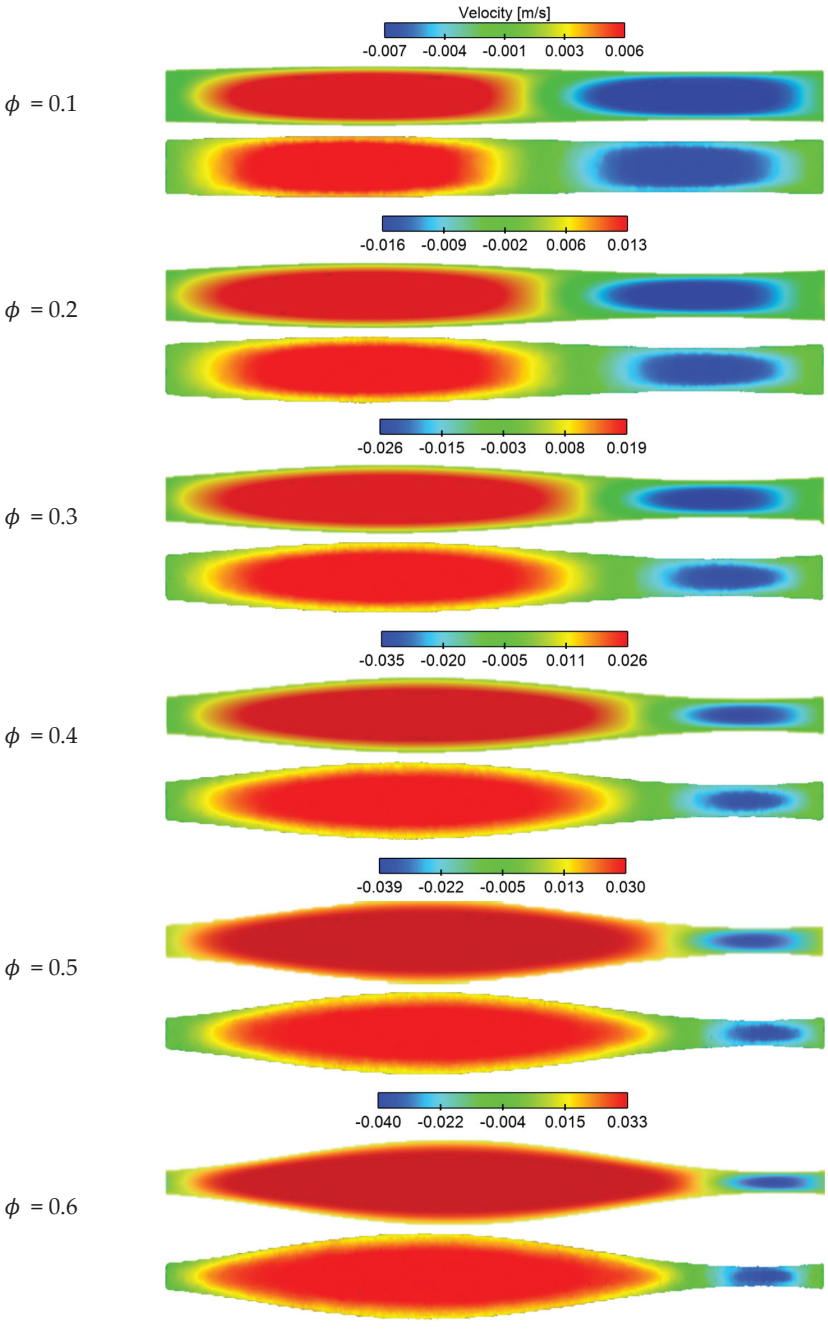

Figure 7. Axial velocity contours at 5 s from the FVM model (top) and the SPH model (bottom).

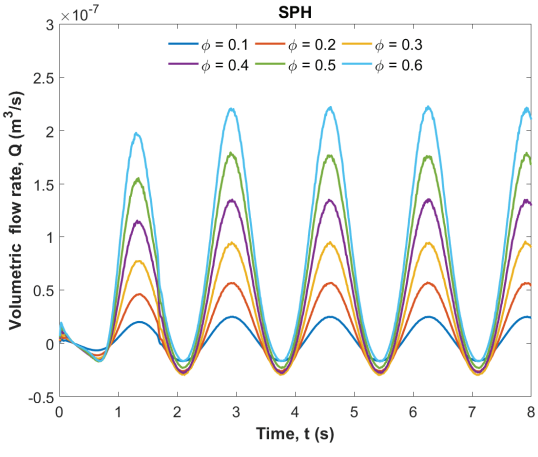

(**a**)

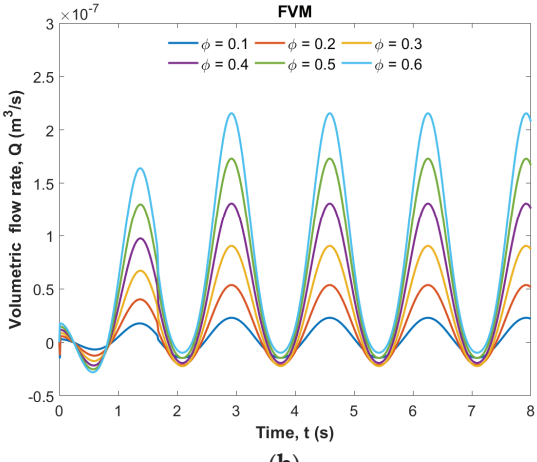

(**b**)

Figure 8. Volumetric flow rate at the mid cross-section over time: (**a**) SPH, (**b**) FVM.

After the initial ramp-up period, there is a strong forward flow with a shorter period of reverse flow that becomes relatively less important as the amplitude ratio is increased. The reverse flow magnitude is sensitive to the applied wave amplitude ratio. At low amplitudes the difference between the forward and backward flow is small making the net flow sensitive to this balance. However, as the wave amplitude is increased there is a significant increase in the forward flow which completely overwhelms the reverse flow. Both methods show very similar behavior.

Figure 9 compares FV and SPH results for volumetric flow rate at different amplitude ratios over time. There is good agreement between the two methods for all the amplitude ratios studied. The volumetric flow rates at the two extremes are slightly different with the SPH model giving slightly higher extreme values compared with the FVM model for all amplitude ratios. However, as the amplitude ratio increases, this difference becomes proportionally smaller bringing the results closer together.

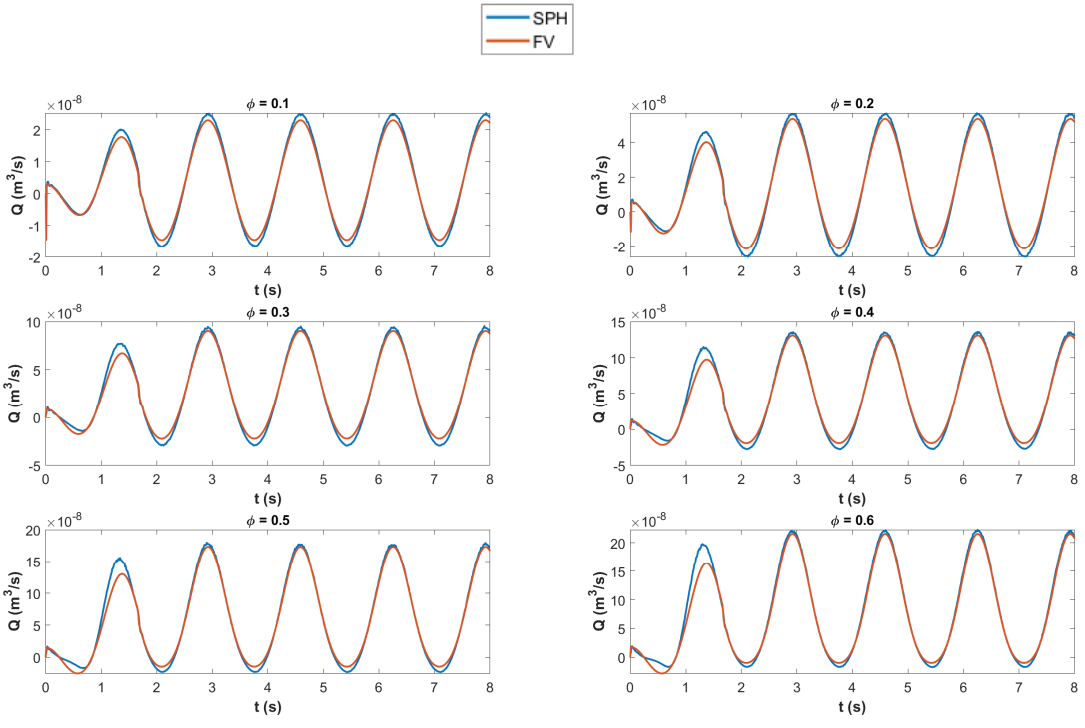

Figure 9. Volumetric flow rate at the mid cross-section over time from both models.

The dimensionless time-averaged volumetric flow (V^*) recorded from both models is then calculated based on the time–mean volumetric flow rate ($\overline{Q}$).

$$V^* = \frac{\overline{Q}}{\pi a^2 c\left(2\phi - \frac{1}{2}\phi^2\right)} \tag{23}$$

The dimensionless results are compared with the analytical solution in Figure 10. The volumetric flows from both models match the analytical solution very well for all occlusion ratios. This shows that both methods are very well suited to this problem and give high and comparable accuracy.

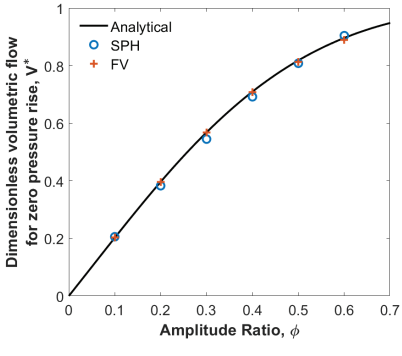

Figure 10. Comparison of computed dimensionless volumetric flow for the two numerical methods with the analytical solution.

5. Sensitivity Study

The influence of numerical parameters is tested here to examine the sensitivity of both methods. In the FVM method, the resolution of a simulation is checked by investigating the sensitivity of the results to both the computational mesh size and the timestep. In the FVM, if the solution is independent of these, the accuracy of the results is then determined by the order of the discretization scheme (typically for the convective term in the equation) and level of convergence (i.e., how well matrix equations are solved) [46]. Typically bounded second-order differencing is used for the temporal and spatial derivatives (albeit that in some regions these must be modified to first order to preserve solution boundedness). This is a highly researched topic and although a huge number of different schemes exist, most software uses a set that has been tried and tested [46].

The situation is much less well-developed in the case of SPH. This arises partly because there has been much less development of this method compared with the FVM but mainly from the difficulty of performing detailed mathematical analysis when the data are stored at the center of disordered particles that can be arranged in an arbitrarily complex manner in space that evolves with the solution. Just as the results from the FVM depend on the computational mesh and choice of the differencing scheme, the SPH results depend on the particle size, choice of the kernel and initial particle separation as discussed earlier.

5.1. SPH Model

5.1.1. Effect of Initial Particle Arrangement

It is non-trivial to populate an arbitrarily shaped region of matter evenly with SPH particles, which is the equivalent of generating a high-quality mesh in the FVM. Certain arrangements are thought to contribute to lower solution quality, for example when a line of particles is compressed perfectly along that line, they can exhibit an artificial resistance to compression followed by a buckling failure. In this work, the aim is to fill a cylinder evenly with a precise volume of SPH particles. Despite the tube geometry (Figure 1) being simple in shape, it has not been established which type of particle packing will lead to optimal results. Thus, three different particle filling approaches are examined: a cubic arrangement, a cylindrical arrangement, and a hybrid of the two above. Here, we describe the properties of each filling approach:

- A cubic arrangement of particles with the center of each adjacent particle located on a cubic grid that is spaced by the particle size in each of the Cartesian directions.
- A cylindrical arrangement of particles with the particle centers one particle diameter apart in the longitudinal direction and arranged in concentric rings around the longitudinal axis of the cylinder that are spaced by one particle diameter and particles in each ring approximately one particle diameter apart on the circumference of the ring.
- A hybrid of the above two approaches: a cylindrical arrangement of one ring of particles near the boundary surface and a cubic arrangement of particles within.

The initial particle arrangements at a cross-section for the three cases described above are shown in Figure 11. The hybrid discretization approach was used in the base case presented above.

A cylindrical packing approach is the most obvious choice for fitting particles evenly but is likely to lead to circumferentially adjacent particles having artificial resistance to radial compression, rather than smoothly re-arranging as randomly located particles would. A cubic packing is easy to implement for any arbitrary geometry but poor initial alignment of fluid particles with boundary particles typically occurs and often leads to non-representative early results as boundary layers of particles are established. A hybrid of both methods where the external surface of the fluid closely matches the boundary surface, but the internal particle distribution minimizes any risk of artificial resistance to compression may prove optimal and is used in the base case here for this reason.

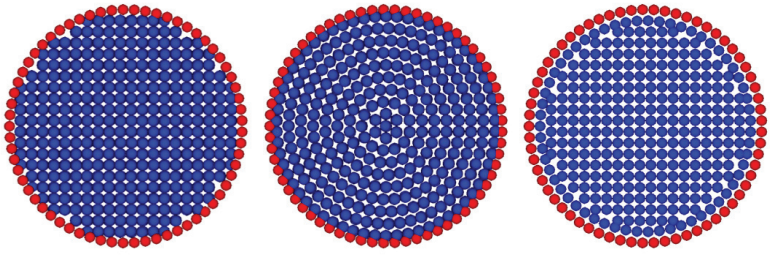

Figure 11. Initial particle arrangement for different assumptions.

The volumetric flow rate history over time shows very similar results for the different initial particle arrangements. The only differences observed are during the ramp time, as shown in Figure 12. The flow pattern for the cylindrical arrangement is less smooth compared with the other two. For the 0.3 amplitude ratio case the cylindrical case also shows greater reverse flow than the other two. The ease of rearrangement of the particles as the tube contracts and expands causes these differences—with the cylindrical packing being harder to rearrange with the cylindrical shells of particles at each radius being able to resist deformation, as expected. The averaged flow rates resulting from the three approaches are compared with the analytical solution in Figure 13. Only small differences are observed, with all three approaches yielding high accuracy, as shown in Table 2.

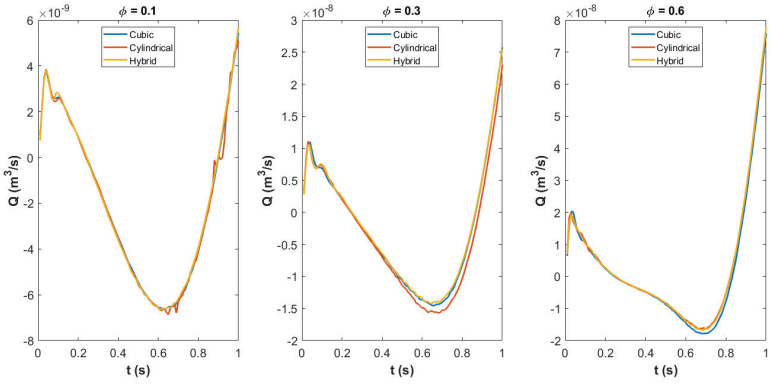

Figure 12. Volumetric flow rate history during the ramp time for different initial particle arrangements.

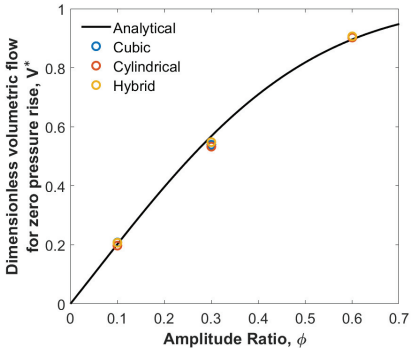

Figure 13. Effect of initial particle arrangement in the SPH model on the dimensionless volumetric flow.

Table 2. Effect of particle arrangement in the SPH simulations.

Arrangement	Normalized Flow Rate	Variation from Analytic Result	Normalized Flow Rate	Variation from Analytic Result	Normalized Flow Rate	Variation from Analytic Result
	$\phi = 0.1$		$\phi = 0.3$		$\phi = 0.6$	
Cubic	0.207	3%	0.540	5%	0.901	0.5%
Cylindrical	0.197	3%	0.529	7%	0.903	0.8%
Hybrid	0.207	2%	0.546	4%	0.904	0.8%

5.1.2. Effect of Kernel Choice

The choice of the kernel is important in this study. A comparison between results obtained with different kernels is given in Figure 14. It shows that the results obtained using the quartic kernel give the best match to the analytic solution. The Wendland kernel shows slightly worse agreement, while the cubic kernel performs the worst of these three commonly used SPH kernels. Figure 15 shows the axial velocity contour at 5 s from the SPH models with different kernels. The quartic kernel provides the smoothest and least diffused pattern compared with the Wendland and cubic kernel, with this effect being most obvious in the $\phi = 0.1$ case, where external forcing is the smallest. Therefore, the quartic option is the best kernel for this problem as it shows the smoothest result and the best agreement with the analytical solution. This can potentially be explained by the shape of the kernels, shown in Figure 3. Firstly, the quartic kernel has larger compact support ($2.5h$ instead of $2h$ for the other two) so can resolve steep gradients better. Secondly, it appears that the greater emphasis placed on the nearest particles of the Wendland kernel compared with the cubic kernel is advantageous in this case. The quartic kernel and to some extent the Wendland kernel capture the boundary layer near the wall better (see Figure 15), which is important in resolving the overall flow field, which in turn determines the net peristaltic flux.

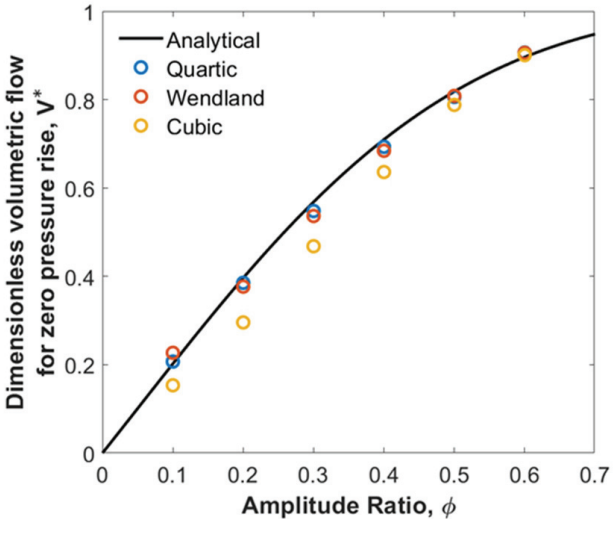

Figure 14. Comparison of dimensionless volumetric flow for the SPH models with different kernels.

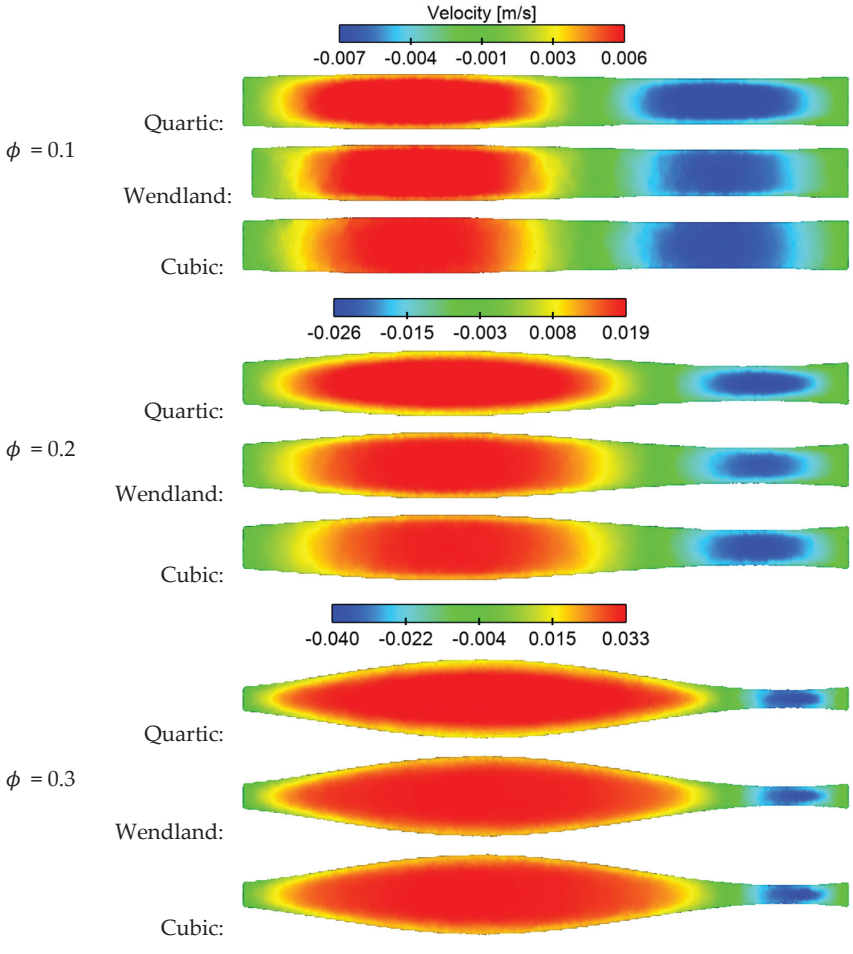

Figure 15. Axial velocity contour at 5 s from the SPH models with different kernels.

5.1.3. Effect of Fluid Sound Speed

As shown in Equations (17) and (19), the local sound of speed (c_s) controls the pressure scale for the fluid flow and the timestep used in the model. In this work, a characteristic velocity, V, is estimated based on the wall wave speed (0.03 m/s). c_s for $\phi = 0.1$ is set to be 20 times the wave speed, making sure the density variation is less than 1%. A numerical convergence study is conducted on the fluid sound speed for the different amplitude ratios listed in Table 3. The results are shown in Figure 16. The chosen base fluid sound speed is acceptable as neither decreasing nor increasing this speed has an impact on the simulation results.

Table 3. Tested sound speed for different amplitude ratios.

c_s (m/s)	ϕ = 0.1	ϕ = 0.3	ϕ = 0.6
Base	0.60	0.68	0.79
Lower (5% lower than base)	0.57	0.64	0.75
Higher (5% higher than base)	0.63	0.71	0.83

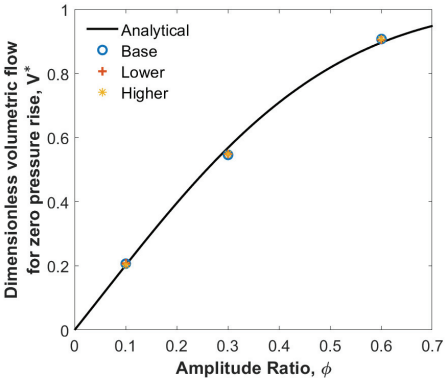

Figure 16. Effect of the fluid sound speed on the net volumetric flow rate for changes in the sound speed.

5.1.4. Effect of Spatial Resolution

A test of convergence is performed on the spatial resolution used in the SPH model. The effect of four different particle sizes (0.15, 0.125, 0.1, and 0.0875 mm) is tested and the results are shown in Table 4. As the particle size decreases, the variation of the normalized flow rate from the analytic results decreases for the different amplitude ratio cases. As shown in Figure 17, the results for particle sizes of 0.1 mm and 0.0875 mm are very close, demonstrating that the solution is well converged and that 0.1 mm particle size is sufficient for accurate prediction, with its results being very close to the analytical solution.

Table 4. Effect of particle size in the SPH simulations.

Particle Size (mm)	Number of Particles	Normalized Flow Rate	Variation from Analytic Result	Normalized Flow Rate	Variation from Analytic Result	Normalized Flow Rate	Variation from Analytic Result
		ϕ = 0.1		ϕ = 0.3		ϕ = 0.6	
0.15	77,000	0.077	62%	0.333	42%	0.583	35%
0.125	124,000	0.185	9%	0.444	22%	0.767	14%
0.1	224,000	0.207	2%	0.546	4%	0.907	1%
0.0875	320,000	0.197	2%	0.550	3%	0.903	1%

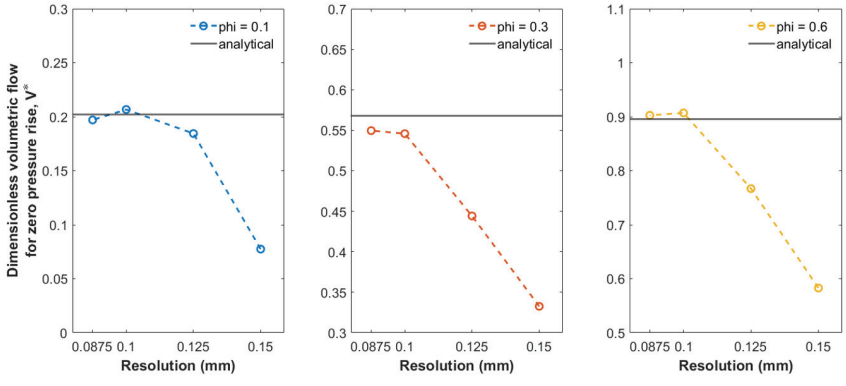

Figure 17. Dimensionless volumetric flow for different particle sizes.

5.2. FVM Model

Mesh and Timestep Independent Studies

A simulation with a refined mesh is made to establish mesh independence. The number of mesh elements was increased from 68,000 to 240,000. The average element size decreased from 0.15 mm to 0.1 mm. A smaller timestep, by a factor of 10, is used to examine the effect of timestep on the numerical results. The results of these analyses are shown in Figure 18. It is evident that the simulations are properly resolved using the original solution parameters.

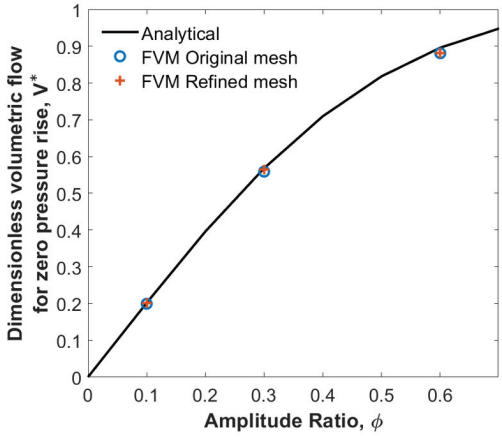

(a) Mesh independence

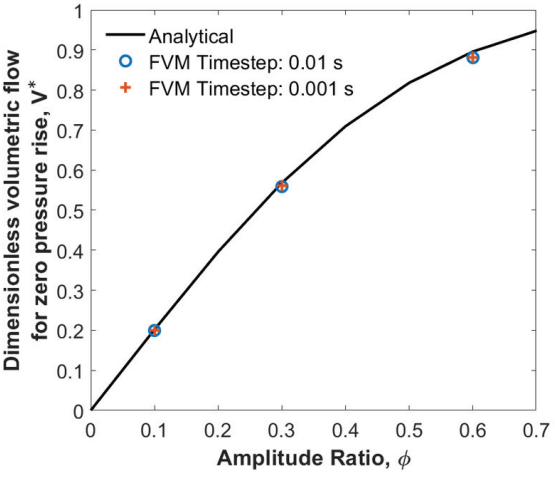

(b) Timestep independence

Figure 18. Mesh and timestep independence studies on the FVM model.

6. Conclusions

Two numerical methods, FVM and SPH, are used to solve a peristaltic flow problem and results from these are compared with the analytical solution. Simulation results show that both methods yield very good agreement with the analytical model results across the large range of occlusion amplitudes that are found in peristalsis. The moving wall boundary condition results in flows in the forward and reverse directions. As the occlusion ratio

increases the forward flow component increases much faster than the negative component resulting in a significant increase in the net flow rate.

The results of both approaches depend on the resolution of the simulation and the choice of solution settings used, but with sufficient resolution, both methods tend to an asymptotic result that matches the analytic model. The spatial resolution in the FVM model depends on the mesh size, while in the SPH model it depends on the chosen particle size. Both methods gave resolution independent results for the base case. In the FVM model, the mesh was refined near the wall but in the SPH model a constant particle size was used.

The dissimilar underlying methodologies of the two solvers meant that different assumptions were made in the two approaches. The FVM model assumed incompressible flow, used implicit time-stepping and solved a Poisson's equation to determine the pressure field. The SPH method assumed a weakly compressible flow, and uses an explicit time integration method, which required a characteristic numerical sound speed to be set based on the expected flow velocities to obtain the pressure field. Despite these differences, both methods gave the same well-resolved solution for the cases presented, in terms of the transient flow history, the net flow over a cycle and the local velocity fields. This work also highlights the very different experience that is needed for use of these complementary solution methods.

Author Contributions: Conceptualization, X.L. and D.F.F.; methodology, X.L., S.M.H., P.W.C. and D.F.F.; software, S.M.H. and P.W.C.; validation, X.L., S.M.H., P.W.C. and D.F.F.; formal analysis, X.L., S.M.H., P.W.C. and D.F.F.; resources, S.M.H. and D.F.F.; writing—original draft preparation, X.L.; writing—review and editing, X.L., S.M.H., P.W.C. and D.F.F.; visualization, X.L.; supervision, D.F.F.; project administration, D.F.F.; funding acquisition, D.F.F. and S.M.H. All authors have read and agreed to the published version of the manuscript.

Funding: This work was partially supported by the Australian Research Council Training center for Australian food processing industry in the 21st century (IC140100026).

Data Availability Statement: Requests for data should be sent to the corresponding author.

Acknowledgments: X.L. received an Australian Government Research Training Program Stipend Scholarship and a supplementary scholarship from the Centre for Advanced Food Engineering (CAFE) of the University of Sydney.

Conflicts of Interest: The authors declare no conflict of interest. One of the authors (D.F.F.) consults to users of Ansys software but this has not influenced the views expressed here.

References

1. Fung, Y.C.; Yih, C.S. Peristaltic transport. *J. Appl. Mech.* **1968**, *35*, 669–675. [CrossRef]
2. Brasseur, J.G. A fluid mechanical perspective on esophageal bolus transport. *Dysphagia* **1987**, *2*, 32–39. [CrossRef] [PubMed]
3. Sinnott, M.D.; Cleary, P.W.; Harrison, S.M. Multiphase Transport in the Small Intestine. In Proceedings of the Eleventh International Conference on CFD in the Minerals and Process Industries, Melbourne, VIC, Australia, 7–9 December 2015; Available online: https://www.cfd.com.au/cfd_conf15/PDFs/131SIN.pdf (accessed on 4 December 2022).
4. Harrison, S.M.; Cleary, P.W.; Sinnott, M.D. Investigating mixing and emptying for aqueous liquid content from the stomach using a coupled biomechanical-SPH model. *Food Funct.* **2018**, *9*, 3202–3219. [CrossRef] [PubMed]
5. Alokaily, S.; Feigl, K.; Tanner, F.X. Characterization of peristaltic flow during the mixing process in a model human stomach. *Phys. Fluids* **2019**, *31*, 103–105. [CrossRef]
6. Li, C.; Jin, Y. A CFD model for investigating the dynamics of liquid gastric contents in human-stomach induced by gastric motility. *J. Food Eng.* **2021**, *296*, 110461. [CrossRef]
7. Huizinga, J.D. Gastrointestinal peristalsis: Joint action of enteric nerves, smooth muscle, and interstitial cells of Cajal. *Microsc. Res. Tech.* **1999**, *47*, 239–247. [CrossRef]
8. Pandey, S.K.; Singh, A. Peristaltic transport in an elastic tube under the influence of dilating forcing amplitudes. *Int. J. Biomath.* **2020**, *13*, 2050027. [CrossRef]
9. Toniolo, I.; Fontanella, C.G.; Foletto, M.; Carniel, E.L. Coupled experimental and computational approach to stomach biomechanics: Towards a validated characterization of gastric tissues mechanical properties. *J. Mech. Behav. Biomed. Mater.* **2022**, *125*, 104914. [CrossRef]
10. Brandstaeter, S.; Fuchs, S.L.; Aydin, R.C.; Cyron, C.J. Mechanics of the stomach: A review of an emerging field of biomechanics. *GAMM-Mitt.* **2019**, *42*, e201900001. [CrossRef]

11. Bornhorst, G.M.; Singh, R.P. Gastric digestion in vivo and in vitro: How the structural aspects of food influence the digestion process. *Annu. Rev. Food Sci. Technol.* **2014**, *5*, 111–132. [CrossRef]
12. Nadia, J.; Olenskyj, A.G.; Stroebinger, N.; Hodgkinson, S.M.; Estevez, T.G.; Subramanian, P.; Singh, H.; Singh, R.P.; Bornhorst, G.M. Tracking physical breakdown of rice- and wheat-based foods with varying structures during gastric digestion and its influence on gastric emptying in a growing pig model. *Food Funct.* **2021**, *12*, 4349–4372. [CrossRef] [PubMed]
13. Bornhorst, G.M.; Roman, M.J.; Rutherfurd, S.M.; Burri, B.J.; Moughan, P.J.; Singh, R.P. Gastric digestion of raw and roasted almonds in vivo and in vitro. *J. Food Sci.* **2013**, *78*, H1807–H1813. [CrossRef] [PubMed]
14. Bornhorst, G.M.; Ferrua, M.; Rutherfurd, S.; Heldman, D.; Singh, R.P. Rheological properties and textural attributes of cooked brown and white rice during gastric digestion in vivo. *Food Biophys.* **2013**, *8*, 137–150. [CrossRef]
15. Bornhorst, G.M.; Chang, L.Q.; Rutherfurd, S.M.; Moughan, P.J.; Singh, R.P. Gastric emptying rate and chyme characteristics for cooked brown and white rice meals in vivo. *J. Sci. Food Agric.* **2013**, *93*, 2900–2908. [CrossRef] [PubMed]
16. Li, C.; Yu, W.; Wu, P.; Chen, X.D. Current in vitro digestion systems for understanding food digestion in human upper gastrointestinal tract. *Trends Food Sci. Technol.* **2020**, *96*, 114–126. [CrossRef]
17. Zhong, C.; Langrish, T. A comparison of different physical stomach models and an analysis of shear stresses and strains in these system. *Food Res. Int.* **2020**, *135*, 109296. [CrossRef]
18. Dupont, D.; Alric, M.; Blanquet-Diot, S.; Bornhorst, G.; Cueva, C.; Deglaire, A.; Denis, S.; Ferrua, M.; Havenaar, R.; Lelieveld, J.; et al. Can dynamic in vitro digestion systems mimic the physiological reality? *Food Sci. Nutr.* **2018**, *59*, 1–17. [CrossRef]
19. Hur, S.J.; Lim, B.O.; Decker, E.A.; McClements, D.J. In vitro human digestion models for food applications. *Food Chem.* **2011**, *125*, 1–12. [CrossRef]
20. Cleary, P.W.; Harrison, S.M.; Sinnott, M.D.; Pereira, G.G.; Prakash, M.; Cohen, R.C.Z.; Rudman, M.; Stokes, N. Application of SPH to single and multiphase geophysical, biophysical and industrial fluid flows. *Int. J. Comput. Fluid Dyn.* **2021**, *35*, 22–78. [CrossRef]
21. Sinnott, M.D.; Cleary, P.W.; Harrison, S.M. Peristaltic transport of a particulate suspension in the small intestine. *Appl. Math. Model.* **2017**, *44*, 143–159. [CrossRef]
22. Sinnott, M.D.; Cleary, P.W.; Arkwright, J.W.; Dinning, P.G. Investigating the relationships between peristaltic contraction and fluid transport in the human colon using Smoothed Particle Hydrodynamics. *Comput. Biol. Med.* **2012**, *42*, 492–503. [CrossRef] [PubMed]
23. Sinnott, M.; Cleary, P.; Arkwright, J.; Dinning, P. Modeling colonic motility: How does descending inhibition influence the transport of fluid? *Gastroenterology* **2011**, *140*, S-865–S-866. [CrossRef]
24. Brasseur, J.G.; Nicosia, M.A.; Pal, A.; Miller, L.S. Function of longitudinal vs circular muscle fibers in esophageal peristalsis, deduced with mathematical modeling. *World J. Gastroenterol.* **2007**, *13*, 1335–1346. [CrossRef]
25. Pal, A.; Indireshkumar, K.; Schwizer, W.; Abrahamsson, B.; Fried, M.; Brasseur, J.G. Gastric flow and mixing studied using computer simulation. *Proc. R. Soc. B Biol. Sci.* **2004**, *271*, 2587–2594. [CrossRef] [PubMed]
26. Ferrua, M.J.; Kong, F.; Singh, R.P. Computational modeling of gastric digestion and the role of food material properties. *Trends Food Sci. Technol.* **2011**, *22*, 480–491. [CrossRef]
27. Du, P.; Paskaranandavadivel, N.; Angeli, T.R.; Cheng, L.K.; O'Grady, G. The virtual intestine: In silico modeling of small intestinal electrophysiology and motility and the applications. *Wiley Interdiscip. Rev. Syst. Biol. Med.* **2016**, *8*, 69–85. [CrossRef] [PubMed]
28. Cleary, P.W.; Harrison, S.M.; Sinnott, M.D. Flow processes occurring within the body but still external to the body's epithelial layer (gastrointestinal and respiratory tracts). In *Digital Human Modeling and Medicine*; Paul, G., Doweidar, M., Eds.; Elsevier: Amsterdam, The Netherlands, 2022.
29. Shapiro, A.H.; Jaffrin, M.Y.; Weinberg, S.L. Peristaltic pumping with long wavelengths at low Reynolds number. *J. Fluid Mech.* **1969**, *37*, 799–825. [CrossRef]
30. Eymard, R.; Gallouët, T.; Herbin, R. Finite volume methods. In *Handbook of Numerical Analysis*; Elsevier: Amsterdam, The Netherlands, 2000; Volume 7, pp. 713–1018.
31. Burns, J.C.; Parkes, T. Peristaltic motion. *J. Fluid Mech.* **1967**, *29*, 731–743. [CrossRef]
32. Barton, C.; Raynor, S. Peristaltic flow in tubes. *Bull. Math. Biophys.* **1968**, *30*, 663–680. [CrossRef]
33. Cleary, P.; Prakash, M.; Ha, J.; Stokes, N.; Scott, C. Smooth particle hydrodynamics: Status and future potential. *Prog. Comput. Fluid Dyn.* **2007**, *7*, 70–90. [CrossRef]
34. Monaghan, J.J. Simulating free surface flows with SPH. *J. Comput. Phys.* **1994**, *110*, 399–406. [CrossRef]
35. Monaghan, J.J. Smoothed particle hydrodynamics. *Rep. Prog. Phys.* **2005**, *68*, 1703–1759. [CrossRef]
36. Cleary, P.W. Modelling confined multi-material heat and mass flows using SPH. *Appl. Math. Model.* **1998**, *22*, 981–993. [CrossRef]
37. Cummins, S.J.; Silvester, T.B.; Cleary, P.W. Three-dimensional wave impact on a rigid structure using smoothed particle hydrodynamics. *Int. J. Numer. Methods Fluids* **2012**, *68*, 1471–1496. [CrossRef]
38. Wendland, H. Piecewise polynomial, positive definite and compactly supported radial functions of minimal degree. *Adv. Comput. Math.* **1995**, *4*, 389–396. [CrossRef]
39. Monaghan, J.J.; Lattanzio, J.C. A refined particle method for astrophysical problems. *Astron. Astrophys.* **1985**, *149*, 135–143. Available online: https://adsabs.harvard.edu/pdf/1985A%26A...149..135M (accessed on 4 December 2022).
40. Monaghan, J.J. Smoothed particle hydrodynamics. *Annu. Rev. Astron. Astrophys.* **1992**, *30*, 543–574. [CrossRef]
41. Courant, R. *Supersonic Flow and Shock Waves: A Manual on the Mathematical Theory of Non-Linear Wave Motion (No. 62)*; Courant Institute of Mathematical Sciences, New York University: New York, NY, USA, 1944; p. 304.

42. Cleary, P.W. New implementation of viscosity: Tests with Couette flows. In *SPH Technical Note 8, Division of Maths and Stats Technical Report DMS—C 96/32*; CSIRO Publishing: New Ryde, NSW, Australia, 1996; Available online: https://publications.csiro.au/rpr/download?pid=procite:ce934b77-8db6-433c-8c12-a58e5bec2e0c&dsid=DS1 (accessed on 4 December 2022).
43. Monaghan, J. On the problem of penetration in particle methods. *J. Comput. Phys.* **1989**, *82*, 1–15. [CrossRef]
44. Ansys Inc. Fluid dynamics verification manual. 2022. Available online: https://ansyshelp.ansys.com/account/secured?returnurl=/Views/Secured/corp/v222/en/fbu_vm/fbu_vm.html (accessed on 4 December 2022).
45. Patankar, S.V. *Numerical Heat Transfer and Fluid Flow*; CRC Press: Boca Raton, FL, USA, 2018.
46. Ferziger, J.H.; Perić, M.; Street, R.L. *Computational Methods for Fluid Dynamics*; Springer: Berlin/Heidelberg, Germany, 2002.

fluids

MDPI

Article

Jet Velocity and Acoustic Excitation Characteristics of a Synthetic Jet Actuator

Nadim Arafa [1], Pierre E. Sullivan [2,*] and Alis Ekmekci [3]

[1] Faculty of Applied Science and Technology, Sheridan College, Brampton, ON L6Y 5H9, Canada
[2] Department of Mechanical and Industrial Engineering, University of Toronto, Toronto, ON M5S 3G8, Canada
[3] Institute for Aerospace Studies, University of Toronto, Toronto, ON M3H 5T6, Canada
* Correspondence: pierre.sullivan@utoronto.ca

Abstract: The effect of the excitation frequency of synthetic jet actuators on the mean jet velocity issuing from an array of circular orifices is investigated experimentally, focusing on the acoustic excitation characteristics of the actuator's cavity. Two cavity configurations are considered. In the first configuration, synthetic jets are generated by exciting a single, large cavity having an array of sixteen orifices via sixteen piezoelectric elements. In the second configuration, the cavity volume of the first configuration is divided into eight isolated compartments, each with two orifices and two piezoelectric elements. Several distinct resonant peaks were observed in the frequency response of the synthetic jet actuator built with a single large-aspect-ratio cavity, whereas the case of compartmentalised cavities exhibited a single resonant peak. Acoustic simulations of the large-aspect-ratio-cavity volume showed that the multiple peaks in its frequency response correspond to the acoustic standing-wave mode shapes of the cavity. Due to its large aspect ratio, several acoustic mode shapes coexist in the excitation frequency range aside from the Helmholtz resonance frequency. When the actuator's cavity volume is compartmentalised, only the Helmholtz resonance frequency is observed within the excitation frequency range.

Keywords: jet noise; synthetic jets; flow control; acoustic simulations

Citation: Arafa, N.; Sullivan, P.E.; Ekmekci, A. Jet Velocity and Acoustic Excitation Characteristics of a Synthetic Jet Actuator. *Fluids* **2022**, *7*, 387. https://doi.org/10.3390/fluids7120387

Academic Editor: Mehrdad Massoudi

Received: 14 October 2022
Accepted: 14 December 2022
Published: 16 December 2022

1. Introduction

Previous work on synthetic jet actuators (SJAs) has proven their potential to delay flow separation over critical aerodynamic surfaces [1–4]. Like many other active flow control techniques [5,6], SJAs have the promising aspect of being tuned to control-separated flow in different conditions. In this technology, flow control is achieved by injecting flow via the external excitation of an enclosed cavity volume. SJAs contain a piezoelectric diaphragm that alternates the air volume in the cavity and produces the synthetic jet through an orifice [7,8]. SJAs are generally smaller than an aircraft wingspan, so they are usually used in array form to cover long spans in aeronautical applications [9,10]. There have been several studies in the literature that first focused on the design of a singular SJA unit and then utilized these units in arrays for a magnified effect. SJAs may comprise a number of discrete cavities excited by isolated piezoelectric elements [11,12] or a large, unified-cavity volume excited simultaneously by several piezoelectric elements. In the latter case, the single, large cavity may have several orifices [10] or a large-aspect-ratio rectangular slot [13,14]. Tang et al. [12] characterized a single cube-shaped cavity-volume unit powered by four piezoelectric elements and used ten of these SJA units, keeping them isolated, in an array form along an aerofoil span. In the frequency response of the single SJA unit, Tang et al. [12] observed a single peak corresponding to the Helmholtz resonance frequency for different excitation voltages. Therefore, they recommended operating the actuator near its Helmholtz frequency to achieve the highest possible jet velocity. Jabbal et al. [9] also used discrete, inclined cavities in an array form, where each chamber was powered

by a single piezoelectric element of its own. They showed that inclining the cavities allows for the overlapping of the actuators and thereby reduces the size of the array with respect to the non-inclined version while maintaining a comparable mean jet velocity. Both Feero et al. [13] and Amitay et al. [15] employed synthetic jets issuing from a large-aspect-ratio rectangular slot to control flow separation over the span of an aerofoil. The internal cavity in their SJAs contained a single large-aspect-ratio cavity covering the length of the rectangular slot. Exciting such a single, large cavity with multiple piezoelectric elements brings the advantage of amplifying the output jet velocity compared to isolated volumes. Both groups showed that SJAs with large cavities and several excitation elements exhibit complex frequency responses when compared to isolated units. Currently, there is no general consensus on the design approach for SJA arrays, and it would be very important to understand the difference between using arrays of isolated SJA units or a single connected unit. Hence, insight into the characteristics of SJA arrays of different cavity types is needed for optimum design and flow-control output.

It is generally recommended to match the excitation frequency of SJAs to a flow instability to improve the flow-control effectiveness of the actuator [16]. Amitay and Glezer [16] showed that when the excitation frequency matches the frequency of the wake instability, unsteady flow reattachment over an aerofoil can be achieved via large-scale vortices that attract the flow towards the trailing edge of the aerofoil. On the other hand, when the excitation frequency matches the frequency of the shear-layer instability—which is approximately one order of magnitude higher than the frequency of the wake instability—flow control is achieved by the induction of small-scale vortices that may suppress the flow separation in a large eddy sheet or the separated layer [17]. Moreover, for efficient SJA performance it is suggested to use an excitation frequency that maximises the mean jet velocity injected into the crossflow to magnify the momentum flux into the crossflow [18]. Therefore, the excitation frequency in a well-designed SJA should match one of the instability frequencies and provide maximum jet velocity. These considerations should also leave some room for fine-tuning. Maximising the jet velocity from a cavity is generally achieved by exciting the cavity at its Helmholtz resonance frequency. Alternatively, the mechanical resonance of the oscillating diaphragm may also be targeted so that the excitation frequency amplifies the jet velocity [19]. Gallas et al. [20] proposed modelling the SJA components as elements of an equivalent electrical circuit using the Lumped Element Modelling (LEM) method to characterise the SJA response based on its geometry and material properties. This method could predict the interaction of the Helmholtz resonance frequency and the mechanical resonance frequency of the oscillating diaphragm when these frequencies are close to each other. The Helmholtz resonance frequency for the cavity volume, f_H, can be estimated theoretically using the cavity and orifice dimensions as follows:

$$f_H = \frac{c}{2\pi}\sqrt{\frac{A}{L_e V}} \tag{1}$$

where c is the speed of sound, A is the cross-sectional area of the orifice, L_e is the equivalent depth of the orifice neck, and V is the cavity volume [21]. However, it should be noted that the Helmholtz equation is formulated for an ideal spherical volume in which the sound-wave propagation matches the volume boundaries. The mechanical-resonance frequency of the diaphragm can be formulated based on its geometric, material, and electrical properties [22]. It is also affected by the clamping condition of the diaphragm circumference, which may deviate the actual resonance frequency of the diaphragm from its theoretical formulation. If the Helmholtz resonance frequency of the cavity and the mechanical resonance frequency of the diaphragm used in the SJA are too close to each other, a coupled frequency response would be obtained in which the two peaks deviate from their theoretically estimated values and merge into one peak, which may maximise the peak jet velocity [22,23]. Such a situation is unpredictable and may be overlooked in the initial design phase, but would be discovered upon SJA implementation.

Another design aspect related to frequency is the noise generated from the actuator. Several studies in the literature were aimed at enhancing the SJA designs by reducing the resulting noise. This was achieved through several methods such as having out-of-phase dual-acting orifices [24], introducing phase miss-matching [25], soundproofing the cavity walls [26], or using different orifice shapes [27]. These studies showed very promising results. However, they also indicated the need for more understanding of the acoustic excitation characteristics of SJAs to reach a better design. Van Buren et al. [23,28] investigated the synthetic-jet-cavity acoustics to determine the effects of the orifice size and cavity volume on the resonance frequency of the SJA. They showed that, for a 'pancake-shaped' (high-aspect-ratio disk) cavity, the Helmholtz equation overestimates the value of the resonance frequency. They concluded that the acoustic resonance frequency is better estimated by a quarter-wavelength resonator equation when the cavity is thin and the orifice opening is relatively large. This is because this cavity volume shape tends towards having the necessary boundaries for the quarter-wavelength excitation (with an open-end condition at the orifice and a closed end at the cavity wall opposite to the orifice). On the other hand, as the width of the cavity increases with respect to diameter (diverging from the pancake shape) and the orifice size decreases, the Helmholtz equation becomes better in determining the resonance frequency while the accuracy of the quarter-wavelength resonator equation reduces. This can be attributed to the fact that the cavity widens and approaches an ideal Helmholtz-resonator shape (more detailed work on the effects of Helmholtz and quarter-wave resonators on cavity acoustics can be found in Ref. [29]). The work of Van Buren et al. [28] demonstrated that the geometry of the cavity volume controls the phenomenon responsible for the acoustic resonance of the SJA cavity. Therefore, the Helmholtz resonance equation may be insufficient to estimate the resonance frequency of SJA cavities, especially when considering geometries that significantly differ from the ideal Helmholtz resonator.

Feero et al. [30] investigated the effect of the synthetic jet injection location on the control of flow past an aerofoil. They used sixteen piezoelectric elements to excite a single large-aspect-ratio-cavity volume (similar to what will be investigated herein). The synthetic jet was introduced through a high-aspect-ratio rectangular slot encompassing a slender cavity volume. They observed that the mean jet-velocity response of the SJA depicts several local peaks at various excitation frequencies. An observation of multiple peaks in the jet-velocity response implies that the acoustic excitation characteristics of their cavity are not as simple as a Helmholtz excitation case and need further understanding. The literature lacks comprehensive studies on the acoustic excitation features of SJA cavities and how they may impact the generated jet velocities. It is crucial to understand all aspects related to the acoustic excitation phenomena in SJA cavities for designing SJAs with maximum actuator performance, which is the main motivation of the current study.

This paper investigates the frequency response of an SJA with emphasis on determining the effect of the cavity shape on the acoustic excitation characteristics of the SJA. Focus is placed on synthetic jets emanating from an array of circular orifices into the span of a flat plate under quiescent flow conditions. The effect of the excitation frequency on the mean jet velocity emanating from the SJA is characterized. Furthermore, on- and off-resonance excitation frequencies are used to capture the impact of the acoustic resonance excitation on the uniformity of the jet velocity along the span of the array. This work also compares the acoustic excitation characteristics of a single, large-aspect-ratio-cavity volume to those resulting from isolated volumes covering the same spanwise length. This shall provide a better understanding of the complex acoustic excitation characteristics of these cavity types.

2. Experimental and Numerical Techniques

The SJA used in this investigation contained an array of sixteen piezoelectric disks, arranged into eight pairs mounted on the facing walls of the SJA cavity, and sixteen circular orifices, as shown in Figure 1a. For this SJA array, two cavity configurations were tested:

(a) *A single, large-aspect-ratio cavity* encompassing the entire array of actuator disks, generated by leaving the region between the piezoelectric elements connected, as depicted in Figure 1a,

(b) *Eight single-cavity isolated compartments*, created by using geometrical dividers between each pair of piezoelectric elements, as shown in Figure 1b.

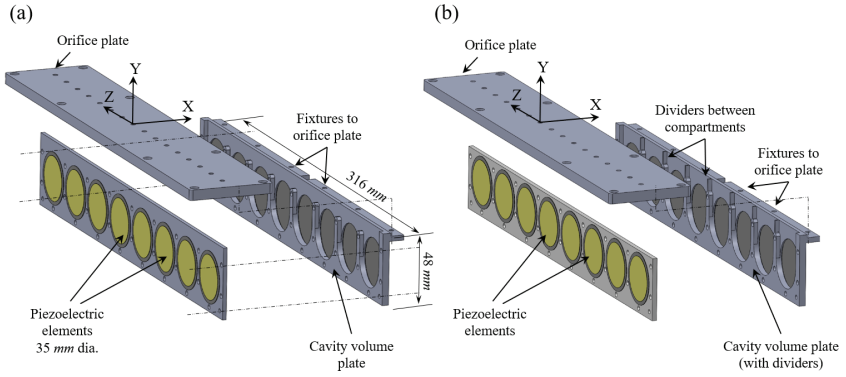

Figure 1. Exploded view of the SJA showing (**a**) the single cavity case, with 16 piezoelectric elements and 16 orifices, and (**b**) 8 single-compartmented cavities, where the cavity volume plate illustrates how the division of the array cavity into 8 equal compartments is achieved. Dashed lines show the assembly lines.

The air volume entrained within each cavity configuration is depicted in Figure 2a. The air volume shown in Figure 2b is 7.54×10^{-6} m^3, which is equal to 1/8th of the large-aspect-ratio-cavity volume depicted in Figure 2a. In both cavity configurations, synthetic jets were developed through sixteen orifices distributed over a span of 285 mm on a flat plate (as seen in Figure 1a) under quiescent conditions. Note that, in the compartmented cavity configuration, each cavity compartment opens to two orifices, depicted in in Figure 2b. Each of the sixteen orifices have a diameter of 3.42 mm and the spacing between the orifices is 19 mm (centre-to-centre).

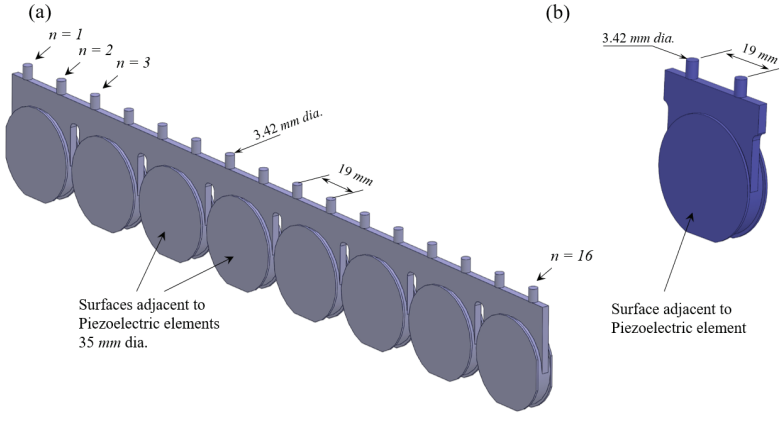

Figure 2. (**a**) The air volume existing inside the single array cavity, excited by the 16 piezoelectric elements, and (**b**) the air volume entrained within one of the cavity compartments, excited by two piezoelectric elements, i.e., this is one of the eight compartments shown in Figure 1b.

All experiments were performed inside an anechoic room located at the University of Toronto Institute for Aerospace Studies. A signal generator (Model: Rigol, DG1022Z) powered all piezoelectric elements simultaneously by providing discrete, sinusoidal ex-

citations which were amplified by a linear power amplifier (Model: Mide QuickPack, QPA3202) to give an amplified excitation amplitude of 150 V_{pp} to all piezoelectric elements (peak-to-peak amplitude). The piezoelectric elements were all operating in-phase through a parallel connection to the amplifier. During the experimental investigations, the jet velocity was measured by a single-sensor hot-wire probe (Dantec miniature probe, 55P11) across and at the centre of each orifice. A two-dimensional traverse mechanism controlled the location of the hot wire in the wall–normal and spanwise directions (i.e., Y and Z directions based on the coordinate system introduced in Figure 1a), with a motion resolution of 0.0025 mm. The velocity was sampled at a 32 kHz sampling frequency over 30 s, which was found to be sufficient to avoid aliasing and any measurement or sampling errors. The sinusoidal input signal sent to the piezoelectric elements was acquired simultaneously with the velocity data to obtain phase-correlated information between the jet velocity and the input excitation signal. The input signal was also used as a reference for the hot-wire measurements conducted non-concurrently over different orifices, eliminating the need for simultaneous measurements above all sixteen of the orifices.

Acoustic simulations were performed to investigate the acoustic excitations of the air volume inside the unified, large-aspect-ratio SJA cavity and its compartmented counterpart. The COMSOL software [31] was utilized to perform an eigenfrequency study for the cavity volumes entrained in both cases (the volumes are shown in Figure 2). Solving the wave equation for the eigenfrequencies and the eigenmodes gave the acoustic natural frequencies and the corresponding acoustic mode shapes or pressure distributions at these frequencies, respectively [32]. This wave equation is given by:

$$\frac{\partial^2 p}{\partial x^2} + \frac{\partial^2 p}{\partial y^2} + \frac{\partial^2 p}{\partial z^2} = \frac{1}{c^2}\frac{\partial^2 p}{\partial t^2} \tag{2}$$

where p is the acoustic pressure and c is the speed of sound. Unstructured tetrahedral elements of various sizes were used to capture all details of the internal cavity geometries. The number of elements used for the large, unified-cavity volume case was 800,000, while around 100,000 elements were utilized for the compartmented cavity. The average meshing element size was 7.5×10^{-2} mm^3. This mesh size was reached following a size-decremental iterative procedure until the values of the acoustic mode frequencies from simulations matched those observed experimentally and did not change any further with the reduction in the mesh size. For the boundary conditions, all solid surfaces were modelled as stagnant walls, the orifices were modelled as pressure openings, and the surfaces adjacent to the piezoelectric diaphragms were modelled as rigid, moving walls. The excitation input was simulated by sinusoidally forcing all surfaces adjacent to piezoelectric diaphragms to oscillate in phase with a uniform amplitude. The elasticity of the diaphragms was not modelled to avoid interaction with structural flexural modes, which are not the focus of this work. It is important to note that the eigenfrequency study presented here provided a standing-wave solution for the natural frequencies and the corresponding acoustic mode shapes. A transient, or time-dependent travelling wave, solution for a specific excitation frequency or amplitude is not the focus of this work, as the motivation for this work was focused more on assessing the frequency response and excitation characteristics rather that the changes in the time domain for a given frequency.

3. Results

3.1. Jet-Velocity Measurements for the Unified, Large-Aspect-Ratio Cavity

Two sets of experiments were performed to characterize the frequency response of the SJA configuration that had one large, unified cavity. First, the mean jet-velocity response at the exit of one of the orifices was determined as a function of the excitation frequency. Second, the mean jet velocities over all sixteen of the orifices were measured at a single excitation frequency to explore whether the jet velocity varied from orifice to orifice over the array. Figure 3a shows the phase-averaged jet velocity at the exit of the orifice that is located in the middle of the array (i.e., the orifice numbered as n = 8 based on the convention used

in Figure 2a, where the measurement point is X/D = Y/D = Z/D = 0) in response to the sinusoidal input signal shown in Figure 3b, which excited the piezoelectric elements at a frequency of f_e = 1220 Hz and an amplitude of E = 150 V_{pp}. Here, for the positive amplitudes of the excitation input signal (i.e., where the phase of the input signal was $0 < \varphi < \pi$) the piezoelectric elements deflected inward into the cavity, leading to the expulsion of the jet, while for the negative excitation amplitudes (i.e., $\pi < \varphi < 2\pi$) the piezoelectric elements deflected outward, corresponding to the ingestion stroke. The velocity signals detected by the single-wire probe used in this investigation were always positive. As a result, the direction of the jet flow could not be distinguished from these velocity signals. However, it was noted that the jet velocity over the return stroke ($\pi < \varphi < 2\,\pi$) seemed marginally lower than the expulsion stroke. This is because some of the returning flow to the cavity was drawn from the edges of the orifice, following a path parallel to the orifice cross-section rather than normal to the orifice cross-section. The error bars in Figure 3a show the standard deviation around the phase-averaged jet velocity at each phase. It should be pointed out here that the hot-wire data always demonstrated a lag (or, in other words, a phase-angle difference) with respect to the input excitation. This phase difference between the hot-wire output and the excitation input was not significant for the case presented in Figure 3a, where the excitation frequency corresponded to a resonant frequency. However, phase-angle variations from orifice to orifice were observed for cases driven by other excitation frequencies, which will be discussed in further detail in Section 4.

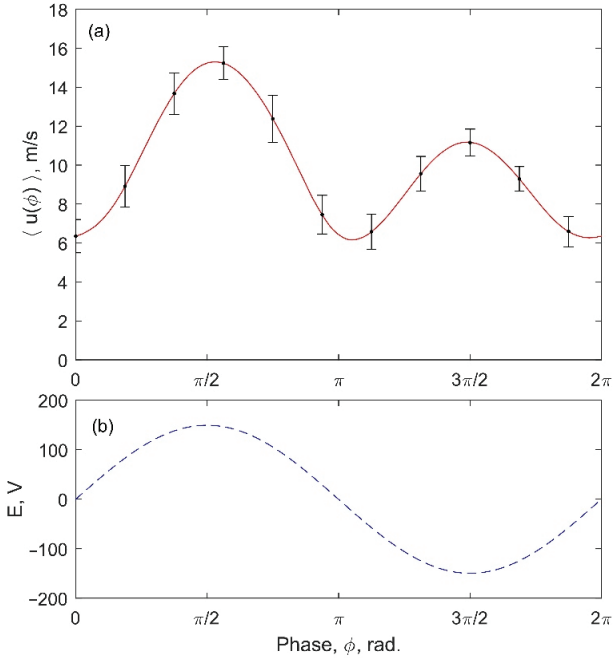

Figure 3. (**a**) Phase-averaged jet velocity, ⟨u(ϕ)⟩, at the exit of the orifice Y/D = 0 in response to (**b**) the sinusoidal excitation at the frequency of f_e = 1220 Hz and the excitation voltage of E = 150 Vpp. Error bars mark the standard deviation in estimating the phase-averaged jet velocity.

It is common in the literature to define the time–mean jet velocity as the time average of the synthetic jet velocity over the expulsion half of the cycle [33]. Hence, it is essential to distinguish the expulsion stroke in the measured velocity signal since the measured data were not phase-locked to the excitation. Given that the measured velocity data had an excitation-frequency-dependent phase-angle difference from the excitation input, as indicated above, the expulsion stroke on the phase-averaged velocity cycle was determined

by taking the phase of the maximum jet velocity as a reference point. The phase-angle range corresponding to the expulsion stroke in a cycle was then considered to be a quarter cycle ($\pi/2$) before and after the phase angle of the maximum jet velocity. Based on this convention, the time–mean jet velocity during the expulsion stroke was found by:

$$\langle \overline{U_J} \rangle = \frac{1}{\tau/2} \int_{t_1}^{t_2} \langle u(t) \rangle \, dt \tag{3}$$

where τ is the period of one cycle, t_1 is the onset time of the expulsion stroke, and t_2 is the ending time of the expulsion stroke. Notice here that, as the expulsion stroke occurred over half of the excitation cycle (i.e., from 0 to $\tau/2$) the denominator in Equation (3) equals $t_2 - t_1 = \tau/2$. In Equation (3), the jet velocity was first phase-averaged and then integrated over the expulsion stroke so that the results were independent of the excitation frequency and the phase-angle difference.

Figure 4 shows the mean jet velocity of the expulsion stroke for the unified-cavity volume configuration, computed using Equation (3) for different excitation frequencies ranging from 300 Hz to 2200 Hz at the exit of the orifice that was located in the middle of the array (i.e., the orifice was numbered as n = 8 and the measurement location was X/D = Z/D = Y/D = 0). This frequency response revealed several peaks in the frequency range of f_e = 800 to 1400 Hz. Equation (1) for the Helmholtz resonance frequency, f_H, can be rearranged for round orifices using lumped elements to:

$$f_H = \frac{c}{2\pi} \sqrt{\frac{3A}{4hV}} \tag{4}$$

where c is the speed of sound, A is the orifice area, h is the depth of the orifice neck, and V is the cavity volume [21]. Using this formula, the theoretical value of the Helmholtz frequency was estimated to be 1232 Hz for the dimensions of the current cavity. This estimation is very close to the resonant peak observed at 1220 Hz in the experimental data presented in Figure 4. However, it can be seen in Figure 4 that, other than this resonant frequency, three more frequencies exist at which the jet velocity peaked. A similar frequency response for the jet velocity was obtained above all other orifices, which confirmed that the existence of these frequency peaks is a characteristic of the cavity excitation affecting the whole actuator.

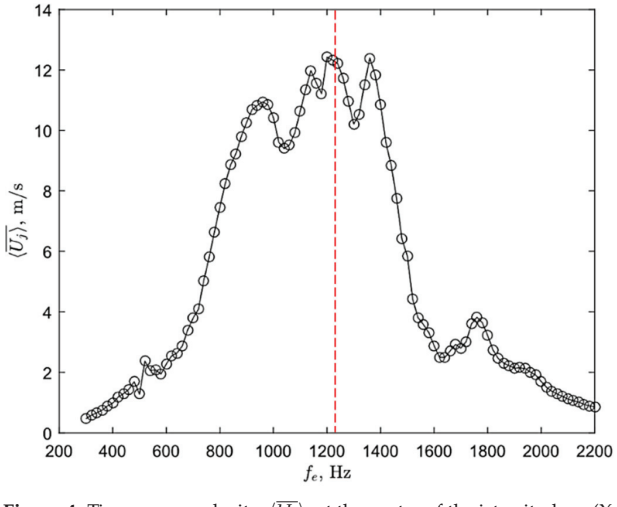

Figure 4. Time–mean velocity, $\langle \overline{U_i} \rangle$, at the centre of the jet exit plane (X/D = Y/D = 0) as a function of the excitation frequency, f_e, for the unified array cavity at the exit of the orifice located in the middle of the array (n = 8), E = 150 V_{pp}. Estimated Helmholtz frequency value is shown by dotted line.

To gain additional insight into these frequency peaks, further measurements and analyses were performed. To begin, the time–mean jet velocity across adjacent synthetic jets was acquired for different excitation frequencies to explore the possibility of an interaction between injected jets from neighbouring orifices. Figure 5 shows the time–mean jet profiles across two consecutive orifices at the height of one orifice diameter above the orifice exits (i.e., at Y/D = 1) for the excitation at the resonance frequency of 1220 Hz. In this figure, the first jet, centred around Z/D = 0, emanated from the orifice located in the middle of the array, n = 8, while the subsequent jet, centred around Z/D = 5.57, was injected from the adjacent orifice, n = 9. It can be observed that both synthetic jets showed a typical mean velocity profile that was similar to that of a steady jet with a local maximum at the centre of each jet, which agrees well with the literature [34,35]. It is also clear that the jets were not interacting with each other. Only a slight difference in the maximum jet velocity at the centreline was observed between these two consecutive jets. Cross-jet profiles captured over orifices located further away from each other depicted a similar jet profile but a significant difference in the peak jet-velocity value. In fact, when the mean jet velocity along all sixteen of the orifices in the array was captured one orifice-diameter above each orifice at the centreline of the jets, a significant variation in jet-velocity peak was observed over the array span. The shape of this variation was found to depend on the excitation frequency, as shown in Figure 6, where the mean jet velocity over the centre of each orifice is depicted for two representative excitation frequencies (the frequencies of f_e = 1200 Hz and f_e = 800 Hz). Notice that the relatively similar values observed for the velocity peaks of the jets issued from the orifices n = 8 and 9 in Figure 5 are also detectable in Figure 6 for the same orifices at the same excitation frequency. It can be seen from Figure 6 that, when the SJA array was excited near the resonant-frequency peak of 1220 Hz, the mean jet velocity increased over two sections: namely, over the orifices n = 3 to 6 and n = 10 to 14. On the contrary, when the excitation was supplied at a frequency of 800 Hz, the orifices n = 2 to 4 showed an increase in jet velocity while the orifices n = 9 to 14 showed a reduction. The origins of the additional resonant peaks, detected in Figure 4, and the rationale behind the variation of the jet velocity over the array of orifices, seen in Figure 6, will be revealed in Section 4 from the acoustic simulation results. However, before delving into these results, it was important to determine if the variation in the jet velocity over the orifice array could be avoided altogether. To this end, the internal cavity volume was divided into separate compartments, as is depicted in Figure 1b. The next section will discuss the experimental results for such a design.

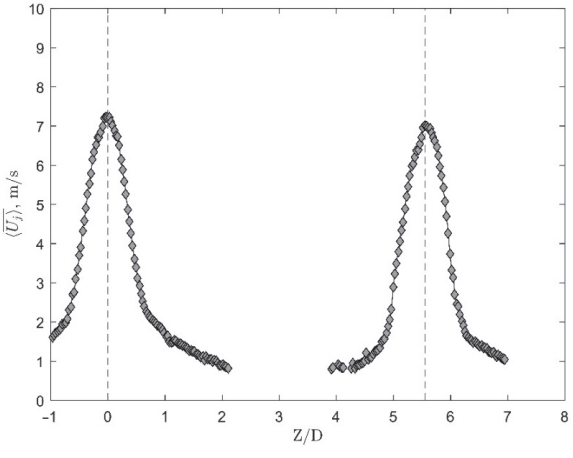

Figure 5. The mean jet velocity during the blowing stroke across two consecutive synthetic jet orifices (n = 8 and n = 9) for the excitation frequency f_e = 1220 Hz. Velocity measurements are performed at one orifice diameter above the exit of the orifices (Y/D = 1). The excitation voltage is E = 150 V_{pp}.

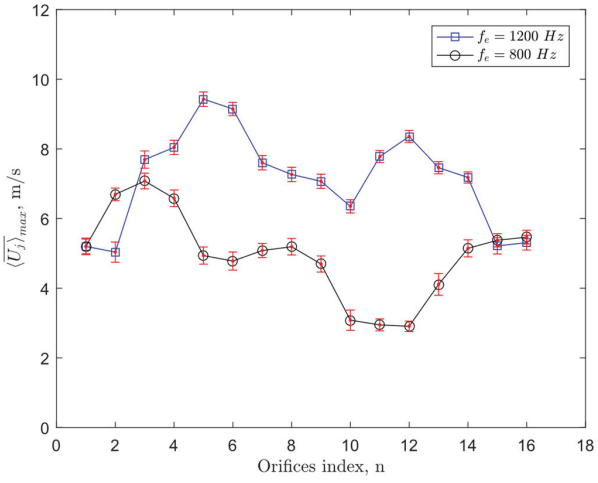

Figure 6. Variation of the peak mean jet velocity during expulsion stroke along the array of orifices at Y/D = 1 (measured at each orifice centreline) for two excitation frequencies (f_e = 800 Hz and 1200 Hz) for the unified-array-cavity volume. Error bars show the standard deviation of measurements at each point. The excitation voltage is E = 150 V_{pp}.

3.2. Jet-Velocity Measurements for the Compartmented Array Cavity

In Figure 7 (below), the time–mean jet velocity over the expulsion stroke from one of the orifices of the compartmented cavity design is given as a function of the excitation frequency with the hot wire located at the centre of the orifice exit. It is observed that this frequency response exhibited only one resonant peak around 1200 Hz, which matches the theoretical Helmholtz resonance frequency estimated earlier. This is a significant difference from the multiple peaks observed for the unified-cavity volume before. Notice that each singular compartment has the same Helmholtz resonance frequency as the unified-cavity case because, when dividing the unified, large-cavity volume into eight isolated compartments, both the cavity volume and the total orifice area in Equation (4) are divided by 8, rendering the same Helmholtz resonance frequency for both configurations. Similar frequency-response graphs were observed when hot-wire measurements were performed above other isolated cavity compartments. The mean jet-velocity profiles above different orifices of the compartmented case were also found to be comparable with no significant differences. In fact, the maximum mean jet velocity, detected at the centre of each jet, varied only slightly for the array of orifices, as is shown in Figure 8. When the compartmented cavities were excited near their resonance frequency, f_e = 1200 Hz, the standard deviation in the maximum time-averaged jet velocity was very small, as the error bars in Figure 8 show. On the other hand, at an off-resonance excitation of f_e = 800 Hz, the standard deviation around the time-averaged value of the time–mean jet velocity was relatively larger. These observations correspond to the characteristics of acoustic excitation of a cavity at its Helmholtz resonance frequency. When the cavity was excited at its Helmholtz resonance frequency, the measured velocity signal was very close to the sinusoidal shape of the tonal-input excitation. Therefore, the standard deviation is relatively small when the signal is phase-averaged. However, in the case of off-Helmholtz resonance excitation, the velocity response to the input excitation was still sinusoidal but exhibited a larger standard deviation (or inconsistencies) in the signal.

The existence of only the Helmholtz resonance peak in the frequency response of every single compartment in the compartmented-cavity design suggests that only one mechanism of exciting the cavity volume can be at play for the compartmented case, and this is the reason why the jet velocity does not exhibit any considerable variation along the array span in this case. The next section discusses acoustic simulations of the two actuator

configurations (the configuration with the unified, large-aspect-ratio cavity and the one with compartmented cavities) to further explore the acoustic excitation mechanisms for each case.

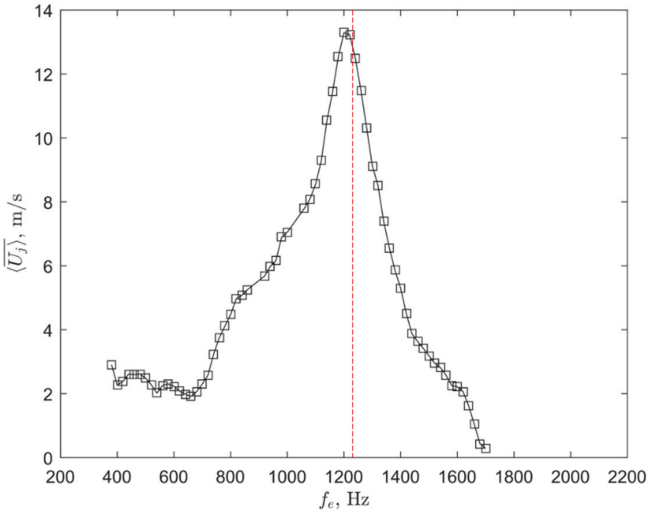

Figure 7. Time–mean velocity, $\langle \overline{U_j} \rangle$, at the jet centre over the expulsion stroke as a function of the excitation frequency, f_e, for one of the eight cavity compartments at the exit of the orifice located in midspan of the array, n = 8. Estimated Helmholtz frequency value is shown by dotted line.

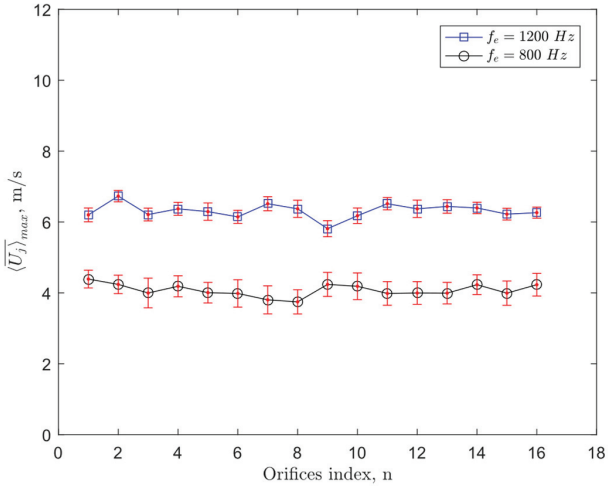

Figure 8. Variation of the time–mean jet velocity during expulsion stroke along the array of orifices at Y/D = 1 (measured at each orifice centreline) for two representative excitation frequencies (f_e = 800 Hz and 1200 Hz) for the case with compartmented cavities.

4. Acoustic Simulations Results

Acoustic simulations of the air volume entrained within each of the two cavity configurations considered in this study were carried out following the methodology explained in Section 2. The simulations were conducted for the exact geometry of the cavity, shown in Figure 2. For the large-aspect-ratio cavity, the simulations gave several eigenfrequencies in the simulated range of excitation frequencies. Some of these frequencies closely matched

the frequency peaks detected experimentally in the jet-velocity measurements (presented in Figure 4), shown in Table 1. Figure 9 shows the instantaneous acoustic-pressure distribution within the entire unified, large-aspect-ratio-cavity volume for the four resonant frequencies shown in Table 1. The acoustic pressure levels resulting from these simulations were arbitrary but comparative due to the nominal boundary condition used at the surfaces of the piezoelectric elements. Therefore, the acoustic pressure levels were normalized by the maximum pressure level detected in the cavity for any given case. Figure 9a reveals that, at the natural frequency of 956 Hz, two parts of the cavity volume exhibited opposing acoustic-pressure distributions (shown by red and blue contours). The opposing direction of the acoustic pressure in these simulations indicated an out-of-phase excitation at these cavity regions. That is, the acoustic pressure fluctuated in an opposite manner between the two parts of the cavity volume when the cavity was excited at this acoustic mode frequency. Figure 9c shows that, at the natural frequency of 1252 Hz, while two parts of the cavity volume exhibited higher acoustic-pressure distributions in one direction (indicated by red contours), the parts at the two ends and in the middle (shown by blue) displayed opposing pressure distributions. The other two natural frequencies, 1126 and 1331 Hz, also exhibited acoustic-pressure variations, giving their respective mode shapes as shown in Figure 9b,d. The acoustic mode distributions in Figure 9a,c for the two frequencies, f_s = 956 and 1252 Hz, agreed well with the experimentally observed variation of the mean jet velocity over the array of orifices for the excitation frequencies of f_e = 800 and 1200 Hz, respectively (see Figure 6), where stronger or weaker jet velocities were obtained above the positive and negative acoustic-pressure regions inside the cavity, respectively.

Inspecting the acoustic simulation results and the experimental results of the mean jet-velocity variation over the orifices, it can be concluded that the excitation of an acoustic mode inside the cavity had a direct effect on the jet velocity exiting from each orifice during the expulsion stroke, which led to the non-uniform jet velocity pattern detected experimentally in Figure 6. It is important to note that the acoustic-pressure distributions shown in Figure 9 corresponded to the peak of the expulsion stroke, i.e., when the piezoelectric elements deflected to their inward-most location. In the other half of the excitation cycle, the acoustic-pressure regions would have been inverted, but that half-cycle would have corresponded to the ingestion stroke (which is not included in the jet-velocity plots discussed earlier). Hence, averaging the jet velocity during the expulsion strokes over the whole sampling time always gave high jet velocity at positive pressure regions and a weaker velocity at the negative pressure regions. Although the excitation of the large-aspect-ratio cavity configuration at the frequency of f_e = 800 Hz was initially thought to be off-resonance, it seems that the fluctuations in acoustic pressure locked onto the closest acoustic mode to this excitation frequency. However, the excitation of the cavity at f_e = 800 Hz generally generated lower jet velocities over the span compared to the f_e = 1200 Hz excitation case. The reason behind the induction of much larger jet velocities for the 1200 Hz excitation frequency could be due to the coupling of one of the acoustic modes with the Helmholtz resonance frequency.

Table 1. Comparison of the natural frequencies, in Hz, obtained from acoustic simulations with resonant frequencies extracted from experimental measurements for the unified, large-aspect-ratio-cavity volume.

Mode Index	**1**	**2**	**3**	**4**
Simulations	956	1126	1252	1331
Experiments	960	1140	1220	1360

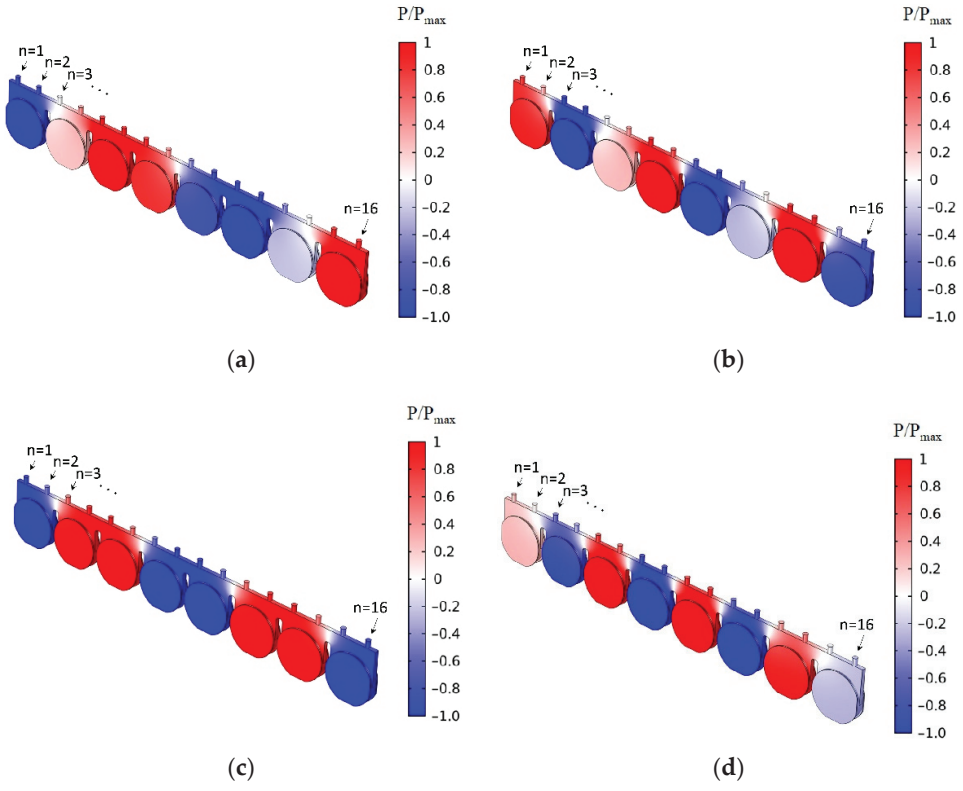

Figure 9. Results of acoustic simulations showing the instantaneous acoustic-pressure distribution, i.e., acoustic mode, within the unified, large-aspect-ratio-cavity volume for different natural frequencies. The frequencies are (**a**) f_{s1} = 956 Hz, (**b**) f_{s2} = 1126 Hz, (**c**) f_{s3} = 1252 Hz, and (**d**) f_{s4} = 1331 Hz.

To gain further insight into the correlation of the excited acoustic mode shape of the cavity with the jet velocities emanating from the orifices, the phase-angle difference of the mean jet velocity between all of the orifices of the SJA array was determined. This phase-angle difference can be extracted from the experimental phase-averaged jet velocity measurements by comparing the phase of the highest phase-averaged jet velocity during the expulsion stroke to the phase of the maximum amplitude of the sinusoidal excitation (see Figure 3). Since the input excitation was recorded simultaneously with the measured jet velocity, the phase-averaged correlation can be extracted and compared for different excitation frequencies. Figure 10a shows the phase-angle variation of the jet velocity over the orifices for the large-aspect-ratio and unified-cavity volumes, determined from experimental measurements at f_e = 1200 Hz, and Figure 10b gives the acoustic mode distribution inside the same cavity volumes extracted from acoustic simulations of the cavity volume for excitation at f_s =1252 Hz. Figure 10b reveals that the excited acoustic mode shape at f_s = 1252 Hz exhibited a negative acoustic-pressure region around the middle of the array (given in blue), i.e., between the orifices n = 8 to 9. As seen in Figure 10a, the phase-angle difference between the phase-averaged jet velocity and the input excitation for these orifices was close to 0 degrees since both orifices were in the same acoustic-pressure region. Figure 10b also shows high acoustic-pressure levels in two regions of the cavity (indicated by red contours), containing the orifices n = 3 to 6 and n = 11 to 14. Around these same orifices, the phase-angle difference between the velocity of the jet and the input excitation was found to be non-zero and generally comparable, indicating the excitation of the acoustic mode shape seen in Figure 10b. Therefore, the jet velocities measured at

the orifices in these two regions were relatively higher than the velocities in the middle and far sides of the cavity, which were observed earlier in Figure 6. It is important to mention again that the exact value of the phase angle itself was not the target here, but the proximity in phase-angle values is an indicator that the jets are synchronized, or that a similar acoustic-pressure distribution persists inside the cavity for these orifice regions.

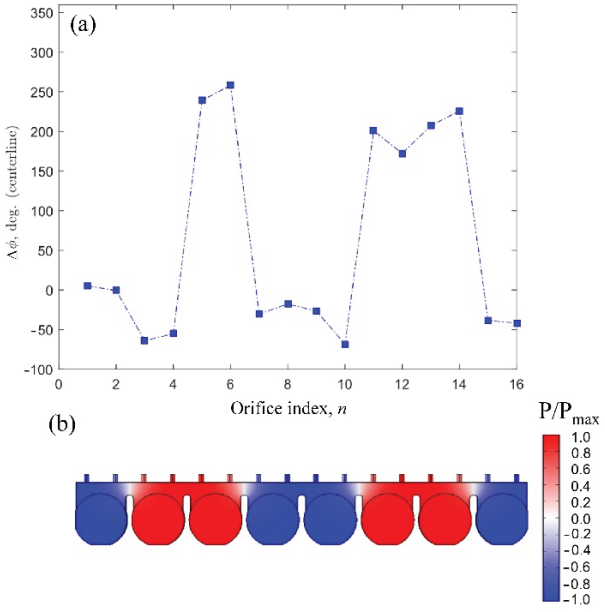

Figure 10. (**a**) Variation of the phase-angle difference between the phase-averaged peak jet velocity at the orifice centre and the peak input excitation along all 16 orifices for the excitation of the unified cavity at the frequency of f_e = 1200 Hz, which is an on-resonance peak, and (**b**) the variation of the instantaneous acoustic pressure within the unified-cavity volume for the corresponding acoustic mode at the natural frequency of f_s = 1252 Hz.

It has been previously discussed that, at the excitation frequency of f_e = 800 Hz, the acoustic-pressure distribution within the large cavity locked onto the closest acoustic mode shape obtained at f_s = 956 Hz, which is given in Figure 11b. For this mode shape, there were two out-of-phase acoustic-pressure regions, shown by the blue and red contours in Figure 11b. These two out-of-phase regions fell somewhere between the orifices n = 5 to 6 and n = 11 to 12. The phase-angle variation of the phase-averaged jet velocity in reference to the input signal for the f_e = 800 Hz case, shown in in Figure 11a, depicted that the jet velocities were within 90 to 120 degrees out of phase between these two regions. The fact that the jet velocities at the two regions were out of phase with each other suggests the excitation of the acoustic mode shape of the f_e = 956 Hz case and explains why there would be a difference in the shape of the jet velocity measured above the array of orifices, as was shown earlier in Figure 6. These results point out a significant challenge for the SJA array, which is achieving a uniform synthetic jet injection along the array of orifices for consistent flow control. The slenderness of the unified, large cavity led to the excitation of different acoustic modes, which was responsible for the variation of the jet velocity over the array. That variation in mean jet velocity depended solely on the excitation frequency and the corresponding acoustic mode shape having been excited in the unified, large-aspect-ratio cavity.

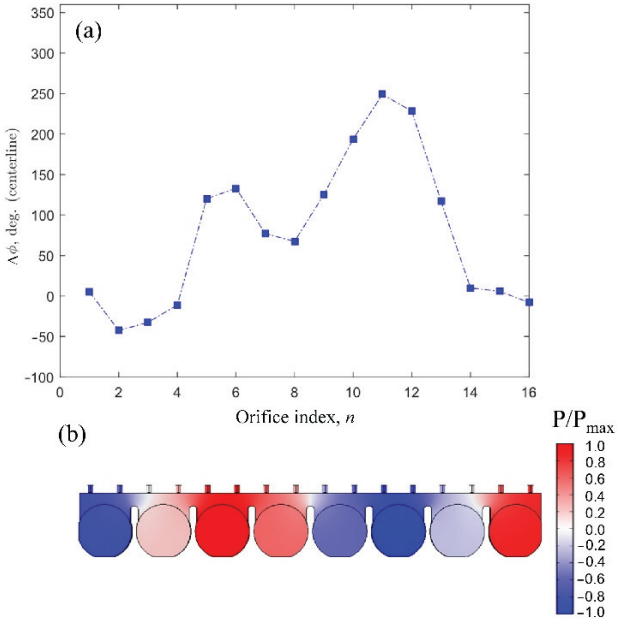

Figure 11. (**a**) Variation of the phase-angle difference between the phase-averaged peak jet velocity at the orifice centre and the peak input excitation along all 16 orifices for the excitation of the unified-cavity configuration at the frequency of f_e = 800 Hz and (**b**) the variation of the instantaneous acoustic pressure within the unified-cavity volume at the closest resonance frequency of an acoustic mode (f_s = 956 Hz).

Acoustic simulations were also performed for the singular case of the compartmented cavity configuration, which had two piezoelectric elements within each unit (see Figure 2b). The instantaneous acoustic-pressure distribution—i.e., acoustic mode shapes—that corresponded to the first two acoustic modes are presented in Figure 12. The simulations also provided several other acoustic modes happening at higher frequencies, listed in Table 2. All of those frequencies were outside of the experimentally tested excitation frequency range, and none of the acoustic-mode frequencies matched the value of the Helmholtz resonance frequency. As a result, a reasonably uniform velocity distribution (seen in Figure 8) was developed over the SJA configuration with compartmentalized cavities when excited by the Helmholtz frequency, given that it was the only observed peak in the frequency response, as is shown in Figure 7. Additionally, at 800 Hz, a uniform jet velocity along the span was observed experimentally (provided earlier in Figure 8) because no acoustic modes exist in this range.

Although the smaller cavity compartment had a similar Helmholtz resonance frequency to that of the large-aspect-ratio–cavity volume, its shape did not result in acoustic modes close to the Helmholtz resonance frequency. The slenderness of the large cavity was the main reason for the generation of acoustic modes within the excitation frequency range, leading to jet-velocity variations. In the present large-aspect-ratio case, one of the acoustic modes also ended up coupling with the Helmholtz resonance frequency, inducing even larger jet velocities. However, this large jet velocity was still associated with large variations along the span following the acoustic mode shape. In conclusion, to gain high jet velocity and avoid spanwise jet-velocity variations over an SJA array, care should be given so that any acoustic modes will fall far away from the Helmholtz resonance frequency.

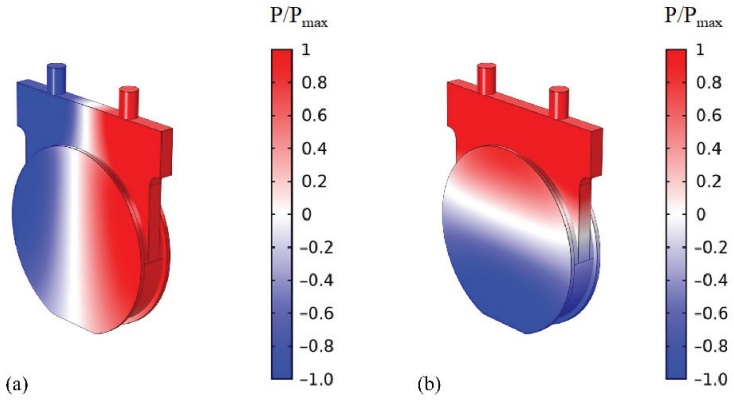

Figure 12. Instantaneous acoustic-pressure distribution, i.e., acoustic mode shape, inside a single compartment from the compartmented cavity configuration for the first two natural frequencies (**a**) f_{s1} = 4664 Hz and (**b**) f_{s2} = 5410 Hz.

Table 2. The natural frequencies (in Hz) corresponding to the acoustic mode shape of the single-cavity unit within the compartmented cavity design.

Mode Index	**1**	**2**	**3**	**4**
Simulations	4664	5410	6890	7667

5. Conclusions

Frequency response and acoustic-cavity-excitation characteristics of synthetic jet actuators (SJAs) with an array of circular orifices were investigated experimentally and numerically. The array consisted of sixteen circular orifices and was powered by sixteen piezoelectric elements with either a single large-aspect-ratio cavity or eight isolated cavity compartments. In the case of a single, unified cavity, several excitation frequencies were observed to yield peaks in the mean jet velocity. For different excitation frequencies, the mean jet velocity of the expulsion stroke showed different spanwise variations over the array of orifices. In the case of isolated cavity compartments, only a single peak was observed in the frequency response and no variation in the mean jet velocity was detected over the array of orifices for the same excitation frequency range used in the unified-cavity configuration. Acoustic simulations of the large-aspect-ratio-cavity volume of the SJA design showed that each resonant frequency peak observed in the frequency response of the SJA corresponded to an acoustic mode shape of the cavity volume. The different mode shapes resulted in a distinct acoustic-pressure distribution within the cavity, leading to a corresponding variation in the jet velocity from one orifice to another within the array. The phase-angle variations of the jet velocity along the orifices were linked to the acoustic mode shapes of the cavity. Additionally, it was shown that if an acoustic mode fell close to the Helmholtz resonance frequency value, the jet velocity at the exit was amplified.

It was also noted that for an acoustic mode shape to form inside the cavity and induce related jet-velocity variations through the orifices, the excitation frequency did not have to be precisely equal to the associated acoustic natural frequency. With an off-resonance input excitation frequency to the SJA, the acoustic-pressure fluctuations within the cavity could still lock onto the closest acoustic mode, inducing a jet velocity variation over the array. The jet velocity and phase-angle variations observed along the orifices point out possible challenges in developing uniform control schemes across long-span aerofoils using an array of circular orifices from a single chamber. In the present work, by dividing the unified, large cavity into isolated cavity compartments, the acoustic mode shapes of each cavity compartment were put outside of the excitation frequency range and away from the

Helmholtz resonance frequency value. As a result, each compartment ejected the same jet velocity, and no variation was observed along the span of the array. This indicates that, while designing an SJA array, cavity/cavities with acoustic mode shapes falling outside of the excitation frequency range of the SJA should be selected to ensure uniform mean jet-velocity output throughout the array. The trade-off is that the resultant jet velocity will be relatively less than what would be obtained when using a large, unified-cavity volume.

Author Contributions: Conceptualization, N.A., P.E.S. and A.E.; methodology, N.A., P.E.S. and A.E.; software, N.A.; validation, N.A.; formal analysis, N.A.; resources, P.E.S. and A.E.; data curation, N.A.; writing—original draft preparation, N.A.; writing—review and editing, P.E.S. and A.E.; supervision, P.E.S. and A.E.; project administration, P.E.S. and A.E.; funding acquisition, P.E.S. and A.E. All authors have read and agreed to the published version of the manuscript.

Funding: This research was funded by the Dean's Strategic Fund (DSF19-30) from the Faculty of Applied Science and Engineering at the University of Toronto.

Data Availability Statement: Not applicable.

Acknowledgments: The authors would also like to acknowledge the licenses and technical support from CMC microsystems for the software used in this work.

Conflicts of Interest: The authors declare no conflict of interest.

References

1. Seifert, A.; Eliahu, S.; Greenblatt, D.; Wygnanski, I. Use of Piezoelectric Actuators for Airfoil Separation Control. *AIAA J.* **1998**, *36*, 1535–1537. [CrossRef]
2. Glezer, A.; Amitay, M. Synthetic Jets. *Annu. Rev. Fluid Mech.* **2002**, *34*, 503–529.
3. Jabbal, M.; Liddle, S.C.; Crowther, W.J. Active Flow Control Systems Architectures for Civil Transport Aircraft. *J. Aircr.* **2010**, *47*, 1966–1981. [CrossRef]
4. Obeid, S.; Ahmadi, G.; Jha, R. NARMAX Identification Based Closed-Loop Control of Flow Separation over NACA 0015 Airfoil. *Fluids* **2020**, *5*, 100. [CrossRef]
5. Ffowcs Williams, J.E. Active Flow Control. *J. Sound Vib.* **2001**, *239*, 861–871. [CrossRef]
6. Löffler, S.; Ebert, C.; Weiss, J. Fluidic-Oscillator-Based Pulsed Jet Actuators for Flow Separation Control. *Fluids* **2021**, *6*, 166. [CrossRef]
7. Smith, B.L.; Glezer, A. The Formation and Evolution of Synthetic Jets. *Phys. Fluids* **1998**, *10*, 2281–2297. [CrossRef]
8. Vasile, J.D.; Amitay, M. Interaction of a Finite-Span Synthetic Jet near the Tip of a Sweptback Wing. *Phys. Fluids* **2015**, *27*, 067102. [CrossRef]
9. Jabbal, M.; Liddle, S.; Potts, J.; Crowther, W. Development of Design Methodology for a Synthetic Jet Actuator Array for Flow Separation Control Applications. *Proc. Inst. Mech. Eng. Part G J. Aerosp. Eng.* **2013**, *227*, 110–124. [CrossRef]
10. Monastero, M.C.; Lindstrom, A.M.; Amitay, M. Effect of Synthetic Jets Spacing on Flow Separation over Swept, Flapped Airfoils. *AIAA J.* **2019**, *57*, 4670–4683. [CrossRef]
11. Liddle, S.C. The Use of Synthetic Jet Actuators to Enhance Deflected Surface Controls. Ph.D. Thesis, University of Manchester, Manchester, UK, 2007.
12. Tang, H.; Salunkhe, P.; Zheng, Y.; Du, J.; Wu, Y. On the Use of Synthetic Jet Actuator Arrays for Active Flow Separation Control. *Exp. Therm. Fluid Sci.* **2014**, *57*, 1–10. [CrossRef]
13. Feero, M.A.; Goodfellow, S.D.; Lavoie, P.; Sullivan, P.E. Flow Reattachment Using Synthetic Jet Actuation on a Low-Reynolds-Number Airfoil. *AIAA J.* **2015**, *53*, 2005–2014. [CrossRef]
14. Amitay, M.; Cannelle, F. Evolution of Finite Span Synthetic Jets. *Phys. Fluids* **2006**, *18*, 054101. [CrossRef]
15. Amitay, M.; Smith, D.R.; Kibens, V.; Parekh, D.E.; Glezer, A. Aerodynamic Flow Control over an Unconventional Airfoil Using Synthetic Jet Actuators. *AIAA J.* **2001**, *39*, 361–370. [CrossRef]
16. Amitay, M.; Glezer, A. Role of Actuation Frequency in Controlled Flow Reattachment over a Stalled Airfoil. *AIAA J.* **2002**, *40*, 209–216. [CrossRef]
17. Yang, E.; Ekmekci, A.; Sullivan, P.E. Phase Evolution of Flow Controlled by Synthetic Jets over NACA 0025 Airfoil. *J. Vis.* **2022**. [CrossRef]
18. Goodfellow, S.D.; Yarusevych, S.; Sullivan, P.E. Momentum Coefficient as a Parameter for Aerodynamic Flow Control with Synthetic Jets. *AIAA J.* **2013**, *51*, 623–631. [CrossRef]
19. Gil, P.; Wilk, J.; Korzeniowski, M. Helmholtz Resonance Frequency of the Synthetic Jet Actuator. *Appl. Sci.* **2021**, *11*, 5666. [CrossRef]
20. Gallas, Q.; Holman, R.; Nishida, T.; Carroll, B.; Sheplak, M.; Cattafesta, L. Lumped Element Modeling of Piezoelectric-Driven Synthetic Jet Actuators. *AIAA J.* **2003**, *41*, 240–247. [CrossRef]

21. Gallas, Q. On the Modeling and Design of Zero-Net Mass Flux Actuators. Ph.D. Thesis, University of Florida, Gainesville, FL, USA, 2005.
22. Gomes, L.D.; Crowther, W.J.; Wood, N.J. Towards a Practical Piezoceramic Diaphragm Based Synthetic Jet Actuator for High Subsonic Applications—Effect of Chamber and Orifice Depth on Actuator Peak Velocity. In Proceedings of the 3rd AIAA Flow Control Conference, San Francisco, CA, USA, 5–8 June 2006; pp. 267–283.
23. Van Buren, T.; Whalen, E.; Amitay, M. Achieving a High-Speed and Momentum Synthetic Jet Actuator. *J. Aerosp. Eng.* **2016**, *29*, 04015040. [CrossRef]
24. Jabbal, M.; Jeyalingam, J. Towards the Noise Reduction of Piezoelectrical-Driven Synthetic Jet Actuators. *Sens. Actuators A Phys.* **2017**, *266*, 273–284. [CrossRef]
25. Guo, Y. Acoustic Analysis of Low-Noise Actuator Design for Active Flow Control. *J. Sound Vib.* **2008**, *311*, 843–860. [CrossRef]
26. Smyk, E.; Markowicz, M. Impact of the Soundproofing in the Cavity of the Synthetic Jet Actuator on the Generated Noise. *Fluids* **2022**, *7*, 323. [CrossRef]
27. Smyk, E.; Markowicz, M. Acoustic and Flow Aspects of Synthetic Jet Actuators with Chevron Orifices. *Appl. Sci.* **2021**, *11*, 652. [CrossRef]
28. Van Buren, T.; Whalen, E.; Amitay, M. Synthetic Jet Actuator Cavity Acoustics: Helmholtz versus Quarter-Wave Resonance. *J. Vib. Acoust. Trans. ASME* **2015**, *137*, 054501. [CrossRef]
29. Bourquard, C.; Noiray, N. Stabilization of Acoustic Modes Using Helmholtz and Quarter-Wave Resonators Tuned at Exceptional Points. *J. Sound Vib.* **2019**, *445*, 288–307. [CrossRef]
30. Feero, M.A.; Lavoie, P.; Sullivan, P.E. Influence of Synthetic Jet Location on Active Control of an Airfoil at Low Reynolds Number. *Exp. Fluids* **2017**, *58*, 99. [CrossRef]
31. COMSOL Inc. Acoustics Module User's Guide. Available online: www.comsol.com/blogs (accessed on 1 December 2020).
32. Kinsler, L.E.; Frey, A.R.; Coppens, A.B.; Sanders, J.V. *Fundamentals of Acoustics*; John Wiley & Sons: Hoboken, NJ, USA, 1999.
33. Holman, R.; Utturkar, Y.; Mittal, R.; Smith, B.L.; Cattafesta, L. Formation Criterion for Synthetic Jets. *AIAA J.* **2005**, *43*, 2110–2116. [CrossRef]
34. Milanovic, I.M.; Zaman, K.B.M.Q. Synthetic Jets in Crossflow. *AIAA J.* **2005**, *43*, 929–940. [CrossRef]
35. Shuster, J.M.; Smith, D.R. Experimental Study of the Formation and Scaling of a Round Synthetic Jet. *Phys. Fluids* **2007**, *19*, 045109. [CrossRef]

fluids

MDPI

Article

Stability of a Regularized Casson Flow down an Incline: Comparison with the Bingham Case

Benedetta Calusi [1,*], Angiolo Farina [1], Lorenzo Fusi [1] and Liviu Iulian Palade [2]

[1] Dipartimento di Matematica e Informatica "U. Dini", Università degli Studi di Firenze, Viale Morgagni 67/A, 50134 Firenze, Italy
[2] CNRS, Institute "Camille Jordan" UMR 5208, INSA-Lyon, Universitè de Lyon, 69621 Villeurbanne, France
* Correspondence: benedetta.calusi@unifi.it

Abstract: In this paper, we study the two-dimensional linear stability of a regularized Casson fluid (i.e., a fluid whose constitutive equation is a regularization of the Casson obtained through the introduction of a smoothing parameter) flowing down an incline. The stability analysis has been performed theoretically by using the long-wave approximation method. The critical Reynolds number at which the instability arises depends on the material parameters, on the tilt angle as well as on the prescribed inlet discharge. In particular, the results show that the regularized Casson flow has stability characteristics different from the regularized Bingham. Indeed, for the regularized Casson flow an increase in the yield stress of the fluid induces a stabilizing effect, while for the Bingham case an increase in the yield stress entails flow destabilization.

Keywords: regularized Casson fluid; regularized Bingham fluid; linear stability analysis; long-wave approximation

Citation: Calusi, B.; Farina, A.; Fusi, L.; Palade, L.I. Stability of a Regularized Casson Flow down an Incline: Comparison with the Bingham Case. *Fluids* **2022**, *7*, 380. https://doi.org/10.3390/fluids7120380

Academic Editor: Mehrdad Massoudi

Received: 4 November 2022
Accepted: 6 December 2022
Published: 9 December 2022

1. Introduction

The rheological behaviour of materials such as suspensions, dispersion, and polymer solutions, is distinctly different from that of Newtonian fluids. In particular, such materials often exhibit flow properties characterized by a critical value of stress (i.e., yield stress, usually denoted as τ_0^*), below which the materials do not deform, and above which they flow accordingly to their rheological properties. They are usually referred as viscoplastic materials, which include, e.g., the Bingham [1], the Herschel–Bulkley [2], and the Casson model [3].

The flow stability analysis of these models can have useful application in several industrial processes (e.g., food and pharmaceutical industries) and environmental phenomena (e.g., debris and lava flow). In general, flows are unstable when the corresponding Reynolds is larger than a critical threshold usually referred to as critical Reynolds number and denoted as Re_c. The pioneering works on stability of Newtonian flow down an incline has been reported in [4,5]. In these papers the authors provide a proportionality relation between the so-called critical Reynolds number, Re_c, and the tilt angle θ and later experimentally validated in [6]. Then, the interest to properly describe fluids with complex rheological behaviour led to an increase in theoretical, numerical, and experimental studies, see e.g., [7–32].

Recently, the onset of instability for viscoplastic fluids, flowing down an incline, has been investigated in [10,16]. In particular, a stability analysis has been performed numerically by using a spectral method in [16] and the long-wave approximation in [10], through a regularization of the Bingham law. The Bingham law describes a material characterized by the presence of a yield stress below which the continuum behaves like a rigid body and above which it flows as a linear viscous fluid. In this paper, we theoretically investigate the flow stability through the long-wave approximation technique following the approach reported in [10] and in [28]. In particular, we focus on a fluid modelled as

a regularized Casson, since it has the advantage of being easy to handle analytically. The Casson constitutive law is widely used to model blood flow [33]. Recently, studies regarding the peristaltic Casson flow (important to understand artery and vein physiology [34,35]), has been developed in [36–41].

In the "ideal" Casson model the stress is undetermined at zero strain rate. The presence of a yield stress has been widely discussed [42–46] and it is still an open debate. The use of a regularized model allows to avoid the problems due to this singularity and so to avoid several analytical and numerical issues [47,48]. Indeed, the singularity at zero strain rate can be smoothed out and the exact model can be recovered through introduction of a positive parameter, chosen quite arbitrarily, which accounts for the accuracy of the approximation [10,16,49,50].

To the best of the authors' knowledge, the analysis of the onset of instability of a flow down an incline when the fluid is modelled as a regularized Casson material has not been presented in the literature before, and this motivates our investigations. Actually, the aim and novelty of this paper is two-fold. First, we study the stability properties of the regularized Casson flow down an incline. Then, we compare the obtained results with the one illustrated in [10] regarding the flow of a regularized Bingham. In particular, our findings highlight that the regularized Bingham fluid and the regularized Casson fluid have stability properties dramatically different. Indeed, although the two models belong to the same "viscoplastic family", they show an opposite stability behaviour as the yield stress increases.

The paper is organized as follows: in Section 2 and 3 we formulate the mathematical problem and the main characteristics of a regularized Casson flow down an incline, respectively. In Section 4, following [10,16,51], we briefly recall linear stability analysis by using the long-wave approximation method. Then, in Section 5 and 6, we report results and some final remarks.

2. Mathematical Model

We proceed similarly to [10,16] briefly reporting the main theoretical background. Throughout the paper the "*" represents a dimensional quantity. Let us consider a reference framework x^*Oy^* as the one depicted in Figure 1. We denote the tilt angle as $\theta \in (0, \pi/2)$ and suppose that the flow domain of the flow is given by

$$\mathcal{D} = \left\{ (x^*, y^*) \in \mathbb{R}^2 | 0 \leq x^* \leq L^*, 0 \leq y^* \leq h^*(x^*, t^*) \right\},$$

where L^* is the length of the domain and $y^* = h^*(x^*, t^*)$ is the upper free surface (not a priori known) and $H^* = \max\{h^*\}$.

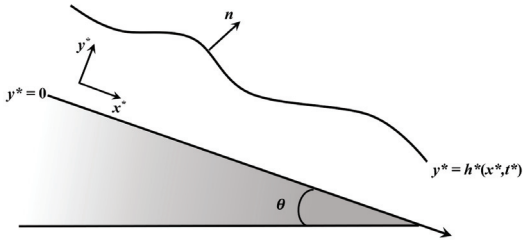

Figure 1. Reference framework.

We denote by $\mathbf{T}^*$ the Cauchy stress tensor and set

$$\mathbf{T}^* = -p^*\mathbf{I} + \boldsymbol{\tau}^*, \tag{1}$$

where $\boldsymbol{\tau}^*$ is the deviatoric part.

The governing equations for the two-dimensional incompressible flow, $\mathbf{v}^* = u^*\mathbf{i} + v^*\mathbf{j}$, are

$$\begin{cases} \rho^*(u^*_{t^*} + u^*u^*_{x^*} + v^*u^*_{y^*}) = -p^*_{x^*} + \tau^*_{11,x^*} + \tau^*_{12,y^*} + \rho^* g^* \sin\theta, \\ \rho^*(v^*_{t^*} + u^*v^*_{x^*} + v^*v^*_{y^*}) = -p^*_{y^*} + \tau^*_{12,x^*} + \tau^*_{22,y^*} - \rho^* g^* \cos\theta, \\ u^*_{x^*} + v^*_{y^*} = 0, \end{cases} \tag{2}$$

where g^* is gravity and ρ^* is the constant material density and, to take the notation as light as possible, we denote $(\cdot)_{t^*} = \dfrac{\partial(\cdot)}{\partial t^*}$, $(\cdot)_{x^*} = \dfrac{\partial(\cdot)}{\partial x^*}$, $(\cdot)_{y^*} = \dfrac{\partial(\cdot)}{\partial y^*}$. We consider the non-slip and impermeability conditions $u^* = v^* = 0$ on $y^* = 0$ and the kinematical–dynamical conditions on h^*, namely

$$\begin{cases} h^*_{t^*} + u^*h^*_{x^*} = v^*, & y^* = h^*, \\ \mathbf{T}^*\mathbf{n} = 0, & y^* = h^*, \end{cases} \tag{3}$$

where $\mathbf{n}$ is the outer normal (see Figure 1).

Exploiting $(2)_3$, we rewrite $(3)_1$ as

$$h^*_{t^*} + \left(\int_0^{h^*} u^* dy^*\right)_{x^*} = 0. \tag{4}$$

We introduce the characteristic quantities

$$\tau^*_c = \frac{\mu^* U^*}{H^*}, \quad p^*_c = \frac{\mu^* U^*}{H^*}, \tag{5}$$

and the strain-rate $\dot{\gamma}^* = 1/2\left(\nabla^*\mathbf{v}^* + \nabla^*\mathbf{v}^{*T}\right)$. Next, we consider the following dimensionless variables

$$\mathbf{x} = \frac{\mathbf{x}^*}{H^*}, \quad \mathbf{v} = \frac{\mathbf{v}^*}{U^*}, \quad t = \frac{U^*}{H^*}t^*, \tag{6}$$

$$h = \frac{h^*}{H^*}, \quad p = \frac{p^*}{p^*_c}, \quad \boldsymbol{\tau} = \frac{\boldsymbol{\tau}^*}{\tau^*_c}, \quad \dot{\gamma} = \frac{H^*}{U^*}\dot{\gamma}^*, \tag{7}$$

where U^* denotes the reference velocity which will be selected to normalize the dimensionless longitudinal velocity. Exploiting (5)–(7), the system (2) becomes

$$\begin{cases} \mathsf{Re}\left(u_t + uu_x + vu_y\right) = -p_x + \tau_{11,x} + \tau_{12,y} + \xi, \\ \mathsf{Re}\left(v_t + uv_x + vv_y\right) = -p_y + \tau_{12,x} + \tau_{22,y} - \xi\cot\theta, \\ u_x + v_y = 0, \end{cases} \tag{8}$$

where

$$\xi = \frac{\mathsf{Re}}{\mathsf{Fr}^2}\sin\theta = \frac{\rho^* g^* H^{*2}}{\mu^* U^*}\sin\theta, \tag{9}$$

and

$$\mathsf{Re} = \frac{\rho^* U^* H^*}{\mu^*}, \qquad \mathsf{Fr}^2 = \frac{U^{*2}}{g^* H^*}, \tag{10}$$

are the Reynolds number and Freude number, respectively.

Finally, we recall that the flow is driven prescribing the inlet discharge which we assume to be constant in time. So, denoting as Q^* the flow rate per unit fluid layer width, we have

$$Q^* = U^* H^* \int_0^1 u(y)dy, \tag{11}$$

provided that the layer is flat and its thickness is H^* (which does not vary in time). From (9) and (10) we have

$$\begin{aligned} H^* &= \left(\frac{\xi \mu^{*2}}{\rho^{*2} g^* \sin\theta}\mathrm{Re}\right)^{1/3}, \\ U^* &= \frac{\mu^*}{\rho^* H^*}\mathrm{Re} = \left(\frac{g^* \mu^* \sin\theta}{\xi \rho^*}\right)^{1/3}\mathrm{Re}^{2/3}. \end{aligned} \tag{12}$$

Therefore, the flow rate Q^* can be rewritten in terms of Re and ξ for given physical (τ_0^*, μ^*, ρ^*) and geometrical (θ) parameters. In the sequel, we shall see that Q^* can be also expressed only on terms of the Reynolds number through the normalization of the dimensionless longitudinal velocity.

3. Regularized Casson

Similarly to [10,16,52], we introduce a dimensional regularization parameter ϵ^* into the dimensionless Casson model, setting

$$\boldsymbol{\tau} = r(|\dot{\boldsymbol{\gamma}}|)\dot{\boldsymbol{\gamma}}, \quad r(|\dot{\boldsymbol{\gamma}}|) = \left(\sqrt{2} + \frac{\sqrt{\mathrm{B}}}{\sqrt{|\dot{\boldsymbol{\gamma}}|} + \sqrt{\epsilon}}\right)^2, \tag{13}$$

where $|\dot{\boldsymbol{\gamma}}| = \sqrt{tr(\dot{\boldsymbol{\gamma}}^2)/2}$, $\mathrm{B} = \dfrac{\tau_0^* H^*}{\mu^* U^*}$ is the Bingham number, which represents the ratio between the yield stress and the characteristic viscous stress, with τ_0^* the yield stress, and $\epsilon = 2\epsilon^* H^*/U^*$, so that when $\epsilon^* \to 0$ we formally retrieve the Casson constitutive law [38].

We recall that for a regularized Bingham fluid the function r, see [10,16], is given by

$$r(|\dot{\boldsymbol{\gamma}}|) = 2 + \frac{\mathrm{B}}{|\dot{\boldsymbol{\gamma}}| + \epsilon}. \tag{14}$$

The plot of r, by using (13) and (14), with respect to $|\dot{\boldsymbol{\gamma}}|$ for selected values of B and ϵ is shown in Figure 2. In particular, the function $r(|\dot{\boldsymbol{\gamma}}|)$ gives the regularized relation between the shear stress τ and shear strain rate $\dot{\gamma}$.

By using (9) and (10) the Bingham number and the regularization parameter can be rewritten in terms of Re, namely

$$\mathrm{B} = X\frac{\xi^{2/3}}{\mathrm{Re}^{1/3}}, \tag{15}$$

with

$$X = \frac{\lambda_1}{(\sin\theta)^{2/3}}, \qquad \lambda_1 = \frac{\tau_0^*}{(g^*\mu^*)^{2/3}\rho^{*1/3}}, \tag{16}$$

and

$$\epsilon = \frac{\lambda_2}{(\sin\theta)^{2/3}}\frac{\xi^{2/3}}{\mathrm{Re}^{1/3}}, \tag{17}$$

with

$$\lambda_2 = \frac{\epsilon^* \mu^{*1/3}}{\rho^{*1/3} g^{*2/3}}, \tag{18}$$

respectively. The parameters λ_1 and λ_2 do not depend on the flow and on the tilt angle θ, so that the parameter X is constant once the fluid and the tilt angle have been selected, i.e., it depends only on the "material" and geometrical properties.

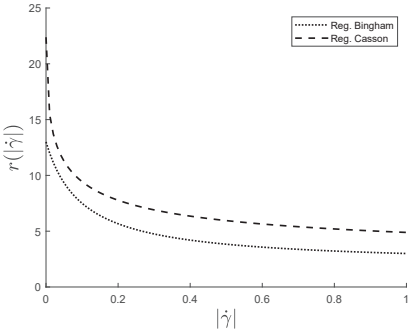

Figure 2. Plot of $r(|\dot{\gamma}|)$ given by (13) and (14) for $\mathsf{B} = 1.1$ and $\epsilon = 0.1$. Although the regularized Bingham and the regularized Casson belong to the same viscoplastic family, they have different behaviour.

We look for a solution in the form $\mathbf{v} = u(y)\mathbf{i}$, $h = 1$, thus system (8) is reduced to

$$\begin{cases} 0 = -p_x + \tau_{12,y} + \xi, \\ \\ 0 = -p_y - \xi \cot\theta, \end{cases} \tag{19}$$

which leads to

$$p = \xi \cot\theta (1 - y). \tag{20}$$

Thus, we have $\tau_{12} = \xi(1-y)$, and, from (13)

$$u_y \left(1 + \frac{\sqrt{\mathsf{B}}}{\sqrt{u_y} + \sqrt{\epsilon}} \right)^2 = \xi(1-y),$$

which, by integrating with respect to y with $u(0) = 0$, leads to

$$u(y) = -\frac{\xi}{4} y^2 - \frac{N_1(y)}{12\xi^{\frac{3}{2}}} y - \frac{1}{12\xi^{\frac{3}{2}}} (N_2(y) + N_3(y) + N_4(y)), \tag{21}$$

where

$$\begin{aligned}
N_1(y) &= M_1(y) M_2(y) - 6\xi^{\frac{5}{2}} + 8a(y)\, \mathsf{B}^{\frac{1}{2}} \xi^{\frac{3}{2}} - 6c, \\
N_2(y) &= -72\epsilon\xi^{\frac{1}{2}} \left(\frac{2\epsilon^{\frac{1}{2}} \mathsf{B}^{\frac{1}{2}}}{3} + \mathsf{B} \right) \log\left(\epsilon^{\frac{1}{2}} - \mathsf{B}^{\frac{1}{2}} + a(y) + M_2(y) \right), \\
N_3(y) &= M_2(y) \left\{ a(y) \left[3\xi^{\frac{3}{2}} + \xi^{\frac{1}{2}} \left(-3\epsilon + 8\epsilon^{\frac{1}{2}} \mathsf{B}^{\frac{1}{2}} + \mathsf{B} \right) \right] - b + \xi^{\frac{1}{2}} \left[\mathsf{B}^{\frac{3}{2}} + \epsilon^{\frac{1}{2}} \left(3\epsilon - 47\epsilon^{\frac{1}{2}} \mathsf{B}^{\frac{1}{2}} + 11\mathsf{B} \right) \right] \right\}, \\
N_4(y) &= -8a(y)\, \xi^{\frac{3}{2}} \mathsf{B}^{\frac{1}{2}} + 8\xi^2 \mathsf{B}^{\frac{1}{2}} + M_3 + M_4, \\
M_1(y) &= -3a(y)\, \xi^{\frac{3}{2}} + b, \\
M_2(y) &= \left[2a(y) \left(\epsilon^{\frac{1}{2}} - \mathsf{B}^{\frac{1}{2}} \right) + c + a^2(y) \right]^{\frac{1}{2}}, \\
M_3 &= \left(3\epsilon^{\frac{1}{2}} + 5\mathsf{B}^{\frac{1}{2}} \right) \xi^{\frac{3}{2}} - \mathsf{B}^{\frac{3}{2}} \xi^{\frac{1}{2}} + \epsilon^{\frac{1}{2}} \xi^{\frac{1}{2}} \left(-3\epsilon + 47\epsilon^{\frac{1}{2}} \mathsf{B}^{\frac{1}{2}} - 11\mathsf{B} \right) - M_5\, \xi \left(-3\epsilon + 8\epsilon^{\frac{1}{2}} \mathsf{B}^{\frac{1}{2}} + \mathsf{B} + 3\xi \right), \\
M_4 &= 72\epsilon\xi^{\frac{1}{2}} \left(-\frac{2\epsilon^{\frac{1}{2}} \mathsf{B}^{\frac{1}{2}}}{3} + \mathsf{B} \right) \log\left(\epsilon^{\frac{1}{2}} - \mathsf{B}^{\frac{1}{2}} + \xi^{\frac{1}{2}} + M_5 \right), \\
M_5 &= \left[\mathsf{B} + 2\mathsf{B}^{\frac{1}{2}} \left(\epsilon^{\frac{1}{2}} - \xi^{\frac{1}{2}} \right) + \left(\epsilon^{\frac{1}{2}} + \xi^{\frac{1}{2}} \right)^2 \right]^{\frac{1}{2}},
\end{aligned} \tag{22}$$

$$a(y) = \xi^{\frac{1}{2}} (1-y)^{\frac{1}{2}}, \quad b = 3\xi^{\frac{3}{2}} \left(\epsilon^{\frac{1}{2}} + \frac{5}{3} \mathsf{B}^{\frac{1}{2}} \right), \quad c = \left(\epsilon^{\frac{1}{2}} + \mathsf{B}^{\frac{1}{2}} \right)^2.$$

Now, we normalize the velocity of the free surface so that $u(1) = 1$, obtaining the implicit relation between Re and ξ, i.e.,

$$\mathcal{F}(\mathrm{Re}, \xi) = 1, \tag{23}$$

where

$$\mathcal{F}(\mathrm{Re}, \xi) = -\frac{4}{\xi^{\frac{3}{2}} \mathrm{Re}^{\frac{1}{3}}} (D_1(\mathrm{Re}, \xi) \log(D_2(\mathrm{Re}, \xi)) + (D_3(\mathrm{Re}, \xi)), \tag{24}$$

and

$$\begin{aligned}
D_1(\mathrm{Re}, \xi) &= -X^{\frac{1}{2}} \epsilon^{\frac{3}{2}} \xi^{\frac{5}{6}} \mathrm{Re}^{\frac{1}{6}} + \frac{3}{2} X \epsilon \xi^{\frac{7}{6}}, \\
D_2(\mathrm{Re}, \xi) &= \epsilon^{\frac{1}{2}} + \xi^{\frac{1}{2}} - \frac{X^{\frac{1}{2}} \xi^{\frac{1}{3}}}{\mathrm{Re}^{\frac{1}{6}}} + A(\mathrm{Re}, \xi), \\
D_3(\mathrm{Re}, \xi) &= D_4(\mathrm{Re}, \xi) + D_5(\mathrm{B}, \xi) + D_6(\mathrm{Re}, \xi), \\
D_4(\mathrm{Re}, \xi) &= \frac{A(\mathrm{Re}, \xi)}{16} \left[\frac{1}{3} \frac{X^{\frac{1}{2}} \xi^{\frac{1}{3}}}{\mathrm{Re}^{\frac{1}{6}}} P_1(\mathrm{Re}, \xi) + P_2(\mathrm{Re}, \xi) \right], \\
D_5(\mathrm{Re}, \xi) &= P_3(\mathrm{Re}, \xi) \log(2\epsilon^{\frac{1}{2}}) \epsilon, \\
D_6(\mathrm{Re}, \xi) &= \frac{P_5(\mathrm{Re}, \xi)}{16} \left(\frac{X^{\frac{1}{2}} \xi^{\frac{1}{3}}}{\mathrm{Re}^{\frac{1}{6}}} P_4(\mathrm{Re}, \xi) + \epsilon^{\frac{3}{2}} \mathrm{Re}^{\frac{1}{3}} \xi^{\frac{1}{2}} + \frac{11}{3} \epsilon^{\frac{1}{2}} X \xi^{\frac{7}{6}} \right) + P_6(\mathrm{Re}, \xi),
\end{aligned}$$

$$\begin{aligned}
P_1(\mathrm{Re}, \xi) &= -X \xi^{\frac{7}{6}} + \mathrm{Re}^{\frac{1}{3}} \left[5\xi^{\frac{3}{2}} + \epsilon^{\frac{1}{2}} \left(47\epsilon^{\frac{1}{2}} \xi^{\frac{1}{2}} - 8\xi \right) \right], \\
P_2(\mathrm{Re}, \xi) &= -\frac{11}{3} \epsilon^{\frac{1}{2}} X \xi^{\frac{7}{6}} + \epsilon^{\frac{1}{2}} \mathrm{Re}^{\frac{1}{3}} \xi^{\frac{3}{2}} - \frac{1}{3} X \xi^{\frac{5}{3}} - \mathrm{Re}^{\frac{1}{3}} \left(\epsilon^{\frac{3}{2}} \xi^{\frac{1}{2}} - \epsilon\xi + \xi^2 \right), \\
P_3(\mathrm{Re}, \xi) &= X^{\frac{1}{2}} \epsilon^{\frac{1}{2}} \xi^{\frac{5}{6}} \mathrm{Re}^{\frac{1}{6}} - \frac{3}{2} X \xi^{\frac{7}{6}}, \\
P_4(\mathrm{Re}, \xi) &= \frac{1}{3} \left(-47\epsilon\xi^{\frac{1}{2}} \mathrm{Re}^{\frac{1}{3}} + X \xi^{\frac{7}{6}} \right), \\
P_5(\mathrm{Re}, \xi) &= \epsilon^{\frac{1}{2}} + \frac{X^{\frac{1}{2}} \xi^{\frac{1}{3}}}{\mathrm{Re}^{\frac{1}{6}}}, \\
P_6(\mathrm{Re}, \xi) &= -\frac{X^{\frac{1}{2}} \xi^{\frac{1}{3}} \mathrm{Re}^{\frac{1}{6}}}{4} \left(\xi^{\frac{3}{2}} \epsilon^{\frac{1}{2}} - \frac{2}{3} \xi^2 \right) - \frac{1}{8} \epsilon \xi^{\frac{3}{2}} \mathrm{Re}^{\frac{1}{3}} - \frac{1}{16} \xi^{\frac{5}{2}} \mathrm{Re}^{\frac{1}{3}} - \frac{1}{8} X \xi^{\frac{13}{6}},
\end{aligned} \tag{25}$$

$$A(\mathrm{Re}, \xi) = \left[2 \frac{X^{\frac{1}{2}} \xi^{\frac{1}{3}}}{\mathrm{Re}^{\frac{1}{6}}} \left(\epsilon^{\frac{1}{2}} - \xi^{\frac{1}{2}} \right) + \frac{X \xi^{\frac{2}{3}}}{\mathrm{Re}^{\frac{1}{3}}} + \left(\epsilon^{\frac{1}{2}} + \xi^{\frac{1}{2}} \right)^2 \right]^{\frac{1}{2}}.$$

As expected, we obtain a one-to-one relation between Re and ξ and we denote by $\hat{\xi}$ the unique solution to (23) such that $u(1) = 1$. The plot $\mathcal{F}(\mathrm{Re}, \xi)$ is displayed in Figure 3. Moreover, we recall that B is expressed in terms of Re through (15), where now $\hat{\xi}$ is the solution of (23). Relation (23) defines as $\mathcal{F}(\mathrm{Re}, \xi) = 1$ which, as expected, is a one-to-one relation between Re and ξ. The plot of $\mathcal{F}(\mathrm{Re}, \xi)$ is displayed in Figure 4, which highlights that, for given λ_1, λ_2, and θ, there exists a unique (Re, ξ) fulfilling (23). Consequently, recalling that Equation (23) derives from the normalization of u, for any Re we obtain a unique value of ξ, which we denoted as $\hat{\xi}$, such that $u(1) = 1$.

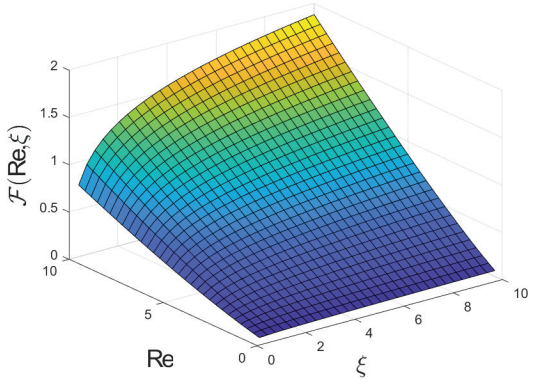

Figure 3. Plot of $\mathcal{F}(\mathrm{Re},\xi)$ for $\lambda_1 = 0.1$ and $\theta = 5^\circ$ for the regularized Casson model (given by (23)).

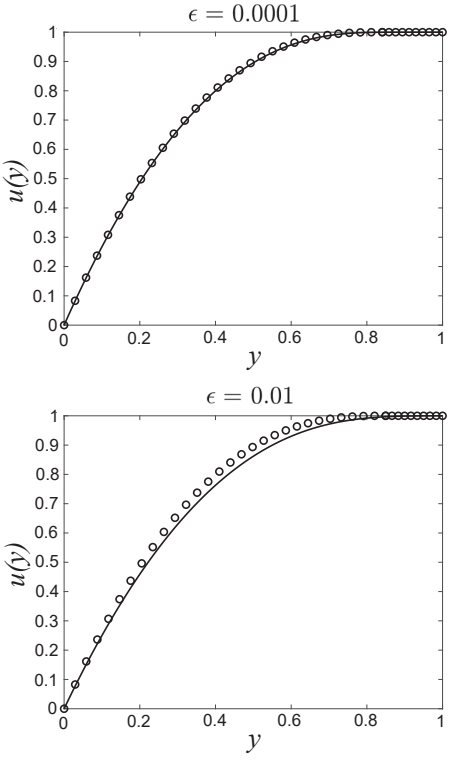

Figure 4. Plot of $u(y)$ given by (21) (empty circles) and (26) (solid line) with $\lambda_1 = 0.1$ and $\theta = 1^\circ$ for different values of ϵ. It is worth noting that the "exact" profile of $u(y)$, given by (26), can be retrieved from the regularized one, given by (21). In fact, the two profiles become very similar when $\epsilon < 10^{-2}$.

We remark that for $\epsilon \to 0$ we retrieve the Casson flow whose normalized velocity field is given by

$$u(y) = \begin{cases} -\frac{\xi y^2}{2} + (\xi\sigma + 2\,\mathsf{B})y + \frac{4\sqrt{\mathsf{B}}\left[-(\xi\sigma+\mathsf{B})^{3/2}+(\xi\sigma-y\xi+\mathsf{B})^{3/2}\right]}{3\xi}, & \text{if } 0 \le y \le \sigma, \\ 1, & \text{if } \sigma \le y \le 1, \end{cases} \tag{26}$$

with

$$\sigma = 1 - \frac{\tau_0^*}{\rho^* g^* H^* \sin\theta} = 1 - \frac{\mathsf{B}}{\xi}, \tag{27}$$

is the flat yield surface [10,16]. The velocity field is normalized so that $u(\sigma) = 1$, i.e.,

$$-\frac{\xi\sigma^2}{2} + (\xi\sigma + 2\,\mathsf{B})\sigma + \frac{4\left[-\sqrt{\mathsf{B}}(\xi\sigma + \mathsf{B})^{3/2} + \mathsf{B}^2\right]}{3\,\xi} = 1, \tag{28}$$

that leads, using (15) and (27), to the following implicit relation between ξ and Re

$$\mathcal{F}(\mathsf{Re}, \xi) = 1, \tag{29}$$

where

$$\mathcal{F}(\mathsf{Re}, \xi) = -\frac{X^2}{6}\xi^{\frac{1}{3}}\mathsf{Re}^{-\frac{2}{3}} - \frac{4}{3}\sqrt{\xi}\sqrt{X\,\xi^{\frac{2}{3}}\mathsf{Re}^{-\frac{1}{3}}} + X\,\xi^{\frac{2}{3}}\mathsf{Re}^{-\frac{1}{3}} + \frac{\xi}{2}. \tag{30}$$

The regularized and the "exact" profiles of $u(y)$ are given by (21) and (26), respectively. They become very similar when $\epsilon < 10^{-2}$ as shown in Figure 4.

It is worth noting that in case $\mathsf{B} = 0$, i.e., Newtonian flow, Equation (23), for $\epsilon \to 0$, and Equation (29) simply reduce to $\mathcal{F} = \xi - 2 = 0$, whose trivial solution is $\hat{\xi} = 2$.

The equations governing the regularized and exact Bingham flow have been reported in [10]. In this paper, we have adopted the same notations as in [10], thus the comparison between the two models can be performed easily.

4. Linear Stability Furthermore, Long-Wave Approximation

In this section, we briefly recall the main characteristic of the linear stability analysis as reported in [10,16,51] and we refer the readers to [10,16] for more details on the derivation of the formulas here summarized.

We consider the basic flow consisting of $h(x,t) = h_b$, with $h_b = 1$, $\mathbf{v}_b = u_b(y)\mathbf{i}$ with u_b given by (21), and, $p = p_b(y)$ where, recalling (20), $p_b(y) = \hat{\xi}\cot\theta(1-y)$. Then, we perturb the basic flow superimposing small disturbances, in the form of travelling waves, so that

$$\begin{aligned} h &= 1 + \hat{h}(y)e^{i\alpha(x-ct)}, \quad u = u_b + \hat{u}(y)e^{i\alpha(x-ct)}, \\ v &= \hat{v}(y)e^{i\alpha(x-ct)}, \qquad p = p_b + \hat{p}(y)e^{i\alpha(x-ct)}, \end{aligned} \tag{31}$$

and

$$\gamma = \gamma_b + \hat{\gamma}, \quad \tau = \tau_b + \hat{\tau}, \tag{32}$$

where $\alpha \in \mathbb{R}$ is the wave number, $c \in \mathbb{C}$ is the complex wave speed and the notation $\hat{(\cdot)}$ represents the infinitesimal disturbance. We write the velocity field in terms of the stream function, i.e.,

$$\hat{\psi}(x,y,t) = \phi(y)e^{i\alpha(x-ct)},$$

as

$$\hat{u} = \hat{\psi}_y = \phi'(y)e^{i\alpha(x-ct)}, \quad \hat{v} = -\hat{\psi}_x = -i\alpha\phi(y)e^{i\alpha(x-ct)}, \tag{33}$$

where, here and in the sequel, $(\cdot)'$ denotes the differentiation with regard to y. Defining by $\Re(c)$ and $\Im(c)$ the real and imaginary part of c, we recall that $\Im(c)$ gives the growth/attenuation factor of the α^{th} mode. Hence, the basic flow h_b, $\mathbf{v}_b$, $p_b(y)$ is unstable when the parameters involved in the problem, namely Re, λ_1, λ_2 and θ, are selected so that $\Im(c) > 0$. The transition between the two regimes is identified by the so-called marginal or neutral curve, i.e., the set of Re, λ_1, λ_2 and θ at which $\Im(c) = 0$.

Then, we consider disturbances of long wavelength $2\pi/\alpha \gg 1$, i.e., $\alpha \ll 1$, expanding ϕ and c in powers of α up to the first order in α, namely

$$\begin{aligned} \phi(y) &= \phi_0(y) + \alpha\phi_1(y), \\ c &= c_0 + \alpha c_1, \end{aligned} \tag{34}$$

where (ϕ_0, c_0) and (ϕ_1, c_1) solve

$$\begin{cases} (s(y)\phi_0(y)'')'' = 0, \\ \phi_0(0) = \phi_0'(0) = 0, \\ \phi_0''(1) - \phi_0(1)\dfrac{\hat{\xi}}{s(1)(c_0-1)} = 0, \\ s(1)\phi_0'''(1) + \phi_0(1)\dfrac{\hat{\xi}s'(1)}{s(1)(c_0-1)} = 0, \end{cases} \tag{35}$$

and

$$\begin{cases} (s(y)\phi_1''(y))'' = i\mathrm{Re}\left[\phi_0''(y)(u_b(y)-c_0) - u_b''(y)\phi_0(y)\right], \\ \phi_1(0) = \phi_1'(0) = 0, \\ \phi_1(1) = 0, \\ \phi_1''(1) + \phi_0(1)\dfrac{\hat{\xi}c_1}{s(1)(c_0-1)^2} = 0, \\ -is(1)\phi_1'''(1) + \phi_0'(1)\mathrm{Re}(c_0-1) - \phi_0(1)\dfrac{\hat{\xi}}{s(1)}\left(\dfrac{s(1)cot\theta}{c_0-1} - i\dfrac{c_1 s'(1)}{(c_0-1)^2}\right) = 0, \end{cases} \tag{36}$$

with

$$s(y) = \frac{1}{2}\left[r\left(\frac{u_b'}{2}\right) + \frac{u_b'}{2}\frac{dr}{dz}\left(\frac{u_b'}{2}\right)\right],$$

and r given by (13). In particular, we have that $\Im(c_0) = 0$, while $\Re(c_1) = 0$, thus

$$\phi(y)e^{i\alpha(x-ct)} = \phi(y) \underbrace{e^{i\alpha(x-c_0 t)}}_{\text{travelling wave}} \underbrace{e^{\alpha^2\Im(c_1)t}}_{\text{growth/attenuation}}. \tag{37}$$

In particular, we can find the critical value of Re, denoted as Re_c, such that

$$\Im(c) = \Im(c_1(\mathrm{Re}_c, \lambda_1, \lambda_2, \theta)) = 0, \tag{38}$$

by prescribing the material characteristics and the tilt angle (i.e., λ_1, λ_2, and θ). Hence, for $\mathrm{Re} < \mathrm{Re}_c$ the α^{th} mode is stable, while instability arises when $\mathrm{Re} > \mathrm{Re}_c$, since $\Im(c_1) < 0$ for $\mathrm{Re} < \mathrm{Re}_c$ and vice versa. Moreover, we eventually remark that the identification of Re_c means, from the practical point of view, the identification of a critical discharge, Q_c^*, above which the flow becomes unstable.

5. Results

The critical value of the Reynolds number, Re_c, is computed by solving the system given by the system of algebraic Equations (23) and (38) with MATLAB® 2022a, using the function FSOLVE.

Figure 5 shows the variation of Re_c with respect to the tilt angle θ for different value of the material parameter λ_1, when $\epsilon = 0.01$ by considering the regularized Bingham and Casson model. Similar to [10], at a given θ, Re_c decreases for increasing values of λ_1 and coincides with $5/4 \cot\theta$, when $\lambda_1 = 0$, i.e., $\mathrm{B} = 0$. However, recalling the proportionality relation (16) between λ_1 and τ_0^*, we have that (see Figure 5A) the yield stress destabilizes the flow when this is modelled using a regularized Bingham flow, while (see Figure 5B) the regularized Casson flow is more stable than the Newtonian flow (i.e., the yield stress has a stabilizing effect on the flow when the material is modelled as a regularized Casson fluid). Coherently, in the case of regularized Casson fluid, Rec is an increasing function of λ_1, namely an increase in the yield stress τ_0^* leads to a flow stabilization (Figure 6C,D). For the regularized Bingham, we have an opposite behaviour. Indeed, Figure 6A,B highlight that Re_c decreases as λ_1 (i.e., τ_0^*) increases. Moreover, it is worth noting that, as physically expected, an increase of θ leads to flow destabilization in both cases.

In Table 1, we report the values of Re_c and c_0 when $\theta = 5^\circ$ for various values of λ_1 when a regularized Bingham and Casson models are considered. We notice that $c_0 = 2$ when $\lambda_1 = 0$, i.e., when the flow is Newtonian, as in [10]. Again, coherently with the results obtained in [10], as λ_1 increases the superficial wave speed increases also for the regularized Casson fluid.

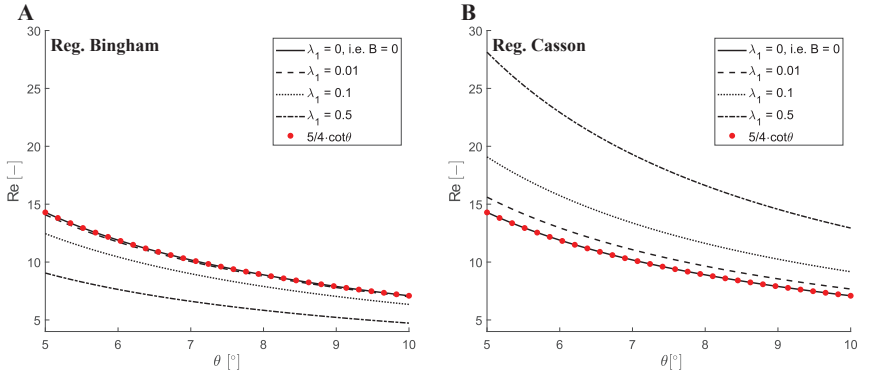

Figure 5. Evolution of the critical Reynolds number, Re_c, with respect to the tilt angle, θ, with $\epsilon = 0.01$ for different values of λ_1 in the case of the flow modelled as a regularized Bingham (**A**) and regularized Casson (**B**) fluid. The theoretical Newtonian flow (i.e., $5/4 \cot\theta$) is given by the red circles. The continuous line is the Newtoian flow computed by our code. We emphasize that the theoretical curve and the computed one coincide.

Table 1. Values of Re_c and c_0 for given values of λ_1 with $\theta = 5^\circ$ and $\epsilon = 0.01$ for both the regularized Bingham and Casson models.

λ_1	Re_c		c_0	
	Reg. Bingham	**Reg. Casson**	**Reg. Bingham**	**Reg. Casson**
0	14.29	14.29	2	2
0.01	14.08	15.61	2.03	2.15
0.1	12.45	19.08	2.34	2.52
0.5	9.05	28.13	4.31	3.30

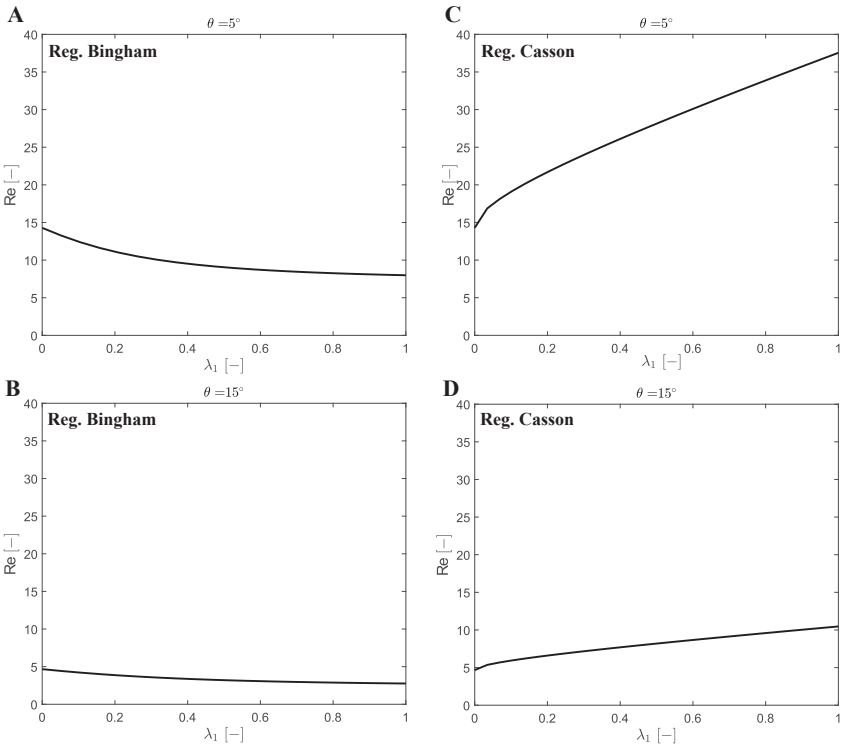

Figure 6. Plot of the critical Reynolds number, Re_c, as a function of λ_1 with $\epsilon = 0.01$ for different values of θ for a regularized Bingham (**A**,**B**) and regularized Casson (**C**,**D**) fluid. The case of Newtonian flow corresponds to $\lambda_1 = 0$, i.e., $\mathrm{B} = 0$.

6. Conclusions

In this paper, the stability analysis of a free surface regularized Casson flow down an incline has been theoretically investigated and compared to the one obtained for the regularized Bingham flow. In both cases the benchmark represented by the Newtonian case (i.e., when $\lambda_1 = 0$, thus $\mathrm{B} = 0$) has been recovered. Our results show that for a regularized Casson fluid Re_c increases with increasing values of the "material" parameter λ_1 (that is proportional to τ_0^* see (16)), while for a regularized Bingham fluid Re_c decreases when λ_1 (i.e., τ_0^*) increases [10,16]. Therefore, our findings (obtained within the long-wave approximation method) show that the flow of the regularized Casson fluid is stabilized by increasing yield stress τ_0^* contrary to what happens with the regularized Bingham.

The stability analysis of the exact Bingham model, investigated in [16], shows that the flow down an incline is unconditionally stable for every Reynolds number. Therefore, our results are unexpected, highlighting that, although in a regularized formulation, models belonging to the same class of viscoplastic fluids can have stability characteristics completely different. Although we are not aware of any studies on the stability of the Casson fluid flowing down an incline, we suppose that the results of [12] can also be extended to this case. Therefore, we show that (as for the regularized Bingham fluid [10]) the regularized Casson can have stability properties that are different from the classic Casson flow. It is worth remarking that the our study has been developed by applying the long-wave approximation to the flow of regularized Bingham and Casson fluids down an incline.

We have in fact shown that the flow along an incline of a Casson-type material becomes increasingly stable as the yield stress increases. Exactly the opposite behaviour occurs with the Bingham fluid. Therefore, this feature can be used, from an experimental point of view,

to highlight the difference between the two rheological models. We believe that our results can pave the way to experimental studies on the flow down an incline.

Author Contributions: Conceptualization, B.C., L.I.P., L.F. and A.F.; methodology, B.C., L.I.P., L.F. and A.F.; software, B.C.; formal analysis, L.F. and A.F.; investigation, B.C., L.I.P., L.F. and A.F.; writing—original draft preparation, B.C., L.I.P., L.F. and A.F.; writing—review and editing, B.C., L.F. and A.F. All authors have read and agreed to the published version of the manuscript.

Funding: This research was partially supported by GNFM of Italian INDAM.

Informed Consent Statement: Not applicable.

Data Availability Statement: Not applicable.

Conflicts of Interest: The authors declare no conflicts of interest.

References

1. Bingham, E.C. *Fluidity and Plasticity*; McGraw-Hill: New York, NY, USA, 1922.
2. Herschel, W.H.; Bulkley, R. Konsistenzmessungen von gummi-benzollosungen. *Kolloid-Z.* **1926**, *39*, 291–300. [CrossRef]
3. Casson, N. A Flow Equation for Pigment-oil Suspensions of the Printing Ink Type. In *Rheology of Disperse Systems*; Mill, C.C., Ed.; Pergamon Press: Oxford, UK, 1959; pp. 84–104 .
4. Benjamin, T.B. Wave formation in laminar flow down an inclined plane. *J. Fluid Mech.* **1957**, *2*, 554. [CrossRef]
5. Yih, C.-S. Stability of liquid flow down an inclined plane. *Phys. Fluids* **1963**, *6*, 321. [CrossRef]
6. Liu, J.; Paul, J.D.; Gollub, J.P. Measurements of the primary instabilities of film flows. *J. Fluid Mech.* **1993**, *250*, 69–101. [CrossRef]
7. Allouche, M.H.; Millet, S.; Botton, V.; Henry, D.; Hadid, H.B.; Rousset, F. Stability of a flow down an incline with respect to two-dimensional and three-dimensional disturbances for Newtonian and non-Newtonian fluids. *Phys. Rev. E* **2015**, *92*, 063010. [CrossRef]
8. Allouche, M.H.; Botton, V.; Millet, S.; Henry, D.; Dagois-Bohy, S.; Güzel, B.; Hadid, H.B. Primary instability of a shear-thinning film flow down an incline: Experimental study. *J. Fluid Mech.* **2017**, *821*, R1. [CrossRef]
9. Balmforth, N.J.; Liu, J.J. Roll waves in mud. *J. Fluid Mech.* **2004**, *519*, 33–54. [CrossRef]
10. Calusi, B.; Farina, A.; Fusi, L.; Rosso, F. Long-wave instability of a regularized Bingham flow down an incline. *Phys. Fluids* **2022**, *34*, 054111. [CrossRef]
11. Chakraborty, S.; Sheu, T.W.-H.; Ghosh, S. Dynamics and stability of a power-law film flowing down a slippery slope. *Phys. Fluids* **2019**, *31*, 013102. [CrossRef]
12. Falsaperla, P.; Giacobbe, A.; Mulone, G. Stability of the plane Bingham–Poiseuille flow in an inclined channel. *Fluids* **2020**, *5*, 141. [CrossRef]
13. Fernandez-Nieto, E.D.; Noble, P.; Vila, J.-P. Shallow water equations for non-Newtonian fluids. *J. Non-Newtonian Fluid Mech.* **2010**, *165*, 712–732. [CrossRef]
14. Forterre, Y.; Pouliquen, O. Long-surface-wave instability in dense granular flows. *J. Fluid Mech.* **2003**, *486*, 21–50. [CrossRef]
15. Fusi, L. Channel flow of viscoplastic fluids with pressure-dependent rheological parameters. *Phys. Fluids* **2018**, *30*, 073102. [CrossRef]
16. Fusi, L.; Calusi, B.; Farina, A.; Rosso, F. Stability of laminar viscoplastic flows down an inclined open channel. *Eur. J. Mech.-B/Fluid* **2022**, *95*, 137–147. [CrossRef]
17. Hu, J.; Millet, S.; Botton, V.; Hadid, H.B.; Henry, D. Inertialess temporal and spatio-temporal stability analysis of the two-layer film flow with density stratification. *Phys. Fluids* **2006**, *18*, 104101. [CrossRef]
18. Hu, J.; Yin, X.Y.; Hadid, H.B.; Henry, D. Linear temporal and spatiotemporal stability analysis of two-layer falling films with density stratification. *Phys. Rev. E* **2008**, *77*, 026302. [CrossRef]
19. Hu, J.; Hadid, H.B.; Henry, D.; Mojtabi, A. Linear temporal and spatiotemporal stability analysis of a binary liquid film flowing down an inclined uniformly heated plate. *J. Fluid Mech.* **2008**, *599*, 269–298. [CrossRef]
20. Hu, T.; Fu, Q.F.; Xing, Y.; Yang, L.J.; Xie, L. Stability of a thin viscoelastic film falling down an inclined plane. *Phys. Rev. Fluids* **2021**, *6*, 083902. [CrossRef]
21. Métivier, C.; Nouar, C. Stability of a Rayleigh–Bénard Poiseuille flow for yield stress fluids—Comparison between Bingham and regularized models. *Int. J. Non-Linear Mech.* **2011**, *46*, 1205–1212. [CrossRef]
22. Millet, S.; Botton, V.; Rousset, F.; Hadid, H.B. Wave celerity on a shearthinning fluid film flowing down an incline. *Phys. Fluids* **2008**, *20*, 031701. [CrossRef]
23. Millet, S.; Botton, V.; Hadid, H.B.; Henry, D.; Rousset, F. Stability of twolayer shear-thinning film flows. *Phys. Rev. E* **2013**, *88*, 043004. [CrossRef]
24. Millet, S.; Usha, R.; Botton, V.; Rousset, F. The mechanism of long-wave instability in a shear-thinning film flow on a porous substrate. *Acta Mech.* **2019**, *230*, 2201–2220. [CrossRef]
25. Mogilevskiy, E. Stability of a non-Newtonian falling film due to three-dimensional disturbances. *Phys. Fluids* **2020**, *32*, 073101. [CrossRef]

26. Ng, C.-O.; Mei, C.C. Roll waves on a shallow layer of mud modelled as a power-law fluid. *J. Fluid Mech.* **1994**, *263*, 151–184. [CrossRef]
27. Noble, P.; Vila, J.-P. Thin power-law film flow down an inclined plane: Consistent shallow-water models and stability under large-scale perturbations. *J. Fluid Mech.* **2013**, *735*, 29–60. [CrossRef]
28. Mounkaila Noma, D.; Dagois-Bohy, S.; Millet, S.; Botton, V.; Henry, D.; Ben Hadid, H. Primary instability of a visco-plastic film down an inclined plane: Experimental study. *J. Fluid Mech.* **2021**, *922*, R2. [CrossRef]
29. Nsom, B.; Ramifidisoa, L.; Latrache, N.; Ghaemizadeh, F. Linear stability of shear-thinning fluid down an inclined plane. *J. Mol. Liquids* **2019**, *277*, 1036–1046. [CrossRef]
30. Pascal, J.P.; D'Alessio, S.J.D. Instability of power-law fluid flows down an incline subjected to wind stress. *Appl. Math. Model.* **2007**, *31*, 1229–1248. [CrossRef]
31. Rousset, F.; Millet, S.; Botton, V.; Hadid, H.B. Temporal stability of carreau fluid flow down an incline. *J. Fluids Eng.* **2007**, *129*, 913–920. [CrossRef]
32. Ruyer-Quil, C.; Chakraborty, S.; Dandapat, B.S. Wavy regime of a powerlaw film flow. *J. Fluid Mech.* **2012**, *692*, 220–256. [CrossRef]
33. Merrill, E.W.; Margetts, W.G.; Cokelet, G.C.; Gilliland, E.R. The Casson equation and rheology of the blood near shear zero. In *Proceedings Fourth International Congress on Rheology*; Copley, A.L., Ed.; Interscience: New York, NY, USA, 1965; Part 4, pp. 135–143.
34. Farina, A.; Fasano, A.; Rosso, F. Mathematical models for some aspects of blood microcirculation. *Symmetry* **2021**, *13*, 1020. [CrossRef]
35. Fasano, A.; Sequeira, A. *Hemomath: The Mathematics of Blood*; Springer: Berlin/Heidelberg, Germany, 2017.
36. Charakopoulos, A.; Karakasidis, T.; Sarris, I. Analysis of magnetohydrodynamic channel flow through complex network analysis. *Chaos* **2021**, *31*, 043123. [CrossRef] [PubMed]
37. Fusi, L. Lubrication flow of a generalized Casson fluid with pressure-dependent rheological parameters. *J. Non-Newton. Fluid Mech.* **2019**, *274*, 104199. [CrossRef]
38. Guadagli, S.; Palade, L.I.; Fusi, L.; Farina, A. On a Casson Fluid Motion: Nonuniform Width Symmetric Channel and Peristaltic Flows. *Fluids* **2021**, *6*, 356. [CrossRef]
39. Reddy, M.G.; Kumara, B.C.P.; Makinde, O.D. Cross Diffusion Impacts on Hydromagnetic Radiative Peristaltic Carreau-Casson Nanofluids Flow in an Irregular Channel. *Defect Diffus. Forum* **2017**, *377*, 62–83. [CrossRef]
40. Sofos, F.; Karakasidis, T.; Spetsiotis, D. Molecular dynamics simulations of ion separation in nano-channel water flows using an electric field. *Mol. Simul.* **2019**, *45*, 1395–1402. [CrossRef]
41. Song, L.; Huo, X.; Zhang, L.; Xie, Y.; Yang, M. Fast estimation on the pressure of detonation products of cyclotetramethylene tetranitramine through molecular dynamics simulations. *Int. J. Mod. Phys. B* **2021**, *35*, 2150106. [CrossRef]
42. Astarita, G. Letter to the editor: The engineering reality of the yield stress. *J. Rheol.* **1990**, *34*, 275–277. [CrossRef]
43. Barnes, H.A. The yield stress—A review or '$\pi\alpha\nu\tau\alpha\ \rho\epsilon\iota$'—Everything flows? *J. Non-Newton. Fluid Mech.* **1999**, *81*, 133–178. [CrossRef]
44. Barnes, H.A.; Walters, K. The yield stress myth? *Rheol. Acta* **1985**, *24*, 323–326. [CrossRef]
45. Frigaard, I.; Nouar, C. On the usage of viscosity regularisation methods for visco-plastic fluid flow computation. *J. Non-Newton. Fluid Mech.* **2005**, *127*, 1–26. [CrossRef]
46. Frigaard, I.A.; Paso, K.G.; de Souza Mendes, P.R. Bingham's model in the oil and gas industry. *Rheol. Acta* **2017**, *56*, 259–282. [CrossRef]
47. Fusi, L.; Farina, A.; Rosso, F. On the mathematical paradoxes for the flow of a viscoplastic film down an inclined surface. *Int. J. Non-Linear Mech.* **2014**, *58*, 139–150. [CrossRef]
48. Fusi, L.; Farina, A.; Rosso, F. Roscani, S. Pressure driven lubrication flow of a Bingham fluid in a channel: A novel approach. *J. Non-Newtonian Fluid Mech.* **2015**, *221*, 66–75. [CrossRef]
49. Bercovier, M.; Engleman, M. A finite-element method for incompressible non-Newtonian flows. *J. Comput. Phys.* **1980**, *36*, 313–326. [CrossRef]
50. Papanastasiou, T.C. Flows of materials with yield. *J. Rheol.* **1987**, *31*, 385–404. [CrossRef]
51. Pascal, J.P. Linear stability of fluid flow down a porous inclined plane. *J. Phys. D Appl. Phys.* **1999**, *32*, 417. [CrossRef]
52. Allouche, M.; Frigaard, I.A.; Sona, G. Static wall layers in the displacement of two visco-plastic fluids in a plane channel. *J. Fluid Mech.* **2000**, *424*, 243–277. [CrossRef]

fluids

MDPI

Article

Single-Mode Solutions for Convection and Double-Diffusive Convection in Porous Media

Chang Liu * and Edgar Knobloch *

Department of Physics, University of California, Berkeley, CA 94720, USA
* Correspondence: chang_liu@berkeley.edu (C.L.); knobloch@berkeley.edu (E.K.)

Abstract: This work employs single-mode equations to study convection and double-diffusive convection in a porous medium where the Darcy law provides large-scale damping. We first consider thermal convection with salinity as a passive scalar. The single-mode solutions resembling steady convection rolls reproduce the qualitative behavior of root-mean-square and mean temperature profiles of time-dependent states at high Rayleigh numbers from direct numerical simulations (DNS). We also show that the single-mode solutions are consistent with the heat-exchanger model that describes well the mean temperature gradient in the interior. The Nusselt number predicted from the single-mode solutions exhibits a scaling law with Rayleigh number close to that followed by exact 2D steady convection rolls, although large aspect ratio DNS results indicate a faster increase. However, the single-mode solutions at a high wavenumber predict Nusselt numbers close to the DNS results in narrow domains. We also employ the single-mode equations to analyze the influence of active salinity, introducing a salinity contribution to the buoyancy, but with a smaller diffusivity than the temperature. The single-mode solutions are able to capture the stabilizing effect of an imposed salinity gradient and describe the standing and traveling wave behaviors observed in DNS. The Sherwood numbers obtained from single-mode solutions show a scaling law with the Lewis number that is close to the DNS computations with passive or active salinity. This work demonstrates that single-mode solutions can be successfully applied to this system whenever periodic or no-flux boundary conditions apply in the horizontal.

Keywords: convection in a porous medium; single-mode solutions; double-diffusive convection

Citation: Liu, C.; Knobloch, E. Single-Mode Solutions for Convection and Double-Diffusive Convection in Porous Media. *Fluids* **2022**, *7*, 373. https://doi.org/10.3390/fluids7120373

Academic Editor: Mehrdad Massoudi

Received: 22 October 2022
Accepted: 29 November 2022
Published: 5 December 2022

Publisher's Note: MDPI stays neutral with regard to jurisdictional claims in published maps and institutional affiliations.

1. Introduction

The single-mode equations ('single-α mean-field theory') obtained from a severely truncated Fourier expansion in the horizontal were likely first proposed by J. Herring [1,2] in analyzing the thermal transport of Rayleigh–Bénard convection (RBC) with either stress-free or no-slip boundary conditions at the top and bottom. Such single-mode equations reduce the governing equations from three spatial dimensions to equations for the vertical solution profile associated with a prescribed horizontal planform. Although the single-mode approach significantly simplifies the horizontal structure, solution profiles in the vertical and the Nusselt number (Nu) from single-mode equations show the expected behavior when compared with experimental measurements [1,2]. The single-mode equations are not only able to provide a useful approximation to steady convection rolls, but their time-dependent behavior also provides a reasonable approximation to that observed in two-dimensional (2D) simulations [3]. The single-mode equations can also incorporate more general planforms such as hexagonal planforms by introducing appropriate self-interaction terms [4,5], again with qualitative agreement with experimental results.

Single-mode equations have also been applied to double-diffusive convection. For example, Gough and Toomre [6] focused on oscillatory double-diffusive convection (ODDC) characterized by the competition between a stabilizing salinity gradient and a destabilizing temperature gradient, a configuration that is subject to a diffusion-driven instability even

when the fluid density is dynamically stable, and showed that the flux ratio is insensitive to the density ratio (called stability parameter there) consistent with experimental measurements [7–9]. Paparella et al. [10] employed single-mode equations allowing for the formation of large-scale shear, and described its interaction with oscillatory convection, producing intermittent overturning of the fluid with significant mixing. Single-mode equations can also be used to characterize the case where a destabilizing salinity gradient competes with a stabilizing temperature gradient, and used to demonstrate that the resulting salt-finger convection may trigger large-scale shear, producing a staircase-like profile in density [11] with mixed regions separated by an interface with a large density gradient. In fact such staircase profiles form even in the absence of shear instabilities, and their stability properties for Prandtl numbers relevant to both oceanographic and astrophysical conditions can be analyzed [12].

The severe truncation of the horizontal Fourier modes within the single-mode equations is expected to be valid for well-organized columnar structures associated with limited interaction between different horizontal harmonics. Such limited interaction between harmonics arises naturally when the dominant flow structures are associated with a small horizontal length scale. This is the case in the asymptotic limit of high wavenumber convection leading to tall and thin flow structures, a limit employed to provide insight into high Rayleigh number RBC [13], convection in a porous medium [14], and salt-finger convection [15]. This high wavenumber asymptotic limit corresponds to small horizontal domain size in two-dimensional numerical simulations. As a result, single-mode solutions show an excellent agreement with DNS results in a small horizontal domain as is the case in vertically confined salt-finger convection [12]. Well-organized columnar flow structures also arise in the presence of strong restraining body forces [16]. For example, rotation constrains the flow variation in the direction of the rotation axis as described by the Taylor–Proudman theorem [17,18]. In the rapidly rotating regime, single-mode solutions of the asymptotically reduced equations show a close agreement with direct numerical simulations (DNS) at moderate reduced Rayleigh numbers; see, e.g., Figures 12 and 13 from [19] and [16,20]. A strong imposed magnetic field plays a similar role, and DNS of rotating magnetoconvection also show results approaching the single-mode solutions [21] at moderate reduced Rayleigh numbers [22]. The stabilizing temperature gradient in salt-finger convection serves as large-scale damping [23,24], leading to well-organized columnar structures known as salt fingers, and single-mode solutions of vertically confined salt-finger convection agree well with DNS near the onset of instability and display scaling laws between the Sherwood number (Sh) and density ratio with a scaling exponent that agrees well with DNS [12].

In this work, we focus on convection in a porous medium modeled by a Darcy law, which also provides large-scale damping as compared with the Navier–Stokes equation describing pure fluids. In contrast to RBC, convection in a porous medium is dominated by well-organized columnar structures even at high Rayleigh numbers as shown in DNS in both 2D [25,26] and 3D [27,28] configurations; see the review [29]. Flow structures in the interior of convection in a porous medium are well approximated by a heat-exchanger model obtained by assuming no vertical variation of fluctuations and a constant mean temperature gradient [25,27,29]. Such well-organized structures are also characterized by a power spectrum density [27] and time-averaged Fourier coefficients [26] that both suggest that a single mode dominates in the interior. The horizontal wavenumber of the dominant flow structures in both the interior and near the boundaries increases with increasing Rayleigh number [25,27,29] leading to improved agreement with the heat-exchanger model at high Rayleigh numbers [27].

Convection and double-diffusive convection in a porous medium have a wide range of geophysical and engineering applications [30–32], for example, in understanding large-scale convection in a geothermal reservoir [33]. Convection in a porous medium driven by concentration gradients models groundwater transport in saline aquifers [34,35] and may

be used to understand the possibility and risks of storing carbon dioxide (CO_2) in large porous underground reservoirs to mitigate CO_2 emissions [36,37].

Porous media convection is also widely studied in enclosures that are closer to an experimental setup [38–45]. Such an enclosure configuration typically adopts impermeable boundary conditions (B.C.) in the horizontal, with no horizontal thermal and salinity fluxes, a configuration that will be referred to as the no-flux case. One major difference between no-flux and periodic boundary conditions in the horizontal is that the latter allow well-defined traveling waves, while no-flux B.C. require a large horizontal domain in order to observe propagating disturbances [43]. Such traveling waves are typically associated with reduced heat transport compared with steady convection rolls [43]. Two-dimensional traveling waves in horizontally periodic domains have been widely studied theoretically in the context of oscillatory double-diffusive convection [46,47] and oscillatory binary fluid convection [48,49] as well as experimentally using Hele-Shaw geometry [50,51]. Moreover, standing waves that are unstable to perturbations in the form of traveling waves within a horizontally periodic domain become stable with no-flux B.C., suggesting that standing waves can also be observed in direct numerical simulations [43].

This work employs single-mode equations to analyze convection and double-diffusive convection in a porous medium and to explore the physics aspects that can be included within this approach. The single-mode equations preserve the nonlinear interaction between the horizontally averaged mode and a single Fourier mode while fully resolving the vertical direction leading to strongly nonlinear solutions. We first focus on thermal convection with salinity as a passive scalar. The single-mode solutions show qualitative agreements with DNS results for the root-mean-square (RMS) temperature, vertical velocity and horizontal velocity. The RMS values in the interior also exhibit certain trends with the Rayleigh number similar to the DNS results [25,27]. We demonstrate that the single-mode solutions are consistent with the heat-exchanger model, which describes well the mean temperature gradient in the interior obtained in DNS [25,27]. The Nusselt number Nu scaling with the Rayleigh number obtained from the single-mode solutions is consistent with that for exact 2D steady convection rolls computed numerically [26] and respects upper bound theory [52].

We further employ single-mode solutions to analyze the influence of active salinity that provides an additional contribution to the buoyancy term, but with a smaller diffusivity than the temperature. The single-mode solutions are able to capture the stabilizing effect of the imposed salinity gradient with progressively lower Nu and Sh as the salinity gradient increases [40]. The single-mode solutions are also able to predict traveling and standing waves and the associated Nu and Sh, both of which are reduced in comparison with steady convection rolls, a prediction also consistent with DNS observations [43]. The Sh obtained from single-mode solutions shows a scaling law with the Lewis number (Le) close to the DNS observation for both active [40] and passive [39] salinity. Single-mode solutions also show agreement with DNS with no-flux boundary conditions in the horizontal [39,40,43] after mirroring the domain.

The remainder of this paper is organized as follows. Section 2 describes the formulation of the single-mode equations for double-diffusive convection in a porous medium. Section 3 then compares the single-mode solutions against a wide range of DNS results [25–28,39,40,43], exact 2D steady convection rolls [26] and upper bound theory [52]. We conclude the paper with a discussion of future directions in Section 4.

2. Single-Mode Solutions for Double-Diffusive Convection in a Porous Medium

We consider a fluid-saturated porous layer between two infinitely long parallel horizontal plates separated by a distance h. The temperature and salinity at these two plates are maintained at constant values with the lower plate maintained at a higher temperature and salinity. The equation of state $(\rho_* - \rho_{r*})/\rho_{r*} = -\alpha(T_* - T_{r*}) + \beta(S_* - S_{r*})$ is linear, with constant expansion/contraction coefficients α, β and reference density, temperature, and salinity $\rho_{r*}, T_{r*}, S_{r*}$, respectively. The subscript $_*$ indicates a dimensional quantity. In the

following, we normalize the temperature T_* by the temperature difference between the bottom and top layer, $T = T_*/\Delta T$ ($\Delta T = T_{\text{bot}} - T_{\text{top}} > 0$), and likewise for the salinity, $S = S_*/\Delta S$ ($\Delta S = S_{\text{bot}} - S_{\text{top}} > 0$). Spatial coordinates are normalized by the height h of the layer while time and velocity are normalized using the time $\sigma h^2/\kappa_T$ and the speed κ_T/h, respectively. Here, σ is the saturated porous medium to fluid heat capacity ratio and κ_T is the thermal diffusivity of the saturated porous medium, respectively. We decompose the temperature and salinity into a linear base state and deviation,

$$T = 1 - z + \tilde{T}, \quad S = 1 - z + \tilde{S}, \tag{1}$$

and introduce the velocity field $\boldsymbol{u} := (u, v, w)$ in Cartesian coordinates (x, y, z) with z as the upward vertical direction. Dropping the tildes and adopting the Darcy–Oberbeck–Boussinesq equations [30] in the infinite Darcy–Prandtl number limit, we arrive at the governing equations:

$$\boldsymbol{u} = -\boldsymbol{\nabla} p + Ra_T (T - R_\rho S)\boldsymbol{e}_z, \tag{2a}$$

$$\boldsymbol{\nabla} \cdot \boldsymbol{u} = 0, \tag{2b}$$

$$\frac{\partial T}{\partial t} + \boldsymbol{u} \cdot \boldsymbol{\nabla} T - w = \nabla^2 T, \tag{2c}$$

$$\varepsilon \frac{\partial S}{\partial t} + \boldsymbol{u} \cdot \boldsymbol{\nabla} S - w = \frac{1}{Le} \nabla^2 S. \tag{2d}$$

Here, the governing non-dimensional parameters include the Rayleigh–Darcy number Ra_T, the density ratio R_ρ, the Lewis number Le and the normalized porosity ε of the porous medium:

$$Ra_T := \frac{g\alpha \Delta T K h}{\kappa_T \nu}, \quad R_\rho := \frac{\beta \Delta S}{\alpha \Delta T}, \quad Le := \frac{\kappa_T}{\kappa_S}, \quad \varepsilon := \frac{\epsilon}{\sigma}, \tag{3}$$

where g is the gravitational acceleration, K is the permeability of the porous medium, ν is the viscosity of the fluid, κ_S is the salinity diffusivity, ϵ is the porosity of the porous medium, and $\boldsymbol{e}_z$ is the unit vector in the vertical direction. In this work, we fix the normalized porosity as $\varepsilon = 1$ and suppose that the top and bottom boundaries are impermeable and maintained at constant temperature and salinity, i.e., that w and the temperature and salinity deviations T and S satisfy

$$w(x, y, z = 0, t) = w(x, y, z = 1, t) \tag{4a}$$

$$= T(x, y, z = 0, t) = T(x, y, z = 1, t) \tag{4b}$$

$$= S(x, y, z = 0, t) = S(x, y, z = 1, t) \tag{4c}$$

$$= 0. \tag{4d}$$

We impose periodic boundary conditions in the horizontal on all variables.

We now formulate the single-mode equations following similar procedure in related problems [1,2,6,12,14]. We decompose the temperature into a horizontally averaged temperature deviation $\bar{T}_0(z, t)$ from the conduction state and a single harmonic in the horizontal direction associated with the wavenumber pair (k_x, k_y) and a complex amplitude $\widehat{T}(z, t)$. The salinity, velocity and pressure are decomposed similarly:

$$\boldsymbol{u}(x, y, z, t) = \bar{\boldsymbol{u}}_0(z, t) + \widehat{\boldsymbol{u}}(z, t)\, e^{\mathrm{i}(k_x x + k_y y)} + c.c., \tag{5a}$$

$$T(x, y, z, t) = \bar{T}_0(z, t) + \widehat{T}(z, t)\, e^{\mathrm{i}(k_x x + k_y y)} + c.c., \tag{5b}$$

$$S(x, y, z, t) = \bar{S}_0(z, t) + \widehat{S}(z, t)\, e^{\mathrm{i}(k_x x + k_y y)} + c.c., \tag{5c}$$

$$p(x, y, z, t) = \bar{p}_0(z, t) + \widehat{p}(z, t)\, e^{\mathrm{i}(k_x x + k_y y)} + c.c., \tag{5d}$$

where *c.c.* indicates a complex conjugate. Equation (5) assumes a horizontal planform in the form of a square ($k_x = k_y$) or a roll ($k_y = 0$), both motivated by the heat-exchanger model (Equation (3.2) from [27]), although more general planforms can be included within the single-mode approach [4,5].

We next substitute (5) into the governing equations (2) and balance the horizontally averaged component and the harmonic components, respectively. Using the boundary conditions in (4) and the momentum equation in (2a), we obtain $\bar{u}_0 = 0$, a major difference from the nonporous case described by Navier–Stokes equations where large-scale shear is allowed and may play an important role [10–12]. We eliminate the horizontally averaged pressure $\partial_z \bar{p}_0 = Ra_T(\bar{T}_0 - R_\rho \bar{S}_0)$ and the harmonic components of the horizontal velocity and pressure using the horizontal momentum equations and the continuity equation:

$$\widehat{u}(z,t) = -\mathrm{i}k_x \widehat{p}(z,t), \;\; \widehat{v}(z,t) = -\mathrm{i}k_y \widehat{p}(z,t), \;\; \widehat{p}(z,t) = -\frac{\partial_z \widehat{w}(z,t)}{k_x^2 + k_y^2}. \tag{6}$$

Dropping all higher-order harmonics, we obtain the desired single-mode equations:

$$\widehat{\nabla}^2 \widehat{w} = \widehat{\nabla}_\perp^2 Ra_T(\widehat{T} - R_\rho \widehat{S}), \tag{7a}$$

$$\frac{\partial \widehat{T}}{\partial t} + \widehat{w}\partial_z \bar{T}_0 - \widehat{w} = \widehat{\nabla}^2 \widehat{T}, \tag{7b}$$

$$\varepsilon \frac{\partial \widehat{S}}{\partial t} + \widehat{w}\partial_z \bar{S}_0 - \widehat{w} = \frac{1}{Le}\widehat{\nabla}^2 \widehat{S}, \tag{7c}$$

$$\frac{\partial \bar{T}_0}{\partial t} + \partial_z(\widehat{w}^* \widehat{T} + \widehat{w}\widehat{T}^*) = \partial_z^2 \bar{T}_0, \tag{7d}$$

$$\varepsilon \frac{\partial \bar{S}_0}{\partial t} + \partial_z(\widehat{w}^* \widehat{S} + \widehat{w}\widehat{S}^*) = \frac{1}{Le}\partial_z^2 \bar{S}_0, \tag{7e}$$

where $\widehat{\nabla}^2 := \partial_z^2 - (k_x^2 + k_y^2)$, $\widehat{\nabla}_\perp^2 := -(k_x^2 + k_y^2)$ and the superscript * denotes a complex conjugate. The corresponding boundary conditions obtained from (4) are:

$$\widehat{w}(z=0,t) = \widehat{w}(z=1,t) \tag{8a}$$

$$= \widehat{T}(z=0,t) = \widehat{T}(z=1,t) = \widehat{S}(z=0,t) = \widehat{S}(z=1,t) \tag{8b}$$

$$= \bar{T}_0(z=0,t) = \bar{T}_0(z=1,t) = \bar{S}_0(z=0,t) = \bar{S}_0(z=1,t) \tag{8c}$$

$$= 0. \tag{8d}$$

The harmonic terms in the single-mode equations in (7a)–(7c) are closely related to the heat exchanger model that is an exact solution in a vertically periodic domain and that describes well the interior of the convecting state in a porous medium [25,27,29]. These harmonic components also resemble the elevator mode that plays an important role in double-diffusive convection; see. e.g., [53–55]. However, the single-mode equations in (7) also apply to a vertically confined domain with the nonperiodic B.C. (8) as well as to the nonlinear interaction between harmonic components and the horizontally averaged modes. As a result, the single-mode equations used here can be understood as an extension of the heat exchanger model to a vertically confined domain with the nonlinear interaction with the horizontally averaged mode included.

In the following, we use the numerical software pde2path [56,57] to compute strongly nonlinear solutions of the single-mode equations in (7) as a function of the system parameters. The vertical direction is discretized using the Chebyshev collocation method with derivatives computed using the Chebyshev differentiation matrix [58] implemented following Uecker [59]. The number of grid points used, including the boundary, is chosen as $N_z = 257$ for the thermal convection results, while all other results use $N_z = 129$. Selected solution profiles of steady convection rolls are validated against the nonlinear boundary value problem (NLBVP) solver in Dedalus [60] with grid points $N_z = 1024$. In order to validate the single-mode equations and associated nonlinear solutions, we reproduce the steady convection rolls of single-mode

equations for RBC [1,2,5] as well as the high wavenumber asymptotic single-mode solutions of RBC (Section 3 in [61]) and convection in a porous medium (Section 3 in [14]). We determine the stability of steady solutions and of traveling waves in a comoving frame from the eigenvalues of the associated Jacobian matrix computed with the `eigs` command focusing on a finite subset of the eigenvalues.

The horizontal translation symmetry in the governing Equation (2) corresponds to the observation that $\widehat{w}$, $\widehat{T}$ and $\widehat{S}$ in (7) multiplied by $e^{i\theta}$ (θ is a constant phase angle) continue to satisfy the equations. The presence of horizontal translation symmetry within the single-mode equations requires a phase condition whenever $k_x \neq 0$ in order to fix the solution phase and obtain a unique solution. The implementation of this condition following Rademacher and Uecker [62] requires the predictor $\boldsymbol{\phi}(z,t)$ from a solution $\boldsymbol{\phi}_{\text{old}}(z,t)$ to be orthogonal to $\mathrm{i}\boldsymbol{\phi}_{\text{old}}(z,t)$:

$$\int_0^1 \mathrm{i}\boldsymbol{\phi}_{\text{old}}(z,t)[\boldsymbol{\phi}(z,t) - \boldsymbol{\phi}_{\text{old}}(z,t)]^* dz = 0, \tag{9}$$

where

$$\boldsymbol{\phi}(z,t) := \left[\widehat{T}(z,t), \widehat{S}(z,t)\right]^{\mathrm{T}}. \tag{10}$$

The horizontally averaged modes are not involved in setting the phase. The vertical velocity $\widehat{w}$ does not need to be involved in (9) because its phase is completely determined by the phase of $\widehat{T}$ and $\widehat{S}$; see Equation (7a).

To compute a steady nonlinear wave traveling in the x direction with speed c, we write Equations (7b)–(7c) in the comoving frame,

$$\frac{\partial \widehat{T}}{\partial t} - \mathrm{i}ck_x\widehat{T} + \widehat{w}\partial_z\bar{T}_0 - \widehat{w} = \widehat{\nabla}^2\widehat{T}, \tag{11a}$$

$$\varepsilon\frac{\partial \widehat{S}}{\partial t} - \mathrm{i}ck_x\varepsilon\widehat{S} + \widehat{w}\partial_z\bar{S}_0 - \widehat{w} = \frac{1}{Le}\widehat{\nabla}^2\widehat{S}, \tag{11b}$$

and set the time derivatives in these equations and in (7d)–(7e) to zero. With the phase condition in (9), the resulting problem has a unique nonlinear eigenvalue c and associated solution profile. Both are updated at each step of the continuation procedure. Steady solutions are associated with $c = 0$.

To compute standing waves, we perform the numerical simulation of single-mode equation using the initial value problem (IVP) solver in Dedalus [60] with the additional assumption that $\widehat{w}$, $\widehat{T}$ and $\widehat{S}$ are real functions. This assumption breaks the horizontal translation symmetry and mimics no-flux boundary conditions in the horizontal. As a result, supercritical but unstable standing waves in a horizontally periodic domain are stabilized, allowing the use of DNS to compute such solutions.

3. Comparisons of Single-Mode Solutions with Direct Numerical Simulations

In this section, we compare the single-mode solutions with DNS for two types of boundary conditions in the horizontal. The first uses periodic boundary conditions [25–28,43,52], and thus the horizontal wavenumber $k_x = 2\pi/L_x$ corresponds to a domain size L_x whenever a single harmonic corresponding to a pair of counter-rotating convection rolls is present. If multiple horizontal modes are present, we use the wavenumber scaling law obtained from DNS data [25,27] as described later. We also compare the single-mode solutions with the corresponding results for an enclosure described by no-flux B.C. in the horizontal, i.e., impermeable boundaries with zero thermal and salinity fluxes corresponding to Neumann boundary conditions (NBC) [39,40,43]. Combining such a no-flux solution with a horizontally reflected solution generates a solution of the periodic B.C. case. Thus, the associated wavenumber is computed as $k_x = n\pi/L_{x,\text{NBC}}$, where n is the number of convection cells in the enclosure and $L_{x,\text{NBC}}$ is the enclosure domain size with no-flux horizontal B.C. Note that traveling wave

solutions are excluded in no-flux cases. We also compare the single-mode solutions with exact 2D steady convection rolls computed by Newton–Kantorovich iteration [26] or reached by DNS [39,40,43]. The exact 2D steady convection rolls obtained by these methods include higher-order harmonics in the horizontal, an effect not included in the single-mode solutions.

3.1. Thermal Convection with Passive Salinity $R_\rho = 0$

In this subsection, we set $R_\rho = 0$, indicating that the salinity is passive, in order to compare the results with thermal convection and transport of a passive scalar in a porous medium without additional contributions to the driving buoyancy term [25–28,39,52]. This subsection first compares the single-mode solutions with DNS results [25–28], as well as exact 2D steady convection rolls [26] and upper bound theory [52], all with periodic boundary conditions in the horizontal. We also compare the single-mode solutions with exact 2D steady convection rolls reached by DNS with no-flux B.C. in the horizontal [39].

Selecting a suitable wavenumber is the main difficulty of applying single-mode solutions [1,4]. Here, we choose $k_y = 0$ to model a 2D flow and the wavenumber scaling $k_x = 0.48 Ra_T^{0.4}$ obtained from the Fourier spectrum at $z = 0.5$ in 2D DNS (Figure 10a in [27]) and (Figure 5 in [29]). For 3D results, we select the wavenumber $k_x = k_y = 0.17 Ra_T^{0.52}$ based on measurement at $z = 0.5$ in 3D DNS (Figure 10a in [27]). These scaling laws represent the best-fit power laws over the range of Ra_T accessible to DNS.

We first compare the harmonic components of single-mode solutions resembling steady convection rolls with the RMS temperature and velocity from DNS. We compute the RMS value over the horizontal direction from steady single-mode convection rolls using

$$T_{\rm rms}(z) = \sqrt{2}|\widehat{T}(z)|, \;\; w_{\rm rms}(z) = \sqrt{2}|\widehat{w}(z)|/Ra_T, \;\; u_{\rm rms}(z) = \sqrt{2}|\widehat{u}(z)|/Ra_T, \tag{12}$$

consistent with the corresponding DNS results [25,27], where the buoyancy velocity scale is employed to normalize velocities. Figure 1 shows that the RMS distribution over the vertical direction z of the single-mode solutions reproduces the qualitative behavior of the RMS values from 3D DNS (Figure 8b in [27]). For example, the temperature RMS values from both the single-mode solutions and the DNS results exhibit a peak near the top and bottom boundaries, and the location of this peak is closer to the boundary at a higher Rayleigh number. The RMS values of both temperature and vertical velocity show a nearly uniform profile in the interior ($z = 0.5$) for both single-mode solutions and DNS results. For the RMS value of the horizontal velocity, the single-mode solutions also reproduce the peak values at the top and bottom boundaries as observed in the DNS. However, the single-mode solutions always predict a zero horizontal velocity RMS in the interior similar to the heat-exchanger model [25,27], although the DNS results indicate a non-zero value.

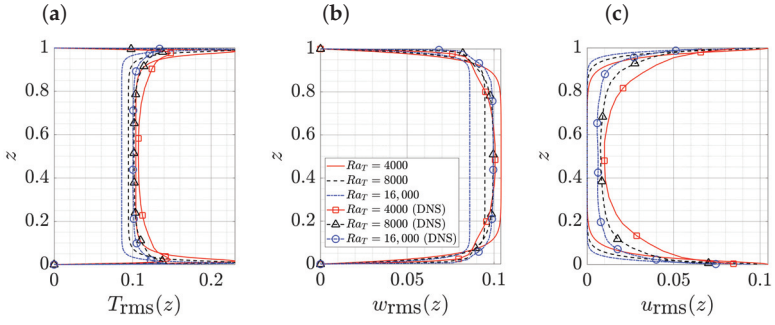

Figure 1. RMS profiles of (**a**) $T_{\rm rms}(z)$, (**b**) $w_{\rm rms}(z)$ and (**c**) $u_{\rm rms}(z)$ at $Ra_T = 4000$, 8000, 16,000 associated with the 3D wavenumber $k_x = k_y = 0.17 Ra_T^{0.52}$ obtained from single-mode solutions (lines) compared with DNS results (Figure 8b in [27]) (lines with markers). Legend for all three panels is provided in panel (**b**).

Figure 2 then compares the mean temperature $1 - z + \bar{T}_0$ obtained from single-mode solutions with DNS results in both 2D (Figure 3a in [25]) and 3D (Figure 7 in [27]) at the corresponding Rayleigh number. Here, we observe that the single-mode solutions accurately reproduce the mean temperature gradient in the interior from DNS, in particular at high Rayleigh numbers. The heat-exchanger model which is an exact solution for unbounded convection in a porous medium was shown to describe well the mean temperature gradient in the interior; see 2D (Equations (3) and (4) in [25]) and 3D (Equation (3.2) in [27]). Considering the single-mode solutions satisfying (7) and making the reasonable assumption $\partial_z^2 \widehat{w}(z = 0.5) = 0$ (cf. Figure 1), we notice that the single-mode solutions reduce to

$$-1 + \partial_z \bar{T}_0(z = 0.5) = -\frac{k_x^2 + k_y^2}{Ra}. \tag{13}$$

The mean temperature gradient in (13) is the same as that within the heat-exchanger model [25,27]. Here, the single-mode solutions also reproduce the trend observed in DNS data [25,27] that the mean temperature gradient is closer to zero (isothermal interiors) at a larger Rayleigh number in 2D results (Figure 2a), but farther from zero in 3D results (Figure 2b), observations based on the assumed wavenumber scaling $k_x \sim Ra_T^{0.4}$ in 2D [25] and $k_x = k_y \sim Ra_T^{0.52}$ in 3D [27]. This wavenumber-Rayleigh-number scaling explains, in conjunction with (13), the different Rayleigh number trends of the interior mean temperature gradient observed in 2D and 3D using single-mode solutions.

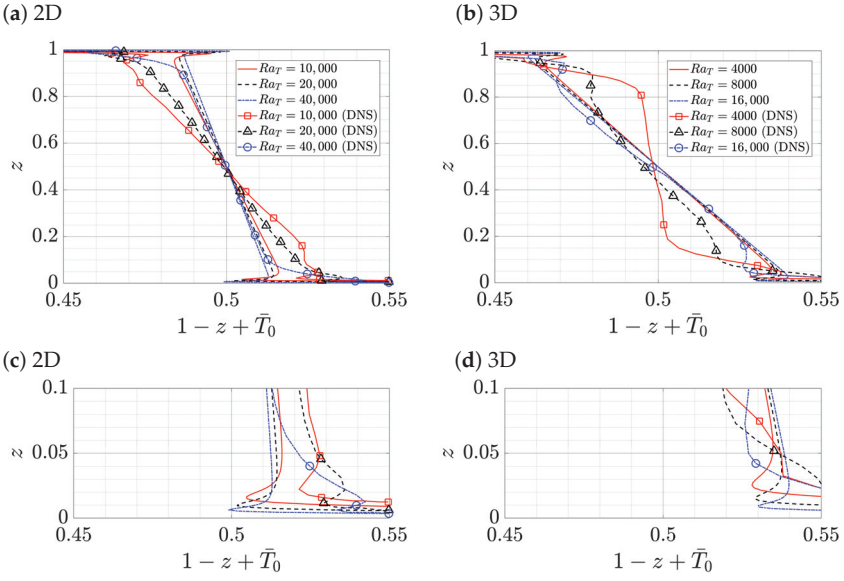

Figure 2. Comparisons of the mean temperature profiles obtained from single-mode solutions (lines) with DNS (lines with markers). Panel (**a**) displays 2D results at $Ra_T = 10,000$, 20,000 and 40,000 using $k_x = 0.48 Ra_T^{0.4}$ and $k_y = 0$ compared with 2D DNS (Figure 3a in [25]). Panel (**b**) shows 3D results at $Ra_T = 4000$, 8000 and 16,000 using $k_x = k_y = 0.17 Ra_T^{0.52}$ compared with 3D DNS (Figure 7 in [27]). Panels (**c**) and (**d**) show zooms of panels (**a**) and (**b**) near the bottom boundary, respectively.

The comparisons presented in Figure 2 also show that the single-mode solutions reproduce the mean temperature overshoot, a thin stably stratified layer near both boundaries. This overshoot appears closer to the boundary at higher Rayleigh numbers, a fact evident in both the single-mode solutions and DNS results; see the zoom near the bottom boundary in Figure 2c,d. Although the precise values of the overshoot temperature in the single-mode solutions are not fully accurate, this observation nonetheless suggests that the single-mode

solutions preserve certain physical mechanisms responsible for this overshot, which is also present in single-mode solutions for RBC [1–3]. In the high Rayleigh number and high wavenumber asymptotic regime of porous media convection, an overshoot near the boundary is also found (Figure 3 in [14]), but is absent in the same asymptotic regime in RBC [13]. Such mixed convective-stably-stratified fluids are extensively studied in penetrative convection (Section 7.3.4 in [63]) using both numerical simulations [64–67] and experiments [67–71]; see the recent review [72].

In Figure 3, we compare the Rayleigh number trend of the RMS values in the interior, at $z = 0.5$, obtained from single-mode solutions with DNS results in both 2D (Figure 3b in [25]) and 3D (Figure 8a in [27]). Evidently, the single-mode theory substantially underestimates $T_{\text{rms}}(z = 0.5)$ and $w_{\text{rms}}(z = 0.5)$ at large Ra_T, which appear to saturate with increasing Ra_T in DNS results, but continue to decrease within single-mode theory, although the latter reproduces the DNS observation that these quantities approach one another at high Ra_T. In fact, the single-mode quantities overlap at large Ra_T, a direct consequence of (7a) and the assumption that $\partial_z^2 \widehat{w}(z = 0.5) = 0$ at high Ra_T, together with (12). However, this relation breaks down at low Rayleigh numbers as shown in both DNS and single-mode solutions. We also examined the profiles of the single-mode solutions at a low Rayleigh number (not shown here), and found that $\widehat{w}$ is no longer uniform in the interior, leading directly to the observed difference between $T_{\text{rms}}(z = 0.5)$ and $w_{\text{rms}}(z = 0.5)$. For high Rayleigh numbers, the DNS results indicate that both $T_{\text{rms}}(z = 0.5)$ and $w_{\text{rms}}(z = 0.5)$ tend to a constant value, which is not observed in the single-mode solutions. Moreover, in single-mode theory $u_{\text{rms}}(z = 0.5)$ remains zero at the Rayleigh numbers reported here, while the DNS data show a non-zero value with a slow decrease to zero as Ra_T increases.

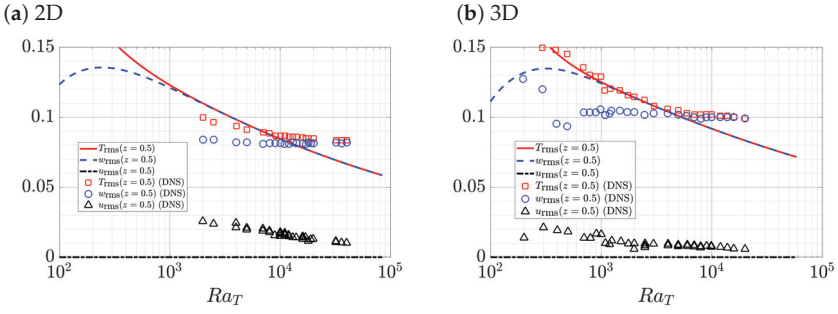

Figure 3. Comparisons of the RMS values at $z = 0.5$ obtained from single-mode solutions (lines) with DNS (markers). Panel (**a**) shows 2D results with DNS data obtained from Figure 3b in [25], while panel (**b**) displays 3D results with DNS data obtained from Figure 8a in [27].

We next analyze the heat transport by computing the Nusselt number

$$Nu := 1 - \langle \partial_z \bar{T}_0(z = 0, t) \rangle_t. \tag{14}$$

where $\langle \cdot \rangle_t$ is the average over time. Figure 4a shows Nu as a function of Ra_T obtained from single-mode solutions with the 2D $k_x = 0.48 Ra_T^{0.4}$ wavenumber scaling compared with 2D DNS data (Figure 2 in [25] and Figure 5b in [26]), exact 2D steady convection rolls (Figure 5b in [26]), and upper bound theory (Figure 5 in [52]). Figure 4b shows the corresponding results with the 3D $k_x = k_y = 0.17 Ra_T^{0.52}$ wavenumber scaling compared with DNS data (Figure 2a in [27] and Table 1 in [28]) and upper bound theory (Figure 5 in [52]). Near onset, $Ra_T \leq 100$, the single-mode solutions deviate from the DNS results because the employed wavenumber scaling based on high Ra_T DNS data may not apply in this regime. Compared with DNS data [25–27], the single-mode solutions overpredict Nu in the small Rayleigh number regime $Ra_T \in [100, 1000]$, but underestimate it in the high Ra_T regime. We also fit Nu over Ra_T for $Ra_T \in [10^3, 8.4 \times 10^4]$ to obtain $Nu \approx 0.154 Ra_T^{0.666}$ for single-mode solutions with the 2D wavenumber scaling. For the 3D results, the Nu scaling

is $Nu \approx 0.108 Ra_T^{0.723}$ for $Ra_T \in [10^3, 5.8 \times 10^4]$. Here, we note that the scaling exponent η of $Nu \sim Ra_T^{\eta}$ is lower than that observed in DNS suggesting $Nu \sim Ra_T$ at high Ra_T [25–28]. Such an inconsistent Nu scaling may result from the underlying single-mode assumption precluding the presence of proto-plumes that emerge near the boundary [25,27] but display a different wavenumber scaling from that employed here (Figure 10 in [27]). The steady-state assumption may also lead to a difference in Nu from DNS results: the exact 2D steady convection rolls involving higher order harmonics computed by Newton–Kantorovich iteration exhibit a scaling law $Nu \sim Ra_T^{0.6}$ [26] that differs from the $Nu \sim Ra_T$ scaling observed in DNS [25–28,52]. Moreover, the secondary Hopf bifurcation of exact 2D steady convection rolls present in DNS leads to secondary boundary modes [26,73–75], but such a secondary bifurcation is absent from the single-mode formulation. However, the Nu scaling obtained from the single-mode solutions remains lower than the upper bound from upper bound theory [52], as shown in Figure 4.

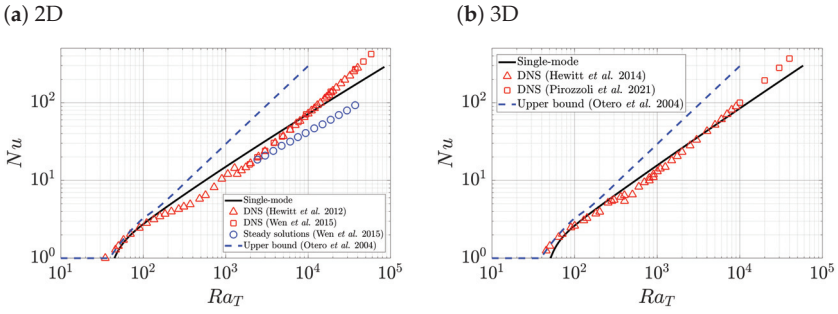

Figure 4. Nu as a function of Ra_T from single-mode solutions (black lines). Panel (**a**) shows 2D results with $k_x = 0.48 Ra_T^{0.4}$, $k_y = 0$ compared with DNS data (Figure 2 in [25] and Figure 5b in [26]), exact 2D steady convection rolls (Figure 5b in [26]), and upper bound theory (Figure 5 in [52]). Panel (**b**) displays 3D results with $k_x = k_y = 0.17 Ra_T^{0.52}$ compared with DNS data (Figure 2a in [27] and Table 1 [28]) as well as upper bound theory (Figure 5 in [52]). The single-mode solutions are stable within this severe truncation.

The Nu scaling obtained from single-mode solutions also depends on the assumed wavenumber, and the single-mode solutions of RBC suggest a suitable wavenumber resulting in Nu close to experimental measurement [5]. Here, we further investigate the wavenumber influence on Nu to identify the parameter regime in which the single-mode solutions provide a valid description of the system, focusing on 2D results ($k_y = 0$). Figure 5 shows Nu for a range of k_x and Ra_T. These values are then compared with the Nu of exact 2D steady convection rolls reached in DNS (Figure 6 and Table 3 in [39]), where the domain size of the enclosure is varied. Note that the enclosure is associated with no-flux horizontal boundary conditions, and thus the associated wavenumber is computed as $k_x = n\pi / L_{x,\mathrm{NBC}}$. In the high wavenumber regime corresponding to a narrow convection cell, the single-mode solutions predict Nu close to the DNS results, but the prediction begins to deviate for larger horizontal domain sizes (smaller k_x). This deviation can be traced to the interaction between different horizontal harmonics present in larger domains that lead to non-sinusoidal solution profiles in the horizontal (Figure 5 in [39]). A similar result is found in salt-finger convection when the corresponding single-mode solutions are compared against DNS results (Figures 2, 6 and 11 in [12]). At lower Ra_T, closer to the onset, the agreement between the single-mode solutions and DNS improves; see Figure 5b, as also found in salt-finger convection (Figure 18 in [12]).

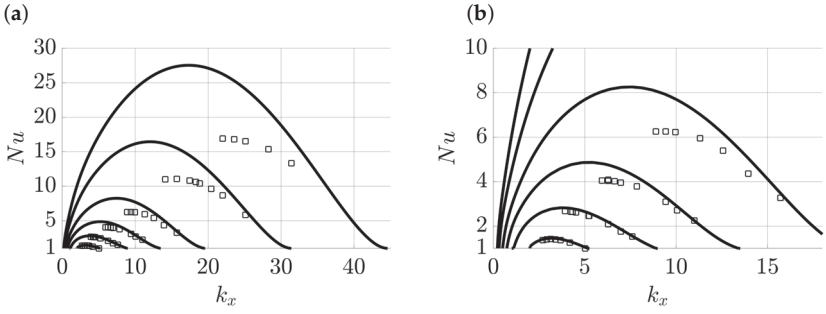

Figure 5. Nu as a function of the horizontal wavenumber k_x for $Ra_T = 50$, 100, 200, 400, 1000 and 2000 (from bottom to top) obtained from single-mode solutions (lines) and compared with DNS results (black squares) with $k_x = n\pi/L_{x,\mathrm{NBC}}$ using n and $L_{x,\mathrm{NBC}}$ appropriate to no-flux horizontal B.C. (Figure 4 and Table 2 in [39]). Panel (**b**) is a zoom of panel (**a**).

Figure 6 shows isocontours of the streamfunction ψ, the total temperature $1 - z + T$ and the total salinity $1 - z + S$. Here, the streamfunction for a two-dimensional flow is constructed as

$$\psi(x, z, t) = \widehat{\psi}(z, t)e^{\mathrm{i}k_x x} + c.c. \text{ with} \tag{15a}$$

$$\widehat{\psi} = \widehat{w}/(\mathrm{i}k_x). \tag{15b}$$

The total temperature and total salinity are both constructed from the single-mode ansatz in (5) and adding the background linear profile as in Equation (1). Figure 6 reproduces the qualitative behavior in the parameter regime of Figure 5 in [39] despite its sinusoidal structure in the horizontal. In fact, the nonsinusoidal nature of the streamfunction of the exact 2D steady convection rolls reached in DNS accounts for the Nu difference between the single-mode equations and DNS shown in Figure 5. The total salinity at the higher Lewis number $Le = 20$ shown in Figure 6d displays a relatively well-mixed interior compared with the corresponding result at $Le = 4$ in Figure 6c, as also found in DNS observations (Figure 5 in [39]).

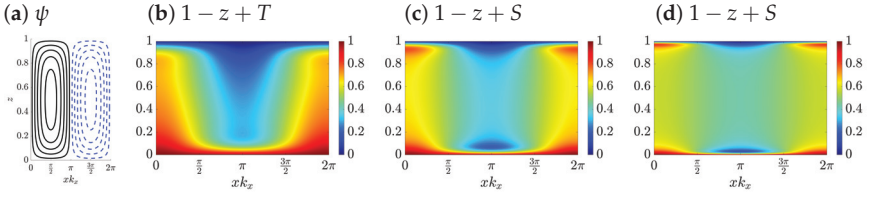

Figure 6. Solution profile of single-mode solutions displaying isocontours of (**a**) streamfunction ψ, (**b**) total temperature $1 - z + T$ and (**c**) total salinity $1 - z + S$ at $Ra_T = 200$, $k_x = 1.89\pi$, and $Le = 4$. Panel (**d**) shows the isocontours of total salinity $1 - z + S$ at $Le = 20$ with other parameters unchanged. This figure is to be compared with the corresponding DNS results (Figure 5 in [39]).

We now turn to the properties of the Sherwood number quantifying salinity transport and defined as

$$Sh := 1 - \langle \partial_z \bar{S}_0(z = 0, t) \rangle_t. \tag{16}$$

Figure 7 shows Sh as a function of Le for passive salinity ($R_\rho = 0$) for a range of Ra_T, compared with the DNS results (Figure 6 and Table 3 in [39]), on the assumption that $k_x = \pi$, 1.25π, 2π, 3π and 5.83π for $Ra_T = 50$, 100, 200, 400 and 1000, respectively, based on the expression $k_x = n\pi/L_{x,\mathrm{NBC}}$ with n and $L_{x,\mathrm{NBC}}$ obtained from [39]. Here, the single-mode solutions predict Sh that overlaps with the DNS results at $Ra_T = 50$ over a wide range

of Le. For high Ra_T and $Le \gtrsim 1$ the single-mode equations over-predict Sh in comparison with the DNS. The single-mode solutions show a scaling law $Sh \sim Le^{\eta}$ with $\eta = 0.52$ for $Ra_T = 50$ and $\eta = 0.51$ for $Ra_T = 100, 200, 400$ and 1000 fitted within $Le \in [10, 100]$. This scaling law is close to the scaling law $Sh \sim Le^{0.5}$ observed in DNS results [39].

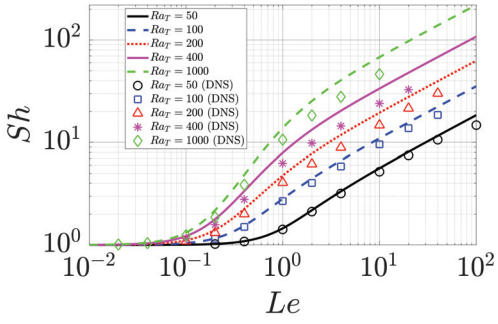

Figure 7. Sh as a function of Le from single-mode solutions (lines) with $R_\rho = 0$ compared with DNS (markers) from Figure 6 and Table 3 in [39]. The horizontal wavenumbers are chosen as $k_x = \pi$, 1.25π, 2π, 3π, 5.83π for $Ra_T = 50$, 100, 200, 400, 1000 based on $k_x = n\pi/L_{x,\mathrm{NBC}}$ with n and $L_{x,\mathrm{NBC}}$ as in [39].

3.2. Double-Diffusive Convection with $R_\rho \neq 0$

In this subsection, we investigate the effect of an active salinity that also contributes to the buoyancy ($R_\rho \neq 0$). Here, $R_\rho > 1$ corresponds to an overall stably stratified (bottom-heavy) configuration. The resulting configuration differs substantially from the passive case $R_\rho = 0$ in that it admits oscillations about the conduction state. This overstable case manifests itself in the presence of a Hopf bifurcation that precedes the steady onset studied in the preceding section. In this subsection we compare the resulting standing waves, traveling waves and steady convection rolls computed from the single-mode equations with the corresponding 2D DNS results using both no-flux and periodic B.C. in the horizontal [40,43].

Figure 8a shows a standing wave (SW) over one oscillation period obtained from a simulation of the single-mode equations with real $[\widehat{w}, \widehat{T}, \widehat{S}]$ in terms of the quantities

$$nu(t) := 1 - \partial_z \bar{T}_0(z = 0, t), \tag{17a}$$

$$sh(t) := 1 - \partial_z \bar{S}_0(z = 0, t), \tag{17b}$$

$$\psi_{\mathrm{mid}}(t) := \max_x \psi(x, z = 0.5, t), \tag{17c}$$

displaying values close to the 2D DNS results with no-flux B.C. in the horizontal (Figure 5 in [43]) as compared in Table 1. The oscillation period from the single-mode equations is $T_p = 1.568$, which is also close to the DNS observation of $T_p = 1.535$ [43], p. 77. Figures 8b,c show isocontours of the streamfunction at the minima and maxima of $\psi_{\mathrm{mid}}(t)$, indicating a complete flow reversal between these instants, in agreement with DNS results (Figure 6 in [43]) and SW observed in related problems [47,76]; the quantities $nu(t)$ and $sh(t)$ are quadratic and so oscillate with half the oscillation period.

Figure 9a shows the bifurcation diagram for the single-mode equations at $Ra_T = 53$, $Le = 5$, $k_x = 2\pi/L_x = \pi$ corresponding to $L_x = 2$. This parameter regime displays traveling waves (TW) in DNS with periodic B.C. in the horizontal at $R_\rho = 0.1$ (Figure 8b in [43]). Here, the single-mode solutions also show a branch of TW (in red) and the TW branch is stable at $R_\rho = 0.1$, consistent with DNS observation [43]. The TW branch loses stability at $R_\rho = 0.0954$ through a secondary Hopf bifurcation prior to its termination on the lower branch of steady convection (in black). Figure 9a shows that both TW and SW bifurcate supercritically from the trivial solution, and that the TW branch displays a larger Nu than the SW branch. This is consistent with the prediction that a stable branch

emerges from a Hopf bifurcation with $O(2)$ symmetry whenever both TW and SW branches bifurcate supercritically and that the larger amplitude branch measured by Nu is then stable [46,48,77].

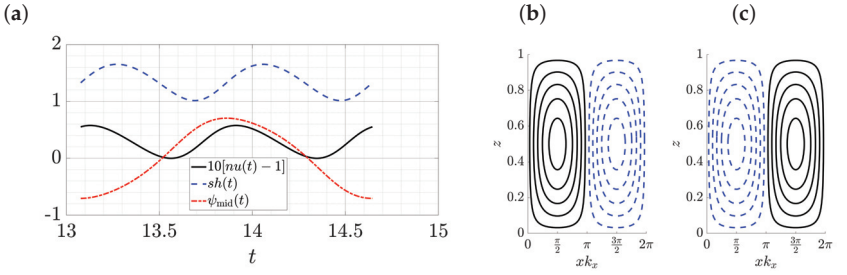

Figure 8. (**a**) One period of a standing wave computed from the single-mode equations at $Ra_T = 55$, $R_\rho = 0.1$, $Le = 5$, $k_x = \pi$ and $k_y = 0$ displaying $10[nu(t) - 1]$, $sh(t)$ and $\psi_{\rm mid}(t)$ as a function of $t \in [13.077, 14.645]$ with oscillation period $T_p = 1.568$. Panels (**b**) and (**c**) show the isocontours of the streamfunction at $t = 13.077$ and $t = 13.861$, respectively. This figure is to be compared with the corresponding DNS results (Figures 5 and 6 in [43]).

Table 1. Comparison of $\max_t \psi_{\rm mid}(t)$, $\max_t nu(t)$, $\max_t sh(t)$ and the oscillation period T_p of standing waves obtained from the single-mode equations and DNS (Figure 5 and p. 77 in [43]) at $Ra_T = 55$, $R_\rho = 0.1$ and $Le = 5$. The single-mode solutions are associated with $k_x = \pi$, $k_y = 0$ while the DNS results [43] are computed with no-flux B.C. in a horizontal domain of size $L_{x,\rm NBC} = \pi/k_x = 1$.

	$\max_t \psi_{mid}(t)$	$\max_t nu(t)$	$\max_t sh(t)$	Period T_p
Standing waves from DNS [43]	0.670	1.052	1.594	1.535
Standing wave from single-mode	0.705	1.058	1.652	1.568

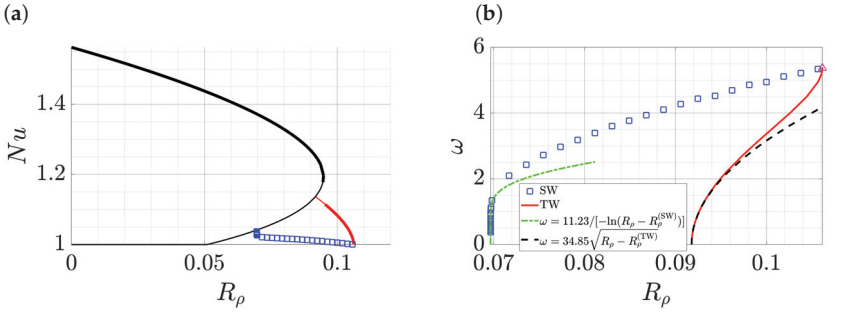

Figure 9. (**a**) Bifurcation diagram of single-mode solutions at $Ra_T = 53$, $Le = 5$, $k_x = \pi$ and $k_y = 0$, showing steady convection rolls (—), SW (□) and TW (—). Thick lines indicate stable solutions and thin lines represent unstable solutions. (**b**) The temporal frequency $\omega = 2\pi/T_p$ of SW (□) and TW (—), the latter computed from $\omega = |c|k_x$. The Hopf frequency is $\omega_{\rm Hopf} = 5.36981$ at the Hopf bifurcation point $R_\rho = 0.10615$ (△) from the trivial solution. Near the termination of the SW branch, the frequency ω decreases to zero at $R_\rho^{(\rm SW)}$ as $\omega \sim 1/[-\ln(R_\rho - R_\rho^{(\rm SW)})]$ (- · -) as predicted theoretically [78]. Near the termination of the TW branch, the phase velocity c of the waves decreases to zero at $R_\rho^{(\rm TW)}$ as $c \sim \sqrt{R_\rho - R_\rho^{(\rm TW)}}$ (– –) as also predicted theoretically [79,80].

Figure 9b displays the oscillation frequency $\omega = 2\pi/T_p$ for both TW and SW. Both start at $\omega_{\rm Hopf} = 5.36981$ at the Hopf bifurcation point $R_\rho = 0.10615$ from the trivial solution, and both decrease to zero with decreasing R_ρ, at which point they terminate on the lower

branch of (unstable) steady rolls. The TW terminate in a local parity-breaking bifurcation at $R_\rho^{(\mathrm{TW})} = 0.0918$ and do so as $\omega \sim \sqrt{R_\rho - R_\rho^{(\mathrm{TW})}}$ [49,79,80] while the SW terminate at $R_\rho^{(\mathrm{SW})} = 0.06966838$ in a global bifurcation and do so as $\omega \sim 1/[-\ln(R_\rho - R_\rho^{(\mathrm{SW})})]$, cf. [48,78]. The resulting bifurcation diagram resembles those found in [47,49,79].

At the slightly different Rayleigh number $Ra_T = 55$, the other parameters being the same ($Le = 5$, $R_\rho = 0.1$, $L_x = 2$), DNS with periodic B.C. in the horizontal instead shows the existence of steady convection rolls (Figure 8a in [43]), while the single-mode solutions also give steady convection rolls, as shown in the top row of Figure 10. For comparison, the bottom row of Figure 10 shows the corresponding solution profiles for the TW at $Ra_T = 53$. Here, both steady convection rolls and traveling waves show streamlines resembling counter-rotating rolls, but the isocontours of the total temperature and total salinity of the traveling waves reveal profiles that are less well-mixed than in steady convection, as also found in DNS (Figure 8 in [43]). The left-right asymmetry of the TW profiles is indicative of propagation.

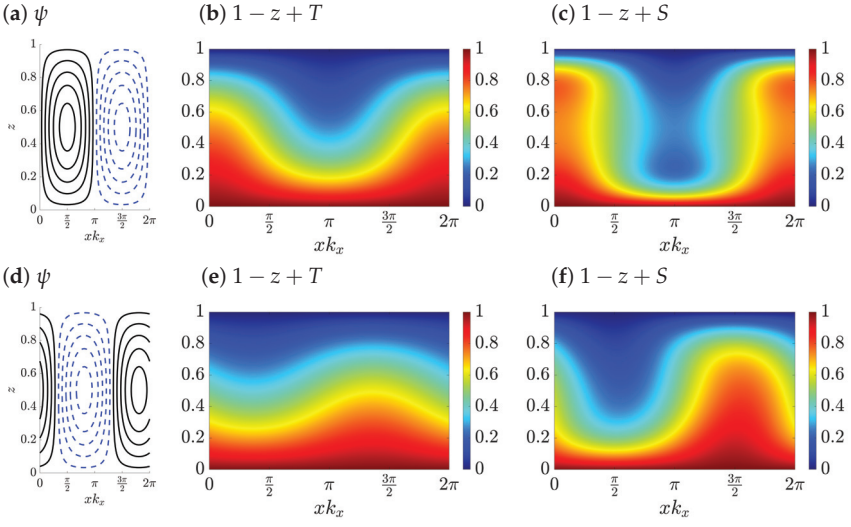

Figure 10. Top: solution profiles for steady convection rolls from the single-mode equations at $Ra_T = 55$ with isocontours of (**a**) streamfunction ψ, (**b**) total temperature $1 - z + T$ and (**c**) total salinity $1 - z + S$. Bottom: solution profiles for a left traveling wave with $c = -1.07$ in the comoving frame from the single-mode equations at $Ra_T = 53$ with isocontours of (**d**) streamfunction ψ, (**e**) total temperature $1 - z + T$ and (**f**) total salinity $1 - z + S$. Other parameters are $R_\rho = 0.1$, $Le = 5$, $k_x = \pi$ and $k_y = 0$ as used in 2D DNS with periodic B.C. in the horizontal and period $L_x = 2\pi/k_x = 2$ (Figure 8 in [43]).

Table 2 further reports the maximum value of streamfunction $\psi_{\max} := \max_{x,\,z,\,t} \psi(x, z, t)$, Nu and Sh of steady convection rolls and traveling waves obtained from single-mode solutions. These values are then compared with the DNS values reported in Figure 8 in [43]. Table 2 also includes the phase speed c of traveling waves obtained from single-mode solutions for comparison with DNS results [43], p. 79. Note that $c = 0$ for steady solutions by definition. The comparison in Table 2 shows that the single-mode solutions quite accurately predict the correct values of $\psi_{\max}$, Nu, Sh and c for both steady convection rolls and traveling waves.

Table 2. Comparison of $\psi_{\max}$, Nu, Sh and c between single-mode solutions and DNS for steady convection rolls at $Ra_T = 55$ and traveling waves at $Ra_T = 53$. Other parameters are $R_\rho = 0.1$, $Le = 5$, $k_x = \pi$ and $k_y = 0$; the DNS results are computed with periodic B.C. in the horizontal with period $L_x = 2\pi/k_x = 2$ (Figure 8 and p. 79 in [43]).

	$\psi_{\max}$	Nu	Sh	c
Steady convection rolls from DNS ($Ra_T = 55$) [43]	1.924	1.371	3.320	0
Steady convection rolls from single-mode ($Ra_T = 55$)	1.812	1.341	3.387	0
Traveling wave from DNS ($Ra_T = 53$) [43]	0.869	1.087	1.865	−1.03
Traveling wave from single-mode ($Ra_T = 53$)	0.848	1.083	1.828	−1.07

Figure 11a shows the bifurcation diagram for $Ra_T = 100$, $Le = 20$, $k_x = \pi$ and $k_y = 0$. Here, the stable TW branch connects to the upper branch of steady convection rolls instead of the lower branch. The connection stabilizes steady rolls for $R_\rho < R_\rho^{(\mathrm{TW})}$. A similar bifurcation diagram with the TW branch terminating at the upper branch was computed for binary fluid convection (Figure 1 in [81]). The transition between the diagrams in Figures 9 and 11 is the result of increasing Ra_T and Le and occurs when the TW termination point $R_\rho^{(\mathrm{TW})}$ passes through the fold on the branch of steady rolls, cf. Figure 3 in [49]. Figure 11a also shows Nu for the unstable SW but these may undergo a fold at lower R_ρ that renders them unstable even with no-flux B.C. Figure 11b displays $\omega = 2\pi/T_p$ for SW and $\omega = |c|k_x$ for TW, both of which start from $\omega_{\mathrm{Hopf}} = 23.40889$ at the Hopf bifurcation point $R_\rho = 0.58548$ from the trivial solution and decrease with decreasing R_ρ. Near $R_\rho^{(\mathrm{TW})} = 0.129$, where the TW branch connects to the upper branch of steady convection rolls, the TW branch once again displays the $c \sim \sqrt{R_\rho - R_\rho^{(\mathrm{TW})}}$ behavior consistent with theoretical analysis [49,79,80].

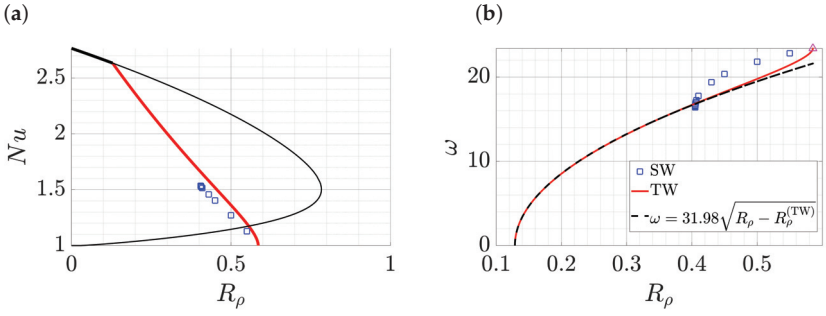

Figure 11. (**a**) Bifurcation diagram of single-mode solutions at $Ra_T = 100$, $Le = 20$, $k_x = \pi$ and $k_y = 0$ showing steady convection rolls (—), SW (□) and TW (—). Thick lines indicate stable solutions and thin lines represent unstable solutions. (**b**) The temporal frequency $\omega = 2\pi/T_p$ of SW (□) and TW (—), the latter computed from $\omega = |c|k_x$. The Hopf frequency is $\omega_{\mathrm{Hopf}} = 23.40889$ at the Hopf bifurcation point $R_\rho = 0.58548$ (△) from the trivial solution. Near the termination of the TW branch the phase velocity c of the waves decreases to zero at $R_\rho^{(\mathrm{TW})}$ as $c \sim \sqrt{R_\rho - R_\rho^{(\mathrm{TW})}}$ (– –) as predicted theoretically [79,80].

Figure 12 shows the solution profile at $R_\rho = 0.4$ for both unstable steady convection rolls and stable traveling waves. Here, the mean temperature of the traveling waves is closer to a linear profile, a fact that is consistent with the lower Nu of traveling waves shown in Figure 11. The isocontours of total temperature and salinity of traveling waves also show profiles that are less well-mixed in the interior than in the corresponding steady convection rolls, cf. Figure 10.

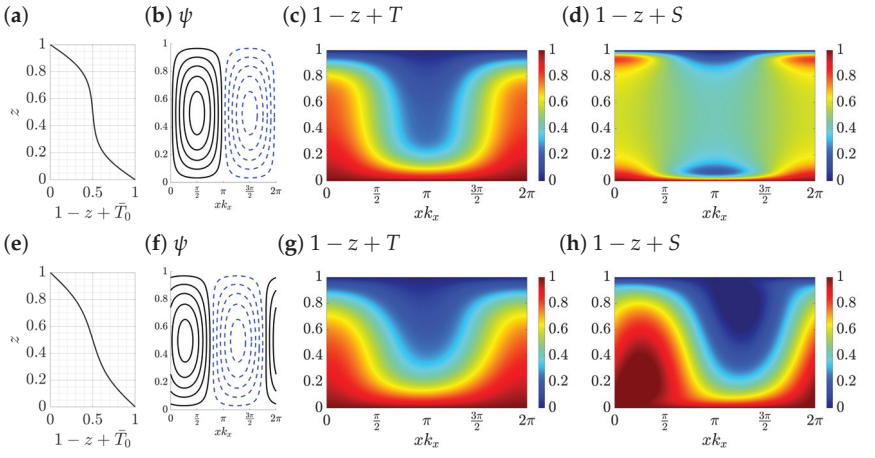

Figure 12. Top: unstable steady convection rolls from single-mode equations showing (**a**) mean temperature $1-z+\bar{T}_0$ and isocontours of (**b**) streamfunction ψ, (**c**) total temperature $1-z+T$ and (**d**) total salinity $1-z+S$. Bottom: stable left traveling wave convection in the comoving frame with phase speed $c=-5.31$ from single-mode equations showing (**e**) mean temperature $1-z+\bar{T}_0$ and isocontours of (**f**) streamfunction ψ, (**g**) total temperature $1-z+T$ and (**h**) total salinity $1-z+S$. The parameters are $Ra_T=100$, $R_\rho=0.4$, $Le=20$, $k_x=\pi$ and $k_y=0$.

Figure 13 shows Sh and Nu for single-mode solutions in the form of steady convection rolls as a function of R_ρ for $Ra_T=100$, 150, 300 and 600 with wavenumbers $k_x=n\pi/L_{x,\mathrm{NBC}}=\pi$, 2π, 2π, and 4π, respectively. We select these wavenumbers based on $L_{x,\mathrm{NBC}}=1$ and the number of convection cells observed in the DNS [40], p. 1266. Here, single-mode solutions also reproduce the qualitative trend observed in DNS (Figure 5 in [40]), namely that Sh and Nu decrease as R_ρ increases, corresponding to a stronger stabilizing effect of the salinity gradient. In particular, the single-mode solutions predict Nu and Sh larger than or equal to those of steady convection rolls reached by DNS for these Ra_T values, similar to the observations in Figures 5 and 7 as well as the comparison in salt-finger convection [12]. Single-mode solutions in the form of steady convection rolls also exist in the stably stratified regime $R_\rho>1$ as a result of diffusivity difference between temperature and salinity. The single-mode solutions fold at $R_\rho=1.665$ when $Ra_T=600$, which is consistent with DNS observation showing that the final state at $R_\rho=3$ is the conduction state (Figure 7 in [40]).

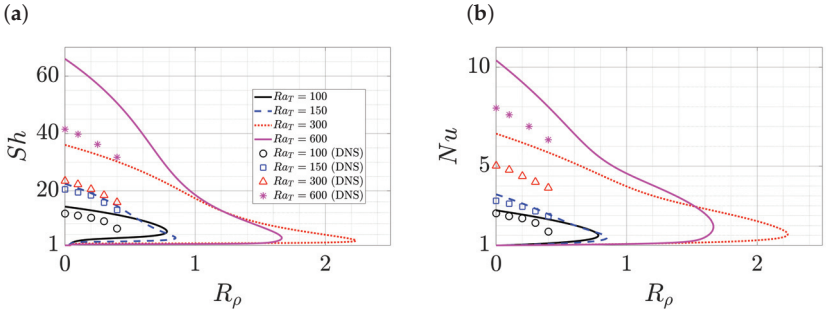

Figure 13. (**a**) Sh and (**b**) Nu, both as a function of R_ρ from the single-mode equations (lines) at $Le=20$, $k_y=0$ and $Ra_T=100$, 150, 300 and 600 with wavenumbers $k_x=n\pi/L_{x,\mathrm{NBC}}=\pi$, 2π, 2π, 4π, respectively, compared with the corresponding DNS results (markers) (Figure 5 in [40]).

Finally, Figure 14 fixes $R_\rho = 0.2$ and presents Sh and Nu as a function of Le. The wavenumber k_x employed for each Ra_T is selected in the same way as in Figure 13 to facilitate direct comparison with the corresponding DNS results (Figure 4 in [40]). We see that for the single-mode solutions $Sh \sim Le^{\eta}$ within $Le \in [10, 100]$ with $\eta = 0.53, 0.56, 0.53$ and 0.54 for $Ra_T = 100$, 150, 300 and 600, respectively. These scaling laws closely follow the trend $Sh \sim Le^{0.5}$ observed in the DNS data [40], although a slight difference exists. The influence of Le on Nu is also relatively smaller compared with Sh, as also found in DNS [40]. Moreover, the plot of Nu as a function of Le within the range $Le \in [10^{-2}, 10^2]$ shows a minimum near $Le \approx 1$ similar to the trend $\psi \sim Le$ at $R_\rho = 0.1$ (Figure 11b in [43]). This is undoubtedly a consequence of the fact that when $Le = 1$ the system ceases to be double-diffusive.

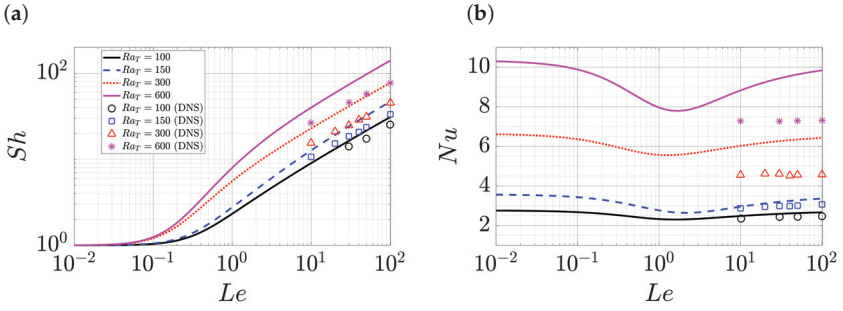

Figure 14. (**a**) Sh and (**b**) Nu, both as a function of Le, from the single-mode equations (lines) at $R_\rho = 0.2$, $k_y = 0$, and $Ra_T = 100$, 150, 300 and 600 and wavenumbers $k_x = n\pi/L_{x,\mathrm{NBC}} = \pi, 2\pi, 2\pi, 4\pi$, respectively, compared with the corresponding DNS results (markers) (Figure 4 in [40]).

4. Conclusions and Future Work

This work employs single-mode equations to analyze both convection and double-diffusive convection in a porous medium where the Darcy law provides large-scale damping. The single-mode equations are obtained from a severely truncated Fourier expansion in the horizontal, but preserve the nonlinear interaction between horizontally averaged mode and a single harmonic mode of the convective state. The single-mode equations fully resolve the vertical direction providing strongly nonlinear solutions. Despite the shortcomings of this approach, we found the single-mode solutions reproduce much of the observed phenomenology identified in high Rayleigh number simulations.

We first considered thermal convection where salinity can be viewed as a passive scalar ($R_\rho = 0$). In this case, convection sets via a steady state bifurcation. The resulting steady convection rolls are well captured by steady solutions of the single-mode equations, which reproduce the qualitative behavior of the RMS profiles (vertical velocity, horizontal velocity and temperature), and the mean temperature profile of the time-dependent state at high Rayleigh numbers, obtained using DNS [25,27]. The single-mode solutions are also consistent with the heat-exchanger model that describes well the mean temperature gradient in the interior [25,27]. The Nu predicted by the single-mode solutions lies below the theoretical upper bound [52] and reveals a scaling law with Rayleigh number close to that followed by exact 2D steady convection rolls [26]. This prediction differs from large aspect ratio DNS results [25–28] where the presence of additional degrees of freedom apparently enhances heat transport but agrees with DNS in small horizontal domains [39] where such degrees of freedom are suppressed.

When the salinity gradient is stabilizing ($R_\rho \neq 0$) the situation is quite different: the system becomes overstable and the conduction state loses stability to oscillations. The resulting traveling and standing waves can still be computed within single-mode theory and both are found to bifurcate supercritically and terminate on the subcritical branch of steady rolls as predicted by theory [78–80]. Of the two competing states, TW and SW, the larger amplitude state as measured by the Nusselt number, is stable, also in agreement with

theoretical prediction [48] and consistent with DNS observations [43]. The *Sh* obtained from single-mode solutions shows a scaling law over *Le* close to DNS observation for both active [40] and passive [39] salinity. The single-mode solutions are derived with the assumption of horizontal periodic boundary conditions, but also show agreement with DNS using no-flux boundary conditions in the horizontal [39,40,43] after mirroring the domain.

The results here suggest the promise of this computationally tractable single-mode approach and open up new directions for future work. For example, single-mode solutions may be further applied to other flow configurations where columnar coherent structures are dominant due to inherent or imposed large-scale damping. The single-mode equations also have the potential to be further improved by systematically including higher-order harmonics in a computationally efficient manner. For example, DNS results show a wavenumber scaling near the boundary different from that in the interior in high Rayleigh number convection [27], directly motivating a "two-mode" reduced-order model. Including higher order harmonics may also suffice to capture the secondary Hopf bifurcation of exact 2D steady convection rolls leading to wall modes [26,73–75], promising further improvement in the predictive power of this approach.

Author Contributions: Conceptualization, methodology, formal analysis, investigation and writing C.L. and E.K.; software, validation and visualization, C.L.; supervision, project administration, and funding acquisition E.K. All authors have read and agreed to the published version of the manuscript.

Funding: This work was supported by the National Science Foundation under Grant No. OCE 2023541.

Institutional Review Board Statement: Not applicable.

Informed Consent Statement: Not applicable.

Data Availability Statement: The data that support the findings of this study are available from the corresponding author upon reasonable request.

Conflicts of Interest: The authors declare no conflict of interest. The funders had no role in the design of the study; in the collection, analyses, or interpretation of data; in the writing of the manuscript; or in the decision to publish the results.

Abbreviations

The following abbreviations are used in this manuscript:

DNS	Direct numerical simulations
RBC	Rayleigh-Bénard convection
ODDC	Oscillatory double-diffusive convection
B.C.	Boundary conditions
NBC	Neumann boundary conditions
CO_2	Carbon dioxide
2D	Two-dimensional
3D	Three-dimensional
c.c.	complex conjugate
RMS	Root mean square
NLBVP	Nonlinear boundary value problem
SW	Standing waves
TW	Traveling waves

References

1. Herring, J.R. Investigation of problems in thermal convection. *J. Atmos. Sci.* **1963**, *20*, 325–338. [CrossRef]
2. Herring, J.R. Investigation of problems in thermal convection: Rigid boundaries. *J. Atmos. Sci.* **1964**, *21*, 277–290. [CrossRef]
3. Elder, J.W. The temporal development of a model of high Rayleigh number convection. *J. Fluid Mech.* **1969**, *35*, 417–437. [CrossRef]
4. Gough, D.O.; Spiegel, E.A.; Toomre, J. Modal equations for cellular convection. *J. Fluid Mech.* **1975**, *68*, 695–719. [CrossRef]
5. Toomre, J.; Gough, D.O.; Spiegel, E.A. Numerical solutions of single-mode convection equations. *J. Fluid Mech.* **1977**, *79*, 1–31. [CrossRef]

6. Gough, D.O.; Toomre, J. Single-mode theory of diffusive layers in thermohaline convection. *J. Fluid Mech.* **1982**, *125*, 75–97. [CrossRef]
7. Turner, J.S. The coupled turbulent transports of salt and and heat across a sharp density interface. *Int. J. Heat Mass Transf.* **1965**, *8*, 759–767. [CrossRef]
8. Crapper, P.F. Measurements across a diffusive interface. *Deep Sea Res. Oceanogr. Abstr.* **1975**, *22*, 537–545. [CrossRef]
9. Marmorino, G.O.; Caldwell, D.R. Heat and salt transport through a diffusive thermohaline interface. *Deep Sea Res. Oceanogr. Abstr.* **1976**, *23*, 59–67. [CrossRef]
10. Paparella, F.; Spiegel, E.A.; Talon, S. Shear and mixing in oscillatory doubly diffusive convection. *Geophys. Astrophys. Fluid Dyn.* **2002**, *96*, 271–289. [CrossRef]
11. Paparella, F.; Spiegel, E.A. Sheared salt fingers: Instability in a truncated system. *Phys. Fluids* **1999**, *11*, 1161–1168. [CrossRef]
12. Liu, C.; Julien, K.; Knobloch, E. Staircase solutions and stability in vertically confined salt-finger convection. *J. Fluid Mech.* **2022**, *952*, A4. [CrossRef]
13. Blennerhassett, P.J.; Bassom, A.P. Nonlinear high-wavenumber Bénard convection. *IMA J. Appl. Math.* **1994**, *52*, 51–77. [CrossRef]
14. Lewis, S.; Rees, D.A.S.; Bassom, A.P. High wavenumber convection in tall porous containers heated from below. *Q. J. Mech. Appl. Math.* **1997**, *50*, 545–563. [CrossRef]
15. Proctor, M.R.E.; Holyer, J.Y. Planform selection in salt fingers. *J. Fluid Mech.* **1986**, *168*, 241–253. [CrossRef]
16. Julien, K.; Knobloch, E. Reduced models for fluid flows with strong constraints. *J. Math. Phys.* **2007**, *48*, 065405. [CrossRef]
17. Taylor, G.I. Motion of solids in fluids when the flow is not irrotational. *Proc. R. Soc. Lond. Ser. A* **1917**, *93*, 99–113.
18. Proudman, J. On the motion of solids in a liquid possessing vorticity. *Proc. R. Soc. Lond. Ser. A* **1916**, *92*, 408–424.
19. Sprague, M.; Julien, K.; Knobloch, E.; Werne, J. Numerical simulation of an asymptotically reduced system for rotationally constrained convection. *J. Fluid Mech.* **2006**, *551*, 141–174. [CrossRef]
20. Grooms, I.; Julien, K.; Weiss, J.B.; Knobloch, E. Model of convective Taylor columns in rotating Rayleigh-Bénard convection. *Phys. Rev. Lett.* **2010**, *104*, 224501. [CrossRef]
21. Calkins, M.A.; Julien, K.; Tobias, S.M.; Aurnou, J.M.; Marti, P. Convection-driven kinematic dynamos at low Rossby and magnetic Prandtl numbers: Single mode solutions. *Phys. Rev. E* **2016**, *93*, 023115. [CrossRef] [PubMed]
22. Calkins, M.A.; Long, L.; Nieves, D.; Julien, K.; Tobias, S.M. Convection-driven kinematic dynamos at low Rossby and magnetic Prandtl numbers. *Phys. Rev. Fluids* **2016**, *1*, 083701. [CrossRef]
23. Yang, Y.; van der Poel, E.P.; Ostilla-Mónico, R.; Sun, C.; Verzicco, R.; Grossmann, S.; Lohse, D. Salinity transfer in bounded double diffusive convection. *J. Fluid Mech.* **2015**, *768*, 476–491. [CrossRef]
24. Xie, J.H.; Julien, K.; Knobloch, E. Jet formation in salt-finger convection: A modified Rayleigh–Bénard problem. *J. Fluid Mech.* **2019**, *858*, 228–263. [CrossRef]
25. Hewitt, D.R.; Neufeld, J.A.; Lister, J.R. Ultimate regime of high Rayleigh number convection in a porous medium. *Phys. Rev. Lett.* **2012**, *108*, 224503. [CrossRef] [PubMed]
26. Wen, B.; Corson, L.T.; Chini, G.P. Structure and stability of steady porous medium convection at large Rayleigh number. *J. Fluid Mech.* **2015**, *772*, 197–224. [CrossRef]
27. Hewitt, D.R.; Neufeld, J.A.; Lister, J.R. High Rayleigh number convection in a three-dimensional porous medium. *J. Fluid Mech.* **2014**, *748*, 879–895. [CrossRef]
28. Pirozzoli, S.; De Paoli, M.; Zonta, F.; Soldati, A. Towards the ultimate regime in Rayleigh–Darcy convection. *J. Fluid Mech.* **2021**, *911*, R4. [CrossRef]
29. Hewitt, D.R. Vigorous convection in porous media. *Proc. R. Soc. A* **2020**, *476*, 20200111. [CrossRef]
30. Nield, D.A.; Bejan, A. *Convection in Porous Media*; Springer: Berlin/Heidelberg, Germany, 2006.
31. Vafai, K. *Handbook of Porous Media*; CRC Press: Boca Raton, FL, USA, 2015.
32. Mojtabi, A.; Charrier-Mojtabi, M.C. Double-diffusive convection in porous media. In *Handbook of Porous Media*; CRC Press: Boca Raton, FL, USA, 2005; pp. 287–338.
33. Cheng, P. Heat transfer in geothermal systems. In *Advances in Heat Transfer*; Elsevier: Amsterdam, The Netherlands, 1979; Volume 14, pp. 1–105.
34. Wooding, R.A.; Tyler, S.W.; White, I. Convection in groundwater below an evaporating salt lake: 1. Onset of instability. *Water Resour. Res.* **1997**, *33*, 1199–1217. [CrossRef]
35. Wooding, R.A.; Tyler, S.W.; White, I.; Anderson, P.A. Convection in groundwater below an evaporating salt lake: 2. Evolution of fingers or plumes. *Water Resour. Res.* **1997**, *33*, 1219–1228. [CrossRef]
36. Huppert, H.E.; Neufeld, J.A. The fluid mechanics of carbon dioxide sequestration. *Annu. Rev. Fluid Mech.* **2014**, *46*, 255–272. [CrossRef]
37. Neufeld, J.A.; Hesse, M.A.; Riaz, A.; Hallworth, M.A.; Tchelepi, H.A.; Huppert, H.E. Convective dissolution of carbon dioxide in saline aquifers. *Geophys. Res. Lett.* **2010**, *37*, L22404. [CrossRef]
38. Caltagirone, J.P. Thermoconvective instabilities in a horizontal porous layer. *J. Fluid Mech.* **1975**, *72*, 269–287. [CrossRef]
39. Trevisan, O.V.; Bejan, A. Mass and heat transfer by high Rayleigh number convection in a porous medium heated from below. *Int. J. Heat Mass Transf.* **1987**, *30*, 2341–2356. [CrossRef]
40. Rosenberg, N.D.; Spera, F.J. Thermohaline convection in a porous medium heated from below. *Int. J. Heat Mass Transf.* **1992**, *35*, 1261–1273. [CrossRef]

41. Goyeau, B.; Songbe, J.P.; Gobin, D. Numerical study of double-diffusive natural convection in a porous cavity using the Darcy-Brinkman formulation. *Int. J. Heat Mass Transf.* **1996**, *39*, 1363–1378. [CrossRef]
42. Mamou, M.; Vasseur, P.; Bilgen, E. Double-diffusive convection instability in a vertical porous enclosure. *J. Fluid Mech.* **1998**, *368*, 263–289. [CrossRef]
43. Mamou, M.; Vasseur, P. Thermosolutal bifurcation phenomena in porous enclosures subject to vertical temperature and concentration gradients. *J. Fluid Mech.* **1999**, *395*, 61–87. [CrossRef]
44. Mahidjiba, A.; Mamou, M.; Vasseur, P. Onset of double-diffusive convection in a rectangular porous cavity subject to mixed boundary conditions. *Int. J. Heat Mass Transf.* **2000**, *43*, 1505–1522. [CrossRef]
45. Bahloul, A.; Boutana, N.; Vasseur, P. Double-diffusive and Soret-induced convection in a shallow horizontal porous layer. *J. Fluid Mech.* **2003**, *491*, 325–352. [CrossRef]
46. Knobloch, E.; Deane, A.E.; Toomre, J.; Moore, D.R. Doubly diffusive waves. *Contemp. Math.* **1986**, *56*, 203–216.
47. Deane, A.E.; Knobloch, E.; Toomre, J. Traveling waves and chaos in thermosolutal convection. *Phys. Rev. A* **1987**, *36*, 2862–2869. [CrossRef] [PubMed]
48. Knobloch, E. Oscillatory convection in binary mixtures. *Phys. Rev. A* **1986**, *34*, 1538–1549. [CrossRef]
49. Knobloch, E.; Moore, D.R. Minimal model of binary fluid convection. *Phys. Rev. A* **1990**, *42*, 4693–4709. [CrossRef]
50. Predtechensky, A.A.; McCormick, W.D.; Swift, J.B.; Rossberg, A.G.; Swinney, H.L. Traveling wave instability in sustained double-diffusive convection. *Phys. Fluids* **1994**, *6*, 3923–3935. [CrossRef]
51. Predtechensky, A.A.; McCormick, W.D.; Swift, J.B.; Noszticzius, Z.; Swinney, H.L. Onset of traveling waves in isothermal double diffusive convection. *Phys. Rev. Lett.* **1994**, *72*, 218–221. [CrossRef]
52. Otero, J.; Dontcheva, L.A.; Johnston, H.; Worthing, R.A.; Kurganov, A.; Petrova, G.; Doering, C.R. High-Rayleigh-number convection in a fluid-saturated porous layer. *J. Fluid Mech.* **2004**, *500*, 263–281. [CrossRef]
53. Stern, M.E. Collective instability of salt fingers. *J. Fluid Mech.* **1969**, *35*, 209–218. [CrossRef]
54. Holyer, J.Y. The stability of long, steady, two-dimensional salt fingers. *J. Fluid Mech.* **1984**, *147*, 169–185. [CrossRef]
55. Radko, T. *Double-Diffusive Convection*; Cambridge University Press: Cambridge, MA, USA, 2013.
56. Uecker, H.; Wetzel, D.; Rademacher, J.D.M. pde2path-A Matlab package for continuation and bifurcation in 2D elliptic systems. *Numer. Math. Theory Methods Appl.* **2014**, *7*, 58–106. [CrossRef]
57. Uecker, H. *Numerical Continuation and Bifurcation in Nonlinear PDEs*; Springer: Berlin/Heidelberg, Germany, 2021.
58. Weideman, J.A.; Reddy, S.C. A MATLAB differentiation matrix suite. *ACM Trans. Math. Software* **2000**, *26*, 465–519. [CrossRef]
59. Uecker, H. pde2path without Finite Elements. 2021. Available online: http://www.staff.uni-oldenburg.de/hannes.uecker/pde2path/tuts/modtut.pdf (accessed on 12 December 2021).
60. Burns, K.J.; Vasil, G.M.; Oishi, J.S.; Lecoanet, D.; Brown, B.P. Dedalus: A flexible framework for numerical simulations with spectral methods. *Phys. Rev. Res.* **2020**, *2*, 023068. [CrossRef]
61. Bassom, A.P.; Zhang, K. Strongly nonlinear convection cells in a rapidly rotating fluid layer. *Geophys. Astrophys. Fluid Dyn.* **1994**, *76*, 223–238. [CrossRef]
62. Rademacher, J.D.M.; Uecker, H. Symmetries, Freezing, and Hopf Bifurcations of Traveling Waves in pde2path. 2017. Available online: https://www.staff.uni-oldenburg.de/hannes.uecker/pde2path/tuts/symtut.pdf (accessed on 15 December 2021).
63. Turner, J.S. *Buoyancy Effects in Fluids*; Cambridge University Press: Cambridge, UK, 1979.
64. Lecoanet, D.; Le Bars, M.; Burns, K.J.; Vasil, G.M.; Brown, B.P.; Quataert, E.; Oishi, J.S. Numerical simulations of internal wave generation by convection in water. *Phys. Rev. E* **2015**, *91*, 063016. [CrossRef]
65. Lecoanet, D.; Quataert, E. Internal gravity wave excitation by turbulent convection. *Mon. Not. R. Astron. Soc.* **2013**, *430*, 2363–2376. [CrossRef]
66. Lecoanet, D.; Schwab, J.; Quataert, E.; Bildsten, L.; Timmes, F.X.; Burns, K.J.; Vasil, G.M.; Oishi, J.S.; Brown, B.P. Turbulent chemical diffusion in convectively bounded carbon flames. *Astrophys. J.* **2016**, *832*, 71. [CrossRef]
67. Couston, L.A.; Lecoanet, D.; Favier, B.; Le Bars, M. Dynamics of mixed convective–stably-stratified fluids. *Phys. Rev. Fluids* **2017**, *2*, 094804. [CrossRef]
68. Le Bars, M.; Lecoanet, D.; Perrard, S.; Ribeiro, A.; Rodet, L.; Aurnou, J.M.; Le Gal, P. Experimental study of internal wave generation by convection in water. *Fluid Dyn. Res.* **2015**, *47*, 045502. [CrossRef]
69. Couston, L.A.; Lecoanet, D.; Favier, B.; Le Bars, M. The energy flux spectrum of internal waves generated by turbulent convection. *J. Fluid Mech.* **2018**, *854*, R3. [CrossRef]
70. Bouffard, M.; Favier, B.; Lecoanet, D.; Le Bars, M. Internal gravity waves in a stratified layer atop a convecting liquid core in a non-rotating spherical shell. *Geophys. J. Int.* **2022**, *228*, 337–354. [CrossRef]
71. Léard, P.; Favier, B.; Le Gal, P.; Le Bars, M. Coupled convection and internal gravity waves excited in water around its density maximum at 4° C. *Phys. Rev. Fluids* **2020**, *5*, 024801. [CrossRef]
72. Le Bars, M.; Couston, L.A.; Favier, B.; Léard, P.; Lecoanet, D.; Le Gal, P. Fluid dynamics of a mixed convective/stably stratified system—A review of some recent works. *Comptes Rendus. Phys.* **2020**, *21*, 151–164. [CrossRef]
73. Aidun, C.K.; Steen, P.H. Transition to oscillatory convective heat transfer in a fluid-saturated porous medium. *J. Thermophys. Heat Transf.* **1987**, *1*, 268–273. [CrossRef]
74. Graham, M.D.; Steen, P.H. Plume formation and resonant bifurcations in porous-media convection. *J. Fluid Mech.* **1994**, *272*, 67–90. [CrossRef]

75. Graham, M.D.; Steen, P.H. Strongly interacting travelling waves and quasiperiodic dynamics in porous medium convection. *Phys. D* **1992**, *54*, 331–350. [CrossRef]
76. Julien, K.; Knobloch, E. Fully nonlinear oscillatory convection in a rotating layer. *Phys. Fluids* **1997**, *9*, 1906–1913. [CrossRef]
77. Knobloch, E.; Silber, M. Travelling wave convection in a rotating layer. *Geophys. Astrophys. Fluid Dyn.* **1990**, *51*, 195–209. [CrossRef]
78. Knobloch, E.; Proctor, M.R.E. Nonlinear periodic convection in double-diffusive systems. *J. Fluid Mech.* **1981**, *108*, 291–316. [CrossRef]
79. Dangelmayr, G.; Knobloch, E. The Takens-Bogdanov bifurcation with O(2)-symmetry. *Philos. Trans. R. Soc. Lond. Ser. A* **1987**, *322*, 243–279.
80. Greene, J.M.; Kim, J.S. The steady states of the Kuramoto-Sivashinsky equation. *Phys. D* **1988**, *33*, 99–120. [CrossRef]
81. Batiste, O.; Knobloch, E.; Alonso, A.; Mercader, I. Spatially localized binary-fluid convection. *J. Fluid Mech.* **2006**, *560*, 149–158. [CrossRef]

fluids

MDPI

Article

Blade Drag Resistance in Windage Operating of Low Pressure Steam Turbines

Antonio Mambro [1], Francesco Congiu [1], Enzo Galloni [2,*] and Davide Lanni [2,*]

[1] GE Power, 5400 Baden, Switzerland
[2] Department of Civil and Mechanical Engineering, University of Cassino, 03043 Cassino, Italy
* Correspondence: galloni@unicas.it (E.G.); davide.lanni@unicas.it (D.L.)

Abstract: On the basis of previous experimental and numerical studies, the windage operation of low-pressure turbine rear stage is investigated. The state of the steam within the rotor channel was correlated to measurements carried out downstream of the blades for different ventilation regimes. Considering very-low-volume flow conditions, the ventilation power was related to the drag force acting on the moving blades. A correlation was identified between the drag coefficient and a Reynolds number relative to the reverse flow height. This correlation can be used in order to predict the power loss of a last-stage moving blade operating at low load.

Keywords: steam turbine; low load operation; ventilation power; drag resistance; Reynolds number

1. Introduction

It is generally recognized that, during low-load operation, steam-turbine rear stages may absorb power from the turbine shaft leading to the so-called "ventilation phenomenon". The absorbed power is converted into heat [1], increasing the temperature of the ventilating stages. The resulting flow and blade-metal temperatures depend on the operational conditions, such as inlet mass flow and temperature, and condenser pressure, and some geometrical parameters such as blade height and pitch-to-chord ratio [2].

Despite this phenomenon having been studied since 1970 [3–5], its importance was mainly confined to the start-up and shut-down of the unit.

Today, with the growing role of renewables energy in the electricity market, steam turbine power plants operate more frequently at a low load [6,7].

Ventilation losses are generated by flow separation and the formation of recirculation zones in the last-stage moving blades [8].

Flow separation starts in correspondence of the blade hub, causing a limited separation in the diffuser cone, as described by Sauchev et al. [9]. There are two different zones that can be identified at the trailing edge of the last-stage moving blades (LSMBs): a reverse-flow region and a through-flow region (Figure 1) [8]. The separated region initially does not have any significant effect on the net power produced by the LSMB. As soon as the volumetric flow reduces, the recirculating region increases, and the reverse flow height increases accordingly [10]. The steam flow starts to be centrifugated in the radial direction, leading to an increase in negative power and flow temperature in correspondence of the tip region of the moving blade. As soon as the dimension of the through-flow region reduces, the net power associated with the last-stage blades decreases accordingly, as reported by Shnee et al. [5]. There is a point where the net power of the last-stage blades becomes negative, producing heat that leads to an increase in flow and blade metal temperatures [11].

Citation: Mambro, A.; Congiu, F.; Galloni, E.; Lanni, D. Blade Drag Resistance in Windage Operating of Low Pressure Steam Turbines. *Fluids* **2022**, *7*, 372. https://doi.org/10.3390/fluids7120372

Academic Editors: Mehrdad Massoudi and Markus Klein

Received: 21 October 2022
Accepted: 2 December 2022
Published: 4 December 2022

Publisher's Note: MDPI stays neutral with regard to jurisdictional claims in published maps and institutional affiliations.

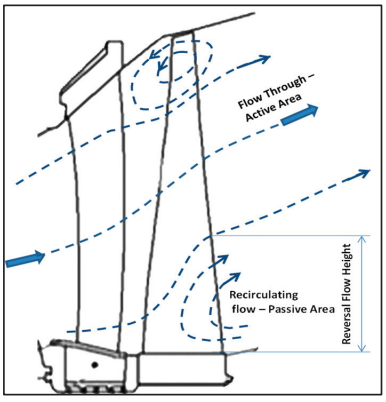

Figure 1. Schematic representation of flow-reversal phenomenon [12].

The capability of accurately assessing the ventilation power and the resulting temperature rise is a key aspect in today's energy market. It enables power plants to:

- Define and operate at the lowest admissible volumetric flow. This has a direct impact on the fixed and variable costs. Fixed costs are related to the potential modifications of the existing steam generator to allow for continuous low-load operation, and in defining the size of any potential auxiliary boiler that can run only when a low load is required [13].
- Run continuously at a low load to avoid cycling operation, which usually has an impact on the lifetime of key mechanical components such as turbine shafts, economizers, and reheater and superheater tubes.
- Optimize hood sprays, minimizing the risk of trailing edge erosion. A cooling system based on water sprays is installed at the low-pressure turbine exhaust. A temperature sensor is installed within the flow path to provide the signal for the automatic start and control of the spray-water quantity. The sizing of the nozzle sprays and the amount of sprayed water must be related to the ventilation power: if the ventilation power is underestimated, there would not be enough water to cool down the exhaust and the LSMB. The unit may trip for high temperature. If the ventilation power is overestimated, the resulting hood sprays are oversized. The injected water does not evaporate because not enough heat is produced by the ventilation power experienced by the LSMB. The droplets sprayed in the exhaust are dragged by the recirculating flow, eroding the trailing edge of the LSMB. This contributes to the degradation of the LSMB performance over the time, and could lead to the generation and propagation of cracks at the trailing edge of the last moving blades. This issue can be critical for blades characterized by high dynamic stresses in correspondence of the root or for moving blades produced from materials that have low fracture toughness such as titanium. Therefore, even when using hood spays, it is very important to assess the ventilation power in the most accurate way. In addition, hood sprays have no effect on the penultimate stages [14].
- Place the expansion line of the low-pressure turbine in the superheated region to avoid water droplet erosion.

In previous works, the authors investigated in depth the windage phenomenon, characterizing it and introducing several useful correlations for turbine design [14,15]. In [16], different ventilation regimes were identified. In particular, for very-low-flow coefficients, the separated flow occupies most of the rotor channel. In this condition, the blade moves in a stagnant fluid, dissipating power because of the drag resistance. The aim of the present paper is to correlate the drag force intensity to the thermofluidic dynamic conditions of the flow by introducing a characteristic drag coefficient. Such a relationship

can be useful in developing models able to predict the operational conditions of turbines running at a very low load.

Some details of both the plots and the mathematical relationships cannot be shown for confidentiality reasons.

2. Experimental and Numerical Methods

In previous works, the low-load phenomenon has been investigated in detail through both experimental and numerical analyses.

Below is shown only a brief summary of the experimental and numerical campaigns carried out. Please refer to the references for more details and insights.

2.1. Experimental Setup

The experimental approach was widely described in [14]. Low-volume tests were carried out in a scaled model steam turbine, which was the same as that described by Megerle in [17]. The maximal output power generated by the steam turbine was between 6 and 8 MW, depending on the condenser pressure and the size of the last-stage blades.

The steam turbine is characterized by four stages (two front stages and two rear stages) and a radial diffuser, which is about 1/3 of the full size. Its configuration and equipment allow for performing detailed measurements relative to the ventilation power absorbed by the penultimate and last stages. Temperature, pressure, and velocity measurements along the blade span were taken on the different planes of CS52, CS61, and CS62, and at the different circumferential locations of S05, S06 and S07 (Figure 2).

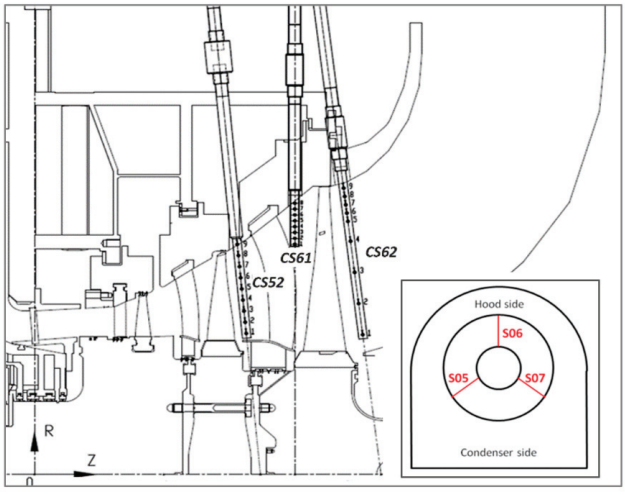

Figure 2. Detailed view of the model steam turbine rear stages and rake temperature measurements [18].

Pressure and velocity measurements were performed with a conventional pneumatic probe or using a dynamic pressure sensor. Temperature measurements were taken with thermocouples of type K installed on a rake. The thermocouples on rake CS62 were not regularly located: the radial pitch in the tip region was rather small in order to ensure the measurement of the maximal flow temperature [12].

2.2. Numerical Setup

The numerical setup was extensively described in previous works, for example, in [12,19]. Briefly, 3D calculations were performed by means of the ANSYS CFX code. The ensemble averaged Navier–Stokes equations coupled to the energy equation and the SST turbulence model were solved by means of an implicit element-based finite-volume formulation. A

streamline curvature correction was also considered in order to overcome some drawbacks due to the eddy viscosity approach.

Steam properties were calculated on the basis of the IAPWS-97 steam table [20].

The whole scaled turbine and the exhaust box were modelled in ANSYS ICEM-CFD and ANSYS Turbogrid, with the front stages as a single pitch, and the rear stages as a full annulus.

By means of the multiple-mixing-plane approach [21], each stage was modelled with 4 sectors, as shown in Figure 3, discretizing in each of them a single stator and a rotor blade.

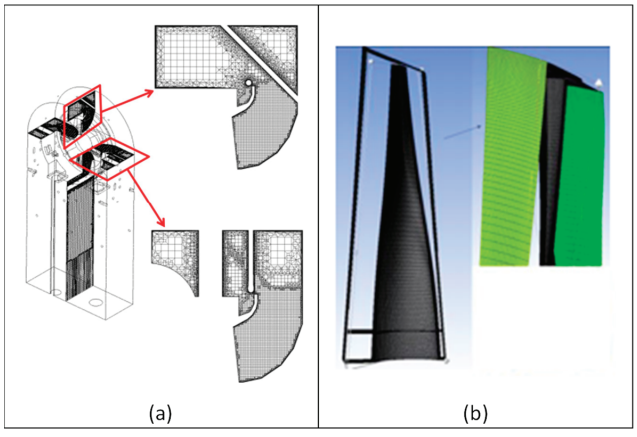

Figure 3. Grid details. (**a**) Multiple mixing plane at the interface between the LSMB and the diffuser and (**b**) last-stage moving blade discretization [19].

As the authors in [12] showed, the CFD model is able to reproduce windage phenomena in the turbine rear stages well. For example, the maximal temperature difference between measurements and calculations was about 10 °C for each considered test case, while the reverse flow height was always well-predicted.

3. Results

3.1. Low-Load Tests

Different sets of rear stages were tested with different thermodynamic boundary conditions and rotational speed levels.

All tests were performed below 10% of the steam turbine nominal load. Therefore, the resulting thermodynamic state of the steam at the last-stage blade outlet was superheated for all the test cases, as reported by Mambro et al. [15].

A summary of the different last-stage blade layout is reported in Table 1, while Table 2 shows some details of the rear stage that are analyzed in this paper [17]. In particular, the low-load test cases reported in Table 3 are considered.

Table 1. Experimental setup of low-pressure turbine rear stages and diffuser.

Full-Size Exhaust Area/Reference Exhaust Area	Free Tip	Snubber	Pitch/Chord (Midsection)
1.6	x	Yes	0.703
1.3	x	Yes	0.703
1.0	x	Yes	0.703
1.1	x	Yes	0.6653
1.0	x	Yes	0.784
1.0	x	no	0.784

Table 2. Main last-stage design parameters for the reference exhaust area.

Last Stage Blades	
Full-size exhaust area/reference exhaust area	1.0
Pitch-to-chord ratio (midsection)	0.784
Hub-to-tip ratio LSMB	0.45
Tip-clearance/moving-blade height ratio (%)	0.8
Part span connection	yes

Table 3. Summary of some representative test cases.

Test Case	Mass Flow (% of Maximal Design Value)	Inlet Temperature (T/T_{ref})	Condenser Pressure (p/p_{ref})	Flow Coefficient (ϕ)
1	5	1.05	1.8	0.022
2	5	1.03	1.25	0.045
3	8	1.13	1.15	0.071
4	8	1.15	1.05	0.09
5	11	1.23	1	0.12

Referring to Table 3, the flow coefficient is defined as:

$$\phi = \frac{C_{ax}}{U_{av}} \tag{1}$$

where C_{ax} is the average axial velocity at the exhaust, and U_{av} is the blade rotational velocity calculates at the midsection. The reference temperature T_{ref} is the minimal tested steam turbine inlet temperature. The reference pressure p_{ref} is the minimal tested condenser pressure.

3.2. Experimental and Numerical Results

Figure 4 shows the distribution of measured axial velocities downstream of the LSMB. They were derived from the direct measurement of the absolute velocity and the rotational speed on the measurement plane. Conventionally, the crossing point between the velocity distribution and the zero axial velocity determines the so-called reverse-flow height [15]. Figure 4 also shows that the reverse-flow height increased when the flow coefficient decreased.

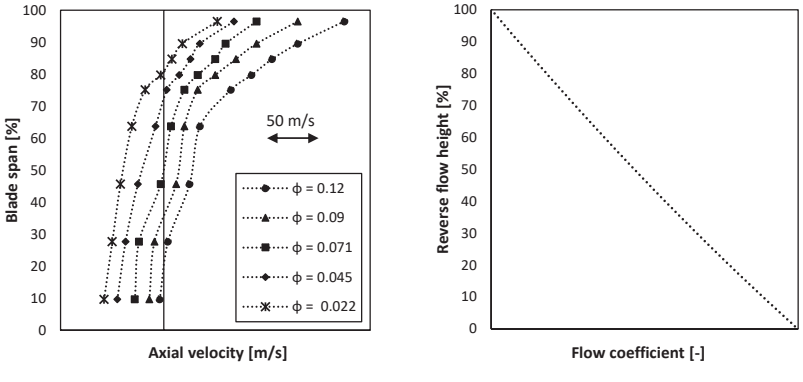

Figure 4. Distribution of the axial velocity along the blade span. (**left**) Mean values on CS62 plane; (**right**) mean reverse flow height. Axial velocity and flow coefficient values are not shown for confidentiality reasons.

The extension of the reverse-flow height also influenced the temperature field, as shown in Figure 5. The measured temperature distribution shifted towards higher values as soon as the flow coefficient decreased. For each test case, as per usual for low-volume-flow operation, the maximal temperature was reached in the upper part of the blade.

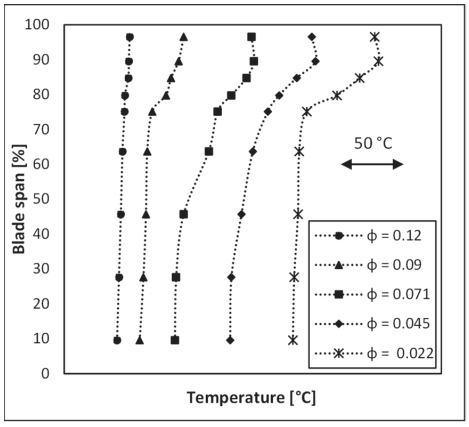

Figure 5. Measured temperature downstream of the LSMB. Temperature values are not shown for confidentiality reasons.

The CFD analyses carried out in [15,16,19] better clarify the experimental results (Figure 6). According to the characteristic ventilation regimes identified in [16], the first two test cases fell within the highest ventilation zone where the recirculating flow downstream of the LSMB was predominant compared to the through-flow area (Zone A). Test Case 3 was characterized by a significant reverse-flow area, but it was still comparable to the active area; the LSMB ventilated, and the overall net power was negative (zone B). Test Cases 4 and 5 fell within the transitional region where the flow started to separate to the hub. The recirculating flow region was negligible; thus, the overall net power produced by the LSMB was positive even though rather small (Zone C).

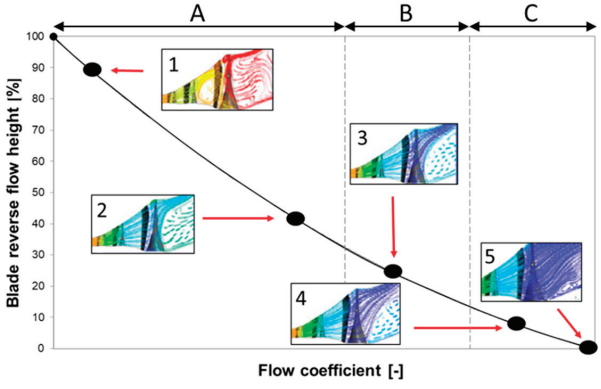

Figure 6. Schematic representation of the variation in blade reverse-flow height for different flow coefficients. (**1**–**5**) show the flow field for the different test cases [16].

When the flow separated to the hub, the recirculating fluid was pushed along the blade span by the centrifugal action. The blade rotated in a stagnant fluid and was subjected to a resistant force that delivered power to the fluid; this power (i.e., the ventilation power) was converted into heat. The extension of the reverse-flow height influenced the ventilation power produced by the blades and the amount of generated heat. The flow coefficient was smaller, and the reverse-flow height and generated heat were larger.

Maximal temperatures were reached at the tip of the blade where the centrifugal action that compressed the fluid against the machine casing was maximal, as shown in

Figure 7. A secondary vortex tended to form at the tip of the blade; however, this secondary recirculation area was much smaller than the main recirculation area.

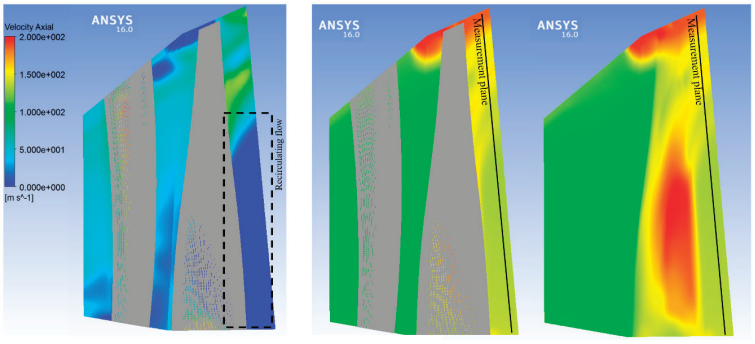

Figure 7. Test Case 2—calculated axial velocity and flow temperature field.

At the blade tip, numerical results also show that the axial velocity field pushed the fluid towards the measurement rake placed downstream of the LSMB. Then, the temperature transducers grasped the maximal temperatures reached in the blade channel.

At the hub, instead, the axial velocities were equal to or less than zero. The measurement rake detected the fluid temperature coming from the exhaust, which was significantly smaller than that inside the blade channel.

However, the radial distribution of the temperature within the majority of the reverse-flow height could be assumed to be uniform both in the blade channel and downstream of the trailing edge, where the measurement rake was located.

Referring to the reverse flow region, Figure 8 shows the difference between the mean temperature calculated into the blade channel and the measured one downstream the blade. For high-enough flow coefficients, there was still a steam expansion between the rotor channel and downstream of the blade (Zone C, Figure 6). The more the flow coefficient reduced, the more the stagnant fluid remaining into the blade channel was compressed, increasing the steam temperature, as shown in Figure 7.

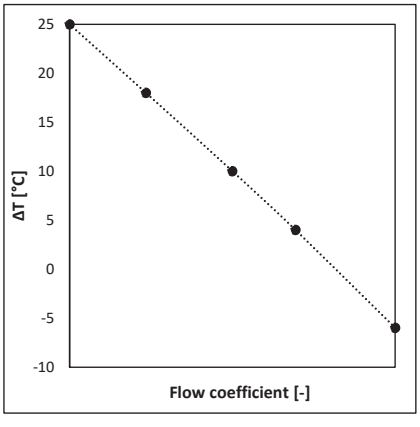

Figure 8. Difference in temperature between calculated data within the blade channel and measurements downstream of the blade. Flow coefficient values are not shown for confidentiality reasons.

The trend shown in Figure 8 is of key importance to build up a transfer function that allows for the assessment of the flow temperature in the reverse-flow region inside the blade

channel where the ventilation phenomena occur from the measured temperature in the exhaust via the rake. This difference depends on the flow coefficient via a linear function.

This correlation can be useful in estimating the properties of steam recirculating within the moving blade channel, starting from data measured downstream of the trailing edge.

Drag Coefficient Estimation

At windage operation, the LSMB delivers work to the steam. This power can be expressed as:

$$P = P_v - P_a \tag{2}$$

where P_v is the power dissipated to move the blade through the stagnant fluid, while P_a is the power that the steam flow delivers to the blades moving through the active area.

For very-low-volume flows, such as for test cases within Zone A, P_a could be neglected, i.e., the measured ventilation power could be considered to be significantly predominant compared to the active power.

Following this approach, the ventilation power due to viscous drag on a blade rotating at rotational speed ω is given by:

$$P_v = \omega RF \tag{3}$$

where F is the frictional force on the blade in the reverse-flow height; R is the radius of the pressure center, approximated to be equal to the mean radius of the reverse-flow height.

The frictional force can be calculated according to Equation (4):

$$F = C_D AK \tag{4}$$

where C_D is a drag coefficient, K is the kinetic energy per volume unit, and A is the characteristic area that is the wetted airfoil area. This is calculated as the airfoil perimeter at the midsection of the reverse-flow height multiplied by the latter, as shown in Figure 9.

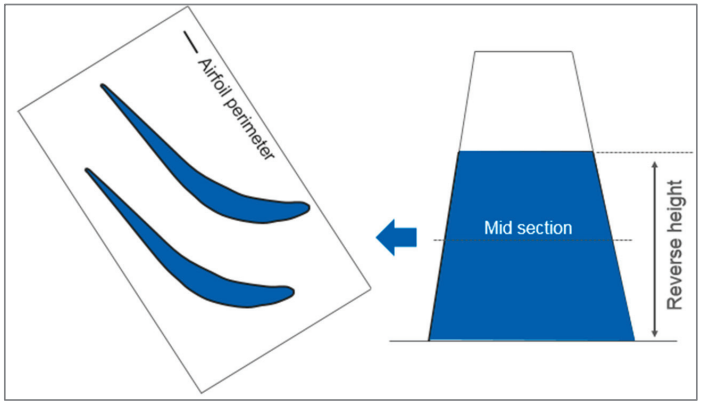

Figure 9. Schematic representation of the airfoil perimeter at the midsection and reverse-flow height.

K is calculated according to Equation (5):

$$K = 0.5\rho U_{rev}^2 , \tag{5}$$

where

$$U_{rev} = \omega R \tag{6}$$

is the average rotational speed of the blade in the reverse flow area, while ρ is the mean steam density in the reverse-flow height.

Lastly, starting from the measured data, the drag coefficient could be calculated according to Equation (7):

$$C_D = \frac{P_v}{0.5 A \rho U_{rev}^3} \tag{7}$$

A relationship between the drag coefficient and a Reynolds number was identified for the last-stage blades of different sizes, pitch-to-chord ratios, and rotational speed levels, as shown in Figure 10, which shows the results relative to a wide range of mass flows, inlet temperatures, and condenser pressures always running the LSMB in windage conditions (i.e., the LSMB always delivering work to the fluid).

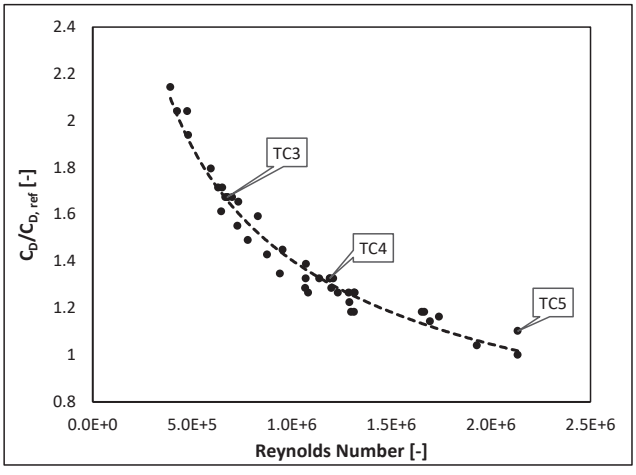

Figure 10. Calculated drag coefficient vs. Reynolds number for different steam turbine last-stage blades—values per blade. $C_{D,ref}$ is the minimal drag coefficient found.

The Reynolds number was related to the reverse-flow height according to Equation (8):

$$Re_{RFH} = \frac{U_{rev} D_{rev}}{\upsilon} \tag{8}$$

where D_{rev} is the outer diameter of the reverse-flow height, and υ is the mean value of the kinematic viscosity of the steam recirculating in this region.

The kinematic viscosity (Equation (8)) and steam density (Equation (5)) were calculated from the condenser pressure and the flow temperature in the reverse-flow height.

The condenser pressure could be used with good approximation because there was practically no pressure recovery in the turbine exhaust due to the separated flow coming from the rear-stage turbine.

According to the measurements and CFD calculations, the flow temperature could also be assumed to be rather uniform in the LSMB channel. This temperature was estimated by correcting the temperature measured downstream of the stage by means of the relationship shown in Figure 8.

As highlighted by the markers relative to Test Cases 3–5, Re_{RFH} increased with the RFH; thus, extreme windage regimes are characterized by the highest values of Re_{RFH}.

Figure 10 also highlights a clear link between the drag coefficient and the Reynolds number for cases in which the recirculation area does not affect the whole blade span (Test Case 3).

This link can be expressed according to Equation (9), for which a coefficient of determination equal to 0.97 was found.

$$C_D = \alpha \cdot Re_{RFH}^{\beta} \tag{9}$$

4. Conclusions

The results presented in this paper are useful in further understanding the behavior of low-pressure turbines operating in windage conditions. In particular, the found relationships can be useful in assessing the ventilation power that the last moving blade delivers to the fluid.

Temperature data measured downstream of the blade were correlated to the mean temperature of the recirculating steam within the blade channel. For high ventilation regimes, this allows for calculating the drag force opposite to the blade motion and the relative blade drag coefficient. A large number of experimental tests prove that this drag coefficient is well-correlated to a Reynolds number defined for the reverse blade height. This good correlation was found not just for extreme windage conditions, but also for each operating condition in which the turbine delivers mechanical power to the steam.

Author Contributions: Conceptualization, A.M., F.C. and E.G.; methodology, A.M. and F.C.; formal analysis, A.M., F.C., E.G. and D.L.; investigation, A.M.; data curation, A.M., F.C., E.G. and D.L.; writing—original draft preparation, A.M., F.C., E.G. and D.L.; writing—review and editing, A.M., E.G. and D.L.; supervision, F.C. and E.G. All authors have read and agreed to the published version of the manuscript.

Funding: This research received no external funding.

Data Availability Statement: Not applicable.

Conflicts of Interest: The authors declare no conflict of interest.

Nomenclature

A	Characteristic area
C_{ax}	Axial velocity
C_D	Drag coefficient
$C_{D,ref}$	Reference drag coefficient
CFD	Computational fluid dynamics
D_{rev}	Outer diameter of the reverse flow height
F	Frictional force on the blade in the reverse flow height
K	Kinetic energy per volume unit
LSMB	Last-stage moving blades
P	Power delivered to the steam by the LSMB at windage operation
P_a	Active power
P_v	Ventilation power
R	Mean radius of reverse flow height
Re_{RFH}	Reynolds number calculated as: $RE_{RFH} = \frac{U_{rev} D_{rev}}{\upsilon}$
RFH	Reverse flow height
T	Inlet temperature
TC	Test case
T_{ref}	Reference temperature
U_{av}	Average circumferential velocity of the blade
U_{rev}	Average rotational speed of the blade in the reverse flow area
α, β	Constant values
υ	Mean value of the kinematic viscosity of the steam recirculating in the reverse flow area
p	Condenser pressure
p_{ref}	Reference pressure
ρ	Mean steam density in the reverse flow height
ϕ	Flow coefficient calculated as: $\phi = \frac{C_{ax}}{U_{av}}$
ω	Rotational speed

References

1. Sigg, R.; Heinz, C.; Casey, M.; Sürken, N. Numerical and experimental investigation of a low-pressure steam turbine during windage. *Proc. Inst. Mech. En.g Part A J. Power Energy* **2009**, *223*, 697–708. [CrossRef]
2. Beevers, A.; Havakechian, S.; Megerle, B. On the Prediction and Theory of the Temperature Increase of Low Pressure Last Stage Moving Blades During Low Volume Flow Conditions, and Limiting it Through Steam Extraction Methods. *J. Turbomach.* **2015**, *137*, 101002. [CrossRef]
3. Neuimin, V.P. Ventilation process in a stage of an axial turbomachine. *Energomashinostronie* **1982**, *11*, 7–12.
4. Lagun, V.; Simoyu, L.; Frumin, Y.Z.; Povolots, L.; Sukharev, F. Distinguishing features of operation of lpc last stages at low loads and under no-load conditions. *Therm. Eng.* **1971**, *18*, 30.
5. Shnee, Y.; Ponomarev, V.; Bystritskii, L. An experimental investigation of partial operating conditions of turbine stages. *Energomashinostroenie* **1977**, *11*, 10–14.
6. Brouwer, A.S.; van den Broek, M.; Seebregts, A.; Faaij, A. Operational flexibility and economics of power plants in future low-carbon power systems. *Appl. Energy* **2015**, *156*, 107–128. [CrossRef]
7. Eser, P.; Singh, A.; Chokani, N.; Abhari, R.S. Effect of increased renewables generation on operation of thermal power plants. *Appl. Energy* **2016**, *164*, 723–732. [CrossRef]
8. Steltz, W.G. An approach to resolving the very low flow in low pressure steam turbines. In *Proceedings of the 1999 International Joint Power Generation Conference*; American Society of Mechanical Engineers: Burlingame, CA, USA, 1999; Volume 2.
9. Sauchev, I.; Neuimin, V.; Zhuchenko, L. Flow separation at blade root in axial flow turbines. *Energomashinostroenie* **1979**, *3*, 9–12.
10. Basirico, J.; Zhou, B.; Mujezinovic, A.; Starodubtsev, Y.; Frolov, B. Testing of Full Speed No Load Operating Conditions in a Subscale Steam Turbine Test Vehicle. In Proceedings of the ASME 2011 Turbo Expo: Turbine Technical Conference and Exposition, Vancouver, BC, Canada, 6–10 June 2011; American Society of Mechanical Engineers: Vancouver, BC, Canada, 2011; pp. 2455–2461. [CrossRef]
11. Filippenko, V.; Frolov, B.; Chernobrovkin, A.; Zhou, B.; Mujezinović, A.; Slepski, J. Analyses of temperature distribution on steam turbine last stage low pressure buckets at low flow operations. In Proceedings of the ASME 2011 Turbo Expo: Turbine Technical Conference and Exposition, Vancouver, BC, Canada, 6–10 June 2011; American Society of Mechanical Engineers: Burlingame, CA, USA, 2011; pp. 2463–2469. [CrossRef]
12. Mambro, A.; Congiu, F.; Galloni, E. Influence of the snubber on temperature distribution at last stage blade exit of a steam turbine during low volume flow operations. *Appl. Therm. Eng.* **2019**, *150*, 937–952. [CrossRef]
13. Mambro, A.; Congiu, F.; Piraccini, F. Application of GE Low Load Package on an Existing District Heating Power Plant: A Case Study. In Proceedings of the ASME 2020 Power Conference collocated with the 2020 International Conference on Nuclear Engineering, Virtual, 4–5 August 2020; American Society of Mechanical Engineers: Burlingame, CA, USA, 2020; Volume 83747, p. V001T09A003.
14. Mambro, A.; Congiu, F.; Galloni, E.; Canale, L. Experimental study and modelling of the ventilation power and maximum temperature of low-pressure steam turbine last stages at low load. *Appl. Energy* **2019**, *241*, 59–72. [CrossRef]
15. Mambro, A.; Galloni, E.; Congiu, F.; Maraone, N. Modelling of low-pressure steam turbines operating at very low flowrates: A multiblock approach. *Appl. Therm. Eng.* **2019**, *158*, 113782. [CrossRef]
16. Mambro, A.; Congiu, F.; Galloni, E. Influence of stage design parameters on ventilation power produced by steam turbine last stage blades during low load operation. *Therm. Sci. Eng. Prog.* **2022**, *28*, 101054. [CrossRef]
17. Megerle, B. Unsteady Aerodynamics of Low Pressure Steam Turbines Operating under Low Volume Flow Conditions. Ph.D. Thesis, Ècole Polytechnicque Fédérale de Lauseanne, Lausanne, Switzerland, 2014.
18. Mambro, A.; Galloni, E.; Congiu, F. Assessment of the heat transfer coefficient for the prediction of ventilation power in steam turbine last stages operating at low load. *Therm. Sci. Eng. Prog.* **2020**, *18*, 100542. [CrossRef]
19. Mambro, A.; Congiu, F.; Galloni, E. CFD Modelling of Steam Turbine Last Stage Blades at Low Load Using Multiple Mixing Plane Approach. In *Turbo Expo: Power for Land, Sea, and Air*; American Society of Mechanical Engineers: Burlingame, CA, USA, 2020; p. V009T23A012.
20. Cooper, J.R.; Dooley, R.B. *Revised Release on the IAPWS Industrial Formulation 1997 for the Thermodynamic Properties of Water and Steam*; The International Association for the Properties of Water and Steam: Lucerne, Switzerland, 2007.
21. Stein, P.; Pfoster, C.; Sell, M.; Galpin, P.; Hansen, T. Cfd modeling of low pressure steam turbine radial diffuser flow by using a novel multiple mixing plane based coupling: Simulation and validation. In *Turbo Expo: Power for Land, Sea, and Air*; American Society of Mechanical Engineers: Burlingame, CA, USA, 2015; Volume 56796, p. V008T26A020.

fluids

MDPI

Article

Mass Transport in Membrane Systems: Flow Regime Identification by Fourier Analysis

Stefan Heinz [1,*], Jakob Heinz [2] and Jonathan A. Brant [3]

[1] Department of Mathematics and Statistics, University of Wyoming, 1000 East University Avenue, Laramie, WY 82071, USA
[2] Department of Biomedical Engineering, Johns Hopkins University, 3400 N. Charles St., Baltimore, MD 21218, USA
[3] Department of Civil & Architectural Engineering, University of Wyoming, 1000 East University Avenue, Laramie, WY 82071, USA
* Correspondence: heinz@uwyo.edu

Abstract: The numerical calculation of local mass distributions in membrane systems by computational fluid dynamics (CFD) offers indispensable benefits. However, the concept to calculate such distributions in response to separate variations of operation conditions (OCs) makes it difficult to address overall, flow-physics-related questions, which require the consideration of the collective interaction of OCs. It is shown that such understanding-related relationships can be obtained by the analytical solution of the advection–diffusion equation considered. A Fourier series model (FSM) is presented, which provides exact solutions of an advection–diffusion equation for a wide range of OCs. On this basis, a new zeroth-order model is developed, which is very simple and as accurate as the complete FSM for all conditions of practical relevance. Advection-dominated blocked and diffusion-dominated unblocked flow regimes are identified (depending on a Péclet number which compares the flow geometry with a length scale imposed by the flow), which implies relevant requirements for the use of lab results for pilot- and full-scale applications. Analyses reveal the equivalence of variations of OCs, which offers a variety of options to accomplish desired flow regime changes.

Keywords: membrane; mass transport; flow regimes

Citation: Heinz, S.; Heinz, J.; Brant, J.A. Mass Transport in Membrane Systems: Flow Regime Identification by Fourier Analysis. *Fluids* **2022**, *7*, 369. https://doi.org/10.3390/fluids7120369

Academic Editor: Mehrdad Massoudi

Received: 10 October 2022
Accepted: 11 November 2022
Published: 30 November 2022

Publisher's Note: MDPI stays neutral with regard to jurisdictional claims in published maps and institutional affiliations.

1. Introduction

Computational studies of membrane systems as illustrated in Figure 1 enable very valuable insight into the effectiveness of performance measures, e.g., with respect to concentration polarization and fouling [1–11], as well as evaluating flow unsteadiness induced by different spacer configurations [12–28]. Such computational insights are invaluable given the experimental challenges associated with directly quantifying such phenomena. In one recent study, Liang et al. [29] used two-dimensional (2D) computational fluid dynamics (CFD; the use of this term refers here to the numerical solution of partial differential equations) simulations to resolve the roles played by bulk flow and slip velocities at a membrane surface for generating shear forces at the membrane surface. From this work, it was determined that the origin of shear induction was less important when compared with the resonant frequency of the perturbations themselves for increasing flux through the disruption of foulant and concentration polarization boundary layers. Similarly valuable insights into improving the hydrodynamic conditions within spiral wound membrane elements were made by Foo et al. [30]. Using CFD, these researchers identified optimum spacer geometries for enhancing water flux (up to a 40% flux enhancement) through a membrane through maximizing unsteady-state shear forces at a membrane surface. Reaching this outcome, as is the case in other similar studies, required computationally intensive evaluations of the hydrodynamic environments within the membrane flow channels. Re-

gardless of the complexities involved, the impacts that such studies have on improving the performance and energy efficiency of membrane processes is obvious.

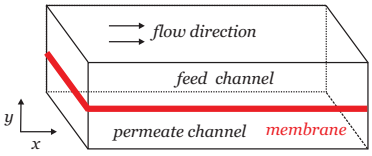

Figure 1. Membrane system illustration.

Despite the indispensable benefits of CFD, the use of such numerical investigation methods is non-trivial, time-consuming, dependent on the availability of numerical codes, and affected by the numerical schemes applied [31–39]. For example, the influence of Péclet numbers (see Equation (6)) has consequences for the equation type considered and the numerical solution of these equations. The equation shows a parabolic (hyperbolic) behavior if the Péclet number is small (large). The numerical solution of such equations becomes increasingly difficult as the Péclet number increases due to the onset of spurious oscillations or excessive numerical damping if standard finite difference or finite element formulations are used [40]. A particular problem is the usual application of Reynolds-averaged Navier–Stokes (RANS) equations. If spacers are involved, separated flow will appear (recirculation zones), and RANS equations are known to not have the capability to deal with such flow features (the latter requires the use of rather sophisticated, partially resolving flow simulation methods [41–48]). On top of knowledge about detailed mass distributions in membrane systems for specific operation conditions OCs provided by CFD, knowledge of specific flow regimes (which may have desired or undesired characteristics) is very helpful for the membrane system design process. Diffusion–advection processes are characterized by diffusion-dominated and advection-dominated flow regimes, which are separated by corresponding Péclet numbers [40,49]: when this number is small (large), then diffusion (advection) dominates. However, there is a large variety of Péclet numbers that can be considered [50], there are often fuzzy criteria for characterizing different flow regimes (such as Péclet numbers larger or smaller than unity), and the practical consequences of such regime separations are not always obvious. So, there are questions regarding the membrane system design (see also Figure 2):

Q1. What determines the existence of qualitatively different mass transport regimes? Which interplay of geometry and OCs is implied, which matters to upscaling?
Q2. How is it possible to accomplish desired flow regime changes by equivalent variations of OCs?
Q3. For different flow regimes, how is it possible to understand the overall mass transport through membranes and characteristic mass distribution features?

The CFD approach often provides an inappropriate basis to address these questions: separate parameter variations hardly allow conclusions about collective parameter effects.

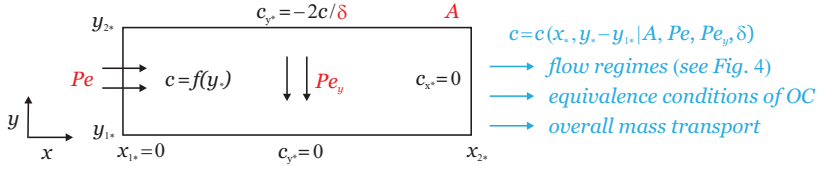

Figure 2. An illustration of the flow configuration considered and flow physics questions addressed (in blue). Operation condition parameters are given in red. Partial derivatives ($c_{x*}$and c_{y*}) are indicated here by subscripts.

In addition to CFD, the use of analytical simulation methods is beneficial because of several reasons. Their use hardly depends on the availability of codes. They are by orders of magnitude more efficient than the numerical integration of partial differential equations in time because of the independence of discretizations and the need to honor numerical stability criteria under significant model parameter variations. Such analytical simulation methods can be used for the verification of numerical solvers because they provide exact results (i.e., independent evidence is not needed to support them). However, first of all, the availability of such models offers the chance to address questions about basic mass transport mechanisms, e.g., regarding the questions Q1–Q3 presented above.

One question related to the use of analytical simulation methods is about their required complexity and simplicity of using them. For the case considered, analytical simulation methods are given by Fourier series representations, there is the question of whether the complexity of such Fourier series representations can be significantly reduced to enhance the clarity of conclusions. Another question related to analytical simulation methods is that their development requires the neglect of effects of spacers, which modify basic flow characteristics implied by geometry, inflow and boundary conditions. The specification of spacer effects on the basic flow configuration varies in the literature [30,51,52]. There are indications that spacers can produce higher fluxes of about 30–40% compared with cases without spacers [30,51,52]. This means analytical simulation methods can be expected to provide valuable guidelines for the characterization of basic flow features, even under conditions where spacers and other effects (flow unsteadiness) are involved. Thus, there are questions in addition to Q1–Q3 considered above:

Q4. What is the most simple analytical model which still enables accurate calculations equivalent to complete Fourier series solutions?

Q5. Given the required approximate representation of the flow field, which arguments support the use of analytical simulation methods under more complex flow conditions?

Analytical solutions obtained by Laplace transforms were presented for a variety of problems, for example, in regard to turbulent dispersion of air pollution [53] and diffusion of oxygen into the blood [54], but no corresponding solutions were presented in regard to membrane systems. The corresponding value of analytical simulation methods is demonstrated here by addressing the questions Q1–Q5 presented above. Fourier analysis is applied for the derivation of analytical results, which offers (via the analysis of eigenvalue regimes) essential new insight. The model development is presented in Section 2 in conjunction with the consideration of questions about the model evaluation and computational aspects. Model applications are reported in Section 3 by focusing on the influence of OCs on species concentration distributions. Section 4 deals with conclusions about the questions considered.

2. Model Development

2.1. Equation Considered

Incompressible flow and a 2D domain are considered, see the illustration in Figure 2. The velocity field is approximated by assuming constant velocities U and V in the x and y directions, which is a requirement to obtain analytical solutions. The suitability of this assumption is considered in Section 4, conclusion #5, in conjunction with mass transport properties. A mixture (e.g., an oil-in-water emulsion) of a continuous phase (e.g., water) and a dispersed phase (e.g., oil at low concentrations) is considered. The solutions presented below are not specific to oil-in-water emulsions, they can be applied to many other systems. According to refs. [7,10,55], the dispersed phase transport equations in the feed/permeate region and membrane region (see Figure 1), respectively, read

$$\frac{\partial c}{\partial t} + U\frac{\partial c}{\partial x} + V\frac{\partial c}{\partial y} = D_M\Big(\frac{\partial^2 c}{\partial x^2} + \frac{\partial^2 c}{\partial y^2}\Big), \qquad \frac{\partial \epsilon_p c}{\partial t} + U\frac{\partial c}{\partial x} + V\frac{\partial c}{\partial y} = D_c\Big(\frac{\partial^2 c}{\partial x^2} + \frac{\partial^2 c}{\partial y^2}\Big). \quad (1)$$

Here, c refers to the dispersed phase concentration, t is time, D_M refers to the molecular diffusion (of oil in water), D_c refers to the capillary diffusion, and ϵ_p is the membrane

porosity. The constant diffusivities D_M and D_c are considered in consistency with the consideration of constant velocities U and V. Diffusion in x direction (which is sometimes neglected) is included. No attempt is made to differentiate between the velocities U and V involved in Equation (1) because these equations are covered by one equation in the following, in particular, the advection–diffusion equation of the membrane region,

$$\frac{\partial c}{\partial t} + \hat{U}\frac{\partial c}{\partial x} + \hat{V}\frac{\partial c}{\partial y} = \hat{D}_c\Big(\frac{\partial^2 c}{\partial x^2} + \frac{\partial^2 c}{\partial y^2}\Big). \tag{2}$$

Here, $\hat{U} = U/\epsilon_p$, $\hat{V} = V/\epsilon_p$, and $\hat{D}_c = D_c/\epsilon_p$ are introduced. The solution obtained can be easily applied as a solution to the feed/permeate region equation by a corresponding adjustment of model parameters (by setting $\epsilon_p = 1$ and replacing D_c by D_M). The domain considered is $0 \le x \le x_2$ and $y_1 \le y \le y_2$; see the illustration in Figure 2. By involving imposed functions $g(x, y)$ and $f(y)$, the initial distribution and x boundary conditions (BCs) at $x = x_1 = 0$ and $x = x_2$ are given by

$$c(x, y, 0) = g(x, y), \quad c(0, y, t) = f(y), \quad \frac{\partial c}{\partial x}(x_2, y, t) = 0. \tag{3}$$

The latter condition applies to the case that diffusion in x direction is included. The y BCs at $y = y_1$ and $y = y_2$ are given by

$$\frac{\partial c}{\partial y}(x, y_1, t) = 0, \qquad c(x, y_2, t)\hat{V}/\delta + \hat{D}_c\frac{\partial c}{\partial y}(x, y_2, t) = 0. \tag{4}$$

The y BCs modify a constant mass transfer (zero gradient) along y by the condition at y_2, which leads to an accumulation of the dispersed phase in the membrane region; see the discussion in the beginning of Section 3. The parameter δ introduced here enables variations of the mass transfer at y_2; Equation (A2) in the Appendix A shows that $2/\delta$ represents the standardized membrane permeability. The introduction of δ is relevant to the identification of the critical Péclet number $Pe_c = 4/(2 + \delta)$ in Section 3.1. The measurement of δ is addressed in Section 3.2. Implications of these BCs may be well seen in figures below (although the effects may be small, see the distributions along x_*).

An important property of the solution $c(x, y, t)$ is its boundedness: if the initial and boundary values of $c(x, y, t)$ lie within a minimum and maximum, $c_{min} \le c \le c_{max}$, then all $c(x, y, t)$ values are bounded by this range [56]. The consideration of an advection–diffusion equation for the dispersed phase is equivalent to the consideration of a stochastic particle model for this phase (a random model for the positions of oil droplets, a Brownian motion model originally applied to describe the motion of pollen grains in water) where the mass concentration represents a non-normalized probability density function (PDF) [57]: the concentration has all the properties of a PDF except that it is not normalized.

It is helpful to introduce normalized variables: $x_* = \hat{U}x/(2\hat{D}_c)$, $y_* = \hat{V}y/(2\hat{D}_c)$, and $t_* = \hat{V}^2 t/(4\hat{D}_c)$. By using these normalized variables, Equation (2) reads

$$\frac{\partial c}{\partial t_*} + 2\frac{U^2}{V^2}\frac{\partial c}{\partial x_*} + 2\frac{\partial c}{\partial y_*} = \frac{U^2}{V^2}\frac{\partial^2 c}{\partial x_*^2} + \frac{\partial^2 c}{\partial y_*^2}. \tag{5}$$

The equations derived in the following reveal that $c = c\big(x_*, y_* - y_{1*}, t_* | x_{2*}, \Delta, \delta, U/V\big)$, where $\Delta = y_{2*} - y_{1*}$. It is convenient to introduce usually applied non-dimensional numbers, the aspect ratio A, the Péclet number Pe, and the Péclet number Pe_y in y direction,

$$A = \frac{x_2}{y_2 - y_1}, \quad Pe = \frac{\hat{U}x_2}{\hat{D}_c}, \quad Pe_y = \frac{\hat{V}(y_2 - y_1)}{\hat{D}_c}. \tag{6}$$

Pe and Pe_y represent the product of corresponding Reynolds numbers ($\hat{U}x_2/\nu$ and $\hat{V}(y_2 - y_1)/\nu$, respectively) with the Schmidt number $\nu/\hat{D}_c$, where ν is the kinematic viscosity. By applying the relationships

$$x_{2*} = Pe/2, \qquad \Delta = Pe_y/2, \qquad U/V = Pe/(APe_y), \tag{7}$$

the solution $c = c\left(x_*, y_* - y_{1*}, t_* | x_{2*}, \Delta, \delta, U/V\right)$ can be written in the following way:

$$c = c(x_*, y_* - y_{1*}, t_* | A, Pe, Pe_y, \delta). \tag{8}$$

The solution $c(x_*, y_*, t_*)$ to Equation (5) involves two ingredients, the stationary solution $s(x_*, y_*)$ for infinitely large t_* and the transitional solution $w(x_*, y_*, t_*)$,

$$c(x_*, y_*, t_*) = s(x_*, y_*) + w(x_*, y_*, t_*). \tag{9}$$

The stationary and transitional solutions $s(x_*, y_*)$ and $w(x_*, y_*, t_*)$, which are referred to as stationary Fourier series model (FSM) and transitional Fourier series model (FSM), are given by Equation (A3) and Equation (A17), respectively; see the explanations in the Appendix A.

2.2. Validation of the Model Implementation

The equations were implemented in an in-house code written for this application. In numerical model applications, the use of the stationary and transitional FSMs obtained ensures exact solutions to the advection–diffusion equation considered. Relatively simple analysis also shows that the use of the structures of $X_n(x_*)$ and $U_n(y_*)$ given in the Appendix A ensures the correct upper and lower y_* BCs and outflow BCs. However, the inflow BCs represented by the sum of Fourier series contributions in the model implementation require validation because they are affected by the numerical implementation, for example, the correct calculation of eigenvalues. This question is addressed in terms of Figure 3, which shows the concentration distribution along y_*/Δ for reference parameters $Pe_y = 1, Pe = 10^2, A = 10^3$, $\delta = 10$, and $\delta = 1$ at $x_* = 0$. The dashed lines represent the imposed profile, the colored lines arise from imitated implementation errors: the neglect of one eigenfunction contribution, and the incorrect calculation of one eigenvalue (β_0^m or β_0^p, respectively) given by a modification by a factor of 2 or 0.5. It may be seen that such incorrect implementations have serious consequences. Both the neglect of one eigenfunction contribution or an eigenvalue modification (by a factor of 2 or 0.5) implies that the model is incapable to correctly provide the imposed profile. Therefore, checks whether concentration calculations are in consistency with imposed profiles are sufficient to conclude that the model implementation is correct. A relatively simple way to provide additional support for the correct model implementation is to ask whether the solutions obtained satisfy the boundedness of mass transport requirement. This is, e.g., not the case for the cases with implementation errors presented in Figure 3: such model results disagree with the boundedness of mass transport because concentration values below zero and above one are obtained. For all the cases presented below, it was found that the boundedness requirements were satisfied by model solutions.

2.3. Computational Cost

The computational cost of the presented method depends very much on the convergence behavior of Fourier representations involved. The stationary solution is driven by the convergence of y_* eigenfunctions. A scaling analysis reveals that $U_n(y_{2*}) \sim (q_1 - q_2)Pe_y/n^2$ at sufficiently high n, where q_1 and q_2 are positive and negative numbers of order unity (which are related to the two contributions to a_n in Table A1). Correspondingly, transitional solution contributions scale with $w_2(y_{2*}, 0) \sim q_1 Pe_y/n^2$, where q_0 is a positive number of order unity. The easiest way to see these scalings is to multiply series contributions with the inverse scaling to demonstrate that series contributions do not change with n and parameter variations. Let us suppose the convergence requirement

that the related Fourier series contributions need to be smaller than 10^{-9}. This implies the condition $Pe_y/N^2 \leq 10^{-9}$, i.e., $N \geq 10^{4.5} Pe_y^{1/2} \approx 3.2 \times 10^4 Pe_y^{1/2}$. For usual values $Pe_y \leq 1$, this condition can be easily satisfied (in less than a minute). A corresponding scaling analysis of x_* eigenfunctions involved in the transitional solution part shows that $w_1(x_{2*}, 0) \sim (-1)^{n+1} qPe(1 + 2/Pe)/n^3$, where q is a positive number of order unity. By using again a convergence criterion that corresponding Fourier series contributions need to be smaller than 10^{-9}, the corresponding convergence condition reads $Pe/N^3 \leq 10^{-9}$ for sufficiently high Pe, this means $N \geq 10^3 Pe^{1/3}$. For $Pe = (10^2, 10^3, 10^4)$, for example, one finds $N \geq (4.6 \times 10^3, 10^4, 2.2 \times 10^4)$. Such simulations take much less than a minute on a personal computer. A very essential observation is the following. In contrast to the stationary solution $s(x_*, y_*)$, the transitional solution $w(x_*, y_*, t_*) = c_{in} w_1(x_*, t_*) w_2(y_*, t_*)$ is given by separated variations in x_* and y_*. This makes computations by orders of magnitude more efficient because a double loop over x_* and y_* eigenvalues does not appear.

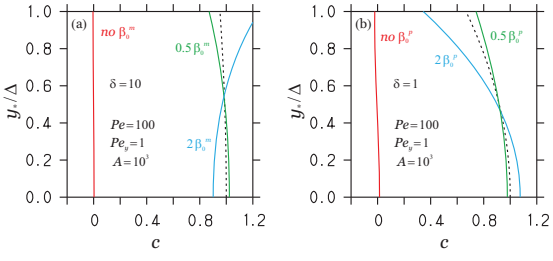

Figure 3. The concentration distribution along y_* from y_{1*} (lower bound) to y_{2*} (upper bound) for reference parameters $Pe_y = 1, Pe = 10^2, A = 10^3$, and $\delta = 10$ in (**a**) and $\delta = 1$ in (**b**) at $x_* = 0$ (dashed lines). The red lines refer to the neglect of β_0^m or β_0^p, respectively, eigenfunction contributions. The blue and green lines refer to a modification of β_0^m or $-\beta_0^p$, respectively, by the given factors (2 and 0.5).

The computational development of the simulation method leads to four observations. (i) The computational method is computationally highly efficient: exact solutions are obtained on a personal computer in less than a minute. (ii) A specific question related to the computational cost is about the scaling of cost with model parameters such as the Péclet numbers involved (Pe and Pe_y). It was shown that such model parameter variations have very minor effects on the solution convergence with respect to both the stationary and transitional solution. (iii) One key element of correct solutions is the exact iterative solution of eigenvalue equations for all parameter regimes, which represents a challenging task. An efficient algorithm for handling this question was presented here. (iv) Another key element is, in particular, the correct identification of the lowest order eigenvalues for all parameter regimes, otherwise the method simply does not work.

3. Model Application

Results using the model obtained are presented now by focusing for simplicity on the stationary solution (the transitional solution is discussed in Section 3.2)

$$c = c(x_*, y_* - y_{1*} | A, Pe, Pe_y, \delta). \tag{10}$$

The parameters involved are given by Equation (6). As shown in the Appendix A in the paragraph below Equation (A6), the critical parameter that separates different eigenvalue regimes is given by $p = 2/\delta - (1 + 2/\delta) Pe_y/2$ (see also the illustration in Figure 4). To restrict attention, it is assumed that $\delta \geq 0$. According to the BC, $s(x_*, y_{2*}) + [\delta/2][\partial s/\partial y_*](x_*, y_{2*}) = 0$, which implies a negative concentration gradient at y_{2*}; this is equivalent to the calculation of a concentration (of oil) that has at the lower boundary y_{1*} a larger value than at the upper boundary y_{2*}. It is worth noting that the

assumption $\delta < 0$, which implies decreasing concentration values toward the lower boundary, may well be in conflict with the boundedness of mass transport for the conditions considered because concentration values larger than unity can be obtained.

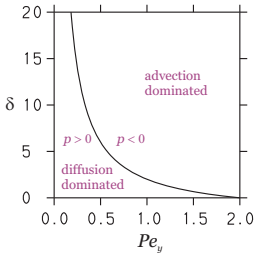

Figure 4. Parameter regimes: the black curve shows Pe_y values for which $p = 2/\delta - (1 + 2/\delta)Pe_y/2 = 0$.

3.1. FSM: Flow Regimes and Equivalent OC

The concentration distribution at $x_* = x_{2*}$and $y_* = y_{1*}$ is shown in Figure 5 for varying parameters A, Pe, Pe_y, and δ. The most relevant observation is that $p = 2/\delta - (1 + 2/\delta)Pe_y/2$, which separates different eigenvalue regimes and also separates different concentration regimes; see Figure 5a. For $p < 0$, one finds high concentration values which do not change much with δ. We refer to this case as blocked flow below. For $p > 0$, one finds much lower concentration values which are, approximately, linearly controlled by δ. We refer to this case below as unblocked flow. The critical Pe_y for which $p = 0$ reads $Pe_c = 4/(2 + \delta)$, which is bounded, $0 \leq Pe_c \leq 2$. Hence, p can be written $p = 2(1 - Pe_y/Pe_c)/\delta$. Here, Pe_y/Pe_c represents a normalized Péclet number. By introducing $L_f = Pe_c\hat{D}_c/\hat{V}$, it can be written $Pe_y/Pe_c = (y_2 - y_1)/L_f$. Correspondingly, the conditions for the unblocked (blocked) flow regimes are given by

$$y_2 - y_1 < L_f \quad (y_2 - y_1 > L_f), \tag{11}$$

respectively. Here, L_f represents a characteristic length scale which depends only on flow properties. Equation (11) state, therefore, the requirement that the domain height has to be sufficiently small to enable unblocked flow. The relationship between unblocked/blocked flow and diffusion/advection-dominated flow regimes can be seen as follows. In unblocked flow, the diffusion dominates: molecular transport governs this regime basically unaffected by the directional influence of advection. It is, therefore, very natural to identify the unblocked (blocked) flow regimes as diffusion (advection)-dominated flow. According to $p = 2(1 - Pe_y/Pe_c)/\delta$, a Péclet number Pe_y/Pe_c smaller (larger) than unity is the condition to have diffusion (advection)-dominated flow.

Figure 5b–d shows the same huge discrepancies between blocked and unblocked flow regimes seen in Figure 5a. Figure 5c,d indicates an equivalence between Pe and inverse A effects. The structure of A curves can be seen as follows. An increased $A^{-1} = (y_2 - y_1)/x_2$ is equivalent to a decreased x_2, which implies a higher $\hat{U}$ to keep $Pe = \hat{U}x_2/\hat{D}_c$ unchanged. The higher the $\hat{U}$, the higher is the concentration reduction. The same mechanism implies Pe effects: an increased Pe is equivalent to a higher $\hat{U}$. With respect to Figure 5b, it is worth noting the following. According to Equation (A4), the x_*/x_{2*} dependence of the concentration distribution is basically controlled by U/V: x_*/x_{2*} variations will disappear if U/V vanishes. This case is almost irrelevant to applications, because usually $U >> V$. For $Pe_y > 1$ in Figure 5b, one finds $Pe/(APe_y) = U/V < 0.1$, i.e., this range of variations is unlikely to be seen in applications. For $Pe_y \leq 1$, the $Pe_y = \hat{V}(y_2 - y_1)/\hat{D}_c$ effects result from the following. An increased Pe_y implies a larger $y_2 - y_1$ and x_2 to keep A unchanged. This implies a smaller $\hat{U}$ to keep Pe constant. Hence, an increased Pe_y increases the concentration.

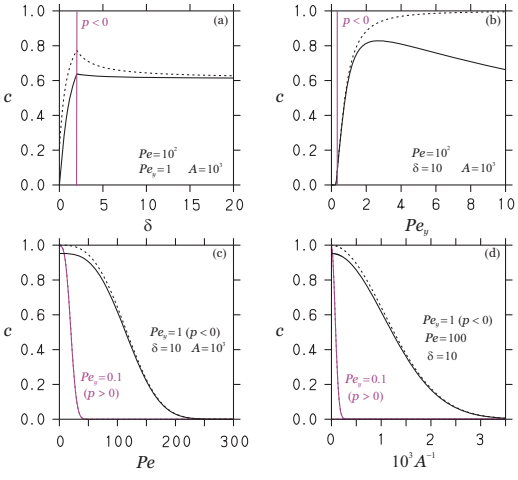

Figure 5. The concentration distribution at $x_* = x_{2*}$, $y_* = y_{1*}$ (dashed lines) and $y_* = y_{2*}$ (solid lines) for reference parameters $\delta = 10$, $Pe_y = 1$, $Pe = 10^2$, and $A = 10^3$. Variations of δ, Pe_y, Pe, A are shown in (**a**), (**b**), (**c**), and (**d**), respectively. The reference parameters kept constant are also given. In (**a**,**b**), the vertical line separates $p > 0$ and $p < 0$ cases. In (**c**,**d**), both $p > 0$ and $p < 0$ cases are shown.

Spatial concentration distributions are shown in Figures 6 and 7. The figures confirm the close relation between Pe, A^{-1} and Pe_y effects. As discussed above, an increase in Pe and A^{-1} reflects an increase in $\hat{U}$, i.e., a change in Pe can be accomplished by a corresponding change in A^{-1}. An analysis of such changes in the blocked flow regime (by looking at requirements for equivalent variations) reveals that increasing Pe by a factor k is approximately equivalent to dividing A by $k^{1.5}$. The relation between Pe_y and A variations is slightly different; see the discussion related to Figure 5. Different patterns can be seen for $U/V < 0.1$. However, according to the discussion related to Figure 5, this is the regime of little relevance to applications. Apart from this regime, an analysis shows that multiplying A by a factor k is approximately equivalent to multiplying Pe_y with a factor slightly larger that k ($1.2k$ or $1.3k$), i.e., there is an equivalence of Pe_y and A variations.

The huge discrepancy between the high-concentration blocked flow and much lower-concentration unblocked flow regimes can be seen again in Figures 6 and 7. In addition to this difference, there is another factor coming into play: $U/V = Pe/(APe_y)$, which controls the x_*/x_{2*} variation according to $R = [1 + (1 + \beta_n^2)U^2/V^2]^{1/2}$. In the small U/V regime, which is of little relevance to applications (see above), one finds the following features. For $U/V = 0.05 - 0.1$, there are almost linear variations; see Figure 7b,c. For $U/V < 0.05$, one finds relatively minor concentration variations along x_*/x_{2*}, including almost constant concentration values if $U/V << 0.05$; see Figure 7b. This is the region where U/V has almost no influence on the concentration distribution. Otherwise, for $U/V > 0.1$, one observes a significant (exponentially) spatial concentration reduction, even for the blocked flow regime; see Figure 7c. Regarding the y_*/Δ variations shown in Figure 6, there are almost homogeneous concentration distributions. The latter is a consequence of two facts: the inflow distribution at $y_* = y_{1*}$, and the boundedness of scalars which excludes the appearance of minimum and maximum values in between boundary values.

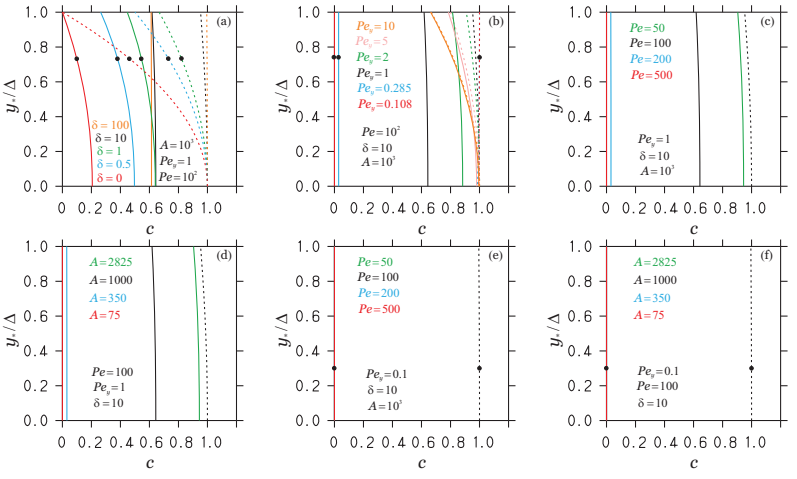

Figure 6. The concentration distribution along y_* from y_{1*} (lower bound) to y_{2*} (upper bound) at $x_* = 0$ (dashed lines) and $x_* = x_{2*}$ (solid lines). Reference values $\delta = 10$, $Pe_y = 1$, $Pe = 10^2$, and $A = 10^3$ are considered in (**a**–**d**) in conjunction with variations of δ, Pe_y, Pe, A. In (**e**,**f**), complementary cases to (**c**,**d**) are considered to cover the $p > 0$ case, where $Pe_y = 0.1$ in contrast to $Pe_y = 1$ in (**c**,**d**). The reference parameters kept constant are also given. The black dots on curves indicate $p > 0$ cases. The $x_* = 0$ profiles are unaffected by Pe, A variations. In (**e**,**f**), all solid curves coincide.

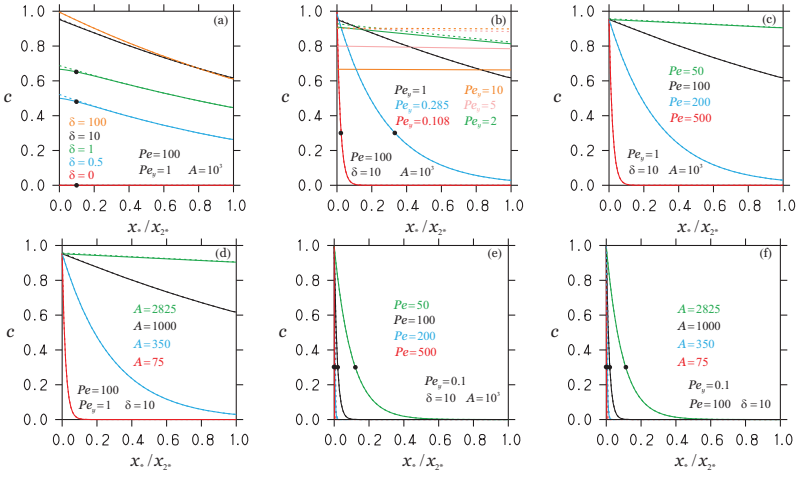

Figure 7. The concentration distribution (**a**–**f**) along x_* at $y_* = y_{2*}$ (solid lines) by following the notation applied in Figure 6. The dashed lines show the results of model Equation (12).

3.2. Zeroth-Order Model

The relevance of the lowest eigenvalue contributions is certainly of interest. To address this question, the stationary FSM is reduced to only these contributions by considering $s_0(x_*, y_*) = e^{y_*} a_0 X_0(x_*) U_0(y_*)$. By involving the BC Equation (A13), a more appropriate writing reads $s_0(x_*, y_*) = f(y_*) X_0(x_*)$, i.e.

$$s_0(x_*, y_*) = \\ = c_1 \left(1 - \frac{(y_* - y_{1*})^2}{\Delta(\Delta+\delta)}\right) e^{(1-R_0)x_*} \frac{1 + R_0 - (1-R_0)e^{-2R_0(x_{2*}-x_*)}}{1 + R_0 - (1-R_0)e^{-2R_0 x_{2*}}}, \tag{12}$$

where $R_0 = [1 + (1 + \beta_0^2)U^2/V^2]^{1/2}$, $x_{2*} = Pe/2$, $\Delta = Pe_y/2$, and $U/V = Pe/(APe_y)$. Depending on negative or positive p values, one needs to use either β_0^m or β_0^p, respectively, in R_0. Here, β_0^p and β_0^m have to be found iteratively by solving Equation (A8) and Equation (A10), respectively; this means they are found via

$$\beta_0^p \Delta = arctan\left\{\frac{\beta_0^p}{1 + \delta(1 + [\beta_0^p]^2)/2}\right\}, \quad \beta_0^m \Delta = arctanh\left\{\frac{\beta_0^m}{1 + \delta(1 - [\beta_0^m]^2)/2}\right\}. \tag{13}$$

Figure 8 demonstrates that simple approximations for these eigenvalues (simple functions of Pe_y or δ) are unavailable, meaning that they need to be determined iteratively via Equation (13). A simple alternative is to use an online calculator [58] to accurately solve the equations considered. According to Figure 8, zero eigenvalues may be found if $Pe_y = Pe_c = 4/(2 + \delta)$. The model Equation (12) is referred to below as zeroth-order model (ZOM). For given model parameters $\Delta(\Delta + \delta) = Pe_y(Pe_y + 2\delta)/4$, R_0, and Pe, this model completely specifies the structure of the concentration distribution via the imposed BC $f(y_*)$ and $X_0(x_*)$, which represents exponential decay along x_*.

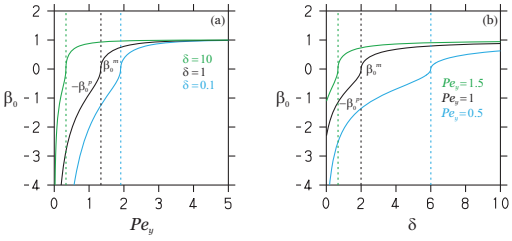

Figure 8. Eigenvalues β_0^m and $-\beta_0^p$ as function of (**a**) Pe_y (depending on δ) and (**b**) δ (depending on Pe_y). The vertical lines separate β_0^m from $-\beta_0^p$.

The performance of Equation (12) is also shown in Figure 7. It may be seen that the performance of this model is excellent with one minor exception: the $U/V < 0.05$ cases in Figure 7b. However, as discussed in relation to Figure 5, this is a case that is almost irrelevant to applications. On the one hand, the performance of Equation (12) reveals the fundamental relevance of including the eigenvalues of lowest order. On the other hand, this performance enables it to perform accurate simulations based on the simple analytical model Equation (12).

Figure 9, where the same cases are considered as in Figure 7, confirms the assumption that the same applies to the transitional solution (a constant initial value $c(x_*, y_*, 0) = c_{in} = 1$ is considered): the reduction of Equations (A17)–(A19) to only considering the lowest eigenvalue contributions results in transitional solutions that do not show any visible difference from the complete solutions (A17)–(A19). As given in regard to the stationary solution, this fact enables the use of a simple analytical formula for performing highly accurate simulations.

First, the ZOM is very beneficial regarding the characterization of the concentration distribution by global maximum and minimum values, which exist because of the boundedness of mass transport. The spatial concentration distributions shown in Figures 6 and 7 reveal a global concentration maximum and minimum at $(x_*, y_*) = (0, y_{1*})$ and $(x_*, y_*) = (x_{2*}, y_{2*})$, respectively. The ZOM then provides the maximum and minimum values

$$s_{min} = s_0(x_{2*}, y_{2*}) = c_1\left[1 - \Delta/(\Delta + \delta)\right]X_0(x_{2*}), \qquad s_{max} = s_0(0, y_{1*}) = c_1. \tag{14}$$

Thus, by involving $Pe_y = 2\Delta$, the stationary ZOM solution is found to be bounded by

$$c_1\left[1-\frac{Pe_y}{Pe_y+2\delta}\right]X_0(x_{2*}) \le s_0(x_*,y_*) \le c_1. \tag{15}$$

Second, the ZOM is very beneficial regarding the estimation of model parameters, which are required to apply the ZOM and FSM and are relevant to scaling questions (upscaling). The aspect ratio $A = x_2/(y_2-y_1)$ is known, but a relevant question is about how δ, $Pe = \hat{U}x_2/\hat{D}_c$, and $Pe_y = \hat{V}(y_2-y_1)/\hat{D}_c$ can be determined. This question is not trivial because $Pe = \hat{U}x_2/\hat{D}_c$ and $Pe_y = \hat{V}(y_2-y_1)/\hat{D}_c$ involve the membrane diffusivity $\hat{D}_c$, which is difficult to measure, and δ, too, is difficult to determine on the basis of $s(x_*,y_{2*}) + [\delta/2][\partial s/\partial y_*](x_*,y_{2*}) = 0$. This question is considered by assuming the measured values of the stationary solution provided by the ZOM. It is possible to address this question in a more general set up, but for simplicity, it is assumed here that U/V is known in addition to A. Because of $X_0(0) = 1$, it is found that $s_0(0,y_*) = f(y_*) = c_1(1-(y_*-y_{1*})^2/[\Delta(\Delta+\delta)])$. Hence, concentration values taken at two appropriate positions enable us to determine $\Delta = Pe_y/2$ and δ. Because U/V is known, δ, Pe_y, and $Pe = APe_yU/V$ are found.

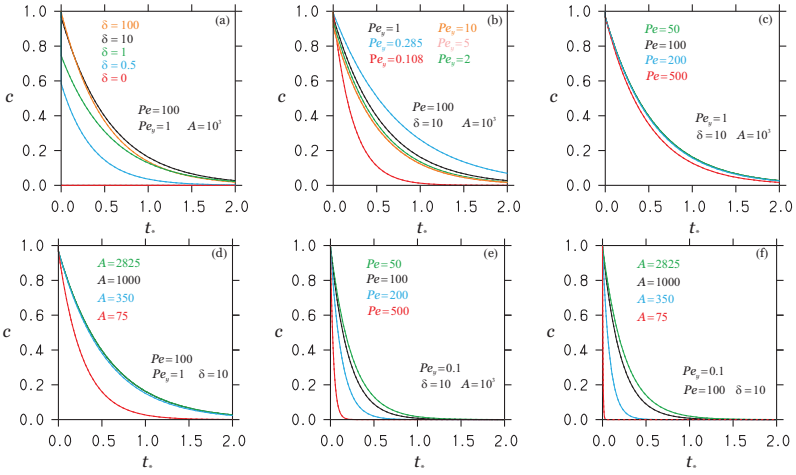

Figure 9. The concentration distribution (**a**–**f**) as function of time t_* at $x_* = x_{2*}$, $y_* = y_{2*}$ (solid lines) by considering the same cases as in Figure 7 (solid lines). The dashed lines show the results of using only the lowest eigenvalue contributions in Equations (A17)–(A19): there is no visible difference to solid curves.

Third, the ZOM can be used to obtain exact conclusions about the equivalence conditions for model parameter variations discussed in Section 3.1. As a first example, let us consider $s_0(x_*,y_{1*}) = c_1X_0(x_*)$ by excluding variations of Pe and δ. In this case, $X_0(x_*)$ is affected by variations of Pe_y and A only via $(1+\beta_0^2)/[Pe/(APe_y)]^2$ in R_0. Then, variations of A can be compensated by variations of Pe_y which ensure an unchanged $X_0(x_*)$. As a second example, let us consider $s_0(x_*,y_{1*}) = c_1X_0(x_*)$ by excluding variations of Pe_y and δ. Then, $X_0(x_*)$ is unchanged in response to A variations if Pe is calculated by the condition to have an unchanged $X_0(x_*)$. As a third example, let us consider the parameter $\Delta/(\Delta+\delta)$, which determines the minimal concentration along y_* according to Equation (15). This parameter can be used to balance membrane fouling reflected by a change in δ from δ_1 to δ_2. The latter requires to determine a change Δ_2 of Δ_1 such that $\Delta_1/(\Delta_1+\delta_1) = \Delta_2/(\Delta_2+\delta_2)$. The latter requirement can also be written $\delta_2/\delta_1 = Pe_{y,2}/Pe_{y,1}$. This means an increase in δ_2 (a reduced flux) can be compensated by a corresponding higher Pe_y.

4. Summary

An analytical FSM for the mass transport in membrane systems is presented here. Our method is computationally highly efficient and exact, i.e., no independent evidence is needed for model results, only the implementation needs justification. Evidence for the validity of results and computational features is described in Sections 2.2 and 2.3. Our conclusions were obtained by Fourier analysis, which provides analytical results that cannot be obtained by experimental or numerical studies.

Let us summarize the answers obtained in regard to the questions Q1–Q5 presented in Section 1. For doing so, the OCs (A, Pe, Pe_y, δ) are assumed to be known; questions in this regard can be addressed by following the discussion at the end of Section 3.2. Based on our core results, the identification of flow separation conditions $y_2 - y_1 \lessgtr L_f$ (see Equation (11)), the discussions of equivalent OC variations (see Section 3), and the ZOM $s_0(x, y) = f(y)X_0(x)$ (see Equation (12)), there are the following conclusions:

1. Arguably, our most relevant observation is that $p = 2(1 - Pe_y/Pe_c)/\delta$, which separates different eigenvalue regimes and also separates different mass transport regimes, in particular diffusion ($p > 0, y_2 - y_1 < L_f$) and advection ($p < 0, y_2 - y_1 > L_f$)-dominated regimes. These regime separation conditions compare geometric conditions (the domain size) with the characteristic length scale L_f imposed by the flow. Given a membrane size considered, knowledge of the regime separation conditions is beneficial for the understanding of upscaling requirements, i.e., the use of lab results for pilot- and full-scale applications; with respect to the same flow properties, upscaling can imply transitions from very efficient to very inefficient flow regimes. A very relevant observation is that diffusion-dominated and advection-dominated flow regimes correspond to unblocked (low concentration values) and blocked (high concentration values) flow. Hence, the mathematical characterization of the dominance of one process has relevant physical consequences. Advection-dominated flow implies blocked flow because the dominance of advection inhibits molecular diffusion, i.e., the reduction in concentration gradients.
2. Knowledge of analytical equivalence conditions for A, Pe and Pe_y parameter variations for cases of practical relevance enables the use of various parameter variations to realize desired effects (under conditions where certain parameter variations are inappropriate). The understanding of several ways to accomplish regime changes enables transitions to preferred flow regimes (see the discussion related to Figure 7). The ZOM can provide exact conclusions about equivalent variations of OCs.
3. The FSM, but in particular the ZOM, provide an answer to question Q3 about the understanding of the overall mass transport and characteristic mass distribution features: for both flow regimes, the ZOM explains the difference between (input and output) boundary values implied by OCs and characteristic concentration variations in between these bounds. In particular, the ZOM enables the explicit calculation of global maximum/minimum concentration values $c_1(1 - Pe_y/[Pe_y + 2\delta])X_0(x_{2*}) \leq s_0(x_*, y_*) \leq c_1$, which is helpful for the understanding of concentration variations.
4. Based on the FSM, the ZOM $s_0(x, y) = f(y)X_0(x)$ was presented, which be can be easily applied. The ZOM performance was found to be excellent for all regimes of practical relevance; see above. The significant advantages offered by the ZOM are described above (see second and third points).
5. According to Equation (2), the mass transport is affected by mass transport properties (diffusivity $\hat{D}_c$), mass transport initial and BCs, and the structure of the velocity field. The transport properties are known, and there is no problem to exactly satisfy mass transport initial and BCs. Although the velocity field is only approximately represented, the boundedness property of mass transport ensures then proper transitions between the imposed exact BCs, i.e., more complex flow conditions can be covered by the method considered.

Our conclusions support the membrane system design via providing relevant guidelines for applications; see the preceding paragraph, in particular the conclusions regarding questions Q1–Q3. It can be expected that the results obtained provide valuable guidelines for CFD and experimental studies, even under conditions where spacers and other effects are present (see the conclusion to question Q5). Direct applications of our method to membrane system design are not the scope of our paper, the latter requires extensive comparisons with corresponding CFD results for a wide range of parameter variations.

The results presented may be seen as modeling of the solute concentration of oil-in an oil-in-water emulsion (see the reference to a corresponding stochastic particle system in Section 2.1). However, in fact, the same equations can be used to model a variety of other systems, as, for example, saltwater systems for brackish water and seawater reverse osmosis. It is worth noting that the method presented actually represents a design strategy that can be applied to other (radial) geometries; it can be extended to three-dimensional analyses, and it can be applied with other initial and boundary conditions. Results obtained on this basis can be expected to provide valuable additional information and conclusions in support of numerical and experimental studies of membrane systems.

Author Contributions: Conceptualization, S.H.; Methodology, J.A.B.; Software, J.H.; Validation, J.H.; Formal analysis, S.H. and J.H.; Investigation, J.H.; Resources, J.A.B.; Data curation, J.H.; Writing—original draft, S.H.; Writing—review & editing, J.H. and J.A.B.; Visualization, J.H.; Supervision, S.H. and J.A.B.; Project administration, J.A.B.; Funding acquisition, J.A.B. All authors have read and agreed to the published version of the manuscript.

Funding: This research was funded by the United States Department of Energy (DOE) grant number DE-FE0031855.

Institutional Review Board Statement: Not applicable.

Informed Consent Statement: Not applicable.

Data Availability Statement: Not applicable.

Acknowledgments: The authors gratefully acknowledge the financial support for this work that was provided by the United States Department of Energy (DOE) under the following Federal Grant Number: DE-FE0031855.

Conflicts of Interest: The authors declare no conflict of interest.

Nomenclature

A	aspect ratio, $x_2/(y_2-y_1)$
c	dispersed phase concentration
c_{in}	initial value in $c(x_*, y_*, 0) = c_{in}$
c_1	model parameter, see Equation (A13)
D_M	molecular diffusion coefficient
D_c	capillary diffusion coefficient
$\hat{D}_c$	D_c/ϵ_p
$f(y)$	imposed boundary condition
$g(x,y)$	imposed initial condition
L_f	characteristic length, $Pe_c\hat{D}_c/\hat{V}$
Pe	Péclet number, $\hat{U}x_2/\hat{D}_c$
Pe_y	Péclet number, $\hat{V}(y_2-y_1)/\hat{D}_c$
Pe_c	critical Péclet number, $4/(2+\delta)$
p	parameter, $2/\delta-(1+2/\delta)Pe_y/2$
R	parameter, $[1+(1+\beta_n^2)U^2/V^2]^{1/2}$
s, w	stationary, transitional solutions
t	time
t_*	non-dim., $\hat{V}^2 t/(4\hat{D}_c)$

U_n	shifted y eigenfunction
U, V	velocities in x, y directions
U/V	non-dim., $Pe/(APe_y)$
$\hat{U}, \hat{V}$	U/ϵ_p, V/ϵ_p
X_n	x eigenfunction
x, y	positions in space
x_1, x_2	x domain bounds
y_1, y_2	y domain bounds
x_*, y_*	non-dim., $\hat{U}x/(2\hat{D}_c)$, $\hat{V}y/(2\hat{D}_c)$
x_{2*}	non-dim., $\hat{U}x_2/(2\hat{D}_c) = Pe/2$
y_{1*}, y_{2*}	non-dim., $\hat{V}y_1/(2\hat{D}_c)$, $\hat{V}y_2/(2\hat{D}_c)$
$\beta_0, \beta_0^m, \beta_0^p$	eigenvalues, see Equations (12) and (13)
Δ	non-dim., $y_{2*} - y_{1*} = Pe_y/2$
δ^{-1}	membrane permeability in Equation (4)
ϵ_p	membrane porosity
ν	kinematic viscosity
$()_{min,max}$	minimum, maximum values
$()_0$	zeroth order contributions

Appendix A. Stationary and Transitional Solutions

Appendix A.1. Stationary Solution

The stationary solution satisfies the stationary partial differential equation

$$2\frac{U^2}{V^2}\frac{\partial s}{\partial x_*} + 2\frac{\partial s}{\partial y_*} = \frac{U^2}{V^2}\frac{\partial^2 s}{\partial x_*^2} + \frac{\partial^2 s}{\partial y_*^2}, \tag{A1}$$

combined with non-homogeneous BCs,

$$\begin{gathered} s(0, y_*) = f(y_*), \quad \tfrac{\partial s}{\partial x_*}(x_{2*}, y_*) = 0, \quad \tfrac{\partial s}{\partial y_*}(x_*, y_{1*}) = 0, \\ s(x_*, y_{2*}) + \tfrac{\delta}{2}\tfrac{\partial s}{\partial y_*}(x_*, y_{2*}) = 0. \end{gathered} \tag{A2}$$

The solution $s(x_*, y_*)$ of Equation (A1) can be obtained by separation of variables [56]. It reads

$$s(x_*, y_*) = \sum_{n=0}^{N} s_n = e^{y_*} \sum_{n=0}^{N} a_n X_n(x_*) U_n(y_*), \tag{A3}$$

where $N \to \infty$ is supposed. The x_* eigenfunctions, which read the eigenvalues β_n of y_* eigenfunctions, are given by

$$X_n(x_*) = e^{(1-R)x_*} \frac{1 + R - (1-R)e^{-2R(x_{2*} - x_*)}}{1 + R - (1-R)e^{-2Rx_{2*}}}, \tag{A4}$$

where $R = [1 + (1 + \beta_n^2)U^2/V^2]^{1/2}$. Equation (A3) applies the modification $Y_n(y_*) = e^{y_*} U_n(y_*)$ of y_* eigenfunctions, which simplifies the ordinary differential equation (ODE) for y_* eigenfunctions because of a vanishing first-order derivative. For $n = 1, 2, \ldots$, the modified eigenfunctions are found to be given by

$$U_n(y_*) = \beta_n cos[\beta_n(y_* - y_{1*})] - sin[\beta_n(y_* - y_{1*})]. \tag{A5}$$

For the case $n = 1, 2, \ldots$ considered, the y_* eigenvalues β_n satisfy the equation

$$\pi^{-1}\beta_n(y_{2*} - y_{1*}) - n = \pi^{-1} arctan\left\{\frac{\beta_n}{1 + \delta(1 + \beta_n^2)/2}\right\}. \tag{A6}$$

This equation can be solved iteratively starting with $\beta_n = n\pi/(y_{2*} - y_{1*})$ on the right-hand side (RHS). The solution is obtained after fewer than 20 iterations. The converged solution

can be written $\beta_n = \nu\pi/(y_{2*} - y_{1*})$, where ν refers to the shifted eigenvalue (in contrast to n). Depending on the BCs (the setting of δ), it turns out that ν is bounded, $n \leq \nu \leq n + 1/2$. Here, the lower and upper limits correspond to $\delta \to \infty$ and $\delta = 0$, respectively.

However, there are also contributions for $n = 0$. In particular, these contributions are determined by the sign of $p = 2/\delta - (1 + 2/\delta)\Delta$, where $\Delta = y_{2*} - y_{1*}$ is applied [56]. Here, p arises from the BCs of U [56]. One finds $0 = U'(y_{1*}) - p_1 U(y_{1*})$ and $0 = U'(y_{2*}) + p_2 U(y_{2*})$, where $p_1 = -1$ and $p_2 = 1 + 2/\delta$. The latter implies $p = p_1 + p_2 + p_1 p_2 \Delta$. Let us consider these two cases in the following two paragraphs (the consideration of $p = 0$ has little practical value because it implies a specific setting for Δ which can be avoided).

(a) Case $p > 0$: In this case, there is one additional positive eigenvalue (denoted by β_0^p, p refers to a positive eigenvalue) below $\beta_1 = \pi/(y_{2*} - y_{1*})$. The eigenfunction follows Equation (A5),

$$U_0^p(y_*) = \beta_0^p cos\Big[\beta_0^p(y_* - y_{1*})\Big] - sin\Big[\beta_0^p(y_* - y_{1*})\Big]. \tag{A7}$$

The eigenvalue β_0^p is determined by the solution of Equation (A6) with $n = 0$,

$$\beta_0^p(y_{2*} - y_{1*}) = arctan\left\{\frac{\beta_0^p}{1 + \delta(1 + [\beta_0^p]^2)/2}\right\}. \tag{A8}$$

This equation was solved iteratively in the same way as Equation (A6) by applying, however, 1000 iterations starting with $\beta_0^m = 10^{-8}$.

(b) Case $p < 0$: In this case, there is one additional negative eigenvalue (denoted by β_0^m, m refers to a negative eigenvalue). The corresponding eigenfunction reads

$$\begin{array}{c} U_0^m(y_*) = \beta_0^m cosh[\beta_0^m(y_* - y_{1*})] - sinh[\beta_0^m(y_* - y_{1*})] = \\ = \frac{\gamma-1}{2} e^{\beta_0^m(y_* - y_{1*})} + \frac{\gamma+1}{2} e^{-\beta_0^m(y_* - y_{1*})}, \end{array} \tag{A9}$$

where β_0^m is given by the solution of

$$\beta_0^m(y_{2*} - y_{1*}) = arctanh\left\{\frac{\beta_0^m}{1 + \delta(1 - [\beta_0^m]^2)/2}\right\}. \tag{A10}$$

An alternative formulation of this equation, which is based on the solution of the quadratic equation for β_0^m, reads

$$\beta_0^m = -\frac{1}{\delta\, tanh(\beta_0^m \Delta)} + \sqrt{\frac{1}{\delta^2 tanh^2(\beta_0^m \Delta)} + 1 + \frac{2}{\delta}}. \tag{A11}$$

The latter equation was found to deal correctly with the limit $\beta_0^m \to 1$. It was numerically solved in the same way as Equation (A8) by applying 1000 iterations starting with $\beta_0^m = 10^{-6}$.

The coefficients a_n in Equation (A3) are chosen such that the stationary solution s matches an imposed boundary function $f(y_*)$ at $x_* = 0$; this means $s(0, y_*) = f(y_*)$. The key for deriving the coefficient formula is to make use of the orthogonality of $U_n(y_*)$ eigenfunction, $\int_{y_{1*}}^{y_{2*}} U_n(y_*) U_m(y_*) dy_* = \delta_{nm} w_n^2$, where the squared norm w_n^2 of U_n is given in Table A1.

Table A1. Fourier coefficients a_n and a_0^m of the stationary solution, where $a_0^p = a_0$.

Positive eigenvalues
$a_n = c_1 \frac{sin(\beta_n \Delta)}{w_n^2} e^{-y_{2*}} - c_1 \frac{e^{-y_{2*}}[k_{1n} cos(\beta_n \Delta) + k_{2n} sin(\beta_n \Delta)] - 4\beta_n e^{-y_{1*}}}{w_n^2 \Delta(\Delta+\delta)(1+\beta_n^2)^2}$,
$k_{1n} = 2\beta_n \left[2 + (1+\beta_n^2)\Delta\right], \qquad k_{2n} = 1 - 2\beta_n^2 + \left[1 + (1+\beta_n^2)\Delta\right]^2$,
$w_n^2 = \frac{1+\beta_n^2}{2}\Delta - \frac{1-\beta_n^2}{4\beta_n} sin(2\beta_n \Delta) + \frac{1}{2} cos(2\beta_n \Delta) - \frac{1}{2}$
Negative eigenvalue
$a_0^m = c_1 \frac{sinh(\beta_0^m \Delta)}{w_m^2} e^{-y_{2*}} - c_1 \frac{e^{-y_{2*}}\left[k_{1m} cosh(\beta_0^m \Delta) + k_{2m} sinh(\beta_0^m \Delta)\right] - 4\beta_0^m e^{-y_{1*}}}{w_m^2 \Delta(\Delta+\delta)(1-[\beta_0^m]^2)^2}$,
$k_{1m} = 2\beta_0^m \left[2 + (1-[\beta_0^m]^2)\Delta\right], \qquad k_{2m} = 1 + 2[\beta_0^m]^2 + \left[1 + (1-[\beta_0^m]^2)\Delta\right]^2$,
$w_m^2 = \frac{1}{2} - \frac{1-[\beta_0^m]^2}{2}\Delta + \frac{(1-\beta_0^m)^2}{8\beta_0^m} e^{2\beta_0^m \Delta} - \frac{(1+\beta_0^m)^2}{8\beta_0^m} e^{-2\beta_0^m \Delta}$

By using this property, one obtains

$$a_n = \frac{1}{w_n^2} \int_{y_{1*}}^{y_{2*}} e^{-y_*} f(y_*) U_n(y_*) dy_*. \tag{A12}$$

The requirement for the imposed function $f(y_*)$ is that it needs to satisfy the BCs. In order to do so, it is assumed that

$$f(y_*) = c_1 \left\{ 1 - \frac{(y_* - y_{1*})^2}{\Delta(\Delta+\delta)} \right\}. \tag{A13}$$

The use of this expression in Equation (A12) provides a_n as given in Table A1. The abbreviations a_0^p and a_0^m are used to refer to the coefficients related to positive and negative eigenvalues, respectively. It is worth noting that w_n^2 and w_m^2 refer to the squared norm of U_n and U_0^m, respectively. In correspondence to the notation used before, w_0^2 refers to the squared norm of U_0^p. With respect to a_0^m, there arises a question about the limit $\beta_0^m \to 1$, which is relevant to some parameter regimes. In this limit case, one finds a_0^m to be given by

$$a_0^m = c_1 \frac{sinh(\beta_0^m \Delta)}{w_m^2} e^{-y_{2*}} - c_1 \frac{1 - e^{-2\Delta}(1 + 2\Delta + 2\Delta^2)}{4 w_m^2 \Delta(\Delta+\delta)} e^{-y_{1*}}. \tag{A14}$$

The latter expression was applied for $|\beta_0^m - 1| \leq 10^{-8}$. The model (A3) obtained in this way represents the stationary Fourier series model (FSM).

Appendix A.2. Transitional Solution

The transitional solution satisfies the non-stationary equation,

$$\frac{\partial w}{\partial t_*} + 2\frac{U^2}{V^2}\frac{\partial w}{\partial x_*} + 2\frac{\partial w}{\partial y_*} = \frac{U^2}{V^2}\frac{\partial^2 w}{\partial x_*^2} + \frac{\partial^2 w}{\partial y_*^2}, \tag{A15}$$

combined with homogeneous BCs,

$$\begin{array}{c} w(0, y_*, t_*) = \frac{\partial w}{\partial x_*}(x_{2*}, y_*, t_*) = \frac{\partial w}{\partial y_*}(x_*, y_{1*}, t_*) = 0, \\ w(x_*, y_{2*}, t_*) + \frac{\delta}{2}\frac{\partial w}{\partial y_*}(x_*, y_{2*}, t_*) = 0, \end{array} \tag{A16}$$

and the initial condition $w(x_*, y_*) = g(x_*, y_*)$. The solution $w(x_*, y_*, t_*)$ of Equation (A15) can be found via separation of variables. It is given by

$$w(x_*, y_*, t_*) = c_{in} w_1(x_*, t_*) w_2(y_*, t_*), \tag{A17}$$

where (by supposing $N \to \infty$ and $M \to \infty$)

$$w_1(x_*, t_*) = \sum_{m=1}^{M} c_m sin(\alpha_m x_*) exp\Big\{x_* - (1+\alpha_m^2)[U/V]^2 t_*\Big\}, \tag{A18}$$

$$w_2(y_*, t_*) = \\ = \sum_{n=0}^{N} b_n \Big[\beta_n cos[\beta_n(y_* - y_{1*})] - sin[\beta_n(y_* - y_{1*})]\Big] exp\{y_* - (1+\beta_n^2)t_*\}. \tag{A19}$$

With respect to $w_2(y_*, t_*)$, the terms of zeroth order are provided in dependence on p as described above regarding the stationary solution; see cases (a) and (b). This means, for $p > 0$ Equation (A19) is applied, whereas $sin[\ldots]$ and $cos[\ldots]$ are replaced by the corresponding $sinh[\ldots]$ and $cosh[\ldots]$ functions for $p < 0$.

In consistency with Table A1, the y_* Fourier coefficients (which were determined by the condition to integrate to one, meaning no initial y_* variation was considered) are given in Table A2.

Table A2. y_* Fourier coefficients b_n and b_0^m of the transitional solution ($b_0^p = b_0$).

Positive eigenvalues
$b_n = \dfrac{sin(\beta_n \Delta)}{w_n^2} e^{-y_{2*}}, \quad w_n^2 = \dfrac{1+\beta_n^2}{2}\Delta - \dfrac{1-\beta_n^2}{4\beta_n} sin(2\beta_n\Delta) + \dfrac{1}{2} cos(2\beta_n\Delta) - \dfrac{1}{2}$
Negative eigenvalue
$b_0^m = \dfrac{sinh(\beta_0^m \Delta)}{w_m^2} e^{-y_{2*}}, \quad w_m^2 = -\dfrac{1-[\beta_0^m]^2}{2}\Delta + \dfrac{1+[\beta_0^m]^2}{4\beta_0^m} sinh(2\beta_0^m\Delta) - \dfrac{1}{2} cosh(2\beta_0^m\Delta) + \dfrac{1}{2}$

The corresponding x_* Fourier coefficients can be calculated on the basis of the orthogonality property of x_* eigenfunctions, $\int_0^{x_{2*}} sin(\alpha_n x_*) sin(\alpha_m x_*) dx_* = \delta_{nm} w_x^2$, where the squared norm of x_* eigenfunctions is given by

$$w_x^2 = \frac{x_{2*}}{2} - \frac{sin(2\alpha_m x_{2*})}{4\alpha_m}. \tag{A20}$$

The x_* eigenvalues α_m in Equation (A18) satisfy the equation

$$\pi^{-1}\alpha_m x_{2*} - n = -\pi^{-1} arctan(\alpha_m). \tag{A21}$$

Here, $n = 1, 2, \ldots$ refers to non-disturbed eigenvalue numbers. The technique to solve this equation for $n = 1, 2, \ldots$ is equivalent to the solution of Equation (A6) related to the stationary solution, where 20 iterations were applied. There is one positive eigenvalue below $\alpha_1 = \pi / x_{2*}$ which is included in the solution of Equation (A22) for $n = 1, 2, \ldots$.

With respect to the x_* Fourier coefficients, the condition reads

$$c_m = \frac{1}{w_x^2} \int_0^{x_{2*}} e^{-x_*} g(x_*) sin(\alpha_m x_*) dx_*, \tag{A22}$$

where $g(x_*)$ is an imposed x_* profile. Regarding the latter,

$$g(x_*) = c_{in} e^{x_* - x_{2*}} \big[1 + (x_{2*} - x_*)(1 + 1/x_{2*})\big] x_* / x_{2*} \tag{A23}$$

is applied. This function follows the e^{x_*} variation of $w_1(x_*, t_*)$; the factor $e^{x_{2*}}$ is included for normalization. The function $g(x_*)$ is positive, bounded, and correctly satisfies the x_* BCs; this means $g(0) = 0$ and $g'(x_{2*}) = 0$. By using Equation (A22), the x_* Fourier coefficients obtained read

$$c_m = \frac{2(1 + 1/x_{2*}) e^{-x_{2*}}}{x_{2*} w_x^2 \alpha_m^3} \big[1 - cos(\alpha_m x_{2*})\big]. \tag{A24}$$

The model Equation (A17) obtained represents the transitional Fourier series model (FSM).

References

1. Gruber, M.F.; Johnson, C.J.; Tang, C.Y.; Jensen, M.H.; Yde, L.; Hélix-Nielsen, C. Computational fluid dynamics simulations of flow and concentration polarization in forward osmosis membrane systems. *J. Membr. Sci.* **2011**, *379*, 488–495. [CrossRef]
2. Gruber, M.F.; Johnson, C.J.; Tang, C.Y.; Jensen, M.H.; Yde, L.; Hélix-Nielsen, C. Validation and analysis of forward osmosis CFD model in complex 3D geometries. *Membranes* **2012**, *2*, 764–782. [CrossRef] [PubMed]
3. Gruber, M.F.; Aslak, U.; Hélix-Nielsen, C. Open-source CFD model for optimization of forward osmosis and reverse osmosis membrane modules. *Sep. Purif. Technol.* **2016**, *158*, 183–192. [CrossRef]
4. Rahimi, M.; Madaeni, S.S.; Abolhasani, M.; Alsairafi, A.A. CFD and experimental studies of fouling of a microfiltration membrane. *Chem. Eng. Process. Process Intensif.* **2009**, *48*, 1405–1413. [CrossRef]
5. Zare, M.; Ashtiani, F.Z.; Fouladitajar, A. CFD modeling and simulation of concentration polarization in microfiltration of oil–water emulsions; Application of an Eulerian multiphase model. *Desalination* **2013**, *324*, 37–47. [CrossRef]
6. Lotfiyan, H.; Ashtiani, F.Z.; Fouladitajar, A.; Armand, S.B. Computational fluid dynamics modeling and experimental studies of oil-in-water emulsion microfiltration in a flat sheet membrane using Eulerian approach. *J. Membr. Sci.* **2014**, *472*, 1–9. [CrossRef]
7. Tashvigh, A.A.; Fouladitajar, A.; Ashtiani, F.Z. Modeling concentration polarization in crossflow microfiltration of oil-in-water emulsion using shear-induced diffusion; CFD and experimental studies. *Desalination* **2015**, *357*, 225–232. [CrossRef]
8. Zoubeik, M.; Salama, A.; Henni, A. A novel antifouling technique for the crossflow filtration using porous membranes: Experimental and CFD investigations of the periodic feed pressure technique. *Water Res.* **2018**, *146*, 159–176. [CrossRef]
9. Behroozi, A.H.; Kasiri, N.; Mohammadi, T. Multi-phenomenal macroscopic investigation of cross-flow membrane flux in microfiltration of oil-in-water emulsion, experimental & computational. *J. Water Process. Eng.* **2019**, *32*, 100962.
10. Behroozi, A.H. A modified resistance model for simulating baffle arrangement impacts on cross–flow microfiltration performance for oily wastewater. *Chem. Eng. Process. Process Intensif.* **2020**, *153*, 107962. [CrossRef]
11. Alshwairekh, A.M.; Alghafis, A.A.; Alwatban, A.M.; Alqsair, U.F.; Oztekin, A. The effects of membrane and channel corrugations in forward osmosis membrane modules–Numerical analyses. *Desalination* **2019**, *460*, 41–55. [CrossRef]
12. Schwinge, J.; Wiley, D.E.; Fletcher, D.F. Simulation of the flow around spacer filaments between narrow channel walls. 1. Hydrodynamics. *Ind. Eng. Chem. Res.* **2002**, *41*, 2977–2987. [CrossRef]
13. Schwinge, J.; Wiley, D.E.; Fletcher, D.F. Simulation of the flow around spacer filaments between channel walls. 2. Mass-transfer enhancement. *Ind. Eng. Chem. Res.* **2002**, *41*, 4879–4888. [CrossRef]
14. Schwinge, J.; Neal, P.R.; Wiley, D.E.; Fletcher, D.F.; Fane, A.G. Spiral wound modules and spacers: Review and analysis. *J. Membr. Sci.* **2004**, *242*, 129–153. [CrossRef]
15. Song, L.; Ma, S. Numerical studies of the impact of spacer geometry on concentration polarization in spiral wound membrane modules. *Ind. Eng. Chem. Res.* **2005**, *44*, 7638–7645. [CrossRef]
16. Siddiqui, A.; Lehmann, S.; Haaksman, V.; Ogier, J.; Schellenberg, C.; Van Loosdrecht, M.C.M.; Kruithof, J.C.; Vrouwenvelder, J.S. Porosity of spacer-filled channels in spiral-wound membrane systems: Quantification methods and impact on hydraulic characterization. *Water Res.* **2017**, *119*, 304–311. [CrossRef]
17. Mojab, S.M.; Pollard, A.; Pharoah, J.G.; Beale, S.B.; Hanff, E.S. Unsteady laminar to turbulent flow in a spacer-filled channel. *Flow Turbul. Combust.* **2014**, *92*, 563–577. [CrossRef]
18. Ranade, V.V.; Kumar, A. Fluid dynamics of spacer filled rectangular and curvilinear channels. *J. Membr. Sci.* **2006**, *271*, 1–15. [CrossRef]
19. Ranade, V.V.; Kumar, A. Comparison of flow structures in spacer-filled flat and annular channels. *Desalination* **2006**, *191*, 236–244. [CrossRef]
20. Keir, G.; Jegatheesan, V. A review of computational fluid dynamics applications in pressure-driven membrane filtration. *Rev. Environ. Sci. Bio/Technol.* **2014**, *13*, 183–201. [CrossRef]
21. Fimbres-Weihs, G.A.; Wiley, D.E. Review of 3D CFD modeling of flow and mass transfer in narrow spacer-filled channels in membrane modules. *Chem. Eng. Process. Process Intensif.* **2010**, *49*, 759–781. [CrossRef]
22. Lau, K.K.; Abu Bakar, M.Z.; Ahmad, A.L.; Murugesan, T. Effect of feed spacer mesh length ratio on unsteady hydrodynamics in 2d spiral wound membrane (swm) channel. *Ind. Eng. Chem. Res.* **2010**, *49*, 5834–5845. [CrossRef]
23. Kostoglou, M.; Karabelas, A.J. On the fluid mechanics of spiral-wound membrane modules. *Ind. Eng. Chem. Res.* **2009**, *48*, 10025–10036. [CrossRef]
24. Koutsou, C.P.; Karabelas, A.J.; Kostoglou, M. Fluid dynamics and mass transfer in spacer-filled membrane channels: Effect of uniform channel-gap reduction due to fouling. *Fluids* **2018**, *3*, 12. [CrossRef]
25. Kavianipour, O.; Ingram, G.D.; Vuthaluru, H.B. Investigation into the effectiveness of feed spacer configurations for reverse osmosis membrane modules using Computational Fluid Dynamics. *J. Membr. Sci.* **2017**, *526*, 156–171. [CrossRef]
26. Kavianipour, O.; Ingram, G.D.; Vuthaluru, H.B. Studies into the mass transfer and energy consumption of commercial feed spacers for RO membrane modules using CFD: Effectiveness of performance measures. *Chem. Eng. Res. Des.* **2019**, *141*, 328–338. [CrossRef]

27. Horstmeyer, N.; Lippert, T.; Schön, D.; Schlederer, F.; Picioreanu, C.; Achterhold, K.; Pfeiffer, F.; Drewes, J. CT scanning of membrane feed spacers–Impact of spacer model accuracy on hydrodynamic and solute transport modeling in membrane feed channels. *J. Membr. Sci.* **2018**, *564*, 133–145. [CrossRef]
28. Liang, Y.Y.; Toh, K.Y.; Fimbres-Weihs, G.A. 3D CFD study of the effect of multi-layer spacers on membrane performance under steady flow. *J. Membr. Sci.* **2019**, *580*, 256–267. [CrossRef]
29. Liang, Y.Y.; Fimbres Weihs, G.A.; Wiley, D.E. Comparison of oscillating flow and slip velocity mass transfer enhancement in spacer-filled membrane channels: CFD analysis and validation. *J. Membr. Sci.* **2020**, *593*, 117433. [CrossRef]
30. Foo, K.; Liang, Y.Y.; Tan, C.K.; Fimbres Weihs, G.A. Coupled effects of circular and elliptical feed spacers under forced-slip on viscous dissipation and mass transfer enhancement based on CFD. *J. Membr. Sci.* **2021**, *637*, 119599. [CrossRef]
31. Appadu, A.R. Numerical solution of the 1D advection-diffusion equation using standard and nonstandard finite difference schemes. *J. Appl. Math.* **2013**, *2013*. [CrossRef]
32. Smith, R. Optimal and near–optimal advection–diffusion finite–difference schemes I. Constant coefficient in one dimension. *Proc. R. Soc. Lond. Ser. A* **1999**, *455*, 2371–2387. [CrossRef]
33. Smith, R. Optimal and near-optimal advection–diffusion finite-difference schemes. II. Unsteadiness and non-uniform grid. *Proc. R. Soc. Lond. Ser. A* **2000**, *456*, 489–502. [CrossRef]
34. Smith, R. Optimal and near-optimal advection—diffusion finite-difference schemes III. Black—Scholes equation. *Proc. R. Soc. Lond. Ser. A* **2000**, *456*, 1019–1028. [CrossRef]
35. Smith, R. Optimal and near-optimal advection-diffusion finite-difference schemes. IV. Spatial non–uniformity. *Proc. R. Soc. Lond. Ser. A* **2001**, *457*, 45–65. [CrossRef]
36. Smith, R.; Tang, Y. Optimal and near–optimal advection–diffusion finite–difference schemes. V. Error propagation. *Proc. R. Soc. Lond. Ser. A* **2001**, *457*, 803–816. [CrossRef]
37. Smith, R.; Tang, Y. Optimal and near–optimal advection–diffusion finite–difference schemes. VI Two–dimensional alternating directions. *Proc. R. Soc. Lond. Ser. A* **2001**, *457*, 2379–2396. [CrossRef]
38. Smith, R. Optimal and near–optimal advection—diffusion finite–difference schemes. VII Radionuclide chain transport. *Proc. R. Soc. Lond. Ser. A* **2001**, *457*, 2719–2740. [CrossRef]
39. Flotron, S.; Rappaz, J. Conservation schemes for convection-diffusion equations with Robin boundary conditions. *ESAIM. Math. Model. Numer. Anal.* **2013**, *47*, 1765–1781. [CrossRef]
40. Singh, K.M.; Tanaka, M. Dual reciprocity boundary element analysis of transient advection-diffusion. *Int. J. Numer. Methods Heat Fluid Flow* **2003**, *13*, 633–646. [CrossRef]
41. Mokhtarpoor, R.; Heinz, S.; Stoellinger, M. Dynamic unified RANS-LES simulations of high Reynolds number separated flows. *Phys. Fluids* **2016**, *28*, 095101/1–095101/36. [CrossRef]
42. Mokhtarpoor, R.; Heinz, S. Dynamic large eddy simulation: Stability via realizability. *Phys. Fluids* **2017**, *29*, 105104/1–105104/22. [CrossRef]
43. Heinz, S. The large eddy simulation capability of Reynolds-averaged Navier-Stokes equations: Analytical results. *Phys. Fluids* **2019**, *31*, 021702/1–021702/6. [CrossRef]
44. Heinz, S.; Mokhtarpoor, R.; Stoellinger, M. Theory-Based Reynolds-Averaged Navier-Stokes Equations with Large Eddy Simulation Capability for Separated Turbulent Flow Simulations. *Phys. Fluids* **2020**, *32*, 065102/1–065102/20. [CrossRef]
45. Heinz, S. A review of hybrid RANS-LES methods for turbulent flows: Concepts and applications. *Prog. Aerosp. Sci.* **2020**, *114*, 100597/1–100597/25. [CrossRef]
46. Heinz, S. The Continuous Eddy Simulation Capability of Velocity and Scalar Probability Density Function Equations for Turbulent Flows. *Phys. Fluids* **2021**, *33*, 025107/1–025107/13. [CrossRef]
47. Heinz, S.; Peinke, J.; Stoevesandt, B. Cutting-Edge Turbulence Simulation Methods for Wind Energy and Aerospace Problems. *Fluids* **2021**, *6*, 288/1–288/15. [CrossRef]
48. Heinz, S. Minimal error partially resolving simulation methods for turbulent flows: A dynamic machine learning approach. *Phys. Fluids* **2022**, *34*, 051705/1–051705/7. [CrossRef]
49. Verrall, D.P.; Read, W.W. A quasi-analytical approach to the advection–diffusion–reaction problem, using operator splitting. *Appl. Math. Model.* **2016**, *40*, 1588–1598. [CrossRef]
50. Huysmans, M.; Dassargues, A. Review of the use of Péclet numbers to determine the relative importance of advection and diffusion in low permeability environments. *Hydrogeol. J.* **2005**, *13*, 895–904. [CrossRef]
51. Phattaranawik, J.; Jiraratananon, R.; Fane, A.G.; Halim, C. Mass flux enhancement using spacer filled channels in direct contact membrane distillation. *J. Membr. Sci.* **2001**, *187*, 193–201. [CrossRef]
52. Yun, Y.; Wang, J.; Ma, R.; Fane, A.G. Effects of channel spacers on direct contact membrane distillation. *Desalin. Water Treat.* **2011**, *34*, 63–69. [CrossRef]
53. Tirabassi, T.; Buske, D.; Moreira, D.M.; Vilhena, M.T. A two-dimensional solution of the advection–diffusion equation with dry deposition to the ground. *J. Appl. Meteorol. Climatol.* **2008**, *47*, 2096–2104. [CrossRef]
54. McKee, S.; Dougall, E.A.; Mottram, N.J. Analytic solutions of a simple advection-diffusion model of an oxygen transfer device. *J. Math. Ind.* **2016**, *6*, 1–22. [CrossRef]
55. Bird, R.B.; Stewart, W.E.; Lightfoot, E.N. *Transport Phenomena*, 2nd ed.; John Wiley & Sons: New York, NY, USA, 2006.
56. Strauss, W.A. *Partial Differential Equations: An Introduction*; John Wiley & Sons: New York, NY, USA, 1992.

57. Heinz, S. *Mathematical Modeling;* Springer: Heidelberg, Gemany, 2011.
58. WolframAlpha. Available online: https://www.wolframalpha.com/input (accessed on 3 October 2022).

fluids

MDPI

Article

From Two-Equation Turbulence Models to Minimal Error Resolving Simulation Methods for Complex Turbulent Flows

Stefan Heinz

Department of Mathematics and Statistics, University of Wyoming, 1000 E. University Avenue, Laramie, WY 82071, USA; heinz@uwyo.edu

Abstract: Hybrid RANS-LES methods are supposed to provide major contributions to future turbulent flow simulations, in particular for reliable flow predictions under conditions where validation data are unavailable. However, existing hybrid RANS-LES methods suffer from essential problems. A solution to these problems is presented as a generalization of previously introduced continuous eddy simulation (CES) methods. These methods, obtained by relatively minor extensions of standard two-equation turbulence models, represent minimal error simulation methods. An essential observation presented here is that minimal error methods for incompressible flows can be extended to stratified and compressible flows, which opens the way to addressing relevant atmospheric science problems (mesoscale to microscale coupling) and aerospace problems (supersonic or hypersonic flow predictions). It is also reported that minimal error methods can provide valuable contributions to the design of consistent turbulence models under conditions of significant modeling uncertainties.

Keywords: computational fluid dynamics (CFD); large eddy simulation (LES); Reynolds-averaged Navier–Stokes (RANS) equations; hybrid RANS-LES methods

Citation: Heinz, S. From Two-Equation Turbulence Models to Minimal Error Resolving Simulation Methods for Complex Turbulent Flows. *Fluids* **2022**, *7*, 368. https://doi.org/10.3390/fluids7120368

Academic Editor: Mehrdad Massoudi

Received: 1 November 2022
Accepted: 21 November 2022
Published: 29 November 2022

Publisher's Note: MDPI stays neutral with regard to jurisdictional claims in published maps and institutional affiliations.

1. Introduction

The introduction of two-equation turbulence models in the frame of Reynolds-averaged Navier–Stokes (RANS) equations is seen to be a very relevant milestone of the development of simulation methods for turbulent flows [1,2]. The specific advantage of such methods is their much improved ability to provide proper scale information (the characteristic length scale of turbulent motions) for turbulent flow simulations. However, it is well known that such methods seriously suffer from their inability to reflect the physics of flows that cannot be properly modeled, as is the case for separated turbulent flows. Reliable simulations of such flows (as illustrated, for example, in Section 3) require the inclusion of flow resolution.

The first method used to overcome this problem is the introduction of flow-resolving simulation methods, as given by large eddy simulation (LES). The LES concept is actually simple. A much smaller characteristic length scale of turbulent motions is applied than that used in RANS. (Usually, the filter width Δ is used as the length scale.) The consequence is the need to use much finer computational grids than those applied in RANS. Thus, LES suffers from its huge computational requirements, especially in regard to simulations of wall-bounded turbulent flows at a high Reynolds number (Re). The practical consequence is that LES is inapplicable to many high Re flows that need to be considered. A concrete illustration of the dimension of this problem is given in Section 3.1.

The second method applied to overcome the fundamental shortcomings of RANS methods is the hybridization of RANS and LES (i.e., the development of hybrid RANS-LES) [3–5]. We have traditionally applied methods such as wall-modeled LES (WM-LES) [6–8] and detached eddy simulation (DES) [4,9–11], as well as a variety of other methods, including scale-adaptive simulation (SAS) methods [4,12,13], lattice Boltzmann (LB) methods [14], Reynolds stress-constrained LES (RSC-LES) [15], unified RANS-LES [16–22], partially averaged Navier–Stokes (PANS) [23], partially integrated transport modeling

(PITM) methods [24,25], and continuous eddy simulation (CES) methods [5,26–32]. The problem is that such hybrid RANS-LES methods suffer from fundamental problems. In particular, under conditions where validation data are unavailable, the problem is that such methods cannot reliably deal with simulations of flows that require flow resolution (see the explanations in Section 2). Thus, such methods face the same problem as RANS equations.

It has to be expected that this development will continue for a long time, as long as there is no clarification of what specifically causes the problems of existing RANS-LES methods, what the implied consequences are, and how it is possible to overcome these issues. The latter questions will be addressed here in Sections 2–4, respectively. Specific emphasis is placed on the explanation of the structure of novel minimal error hybrid simulation methods, which generalize CES methods (see the illustration in Figure 1). These methods may be seen as a relatively simple, mathematically exact modification of the originally introduced RANS two-equation turbulence models. A specific motivation is to significantly extend the corresponding methods developed thus far to the modeling of stratified and compressible flows. Section 5 describes applications of the novel methods presented thus far, and the conclusions are presented in Section 6.

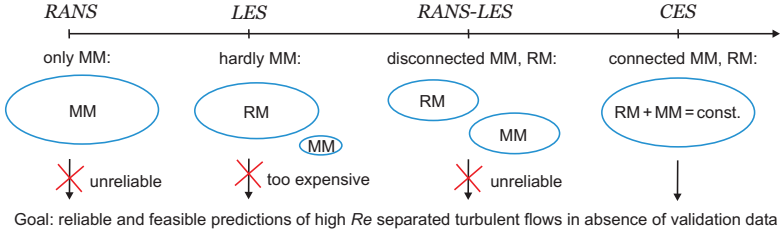

Figure 1. Abilities of computational methods in regard to reliable and feasible predictions of high *Re* flows that require flow resolution. Here, hybrid RANS-LES refers to popular methods, MM (RM) refers to modeled (resolved) motion, and CES refers to continuous eddy simulation.

2. Basic Problems of Existing Hybrid RANS-LES Methods

The most relevant problem $\mathcal{P}_1$ of hybrid RANS-LES is (particularly under conditions where validation data are unavailable) the lack of predictive power of flow simulations that require the inclusion of flow resolution. A physically correct simulation mechanism requires a swing between the amounts of resolved motion (fluctuations implied by the grid and *Re*) and the modeled motion imposed by the model equations. The model's contribution needs to decrease (increase) in response to a higher (lower) amount of resolved motion. However, in existing hybrid RANS-LES methods, the model does not receive (correct) information about the amount of resolved motion [32], which does not allow a (proper) model response. This implies the following: simulations for which validation data are hardly available (see the challenges described in Section 3) will involve a certain amount of resolved motion, which changes with the grid and *Re*. Then, if there is no guidance about an appropriate set-up of modeled motion, such simulations will produce random results in general. In particular, *Re* effects calculated on this basis cannot be considered to be reliable. By taking reference to Figure 1, an illustration of this problem is given in Figure 2.

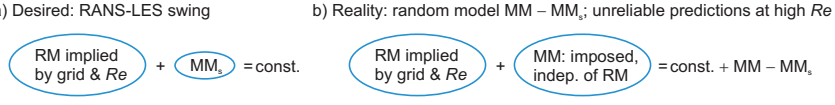

Figure 2. Problem $\mathcal{P}_1$ illustration. MM (RM) refers to modeled (resolved) motion, and MM_s is MM implied by swing. (**a**) Desired: RANS-LES swing. (**b**) Reality: random model MM – MM_s, with unreliable predictions at high *Re*.

The second problem $\mathcal{P}_2$ is closely related to $\mathcal{P}_1$. In many cases, we need reliable hybrid methods that are (1) applicable on coarse grids in almost RANS mode and (2) reliable hybrid methods that are applicable in almost resolving mode independent of the LES resolution requirements (which are hard to assess and control). The essential ingredients to properly deal with these requirements are (1) a stable dependence of the modeled length scale on the resolved length scale (the latter reflects fluctuations (i.e., this stable dependence of length scales ensures a stable involvement of fluctuations even under almost RANS conditions)) and (2) an appropriate representation of the characteristic LES length scale independent of the filter width Δ. Existing hybrid RANS-LES methods do not involve these ingredients (i.e., they cannot reliably cover these two regimes).

The third problem $\mathcal{P}_3$ of existing popular hybrid RANS-LES methods is the lack of guidance through exact theory, which has several consequences. Most hybrid RANS-LES methods were introduced on the basis of empirical reasoning, but some hybrid RANS-LES methods were introduced on the basis of sound theoretical concepts [5]. However, there is the question of which theoretical concept should be preferred. The lack of an answer to this question leads to a large variety of potential methods that can be used in applications. In addition, existing hybrid RANS-LES methods suffer from significant uncertainty in their predictions in the absence of validation data. For example, the WMLES, DES, and PANS results depend significantly on the model option settings [5]. Thus, it is usual practice to choose such settings to produce the best possible agreement with the available data. The search for the best model and best model set-up is demanding and time-consuming. Another problem is implied by the fact that hybrid RANS-LES methods include a RANS component, but such RANS equations can be significantly affected by modeling uncertainties, in particular for stratified and compressible flows.

3. Challenges

Concrete examples for the relevance of such RANS problems will be given next. In particular, Section 3.1 addresses the need to overcome the problem $\mathcal{P}_1$, whereas Sections 3.2 and 3.3 illustrate the requirement to also overcome the problems $\mathcal{P}_2$ and $\mathcal{P}_3$.

3.1. NASA's CFD 2030 Vision

There are many computational challenges related to incompressible flow, such as NASA's 2030 Computational Fluid Dynamics (CFD) Vision Report challenge to accomplish LES of a powered aircraft configuration across the full flight envelope [33–36]. This case focuses on the ability of CFD to simulate the flow about a complete aircraft geometry at the critical corners of the flight envelope including low-speed approach and takeoff conditions, transonic buffet, and possibly undergoing dynamic maneuvers, where aerodynamic performance is highly dependent on the prediction of turbulent flow phenomena such as smooth body separation and shock–boundary layer interaction [34]. A specific overview of the essential further steps required to deal with the challenge was provided by Slotnick and Mavriplis [37].

A specific indication of this challenge arises from the computational cost analysis offered by Probst et al. [35] and the Federal Republic of Germany's research centre for aeronautics and space (DLR), which considers the cost of resolving LES simulations of a full three-dimensional (3D) wing of an aircraft at flight Re. The conclusion of this conservative cost estimation was the following: Even with exclusive access to the largest existing cluster of Xeon-CPUs comparable to DLR's "Tianhe-2A" with almost 5 million cores, such a simulation would take around 650 years when extrapolated linearly. The computational cost required for addressing this partial problem clearly demonstrates the relevance of properly functioning hybrid RANS-LES models. In particular, as pointed out by Slotnick et al., progress toward this goal can be measured through the demonstration of effective hybrid RANS-LES and WMLES simulations with increasing degrees of modeled versus resolved near-wall turbulence structures with increasing geometric complexity [34].

However, existing hybrid RANS-LES methods face significant problems in this regard (see Section 2).

3.2. Atmospheric Mesoscale to Microscale Coupling

Another motivation for the development of exact hybrid RANS-LES models arises from the coupling of atmospheric mesoscale and microscale simulations (The term microscale simulation refers here to methods aiming at flow resolution, in contrast to flow modeling). The latter is an essential requirement to predict, for example, the performance of wind farms under the influence of large-scale weather processes. The usually related problems of such simulations are shown in Figure 3. A direct coupling of simulation methods as illustrated in Figure 3 is inappropriate, as the outer RANS simulation blocks the simulation of resolved motions in the inner domain, and (depending on the set-up) the abrupt decay of modeled motion in the transition region can provide inappropriate boundary conditions for the outer RANS simulation. Thus, it needs a transitional region between the two RANS and LES regions which applies relatively coarse grids. This implies a fundamental problem (referred to as the Terra Incognita problem by Wyngaard [38]): such simulations contradict basic RANS or LES principles, their value is at least questionable.

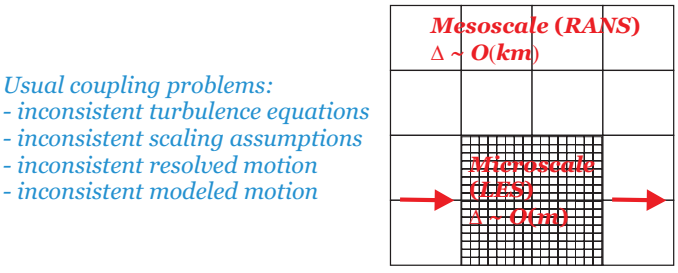

Figure 3. Typical problems related to the coupling of mesoscale (RANS) and microscale (LES) methods, where Δ refers to the characteristic grid size used in simulations.

There are obvious requirements for dealing with this problem. It needs hybrid RANS-LES equations that are able to cover both LES and RANS regimes (including the need that the length scale information used in the RANS is able to provide correct length scale information for LES independent of the LES filter width Δ). The most important requirement is the model's ability to respond correctly to the amount of resolved motion by appropriate changes of the model's contribution to the simulation. In other words, it needs minimal error hybrid RANS-LES models, which have this ability. Because of the coarse grids that usually need to be applied for atmospheric boundary layer (ABL) simulations, a specific aspect of the problem considered is the need for hybrid RANS-LES simulation methods that work stably in the almost RANS regime. As a matter of fact, it also needs a significant extension of previously developed methods: the inclusion of stratification effects, which is needed to simulate ABL processes. The latter is affected by modeling questions (see the discussion below Equation (22)). Thus, in addition to the need to deal with problem $\mathcal{P}_1$ described Section 2, it also requires solutions to problems $\mathcal{P}_2$ and $\mathcal{P}_3$ in this case.

3.3. High Angle of Attack Supersonic and Hypersonic Flow Predictions

The challenges described in Section 3.1 are significantly enhanced if aircraft are considered which fly at very high (supersonic or hypersonic) speeds. Commercial transports rarely fly at an angle of attack larger than 10°, but tactical aircraft and missiles can fly at much higher angles of attack [39]. Therefore, on top of the problems described in Section 3.1, additional challenges arise from the much bigger variety of flow separation induced by angle of attack variations and structural flow variations induced by compressibility [16]. Arguably, the biggest challenge of such flow simulations arises from the questionable

basis given by model equations for compressible flows. There is, for example, an ongoing debate about the structure of the dissipation rate equation considered in conjunction with the modeled kinetic energy equation (see [40,41] and the discussion below Equation (26)). It is worth noting that such RANS model issues are transferred to LES models via the required k transport equation [42]. Correspondingly, existing hybrid RANS-LES methods that combine RANS and LES components suffer from the same problem.

First, the conclusion is the same as in regard to the problems described in Section 3.1: it needs hybrid RANS-LES models which properly function under significant variations of resolved motion. Second, another question concerns the theoretical basis of such simulations. The possibility to develop minimal error hybrid methods depends on the structure of the model equations considered. This leads to the question of whether the minimal error design approach can provide valuable guidelines for the establishment of compressible flow models. Given the lack of a theoretical basis to deal directly with this issue, it is difficult to see which other approaches can help to overcome this relevant problem. Third, the development of exact hybrid RANS-LES models is needed because of the following. Different from the need for such methods described in Section 3.2 (which requires well-functioning methods under almost RANS conditions), for highly compressible flows, we need methods that can be used as resolving methods independent of the LES resolution requirements. This ability is is the most reliable way to deal with several flow physics questions (e.g., about structural compressibility effects) that need clarification. Thus, in addition to the need to address the problem $\mathcal{P}_1$ described in Section 2, we see here again the need for solutions to the problems $\mathcal{P}_2$ and $\mathcal{P}_3$.

4. Minimal Error Methods

Mimimal error hybrid simulation methods will be presented in the following three subsections in regard to incompressible flows, stratified flows, and compressible flows. It is worth noting that the presentation of such methods for incompressible flows in Section 4.1 provides the technical basis for extensions to the stratified and compressible flows in Sections 4.2 and 4.3, respectively.

4.1. Incompressible Flows

The design of minimal error methods will be described first for incompressible flows with respect to the widely used $k-\epsilon$ model (other turbulence models were considered elsewhere [32]). The suitability of this model is well known in the context of RANS equations. Evidence for the suitability of this model to also provide resolved motions on appropriate grids is given by corresponding PANS [23] and PITM [24,25] methods. The model considered is given by the incompressible continuity equation $\partial\widetilde{U}_i/\partial x_i = 0$ and the momentum equation

$$\frac{D\widetilde{U}_i}{Dt} = -\frac{\partial(\widetilde{p}/\rho + 2k/3)}{\partial x_i} + 2\frac{\partial(\nu+\nu_t)\widetilde{S}_{ik}}{\partial x_k}. \tag{1}$$

Here, $D/Dt = \partial/\partial t + \widetilde{U}_k\partial/\partial x_k$ denotes the filtered Lagrangian time derivative, and the sum convention is used throughout this paper. $\widetilde{U}_i$ refers to the i^{th} component of the spatially filtered velocity. We have here the filtered pressure $\widetilde{p}$, the constant mass density ρ, the modeled energy k, the constant kinematic viscosity ν, and the rate-of-strain tensor $\widetilde{S}_{ij} = (\partial\widetilde{U}_i/\partial x_j + \partial\widetilde{U}_j/\partial x_i)/2$. The modeled viscosity is given by $\nu_t = C_\mu k\tau = C_\mu k^2/\epsilon$. Here, ϵ is the modeled dissipation rate of the modeled energy k, $\tau = k/\epsilon$ is the dissipation time scale, and C_μ has a standard value $C_\mu = 0.09$. For k and ϵ, we consider the transport equations

$$\frac{Dk}{Dt} = P - \epsilon + D_k, \qquad \frac{D\epsilon}{Dt} = C_{\epsilon_1}\frac{\epsilon^2}{k}\left(\frac{P}{\epsilon} - \alpha\right) + D_\epsilon. \tag{2}$$

The diffusion terms reads $D_k = \partial[\nu_t\,\partial k/\partial x_j]/\partial x_j$, $D_\epsilon = \partial[(\nu_t/\sigma_\epsilon)\,\partial\epsilon/\partial x_j]/\partial x_j$, and $P = \nu_t S^2$ is the production of k, where $S = (2\widetilde{S}_{mn}\widetilde{S}_{nm})^{1/2}$ is the characteristic shear rate. C_{ϵ_1} is a constant with a standard value $C_{\epsilon_1} = 1.44$, and $\sigma_\epsilon = 1.3$. In RANS, $\alpha = C_{\epsilon_2}/C_{\epsilon_1}$, where $C_{\epsilon_2} = 1.92$ [2] implies $\alpha = 1.33$.

One possibility to hybridize Equation (2) is to consider a variable α^* (instead of a constant α) combined with an appropriate calculation of α^*:

$$\frac{Dk}{Dt} = P - \epsilon + D_k, \qquad \frac{D\epsilon}{Dt} = C_{\epsilon_1}\frac{\epsilon^2}{k}\Big(\frac{P}{\epsilon} - \alpha^*\Big) + D_\epsilon. \tag{3}$$

The diffusion terms are adjusted accordingly such that we have the expressions $D_k = \partial[\nu_t^*\,\partial k/\partial x_j]/\partial x_j$ and $D_\epsilon = \partial[(\nu_t^*/\sigma_\epsilon)\,\partial\epsilon/\partial x_j]/\partial x_j$. The setting of ν_t^* will be addressed below. The determination of α^* will be described by applying variational analysis. We consider variations of model parameters (α^*) and related variations of model variables (such as k and ϵ). The question is which model coefficient satisfies the variation equations implied by the turbulence model considered. The analysis follows the approach presented in [26]. The technical framework applied to derive these results was provided by an analysis of Friess et al. [11]. The significant difference with the latter findings is that Friess et al. focused on a different question: for given PANS/PITM-type relations between model coefficients and resolution indicators, they determined the equivalence criteria for hybrid methods based on other turbulence models. A relevant assumption made throughout this paper is that the energy partition ($\delta k/k$ and $\delta\epsilon/\epsilon$; see below) does not change in space and time. This assumption is not a restriction but a desired stability requirement, as it ensures that physically equivalent flow regions are equally resolved without significant oscillations of $\delta k/k$ or $\delta\epsilon/\epsilon$ [26–28].

In an exact analysis option $\mathcal{O}_1$, we set $\nu_t^* = \nu_{t,tot}$ in $D_k = \partial[\nu_t^*\,\partial k/\partial x_j]/\partial x_j$ and $D_\epsilon = \partial[(\nu_t^*/\sigma_\epsilon)\,\partial\epsilon/\partial x_j]/\partial x_j$ and introduce a hybridization error λ_1 as a residual of the ϵ equation:

$$\lambda_1 = C_{\epsilon_1}\frac{\epsilon^2}{k}\Big(\frac{P}{\epsilon} - \alpha_1^*\Big) + D_\epsilon - \frac{D\epsilon}{Dt} = C_{\epsilon_1}\frac{\epsilon^2}{k}\Big(\frac{1}{\epsilon}\frac{Dk}{Dt} + 1 - \frac{D_k}{\epsilon} - \alpha_1^*\Big) + D_\epsilon - \frac{D\epsilon}{Dt}, \tag{4}$$

where the k equation is used to replace P/ϵ in the previous expression. The subscript 1 refers to option $\mathcal{O}_1$. The normalized error reads as follows:

$$\frac{\lambda_1}{\epsilon} = \frac{C_{\epsilon_1}}{\tau}(1 - \alpha_1^*) + \frac{C_{\epsilon_1}}{k}\Big(\frac{Dk}{Dt} - D_k\Big) - \frac{1}{\epsilon}\Big(\frac{D\epsilon}{Dt} - D_\epsilon\Big). \tag{5}$$

Justification for the normalization applied can be obtained by taking the variation of λ_1 and combining the terms that involve λ_1. In the first order of variations (denoted by δ), we have

$$\frac{\delta(Dk/Dt)}{Dk/Dt} = \frac{\delta D_k}{D_k} = \frac{\delta k}{k}, \qquad \frac{\delta(D\epsilon/Dt)}{D\epsilon/Dt} = \frac{\delta D_\epsilon}{D_\epsilon} = \frac{\delta\epsilon}{\epsilon}. \tag{6}$$

Correspondingly, we find that the variation of the last two terms in Equation (5) disappears because of

$$\delta\Big[\frac{1}{k}\frac{Dk}{Dt}\Big] = \delta\Big[\frac{D_k}{k}\Big] = \delta\Big[\frac{1}{\epsilon}\frac{D\epsilon}{Dt}\Big] = \delta\Big[\frac{D_\epsilon}{\epsilon}\Big] = 0. \tag{7}$$

Thus, the variation of Equation (5) provides

$$\delta\Big(\frac{\lambda_1}{\epsilon}\Big) = \frac{C_{\epsilon_1}}{\tau}(1 - \alpha_1^*)\Big[\frac{\delta\alpha_1^*}{\alpha_1^* - 1} - \frac{\delta\tau}{\tau}\Big]. \tag{8}$$

An extremal error is found by setting the first variation equal to zero:

$$\frac{\delta\alpha_1^*}{\alpha_1^* - 1} = \frac{\delta\tau}{\tau}. \tag{9}$$

This equation can be integrated from the RANS state to a state with a certain level of resolved motion $\int_{\alpha}^{\alpha_1^*} dx/(x-1) = \int_{\tau_{tot}}^{\tau} dy/y$. We obtain it in this way:

$$\alpha_1^* = 1 + \tau_+(\alpha - 1), \tag{10}$$

where $\tau_+ = \tau/\tau_{tot}$ refers to the modeled-to-total time scale ratio, which is calculated as L_+ (see the explanations in regard to option $\mathcal{O}_2$ below). For all models considered in this paper, we find a zero second variation, and we need to ask whether λ_1 provides a minimum or maximum error. The results were equal to the variational results obtained by considering $\lambda_1 = 0$; that is, the analysis presented implies minimal error models.

A different analysis option $\mathcal{O}_2$ is as follows. The analysis option $\mathcal{O}_1$ is exact, but the disadvantage is the need to involve $\nu_{t,tot}$ in the equations solved in the simulations. The latter is avoided in analysis option $\mathcal{O}_2$, where the substantial derivatives Dk/Dt and $D\epsilon/Dt$ are neglected in regard to the derivation of model coefficients. This approach appears to be well justified for most applications. It was found to work very well in previous applications to periodic hill flows [27]. Correspondingly, we consider (the subscript 2 refers to the analysis option $\mathcal{O}_2$) $\nu_t^* = \nu_t$ in D_k and D_ϵ in conjunction with the hybridization error:

$$\lambda_2 = C_{\epsilon_1}\frac{\epsilon^2}{k}\Big(\frac{P}{\epsilon} - \alpha_2^*\Big) + D_\epsilon = C_{\epsilon_1}\frac{\epsilon^2}{k}\Big(1 - \frac{D_k}{\epsilon} - \alpha_2^*\Big) + D_\epsilon, \tag{11}$$

where the k equation is used again to replace P/ϵ in the previous expression. The normalized error reads as follows:

$$\frac{\lambda_2}{k^2} = \frac{C_{\epsilon_1}}{L^2}\Big(1 - \alpha_2^*\Big) - C_{\epsilon_1}\frac{\epsilon D_k}{k^3} + \frac{D_\epsilon}{k^2}, \tag{12}$$

where the modeled length scale $L = k^{3/2}/\epsilon$ is introduced in the first term on the right-hand side (RHS). Because of $\nu_t^* = \nu_t$, we find in the option $\mathcal{O}_2$ in the first order of variations the relations

$$\delta D_k/D_k = 3\delta k/k - \delta\epsilon/\epsilon, \qquad \delta D_\epsilon/D_\epsilon = 2\delta k/k, \tag{13}$$

which imply that the variation of the last two terms in Equation (12) disappears because of

$$\delta\Big[\frac{\epsilon D_k}{k^3}\Big] = \frac{\epsilon D_k}{k^3}\Big[\frac{\delta D_k}{D_k} + \frac{\delta\epsilon}{\epsilon} - 3\frac{\delta k}{k}\Big] = 0, \qquad \delta\Big[\frac{D_\epsilon}{k^2}\Big] = \frac{D_\epsilon}{k^2}\Big[\frac{\delta D_\epsilon}{D_\epsilon} - 2\frac{\delta k}{k}\Big] = 0. \tag{14}$$

Thus, the variation of Equation (12) provides

$$\delta\Big[\frac{\lambda_2}{k^2}\Big] = \frac{C_{\epsilon_1}}{L^2}\Big(1 - \alpha_2^*\Big)\Big[\frac{\alpha_2^*}{\alpha_2^* - 1} - \frac{\delta L^2}{L^2}\Big]. \tag{15}$$

An extremal error is found by setting the first variation equal to zero:

$$\frac{\delta\alpha_2^*}{\alpha_2^* - 1} = \frac{\delta L^2}{L^2}. \tag{16}$$

This equation can be integrated from the RANS state to a state with a certain level of resolved motion: $\int_{\alpha}^{\alpha_2^*} dx/(x-1) = \int_{L_{tot}^2}^{L^2} dy/y$. We obtain in this way

$$\alpha_2^* = 1 + L_+^2(\alpha - 1), \tag{17}$$

where $L_+ = L/L_{tot}$ refers to the modeled-to-total length scale ratio. A relevant technical detail is the calculation of L_+ (τ_+ is calculated correspondingly). The turbulence length scale resolution ratio $L_+ = L/L_{tot}$ involves the modeled (L) and total contributions (L_{tot}) [26]. The modeled contribution is calculated by $L = \langle k\rangle^{3/2}/\langle\epsilon\rangle$, where the brackets refer to the averaging over time. The total length scale is calculated correspondingly by

$L_{tot} = k_{tot}^{3/2}/\epsilon_{tot}$. Corresponding to $k_{tot} = \langle k \rangle + k_{res}$, ϵ_{tot} is the sum of the modeled and resolved contributions $\epsilon_{tot} = \langle \epsilon \rangle + \epsilon_{res}$. Here, the resolved contributions are calculated by $k_{res} = \left(\langle \widetilde{U}_i \widetilde{U}_i \rangle - \langle \widetilde{U}_i \rangle \langle \widetilde{U}_i \rangle \right)/2$, $\epsilon_{res} = \nu \left(\langle \partial \widetilde{U}_i / \partial x_j \partial \widetilde{U}_i / \partial x_j \rangle - \langle \partial \widetilde{U}_i / \partial x_j \rangle \langle \partial \widetilde{U}_i / \partial x_j \rangle \right)$.

The consideration of Equation (3) is one possibility to hybridize the equations considered. Another possibility is to consider

$$\frac{Dk}{Dt} = P - \psi_\alpha \epsilon + D_k, \qquad \frac{D\epsilon}{Dt} = C_{\epsilon_1} \frac{\epsilon^2}{k} \left(\frac{P}{\epsilon} - \alpha \right) + D_\epsilon, \tag{18}$$

where the dissipation ϵ in the k equation is modified by introducing the unknown ψ_α. By following the analysis of Equation (3), we consider the hybridization error λ_1 in analysis option $\mathcal{O}_1$:

$$\lambda_1 = C_{\epsilon_1} \frac{\epsilon^2}{k} \left(\frac{P}{\epsilon} - \alpha_1 \right) + D_\epsilon - \frac{D\epsilon}{Dt} = C_{\epsilon_1} \frac{\epsilon^2}{k} \left(\frac{1}{\epsilon} \frac{Dk}{Dt} + \psi_\alpha - \frac{D_k}{\epsilon} - \alpha_1 \right) + D_\epsilon - \frac{D\epsilon}{Dt}, \tag{19}$$

where the k equation is used to replace P/ϵ in the previous expression. The comparison with Equation (4) shows the equivalence of both approaches, provided that $\alpha^* = 1 + \alpha - \psi_\alpha$. The comparison of the corresponding λ_2 in analysis option $\mathcal{O}_2$ leads to the same conclusion.

4.2. Stratified Flows

In regard to stratified flows, we begin with describing the typical structure of an ABL microscale model [43]. We have the incompressible continuity equation $\partial \widetilde{U}_i / \partial x_i = 0$, and the momentum and potential temperature equations read as follows:

$$\frac{D\widetilde{U}_i}{Dt} = -\frac{\partial (\widetilde{p}/\rho + 2k/3)}{\partial x_i} + 2 \frac{\partial (\nu + \nu_t) \widetilde{S}_{ik}}{\partial x_k} - \epsilon_{ikn} f_k \widetilde{U}_n - g_i, \tag{20}$$

$$\frac{D\widetilde{\Theta}}{Dt} = \frac{\partial}{\partial x_k} \left[\left(\frac{\nu}{Pr} + \frac{\nu_t}{Pr_t} \right) \frac{\partial \widetilde{\Theta}}{\partial x_k} \right] + S_\theta. \tag{21}$$

Here, $\widetilde{\Theta}$ is the potential temperature. In addition, g_i is the gravity vector, f_k is the Coriolis vector, and ϵ_{ijk} is the Levi-Civita symbol. In the $\widetilde{\Theta}$ equation, we have the molecular and turbulent heat diffusivities ν/Pr and ν_t/Pr_t, where Pr and Pr_t are the Prandtl number and turbulent Prandtl number, respectively. The effect of radiation can be taken into account via the source term S_θ. Equations (20) and (21) are combined with the $k - \epsilon$ model [43]:

$$\frac{Dk}{Dt} = P + P_b - \epsilon + D_k, \qquad \frac{D\epsilon}{Dt} = C_{\epsilon_1} \frac{\epsilon^2}{k} \left(\frac{P}{\epsilon} + C_b \frac{P_b}{\epsilon} - \alpha \right) + D_\epsilon. \tag{22}$$

The diffusion terms read $D_k = \partial [\nu_t \, \partial k / \partial x_j] / \partial x_j$ and $D_\epsilon = \partial [(\nu_t/\sigma_\epsilon) \, \partial \epsilon / \partial x_j] / \partial x_j$, and $P = \nu_t S^2$ is the production of k. In regard to Equation (2), C_{ϵ_1} has a standard value $C_{\epsilon_1} = 1.44$, $\sigma_\epsilon = 1.3$, and $\alpha = C_{\epsilon_2}/C_{\epsilon_1} = 1.33$ in RANS equations. The effect of buoyancy is reflected by the buoyancy production $P_b = -RiP/Pr_t$, where $Ri = \beta g \partial \widetilde{\Theta} / \partial x_3 S^{-2}$ is the gradient Richardson number [16,44–46]. The buoyancy coefficient C_b is characterized by a large uncertainty: its values range from -1.4 to $+1.45$ [47,48], including $C_b = 1$ [49]. For simplicity, we assume $C_b = 1$ in the following, in line with the recommendation of Mellor and Yamada [49].

Corresponding mesoscale models actually represent equivalent or simplified versions of the microscale model given by Equations (20)–(22). A hierarchy of model versions can be considered [50–54]. Several options will be considered in the following with the understanding that the model version considered is applied to both the microscale and mesoscale.

The first option is referred to as CES-MIME. CES stands for continuous eddy simulation, and MIME stands for microscale-mesoscale model, meaning that the model can be continuously applied through microscales and mesoscales. This model is equivalent to Equations (20)–(22). Although the use of this model on the mesoscale is not the common

choice, there exist several applications of corresponding models [55–59]. One possibility for hybridizing this model is to consider a variable α^* (instead of a constant α) combined with an appropriate calculation of α^*. Hence, in conjunction with $C_b = 1$, we consider

$$\frac{Dk}{Dt} = P + P_b - \epsilon + D_k, \qquad \frac{D\epsilon}{Dt} = C_{\epsilon_1}\frac{\epsilon^2}{k}\Big(\frac{P}{\epsilon} + \frac{P_b}{\epsilon} - \alpha^*\Big) + D_\epsilon. \tag{23}$$

We introduce the hybridization error according to the analysis option $\mathcal{O}_1$ in conjunction with replacing ν_t in $D_k = \partial[\nu_t\,\partial k/\partial x_j]/\partial x_j$ and $D_\epsilon = \partial[(\nu_t/\sigma_\epsilon)\,\partial\epsilon/\partial x_j]/\partial x_j$ by $\nu_{t,tot}$:

$$\lambda_1 = C_{\epsilon_1}\frac{\epsilon^2}{k}(p - \alpha_1^*) + D_\epsilon - \frac{D\epsilon}{Dt} = C_{\epsilon_1}\frac{\epsilon^2}{k}\Big(\frac{1}{\epsilon}\frac{Dk}{Dt} + 1 - \frac{D_k}{\epsilon} - \alpha_1^*\Big) + D_\epsilon - \frac{D\epsilon}{Dt}, \tag{24}$$

where the abbreviation $p = (P + P_b)/\epsilon$ is used. It turns out that this equation is equal to Equation (4), which means that the implications presented above are recovered. The same conclusion is obtained in regard to the analysis according to option $\mathcal{O}_2$, where ν_t is not replaced by $\nu_{t,tot}$ in the diffusion terms. Another possibility for hybridizing the CES-MIME model version is to hybridize the k equation via introducing ψ_α. This means we consider

$$\frac{Dk}{Dt} = P + P_b - \psi_\alpha\epsilon + D_k, \qquad \frac{D\epsilon}{Dt} = C_{\epsilon_1}\frac{\epsilon^2}{k}\Big(\frac{P}{\epsilon} + \frac{P_b}{\epsilon} - \alpha\Big) + D_\epsilon. \tag{25}$$

The same analysis as that presented in Section 4.1 leads to the conclusion that this approach represents an equivalent approach as long as the model coefficients are properly related by $\alpha^* = 1 + \alpha - \psi_\alpha$.

The second option is the CES-MIME-AE model. This model is a reduced version of CES-MIME, where ϵ in Equations (20)–(22) is provided by an algebraic expression (AE refers to an algebraic ϵ equation). This option is, for example, applied in conjunction with Mellor and Yamada's level 2.5 closure model [49] (see also the last paragraph of Section 4.2), which is a standard model applied for mesoscale simulations [60]. A usually applied ϵ expression reads $\epsilon = C_\mu k^{3/2}/(\sqrt{2}S_m l)$. Here, S_m is a stability function, and l is a length scale that is algebraically provided [43]. A corresponding analysis of the CES-MIME-AE model version is presented in Appendix A.

A third option is the CES-MIME-HH set-up, which is a reduced version of either the CES-MIME or CES-MIME-AE model where horizontal transport processes are neglected [49,61,62] (HH refers to horizontal homogeneity of the ABL). With respect to this model option, the analysis in Section 4.2 shows that this option is independent of the hybridization, and the hybridization functions α^* and ψ_α are unaffected. Given that the neglect of horizontal transport is often considered to be appropriate in a mesoscale model, the consequence of this simplification will be a discontinuous transition between mesoscale and microscale models, (Usually, the neglect of horizontal transport processes will be at least questionable for microscale simulations.) but this assumption will not hamper the combined model's ability to maintain a meaningful balance of resolved and modeled motions.

Another often-applied approximation is to replace the turbulent viscosity ν_t with algebraic expressions depending on the vertical coordinate and stability. In this case, there is no need for a k or an ϵ equation [43]. However, this modeling assumes that the turbulent viscosity is always fully modeled in terms of RANS-type variables (total variables). This concept does not provide a meaningful basis for hybridization. Thus, this option is not considered here.

In regard to the developments presented here, it is worth noting that the applicability of these methods is not limited to eddy viscosity models, applied for simplicity. The same approach can be applied, for example, in the frame of Reynolds stress models, as given by Mellor and Yamada's closure model [49,60] (see the explanations given in Appendix B). A Reynolds stress model is a k equation extended by Reynolds stress anisotropy and combined with a scale model (usually for ϵ), which provides scale information for the Reynolds stress model via $\tau = k/\epsilon$ or $L = k^{3/2}/\epsilon$. If an ϵ transport equation is involved,

then the hybridization can be driven through the ϵ equation as described above. If an algebraic ϵ expression is applied, then the hybridization can be driven by the k equation implied by the Reynolds stress model as described above. This case is usually considered in Mellor and Yamada's closure model because the original Mellor and Yamada master length scale formulation provides inappropriate results [60].

4.3. Compressible Flows

Compressible flow modeling will be addressed by considering the spatially filtered mass density $\bar{\rho}$, and tilde variables will be used to reflect the mass density-weighted variables by following the notation used above. The continuity and momentum equations considered are then given by

$$\frac{D\bar{\rho}}{Dt} = -\bar{\rho}\widetilde{S}_{kk}, \qquad \frac{D\widetilde{U}_i}{Dt} = -\frac{1}{\bar{\rho}}\frac{\partial(\widetilde{p} + 2\bar{\rho}k/3)}{\partial x_i} + \frac{2}{\bar{\rho}}\frac{\partial\bar{\rho}(\nu + \nu_t)\widetilde{S}_{ik}}{\partial x_k}. \tag{26}$$

Here, $D/Dt = \partial/\partial t + \widetilde{U}_k\partial/\partial x_k$, and the modeled viscosity is given by $\nu_t = C_\mu k\tau = C_\mu k^2/\epsilon$. Many different methods have been applied to provide k and ϵ for compressible flows [16,40,41,63–65]. We follow the usual approach of involving explicit compressibility corrections (the dilatational dissipation ϵ_d and pressure dilation Π_d) only in the k equation [63–65]:

$$\frac{Dk}{Dt} = P + \frac{\Pi_d}{\bar{\rho}} - \epsilon - \epsilon_d + D_k, \qquad \frac{D\epsilon}{Dt} = C_{\epsilon_1}\frac{\epsilon^2}{k}\Big(\frac{P}{\epsilon} - \alpha\Big) + D_\epsilon. \tag{27}$$

The production is given here by $P = \nu_t S^2 - (2k/3)\widetilde{S}_{nn}$. The usual models for ϵ_d and Π_d, which are not applied because there is no need to do so, are $\epsilon_d = \alpha_1 M_t^2\epsilon$ and $\Pi_d/\bar{\rho} = -\alpha_2 M_t^2 P + \alpha_3 M_t^2\epsilon$ [63], where α_1, α_2 , and α_3 are the model parameters and the turbulence Mach number is defined by $M_t^2 = 2k/a^2$, where a refers to the speed of sound.

For simplicity, we only consider the option to hybridize the k equation via introducing ψ_α in the following. This means we consider

$$\frac{Dk}{Dt} = P - (\psi_\alpha + p_d)\epsilon + D_k, \qquad \frac{D\epsilon}{Dt} = C_{\epsilon_1}\frac{\epsilon^2}{k}\Big(\frac{P}{\epsilon} - \alpha\Big) + D_\epsilon, \tag{28}$$

where $p_d = [\epsilon_d - \Pi_d/\bar{\rho}]/\epsilon$, the production to dissipation ratio due to dilatational compressibility effects, is introduced as an abbreviation. These equations are equivalent to Equation (18), where ψ_α is replaced with $\psi_\alpha + p_d$. The same analysis presented above implies that $\alpha^* = 1 + p_{d,tot} + \alpha - \psi_\alpha - p_d$, where $p_{d,tot}$ refers to the total value of p_d. In the two options $\mathcal{O}_1$ and $\mathcal{O}_2$ considered, we have $\alpha_1^* = 1 + \tau_+(\alpha - 1)$ and $\alpha_2^* = 1 + L_+^2(\alpha - 1)$ (see Equation (10) and Equation (17)). Hence, the incompressible flow models presented above can be easily extended to the compressible flow.

5. Applications: Periodic Hill Flow Simulations

In regard to the problems $\mathcal{P}_1$, $\mathcal{P}_2$, and $\mathcal{P}_3$ of the hybrid RANS-LES model described in Section 2, we observe the following. The analysis presented in Section 4 provides the desired guideline with respect to problem $\mathcal{P}_3$. For several turbulence model structures and hybridization types, the use of the minimal error technique provides exactly one optimal computational method. A question that is unaddressed in this way is about the computational performance differences of different model structures and hybridization options. The analysis presented in Section 4 also provides a solution to the problem $\mathcal{P}_2$. With respect to the almost RANS regime, the relationship $\alpha_2^* = 1 + L_+^2(\alpha - 1)$, (for an example, see Equation (17)), implies a stable dependence of the modeled length scale $L = k^{3/2}/\epsilon$ calculated via the $k - \epsilon$ model on the resolved length scale involved in the definition of L_+. In regard to the almost LES regime, the modeled length scale $L = k^{3/2}/\epsilon$ calculated via the $k - \epsilon$ model can serve as an LES length scale independent of the LES filter

width Δ (i.e., the usual LES resolution requirement that Δ needs to be sufficiently small does not apply). However, an answer to the question of whether the methods presented in Section 4 can also overcome the problem $\mathcal{P}_1$, which requires a well functional "RANS-LES swing", requires computational evidence.

The latter question was addressed by the simulations of periodic hill flows reported in [27]. Figure 4 illustrates the flow configuration considered, a channel flow (flowing from the left to the right) with periodic restrictions (hills). This considered flow configuration is often used for the evaluation of turbulence models. It creates a variety of relevant flow features such as separation, recirculation, and natural reattachment. The hill crest is located at $(x/h, y/h) = (0, 1)$. The height h and bulk velocity U_b are used as scaling variables, they define Re. The simulations were performed by using the OpenFOAM CFD Toolbox [66]. A CES model formulation corresponding to option $\mathcal{O}_2$ was applied, including the comparison of different hybridization options. A range of Re and grids was considered. Re ranged from $Re = 37,000$ to $Re = 500,000$. The data for model validation were only available for the $Re = 37K$ case [67]. Several grids were used, with the finest (coarsest) grid applied having $500,000$ ($120,000$) grid points. The grids were referred to as G_{500} and G_{120}, respectively. An almost complete flow resolution was accomplished at $Re = 37K$ using the finest G_{500} grid, and an almost RANS simulation was accomplished at $Re = 500,000$ using the coarsest grid (G_{120}).

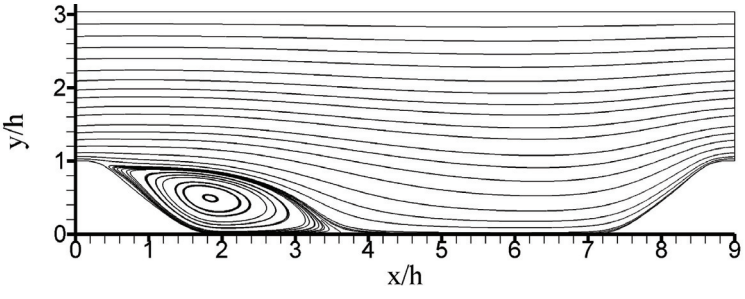

Figure 4. Periodic hill flow velocity streamlines obtained by CES at $Re = 37,000$ on G_{500} (G_{500} refers to $500,000$ grid points). Reprinted with permission from [27]. Copyright 2020 AIP Publishing.

The observations obtained by these simulations are the following:

- Problem $\mathcal{P}_1$: The most relevant fact is the conclusion that the "RANS-LES swing" was fully functional. There was a stable redistribution between the resolved and modeled motions, depending on the grid and Re variations. In particular, a spatially relatively uniform mode variation reflected by the resolution indicator L_+ was found.
- Problem $\mathcal{P}_2$: In regard to the almost RANS regime, a stable generation mechanism of turbulent velocity fluctuations was observed. In particular, fluctuations were not extinguished even for very high Re values and very coarse grids. In regard to the almost LES regime, it was found that the characteristic length scale provided by CES, which was independent of the LES filter width Δ, properly worked. The LES simulations performed on this basis (with $500,000$ grid points) showed better performance than almost resolving LES using 20 million grid points.
- Problem $\mathcal{P}_3$: Another relevant observation is that different model hybridization options worked equally well; there were hardly differences regarding the simulation results obtained. This fact confirms the applicability of the CES approach to at least several turbulence model structures, as long as the "RANS-LES swing" is functional.

6. Summary

The current stagnation of the development of computational simulation methods for turbulent flows was addressed here by clarification of what specifically causes the problems of existing RANS-LES methods, what the implied consequences are, and how it is possible

to overcome these issues (see Sections 2–4). The facts presented here can be summarized as follows:

1. The minimal error approach presented here (which generalizes CES methods) minimizes the hybridization error among many other hybrid RANS-LES methods. It provides a theoretical solution to the problems $\mathcal{P}_1$, $\mathcal{P}_2$, and $\mathcal{P}_3$. Applications demonstrated the excellent performance of such simulation methods (see Section 5). It is essential to note that these methods represent a relatively minor extension of standard two-equation turbulence models.
2. An essential observation presented here is that minimal error methods for incompressible flows [32] can be extended to stratified and compressible flows. This opens the way to addressing relevant atmospheric science problems (mesoscale to microscale coupling) and aerospace problems (supersonic and hypersonic flow predictions) (see the discussions in Section 3). It was argued that such simulations need, in particular, the ability to perform reliable predictions under almost RANS and almost LES conditions.
3. Hybrid RANS-LES models are based on RANS equations, and such RANS equations face relevant modeling questions, particularly for stratified and compressible flows. Minimal error methods are in line with standard modeling options, and they exclude many other options. Thus, minimal error methods can provide valuable contributions to the design of consistent turbulence models. In regard to compressible flows, models are excluded that include a variety of compressibility effects in the ϵ equation [40,41]. In regard to stratified flows, a welcome byproduct of considering the hybridization of the closure model of Mellor and Yamada [49] (see Appendix B) is the correct specification of the length scales involved, which is seen as a major issue of such simulations.
4. From a more general view point, the relevance of the minimal error methods presented is the following. We need reliable methods to simulate high Re flows. LES models and experiments are restricted by resolution requirements, and popular hybrid RANS-LES models are known to be unreliable. In this situation, minimal error methods can provide an error-free simulation contribution in response to the flow resolution (see the illustration in Figure 2). The latter is the essential requirement for providing reliable predictions under conditions where validation data are unavailable.

Funding: This work received no external funding.

Institutional Review Board Statement: Not applicable.

Informed Consent Statement: Not applicable.

Data Availability Statement: Not applicable

Acknowledgments: I would like to acknowledge support from the National Science Foundation (AGS, Grant No. 2137351, with N. Anderson as Technical Officer) and support from the Hanse-Wissenschaftskolleg (Delmenhorst, Germany, with M. Kastner as Technical Officer). This work was supported by the Wyoming NASA Space Grant Consortium (NASA Grant No. 80NSSC20M0113) and the University of Wyoming School of Computing (Wyoming Innovation Partnership grant).

Conflicts of Interest: The authors declare no conflict of interest.

Appendix A

Let us consider the CES-MIME-AE model, which makes use of an algebraic expression for ϵ instead of using the transport equation considered in the CES-MIME version. Because of the lack of an ϵ transport equation, the basis for this approach is given by the k equation

$$\frac{Dk}{Dt} = P + P_b - \psi_\alpha \epsilon + D_k = (p - \psi_\alpha)\epsilon + D_k. \tag{A1}$$

Here, ψ_α appears as an unknown function considered for setting up the hybridization, and the abbreviation $p = (P + P_b)/\epsilon$ was used. Then, the latter equation can be written:

$$p - \psi_\alpha = \frac{1}{\epsilon}\frac{Dk}{Dt} - \frac{D_k}{\epsilon}. \tag{A2}$$

In an exact analysis option $\mathcal{O}_1$, we have $D_k = \partial[\nu_{t,tot}\,\partial k/\partial x_j]/\partial x_j$, and Dk/Dt is involved. The hybridization error λ_1 divided by k reads as follows:

$$\frac{\lambda_1}{k} = \frac{\psi_\alpha - p}{k} + \frac{1}{k\epsilon}\Big(\frac{Dk}{Dt} - D_k\Big). \tag{A3}$$

Here, ϵ is unaffected by variations. This is a requirement, the assumption of an algebraic model is equivalent to assuming that ϵ is given by its total value. Equation (7) applies, leading to the fact that the variation in the last two terms on the RHS disappears. The variation of Equation (A3) then implies

$$\delta\Big[\frac{\lambda_1}{k}\Big] = \frac{\psi_\alpha - p}{k}\Big(\frac{\delta(\psi_\alpha - p)}{\psi_\alpha - p} - \frac{\delta k}{k}\Big). \tag{A4}$$

By setting the first variation equal to zero, we have

$$\frac{\delta(\psi_\alpha - p)}{\psi_\alpha - p} = \frac{\delta k}{k}. \tag{A5}$$

We can integrate from the RANS state to a state with a certain level of resolution to obtain

$$\psi_\alpha = p + k_+(1 - p_{tot}), \tag{A6}$$

where p_{tot} refers to the total value of p (including contributions such as k_{tot} and ϵ_{tot}).

In the analysis option $\mathcal{O}_2$, we have $D_k = \partial[\nu_t\,\partial k/\partial x_j]/\partial x_j$, and Dk/Dt is not involved. The hybridization error λ_2 divided by k^3 reads as follows:

$$\frac{\lambda_2}{k^3} = \frac{\psi_\alpha - p}{k^3} - \frac{D_k}{k^3\epsilon}. \tag{A7}$$

According to Equation (14), the variation of the last term on the RHS disappears, and we obtain the variational equation

$$\delta\Big[\frac{\lambda_2}{k^3}\Big] = \frac{\psi_\alpha - p}{k^3}\Big(\frac{\delta(\psi_\alpha - p)}{\psi_\alpha - p} - 3\frac{\delta k}{k}\Big). \tag{A8}$$

We set the first variation equal to zero and obtain

$$\frac{\delta(\psi_\alpha - p)}{\psi_\alpha - p} = 3\frac{\delta k}{k} \tag{A9}$$

Then, we integrate from the RANS state to a state with a certain level of resolution to obtain

$$\psi_\alpha = p + k_+^3(1 - p_{tot}). \tag{A10}$$

Appendix B

We consider a usual, incompressible flow Lagrangian stochastic particle model for the position x_i^*, velocity U_i^*, and scalar (potential temperature) Θ^* [16]. We have $dx_i^*/dt = U_i^*$ combined with

$$\frac{dU_i^*}{dt} = \widetilde{\Gamma}_i - \Big[\frac{c_1^*}{2\tau}\delta_{ik} - c_2^*\frac{\partial\widetilde{U}_i}{\partial x_k}\Big]\big(U_k^* - \widetilde{U}_k\big) + F_i + (C_0\epsilon)^{1/2}\frac{dW_i}{dt},$$

$$\frac{d\Theta^*}{dt} = \widetilde{\Omega} - \frac{c^*_{\theta 1}}{\tau_\theta}\left(\Theta^* - \widetilde{\Theta}\right). \tag{A11}$$

The terms $\widetilde{\Gamma}_i$ and $\widetilde{\Omega}$ ensure consistency with the mean velocity and potential temperature equations, respectively [16]. With respect to the velocity field, we applied the usual Rotta assumption. In regard to the scalar field, we excluded a stochastic source term and specified the scalar mixing frequency with $c^*_{\theta 1}/\tau_\theta$. This mixing frequency is not assumed to be proportional to τ^{-1} (τ_θ refers to the scalar dissipation time scale and is related to the scalar dissipation rate by $\epsilon_\theta = k_\theta/\tau_\theta$, where $k_\theta = \widetilde{\theta^2}/2$). In addition, dW_i/dt refers to the derivative of a Wiener process [16], and c^*_1, c^*_2, $c^*_{\theta 1}$, and C_0 are the model parameters. The body forces involved are represented by $F_i = -\epsilon_{ikn} f_k U^*_n - \beta_\theta g_i \Theta^*$. Here, β_θ is the coefficient of thermal expansion (the inverse reference temperature).

The particle model Equation (A11) implies the following exact Reynolds stress equations [16,28]:

$$\begin{aligned}
&\frac{D\widetilde{u_i u_j}}{Dt} + \frac{\partial \tau_{ijk}}{\partial x_k} - P_{ij} + \beta_\theta\left(g_j\widetilde{u_i\theta} + g_i\widetilde{u_j\theta}\right) + f_k\left(\epsilon_{jkn}\widetilde{u_n u_i} + \epsilon_{ikn}\widetilde{u_n u_j}\right)\\
&= -\frac{c^*_1}{\tau}\left(\widetilde{u_i u_j} - \frac{2k}{3}\delta_{ij}\right) + 2c^*_2\left(\frac{\partial \widetilde{U}_i}{\partial x_k}\widetilde{u_k u_j} + \frac{P_*}{3}\delta_{ij}\right) - \frac{2}{3}\left(c^*_1 + c^*_2\frac{P_*}{\epsilon} - \frac{3}{2}C_0\right)\epsilon\delta_{ij},
\end{aligned} \tag{A12}$$

$$\frac{D\widetilde{u_i\theta}}{Dt} + \frac{\partial \tau_{ik\theta}}{\partial x_k} - P_{i\theta} + \beta_\theta g_i\widetilde{\theta^2} + f_k\epsilon_{ikn}\widetilde{u_n\theta} = -\left[\frac{c^*_1}{2\tau} + \frac{c^*_{\theta 1}}{\tau_\theta}\right]\widetilde{u_i\theta} + c^*_2\widetilde{u_k\theta}\frac{\partial \widetilde{U}_i}{\partial x_k}, \tag{A13}$$

$$\frac{D\widetilde{\theta^2}}{Dt} + \frac{\partial \tau_{k\theta\theta}}{\partial x_k} - 2P_\theta = -2\frac{c^*_{\theta 1}}{\tau_\theta}\widetilde{\theta^2}. \tag{A14}$$

We have here $P_* = -\widetilde{u_k u_n}\partial\widetilde{U}_n/\partial x_k$, where τ_{ijk}, $\tau_{ij\theta}$, and $\tau_{i\theta\theta}$ refer to the corresponding triple correlations, and we introduce the abbreviations

$$P_{ij} = -\widetilde{u_k u_j}\frac{\partial \widetilde{U}_i}{\partial x_k} - \widetilde{u_k u_i}\frac{\partial \widetilde{U}_j}{\partial x_k}, \quad P_{i\theta} = -\widetilde{u_i u_k}\frac{\partial \widetilde{\Theta}}{\partial x_k} - \widetilde{u_k\theta}\frac{\partial \widetilde{U}_i}{\partial x_k}, \quad P_\theta = -\widetilde{u_k\theta}\frac{\partial \widetilde{\Theta}}{\partial x_k}. \tag{A15}$$

The consistency of these equations with the definitions of the dissipation rates $\epsilon = k/\tau$ and $\epsilon_\theta = k_\theta/\tau_\theta$ in the transport equations for $k = \widetilde{u_n u_n}/2$ and $k_\theta = \widetilde{\theta^2}/2$ requires two coefficient relations:

$$c^*_1 + c^*_2 P_*/\epsilon - 3C_0/2 = 1, \qquad c^*_{\theta 1} = 1/2. \tag{A16}$$

Equations (A12)–(A14) agree with the level 4 closure model of Mellor and Yamada [49], with the exception of Mellor and Yamada's neglect of higher-order anisotropy effects, leading to an isotropic version of the c^*_2 term on the RHS of Equation (A12) (which then reads $8kc^*_2\widetilde{S}_{ij}/3$) and the neglect of the last term in Equation (A13). A comparison of the coefficients applied here with coefficients ℓ_1, ℓ_2, Λ_1, and Λ_2 applied by Mellor and Yamada reveals, in conjunction with $c^*_{\theta 1} = 1/2$, the relations

$$\frac{c^*_1}{\tau} = \frac{(2k)^{1/2}}{3\ell_1}, \quad \frac{4c^*_2}{3} = 2C_1, \quad \epsilon = \frac{(2k)^{3/2}}{\Lambda_1}, \quad \frac{c^*_1}{2\tau} + \frac{1}{2\tau_\theta} = \frac{(2k)^{1/2}}{3\ell_2}, \quad \frac{c^*_{\theta 1}}{\tau_\theta} = \frac{(2k)^{1/2}}{\Lambda_2}, \tag{A17}$$

We find, in addition to the relationship $C_1 = 2c^*_2/3$, the following condition for ℓ_1, ℓ_2, Λ_1 and Λ_2:

$$(\ell_1, \Lambda_1, \ell_2, \Lambda_2) = \left(\frac{1}{2c^*_1}, 3, \frac{1}{c^*_1 + \Gamma}, \frac{3}{2c^*_{\theta 1}\Gamma}\right)\frac{2^{3/2}}{3}L. \tag{A18}$$

Here, $L = k^{1/2}\tau$ and the mechanical-to-scalar time scale ratio $\Gamma = \tau/\tau_\theta$ are involved. (A constant $\Gamma = 1.5$ was applied for stratified flow [68,69]) Equations (A12)–(A14) receive

scale information via τ or L; that is, τ or L needs to be provided in a physically meaningful way under changing stratification.

References

1. Pope, S.B. *Turbulent Flows*; Cambridge University Press: Cambridge, UK, 2000.
2. Wilcox, D.C. *Turbulence Modeling for CFD*, 2nd ed.; DCW Industries: La Canada, CA, USA, 1998.
3. Fröhlich, J.; Terzi, D.V. Hybrid LES/RANS methods for the simulation of turbulent flows. *Prog. Aerosp. Sci.* **2008**, *44*, 349–377. [CrossRef]
4. Chaouat, B. The state of the art of hybrid RANS/LES modeling for the simulation of turbulent flows. *Flow Turbul. Combust.* **2017**, *99*, 279–327. [CrossRef] [PubMed]
5. Heinz, S. A review of hybrid RANS-LES methods for turbulent flows: Concepts and applications. *Prog. Aerosp. Sci.* **2020**, *114*, 100597. [CrossRef]
6. Piomelli, U. Large eddy simulations in 2030 and beyond. *Phil. Trans. R. Soc. A* **2014**, *372*, 20130320. [CrossRef] [PubMed]
7. Larsson, J.; Kawai, S.; Bodart, J.; Bermejo-Moreno, I. Large eddy simulation with modeled wall-stress: recent progress and future directions. *Mech. Eng. Rev.* **2016**, *3*, 15-00418. [CrossRef]
8. Bose, S.T.; Park, G.I. Wall-modeled large-eddy simulation for complex turbulent flows. *Annu. Rev. Fluid Mech.* **2018**, *50*, 535–561. [CrossRef]
9. Spalart, P.R.; Jou, W.H.; Strelets, M.; Allmaras, S.R. Comments on the feasibility of LES for wings, and on a hybrid RANS/LES approach. In *Advances in DNS/LES*; Liu, C.; Liu, Z., Eds.; Greyden Press: Dayton, OH, USA , 1997; pp. 137–147.
10. Spalart, P.R. Detached-eddy simulation. *Annu. Rev. Fluid Mech.* **2009**, *41*, 181–202. [CrossRef]
11. Friess, C.; Manceau, R.; Gatski, T.B. Toward an equivalence criterion for hybrid RANS/LES methods. *Comput. Fluids* **2015**, *122*, 233–246. [CrossRef]
12. Menter, F.R.; Egorov, Y. The scale-adaptive simulation method for unsteady turbulent flow prediction: Part 1: Theory and model description. *Flow Turbul. Combust.* **2010**, *78*, 113–138. [CrossRef]
13. Jakirlić, S.; Maduta, R. Extending the bounds of "steady" RANS closures: Toward an instability-sensitive Reynolds stress model. *Int. J. Heat Fluid Flow* **2015**, *51*, 175–194. [CrossRef]
14. Li, J.; Zhong, C.; Pan, D.; Zhuo, C. A gas-kinetic scheme coupled with SST model for turbulent flows. *Comput. Math. Appl.* **2019**, *78*, 1227–1242. [CrossRef]
15. Chen, S.; Xia, Z.; Pei, S.; Wang, J.; Yang, Y.; Xiao, Z.; Shi, Y. Reynolds-stress-constrained large-eddy simulation of wall-bounded turbulent flows. *J. Fluid Mech.* **2012**, *703*, 1–28. [CrossRef]
16. Heinz, S. *Statistical Mechanics of Turbulent Flows*; Springer: Berlin, Germany, 2003.
17. Heinz, S. Comment on "A dynamic nonlinear subgrid-scale stress model" [Phys. Fluid 17, 035109 (2005)]. *Phys. Fluids* **2005**, *17*, 099101. [CrossRef]
18. Heinz, S. Unified turbulence models for LES and RANS, FDF and PDF simulations. *Theoret. Comput. Fluid Dynam.* **2007**, *21*, 99–118. [CrossRef]
19. Gopalan, H.; Heinz, S.; Stöllinger, M. A unified RANS-LES model: Computational development, accuracy and cost. *J. Comput. Phys.* **2013**, *249*, 249–279. [CrossRef]
20. Mokhtarpoor, R.; Heinz, S.; Stoellinger, M. Dynamic unified RANS-LES simulations of high Reynolds number separated flows. *Phys. Fluids* **2016**, *28*, 095101. [CrossRef]
21. Mokhtarpoor, R.; Heinz, S. Dynamic large eddy simulation: Stability via realizability. *Phys. Fluids* **2017**, *29*, 105104. [CrossRef]
22. Stöllinger, M.; Heinz, S.; Zemtsop, C.; Gopalan, H.; Mokhtarpoor, R. Stochastic-based RANS-LES simulations of swirling turbulent jet flows. *Int. J. Nonlinear Sci. Numer. Simul.* **2017**, *18*, 351–369. [CrossRef]
23. Girimaji, S. Partially-averaged Navier-Stokes method for turbulence: A Reynolds-averaged Navier-Stokes to direct numerical simulation bridging method. *ASME J. Appl. Mech.* **2006**, *73*, 413–421. [CrossRef]
24. Chaouat, B.; Schiestel, R. A new partially integrated transport model for subgrid-scale stresses and dissipation rate for turbulent developing flows. *Phys. Fluids* **2005**, *17*, 065106. [CrossRef]
25. Chaouat, B.; Schiestel, R. Analytical insights into the partially integrated transport modeling method for hybrid Reynolds averaged Navier-Stokes equations-large eddy simulations of turbulent flows. *Phys. Fluids* **2012**, *24*, 085106. [CrossRef]
26. Heinz, S. The large eddy simulation capability of Reynolds-averaged Navier-Stokes equations: Analytical results. *Phys. Fluids* **2019**, *31*, 021702. [CrossRef]
27. Heinz, S.; Mokhtarpoor, R.; Stoellinger, M.K. Theory-Based Reynolds-Averaged Navier-Stokes Equations with Large Eddy Simulation Capability for Separated Turbulent Flow Simulations. *Phys. Fluids* **2020**, *32*, 065102. [CrossRef]
28. Heinz, S. The Continuous Eddy Simulation Capability of Velocity and Scalar Probability Density Function Equations for Turbulent Flows. *Phys. Fluids* **2021**, *33*, 025107. [CrossRef]
29. Heinz, S. Theory-Based Mesoscale to Microscale Coupling for Wind Energy Applications. *Appl. Math. Model.* **2021**, *98*, 563–575. [CrossRef]
30. Heinz, S.; Peinke, J.; Stoevesandt, B. Cutting- Edge Turbulence Simulation Methods for Wind Energy and Aerospace Problems. *Fluids* **2021**, *6*, 288. [CrossRef]

31. Fagbade, A.; Heinz, S. Application of Mode-Controlled Hybrid RANS-LES to the NASA Wall-Mounted Hump Flow. In Proceedings of the 2022 AIAA SciTech Forum, 2022; AIAA Paper 22-0180; pp. 1–16.
32. Heinz, S. Minimal error partially resolving simulation methods for turbulent flows: A dynamic machine learning approach. *Phys. Fluids* **2022**, *34*, 051705. [CrossRef]
33. Slotnick, J.; Khodadoust, A.; Alonso, J.; Darmofal, D.; Gropp, W.; Lurie, E.; Mavriplis, D. CFD vision 2030 study: A path to revolutionary computational aerosciences. NASA/CR-2014-218178, 2014. Available online: https://ntrs.nasa.gov/search.jsp?R=20140003093 (accessed on 10 October 2022).
34. Slotnick, J.P.; Khodadoust, A.; Alonso, J.J.; Darmofal, D.L.; Gropp, W.D.; Lurie, E.A.; Mavriplis, D.J.; Venkatakrishnan, V. Enabling the environmentally clean air transportation of the future: A vision of computational fluid dynamics in 2030. *Philos. Trans. Royal Soc. A* **2014**, *372*, 20130317. [CrossRef]
35. Probst, A.; Knopp, T.; Grabe, C.; Jägersküpper, J. HPC requirements of high-fidelity flow simulations for aerodynamic applications. In Proceedings of the European Conference on Parallel Processing, Warsaw, Poland, 24–28 August; Springer: Berlin/Heidelberg, Germany, 2020; pp. 375–387.
36. Goc, K.A.; Lehmkuhl, O.; Park, G.I.; Bose, S.T.; Moin, P. Large eddy simulation of aircraft at affordable cost: a milestone in computational fluid dynamics. *Flow* **2021**, *1*, E14. [CrossRef]
37. Slotnick, J.P.; Mavriplis, D. A Grand Challenge for the Advancement of Numerical Prediction of High Lift Aerodynamics. In Proceedings of the AIAA SciTech Forum, 2021; AIAA Paper 22-0955; pp. 1–21.
38. Wyngaard, J.C. Toward numerical modeling in the "Terra Incognita". *J. Atmos. Sci.* **2004**, *61*, 1816–1826. [CrossRef]
39. Cummings, R.M.; Forsythe, J.R.; Morton, S.A.; Squires, K.D. Computational challenges in high angle of attack flow prediction. *Prog. Aerosp. Sci.* **2003**, *39*, 369–384. [CrossRef]
40. Chassaing, P. The modeling of variable density turbulent flows. A review of first-order closure schemes. *Flow, Turb. Combust.* **2001**, *66*, 293–332. [CrossRef]
41. Chassaing, P.; Antonia, R.A.; Anselmet, F.; Joly, L.; Sarkar, S. *Variable Density Fluid Turbulence*; Volume 69; Springer Science & Business Media: Dordrecht, The Netherlands, 2002.
42. Park, N.; Mahesh, K. Numerical and modeling issues in LES of compressible turbulence on unstructured grids. In Proceedings of the 45th AIAA Aerospace Sciences Meeting and Exhibit, Reno, NV, USA, 8–11 January 2007; AIAA Paper 07-0722; pp. 1–18.
43. Temel, O.; Porchetta, S.; Bricteux, L.; van Beeck, J. RANS closures for non-neutral microscale CFD simulations sustained with inflow conditions acquired from mesoscale simulations. *Appl. Math. Model.* **2018**, *53*, 635–652. [CrossRef]
44. Heinz, S. Nonlinear Lagrangian equations for turbulent motion and buoyancy in inhomogeneous flows. *Phys. Fluids* **1997**, *9*, 703–716. [CrossRef]
45. Heinz, S. Connections between Lagrangian stochastic models and the closure theory of turbulence for stratified flows. *Int. J. Heat Fluid Flow* **1998**, *19*, 193–200. [CrossRef]
46. Heinz, S.; van Dop, H. Buoyant plume rise described by a Lagrangian turbulence model. *Atmos. Environ.* **1999**, *33*, 2031–2043. [CrossRef]
47. Baumert, H.; Peters, H. Second-moment closures and length scales for weakly stratified turbulent shear flows. *J. Geophys. Res. Oceans* **2000**, *105*, 6453–6468. [CrossRef]
48. Sogachev, A. A note on two-equation closure modelling of canopy flow. *Boundary Layer Meteorol.* **2009**, *130*, 423–435. [CrossRef]
49. Mellor, G.L.; Yamada, T. Development of a turbulence closure model for geophysical fluid problems. *Rev. Geophys.* **1982**, *20*, 851–875. [CrossRef]
50. Muñoz-Esparza, D.; Kosović, B.; Mirocha, J.; van Beeck, J. Bridging the transition from mesoscale to microscale turbulence in numerical weather prediction models. *Boundary Layer Meteorol.* **2014**, *153*, 409–440. [CrossRef]
51. Sanz Rodrigo, J.; Chavez Arroyo, R.A.; Moriarty, P.; Churchfield, M.; Kosović, B.; Réthoré, P.E.; Hansen, K.S.; Hahmann, A.; Mirocha, J.D.; Rife, D. Mesoscale to microscale wind farm flow modeling and evaluation. *Wires Energy Environ.* **2017**, *6*, e214. [CrossRef]
52. Veers, P.; Dykes, K.; Lantz, E.; Barth, S.; Bottasso, C.L.; Carlson, O.; Clifton, A.; Green, J.; Green, P.; Holttinen, H.; et al. Grand challenges in the science of wind energy. *Science* **2019**, *366*, eaau2027. [CrossRef] [PubMed]
53. Meneveau, C. Big wind power: Seven questions for turbulence research. *J. Turbul.* **2019**, *20*, 2–20. [CrossRef]
54. Haupt, S.E.; Berg, L.; Churchfield, M.; Kosović, B.; Mirocha, J.; Shaw, W. Mesoscale to Microscale Coupling for Wind Energy Applications: Addressing the Challenges. *J. Phys. Conf. Ser.* **2020**, *1452*, 012076. [CrossRef]
55. Detering, H.W.; Etling, D. Application of the E-ε turbulence model to the atmospheric boundary layer. *Boundary Layer Meteorol.* **1985**, *33*, 113–133. [CrossRef]
56. Duynkerke, P.; Driedonks, A. A model for the turbulent structure of the stratocumulus–topped atmospheric boundary layer. *J. Atmos. Sci.* **1987**, *44*, 43–64. [CrossRef]
57. Duynkerke, P.G. Application of the E–ε turbulence closure model to the neutral and stable atmospheric boundary layer. *J. Atmos. Sci.* **1988**, *45*, 865–880. [CrossRef]
58. Zhang, C.; Wang, Y.; Xue, M. Evaluation of an E–ε and three other boundary layer parameterization schemes in the WRF model over the Southeast Pacific and the Southern Great Plains. *Mon. Weather Rev.* **2020**, *148*, 1121–1145. [CrossRef]
59. Tran, V.; Ng, E.Y.K.; Skote, M. CFD simulation of dense gas dispersion in neutral atmospheric boundary layer with OpenFOAM. *Meteorol. Atmos. Phys.* **2020**, *132*, 273–285. [CrossRef]

60. Juliano, T.W.; Kosović, B.; Jiménez, P.A.; Eghdami, M.; Haupt, S.E.; Martilli, A. "Gray Zone" simulations using a three-dimensional planetary boundary layer parameterization in the Weather Research and Forecasting Model. *Mon. Weather Rev.* **2022**, *150*, 1585–1619. [CrossRef]
61. Hong, S.Y.; Noh, Y.; Dudhia, J. A new vertical diffusion package with an explicit treatment of entrainment processes. *Mon. Weather Rev.* **2006**, *134*, 2318–2341. [CrossRef]
62. Nakanishi, M.; Niino, H. Development of an improved turbulence closure model for the atmospheric boundary layer. *J. Meteorol. Soc. Japan Ser. II* **2009**, *87*, 895–912. [CrossRef]
63. Sarkar, S. The pressure–dilatation correlation in compressible flows. *Phys. Fluids A* **1992**, *4*, 2674–2682. [CrossRef]
64. Suzen, Y.; Hoffmann, K. Investigation of supersonic jet exhaust flow by one-and two-equation turbulence models. In Proceedings of the 36th AIAA Aerospace Sciences Meeting and Exhibit, Las Vegas, NV, USA, 24–28 July 1998; AIAA Paper 98-0322; pp. 1–18.
65. Forsythe, J.R.; Hoffmann, K.A.; Cummings, R.M.; Squires, K.D. Detached-eddy simulation with compressibility corrections applied to a supersonic axisymmetric base flow. *J. Fluids Eng.* **2002**, *124*, 911–923. [CrossRef]
66. Openfoam Documentation; Technical Report. 2009. Available online: (accessed on 10 May 2020).
67. Rapp, C.; Manhart, M. Flow over periodic hills – an experimental study. *Exp. Fluids* **2011**, *51*, 247–269. [CrossRef]
68. Warhaft, Z. Passive scalars in turbulent flows. *Annual Rev. Fluid Mech.* **2000**, *32*, 203–240. [CrossRef]
69. Das, S.K.; Durbin, P.A. A Lagrangian stochastic model for dispersion in stratified turbulence. *Phys. Fluids* **2005**, *17*, 025109. [CrossRef]

fluids

MDPI

Article

Measurement of Mass Transfer Intensity in Gas–Liquid Medium of Bioreactor Circuit Using the Thermometry Method

Ilya Starodumov [1], Irina Nizovtseva [1,2,*], Sergey Lezhnin [1,3], Sergey Vikharev [1], Vladislav Svitich [1], Pavel Mikushin [1], Dmitri Alexandrov [1], Nikolay Kuznetsov [1] and Dmitri Chernushkin [4]

[1] Laboratory of Multiphase Physical and Biological Media Modeling, Department of Theoretical and Mathematical Physics, Ural Federal University, Ekaterinburg 620000, Russia
[2] Otto-Schott-Institut fur Materialforschung, Friedrich-Schiller University of Jena, 07743 Jena, Germany
[3] S. S. Kutateladze Institute of Thermophysics, Siberian Branch of the Russian Academy of Sciences, Novosibirsk 630090, Russia
[4] NPO Biosintez Ltd., Moscow 109390, Russia
* Correspondence: nizovtseva.irina@gmail.com

Abstract: The development of energy-efficient solutions for large-scale fermenters demands a deep and comprehensive understanding of hydrodynamic and heat and mass transfer processes. Despite a wide variety of research dedicated to measurements of mass transfer intensity in bubble flows, this research subject faces new challenges due to the topical development of new innovative bioreactor designs. In order to understand the fluid dynamics of the gas–liquid medium, researchers need to develop verified CFD models describing flows in the bioreactor loop using a progressive physical and mathematical apparatus. In the current paper, we represent the results of evaluating the key performance indicator of the bioreactor, namely the volumetric mass transfer coefficient (k_La) known as a parameter of dominant importance for the design, operation, scale-up, and optimization of bioreactors, using the developed thermometry method. The thermometry method under consideration was examined within a series of experiments, and a comparative analysis was provided for a number of various regimes also being matched with the classical approaches. The methodology, experiment results, and data verification are given, which allow the evaluation of the effectiveness and prediction of the fluid flows dynamics in bioreactors circuits and ultimately the operational capabilities of the fermenter line.

Keywords: gas–liquid flow; bioreactor; fermentation; mass transfer coefficient; thermometry method; kLa; two-phase media; multiphase flows; scale-up; numerical modeling; jet fermenter

Citation: Starodumov, I.; Nizovtseva, I.; Lezhnin, S.; Vikharev, S.; Svitich, V.; Mikushin, P.; Alexandrov, D.; Kuznetsov, N.; Chernushkin, D. Measurement of Mass Transfer Intensity in Gas–Liquid Medium of Bioreactor Circuit Using the Thermometry Method. *Fluids* **2022**, *7*, 366. https://doi.org/10.3390/fluids7120366

Academic Editors: Ashwin Vaidya and Mehrdad Massoudi

Received: 10 October 2022
Accepted: 23 November 2022
Published: 25 November 2022

1. Introduction

Despite the impressive recent development of the practice of applying modern numerical and computational methods to hydrodynamic flow analysis [1–9], as well as machine learning methods [10–13] for modeling, analyzing, and evaluating the performance parameters of various engineering solutions in the field of fermentation [14,15], a number of questions remain as an open challenge for the scientific community [16–18]. Among them lies a fair assessment of fermenters' performance indicators [19–21] for the case of the large-scale transition from laboratory to industrial solutions. Another indisputable challenge for researchers in the field of biotechnology is the development and implementation of analytical modules for the control system of mass transfer characteristics of the fermentation process [22–25]. Both of these problems require an adequate verified description of the behavior of bubbles in a two-phase gas–liquid medium of a bioreactor [26–29], in particular, the development of relevant experiments and methods for evaluating the mass transfer in the system [14,30–32]. The latter is particularly relevant since, together with the energy consumption associated with the fermenter's performance and therefore the direct economic effect when choosing the bioreactors types, the (k_La) coefficient must be measured by methods that do not involve shutting down the fermentation process at

the plant and, moreover, do not require any sort of chemical interventions in the circuit of the plant (as, e.g., i is assumed in the case of a number of classical approaches such as the sulfite method). Thus, the requirements of maximum non-interference in the fermentation process, the need to carry out measurements in parallel with the main (complicated microbiological) processes, and reasonable considerations regarding the final cost of resources for such regular measurements lead researchers to the need to find new methods that meet the above claims. The present study is devoted to solving the aforementioned problem based on a sample stand of a mass transfer apparatus designed for the process of growing microorganisms on various types of substrates [9,26,33], namely a jet bioreactor with the recirculation of liquid and gas phases of an air–water and air–model liquid of a given rheology system. Studied experimentally on various scales of plantsand evaluated critically from the point of view of compliance with the results of other measurement methods, the presented thermometric method was proven indeed to be a promising tool for measuring the efficiency in mass transfer apparatuses, including large-scale (in our experiment, up to 1000 cubic meters) fermentation plants. An experimental study of the life-cycle analysis of bubbles, its evolution, and mass transfer characteristics in jet bioreactors (when mixing is carried out due to a falling jet of liquid initiated by pump operation) was provided when the bubbles passed through a closed circuit of the fermenter. The experimental module was designed in order to include a set up wide enough to evaluate hydrodynamics and calculate the mass-transfer parameters of the fermenter depending on the performance of the circulation pump, the amount of air supplied, and the degree of filling of the apparatus circuit etc. The thermometry method for volumetric mass transfer coefficient (k_La) evaluation based on the transition of the mechanical form of energy into heat due to the operation of the pump [34] was investigated and verified in particular with sulfite method and k_La calculations performed on the basis of input mechanical energy. We have also focused on investigating the limits of applicability of these methods for various operating modes and scales of experimental setup, investigating the influence of concrete numerical values and corridors of input parameters on the behavior of gas–liquid flows.

2. Materials and Methods

2.1. Theory of the Thermometry Method

The cornerstone of the fermentation process, namely the aforementioned calculation of the volumetric mass transfer rate, depends directly on the type of installation (fermenter) that provides the gas–liquid fluid flow transition. One knows a number of various empirical formulas for determining the dissolution of gas (oxygen) for bubbling, bubbling-airlift, gas-lift, nozzle gas distribution [35], and finally jet units, which are considered in the current manuscript. At least two main, physically natural, parameters in these formulas are worth mentioning, namely (1) specific input energy (power) spent on mixing and aeration N_v, kW/m^3, since diffusion processes in a liquid are intensified with an increase in the Reynolds number in terms of the relative velocity of the liquid and gas phases [36], and thus the energy dissipation of the gas flow was carried out as a result of the work of the gas flow against friction velocity, and (2) and true volumetric gas fraction (void fraction) φ. The volumetric gas fraction in the apparatus could thus be defined as the ratio of the volume of the gas phase to the volume of the gas–liquid mixture. As φ increases, the specific interfacial surface also increases. In a particular idealized case, e.g., in a monodisperse bubble medium, the interfacial area per unit volume is equal to $6\ \varphi/\ D$, where D is the gas-bubble diameter. This fact can be explained by an example. Let us denote $V_b = \pi D^3/6$ as bubble volume. The number of bubbles per unit volume $N = \varphi/V_b = 6\ \varphi/\pi D^3$, and the total area of the interfacial surface per unit volume $N\pi D^2 = 6\ \varphi/D$. When designing a jet fermenter of an overflow type, the ratio of the volume of the gas phase to the volume of the gas–liquid mixture is taken to be equal to $\varphi = 1$. We also take into account [34] the following formula outflow for the k_La definition:

$$k_La = A \cdot N_v^n \cdot \varphi^m, \quad (1)$$

where A, n, and m are coefficients assigned specifically for the type of apparatus under consideration. In jet fermenters, when mixing is provided through the falling jet of liquid caused by the operation of the pump, with natural ejection of the gas by a liquid jet, the mass transfer coefficient in the liquid phase is thus proposed to be calculated using the following formula [37]:

$$k_L a = 350 \cdot N_v^{0.85}, \quad (2)$$

The specific input power spent on mixing and aeration N_v represents itself as the mechanical (useful) power of the rotary pump. It should be noted that in real experiments, the calculated power consumption of the pump might differ significantly from N_v since asynchronous motors are widely in use for pump operation and thus the efficiency depends on the load lying in practice from 75% to 96%. In other words, considering that N_v equal to the measured power consumption appears to be incorrect, and taking into account [38], N_v is rather spent on the following:

1. Averaged and turbulent (pulsation) kinetic energy of the flow,
2. Change in the potential energy of the fluid in the gravitational field,
3. Enthalpy change (heating of liquid due to thermal dissipation),
4. Heat of gas dissolution (negative),
5. External heat losses of the circuit,
6. Interfacial "liquid–gas" energy.

In stationary (quasi-stationary) modes of operation of the closed circuit of the bioreactor, the kinetic and potential energies of the flow (1 and 2) do not change. If one neglects the heat of condensation and heat losses (4 and 5), the specific input power for mixing the medium in the apparatus might be calculated as follows:

$$N_v^{heat} = C_p \Delta T / \Delta t, \quad (3)$$

where C_p is the specific heat of the liquid (the heat capacity of the apparatus walls is considered negligible). Expression ΔT denotes liquid temperature difference during the determination time, °C; and Δt is the relative measurement period.

It is worth mentioning that when thermometry method is applied, it is crucial to make the first measurement of the temperatures when achieving the steady flow regime. In turn, this is determined by the time of establishment of the stationary turbulent spectrum in the flow. For regular contour sizes (internal diameters of pipes are centimeters or tens of centimeters) and Reynolds number (tens or hundreds of thousands, which corresponds to developed turbulent regime), this time is on the order of a few seconds. During this time period, the "gas–liquid" interfacial surface most likely formed.

In general, this formula can be modified in cases when significant external heat losses or significant heat of dissolution takes place. If the circuit is not closed and during the circulation of the liquid a complete or partial renewal of the liquid takes place, it is obligatory to take into account the change in the kinetic and potential energy of the flow, as well as the change in the interfacial surface since the intake and removal of fluid can be carried out at various speeds and on various heights, a new interfacial surface is additionally formed. Finally, with a constant gas supply, it is necessary to take into account its excess enthalpy, which is meanwhile partially expended on the gas dissolution. According to the assessment, the external heat losses of the circuit make a significant contribution to determining the specific input power since the surface of the apparatus is extensive and not thermally isolated:

$$Q_{loss} = \alpha_{tot} \, \Delta t \, A_{surf} \, (T_{surf} - T_{out}), \quad (4)$$

where $\alpha_{tot} = (9.3 \pm 0.06)$ [W/m^2 °C] represents total coefficient of heat transfer by radiation and convection; A_{surf} is responsible for heat exchange surface area of the apparatus, and T_{surf} for its surface temperature. Accordingly, T_{out} corresponds to ambient temperature.

2.2. Design and Procedure of the Experiment

Verification of the thermometric method was carried out on the developed experimental setup (Figure 1), designed especially to recreate the complete operation of a jet ejection bioreactor with a working volume of 0.1 m^3 in terms of hydrodynamic flows. The setup is represented as a closed hydrodynamic circuit with free input for the gas phase injections. For additional verification and comparative analysis of the range of applicability of various methods for k_La measurement, the archive data were used for the analogous setup of a similar design type, but eight times bigger by working volume than the main experimental setup (see also Section 3).

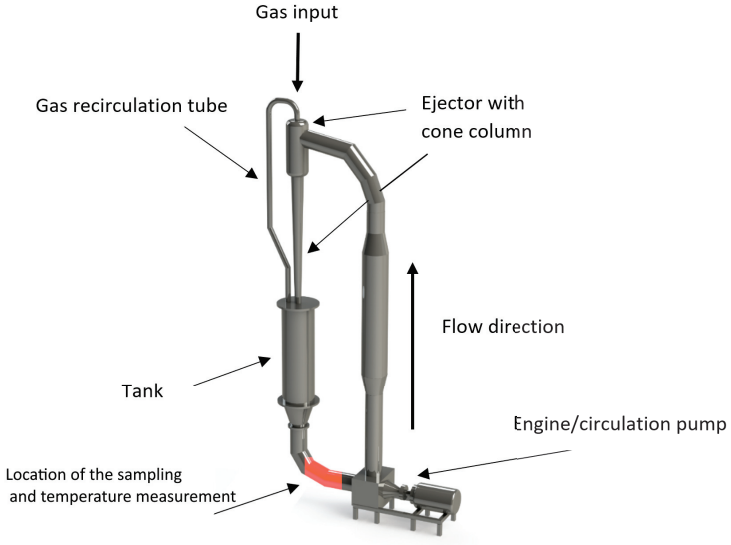

Figure 1. Experimental setup for measuring the mass transfer of the air–liquid flow. The design of the experimental setup corresponds to the real field jet bioreactor for manufacturing the microbiological single-cell protein and corresponding high-added-value products.

The principle of operation of the designed experimental setup is shown on Figure 1. The motor rotates the circulation pump, which ensures the rise of liquid through the circulation circuit into the overflow ejector. Once in the ejector, the liquid, subjected to gravitational force, falls into the tank, entraining the air through the inlet valve, as well as from the recirculation tube connecting the tank and the ejector. The device absorbs the air up to a state of saturation. Meanwhile, in the ejection column, a bubbly medium is formed, which provides the most intensive mass transfer and saturation of the liquid with dissolved gas. During the operation, the experimental setup is controlled by a single parameter: the pressure-flow characteristic of the pump, determined by the consumed energy of the engine. The tactical task of the planned experiments was to determine the rate of oxygen dissolution, as well as to calculate the volumetric mass transfer coefficient. The experiments were carried out for the media characteristics represented in Table 1.

The above-mentioned special model liquid was determined as a mixture of water and glycerin at a ratio of 11.5:1. Such a fluid satisfactorily models the rheology of a biological fluid used in industrial bioreactors [9]. On the initial phase, the experimental setup was filled with liquid up to a working volume of 0.125 m^3 and preheated up to the ambient (air) temperature. Then, the pump was started, and the experimental setup was saturated with air (air absorption in the ejector then stops), and the procedure of temperature measurement of the liquid in front of the pump was initialized (see Figure 1). The measurement series were made accurately every 300 s using a GMH 3230 digital high-precision, low-inertia thermometer. The results of thermometric measurements, namely the dependence of water

temperature on time for various pump operation modes, are shown in Figure 2. The corresponding specific volumetric power values on the pump impeller for these modes are given in the figure's legend. The graph shows that a greater specific input power corresponds to a greater slope of the graph. Accordingly, larger angles of inclination correspond to larger thermal outputs.

Table 1. Experimental media and hydrodynamic regimes parameters.

Specific Input Power N_v (Experimental Setup Regime), kW/m^3	Liquid Type	Heat Capacity, W h/kg °C	Density, kg/m^3	Air Temperature, °C
Thermometry method				
0.940	Water	1.17	1000	20.4
1.042	Water	1.17	1000	28.4
1.605	Water	1.17	1000	26.2
1.915	Water	1.17	1000	30.1
2.243	Water	1.17	1000	30
1.062	Model liquid	0.56	1020	27.9
1.636	Model liquid	0.56	1020	28
2.286	Model liquid	0.56	1020	28
Sulfite method				
1.052	Water	1.17	1000	29
1.620	Water	1.17	1000	29
2.264	Water	1.17	1000	29

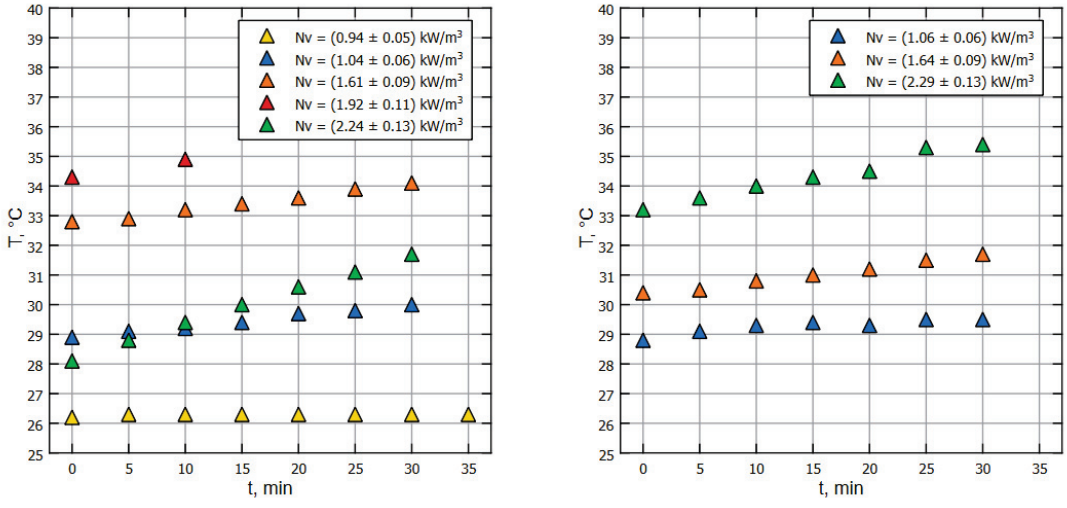

Figure 2. Relative temperature of the liquid changes with time, thermometry method applied on water (**left**) and model liquid (**right**).

In order to determine the reasonably applicable intervals of the thermometric method, as well as to confirm the relevance of the obtained absolute values measured and calculated, the sulfite method of measurement of the the intensity of oxygen dissolution in water [39–42] was used as a reference. The choice of the sulfite method for studying mass transfer in the liquid phase was determined due to the fact that the oxidation reaction of sodium sulfite occurs in the bulk of the liquid, and the process of chemisorption of air oxygen by an aqueous solution of sodium sulfite is determined by the diffusion of oxygen

in the liquid boundary film. Since the resistance in the gas phase is negligible, the entire process of sodium sulfite oxidation is limited by mass transfer in the liquid phase. An aqueous solution of copper sulfate with a concentration of more than 10 kmol/m^3 at a concentration in a solution lies within the range of 4–50 g/L depending on the quality of mass transfer (the higher the rate of dissolution of oxygen, the more we take the concentration for the accuracy of determination due to the measurement technique). According to a number of researchers [37], the rate of a chemical reaction in the presence of copper ions does not depend on the concentration of sodium sulfite. The latter makes it possible to neglect the degree of mixing of the liquid when calculating the driving force of the process. In the presence of a catalyst, the reaction proceeds in the diffusion region, where the rate of sulfite oxidation is limited by the resistance in the liquid phase, so the core of the sulfite method is based on the oxidation reaction of sodium sulfite in the presence of a catalyst—copper or cobalt ions: $2Na_2SO_3 + O_2 - {}^{Co^{2+}Cu^{2+}} \rightarrow 2Na_2SO_4$. The excess sulfite remaining is determined by iodometric back-titration [39,41]. Sulfite concentrations applied range from 0.2 n up to 1 n. Note that the rate of the chemical reaction of sulfite oxidation is much higher than the rate of absorption, so the overall rate of the process is determined by the rate of absorption. The sulfite coefficient (sulfite number) M determined by this method characterizes the rate of oxygen absorption in the experimental setup (normal range is from 0.5 to 5 and rarely reaches 10 mmol/L min for O_2. Parameter M might be determined by the physical–chemical properties of the sulfite solution and the hydrodynamic parameters of the system. Since the reaction between dissolved oxygen and sulfite is close to instantaneous and the concentration of dissolved oxygen is zero, we have:

$$M = k_L a \, C_{O_2}. \quad (5)$$

It is worth mentioning that normally the $k_L a$ value, determined by the sulfite method, is higher than what might be determined by the direct method [37,40,42]. The experimental setup was filled with liquid up to a working volume of 0.125 m^3, heated preliminarily up to the ambient (air) temperature; the pump was started, and the process of sampling from the line in the position in front of the pump was begun (see Figure 1). Sampling was carried out every 180 s, and each iteration demanded sample volume as of 50 mL of liquid. The results of the measurements of sulfite spent for the titration are represented on Figure 3.

Note that for both of Figures 2 and 3, dots of the same color correspond to the same pump's RPM, but the specific power on the impeller is different due to the properties of the liquids (water and model liquid).

The sulfite M number can be determined according to the formula [37,40,42] $M = 24/\Delta t \, (a_f - a_i)$, where: Δt is experience exposure and a_f and a_i are final and initial amount of 0.1 N solution of sodium hyposulfite spent for the titration. Typically, the time intervals with the highest sulfite consumption are used [40,42]. Finally, the mass transfer coefficient in the liquid phase was determined by the ratio $k_L a = M/(C^*_{O_2} - C_{O_2})£$, where $C^*_{O_2}$ is equilibrium oxygen concentration in relation to the gas phase (7.15 mg/L, 0.0076 kg/m^3 is taken for calculations) for the experimental conditions; C_{O_2} is the concentration of oxygen dissolved in the liquid, equal to zero in our case; £ is the coefficient of acceleration of the process of oxygen chemisorption in relation to biosorption $(£ = 1.5)$, and this coefficient is taken based on the design of the fermenter.

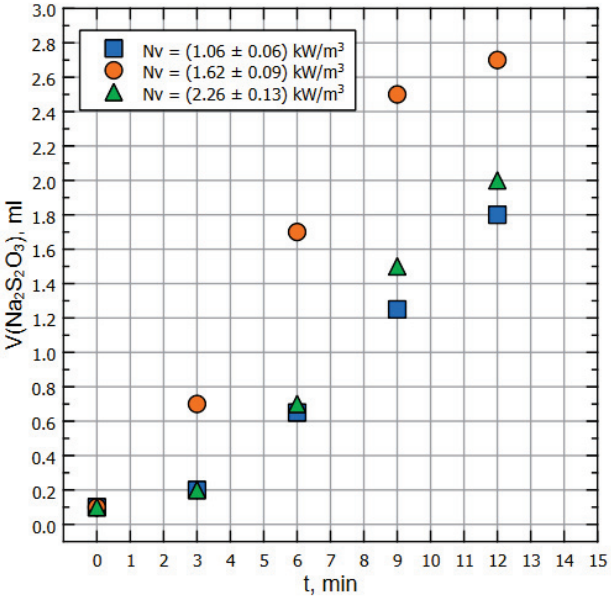

Figure 3. Amount of thiosulfite used for titration, mL per minute.

3. Results

Figure 4 shows the dependence of k_La on N_v for various liquids (water and special model liquid) and methods for k_La measurements on the experimental setup designed in strict accordance with real jet-fermentation apparatuses. Note that the measurements were carried out in the steady state mode of heat exchange between the reactor and the environment according to the measurement protocols. In Figure 4, the black curve corresponds to calculated dependence, and blue dots correspond to the data obtained using the thermometric method for the water $(\rho = 1000\ \mathrm{kg/m^3}, \mathrm{C} = 4200\ \mathrm{J/kg\ ^\circ C}$ at different setup regimes (see Table 1); green dots correspond to the data obtained using the thermometric method for the model liquid ($\rho = 1019\ \mathrm{kg/m^3}, \mathrm{C} = 2000\ \mathrm{J/kg\ ^\circ C}$) at different setup regimes (see Table 1). Finally, red dots represent the data obtained according to the sulfite methodology $(\rho = 1008\ \mathrm{kg/m^3}, \mathrm{C} = 4200\ \mathrm{J/kg\ ^\circ C})$, with the same regime range.

It should be noted that an increase in engine speed leads to an increase in the specific input power (in the operating frequency range): the location of the data points on the graph (Figure 4) allows one to observe the tendency for k_La to increase with an increase in N_v (in the operating frequency range). The shift in N_v values for the same pump motor speed is explained by the fact that at the same head and volume flow, a liquid with a higher density will provide a greater specific input power. Thus, with rounding taken into account, water, $N_v = (1.61 \pm 0.09)\ \mathrm{kW/m^3}; \rho = 1000\ \mathrm{kg/m^3}$; sulfite solution, $N_v = (1.62 \pm 0.09)\ \mathrm{kW/m^3}$; $\rho = 1008\ \mathrm{kg/m^3}$; model fluid, $N_v = (1.64 \pm 0.09)\ \mathrm{kW/m^3}$; $\rho = 1019\ \mathrm{kg/m^3}$. One can see that within the operating power range (sub-critical modes), there is a coincidence of k_La values within the calculation errors range for all methods used, with the understanding that the acceptable difference between the k_La values for water and the model liquid is caused by the properties of the liquid such as change in viscosity, heat capacity, etc.

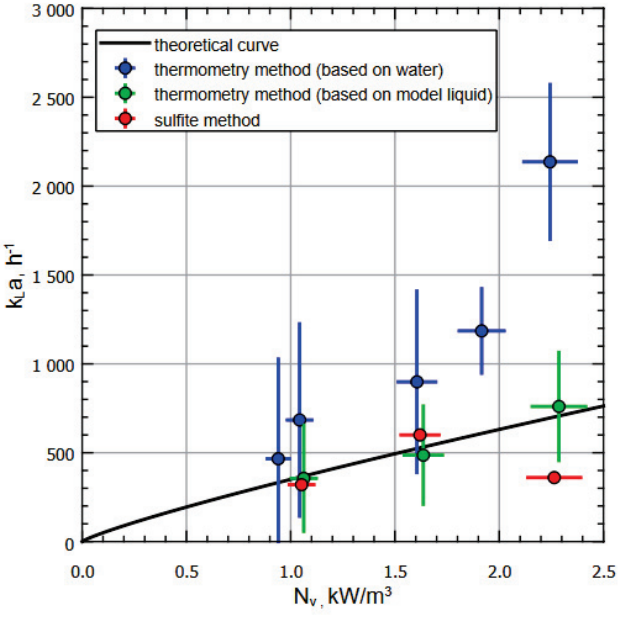

Figure 4. Dependence of $k_L a$ on N_v for various liquids and methods of measuring $k_L a$ on an experimental apparatus. The measurements were carried out in the steady state mode of heat exchange between the reactor and the environment according to the measurement protocol.

The characteristic increase in $k_L a$ in experiments with water at specific input powers above 1.6 kW/m^3 and, accordingly, the drop of $k_L a$ for the sulfite method, can be explained by the peculiarities of the fermenter operation, namely reaching critical values of the ejector's normal operation due to the overfilling of the mixing chamber, which led to a decrease in relative velocities in the gas-phase pickup zone and, as a result, to a decrease in the volume of ejected air. The calculation errors were estimated using the formulas for indirect measurements, taking into account the random and instrumental components for the corresponding values.

Additional series of calculations were performed for the archived data measurements provided for the similar apparatus of greater volume (bigger by one order in volume than the experimental setup considered above). The corresponding calculations are represented on Figure 5, showing, similarly to Figure 4, the plot of $k_L a$ for various methods of measuring volumetric mass transfer coefficients. Again, the black curve corresponds to calculated dependence, blue dots correspond to thermometry method applied for the gas–water system, and the red dots correspond to sulfite method measurements.

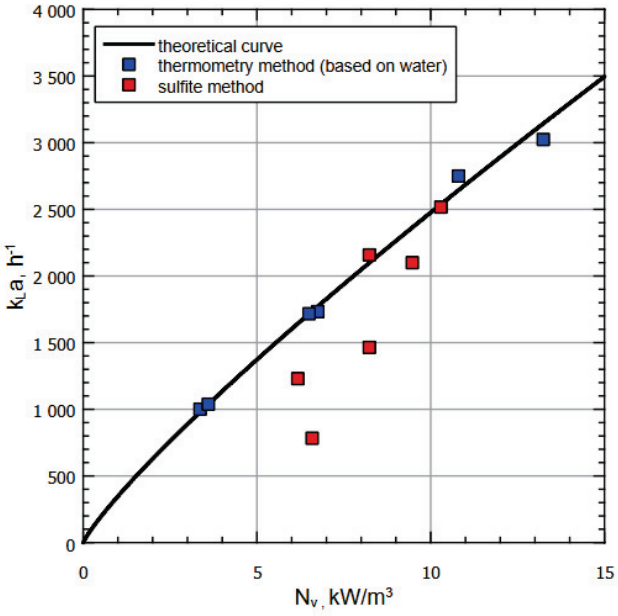

Figure 5. Dependence of $k_L a$ on N_v for various liquids and methods of measuring $k_L a$ based on archive data (with working volume of the next order than the experimental setup considered above.

4. Discussion

The experimental and theoretical analyses of one of the key characteristics of fermentation apparatuses, namely the volumetric mass transfer coefficient, provided with various methods, are believed to be the first of their kind conducted for various input parameters of the system (frequency, various types of liquid, including the model one, corresponding in rheology to real cultural liquid of biotechnological productions) for various scales of experimental setups of jet bioreactors. At the same time, the authors would like to draw the readers' attention to a number of requirements for both the experiments and the conclusions following from the analysis of the data. Thus, special requirements should be imposed on minimizing the spread of ambient temperature (which corresponds to the temperature difference during the analysis according to the thermometric method): the temperature measurement calculation error has the same order of magnitude with the temperature difference during thermometry at low powers or at short measurement times. Among the conclusions obtained, we should especially note that all the studied methods for $k_L a$ measurements have their limitations in terms of ranges of applicability. For example, for the thermometric method on the one hand, at low pump powers, the thermal power of heating the liquid is comparable to the error in thermal power due to specific of instruments, which allows evaluate the lower limit of applicability. On the other hand, at high powers, the excessive heating of the liquid will overestimate the specific input power, since only a part of the thermal power corresponds to the power used to dissolve oxygen. In this vein, it would be reasonable to introduce a correction factor that depends on the thermal power as a function that decreases outside the primary range of applicability of the method, which in the future will allow it to be expanded. For thermometric measurements, the heat capacity of the final solution is also important: this must be taken into account when choosing a model liquid. We also note that there are other options for obtaining empirical dependencies of $k_L a$ on the specific input power, since even when using the dependence given in the article, variation in multipliers and power exponents is allowed. We especially

note that it requires the fitting of the methodological parameters for each specific apparatus. The mechanism of energy distribution in the jet bioreactors requires further research and is one of the prospects for this project's team.

5. Conclusions

The key characteristic of fermentation apparatuses considered in this manuscript, namely the volumetric mass transfer coefficient, indeed draws researchers' attention both in terms of their fundamental interest in fluid flow research and measurement techniques in closed mass transfer apparatuses circuits and in terms of industry demands. It should be especially highlighted that the k_La measurement technique is particularly challenging and requires adjustments for various bioreactor designs, while classical approaches do not provide the corresponding measurements by, e.g., the sulfite method due to the large scale of installations in industrial solutions. Thus, a verified method for obtaining data on the volumetric mass transfer coefficient with the determination of the objective horizons of application is required, and exactly this approach was demonstrated for the first time in this work. In the presented study, the experimental hydrodynamic and mass transfer characteristics of the jet fermenter were obtained, and the verification of the thermometric approach for estimating the volumetric mass transfer coefficient based on experimental data and the reference sulfite method was carried out. The intervals of applicability of these methods were analyzed, and the critical values for the operating modes of the experimental installations under consideration, designed in full accordance with jet bioreactors in terms of hydrodynamic characteristics, were determined. This study demonstrates the need for a comprehensive analysis of the system using various methods to determine the values of the volumetric mass transfer coefficient. The presented thermometric method for determining the rate of dissolution of atmospheric oxygen can be used in the microbiological and food industries in the development of new types of fermentation equipment in order to determine the best indicators for mass transfer, as well as to compare various types of apparatus that differ in design and energy input for mixing and aeration, and also to determine the mass-transfer parameters of industrial mass-exchange/fermentation apparatuses of large unit power. The development of the various novel engineering solutions, techniques, and methodology in fermentation are aimed to improve process efficiency, safety, and other process parameters, which are crucial to shaping a wide spectrum of biotechnology products' quality.

Author Contributions: Conceptualization, I.S. and I.N.; methodology, V.S. and D.C.; software, P.M. and S.V.; formal analysis, S.L. and N.K.; investigation, I.S., V.S., I.N. and S.L.; resources, D.C.; data curation, I.S. and P.M.; writing—original draft preparation, I.S., I.N., P.M., S.L., N.K. and V.S.; writing—review and editing, I.S., I.N., P.M., S.L. and V.S.; visualization, I.S. and P.M.; supervision, S.L. and D.C.; project administration, D.A. and D.C.; funding acquisition, I.S. and D.C. All authors have read and agreed to the published version of the manuscript.

Funding: The research funding from the Ministry of Science and Higher Education of the Russian Federation (Ural Federal University Program of Development within the Priority-2030 Program) is gratefully acknowledged.

Acknowledgments: The authors express their heartfelt gratitude to Professor Evgeny L. Listov for their professional consultation, historical references, and friendly support of the study.

Conflicts of Interest: The authors declare no conflicts of interest.

Nomenclature

ρ	density of the liquid, (kg/m^3)
C_{O_2}	dissolved oxygen concentration in the liquid, (kg/L)
$C^*_{O_2}$	equilibrium dissolved oxygen concentration in the liquid, (kg/L)
Q_{loss}	heat loss, (J)
α_{tot}	total coefficient of heat transfer by radiation and convection, $(W/(m^2\,^\circ C)$
A_{surf}	heat exchange surface area, (m^2)
T_{surf}	surface temperature of the apparatus, $(^\circ C)$
T_{out}	ambient temperature, $(^\circ C)$
Δt	measurement period, (s)
T	temperature of the liquid, $(^\circ C)$
ΔT	liquid temperature difference during the measurement, $(^\circ C)$
C_p	specific heat capacity of the liquid, $(kJ/(kg\,^\circ C))$
N_v^{heat}	specific input power (thermal), (kW/m^3)
N_v	specific input power (at the pump impeller), (kW/m^3), calculated taking into account pump and liquid specific characteristics
k_La	volumetric mass transfer coefficient, $\left(h^{-1}\right)$

References

1. Guseva, E.M.N.; Safarov, R.; Boudrant, J. An approach to modeling, scaling and optimizing the operation of bioreactors based on computational fluid dynamics. *Int. J. Softw. Prod. Syst.* **2015**, *112*, 249–255.
2. Petersen, L.A.; Villadsen, J.; Jørgensen, S.B.; Gernaey, K.V. Mixing and mass transfer in a pilot scale U-loop bioreactor. *Biotechnol. Bioeng.* **2017**, *114*, 344–354. [CrossRef] [PubMed]
3. Prasser, H.M.; Häfeli, R. Signal response of wire-mesh sensors to an idealized bubbly flow. *Nucl. Eng. Des.* **2018**, *336*, 3–14. [CrossRef]
4. Krychowska, A.; Kordas, M.; Konopacki, M.; Grygorcewicz, B.; Musik, D.; Wójcik, K.; Jędrzejczak-Silicka, M.; Rakoczy, R. Mathematical modeling of hydrodynamics in bioreactor by means of CFD-based compartment model. *Processes* **2020**, *8*, 1301. [CrossRef]
5. Yao, Y.; Fringer, O.B.; Criddle, C.S. CFD-accelerated bioreactor optimization: Reducing the hydrodynamic parameter space. *Environ. Sci. Water Res. Technol.* **2022**, *8*, 456–464. [CrossRef]
6. Panunzi, A.; Moroni, M.; Mazzelli, A.; Bravi, M. Industrial Case-Study-Based Computational Fluid Dynamic (CFD) Modeling of Stirred and Aerated Bioreactors. *ACS Omega* **2022**, *7*, 25152–25163. [CrossRef]
7. Ramírez, L.A.; Pérez, E.L.; García Díaz, C.; Camacho Luengas, D.A.; Ratkovich, N.; Reyes, L.H. CFD and Experimental Characterization of a Bioreactor: Analysis via Power Curve, Flow Patterns and k_La. *Processes* **2020**, *8*, 878. [CrossRef]
8. Cappello, V.; Plais, C.; Vial, C.; Augier, F. Scale-up of aerated bioreactors: CFD validation and application to the enzyme production by Trichoderma reesei. *Chem. Eng. Sci.* **2021**, *229*, 116033. [CrossRef]
9. Nizovtseva, I.G.; Starodumov, I.O.; Schelyaev, A.Y.; Aksenov, A.A.; Zhluktov, S.V.; Sazonova, M.L.; Kashinsky, O.N.; Timkin, L.S.; Gasenko, V.G.; Gorelik, R.S.; et al. Simulation of two-phase air–liquid flows in a closed bioreactor loop: Numerical modeling, experiments, and verification. *Math. Methods Appl. Sci.* **2022**, *45*, 8216–8229. [CrossRef]
10. Biessey, P.; Bayer, H.; Theßeling, C.; Hilbrands, E.; Grünewald, M. Prediction of Bubble Sizes in Bubble Columns with Machine Learning Methods. *Chem. Ing. Tech.* **2021**, *93*, 1968–1975. [CrossRef]
11. Cruz, I.A.; Chuenchart, W.; Long, F.; Surendra, K.; Andrade, L.R.S.; Bilal, M.; Liu, H.; Figueiredo, R.T.; Khanal, S.K.; Ferreira, L.F.R. Application of machine learning in anaerobic digestion: Perspectives and challenges. *Bioresour. Technol.* **2022**, *345*, 126433. [CrossRef] [PubMed]
12. Hessenkemper, H.; Starke, S.; Atassi, Y.; Ziegenhein, T.; Lucas, D. Bubble identification from images with machine learning methods. *arXiv* **2022**, arXiv:2202.03107.
13. Yu, S.I.; Rhee, C.; Cho, K.H.; Shin, S.G. Comparison of different machine learning algorithms to estimate liquid level for bioreactor management. *Environ. Eng. Res.* **2022**, *28*, 220037. [CrossRef]
14. Rathore, A.S.; Kanwar Shekhawat, L.; Loomba, V. Computational Fluid Dynamics for Bioreactor Design . In *Bioreactors: Design, Operation and Novel Applications*; Wiley Online Library: Hoboken, NJ, USA, 2016; pp. 295–322.
15. Ansoni, J.L.; Seleghim, P., Jr. Optimal industrial reactor design: Development of a multiobjective optimization method based on a posteriori performance parameters calculated from CFD flow solutions. *Adv. Eng. Softw.* **2016**, *91*, 23–35. [CrossRef]
16. Charles, M. Fermentation scale-up: Problems and possibilities. *Trends Biotechnol.* **1985**, *3*, 134–139. [CrossRef]
17. Gill, N.; Appleton, M.; Baganz, F.; Lye, G. Quantification of power consumption and oxygen transfer characteristics of a stirred miniature bioreactor for predictive fermentation scale-up. *Biotechnol. Bioeng.* **2008**, *100*, 1144–1155. [CrossRef]
18. Petříček, R.; Labík, L.; Moucha, T.; Rejl, F.J.; Valenz, L.; Haidl, J. Volumetric Mass Transfer Coefficient in Fermenters: Scale-up Study in Viscous Liquids. *Chem. Eng. Technol.* **2017**, *40*, 878–888. [CrossRef]

19. Schügerl, K. Comparison of different bioreactor performances. *Bioprocess Eng.* **1993**, *9*, 215–223. [CrossRef]
20. Moser, A. Bioreactor Performance: Process Design Methods. In *Bioprocess Technology*; Springer: Berlin/Heidelberg, Germany, 1988; pp. 307–405.
21. Stanbury, P.F.; Whitaker, A.; Hall, S.J. *Principles of Fermentation Technology*; Elsevier: Amsterdam, The Netherlands, 2013.
22. Halme, A.; Kiviranta, H.; Kiviranta, M. Study of a single-cell protein fermentation process for computer control. *Ifac Proc. Vol.* **1977**, *10*, 407–415. [CrossRef]
23. Pilarek, M.; Sobieszuk, P.; Wierzchowski, K.; Dąbkowska, K. Impact of operating parameters on values of a volumetric mass transfer coefficient in a single-use bioreactor with wave-induced agitation. *Chem. Eng. Res. Des.* **2018**, *136*, 1–10. [CrossRef]
24. Šulc, R.; Dymák, J. Hydrodynamics and Mass Transfer in a Concentric Internal Jet-Loop Airlift Bioreactor Equipped with a Deflector. *Energies* **2021**, *14*, 4329. [CrossRef]
25. Bun, S.; Wongwailikhit, K.; Chawaloesphonsiya, N.; Lohwacharin, J.; Ham, P.; Painmanakul, P. Development of modified airlift reactor (MALR) for improving oxygen transfer: Optimize design and operation condition using 'design of experiment'methodology. *Environ. Technol.* **2020**, *41*, 2670–2682. [CrossRef] [PubMed]
26. Hibiki, T.; Goda, H.; Kim, S.; Ishii, M.; Uhle, J. Experimental study on interfacial area transport of a vertical downward bubbly flow. *Exp. Fluids* **2003**, *35*, 100–111. [CrossRef]
27. Kreitmayer, D.; Gopireddy, S.R.; Matsuura, T.; Aki, Y.; Katayama, Y.; Nakano, T.; Eguchi, T.; Kakihara, H.; Nonaka, K.; Profitlich, T.; et al. CFD-Based and Experimental Hydrodynamic Characterization of the Single-Use Bioreactor XcellerexTM XDR-10. *Bioengineering* **2022**, *9*, 22. [CrossRef] [PubMed]
28. Vaidheeswaran, A.; Hibiki, T. Bubble-induced turbulence modeling for vertical bubbly flows. *Int. J. Heat Mass Transf.* **2017**, *115*, 741–752. [CrossRef]
29. Ohba, K.; Yuhara, T.; Matsuyama, H. Simultaneous measurements of bubble and liquid velocities in two-phase bubbly flow using laser Doppler velocimeter. *Bull. JSME* **1986**, *29*, 2487–2493. [CrossRef]
30. Maischberger, T. Optimized process and bioreactor characterization. *Chem. Ing. Tech.* **2019**, *91*, 1719–1723. [CrossRef]
31. Bun, S.; Chawaloesphonsiya, N.; Ham, P.; Wongwailikhit, K.; Chaiwiwatworakul, P.; Painmanakul, P. Experimental and empirical investigation of mass transfer enhancement in multi-scale modified airlift reactors. *Multiscale Multidiscip. Model. Exp. Des.* **2020**, *3*, 89–101. [CrossRef]
32. Richard, H.; Irina, N.; Dmitri, C.; Kalyuzhnaya, M.G. C1-Proteins Prospect for Production of Industrial Proteins and Protein-Based Materials from Methane. In *Algal Biorefineries and the Circular Bioeconomy*; CRC Press: Boca Raton, FL, USA, 2022; pp. 251–276.
33. Strong, P.; Kalyuzhnaya, M.; Silverman, J.; Clarke, W. A methanotroph-based biorefinery: Potential scenarios for generating multiple products from a single fermentation. *Bioresour. Technol.* **2016**, *215*, 314–323. [CrossRef]
34. Listov, E.L.; Chernushkin, D.V.; Burov, S.N.; Dibtsov, V.P.; Sorokin, A.G.; Butorova, I.A.; Aksyutin, O.E.; Ishkov, A.G.; Bondarenko, K.N.; Shajkhutdinov, A.Z.; et al. Method for Determining Mass-Exchange Apparatus Efficiency. RUS Patent RU 2702539 C1, 20 February 2019. .
35. Wallis, G. *One-Dimensional Two-Phase Flow*; McGraw Hill: New York, NY, USA, 1969.
36. Levich, V. *Physicochemical Hydrodynamics*; Prentice-Hall: Upper Saddle River, NJ, USA, 2017.
37. Viestur, U.; Kuznetsov, A.; Savenkov, B. *Sistemy Fermentacii*; Zinatne: Riga, Latvia, 1986.
38. Kirillin, V.; Sychev, V.; Sheindlin, A. *Technical Thermodynamics*; Izdatel Energiia: Moscow, Russia, 1974.
39. Nazarov, V. Processes and devices of microbiological productions. *J. Tech. Res.* **2016**, *2*, 4.
40. Vinogradova, A.; Anashkina, E. *Obshchaya Biotekhnologiya*; Perm University Press: Perm Krai , Russia, 2008.
41. Khabibrahmanov, R.; Muhachev, S. Issledovanie massoobmennyh harakteristik apparatov s perforirovannymi meshalkami sul'fitnym metodom. *Vestn. Kazan. Tekhnologicheskogo Univ.* **2014**, *17*, 140–143.
42. Mironov, M.; Tokareva, M. *Metody Rascheta Oborudovaniya Biotekhnologicheskih Proizvodstv*; Urals University Press: Chelyabinsk, Russia, 2017.

fluids

MDPI

Article

Bubble Growth in Supersaturated Liquids

Raj Kumar Nayak Maloth, Roger E. Khayat * and Christopher T. DeGroot

Department of Mechanical and Material Engineering, University of Western Ontario, London, ON N6A 3K7, Canada
* Correspondence: rkhayat@uwo.ca

Abstract: Bubble formation and dissolution have a wide range of industrial applications, from the production of beverages to foam manufacturing processes. The rate at which the bubble expands or contracts has a significant effect on these processes. In the current work, the hydrodynamics of an isolated bubble expanding due to mass transfer in a pool of supersaturated gas–liquid solution is investigated. The complete scalar transportation equation (advection–diffusion) is solved numerically. It is observed that the present model accurately predicted bubble growth when compared with existing approximated models and experiments. The effect of gas–liquid solution parameters such as inertia, viscosity, surface tension, diffusion coefficient, system pressure, and solubility of the gas has been investigated. It is found that the surface tension and inertia have a very minimal effect during the bubble expansion. However, it is observed that the viscosity, system pressure, diffusion, and solubility have a considerable effect on bubble growth.

Keywords: bubble growth; hydrodynamics; supersaturated liquids; 1-d moving interface; advection–diffusion process

Citation: Maloth, R.K.N.; Khayat, R.E.; DeGroot, C.T. Bubble Growth in Supersaturated Liquids. *Fluids* **2022**, *7*, 365. https://doi.org/10.3390/fluids7120365

Academic Editor: Mehrdad Massoudi

Received: 18 October 2022
Accepted: 22 November 2022
Published: 25 November 2022

Publisher's Note: MDPI stays neutral with regard to jurisdictional claims in published maps and institutional affiliations.

1. Introduction

A gas bubble is formed when an atomically or molecularly dissolved gas becomes supersaturated in a liquid solvent as a result of the reduction in imposed gas pressure, change in liquid temperature, or change in solute or solvent character Rosner et al., 1972, [1]. The study of gas bubbles is of major interest due to their appearance in many real-world problems. One of the important applications of bubble hydrodynamics is in chemical process industries, for example in the production of foamed plastics Elshereef et al., 2010, [2]. When a gas-generating substance such as a blowing agent is mixed with a high-pressure molten polymer, the resulting product turns out to be thermoplastic Arefmanesh et al., 1992, [3]. In this process, gas bubbles emerge and have a considerable effect on product quality. Therefore, it is necessary to understand the behavior of bubbles under different process parameter conditions. High-density foamed thermoplastics, otherwise called cellular plastics, are used in household furniture, transportation, and building products; on the other hand, low-density thermoplastics are frequently used in rigid packing Lee et al., 1996, [4]. The formation and growth of bubbles due to de-gassing or reduction in pressure in a supersaturated gas–liquid solution is observed in a broader spectrum of industrial and natural processes. For example, a very well-known process in which de-gassing is observed are carbonated beverages, such as beer, soda, and champagne (Bisperink et al., 1994, [5]; Jones et al., 1999, [6]; Barker et al., 2002, [7]; Liger-Belair 2005, [8]; Lee et al., 2011, [9]; Enríquez et al., 2013, [10] Enríquez et al., 2014, [11]). The study of bubble dynamics is vital in production industries, where molten polymers, metals, and glasses are of major interest Amon and Denson, 1984, [12] and a bubble prediction theory is important in the exsolution of gases during oil extraction Pooladi-Darvish et al., 1999, [13].

Several mathematical models have been developed to predict the bubble size evolution in various industrial processes. For instance, Epstein and Plesset, 1950, [14] derived

an approximate analytical solution, by neglecting inertia, to an unbounded single bubble growth/dissolution in a gas–liquid solution due to pure mass transfer (diffusion) for supersaturated and undersaturated conditions. Epstein's formulation suggests that the bubble grows as the square root of time, i.e., $\overline{R} \propto \sqrt{\overline{t}}$, where $\overline{R}$ is the radius of the bubble. However, their formulation lacks in explaining the hydrodynamic effects on bubble growth, including inertia, surface tension, etc. Barlow and Langlois, 1962, [15] were the first to combine diffusion with hydrodynamics, wherein they introduced a very complicated integro-differential equation based on a thin shell assumption. The formulation of Barlow et al. is complicated and computationally time-consuming to solve for larger bubble growth rates. Rosner and Epstein, 1972, [1] assumed a parabolic concentration profile in a thin boundary layer to generate an approximate solution of the diffusion equation. This work has been adopted by many researchers including Elshereef et al., 2010, [2], Patel, 1980, [16] and Han and Yoo, 1981, [17] formulation does not account for the change in gas pressure inside the bubble with time. Patel, 1980, [16] developed two coupled ordinary differential equations (ODEs) for predicting the unbounded growth of a single bubble in a Newtonian liquid; however, he neglected the effect of inertia in his formulation. Later, Amon and Denson, 1984, [12] introduced a cell-based model that incorporates the effect of available gas from the surrounding bubbles. Amon and Denson's formulation is developed based on a cell model assumption, where they have considered the foam as a summation of an equal microscopic unit of spherical cells with a constant mass in it and every cell has a spherical gas bubble that grows by diffusion of gas from the microscopic unit.

As discussed earlier, Barlow et al., 1962, [15] and Patel, 1980, [16] developed models for pure Newtonian fluid cases, hence neglected the effect of the elastic nature of the polymer. To fill this gap, Han and Yoo, 1981, [17] and Ramesh et al., 1991, [18] introduced a model that includes the effect of the elasticity of the fluid (polymer). Elshereef et al., 2010, [2] compared two popular bubble growth models. The first model is known as the Patel model or single bubble growth model, which is developed on assumption that a single bubble grows in a pool of liquid with infinite availability of gas, and the second model is called a cell model or Amon and Denson model, which is developed by incorporating the finiteness of gas availability and considering the proximity of gas bubbles. The main motivation of the Elshereef et al., 2010, [2] investigation was to compare these two models in terms of numerical implementations and accuracy in bubble growth prediction. In this regard, they compared the models with Han and Yoo's experimental findings. In recent years, Soto et al., 2019, 2020, [19,20] investigated experimentally carbon dioxide (CO_2) and nitrogen (N_2) bubble growth in water solutions with and without confinements. Their finding suggests that after the initial period of diffusion-driven bubble growth, the mass transfer is further accelerated due to density-driven convective flow.

Although researchers have performed ample work in understanding the hydrodynamics of the bubbles in different processes, clear insight into the diffusion process coupling with hydrodynamics and an explanation of process flow parameters' effects on hydrodynamics are lacking. The current work emphasizes solving the diffusion process numerically and closely studying how different liquid parameters such as liquid viscosity, surface tension, diffusion coefficient, system pressure, and solubility of gas affect the hydrodynamics of bubble growth. Though the current numerical framework developed in this work is for Newtonian liquids, the authors aim to explore how the current model compares with the different Newtonian liquid models of Elshereef et al., 2010, [2] and the viscoelastic experimental data of Han and Yoo, 1981, [17].

2. Physical Domain and Problem Formulation

2.1. The Physical Domain

The hydrodynamics of an isolated, spherically symmetrical gas bubble of radius $\overline{R}(\overline{t})$, where $\overline{t}$ is the time, in an incompressible gas–liquid solution is examined in spherical coordinates $(\overline{r}, \overline{\theta}, \overline{\phi})$. Barred variables denote dimensional quantities. We assume a stationary single bubble of initial radius $\overline{R}_0$ and a gas pressure $\overline{p}_{g0}$ nucleating in a saturated solution

of gas and liquid with the partial pressure of the gas in the liquid $\overline{p}_0$ and concentration $\overline{c}_0$, as shown in Figure 1. Denoting the interfacial tension by σ, then $\overline{p}_{g0} = \frac{\sigma}{\overline{R}_0} + \overline{p}_0$. At $\overline{t} = 0^+$, the gas–liquid solution is suddenly exposed to a drop in pressure when the atmospheric pressure $\overline{p}_a$ is applied in the bulk liquid region far from the gas bubble, and where it is assumed maintained for all time $\overline{t} > 0$. We denote by $\overline{p}_R(\overline{t})$ the pressure at the gas–liquid interface and by $\overline{p}_g(\overline{t})$, the gas pressure inside the bubble. The concentration of the gas in the liquid at a given time and position is denoted by $\overline{c}(\overline{r}, \overline{t})$, whereas the concentration at the interface of the bubble is $\overline{c}_R(\overline{t}) \equiv \overline{c}(\overline{r} = \overline{R}, \overline{t})$. Due to the spherical symmetry assumption the velocity components $\overline{v}$ and $\overline{w}$ in the direction $\overline{\theta}$ *and* $\overline{\phi}$ vanishes. Therefore, the only non-vanishing liquid velocity component is in radial direction and denoted by $\overline{u}(\overline{r}, \overline{t})$ and the bubble interface velocity is given by $\frac{d\overline{R}}{d\overline{t}} = \overline{u}(\overline{r} = \overline{R}, \overline{t})$ Maloth, 2020, [21]. Henry's law is assumed to apply initially so that $\overline{c}_0 = k_H \overline{p}_0$ and at the interface so that $\overline{c}_R(\overline{t}) = k_H \overline{p}_R(\overline{t})$, where k_H is Henry's constant. Finally, as it is customarily done in the literature, we assume that the concentration far from the bubble retains its initial level as it is not affected by the sudden drop in pressure during the transient process of bubble growth. Thus, $\overline{c}(\overline{r} \to \infty, \overline{t}) \sim \overline{c}_0$.

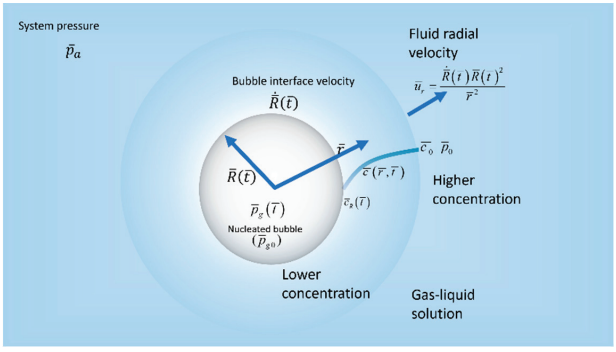

Figure 1. Schematic diagram of a single bubble in a liquid–gas solution.

2.2. Conservation of Mass and Linear Momentum

The flow of the Newtonian liquid of density ρ_L and viscosity μ_L is assumed to be spherically symmetric, thus reducing to a transient one-dimensional problem in the radial direction, $\overline{r}$. The conservation of mass and momentum in the liquid region reduces to

$$\frac{\partial \overline{u}}{\partial \overline{r}} + 2\frac{\overline{u}}{\overline{r}} = 0 \tag{1}$$

$$\rho_L\left(\frac{\partial \overline{u}}{\partial \overline{t}} + \overline{u}\frac{\partial \overline{u}}{\partial \overline{r}}\right) = -\frac{\partial \overline{p}}{\partial \overline{r}} + 2\mu_L\left(\frac{\partial^2 \overline{u}}{\partial \overline{r}^2} + \frac{1}{\overline{r}}\frac{\partial \overline{u}}{\partial \overline{r}} - \frac{1}{\overline{r}^2}\overline{u}\right). \tag{2}$$

These equations are subject to the following initial and boundary conditions. Initially, the bubble is assumed to be of radius $\overline{R}_0$ and at rest, so that

$$\overline{R}(t = 0) = \overline{R}_0,\ \overline{u}(\overline{r}, \overline{t} = 0) = 0. \tag{3}$$

The kinematic and dynamic boundary conditions at the interface take the form:

$$\overline{u}(\overline{r} = \overline{R}, \overline{t}) = \frac{d\overline{R}}{d\overline{t}} \tag{4}$$

$$\overline{p}_g(\overline{t}) = 2\frac{\sigma}{\overline{R}(\overline{t})} + \overline{p}(\overline{r} = \overline{R}, \overline{t}) + 4\frac{\mu_L}{\overline{R}(\overline{t})}\overline{u}(\overline{r} = \overline{R}, \overline{t}), \tag{5}$$

where σ is the interfacial tension. In stating condition (5), the gas inside the bubble is assumed to be motionless. Integrating Equation (1) and using condition (4) leads to

$$\overline{u}(\overline{r},\overline{t}) = \frac{\overline{R}^2}{\overline{r}^2}\frac{d\overline{R}}{d\overline{t}}. \tag{6}$$

Substituting this expression for the radial velocity and integrating Equation (2) over the interval $\overline{r} \in (\overline{R},\infty)$, and eliminating the pressure at the interface from conditions (5) yields the Rayleigh–Plesset equation:

$$\rho_L\left[\overline{R}\frac{d^2\overline{R}}{d\overline{t}^2} + \frac{3}{2}\left(\frac{d\overline{R}}{d\overline{t}}\right)^2\right] = \overline{p}_g(\overline{t}) - 2\frac{\sigma}{\overline{R}} - 4\frac{\mu_L}{\overline{R}}\frac{d\overline{R}}{d\overline{t}} - \overline{p}_a. \tag{7}$$

Here, the growth of the bubble is dictated by the pressure difference $\overline{p}_g - \overline{p}_a$, where $\overline{p}_g > \overline{p}_a$. We note that the pressure at infinity is the surrounding or ambient pressure of the liquid and is equal to $\overline{p}_a$. Equation (7) can be solved once and $\overline{p}_g(\overline{t})$ is determined. The evolution of the gas pressure inside the bubble is directly related to the evolution and distribution of the gas concentration in the liquid, which is formulated next.

2.3. Concentration and Mass Transfer

In a supersaturated liquid, bubbles grow due to the diffusion of mass across the interface. Therefore, the diffusive mass flux across the interface is equal to the rate of change in mass inside the gas bubble. According to Fick's first law, the time rate of change in mass flux $\dot{m}_R$ at the interface of the spherical bubble is then given by

$$\frac{d\overline{m}_R}{d\overline{t}} = 4\pi\overline{R}^2 D\left(\frac{\partial\overline{c}}{\partial\overline{r}}\right)_{\overline{R}}. \tag{8}$$

Here, $\left(\frac{\partial\overline{c}}{\partial\overline{r}}\right)_{\overline{R}} = \frac{\partial\overline{c}}{\partial\overline{r}}(\overline{r}=\overline{R},\overline{t})$ is the concentration gradient of the gas at the interface and D (m^2/s) is the diffusion coefficient of the gas–liquid solution. Now, let the mass of the gas inside the bubble be $\overline{m}_g(\overline{t}) = \frac{4}{3}\pi\overline{\rho}_{g0}(\overline{t})\overline{R}^3(\overline{t})$, where $\overline{\rho}_g(\overline{t})$ is the gas density. Then, the rate of change in mass inside the spherical bubble is

$$\frac{d\overline{m}_g}{d\overline{t}} = 4\pi\overline{R}^2\left(\overline{\rho}_g\dot{\overline{R}} + \frac{\overline{R}}{3}\dot{\overline{\rho}}_g\right). \tag{9}$$

Assuming that the gas inside the bubble follows the ideal gas law, the density of the gas can be eliminated in terms of the pressure as $\overline{\rho}_g(\overline{t}) = \frac{\overline{p}_g(\overline{t})M}{R_g\overline{T}_g}$, where R_g is the universal gas constant; $\overline{T}_g$ is the temperature of the gas, which is assumed to remain constant throughout the transient process; and M is the molar gas weight. We also assume that, after nucleation, the pressure inside the bubble is in equilibrium with the initial saturation pressure $\overline{p}_{g0}$ and density $\overline{\rho}_{g0}$. In this case, we can write $\overline{\rho}_g(\overline{t}) = \frac{\overline{\rho}_{g0}}{\overline{p}_{g0}}\overline{p}_g(\overline{t})$, and Equation (9) becomes

$$\frac{d\overline{m}_g}{d\overline{t}} = 4\pi\frac{\overline{\rho}_{g0}}{\overline{p}_{g0}}\overline{R}^2\left(\overline{p}_g\frac{d\overline{R}}{d\overline{t}} + \frac{\overline{R}}{3}\frac{d\overline{p}_g}{d\overline{t}}\right) \tag{10}$$

Upon introducing (10) into Equation (8), we obtain the desired equation for the pressure inside the gas bubble:

$$\frac{d\overline{p}_g}{d\overline{t}} = 3\frac{\overline{p}_{g0}}{\overline{\rho}_{g0}}D\frac{1}{\overline{R}}\left(\frac{\partial\overline{c}}{\partial\overline{r}}\right)_{\overline{R}} - 3\frac{\overline{p}_g}{\overline{R}}\frac{d\overline{R}}{d\overline{t}}. \tag{11}$$

This is the pressure equation resulting from the thermodynamic equilibrium at the interface. This first-order equation requires one initial condition on the pressure inside the bubble, which is formally written as

$$\overline{p}_g(\bar{t}=0) = \overline{p}_{g0}. \tag{12}$$

Equations (7) and (11) reflect the coupling between the bubble growth and pressure evolution inside the bubble. The presence of the concentration gradient at the interface in (11) also signals an additional coupling with the gas concentration across the saturated liquid, which is governed by an advection–diffusion equation, as shown next.

The concentration of gas in the liquid $\overline{c}(\overline{r},\bar{t})$ can be described by the scalar transport advection–diffusion equation which, when the velocity is substituted from (6) in the convective term, becomes

$$\frac{\partial \overline{c}}{\partial \bar{t}} + \frac{\overline{R}^2}{\overline{r}^2}\frac{d\overline{R}}{d\bar{t}}\frac{\partial \overline{c}}{\partial \overline{r}} = D\left(\frac{2}{\overline{r}}\frac{\partial \overline{c}}{\partial \overline{r}} + \frac{\partial^2 \overline{c}}{\partial \overline{r}^2}\right). \tag{13}$$

The initial condition for Equation (13) comes from the assumption that, after the nucleation of the bubble, the concentration is uniformly distributed in the liquid, and it is equal to the dissolved concentration $\overline{c}_0$. Therefore, it is written as

$$\overline{c}(\overline{r},\bar{t}=0) = \overline{c}_0. \tag{14}$$

The remaining two boundary conditions for Equation (13) are the equilibrium condition of the concentration at the interface, which is described by Henry's law,

$$\overline{c}(\overline{r}=\overline{R},\bar{t}) = \overline{c}_R(\bar{t}) = k_H \overline{p}_g(\bar{t}), \tag{15}$$

where k_H is Henry's constant. The concentration far from the bubble is assumed to be equal to the saturation concentration:

$$\overline{c}(\overline{r}\to\infty,\bar{t}) \sim \overline{c}_0 = k_H\overline{p}_0 = k_H\left(\overline{p}_{g0} - 2\frac{\sigma}{\overline{R}_0}\right). \tag{16}$$

This completes the formulation of the problem, which illustrates the non-linear coupling among the bubble growth, gas pressure, and concentration in the liquid region.

Equation (11) is similar to the pressure formulation of Elshereef et al., 2010, [2]. However, they assumed an approximate analytical solution to calculate the concentration gradient that appears in Equation (11). In the present work, one of the main goals is to solve the fully coupled problem numerically using a finite difference approach and compare it with the approximated analytical results.

3. Non-Dimensionalization and Solution Procedure

3.1. The Dimensionless Problem

The equations and their initial and boundary conditions are non-dimensionalized as follows. The velocity scale is taken as $\overline{V} = \sqrt{\frac{(\overline{p}_{g0}-\overline{p}_a)}{\rho_L}}$, which is related to the initial driving pressure difference, the length scale is the initial bubble radius $\overline{R}_0$, the pressure scale is the initial gas pressure $\overline{p}_{g0}$, and the concentration scale is the equilibrium concentration $\overline{c}_0$. In this case, the time scale is naturally $\frac{\overline{R}_0}{\overline{V}}$. The dimensionless variables become

$$r = \frac{\overline{r}}{\overline{R}_0},\ c = \frac{\overline{c}}{\overline{c}_0},\ t = \frac{\overline{V}}{\overline{R}_0}\bar{t},\ R = \frac{\overline{R}}{\overline{R}_0},\ p = \frac{\overline{p}}{\overline{p}_{g0}}\ . \tag{17}$$

There are five non-dimensional groups appearing in the problem, three familiar groups: the Reynolds number Re, the capillary number Ca and the Péclet number Pe. More explicitly:

$$Re = \frac{\rho_L \overline{V}\, \overline{R}_0}{\mu_L}, \tag{18a}$$

$$Ca = \frac{\rho_L \overline{V}^2 \overline{R}_0}{\sigma} = \frac{(\overline{p}_{g0} - \overline{p}_a)\overline{R}_0}{\sigma}, \tag{18b}$$

$$Pe = \frac{\overline{V}\, \overline{R}_0}{D}. \tag{18c}$$

Here, the Reynolds number (Re) compares the inertial force due to bubble growth in the liquid region with the liquid viscosity. The capillary number (Ca) weighs between viscous forces from the liquid to the surface tension forces at the interface of the bubble and the liquid and the Péclet number describes the ratio between the convection mass transfer to the diffusive mass transfer of gas from the liquid into the bubble.

The additional two new non-dimensional parameters are denoted by P and C, the former being the ratio of the initial pressure to the pressure difference, and the latter reflects the initial level of gas solubility:

$$P = \frac{\overline{p}_{g0}}{\overline{p}_{g0} - \overline{p}_a} = \frac{1}{1 - p_a}, \tag{19a}$$

$$C = \frac{\overline{c}_0}{\overline{p}_{g0}}. \tag{19b}$$

Finally, a sixth additional parameter in the problem is the dimensionless atmospheric-to-gas pressure ratio $p_a = \frac{\overline{p}_a}{\overline{p}_{g0}}$.

3.2. Domain Mapping

The interface of the bubble changes with time, which makes the numerical procedure for solving the concentration distribution in the liquid more complicated and time-consuming. We implement an implicit finite difference in space and integrate the resulting equations with respect to time. One obvious but costly approach is to track the interface of the bubble with time and re-mesh the computational domain at each time step.

Alternatively, we recast the concentration Equation (13) in terms of Lagrangian coordinates $\overline{x}(\overline{r}, \overline{t}) = \overline{r} - \overline{R}(t)$, such that at all time intervals the interface is fixed. Therefore, after non-dimensionalization and coordinate transformation the Equations (7), (11) and (13) takes the form:

$$R\frac{d^2R}{dt^2} + \frac{3}{2}\left(\frac{dR}{dt}\right)^2 = P(p_g - p_a) - \frac{2}{CaR} - \frac{4}{ReR}\frac{dR}{dt}. \tag{20}$$

$$\frac{dp_g}{dt} = 3\frac{C}{RPe}\left(\frac{\partial c}{\partial x}\right)_{\mathrm{x=0}} - 3\frac{p_g}{R}\frac{dR}{dt} \tag{21}$$

$$\frac{\partial c}{\partial t} + \frac{\partial c}{\partial x}\left(\frac{\dot{R}R^2}{(x+R)^2} - \dot{R}\right) = \frac{1}{Pe}\left(\frac{2}{x+R}\frac{\partial c}{\partial x} + \frac{\partial^2 c}{\partial x^2}\right) \tag{22}$$

The rescaled initial and boundary conditions are deduced from (3), (12), and (14) to:

$$R(t=0) = 1, \tag{23a}$$

$$\dot{R}(t=0) = 0, \tag{23b}$$

$$p_g(t=0) = 1, \tag{23c}$$

$$c(x, t = 0) = 1. \tag{23d}$$

$$c(x = 0, t) = p_g(t), \tag{24a}$$

$$c(\, x \to \infty, t\,) = 1. \tag{24b}$$

3.3. Numerical Implementation

Equation (20) is a non-linear, second-order ODE that describes the bubble growth. If the pressure in the bubble is constant, Equation (20) can be solved for the bubble growth $R(t)$ and its interface velocity $\dot{R}(t)$ with the use of any readily available numerical time integration solver, such as ode45 in MathWorks MATLAB version R2019b. However, the difficulty arises when the pressure inside the bubble varies with time, and it then needs to be coupled with the scalar diffusion equation to solve for the concentration gradient at the interface. Additionally, the scalar diffusion Equation (22) contains a highly non-linear convective term in terms of bubble radius and interface velocity. This combination makes the equations stiffer and involves solving Equations (20)–(22) simultaneously. Therefore, solving the highly stiff equations with ode45 takes a tremendous amount of time. Instead of ode45, a variable order of accuracy solver, ode15s, is used to integrate the equations. Here, ode15s uses first to fifth orders, changing the order as required. This solver takes much less time compared to the ode45 solver without compromising accuracy.

To solve these two equations simultaneously, the second-order non-linear hydrodynamic Equation (20) primarily needs to be converted into the system of first-order ODEs by letting $R = y_1$. Therefore, the system of first-order ODEs is given as

$$\frac{dR}{dt} = y_2 \tag{25}$$

$$\frac{dy_2}{dt} = \frac{1}{y_1}\left(P(p_g - p_a) - \frac{2}{y_1 Ca} - \frac{4y_2}{y_1 Re} - \frac{3}{2}y_2^2\right) \tag{26}$$

This way, when Equation (25) is integrated, one can obtain y_2, which is bubble interface velocity, and similarly Equation (26) is integrated to obtain y_1, which is the bubble radius. Since Equation (26) includes partial derivates in time and space, one can approximate either time or space using the finite difference methods. For convenience, the space partial derivative is approximated with a finite difference, up to second-order accuracy.

Let i be the node position and N be the total number of nodes (see Figure 2) in the gas–liquid solution, starting from the interface $x = 0$ to infinity. The central difference scheme is adopted for the derivates. Therefore, the finite difference approximation for the first- and second-order derivatives with central difference schemes are written as

$$\frac{\partial c}{\partial x} = \frac{c_{i+1} - c_{i-1}}{2dx} \tag{27}$$

$$\frac{\partial^2 c}{\partial x^2} = \frac{c_{i+1} - 2c_i + c_{i-1}}{dx^2} \tag{28}$$

The discretized form of the scalar diffusion equation using Equations (27) and (28) takes the form

$$\frac{dc_i}{dt} = \frac{1}{Pe}\left(\frac{2}{(x_i + R)}\left(\frac{c_{i+1} - c_{i-1}}{2dx}\right) + \left(\frac{c_{i+1} - 2c_i + c_{i-1}}{dx^2}\right)\right) - \left(\frac{c_{i+1} - c_{i-1}}{2dx}\right)\left(\frac{\dot{R}R^2}{(x_i + R)^2} - \dot{R}\right) \tag{29}$$

The discretized form of diffusion Equation (29) needs to be solved at $N - 2$ $(1 < i < N)$ nodes, starting from $i = 2$ to $i = N - 1$. Whereas at the interface, i.e., at $i = 1$, the boundary condition (24a) can be written in terms of ODE as

$$\frac{dc_1}{dt} = \left(\frac{k_h \overline{p}_{g0}}{\overline{c}_0}\right)\frac{dp_g}{dt} \tag{30}$$

The final node serves as a boundary and the value of concentration is known from the boundary condition (24b), therefore at $i = N$,

$$c_N = 1 \tag{31}$$

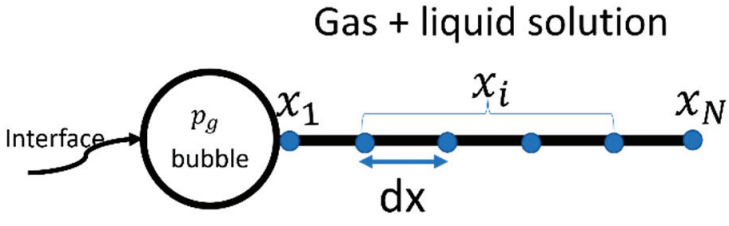

Figure 2. Numerical domain.

Similarly, the concentration gradient at the interface in Equation (21) is discretized using a forward finite difference scheme and is given as

$$\frac{\partial c}{\partial x} = \frac{c_{i+1} - c_i}{dx}, \tag{32}$$

and substituting Equation (32) in (21) results in

$$\frac{dp_g}{dt} = \frac{3I}{RPe}\left(\frac{c_{i+1} - c_i}{dx}\right) - 3\overline{p}_g\left(\frac{\dot{R}}{R}\right) \tag{33}$$

To be consistent with the notation used for the hydrodynamic ODEs (25) to (26), Equations (29) to (33) are rewritten in terms of y as follows:

For the nodes between 1 and N ($1 < i < N$) is written as

$$\begin{aligned}\frac{dy_{3+i}}{dt} = \frac{1}{Pe}\left(\frac{2}{(x_i+y_1)}\left(\frac{y_{3+(i+1)}-y_{3+(i-1)}}{2dx}\right) + \left(\frac{y_{3+(i+1)}-2y_{3+i}+y_{3+(i-1)}}{dx^2}\right)\right)\\ -\left(\frac{y_{3+(i+1)}-y_{3+(i-1)}}{2dx}\right)\left(\frac{y_2{y_1}^2}{(x_i+y_1)^2} - y_2\right)\end{aligned} \tag{34}$$

at the interface node $(i = 1)$,

$$\frac{dc_{y_3+i}}{dt} = \frac{dy_3}{dt} \tag{35}$$

and at the final boundary node $i = N$,

$$y_{N+3} = 1. \tag{36}$$

Finally, the pressure equation takes the form:

$$\frac{dy_3}{dt} = \frac{3I}{y_1 Pe}\left(\frac{y_5 - y_4}{dx}\right) - 3y_3\left(\frac{y_2}{y_1}\right) \tag{37}$$

Therefore, the total (N +3) equations starting from (25) to (37) are the final system of ODEs that has to be solved simultaneously subjected to the initial and boundary conditions (23) to (24).

3.4. Grid Independence Test

For the numerical simulations, the infinite spatial domain is assumed to be 10 times the maximum radius of the bubble. Furthermore, the maximum radius of the bubble is anticipated to be 250 μm. This suggests that the physical infinity of the domain is 250 × 10 = 2500 μm and in terms of x_∞ it is 2250. (Note that $x = r - R(t)$). The grid independence test seeks to minimize discretization error by making the numerical solution independent of the grid

spacing. Figure 3 shows that the solution converges with increasing number of nodes. When the domain is discretized from 100 to 1000 nodes a 15% of maximum error is observed in the bubble radius and the error reduced to 2% as the number of nodes increased from 1000 to 3000; Therefore, to achieve accurate results in the numerical simulations, the domain is equally discretized with 3000 nodes.

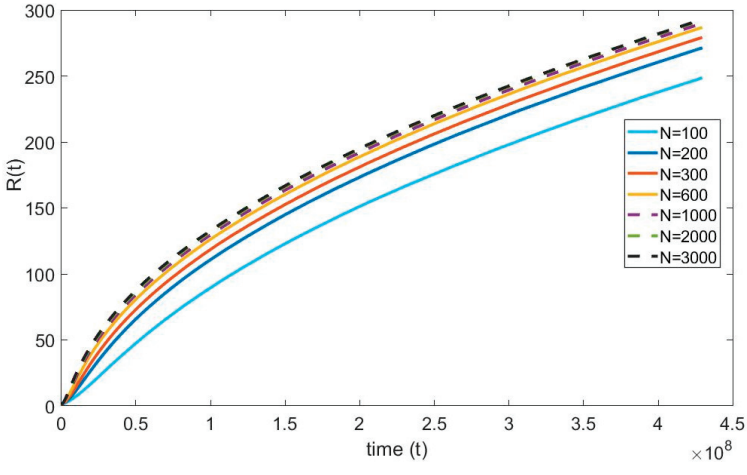

Figure 3. Grid independence test of the diffusion equation.

4. Results and Discussion

4.1. Comparison with Existing Experiments and Theory

A comparison has been made between the present model and experiment data of Han and Yoo, 1981, [17] along with the Patel, 1980, [16] and Amon and Denson, 1984, [12] models in Figure 4. The comparison is carried out based on Han and Yoo, 1981, [17] viscoelastic bubble growth experimental data for $Re = 4.5 \times 10^{-6}$, $Ca = 13.17$, $P = 1.27$, $C = 0.3$, and $Pe = 3.7 \times 10^{4}$. It is evident from the plot that the present numerical model was able to capture the experimental data more accurately than the other two models. In the initial stages, it is observed that there is a discrepancy between all the bubble growth models when compared to the experimental data of Han and Yoo, 1981, [17]. This type of divergence at the initial stage is expected, since the polymer used by Han and Yoo for the experiment exhibits the viscoelastic effect, whereas other numerical models stated in the work including the present numerical model were developed based on pure Newtonian fluid assumptions. This indicates that the viscoelastic nature of the liquid is of importance only at the initial stages and has minimum to no effects on the later stages of bubble growth.

Similarly, Figure 4 shows that the trend of the models proposed by Patel and Amon and Denson were similar at their initial and later stages. Amon and Denson's model deviates from the Patel model and moves toward the present numerical model. It is worth mentioning that the slight deviation of the aforementioned models from the present model is because of the cell model assumptions carried out by the authors in their work, whereas the present model is solved completely with the numerical approach. Overall, the present model shows more promising and accurate predictions than previous models.

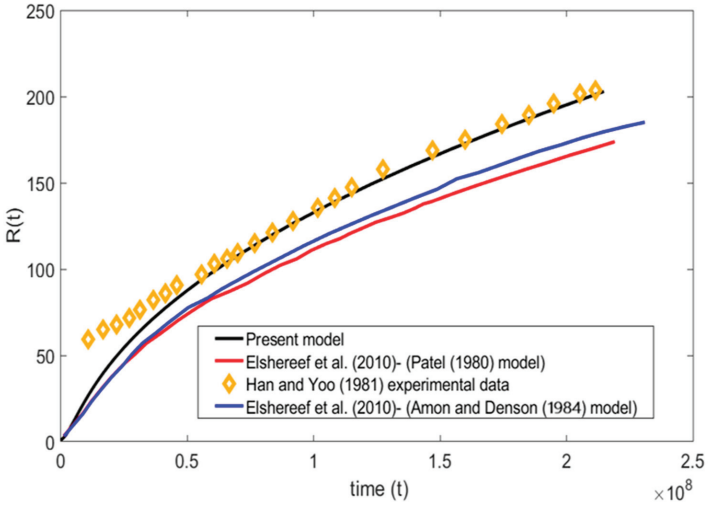

Figure 4. Present model comparison with experiment data of Han and Yoo, 1981, [17] and theory of Elshereef et al., 2010, [2], Amon and Denson, 1984, [12] and Patel, 1980, [16] ($Re = 4.5 \times 10^{-6}$, $Ca = 13.17$, $P = 1.27$, $C = 0.3$, and $Pe = 3.7 \times 10^4$).

4.2. Concentration in the Liquid

In the literature, the variation in concentration of gas in the liquid medium has not been reported or investigated thoroughly. For instance, Elshereef et al., 2010, [2] reported that his second comparison model, which is developed by Amon and Denson, 1984, [12], has solved the advection–diffusion equation using finite difference approximation. However, the concentration profiles in the liquid side were not reported. In this section, we present the concentration profile of the gas in the liquid explicitly.

Figures 5 and 6, represent the transient concentration profiles at different locations and time instances. The positional concentration profiles (Figure 5) are shown from the bubble interface, i.e., $x = 0$, to the location where the concentration gradient disappears, i.e., $x = 400$. Additionally, the time instances (Figure 6) are shown from 0.01 to 20 s. It is expected that as we move farther from the interface, the concentration gradient decreases, and this trend can be observed in Figure 5. Similarly, Figure 6 shows that at the initial time steps the concentration profile at the interface starts developing and eventually reaches a steady state with larger gradients at a larger time period.

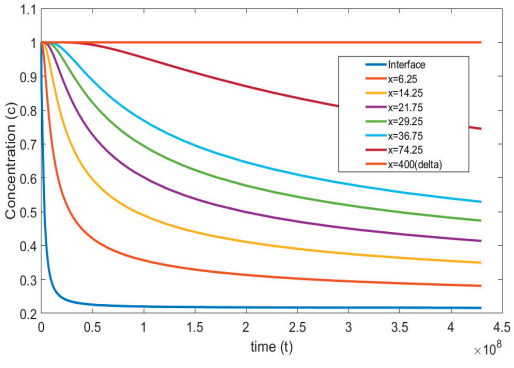

Figure 5. Concentration profiles reported at different positions with dimensionless time ($Re = 4.5 \times 10^{-6}$, $Ca = 13.17$, $P = 1.27$, $C = 0.3$, $Pe = 3.7 \times 10^4$, $t = 4.5 \times 10^8$).

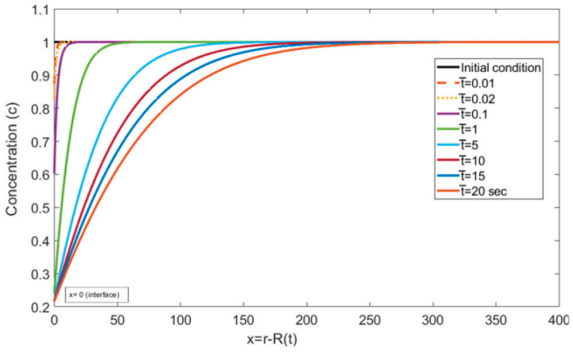

Figure 6. Concentration profiles reported in the liquid at different dimensionless time values ($Re = 4.5 \times 10^{-6}$, $Ca = 13.17$, $P = 1.27$, $C = 0.3$, and $Pe = 3.7 \times 10^{4}$).

4.3. Parametric Study of Bubble Growth

Equations (20) to (22), which constitute the full bubble growth model, emphasize that Equations (18a–c) and (19a,b), i.e., Re, Ca, Pe, P, and C, are the numbers that control bubble growth. A small change in these field parameters may affect bubble growth. In this section, an extensive study is carried out to determine the effect of these parameters on bubble growth. To do so, we only change a single parameter in non-dimensional numbers that is independent of other non-dimensional numbers. This is because if we closely observe the non-dimensional groups, they are coupled to one another by the liquid density (ρ_L), velocity ($\overline{V}$), and initial bubble radius ($\overline{R}_0$). For example, to study the effect of viscosity of the liquid, we can only change the μ_L parameter in the Reynolds number Equation (18a), and to study the effect of surface tension, we only change the σ in the capillary number Equation (18b), and so on. To observe the effects of these parameters, we need a primary or base case result to perform a relative comparison. Therefore, we consider the present numerical model results shown in Figure 4 as the primary case.

4.3.1. Effect of Viscosity on the Bubble Growth

To observe the effect of viscosity, only Reynolds number is varied, keeping other non-dimensional numbers constant. In the base case, Reynolds number is 4.5×10^{-6}, and this number is varied between 4.5×10^{-7} and 4.5×10^{-5}. In Figure 7a, at higher Reynolds numbers ($Re = 4.5 \times 10^{-5}$), the bubble growth is faster, and at lower Reynolds numbers ($Re = 4.5 \times 10^{-7}$), the bubble growth is slower. This type of behavior is expected because, at lower viscosity, the normal stress in the liquid is lower, which results in a more rapid bubble growth rate. Although the figure depicts a change in the qualitative trend with time when Re is increased, this change is only in appearance, at least initially. In fact, the slope at $t = 0$ is always zero, but the radius grows too rapidly for this to be visible; this becomes clear when we next examine the interfacial velocity.

Figure 7b shows that, if the viscosity is high, the normal stress is high, which retards bubble growth. This behavior can be well understood from Figure 7b, where the initial interface bubble velocity is high at a higher Reynolds number, suggesting rapid bubble growth. Additionally, at a lower Reynolds number, retardation of bubble interface velocity is observed, expressing that the bubble growth rate is slower. At a relatively low Re, the interfacial velocity grows slowly, reflecting a weak acceleration of the bubble, which continues to weaken with time until it vanishes, at which time the velocity reaches a maximum, reflected in the change in concavity in Figure 7a. The bubble continues to grow, but at a slower pace. This trend is similar at higher Re, but the initial growth is much faster, and the maximum is reached earlier, leading to a stronger deceleration. The change in concavity for the radius happens for any Re, but is most visible for the lowest Re shown in Figure 7a,b.

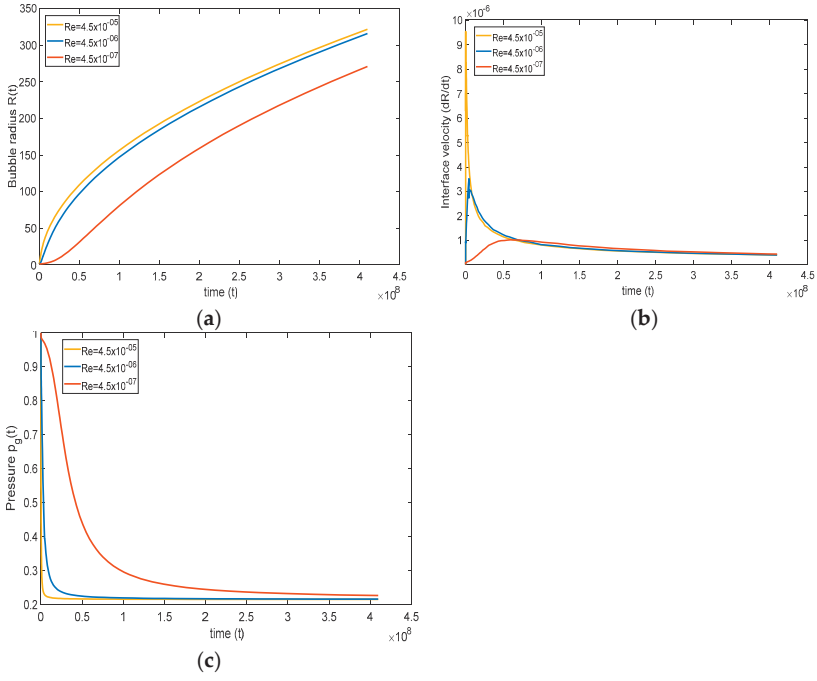

Figure 7. Effect of Reynolds number on (**a**) bubble radius, (**b**) interface velocity, and (**c**) pressure inside the gas (Ca = 13.17, P = 1.27, C = 0.3, and $Pe = 3.7 \times 10^4$).

The response in the pressure of the gas is dictated by (21), and is influenced by an intricate coupling between the evolution of the interfacial concentration gradient and the velocity. The evolution of the pressure is depicted in Figure 7c between the high and low Reynolds numbers. Typically, the pressure drops initially at a rate dominated primarily by the concentration gradient since the interface velocity is close to zero. The drop rate decreases gradually as the interface velocity increases with time. At lower Reynolds number, the pressure inside the bubble decreases slowly, reflecting a lower pressure drop, thus remaining closer to atmospheric pressure, causing slower bubble growth. On the other hand, at a high Reynolds number, the pressure inside the bubble decreases rapidly, which in turn enhances bubble growth. Finally, the maximum in the interface velocity occurs when the acceleration vanishes, and the maximum is then given by

$$\dot{R}_{\max} = -\frac{4}{3ReR} + \sqrt{\frac{16}{9Re^2R^2} + \frac{2P}{3}\Delta p - \frac{4}{3CaR}} \tag{38}$$

Clearly, the maximum vanishes if the driving pressure balances with the surface tension force. If surface tension is dominant, the maximum does not occur (see next section)

4.3.2. Effect of Surface Tension of the Liquid on the Bubble Growth

The effect of surface tension on the bubble growth is carried out with a similar approach that was demonstrated in the previous section. The capillary number is varied from the reference number while keeping other non-dimensional numbers constant. The reference capillary number is 13.17, and is varied in the range of low magnitudes Ca = 1.9 and Ca = 3. It is expected that the interfacial tension tends to retard the bubble growth by opposing the motion of the bubble boundary, and similar behavior is observed from the numerical simulations. Equation (20) clearly illustrates the competition among gas pressure, surface tension, and viscous forces on the right-hand side, as they simultaneously influence the

bubble growth. If surface tension effects are weak, then the bubble growth is dictated mainly by the gas pressure. If surface tension is increased, then the growth can be neutralized, or even reversed, as illustrated in Figure 8. The growth or collapse hinges on the initial stage, and is reflected by the initial concavity in R. If the surface tension effect is weak, then $\ddot{R}(t=0) \approx P(1-p_a) > 0$, leading to the ensuing bubble growth. On the other hand, for small Ca, $\ddot{R}(t=0) \approx -\frac{2}{Ca} < 0$, and the bubble collapses from its initial size $R(t=0) = 1$. Finally, when $Ca = \frac{2}{P(1-p_a)}$, no growth or collapse occurs.

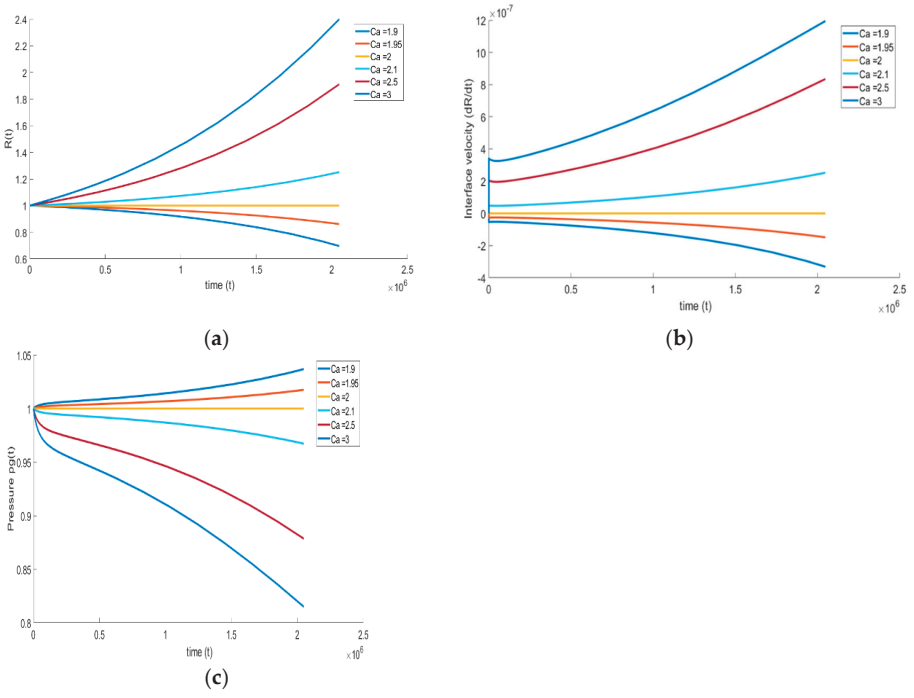

Figure 8. Effect of surface tension on (**a**) bubble growth, (**b**) interface velocity, and (**c**) pressure inside the bubble ($Re = 4.5 \times 10^{-6}$, $P = 1.27$, $C = 0.3$, and $Pe = 3.7 \times 10^4$).

We see that at approximately $Ca = 2$, the slope of the bubble growth shifts toward the positive trend, highlighting that the critical capillary number is ~2. At $Ca > 2$, the surface tension effect results in positive bubble growth. On the other hand, for $Ca < 2$ surface tension becomes dominant, and the bubble collapses. These effects can also be understood by examining the bubble interface velocity (Figure 8b) and evolution of gas pressure inside the bubble (Figure 8c). During bubble growth, the increase in interface velocity and decrease in bubble pressure is noticed; during bubble shrinkage, the decrease in interface velocity and increase in gas pressure is noticed. Finally, and as reflected in (38), we note that no maximum occurs in the interface velocity as a result of the relative dominance of surface tension.

4.3.3. Effect of Ambient Pressure on the Bubble Growth

In this section, the effect of ambient pressure (p_a) is studied. The system pressure is the ambient pressure where the growth of the bubble takes place. For instance, in the case of foaming, the system pressure is considered as the mold pressure, where the bubble growth occurs upon injecting polymer melts Han and Yoo, 1981, [17]. Similarly, in carbonated beverages, the system pressure becomes the ambient pressure.

It is important to see how the system pressure affects the overall growth of the bubble. Therefore, three cases are considered: the reference case $p_a = 0.21$ of Han and Yoo, 1981, [17], and the cases of high pressure $p_a = 0.31$ and low pressure $p_a = 0.10$. Note that the initial gas pressure (P_{g0}) in the bubble is kept constant for all the cases. One can see from Equation (20) the initial magnitude of $(p_g - p_a)$ defines the rate of bubble growth. Since the initial pressure $p_g = 1$ is the same for all the cases, and $1 > p_a$, then a higher p_a leads to a lower pressure difference and slower bubble growth, as reflected in Figure 9a–c. As the system pressure increases, bubble growth decreases, and vice versa. On decreasing the system pressure, we observe a large deviation between the base case and lower system pressure case. On the other hand, while increasing the system pressure, we observe a comparatively smaller deviation between the base case and lower system pressure case. Figure 9c indicates that the pressure drops sharply initially, at a rate that is slightly lower for higher system pressure. After the initial drop, the pressure rapidly reaches the system pressure, and bubble growth slows mainly as a result of surface tension and viscous effects.

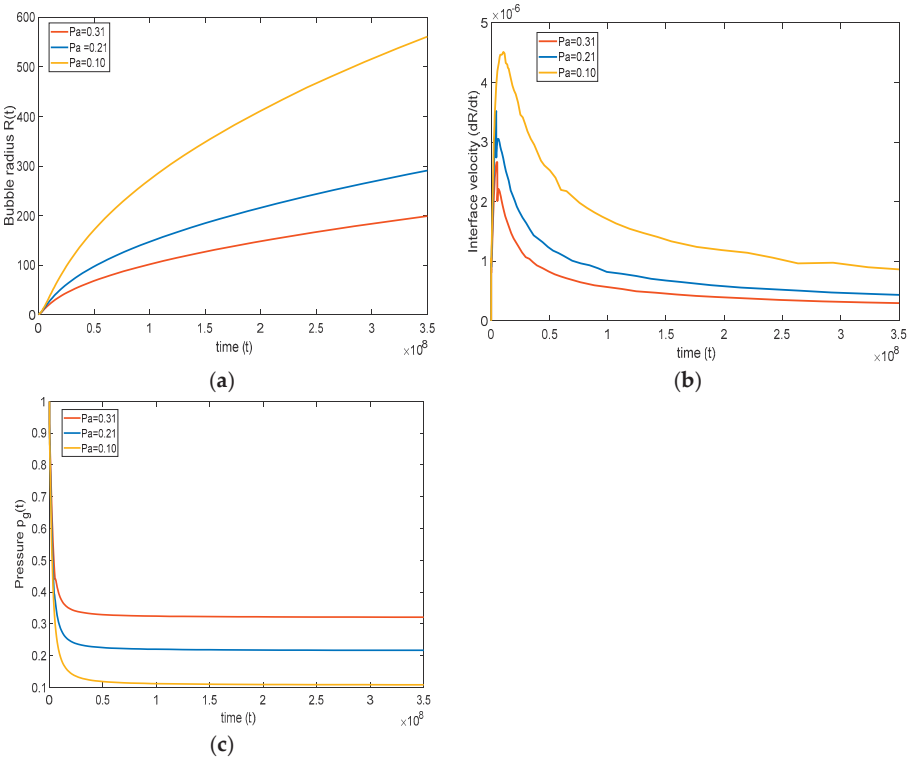

Figure 9. Effect of system pressure on (**a**) bubble growth, (**b**) interface velocity, and (**c**) pressure inside the bubble ($Re = 4.5 \times 10^{-6}$, $Ca = 13.17$, $P = 1.27$, $C = 0.3$, and $Pe = 3.7 \times 10^4$).

4.3.3.1. Effect of Solubility and Diffusion Parameters on Bubble Growth

The solubility and diffusivity of the gas in the liquid solution plays a major role in the bubble growth process. The present part focuses on studying the effect of both parameters. From the definition of Péclet number (see equation (18c)), only the diffusion coefficient is varied to maintain the other parameters as unchanged.

Therefore, a lower $Pe = 3.7 \times 10^3$ (high diffusion coefficient) and higher Péclet number $Pe = 3.7 \times 10^5$ (low diffusion coefficient) are considered. The magnitudes are compared with the base case, $Pe = 3.7 \times 10^4$. Figure 10a shows that at a lower Péclet number, the growth rate of the bubble is higher; at a higher Péclet number, the growth rate is slower.

This type of trend is predicted since, at a higher diffusion coefficient, the rate of gas flow through the interface is high, and vice versa.

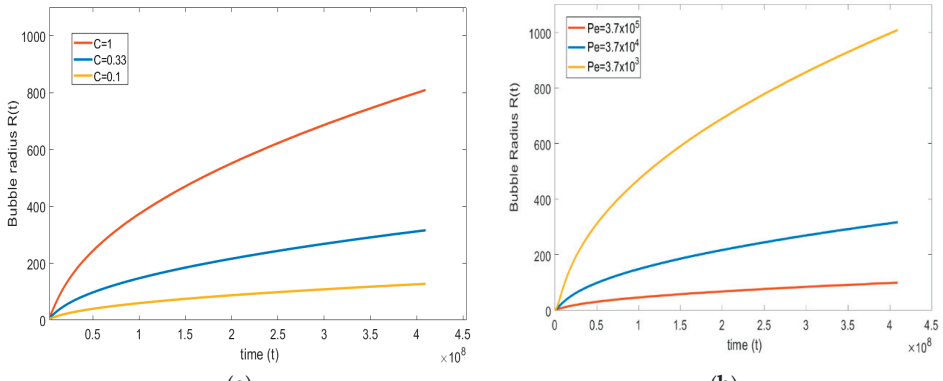

(**a**) (**b**)

Figure 10. (**a**) Effect of diffusion coefficient on bubble growth; (**b**) effect of Henry's constant on bubble growth ($Re = 4.5 \times 10^{-6}$, $Ca = 13.17$, $P = 1.27$, and $C = 0.3$).

Similarly, to see the effect of solubility on bubble growth, the non-dimensional number C (see Equation (19b)), which relates to Henry's constant k_h, is varied. Here, the non-dimensional number C increases with increasing k_h and decreases by decreasing the k_h. The magnitude of the non-dimensional number C for the base case is 0.33, and this is varied between the lower number $C = 0.1$ to a higher number $C = 1$.

Figure 10b suggests that, on increasing the solubility of a gas in the liquid, the bubble growth rate is faster, and the lower the solubility of the gas in the liquid, the growth rate is lower. This result is close to physical observations; i.e., at higher solubility, the amount of gas available in the liquid is high, because the mass transfer from the liquid side to the bubble is high, resulting in a higher bubble growth rate.

5. Concluding Remarks

The hydrodynamics of a single bubble in the pool of Newtonian liquid that expands due to mass transfer was investigated in the current work. This study directly relates to foaming processes, carbonated beverages, and any other problem in which the bubble grows due to mass transfer.

Rigorous non-dimensional formulations were derived to incorporate interfacial, viscosity, diffusivity, and solubility effect on bubble growth. Especially the inertia of the liquid was included in the formulation, along with full scalar advection–diffusion processes. A strong numerical approach to the highly non-linear stiff coupled equations was discussed. The moving interface of the bubble was tackled by mapping the domain to the new coordinate (x).

The results obtained with the present formulation and numerical solution to the advection–diffusion equation was compared with the Elshereef et al., 2010, [2] models. The present numerical model predicts accurate bubble growth in comparison to Elshereef et al., 2010, [2] models. These results were validated by comparing with the Han and Yoo, 1981, [17] experimental data set.

To our knowledge, the influence and behavior of the concentration of the gas in the liquid has not been reported in the literature. In this work, a clear insight is provided on the concentration profiles of gas in the liquid and a boundary layer variation around the bubble. A simple numerical investigation was conducted to compare the variation in the approximated diffusion equation results against the present numerical results. We showed that that the gas concentration profile in the liquid deviates from the traditional concentration profile.

With the validated numerical model, a comprehensive parametric study was performed on the bubble growth. The results show that the rate of bubble growth depends primarily on the viscosity of the liquid, initial pressure difference, diffusion, and solubility. The effect of surface tension on the overall bubble growth process is limited.

We showed that the higher viscosity of the liquid lowers the bubble growth rate, and vice versa. The initial pressure difference between the bubble and the system has a significant effect on the overall bubble growth process. The higher the initial pressure difference, the greater is the bubble growth. With a lower initial pressure difference, the bubble growth is limited.

The investigation shows that the effect of diffusion and solubility of the gas in the liquid play an important role in the overall bubble growth process. Higher magnitude of these parameters leads to a higher bubble growth rate, and vice versa. It is concluded that these parameters have a similar effect on bubble growth.

Author Contributions: Conceptualization, R.K.N.M.; Methodology, R.K.N.M., R.E.K. and C.T.D.; Software, R.K.N.M.; Writing—original draft, R.K.N.M.; Writing—review and editing, R.E.K. and C.T.D. All authors have read and agreed to the published version of the manuscript.

Funding: This research received no external funding.

Institutional Review Board Statement: Not applicable.

Informed Consent Statement: Not applicable.

Data Availability Statement: Not applicable.

Conflicts of Interest: The authors declare no conflict of interest.

References

1. Rosner, D.E.; Epstein, M. Effects of interface kinetics, capillarity and solute diffusion on bubble growth rates in highly supersaturated liquids. *Chem. Eng. Sci.* **1972**, *27*, 69–88. [CrossRef]
2. Elshereef, R.; Vlachopoulos, J.; Elkamel, A. Comparison and analysis of bubble growth and foam formation models. *Eng. Comput.* **2010**, *27*, 387–408. [CrossRef]
3. Arefmanesh, A.; Advani, S.G.; Michaelides, E.E. An accurate numerical solution for mass diffusion-induced bubble growth in viscous liquids containing limited dissolved gas. *Int. J. Heat Mass Transf.* **1992**, *35*, 1711–1722. [CrossRef]
4. Lee, S.T.; Ramesh, N.S.; Campbell, G.A. Study of thermoplastic foam sheet formation. *Polym. Eng. Sci.* **1996**, *36*, 2477–2482. [CrossRef]
5. Bisperink, C.G.J.; Prins, A. Bubble growth in carbonated liquids. *Colloids Surf. A Physicochem. Eng. Asp.* **1994**, *85*, 237–253. [CrossRef]
6. Jones, S.; Evans, G.; Galvin, K. The cycle of bubble production from a gas cavity in a supersaturated solution. *Adv. Colloid Interface Sci.* **1999**, *80*, 51–84. [CrossRef]
7. Barker, G.S.; Jefferson, B.; Judd, S.J. The control of bubble size in carbonated beverages. *Chem. Eng. Sci.* **2002**, *57*, 565–573. [CrossRef]
8. Liger-Belair, G. The Physics and Chemistry behind the Bubbling Properties of Champagne and Sparkling Wines: A State-of-the-Art Review. *J. Agric. Food Chem.* **2005**, *53*, 2788–2802. [CrossRef] [PubMed]
9. Lee, W.T.; McKechnie, J.S.; Devereux, M.G. Bubble nucleation in stout beers. *Phys. Rev. E Stat. Nonlinear Soft Matter Phys.* **2011**, *83*, 1–5. [CrossRef] [PubMed]
10. Enríquez, O.R.; Hummelink, C.; Bruggert, G.-W.; Lohse, D.; Prosperetti, A.; Van Der Meer, D.; Sun, C. Growing bubbles in a slightly supersaturated liquid solution. *Rev. Sci. Instruments* **2013**, *84*, 65111. [CrossRef] [PubMed]
11. Enríquez, O.R.; Sun, C.; Lohse, D.; Prosperetti, A.; van der Meer, D. The quasi-static growth of CO2 bubbles. *J. Fluid Mech.* **2014**, *741*, 1–9. [CrossRef]
12. Amon, M.; Denson, C.D. A study of the dynamics of foam growth: Analysis of the growth of closely spaced spherical bubbles. *Polym. Eng. Sci.* **1984**, *24*, 1026–1034. [CrossRef]
13. Pooladi-Darvish, M.; Firoozabadi, A. Solution-gas drive in heavy oil reservoirs. *J. Can. Pet. Technol.* **1999**, *38*, 54–60. [CrossRef]
14. Epstein, P.S.; Plesset, M.S. On the stability of gas bubbles in liquid-gas solutions. *J. Chem. Phys.* **1950**, *18*, 1505–1509. [CrossRef]
15. Barlow, E.J.; Langlois, W.E. Diffusion of Gas from a Liquid into an Expanding Bubble. *IBM J. Res. Dev.* **1962**, *6*, 329–337. [CrossRef]
16. Patel, R.D. Bubble growth in a viscous Newtonian liquid. *Chem. Eng. Sci.* **1980**, *35*, 2352–2356. [CrossRef]
17. Han, C.D.; Yoo, H.J. Studies on structural foam processing. IV. Bubble growth during mold filling. *Polym. Eng. Sci.* **1981**, *21*, 518–533. [CrossRef]

18. Ramesh, N.S.; Rasmussen, D.H.; Campbell, G.A. Numerical and experimental studies of bubble growth during the microcellular foaming process. *Polym. Eng. Sci.* **1991**, *31*, 1657–1664. [CrossRef]
19. Soto, Á.M.; Enríquez, O.R.; Prosperetti, A.; Lohse, D.; van der Meer, D. Transition to convection in single bubble diffusive growth. *J. Fluid Mech.* **2019**, *871*, 332–349. [CrossRef]
20. Soto, M.; Lohse, D.; van der Meer, D. Diffusive growth of successive bubbles in confinement. *J. Fluid Mech.* **2020**, *882*, A6. [CrossRef]
21. Maloth, R.K.N. The Study of Bubble Growth Hydrodynamics in the Supersaturated Liquids. Master's Thesis, University of Western Ontario, London, ON, Canada, 2020.

fluids

MDPI

Article

Computational Fluid Dynamics Approach for Oscillating and Interacting Convective Flows

Attila Gergely and Zoltán Néda *

Department of Physics, Babeş-Bolyai University, 400084 Cluj-Napoca, Romania
* Correspondence: zoltan.neda@ubbcluj.ro; Tel.: +40-745-310531

Abstract: The oscillation and collective behavior of convective flows is studied by a computational fluid dynamics approach. More specifically, the rising dynamics of heated fluid columns is simulated in gravitational field using a simplified 2D geometry. The numerical method uses the FEniCS package for solving the coupled Navier–Stokes and heat-diffusion equations. For the flow of a single heated fluid column, the effect of the inflow yield and the nozzle diameter is studied. In agreement with the experiments, for a constant nozzle diameter the oscillation frequency increases approximately linearly as a function of the the flow rate, while for a constant flow rate the frequency decreases as a power law with the increased nozzle diameter. For the collective behavior of two nearby flows, we find a counter-phase synchronization and a decreasing trend of the common oscillation frequency with the distance between the jets. These results are in agreement with the experiments, and our computational study also suggests that the phenomenon is present on largely different length-scales.

Keywords: computational fluid dynamics; convective flows; oscillations; instabilities; synchronization

Citation: Gergely, A.; Néda, Z. Computational Fluid Dynamics Approach for Oscillating and Interacting Convective Flows. *Fluids* **2022**, *7*, 339. https://doi.org/10.3390/fluids7110339

Academic Editor: Mehrdad Massoudi

Received: 10 September 2022
Accepted: 13 October 2022
Published: 24 October 2022

Publisher's Note: MDPI stays neutral with regard to jurisdictional claims in published maps and institutional affiliations.

1. Introduction

Our recent experimental results reported that rising gas columns can perform oscillations and their interaction leads to fascinating collective behavior [1]. The oscillations and their related instabilities have been previously known (see for example [2–6]), and this problem is still actively in the focus of the scientific community [7,8]. Besides many refined experiments, theoretical studies based on simple hydrodynamics [1,5], theory of dynamical systems [5], impulse response [2], scaling theory [8], linear stability analyses [2,9], and numerical fluid dynamics [6,7] were considered. Although the emerging oscillations are well-studied, to the best of our knowledge there are no theoretical studies on the interaction and collective behavior of nearby jets.

The collective behavior of convective flows can be discussed in analogy with the very similar phenomena known for diffusive flames [10–18]. For interactive jets, the toy-model presented in Ref. [1] is inadequate to explain the fine details of the observed phenomena, therefore a more sophisticated theoretical approach is needed. On the other hand, we also believe that this intriguing phenomena is present on larger length-scales as well, being relevant to industrial processes also. The present study contributes in this sense, by considering a numerical hydrodynamics approach to this puzzling phenomenon.

For experimental results, we consider as a reference our previous study realized with a controlled flow of Helium into air [1]. In these experiments, the Schlieren technique [19,20] was used to visualize the flow, also allowing a digital processing of the oscillations. From the images processed by the Otsu method [21,22], the characteristic frequency and the relevant synchronization order parameter was derived. For a better understanding of the phenomena, some sample movies with original recordings and the ones processed with the Otsu method are provided on our YouTube channel [23] and are uploaded also as Supplementary Materials for this article. For a single flow column, the experiments investigated the effect of the nozzle diameter and flow rate on the observed oscillation frequency. For the

collective behavior of two nearby flows, our experiments investigated as a function of the separation distance between the flows (i) the phase difference between the oscillations, (ii) their common oscillation frequency, and (iii) a proper synchronization order parameter.

At constant Helium flow, the oscillation frequency of the rising gas column decreases in form of a power law as a function of the nozzle diameter. This finding is similar with the observed oscillation frequency of the flames of candle bundles as a function of the number of candles in the bundle [18]. For a constant nozzle diameter it was found that the oscillation frequency of the flow increases linearly with the flow yield. For the collective behavior of two nearby and clearly separated flow columns with similar flow parameters, only counter-phase synchronization was observed. This is somehow different from the phenomena observed for candle bundle flames, where both in-phase and counter phase synchronization is present depending on the distance between the flames [18]. The experiments concluded that for short distances, the oscillation frequency of the flow column becomes significantly higher than the frequency observed for non-interacting Helium columns with the same parameters (flow rate and nozzle diameter). All the above summarized results should be a test for any model and numerical approach on this intriguing phenomenon.

Due to the complexity of the problems related to flows in different spatial configurations and environments, the computation approaches are often the only theoretical possibilities to realistically model such phenomena (see for example Refs. [24,25]). Even with such a modeling methodology, imposing the right boundary conditions and offering a proper discretization of space and time raises many technical challenges [26]. The incredible revolution we experience nowadays in computational resources and methods have helped us overcome much of these difficulties, and computational fluid dynamics have become the primary tool to investigate theoretical problems related to fluid dynamics. However, even with the presently available computational power, we are often forced to investigate a simpler flow topology and reduce the dimensionality of the problem [27]. This is nowadays a standard procedure for cases where the problem becomes computationally difficult in 3D. A two-dimensional simplification is usually considered when the periodicity and symmetry of the considered flow allows for it. Assuming in the following a cylindrical symmetry for the flow, we consider a two-dimensional numerical fluid dynamics approach for the above mentioned phenomenon. First, we discuss the theoretical background on which our approach is built and the details of the applied numerical method. Using simple and straightforward examples, we thoroughly test the simulation environment to gain confidence in the method. After this methodological part, we approach the proposed problem and compare the results of the simulations with the experimental data from Ref. [1]. Finally, the conclusions are drawn and the universality features of this intriguing phenomenon are discussed.

Before presenting our simulation methodology, we have to mention that we use equations and system parameters in a dimensional form, rather than following the accepted methodology with dimensionless variables. The reason for this is that in our approach we need to take into account the spatial and temporal variation of the density that is connected with the temperature field. In such cases we cannot use a constant Reynolds number, and the numerical advantage of the dimensionless formalism is not obvious. On the other hand, by using dimensional variables and parameters, the connections with the experimental conditions, time, and length-scales are more straightforward.

2. The Numerical Approach

We present here a 2D numerical approach, which is suitable for modeling the oscillations and collective behavior observed in the rising gas columns. In order to further simplify the problem, instead of a Helium column injected from the bottom we consider the flow of the same incompressible fluid as the surrounding, heated in a restricted region at the bottom of the simulated area. In such a manner we get a rising gas column that is also realizable in experiments.

Using the same Schlieren technique as previously, in Figure 1 and in the movies presented in Ref. [28], we show that very similar instabilities and oscillations occur. In these experiments the heating is realized by a simple heating coil in which one controls the dissipated electric power. Unfortunately, in such experiments there is no good control over the flow debit, therefore one cannot conduct such carefully monitored experiments as the ones done for Helium. The numerical results are therefore compared with our earlier experiments [1].

The advantage of the proposed setup is that we do not have to apply the numerical fluid dynamics method for two component gases. We do pay however for this simplification by the non-homogeneous temperature field, therefore extra transports and gradients have to be taken into account.

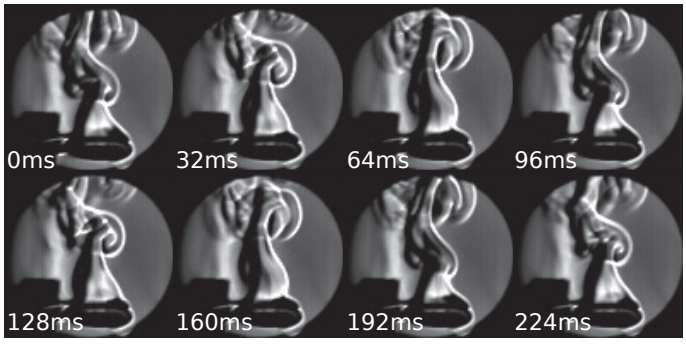

Figure 1. Visualization of a rising hot-air column using the Schlieren technique. Similar instabilities and oscillations appear in rising Helium gas columns.

In our approach, the fluid is considered to be ideal, as described by the Navier–Stokes equation. For an incompressible fluid in a gravitational field, the Navier–Stokes equation is written in the following form:

$$\rho \frac{\partial \mathbf{u}}{\partial t} + \rho\,(\mathbf{u}\cdot\nabla)\mathbf{u} = -\nabla p + \mathbf{g}\,\rho + \mu\,\Delta\mathbf{u} \tag{1}$$

$$\nabla\cdot\mathbf{u} = 0 \tag{2}$$

Here ρ denotes the density, p is the pressure, $\mathbf{g}$ the gravitational acceleration, $\mathbf{u}$ is the velocity of the fluid, and μ denotes the fluid's viscosity. The quantities $\mathbf{u}$, ρ and p can be time- and position-dependent in the flow-space.

For the considered problem, the convective flow due to the temperature difference plays a key role, therefore in the Navier–Stokes equation, we will take into account the temperature dependence of the density and also describe the time evolution of the temperature inside the fluid. As previously emphasized, this is the main reason as to why the dimensionless form of the equation does not reduce the numerical complexity of the problem.

The evolution of the temperature and the temperature dependence of the density are approximated by the following equations:

$$\begin{aligned} \rho &= \frac{\rho_0}{1+(T-T_0)\cdot\alpha} \\ \frac{\partial T}{\partial t} &= D\cdot\Delta T - (\mathbf{u}\cdot\nabla)\cdot T \end{aligned} \tag{3}$$

In the above equations, ρ_0 is the density at T_0, T is the temperature of the fluid at a given spatial position and in a given time-moment, D is the diffusion constant, and T_0 is the ambient temperature. The numerical solution of the coupled systems of partial differential Equations (2) and (3) was done by using the "FEniCS" software package [29].

FEniCS is an open-source platform developed for solving Partial Differential Equation (PDE) systems. We chose this platform because it has high-level programming interfaces (C ++, Python), the shape of the equations in the program code is similar to their symbolic form, and the program is optimized for a wide range of hardware from laptops to high-performance clusters.

2.1. The Simulation Code

FEniCS uses finite element methods to solve PDEs. As an example in Appendix A.1, we illustrate how to solve the simple 2D Poison equation with FEniCS. For our specific problem we first deal with the term describing the evolution of the temperature:

$$\frac{\partial T}{\partial t} = D \cdot \Delta T - (\mathbf{u} \cdot \nabla) \cdot T \tag{4}$$

This equation contains a time derivative, so in addition to the coordinates we also have to discretize time. This is done by the Euler method, as follows:

$$\frac{T(t+dt) - T(t)}{dt} = D \cdot \Delta T(t) - (\mathbf{u} \cdot \nabla) \cdot T(t), \tag{5}$$

We then bring each term to the left hand side of the equation, we multiply the equation by a τ test function, and integrate the equation over the entire simulated domain:

$$\int_\Omega [T(t+dt) - T(t) - D \cdot \Delta T(t) \cdot dt + (\mathbf{u} \cdot \nabla) \cdot T(t) \cdot dt] \cdot \tau \, d\Omega = 0 \tag{6}$$

The equations above contain a second-order derivative for the coordinates, which is eliminated by partial integration:

$$\int_\Omega (\nabla^2 \cdot T(t)) \cdot \tau \, d\Omega = \int_{\partial\Omega} \left(\frac{\partial T(t)}{\partial \mathbf{n}} \right) \cdot \tau \, ds - \int_\Omega \nabla T(t) \cdot \nabla \tau \, d\Omega \tag{7}$$

Here we denoted by $\mathbf{n}$ the unit normal vector to the $\partial\Omega$ surface. The derivative with respect to $\mathbf{n}$ is defined as:

$$\frac{\partial T}{\partial \mathbf{n}} = (\nabla T) \cdot \mathbf{n} \tag{8}$$

Rewriting Equation (6) using the above result and the fact that under the Dirichlet and free boundary conditions the surface integral disappears, we obtain the final form:

$$\int_\Omega ([T(t+dt) - T(t) + (\mathbf{u} \cdot \nabla) \cdot T(t) \cdot dt] \cdot \tau \; + D \cdot \nabla T(t) \cdot \nabla \tau \cdot dt \;) \, d\Omega = 0 \tag{9}$$

The incompressible Navier–Stokes equation (2) was solved using the IPCS (Incremental Pressure Correction Scheme) scheme [30]. The IPCS method consists of three steps, but before specifying the steps we introduce the following functions and notation:

$$\begin{aligned} [\varepsilon(\mathbf{u})] &= \frac{1}{2} \cdot ([\nabla \otimes \mathbf{u}] + [\nabla \otimes \mathbf{u}]^T) \\ [\sigma(\mathbf{u}, p)] &= 2 \cdot \mu \cdot \varepsilon(\mathbf{u}) - p \cdot I \\ \langle \mathbf{f}, \mathbf{g} \rangle_\Omega &= \int_\Omega \mathbf{f} \cdot \mathbf{g} \, d\Omega \\ \langle [A], [B] \rangle_\Omega &= \int_\Omega [A] : [B] \, d\Omega \end{aligned} \tag{10}$$

The $\otimes$ product defines a matrix with the following elements:

$$\nabla \otimes \mathbf{u} = \left[\frac{\partial u_j}{\partial x_i} \right] \tag{11}$$

We denoted by [...] a square matrix, by $[...]^T$ the transpose of a matrix, and by : the inner product of matrices:

$$[A] : [B] \equiv \sum_{i,j} A_{ij} B_{ij} \tag{12}$$

Using the ε and σ functions and the specified notation, the steps of the method will be described in the following. First we reconsider the Navier–Stokes equation using a set of test functions:

$$\rho \cdot \left\langle \frac{\mathbf{u}^* - \mathbf{u}(t)}{dt}, \mathbf{v} \right\rangle_\Omega + \rho \cdot \langle \mathbf{u}(t) \cdot \nabla \mathbf{u}(t), \mathbf{v} \rangle_\Omega + \left\langle \left[\sigma\left(\frac{\mathbf{u}(t)+\mathbf{u}^*}{2}, p(t) \right) \right], [\varepsilon(\mathbf{v})] \right\rangle_\Omega + \\ + \langle p(t) \cdot \mathbf{n}, \mathbf{v} \rangle_{\partial\Omega} - \left\langle \mathbf{n} \cdot [\nabla \otimes \left(\frac{\mathbf{u}(t)+\mathbf{u}^*}{2} \right)]^T, \mathbf{v} \right\rangle_{\partial\Omega} = \rho \cdot \langle \mathbf{g}, \mathbf{v} \rangle_\Omega \tag{13}$$

Here **v** is the test function. For more information on making this choice, one should consult [29] The first step of the method is the calculation of an intermediate velocity $\mathbf{u}^*$ from which the pressure will be determined. Then, the pressure is determined in the $t + dt$ step in equation:

$$\langle \nabla p(t+dt), \nabla q \rangle_\Omega = \langle \nabla p(t), \nabla q \rangle_\Omega - \frac{\langle \nabla \mathbf{u}^*, q \rangle_\Omega}{dt} \cdot \rho \tag{14}$$

In the equation above, q is a test function for the pressure. In the last step, the velocity in the $t + dt$ time step is determined based on the pressure and the intermediate velocity:

$$\langle \mathbf{u}(t+dt), \mathbf{v} \rangle_\Omega = \langle \mathbf{u}^*, \mathbf{v} \rangle_\Omega - \frac{dt \cdot \langle \nabla (p(t+dt) - p(t)), \mathbf{v} \rangle_\Omega}{\rho} \tag{15}$$

The method described above for solving the incompressible Navier–Stokes equation is implemented in 2D. FEniCS uses a triangular adaptive grid to solve the 2D partial differential equation. We carefully verified the grid independence of the results, aspects which will be discussed in the next section. Here, in Figure 2, we illustrate the topology of the grid we used in the simulation space.

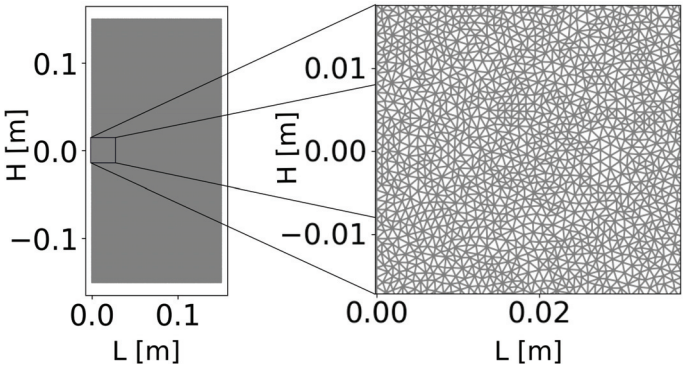

Figure 2. The topology of the used grid. On the left panel, due to the finite scale of the lines, it is not possible to visualize the grid of the whole simulation area. A magnified image of the marked region is illustrated in the panel on the right.

In order to solve the equations numerically, we need boundary conditions in addition to discretization. We used Dirichlet and free boundary conditions. The Dirichlet boundary condition means that the value of the quantity at a given point is fixed. In the case of the free boundary condition, the derivative as a function of the coordinates of the quantity at the given point is 0.

We visually tested our 2D simulation environment on two simple problems. First we intended to reproduce the Karman vortices in the flow of a fluid around an obstacle

(Appendix A.2). Second, we simulated the expansion and rising of a heated sphere, verifying the code for non-homogeneous temperature conditions as well (Appendix A.3). The test simulations reproduced the expected realistic behavior for these known problems, giving confidence for the correct implementation of the relevant equations discussed above.

2.2. Simulating the Rising Hot Air Column

In the followings we provide the details for implementing the simulations, aiming to reproduce the characteristic oscillations observed in a rising gas column. The boundary conditions introduced for velocity and temperature will be justified, and we explain how the time series of the characteristic oscillations were obtained and how the oscillation frequency was calculated.

We consider the inflow geometry presented in Figure 3, leading to the flow illustrated in Figure 4a. On the sidewalls, the value of the velocity is fixed to 0, on the lower boundary, the x-direction component of the velocity is considered as 0, and the y-direction component is given by the following parabolic-like kernel (see Figure 3)

$$v_y(x,0) = c_1 f\left(x, \tfrac{d}{2}\right)\left(\tfrac{d}{2} - x\right)\left(x + \tfrac{d}{2}\right) + c_2 f\left(x, \tfrac{H}{2}\left(1 - \tfrac{1}{30}\right)\right), \tag{16}$$

with:

$$f(a,b) = \frac{1}{e^{-c_3\cdot(b+a)}+1} - \frac{1}{e^{c_3\cdot(b-a)}+1}. \tag{17}$$

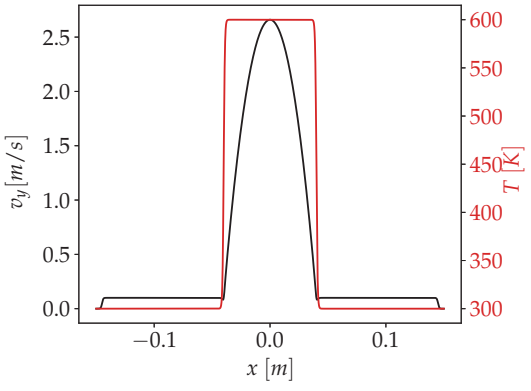

Figure 3. An example of the y-component of velocity, $v_y(x,0)$, and temperature profile, $T(x,0)$, of the heated fluid column at the bottom boundary of the simulated space. The following parameters were used: $c_1 = 1600\ \mathrm{m^{-1}{\cdot}s^{-1}}$, $c_2 = 0.1\ \mathrm{m{\cdot}s^{-1}}$, $c_3 = 2000\ \mathrm{m^{-1}}$, $d = 0.08$ m, $T_0 = 300$ K, $H = 0.3$ m.

In the equation from above, d denotes the nozzle diameter, H denotes the width of the simulated space, the parameters c_1, c_2 determine the incoming flow rate of the fluid, and c_3 is a tuning parameter governing the cut in each profile.

At the upper boundary (height L), free boundary conditions are applied for the y component of the velocity, and for the x component the Dirichlet condition is applied, i.e., $v_x(x,L) = 0$. For pressure, Dirichlet boundary conditions were used in the upper part of the simulated volume, $p(x,L) = g \cdot \rho_0 \cdot l$, and for the free boundary condition for the other boundaries. The temperature on the walls is fixed to T_0. On the upper boundary we consider T_0 if the y-direction component of the velocity is negative, otherwise free boundary conditions are used. The temperature at the lower boundary is determined by using the following equation:

$$T(x,0) = T_0 + T_{heating} f\left(x, \tfrac{d}{2}\right) \tag{18}$$

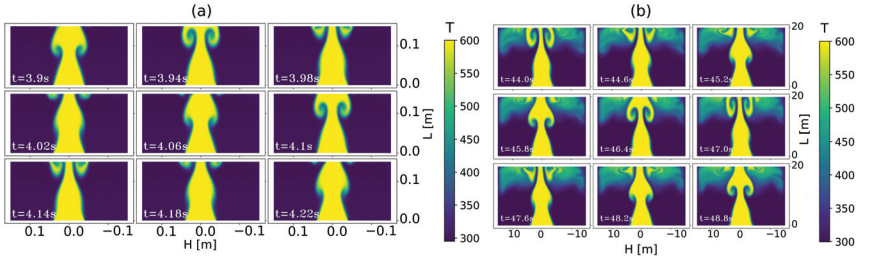

Figure 4. Oscillation of a heated air column in snapshots. The images show the temperature space at the specified t time moments for two different length scales (**a**,**b**). The gravity acts in the negative direction of the y-axis and the parameters of the simulation were chosen as follows: (**a**) $\alpha = 0.33 \cdot 10^{-2}$ K^{-1}, $\rho_0 = 1.2$ kg·m^{-2}, $T_0 = 300$ K, $D = 10^{-4}$ m^2·s^{-1}·K^{-1}, $g_y = -9.81$ m·s^{-2}, $\mu = 1.96 \cdot 10^{-5}$ kg·s^{-1}, $c_2 = 0.1$ m·s^{-1}, $c_3 = 2000$ m^{-1}, $d = 0.08$ m, $c_1 = 1600$ m^{-1}·s^{-1}, (**b**) $\alpha = 10^{-3}$ K^{-1}, $\rho_0 = 1$ kg·m^{-2}, $T_0 = 300$ K, $D = 5 \cdot 10^{-2}$ m^2·s^{-1}·K^{-1}, $g_y = -9.81$ m·s^{-2}, $\mu = 5 \cdot 10^{-2}$ kg·s^{-1}, $c_2 = 0.4$ m·s^{-1}, $c_3 = 5$ m^{-1}, $d = 8$ m, $c_1 = 0.375$ m^{-1}·s^{-1}.

Here, the $T_{heating}$ temperature governs the form of the temperature profile at $y = 0$ height. For simplicity reasons we have used in all the presented results $T_{heating} = T_0$. In the first attempts at the upper part of the simulated box, the free boundary condition was considered for the velocity. However in such cases, unexpected instabilities occurred and after a certain time the heated fluid column was pushed to one of the sidewalls. We have carefully examined this phenomenon and concluded that a self-amplifying effect is responsible for its development. Due to the convective flow, the amount of fluid leaving the simulation box is larger than the volume of fluid flowing into the simulation box through the lower boundary. Since the fluid is incompressible, the fluid must flow back into the simulation box through the upper boundary. Since there is always an asymmetry in the profile of the fluid inflow, this will slightly deflect the outflowing column. In the direction of the deflection, the inflow area decreases, so the asymmetry in the fluid inflow increases. An increase in asymmetry over time will result in the fluid flowing along one of the walls. This is the simple explanation of the observed instabilty.

Two methods were used to eliminate these instabilities. The first method is to flow a fluid of ambient temperature T_0 at a constant rate on both sides of the heated air column. Since the flow is two-dimensional, the fluid flowing on a given side can only leave on the same side and this will always provide a minimum distance from the wall for the rising jet. The second method is to allow only the y-direction component of the velocity at the upper boundary. Combining these two methods will eliminate the tendency of the jet to approach one of the sidewalls.

For the upper boundary, a proper boundary condition has to be applied for the inflowing fluid temperature as well. At the upper boundary, an inflow is also necessary in order to respect the incompressibility of the fluid. Since the temperature of the outflowing fluid varies over a wide range we cannot apply the Dirichlet boundary condition to the whole upper boundary because this would cause unmanageable gradients. Avoiding large gradients due to large temperature differences was solved by applying the boundary condition only to those points where the y-direction component of the velocity became negative.

Before performing our large-scale computations we have checked that the used space-discretization (grid) and chosen time-step does not influence the observed trends. Grid independence was proved by reducing and increasing space and/or time discretization consecutively, and comparing the trends and values for the relevant numerical parameters. In Figure 5, we illustrate the grid independence by plotting the time series of the observed oscillations for different grid sizes. More precisely we plot the number of pixels with an intensity above a given threshold detected at bottom of the simulated area (up to height:

$L/3$). The observed oscillation frequency is practically independent of the grid size in case of the refined grids considered in the simulations.

The time series for the relevant hydrodynamical parameters were generated by following the temperature distribution in the simulated space. The characteristic frequency was determined by a Fourier transform and from the Power Spectral Density (PSD) the characteristic frequency was calculated. The used signal is the average of the pixel intensities in the lower part of the simulated area (height smaller than L/3). A characteristic signal and the corresponding PSD is sketched in Figure 6.

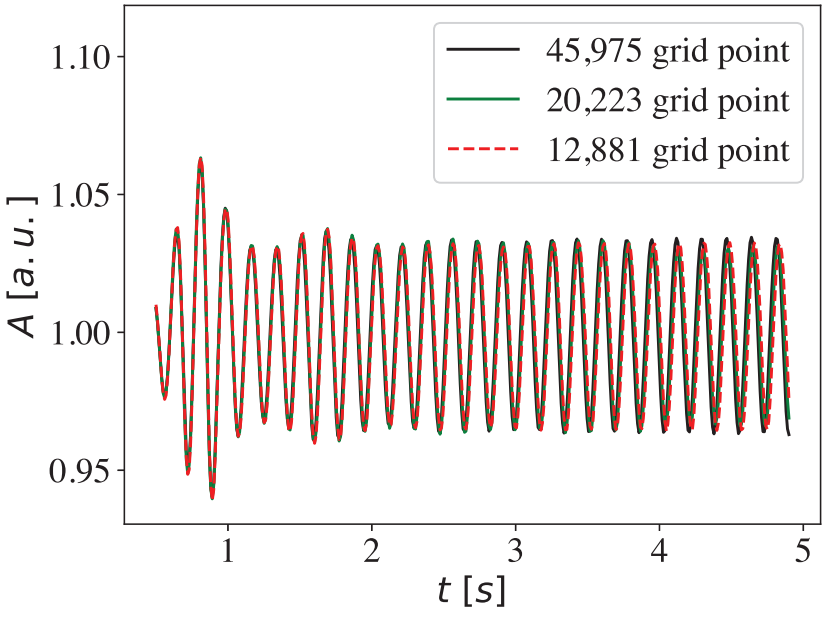

Figure 5. Oscillations observed in the flow when using different grid-sizes.

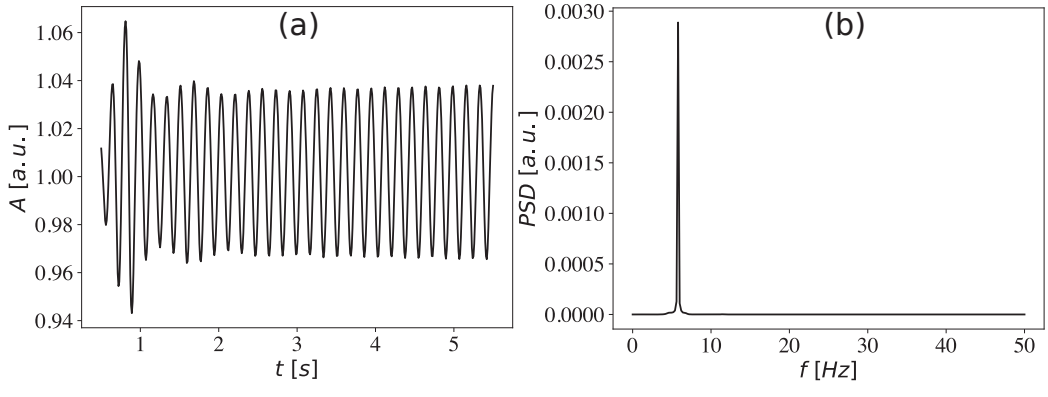

Figure 6. (**a**) Characteristic oscillation of the average temperature in the lower simulation area (height < $L/3$) and (**b**) the corresponding Power Spectral Density (PSD) with the characteristic peak.

For realistically chosen parameters, it was shown that the model is capable of producing an oscillation similar to the one observed in the case of the Helium column. Interestingly, it was found that such oscillations are possible even on largely different length-scales. The observed oscillation is shown in Figure 4a,b. where we illustrate the temperature space at subsequent time moments. For the simulations presented in Figure 4, we used the parameters specified in the figure caption.

For a quantitative evaluation of the simulated dynamics, the Otsu method was applied for the 2D temperature field. To obtain the time series, in uniform time intervals the Otsu processed pixels were summed up to a certain height, after this the obtained time series was divided by its average value. The oscillation frequency was calculated in a similar manner with the experiments, based on the above generated time series. In the first step, a Fourier transform was applied to the time series and then the value of the frequency belonging to the largest peak was determined as the relevant oscillation frequency.

With the implemented simulation code we examined how the inflow rate (yield) of the heated fluid column and the nozzle diameter affects its oscillation frequency. We also investigated the collective behavior for the oscillation of two columns placed nearby each other.

2.3. Numerical Results for the Oscillation Frequency

The effect of flow yield and nozzle diameter was examined on two different length-scales. To study the flow yield we used the parameter sets (a) and (b) introduced above, and the nozzle diameters were $d = 0.08$ m and $d = 8$ m, respectively. For constant c_3, c_2, and d parameters, the yield (flow debit) of the heated fluid only depends on c_1:

$$\Phi = \int_{-\frac{d}{2}}^{\frac{d}{2}} v_y(x,0)\,dx = \tag{19}$$
$$= \int_{-\frac{d}{2}}^{\frac{d}{2}} [c_1 f\left(x, \tfrac{d}{2}\right)\left(\tfrac{d}{2} - x\right)\left(x + \tfrac{d}{2}\right) + c_2 f\left(x, \tfrac{H}{2}(1 - \tfrac{1}{30})\right)]dx$$

The computed oscillation frequency of the heated fluid column as a function of the Φ parameter is plotted in Figures 7a and 8a. One can observe that the oscillation frequency increases as the flow rate Φ increases, and this increasing trend can be well approximated by a linear fit in good agreement with the experimental results plotted in Figure 9.

The effect of nozzle diameter on the oscillation frequency was investigated at a constant inflow yield. Since the yield Φ depends on d according to Equation (19), for different nozzle diameters we must rescale the parameters c_1 so that the flow rate remains constant. For the smaller length-scale simulations, we used $\Phi_1 = 0.076$ m^2/s flow yield and for the larger scale simulations, we used $\Phi_2 = 29$ m^2/s flow yield. To keep the flow yield for different nozzle diameters constant, we varied the value of the c_1 parameter. The c_1 values for the different nozzle diameters are shown in Tables 1 and 2.

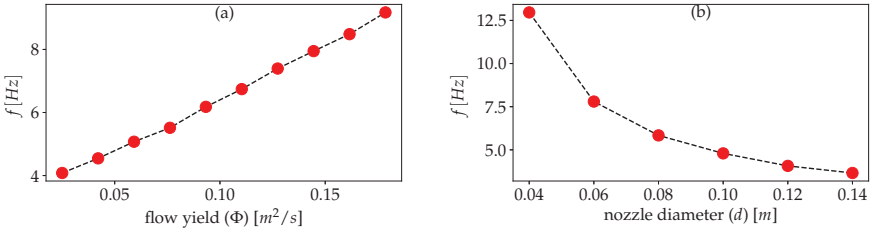

Figure 7. Simulation results for the smaller length-scale. (**a**) shows the oscillation frequency of the heated fluid column as a function of the flow yield Φ fixed by Equation (19) for $d = 0.08$ m inflow diameter. (**b**) shows the oscillation frequency of the heated fluid column as a function of the d nozzle diameter. The other parameters used are the same as the ones specified in the caption of Figure 4, the value of c_1 for the different nozzle diameters are given in Table 1.

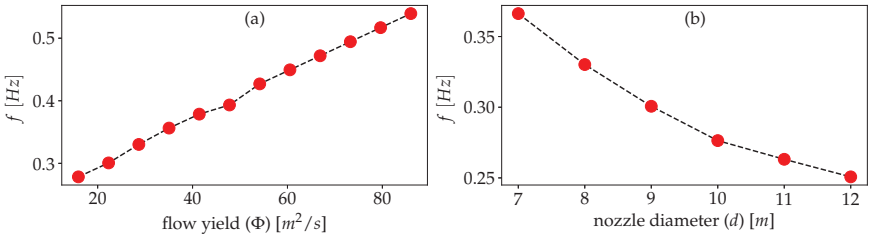

Figure 8. Simulation results for the larger length-scale. (**a**) shows the oscillation frequency of the heated fluid column as a function of the flow yield Φ fixed by Equation (19) for $d = 8$ m inflow diameter. (**b**) shows the oscillation frequency of the heated fluid column as a function of the d nozzle diameter. The other parameters are the same as the ones specified in the caption of Figure 4. The value of c_1 for the different nozzle diameters are given in Table 2.

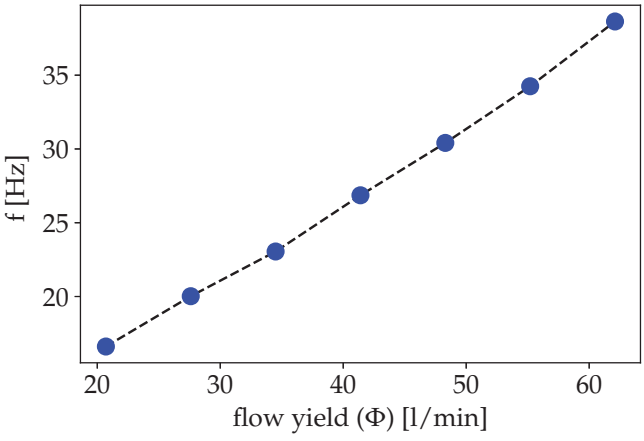

Figure 9. Experimentally observed oscillation frequency of a Helium column as a function of the yield (flow debit) obtained for a setup with a nozzle diameter of 2 cm. With the increasing flow yield, the frequency of the oscillation increases in an almost linear manner. The plot is done by using our experimental results detailed in Ref. [1].

Table 1. Value of the c_1 parameter for different nozzle diameters d, in order to keep the flow rate $\Phi_1 = 0.076\ \mathrm{m}^2/\mathrm{s}$.

d [m]	**0.04**	**0.06**	**0.08**	**0.1**	**0.12**	**0.14**
c_1 [$\mathrm{m}^{-1}\cdot\mathrm{s}^{-1}$]	6781	1952	800	398	223	136

Table 2. Value of the c_1 parameter for different nozzle diameters d, in order to keep the flow rate $\Phi = 29\ \mathrm{m}^2/\mathrm{s}$.

d [m]	**7**	**8**	**9**	**10**	**11**	**12**
c_1 [$\mathrm{m}^{-1}\cdot\mathrm{s}^{-1}$]	0.45	0.3	0.21	0.153	0.11	0.088

For both length scales, a decreasing trend of the oscillation frequency as a function of the nozzle diameter was observed. The results in such sense are plotted in Figures 7b and 8b, the trend is in good agreement with the experimental results shown in Figure 10.

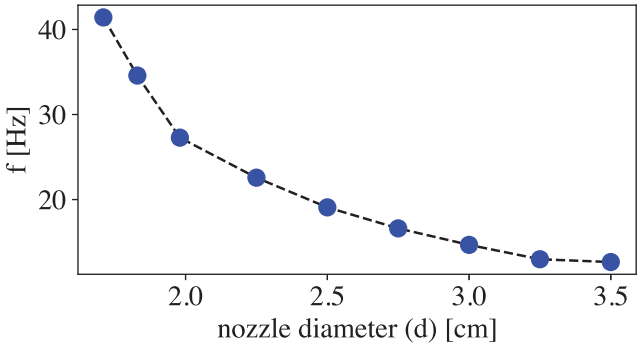

Figure 10. Experimentally observed oscillation frequency of a Helium column as a function of the nozzle diameter for a yield of Φ =46 $\pm$ 2.3 L/min. The plot is done by using our experimental results detailed in Ref. [1].

2.4. Numerical Results for the Collective Behavior

We now turn our attention to reproducing the experimentally observed collective behavior in form of anti-phase synchronization.

The dimensions of the simulation boxes used to study the collective behavior are as follows: 46 m wide (H = 46 m) and 30 m high (L = 30 m) for the large length-scale and 0.3 m wide (H = 0.3 m) and 0.15 m high (L = 0.15 m) at the smaller length-scale. At the lower boundary, the x component of the inflow fluid velocity is 0, and the y component is given by the following kernel function:

$$\begin{aligned} v_y(x,0) = c_1 f\left(x - d_0, \tfrac{d}{2}\right)\left(d_0 - x + \tfrac{d}{2}\right)\left(x - d_0 + \tfrac{d}{2}\right) + \\ + c_1 f\left(x + d_0, \tfrac{d}{2}\right)\left(\tfrac{d}{2} - d_0 - x\right)\left(x + d_0 + \tfrac{d}{2}\right) + c_2 f\left(x, \tfrac{H}{2} - c_4\right) \end{aligned} \quad (20)$$

Here the value of c_4 is 0.5 m for the large scale system and 0.005 m for the small scale system.

This leads to an inflow profile with two peaks, where the centers are separated at a distance of $2d_0$, as illustrated in Figure 11. The temperature profile is adjusted accordingly:

$$T(x,0) = T_0 + T_{heating} f\left(x - d_0, \tfrac{d}{2}\right) + T_{heating} f\left(x + d_0, \tfrac{d}{2}\right) \quad (21)$$

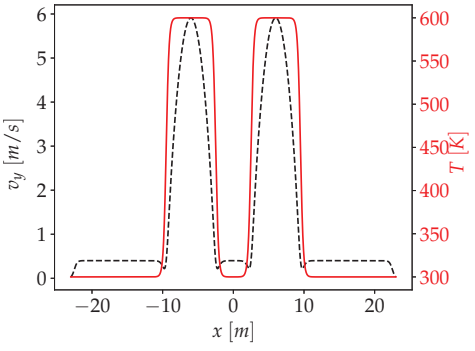

Figure 11. An example for the y-component velocity $v_y(x,0)$ and temperature, $T(x,0)$ profiles of the heated fluid columns at the bottom boundary of the simulated space. The following parameters were used: $c_1 = 0.45\ \mathrm{m}^{-1} \cdot\ \mathrm{s}^{-1}$, $c_2 = 0.4\ \mathrm{m} \cdot \mathrm{s}^{-1}$, $c_3 = 5\ \mathrm{m}^{-1}$, $d = 7$ m, $d_0 = 6$ m, $T_0 = 300$ K, $H = 46$ m.

We used the same simulation parameters as before and fixed $d = 7$ m, $c_1 = 0.45\,\mathrm{m}^{-1} \cdot \mathrm{s}^{-1}$ values for the large length-scale and $d = 0.04$ m, $c_1 = 6400\,\mathrm{m}^{-1} \cdot \mathrm{s}^{-1}$ values for the small length-scale system. Again, for the presented results we considered $T_{heating} = T_0$. The experimental results from Ref. [1] show that at a small separation distance, collective behavior in form of counter-phase synchronization appears. A snapshot for a simulated stable collective behavior is visible in Figure 12, successfully reproducing this counter phase synchronization on the smaller length-scale. Similar behavior is observable for the larger length-scales as well.

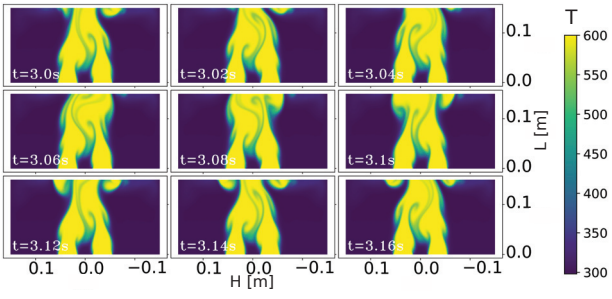

Figure 12. Counter-phase synchronization of two nearby heated columns. Computer simulation results with the following parameters: $\alpha = 0.33 \cdot 10^{-2}\ \mathrm{K}^{-1}$, $\rho_0 = 1.2\ \mathrm{kg{\cdot}m^{-2}}$, $T_0 = 300$ K, $D = 10^{-4}\ \mathrm{m^2{\cdot}s^{-1}{\cdot}K^{-1}}$, $g_y = -9.81\ \mathrm{m{\cdot}s^{-2}}$, $\mu = 1.96 \cdot 10^{-5}\ \mathrm{kg{\cdot}s^{-1}}$, $c_2 = 0.1\ \mathrm{m{\cdot}s^{-1}}$, $c_3 = 2000\ \mathrm{m^{-1}}$, d=0.04 m, $c_1 = 6400\ \mathrm{m^{-1}{\cdot}s^{-1}}$, $H = 0.3$ m, $2 \cdot d_0 = 0.03$ m.

For the pictures processed with the Otsu method, the collective oscillation of nearby heated fluid columns are shown in Figure 13a,b, for the small and large length-scales, respectively.

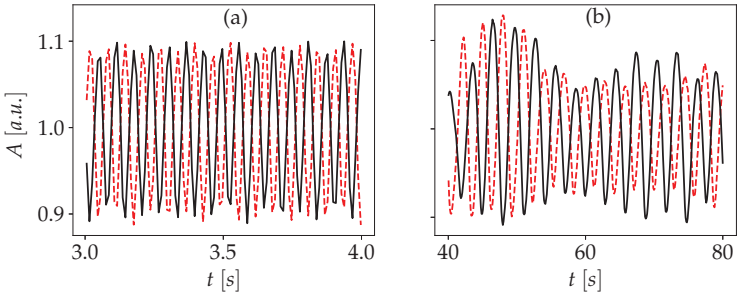

Figure 13. Simulated time series for the oscillations of nearby heated fluid columns. The motion of the interface is detected by the Otsu method at the same height from the nozzle. For smaller separation distances and for the two different nozzle diameters considered in the simulations ((**a**) $2 \cdot d_0 = 0.03$ m, (**b**) $2 \cdot d_0 = 5$ m) a clear counter-phase synchronization is observable. The parameters of the simulations are (**a**): $\alpha = 0.33 \cdot 10^{-2}\ \mathrm{K}^{-1}$, $\rho_0 = 1.2\ \mathrm{kg{\cdot}m^{-2}}$, $T_0 = 300$ K, $D = 10^{-4}\ \mathrm{m^2{\cdot}s^{-1}{\cdot}K^{-1}}$, $g_y = -9.81\ \mathrm{m{\cdot}s^{-2}}$, $\mu = 1.96 \cdot 10^{-5}\ \mathrm{kg{\cdot}s^{-1}}$, $c_2 = 0.1\ \mathrm{m{\cdot}s^{-1}}$, $c_3 = 2000\ \mathrm{m^{-1}}$, $d = 0.04$ m, $c_1 = 6400\ \mathrm{m^{-1}{\cdot}s^{-1}}$, $2 \cdot d_0 = 0.03$ m. (**b**): $\alpha = 10^{-3}\ \mathrm{K}^{-1}$, $\rho_0 = 1\ \mathrm{kg{\cdot}m^{-2}}$, $T_0 = 300$ K, $D = 5 \cdot 10^{-2}\ \mathrm{m^2{\cdot}s^{-1}{\cdot}K^{-1}}$, $g_y = -9.81\ \mathrm{m{\cdot}s^{-2}}$, $\mu = 5 \cdot 10^{-2}\ \mathrm{kg{\cdot}s^{-1}}$, $c_2 = 0.4\ \mathrm{m{\cdot}s^{-1}}$, $c_3 = 5\ \mathrm{m^{-1}}$, $d = 8$ m, $c_1 = 0.375\ \mathrm{m^{-1}{\cdot}s^{-1}}$, $2 \cdot d_0 = 0.03$ m and we have fixed $d = 7$ m and $c_1 = 0.45\ \mathrm{m^{-1}{\cdot}s^{-1}}$.

For the indicated separation distances, an almost perfect counter-phase synchronization develops. For larger separation distances, the phases of the oscillations will begin to shift relative to each other and no clear phase-difference blocking is observable.

For the simulations performed on the smaller length-scale, corresponding to the experimental conditions in Ref. [1], we computed the synchronization order parameter, which is

meant to characterize the collective oscillation. We used the same z synchronization order parameter as the one used in Refs. [1,18]. The computationally derived synchronization parameter is plotted in Figure 14a. Its values in the neighborhood of -1 indicates that we have counter-phase synchronization for the studied distances. In Figure 14b we also show the oscillation frequency of the two synchronized heated fluid columns as a function of their separation distance. This frequency decreases as we increase the separation distance between the columns, similarly to what has been reported in our experiments for the Helium columns [1].

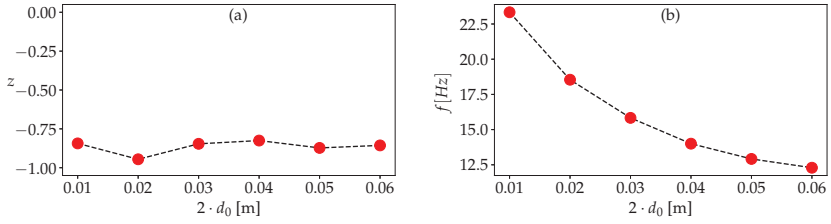

Figure 14. Simulation results for the collective behavior of two heated columns. (**a**) The synchronization order parameter of two interacting heated fluid columns and (**b**) shows the collective oscillation frequency, both as a function of the separation distance between the columns. The following simulation parameters were considered: $\alpha = 0.33 \cdot 10^{-2}$ K^{-1}, $\rho_0 = 1.2$ kg·m^{-2}, $T_0 = 300$ K, $D = 10^{-4}$ m^2·s^{-1}·K^{-1}, $g_y = -9.81$ m·s^{-2}, $\mu = 1.96 \cdot 10^{-5}$ kg·s^{-1}, $c_2 = 0.1$ m·s^{-1}, $c_3 = 2000$ m^{-1}, $d = 0.04$ m, $c_1 = 6400$ m^{-1}·s^{-1}.

Similarly with the case of the oscillations for a single flow, we have tested the grid independence of the results for synchronization. On Figure 15, we illustrate the observed collective behavior for two different grid sizes, using the same values for all the other simulation parameters.

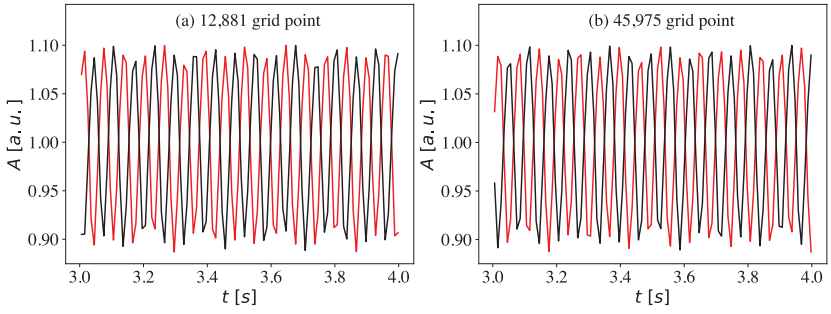

Figure 15. Grid independence of the observed anti-phase synchronization. Figures (**a**,**b**) shows that apart from some minor differences in the amplitudes, the grid size at the used high resolution does not influence the observed frequencies and the synchronization order parameter.

3. Discussion and Conclusions

In our previous study [1], we used both experimental and theoretical approaches to investigate whether the hydrodynamic instabilities that occur in rising gas columns are also responsible for the oscillations observed for the diffusion flames [18]. It was shown that this is indeed the case: Helium columns ascending in air from a circular nozzle produce similar oscillations with the ones observed in diffusion flames. In addition, the similar collective behavior of these oscillations (counter-phase synchronization) for Helium columns and flickering candle flames suggest that the hydrodynamic processes by their own are enough to explain these phenomenon. For modeling the observed oscillations, a simplified but analytically treatable hydrodynamic approach was used. The model predicted the right

trends for the oscillation frequencies as a function of the relevant parameters, but was unsuitable to approach the collective behavior.

In this study, we offered improved modeling by considering a 2D numerical hydrodynamics computer simulation where, for computational simplicity, heated fluid columns were considered instead of ascending Helium columns. This approach proved to be successful for reproducing the experimentally observed features. For a constant nozzle diameter, the numerics led to an oscillation frequency that increased roughly linearly with the flow yield, which is in agreement with the experimental results. For constant flow yield, the numerical results suggested a decreasing trend of the oscillation frequency as a function of the nozzle diameter, confirming the experimental results. The exact shape of the simulated trend was however slightly different from the one observed in the experiments. The main reason for this discrepancy is most likely the reduction of the real 3D problem to a 2D topology. Finally, the presented computer simulations were successful also in reproducing the counter-phase synchronization of the two heated fluid columns placed nearby each other. The computed trends for the synchronization order-parameter and the collective frequency were also in agreement with the experimental results obtained for Helium columns rising in air.

From a more general physical point of view it is important to notice once again the generality of the spontaneous synchronization phenomena in interacting oscillatory systems. Similarly with the analogous candle flame synchronization, the investigated fluid-dynamical system offers yet another fascinating example in this sense. The Navier–Stokes equation for incompressible fluids coupled with the classical heat-diffusion equation, and by considering a temperature dependent density in a 2D approach, is seemingly enough for reproducing the experimentally observed trends. The use of a 2D topology is based on the assumption of the jet's cylindrical symmetry. Future experiments will decide whether this is a reasonable approximation. However, performing a realistic 3D fluid dynamical simulation with the FEniCS method was not viable with our available computational resources.

It worth mentioning here that the computer simulations were performed both in the laboratory and for a much larger length-scale than the experiments. The qualitative agreement between the results (trends and collective behavior) on these different length-scales suggests that the investigated phenomenon is more general than it was thought to be, and might have further, yet unexplored, connections.

Supplementary Materials: The following supporting information can be downloaded at: https://www.mdpi.com/article/10.3390/fluids7110339/s1, Video S1: Experimental and Otsu processed movies for the oscillation and collective behavior of Helium jets.

Author Contributions: Conceptualization Z.N.; methodology A.G. and Z.N.; validation A.G.; formal analysis A.G.; funding acquisition Z.N.; first draft of the manuscript by Z.N. All authors have read and agreed to the published version of the manuscript.

Funding: This research was supported by funding from the UEFISCDI grant PN-III-P4-ID-PCE-2020-0647.

Data Availability Statement: Not applicable.

Acknowledgments: The work was supported by the Romanian UEFISCDI PN-III-P4-ID-PCE-2020-0647 research grant. The work of Attila Kelemen is supported by the Collegium Talentum Programme of Hungary. We acknowledge M. Ercsey-Ravasz, B. Molnár and G.C. Silaghi, all from the Babes-Bolyai University in helping us with the computational resources for running our simulation codes.

Conflicts of Interest: The authors declare no conflict of interest.

Appendix A

Appendix A.1. Solving the 2D Poisson Equation in FEniCS

Here we illustrate how to solve a PDE in FEniCS using the 2D Poisson equation. The Poisson equation can be given in the following form:

$$-\Delta\varphi = f \tag{A1}$$

If we have a simple rectangular space, then the above equation can be easily given in the finite element form

$$-\frac{\varphi_{i-1,j} - 2\varphi_{i,j} + \varphi_{i+1,j}}{h^2} - \frac{\varphi_{i,j-1} - 2\varphi_{i,j} + \varphi_{i,j+1}}{h^2} = f_{i,j}, \tag{A2}$$

however, with this simple and intuitive approach, we soon run into problems, because even for a circle it is impossible to map the boundary with an acceptably small number of squares. The FEniCS program [29] uses a triangular grid instead of a square grid to cover the simulated space, in which case we can always select the grid so that the grid points are on the boundary surfaces.

Discretization alone does not solve the equation, the next question is how to determine the solution at each lattice point. As the first step, we write the $\varphi(x_1, x_2)$ function in the following form:

$$\varphi(x_1, x_2) = \sum_{i=0}^{N} c_i \phi_i(x_1, x_2) \tag{A3}$$

In the above equation, $\phi_i(x_1, x_2)$ is a given k-th order polynomial, c_i are the coefficients that determine $\varphi(x_1, x_2)$, and N + 1 is the number of the grid points. The c_i coefficients are determined by multiplying the Poisson equation by N + 1 different $v(x_1, x_2)$ so-called test functions and integrating the product over the whole domain to obtain N + 1 linearly independent equations from which the c_i coefficients can be calculated. All this can be formally given in the following form:

$$\int_\Omega -v\,\Delta\varphi\; d\Omega = \int_\Omega f v\; d\Omega \tag{A4}$$

We used the notation $d\Omega = dx_1 dx_2$. The above form of PDE is called the weak formulation of the equation and this is what is calculated by the FEniCS program. The second-order derivative after the coordinates in the above equation means that the polynomials used need to be twice differentiable. Because the use of polynomials with large degrees requires more memory and computation, we always strive to keep the degree of polynomials to a minimum. In the above equation, the reduction of the order of derivatives can be done by Gauss–Green integration as follows:

$$\int_\Omega -v\,\Delta\varphi\; d\Omega = \int_\Omega \nabla v \nabla\varphi\; d\Omega - \int_{\partial\Omega} \frac{\partial\varphi}{\partial \mathbf{n}} v\; ds \tag{A5}$$

Since we use Dirichlet boundary conditions for the Poisson problem, the value of v at the boundary is 0, so the Equation (A4) can be written in the following form:

$$\int_\Omega \nabla v \nabla\varphi\; d\Omega = \int_\Omega f\, v\; d\Omega \tag{A6}$$

We have seen above how to rewrite the 2D Poisson problem in a form that can be solved with the FEniCS program, and now we show the implementation of the solution in Python.

```
from fenics import *    #
import numpy as np #Numpy is required for error calculation
import matplotlib.pyplot as plt #We plot the result with the matplotlib
```

```
Nx=10#The number of grid points in the x directions
Ny=10#The number of grid points in the y directions
mesh=UnitSquareMesh(Nx,Ny)
V=FunctionSpace(mesh,'P',1)#space containing first degree polynomials
fi_D=Expression('1+x[0]*x[0]+2*x[1]*x[1]',degree=2)
#boundary conditions equation (on boundarys fi(x,y)=x^2+2y^2+1)
def boundery(x,on_boundary):
return on_boundary
bc=DirichletBC(V,fi_D,boundery)#boundary conditions
fi=TrialFunction(V)
v=TestFunction(V)
f=Constant(-6)
a=dot(grad(fi),grad(v))*dx#right side of equation
L=f*v*dx#left side of equation
fi=Function(V)
solve(a==L,u,bc)#solve the~equation

c = plot(interpolate(fi, V), mode='color')
plt.colorbar(c)
plot(fi)
plt.savefig('result1.png')
plt.show()
vertex_v_ud=fi_D.compute_vertex_values(mesh)
vertex_v_u=fi.compute_vertex_values(mesh)
err_max=np.max(np.abs(vertex_v_ud-vertex_v_u))
print("maximum error: ",err_max)
```

The above program solves Equation (A1) on the unit square of $\{(0,0),(1,1)\}$. The largest difference between the theoretically expected and the numerically obtained value was of the order of the precision of the numerical representation of the numbers, giving us confidence for the use of the numerical solution.

Appendix A.2. Test for the 2D Fluid Dynamics Simulations—Karman Vortices

The first phenomenon we aimed to reproduce using our fluid dynamics simulation is the formation of Karman vortices in the flow of fluids around an obstacle. With this test we aimed to check visually whether the Navier–Stokes equation has been correctly implanted, since the temperature of the fluid at all points is considered fixed: T_0. Therefore, for this test, the density in the simulated volume is constant.

In these simulations, the length of the simulated volume was considered as 2.2 m, the width of the simulated volume as 0.41 m and in the middle of the simulated coordinate space a circular obstacle with a radius of 0.05 m is placed. The coordinates of the center of this obstacle was taken at (0.2 m, 0.2 m). The density of the fluid was taken as unity (1 kg/m^2), the viscosity is 0.001 kg/s, and no gravitational field is considered. For input (the left region of the space in Figure A1) we considered that the velocity in the y direction is 0, and the velocity in the x direction has a parabolic profile with a maximum value of 1.5 m/s. On the horizontal walls and on the boundary of the obstacle we consider no-slip conditions, thus the velocity is fixed to 0. For the output (right-sight region) we have also imposed for the y direction velocity to be zero, and the pressure at the output is also fixed to 0. Otherwise, there are free boundary conditions for the pressure. The temperature is fixed at $T_0 = 300$ K at input and on the horizontal walls.

The velocity vector spaces obtained from the simulations are shown in Figure A1 for four time moments, as indicated on the left side of the images. One can observe that the simulation successfully reproduces the expected Karman vortices.

Appendix A.3. Test for the 2D Fluid Dynamics Simulations—Heat Induced Mushroom Cloud

In this second test we aimed to implement the density and temperature evolution of a heated gas sphere in a gravitational field. It is expected that the shape of the heated gas will follow the known dynamics of a mushroom cloud in a nuclear explosion.

In the performed simulations, the density at T_0 was chosen as unity (1 kg/m^2), the ambient temperature T_0 is 300 K, the α parameter in Equation (3) is $\alpha = 0.001$ K^{-1}, the thermal

diffusion constant D is 0.3 m^2/s, the initially heated sphere temperature is 600 K, the fluid viscosity is taken as $\mu = 0.05$ kg/s, the gravitational acceleration is $g_y = -9.81$ m/s^2, and the size of the simulated volume is 30 m^2 in both the x and y directions.

At the bottom and walls of the simulated space, the velocity is fixed to 0. At the upper boundary we fix the x component of the velocity to $v_x = 0$. For the pressure, the value of $g \cdot \rho_0 \cdot l$ is fixed for the upper boundary, and free boundary conditions are applied to all the other boundaries. For temperature, free boundary condition is applied at the upper boundary if the y direction component of the velocity is positive, otherwise the temperature is fixed to $T_0 = 300$ K units on the upper boundary and on the side-walls. The temperature is fixed to a higher value of 450 K units at the bottom-wall of the simulated area. This is necessary in order to make the resulting flow visible in the temperature space. Initially, the velocity in the whole simulated volume is 0 and the volume contains a sphere (disk) with a radius of 5 m, in which the temperature is 600 K. The center of the sphere is at the coordinates (0 m, 7 m), the temperature around the sphere is fixed to 300 K, and the temperature between the center, and the surface of the disk is given by an interpolation with a sigmoid function.

The time-evolution of the temperature map derived from the simulation is shown in Figure A2. The effect of thermal diffusion can be observed in the first two frames. As a result of this diffusion, the initially sharp boundary line between the high and low temperature regions becomes blurred. The subsequent frames show the displacement due to convective flow and as a result of this the characteristic mushroom cloud shape is formed.

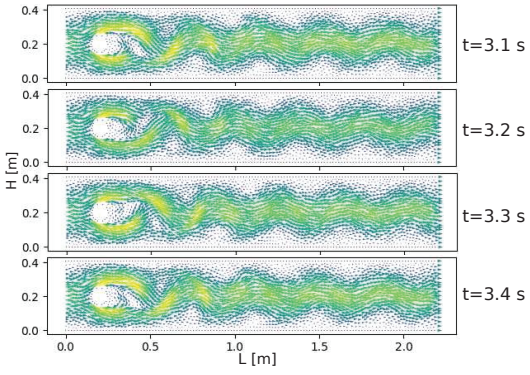

Figure A1. Velocity fields obtained from the simulation of the Karman vortices at four consecutive time moments.

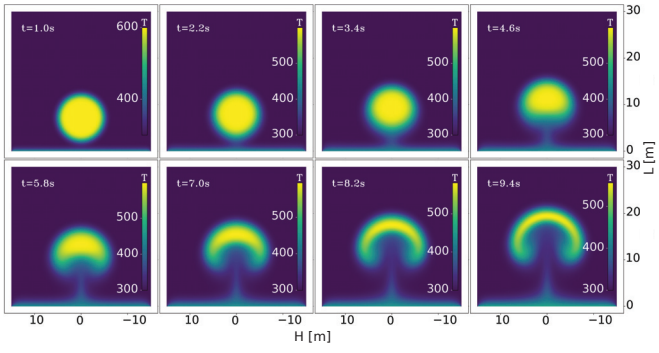

Figure A2. Snapshots of the time evolution of a heated gas sphere. The parameters and details of the simulation can be found in the text.

References

1. Gergely, A.; Paizs, C.; Tötös, R.; Néda, Z. Oscillations and collective behavior in convective flows. *Phys. Fluids* **2021**, *33*, 124104. [CrossRef]
2. Monkewitz, P.; Sohn, K. Absolute instability in hot jets. *AIAA J.* **1988**, *26*, 911–916. [CrossRef]
3. Sreenivasan, K.; Raghu, S.; Kyle, D. Absolute instability in variable density round jets. *Exp. Fluids* **1989**, *7*, 309. [CrossRef]
4. Yuan, T.; Durox, D.; Villermaux, E. An analogue study for flame flickering. *Exp. Fluids* **1994**, *17*, 337–349. [CrossRef]
5. Monkewitz, P.; Bechert, D.; Barsikow, B.; Lehmann, B. Self-excited oscillations and mixing in a heated round jet. *J. Fluid Mech.* **1990**, *213*, 611–639. [CrossRef]
6. Lesshafft, L.; Huerre, P.; Sagaut, P. Frequency selection in globally unstable round jets. *Phys. Fluids* **2007**, *19*, 054108. [CrossRef]
7. Boguslawski, A.; Tyliszczak, A.; Drobniak, S.; Asendrych, D. Self-sustained oscillations in a homogeneous-density round jet. *J. Turbul.* **2013**, *14*, 25–52. [CrossRef]
8. Pawlowska, A.; Boguslawski, A. The Dynamics of Globally Unstable Air-Helium Jets and Its Impact on Jet Mixing Intensity. *Processes* **2020**, *8*, 1667. [CrossRef]
9. Jendoubi, S.; Strykowski, P. Absolute and convective instability of axisymmetric jets with external flow. *Phys. Fluids* **1994**, *6*, 3000. [CrossRef]
10. Chamberlin, D.; Rose, A. The flicker of luminous flames. *Proc. Symp. Combust.* **1948**, *1–2*, 27–32. [CrossRef]
11. Durox, D.; Yuan, T.; Baillot, F.; Most, J. Premixed and diffusion flames in a centrifuge. *Combust. Flame* **1995**, *102*, 501–511. [CrossRef]
12. Durox, D.; Yuan, T.; Villermaux, E. The Effect of Buoyancy on Flickering in Diffusion Flames. *Combust. Sci. Technol.* **1997**, *124*, 277–294. [CrossRef]
13. Huang, Y.; Yan, Y.; Lu, G.; Reed, A. On-line flicker measurement of gaseous flames by image processing and spectral analysis. *Meas. Sci. Technol.* **1999**, *10*, 726–733. [CrossRef]
14. Kitahata, H.; Taguchi, J.; Nagayama, M.; Sakurai, T.; Ikura, Y.; Osa, A.; Sumino, Y.; Tanaka, M.; Yokoyama, E.; Miike, H. Oscillation and Synchronization in the Combustion of Candles. *J. Phys. Chem. A* **2009**, *113*, 8164–8168. [CrossRef]
15. Ghosh, S.; Mondal, S.; Mondal, T.; Mukhopadhyay, A.; Sen, S. Dynamic Characterization of Candle Flame. *Int. J. Spray Combust. Dyn.* **2010**, *2*, 267–284. [CrossRef]
16. Okamoto, K.; Kijima, A.; Umeno, Y.; Shima, H. Synchronization in flickering of three-coupled candle flames. *Sci. Rep.* **2016**, *6*, 1–10. [CrossRef]
17. Chen, T.; Guo, X.; Jia, J.; Xiao, J. Frequency and Phase Characteristics of Candle Flame Oscillation. *Sci. Rep.* **2019**, *9*, 1–13. [CrossRef]
18. Gergely, A.; Sándor, B.; Paizs, C.; Tötös, R.; Néda, Z. Flickering candle flames and their collective behavior. *Sci. Rep.* **2020**, *10*, 1–13. [CrossRef]
19. Settles, G.S. *Schlieren and Shadowgraph Techniques: Visualizing Phenomena in Transparent Media*; Springer: Berlin/Heidelberg, Germany, 2001.
20. Leptuch, P.A.; Agrawal, A.K. High-speed rainbow schlieren visualization of an oscillating helium jet undergoing gravitational change. *J. Vis.* **2006**, *9*, 101–109. [CrossRef]
21. Otsu, N. A Threshold Selection Method from Gray-Level Histograms. *IEEE Trans. Syst. Man, Cybern.* **1979**, *9*, 62–66. [CrossRef]
22. FreddyCree. Wikipedia, Otsu's Method. 2017. Available online: https://en.wikipedia.org/wiki/Otsu's_method (accessed on 10 July 2021).
23. Gergely, A. 2020. Available online: https://youtube.com/playlist?list=PLamJmxTyiR_3sy-fYUEDEXW4NtbsnsXnW (accessed on 15 July 2022).
24. Joel, H. Ferziger, M.P.; Street, R.L. *Computational Methods for Fluid Dynamics*, 4th ed.; Springer International Publishing: Berlin/Heidelberg, Germany, 2020.
25. Wendt, J.F. *Computational Fluid Dynamics*; Springer: Berlin/Heidelberg, Germany, 2009.
26. Venkatakrishnan, V.; Salas, M.D.; Chakravarthy, S.R. *Barriers and Challenges in Computational Fluid Dynamics*; Springer Science+Business Media Dordrecht: Berlin/Heidelberg, Germany, 1998.
27. Correa, P.G.; MacIntyre, J.; Gomba, J.; Cachile, M.; Hulin, J.; Auradou, A. Three-dimensional flow structures in X-shaped junctions: Effect of the Reynolds number and crossing angle. *Phys. Fluids* **2019**, *31*, 043606. [CrossRef]
28. Gergely, A. Heated Air Column. 2020. Available online: https://youtube.com/playlist?list=PLamJmxTyiR_0fNk5bzTD5GyRF_dOrmB2E (accessed on 10 July 2022).
29. Langtangen, H.P.; Logg, A. *Solving PDEs in Python*; Springer: Berlin/Heidelberg, Germany, 2017. [CrossRef]
30. Logg, A.; Mardal, K.A.; Wells, G.N. *Automated Solution of Differential Equations by the Finite Element Method*; Springer: Berlin/Heidelberg, Germany, 2012. [CrossRef]

fluids

MDPI

Article

Effect of the Pore Geometry on the Driving Pressure across a Bubble Penetrating a Single Pore

Shadi Ansari and David S. Nobes *

Department of Mechanical Engineering, University of Alberta, Edmonton, AB T6G 2R3, Canada
* Correspondence: dnobes@ualberta.ca

Abstract: The passage of a bubble and the required energy for its motion through a confining pore can potentially be affected by the surface roughness and geometry of the pore. The motion of an isolated bubble passing through four different pore geometries (three circular pores, a smooth pore and 2 with different roughness, and a sharp triangular pore) is investigated. The shape of the deformed bubble passing these geometries was evaluated to determine the pressure drop across the bubble and hence the driving force to cause motion. The results of investigating the motion of the bubbles and the change in the pressure and velocity of the bubbles showed that the pore shape and surface roughness have a significant effect on the passage of the isolated phase. The motion of the bubble entering the entrance of the circular pores was similar for all circular cases. On exiting, however, a clear difference between the cases due to the presence of the peaks of the roughness was observed. These results indicate that, in addition to the critical pressure at the entrance of the pore, extra resistance will be introduced due to bubble phase pinning at the exit caused by roughness of the pore.

Keywords: PIV; laplace pressure; critical pressure; phase trapping; phase pinning; confined geometry; bubble; multi-phase flow; surface roughness; transit time

Citation: Ansari, S.; Nobes, D.S. Effect of the Pore Geometry on the Driving Pressure across a Bubble Penetrating a Single Pore. *Fluids* **2022**, *7*, 333. https://doi.org/10.3390/fluids7100333

Academic Editor: Mehrdad Massoudi

Received: 9 September 2022
Accepted: 18 October 2022
Published: 20 October 2022

1. Introduction

Multi-phase flow motion in a porous media is broadly observed in different applications such as oil recovery [1], food processing [2], and macromolecular delivery [3]. The motion of an immiscible phase having different motility in the pore space will lead to the trapping of the dispersed phase caused by the snap-off or the bypass of the phases within the pore structures [4,5]. The mobilization of the trapped phase is important for many applications such as trap oxygen gas bubbles in contaminated groundwater or residual oil in the recovery of oil reserves [5–9]. Having a better understanding of the motion of the phases and their interaction with the surrounding fluid and solid geometry is beneficial to predict the required energy needed to mobilize the isolated phase.

Over the past two decades, the motion of multi-phase flows in porous media has been studied by groups of researchers at a macro and micro scale [10–19]. The comparison between the motion of single-phase and multi-phase flow indicates that higher resistance to the flow is observed for multi-phase flows [20–25]. The resistance is introduced due to the deformation of the dispersed phase which arises from the interfacial interaction between the phases and the flow passage [26–28]. Phase trapping in the pore geometry occurs due to the critical pressure introduced by the interaction of the dispersed phase and the solid interface at the entrance of the confined geometry [29]. To mobilize the trapped phase in the pore geometry, a critical driving force is needed to overcome the entrance pressure [8].

Various factors have an impact on the motion of the isolated dispersed phase in a pore structure such as the velocity [30–34] and rheology of the carrying fluid [35–37] the pressure of the system [38], the relative size of the dispersed phase compared to the pore [39–41] and the capillary number [39–43]. Studies on the interaction of the solid surface and the trapped isolated phase has shown that pore structure [44], grain morphology, and wettability of

the surface play important roles in the motion of isolated dispersed phases in the pore structure [44–47]. Other studies [22,41] on the effect of the pore structure on the motion of multi-phase flow have mainly focused on the overall phase trapping in the pore space and phase residual. Overall, these studies did not focus on the fundamentals of the interaction of an isolated dispersed phase and solid geometry and the effect of the grain morphology on the motion of the dispersed phase through a pore geometry.

Research work focusing on the pore-scale interaction of an isolated dispersed phase and pore geometry [38,39] showed that in addition to the entrance critical pressure, the strong interaction of the solid interface and the pore geometry can lead to an extra critical pressure at the exit of the pore geometry [48]. The introduced flow restrictions will lead to different flow motions within the geometry and the calculation of the critical entrance pressure is not sufficient to predict the required driving force for the mobilization of the trapped phase in the solid geometry [49,50]. The surface properties of the confined geometry are an important component for emulsion flows in porous media [14–23].

The main objective of this study is to investigate the pore-scale effects of shape and surface roughness of a confined geometry on pressure distribution within the multi-phase flow and the required transit time for the phase to pass the confined geometry. To achieve this goal, an isolated bubble is considered as a dispersed phase to pass through a pore space and its deformation and velocity will be monitored using a shadowgraph imaging method. The interaction of the bubble and the interface is visualized by the deformation of the phase at different stages and velocity and pressure distribution were selected as representative parameters for the flow properties. The pressure in this study is calculated using an indirect method proposed in our previous studies [33,51]. The results of this study will aim to provide a better understanding of the effect of pore surface properties on pore-scale capillary pressure and fluid motion within a porous media.

2. Pressure Calculation from Shape Analysis

The pressure changes across a dispersed phase passing through a confined geometry or its driving pressure, can be determined using the theory introduced by Jamin (1860) [52] which was derived from the Young–Laplace equation. According to this theory, the pressure changes within the deformed dispersed phase (ΔP^*) is inversely proportional to the change in the radii of curvature of the trailing (R_T) and leading-edge (R_L) as defined in Figure 1a and proportional to the interfacial tension (γ_{cd}) as:

$$\Delta P^* = \gamma_{cd}\left(\frac{1}{R_L} - \frac{1}{R_T}\right), \quad (1)$$

The change in the pressure within the phase (ΔP^*) showed that a different local pressure change along the phase can be expected depending on the location of the dispersed phase within the pore geometry. A sample of the different stages of bubble deformation and their corresponding change in the pressure of the phase is shown in Figure 1b. The deformation of bubble can be monitored by the relative location of the centroid of the projected area of the bubble (y_c) with respect to the pore throat (y_p). Where the bubble will have similar $R_L = R_T$ at $y_c - y_p = 0$ leading to $\Delta P^* = 0$.

The pressure gradient generated within the dispersed phase is positive as the droplet enters the pore in the stage seen in Figure 1b ($R_L < R_T$) leading to an extra resistance to the droplet passage [21,35]. Negative ΔP^* occurs when the dispersed phase exists the pore which results in the acceleration of the dispersed phase (Figure 1b ($R_L > R_T$). Zero ΔP^* occurs when the pressure distribution is uniform between the leading and trailing edge of the bubble $R_L = R_T$. To monitor the instantaneous change in the motion of isolated bubbles passing through a pore geometry, an image processing technique developed in our previous studies [41,53] can be utilized. As reported in our previous study [49], the maximum uncertainty for detection will result to a 5.5% error in calculation of the change in the radius of curvature. The proposed methodology to evaluate the motion of the phase can detect the critical pressure required for mobilization of the phase in the pore geometry

(ΔP_c). The critical pressure can be determined from the first peak detected in the motion of the dispersed phase on entrance into the confined geometry.

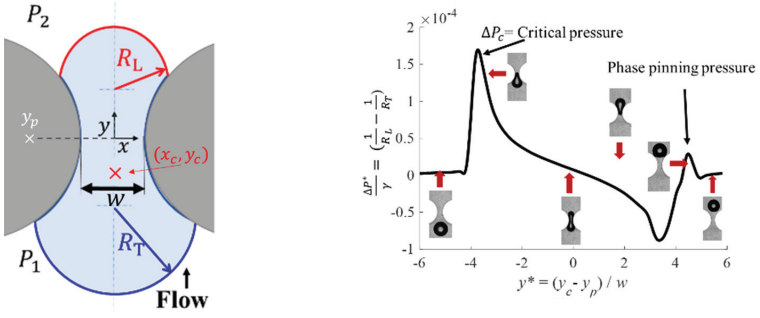

(**a**) (**b**)

Figure 1. (**a**) Schematic of bubble deformation and (**b**) an example of the determined pressure difference across an isolated bubble passing through a pore and its corresponding locations.

3. Experimental Setup and Image Processing

An optical setup was used to measure and track the motion and deformation of a bubble passing through a pore geometry is shown in Figure 2. The setup consists of two main sections of an imaging system containing a camera (4M180, IO Industries Inc., London, UK), a light source (BX0404-520 nm; Advanced Illumination Inc., Rochester, VT, USA), and data acquisition (DVR Express Core 2, IO Industries Inc., London, UK) [54–56]. The second section, the flow loop, consisted of two syringe pumps for each phase (PHD 2000, Harvard Apparatus, Holliston, MA, USA) and a flow channel, as highlighted in the figure.

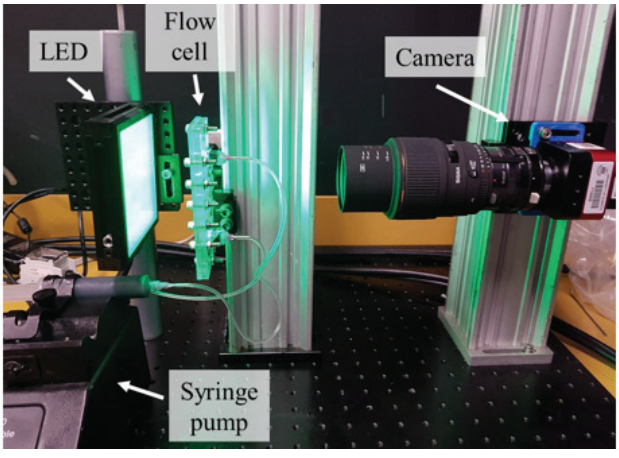

Figure 2. A picture of the experimental setup showing the main components.

The designs of the flow channels used to study different pore geometries are shown in Figure 3. The flow channels consisted of two assembled layers of an optical access window and the main flow channel. The window access is made of acrylic sheet and manufactured using a laser cutter (VersaLaser VLS Version 3.50; Universal Laser Systems, Scottsdale, AZ, USA). The design main flow channels with the desired features were manufactured from a photo-reactive resin using the stereolithography (SLA) additive manufacturing technique (Form 2, Formlabs Inc., Somerville, MA, USA). The flow channels are manufactured with resolution of 25 μm for each layer.

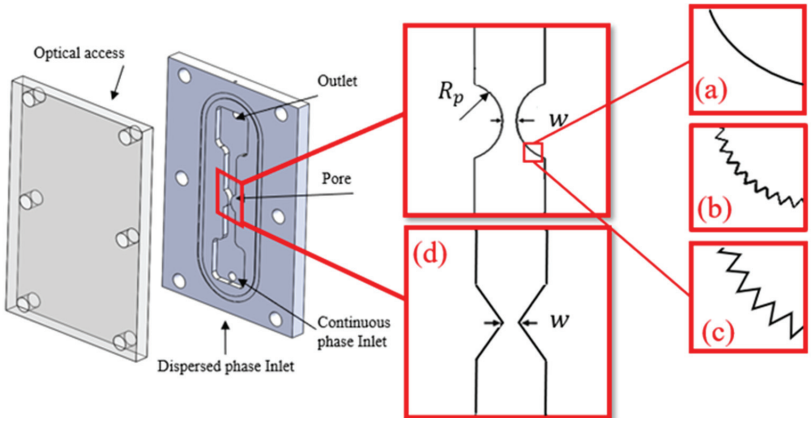

Figure 3. Design of flow channels containing different shapes of pore space (**a**) circular pore (**b**) circular pore with 0.2 mm surface roughness, (**c**) circular pore with 0.4 mm surface roughness, and (**d**) pore with a sharp corner. In the current study, w = 1 mm and R_p = 2 mm.

Two separate inlets for the continuous and the dispersed phase were designed at the bottom of the flow channel as highlighted in Figure 3. Glycerol (100% Pure Glycerol (Molecular Biology), Fisher BioReagents™, Pittsburgh, PA, USA) was used as the continuous flow and air was used as the dispersed phase. The glycerol had a viscosity of 1.412 Pa.s, density of 1.26 g/cm and surface tension of 64 mN/m [57,58]. The continuous phase in each experiment was injected with different flow rates of 0.1, 0.2, and 0.3 mL/min. Air, as a dispersed phase, was injected at time intervals to generate an isolated bubble. The content angle measurement between the phases was obtained using a SLA sample piece manufactured with the same setting as the flow channel. The contact angle between a glycerol droplet and the solid interface is 130°.

The motion of the multi-phase flow in the pore space was studied by modeling the pore space of two adjacent particles in the flow channels. Four different pore geometries were designed as shown in the detailed views of Figure 3. These pore geometries are a smooth circular pore, circular pore with two different roughness (0.2 and 0.4 mm), and a sharp pore. In these channels, two cylindrical pillars were used to mimic the geometry of two adjacent particles in the pore space with smooth surfaces. The diameter pillars (R_p) were 2 mm and they were separated by w = 1 mm at the pore throat. The detail view (a) of Figure 3 represents the design of the smooth circular pore. Two different roughness of 0.2 and 0.4 mm, shown in the detail view (b) and (c), were used to compare the effect of roughness. A sharp pore geometry with the same aperture was also considered to account for the effect of the change of the convergence of the pore on the pressure distribution. In this case, two adjacent rectangles were considered as shown in the detail view (d). For all cases, the depth of the channel was 3 mm. Figure 4 shows the pictures of the pore geometries after manufacturing on the left for each pore geometry and their corresponding original designs are shown on the right.

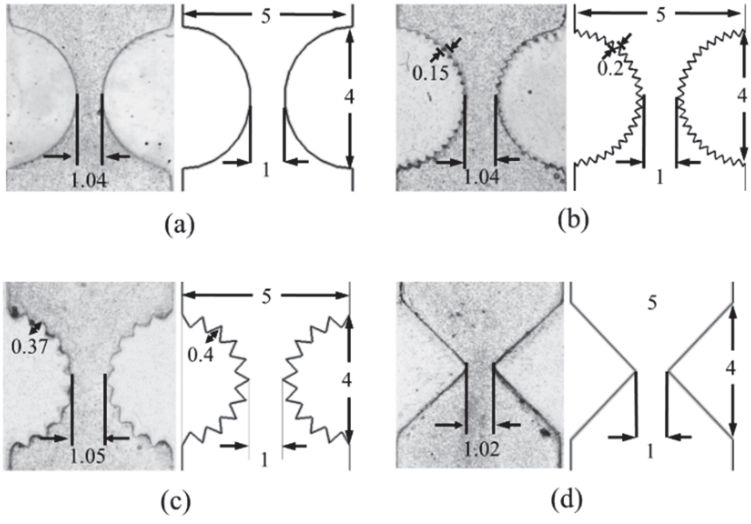

Figure 4. Picture of the manufactured pore and designed geometry (**a**) smooth circular pore, (**b**) sharp pore, (**c**) circular pore with 0.2 mm roughness, and (**d**) circular pore with 0.4 mm roughness (all dimensions are in mm).

A sample of a raw image of a bubble and the surrounding fluid passing through a circular pore is shown in Figure 5a. The images are collected in the mid-plane of channel to evaluate the deformation of the bubble in the symmetry plane. The bubble is reflected as a black hollow region as shown in the picture due to the difference between the refractive indexes of glycerol and air. To have better detection of the deformation of the bubble and remove noise of the background, the images need to be pre-processed. The details of these procedures can be seen in [33,41,53]. The deformation of the dispersed phase in the pore geometry will be then detected by the radius of the leading and trailing edge at each location as shown in Figure 5c. Having the curvature of the leading and trailing edges, the pressure change across the bubble can be evaluated using Equation (1).

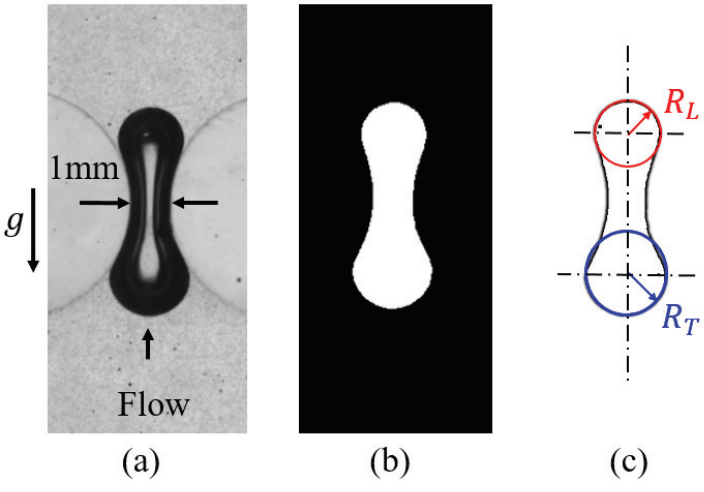

Figure 5. An example of (**a**) a raw image, (**b**) the isolated dispersed phase, and (**c**) processed image defining the leading and trailing geometry.

4. Results

4.1. Flow Visualization of Bubbles Deformation Passing Different Pore Geometries

A series of images showing the passage of the bubble and its deformation for bubbles having a similar equivalent radius (radius of bubble, R_b ~3 mm) passing through the different pore geometries are shown in Figure 6. The images were selected based on the location of the centroid of the projected area of the bubble from the pore throat to highlight the bubble shape at these locations for the different surface conditions. As shown in location (a) for all pore geometries, the bubbles are symmetric and have a similar radius of the curvature of leading and trailing edges. They are slightly oval at this position due to the presence of a confining wall effect on the bubble's interface as was reported in [59]. The results of the pressure calculation for the bubble passage are unique for the current experiment due to the presence of the confining wall. As the size of the bubble considered in this study is same, the results of the trend of the change in the pressure and the radius of curvature is general and can be applied for any confining geometry condition.

As the bubbles approach the pore geometry, their leading-edge deforms slightly as shown in location (b) in Figure 6. The deformation in this location leads to the decrease in the radius of curvature of the leading edge compared to the trailing edge of the bubble. The decrease in the leading edge continues until it passes the pore throat as shown in Figure 6c. After this location, the leading-edge radius of curvature increases and reaches an equilibrium condition after the bubble has passed through the pore geometry.

As shown in Figure 6, there is a significant difference between the motion of bubbles exiting the pore geometries with different roughness. The effect of the surface condition of the pore geometry on the motion of the bubble can be observed by the deformation of the trailing edge at different locations along the pore. In the case of a smooth circular pore, shown in Figure 6I, the bubbles trailing edge decreases as it enters the pore geometry. The trailing edge maintains its convex curvature during its passage in the pore. As it reaches the exit of the pore, in location (h) of case (I), the interaction between the pore solid interface and the bubble leads to the development of phase pinning. Change in the detachment of the bubble exiting a circular pore geometry is highly affected by the relative size of the bubble with the pore and the continuous phase flow rate. A sample of the effect of the continuous phase flow rate is shown in Figure 7. The bubble's trailing edge interface becomes flat for lower flow rates and as the flow rate increases, the bubbles trailing interface becomes concave.

The motion of a bubble passing through a circular pore with roughness is shown in Figure 6II,III. Having a closer look at the interaction of the bubble and pore geometry shows that the bubble deforms to fill the pore roughness. It does not block the valleys of the pore roughness and the phases are mostly in contact at the peak of the roughness of the pore. The higher contact area between the bubble and the solid surface in this condition results in more interaction between the surface and the trailing region of the bubble. Therefore, phase pinning occurs at each peak of the roughness of the pore interface shown in locations (g) and (h) for cases (II), and (III).

For rough pores, the interface of the trailing edge of the bubble goes through different steps due to pinning at each peak of the pore. The details of the change in the curvature of the bubble passing a 0.4 mm roughness are shown in Figure 8. As shown in the detailed view of Figure 8a, the bubble has a convex curvature before its trailing edge reaches the peak of the roughness. As the bubble moves further into the pore, the bubble's trailing edge and reaches the same elevation of the pore the roughness in Figure 8b, the bubble has a flat trailing edge due to the pinning of the phase. On breaking of the pinning, in Figure 8c the trailing edge curvature has become concave. As the bubble is not in contact with the valleys of the pore, the trailing edge becomes unstable, and the bubbles' trailing edge moves to the next pore peak as shown in Figure 8d. The same deformation steps for the trailing edge were observed at each peak of the roughness. Similar interaction of the phase was observed in the case of a bubble moving through a pore with a roughness of 0.2 mm.

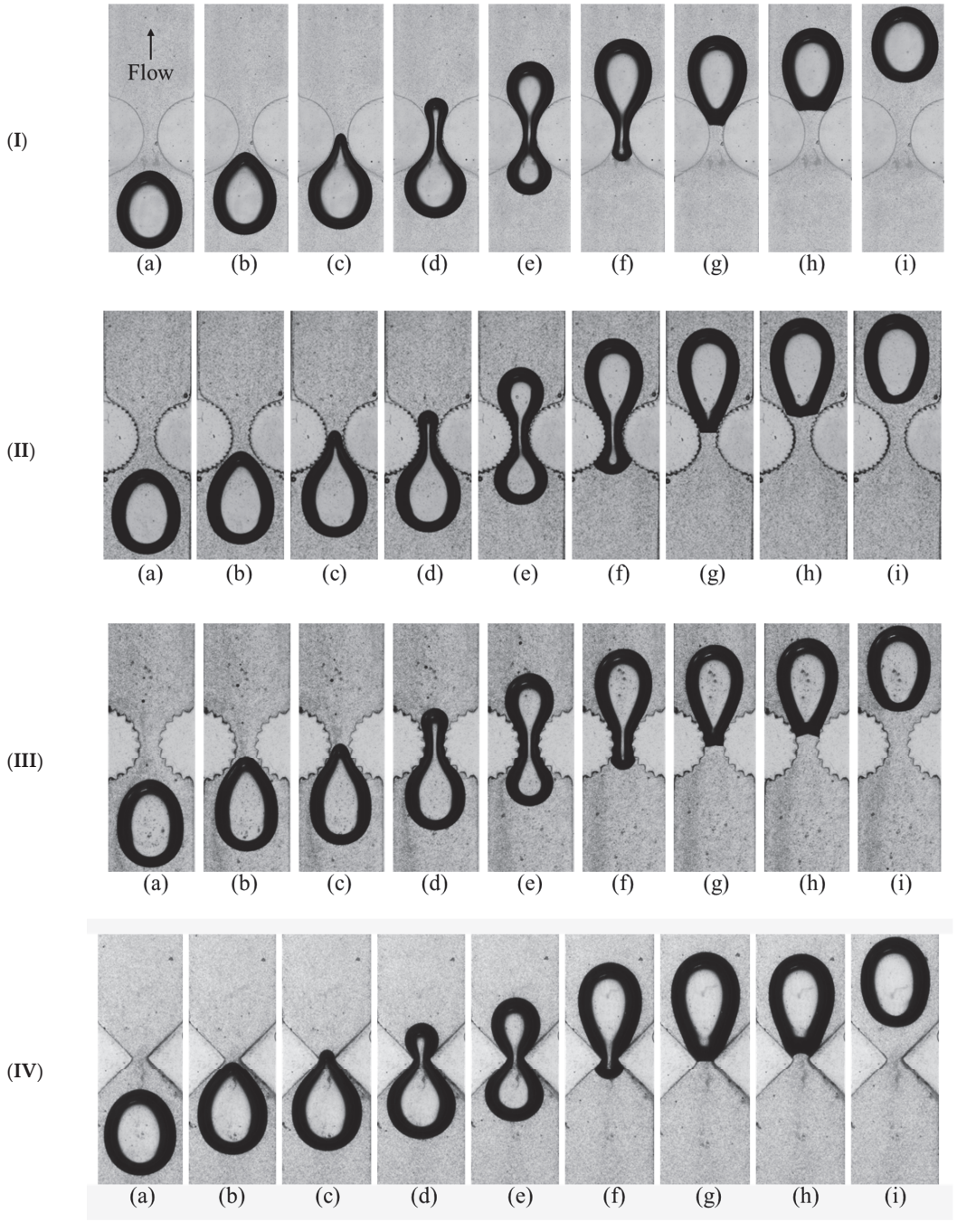

Figure 6. Bubble passing through (**I**) circular pore (**II**) circular pore with 0.2 mm surface roughness, (**III**) circular pore with 0.4 mm surface roughness, and (**IV**) pore with a sharp corner.

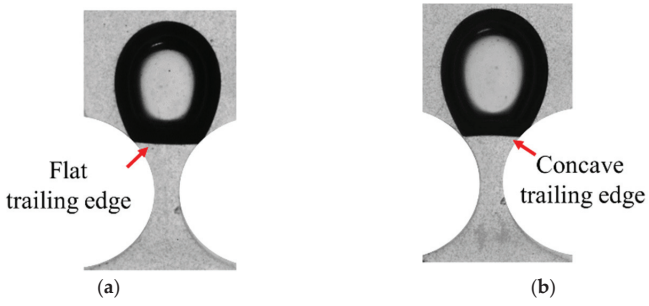

Figure 7. Pinning of a bubble existing a smooth pore interface at (**a**) 0.1 mL/min and (**b**) 0.3 mL/min.

For the case of the flow in the sharp pore geometry shown in Figure 6IV, the bubble has a smooth transition in the pore geometry. Due to the lower gradient of the change in the available cross-sectional area of the pore geometry, the curvature of the leading and trailing edges has more variation. The bubble has the same trend of change in the leading and trailing edge. Pinning of the phase was observed after the bubble passes the pore throat as shown in location (g) of Figure 6IV.

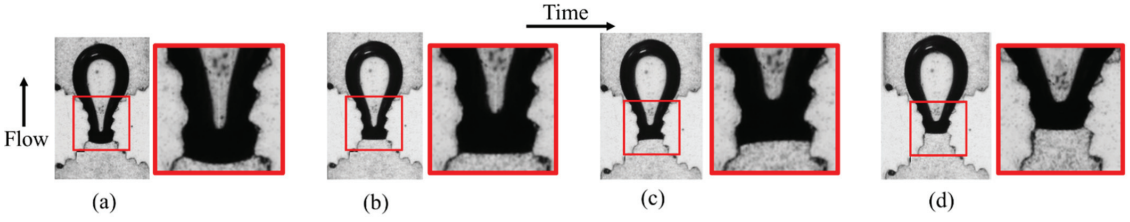

Figure 8. Phase pinning of a bubble. (R_b~1.95 mm) at different stages passing through a rough pore space having (**a**) convex, (**b**) flat, (**c**) concave, and (**d**) flat trailing edge.

4.2. Change in the Bubble's Pressure and Velocity While Passing through Smooth Circular Pore

The instantaneous change of the absolute value of the radius of curvature of the leading and trailing edges of a bubble passing through a circular pore (geometry shown in Figure 4a) is represented in Figure 9a. The location of the bubble, symbolized by y^*, is the normalized location of the centroid of the projected area (y_c) along the pore geometry by the width of the channel (w). The location was also offset by the pore throat (y_p) so the location $y^* = 0$ represents the condition when the bubbles centroid is aligned with the pore throat.

As indicated in Figure 9a the bubble has the same radius of curvature of the leading and trailing edge before it enters the pore geometry ($y^* < -4$). This condition is also shown in location (a) of Figure 6I. As the bubble enters the pore, indicated in location (b) in Figure 6I, the bubbles leading edge decreases due to the decrease in the available cross-sectional area. The minimum radius occurs at $y^* \sim -3$ where the leading edge is aligned with the pore throat. The deformation of the leading edge continues until location (g) of Figure 6I when the bubbles leading edge passes through the pore geometry, and it regains its original radius of curvature for $y^* > 4$.

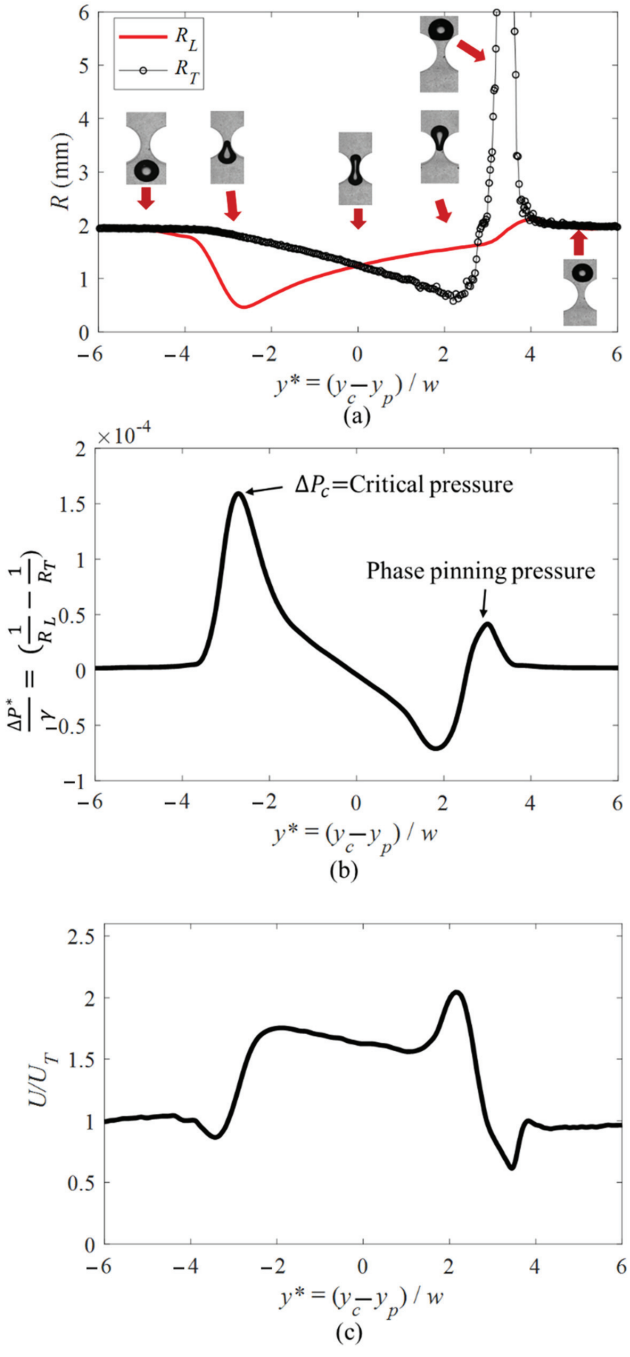

Figure 9. Plots of (**a**) change in the radii of curvature of leading and trailing edge of a bubble, (**b**) pressure along the bubble, and (**c**) velocity of the centroid of the projected area of a bubble (R_b ~1.95 mm) passing through a smooth circular pore surface. (Sample images of different conditions are shown in Figure 6I).

It can be seen that the deformation of the bubble's trailing face occurs further into the pore ($y^* \sim -3$) compared to the leading edge. The bubbles trailing edge reaches its minimum value as it aligns with the pore throat ($y^* \sim 2.5$). At $y^* \sim 3.5$ the radius increases to infinity and decreases to a constant value. The increase in the radius is caused by the pinning of the bubbles trailing edge before it exits the pore. In this condition, the bubbles trailing edge becomes flat and again regains its convex shape. After $y^* > 5$, the bubble detaches from the surface, and its radius of curvature of leading and trailing edge becomes equivalent.

The change in the pressure of the bubble at different locations along the pore was determined by the change in the radius of curvature shown in Figure 9a and Equation (1). The pressure is plotted as the ratio of the pressure and the interfacial tension that shows the pressure drop is only function of radii of the change in the trailing and the leading edge. In this study the $\frac{\Delta P^*}{\gamma_{cd}}$ has the unit of mm^{-1}. As shown in Figure 9b, the pressure across the bubble was similar at the entrance and exit when the bubble is well away from the pore. As it enters the pore, the pressure across the bubble increases to a maximum value at ($y^* \sim -3$). This positive pressure is known as the critical pressure required for the bubble to enter the pore. This pressure is highly affected by the relative size of the dispersed phase and pore geometry, flow rate, and interfacial tension of the phases. In the current study, the bubble can pass this region in the pore as the driving force of the carrying fluid overcomes the introduced pressure and the phase can deform further to pass the pore geometry.

As the bubble passes the stages corresponding to the critical pressure, the pressure drop across the bubble decreases and it reaches a minimum value. This negative value of the pressure represents the direction of the pressure gradient across the bubble and corresponds to the high velocity observed when the bubble passes through the pore throat. The pinning of the phase at the exit of the pore results in another positive pressure. The introduced pressure due to the pinning of the bubble, in this case, is lower than the critical pressure at the entrance. The driving force also can again overcome this pressure and the bubble can exit the pore geometry.

The change in the pressure across the bubble results in a variation in the velocity of the of the projected area of the bubble (U) as depicted in Figure 9c. The bubble reaches the pore geometry with a constant velocity corresponding to its terminal velocity (U_T). A slight decrease in the velocity is detected as the bubble gets closer to the pore geometry. The deceleration is caused by the development of the critical pressure needed to deform the bubble, allowing it to enter the pore. As the bubble passes this location it accelerates as it enters the pore throat. The introduced pinning pressure will result in a decrease of the velocity at the exit of the pore. The bubble accelerates as it detaches from the surface of the pore, returning to its terminal velocity.

4.3. Change in the Bubble's Pressure and Velocity while Passing through Circular Pore with 0.2 mm Roughness

The variation in the radius of curvature, pressure, and velocity of a bubble passing through a circular pore with 0.2 mm roughness are shown in Figure 10. The leading edge experiences the same deformation as discussed for the smooth circular pore. The trailing edge, however, has a different set of deformation characteristics as the bubble's centroid passes through the pore throat ($y^* > 0$). The interaction of the moving interface of the bubble and the peak of the solid interface leads to pinning of the phase at different locations after the pore throat. The bubble interface shape changes at each peak of the pore roughness which results in an increase in the radius of curvature. These conditions are represented by the peaks detected in Figure 10a.

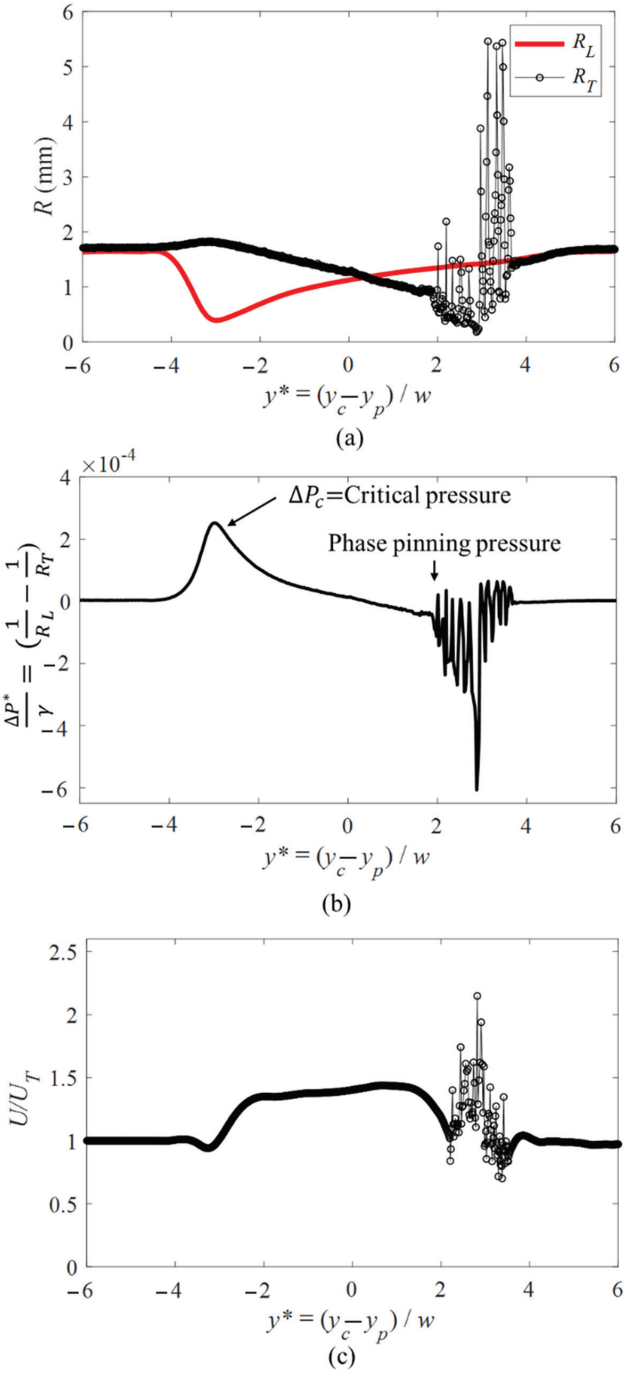

Figure 10. Plots of (**a**) change in the radii of curvature of leading and trailing edge of a bubble, (**b**) pressure along the bubble, and (**c**) velocity of the centroid of a bubble (R_b ~1.95 mm) passing through a circular pore with 0.2 mm roughness on the surface (Sample images of different conditions are shown in Figure 6II).

The effect of pinning of the phase in this pore geometry on the instantaneous change in the pressure of the bubble at different locations is shown in Figure 10b. The overall trend of the change in the pressure is similar to the circular pore discussed in the previous section. A similar critical pressure is detected in this case as shown for the smooth surface pore. The phase pinning of the bubble trailing edge at different locations along the pore results in multiple positive pressure peaks as the bubble passes the pore throat.

The velocity of the of the projected area of the bubble passing through the rough pore is shown in Figure 10c. The velocity of the bubble is constant before it reaches the pore and as it enters the pore, the bubble accelerates due to the decrease in the available area. The bubble decelerates as its centroid passes the pore throat as the area available for the flow increases. At each pinning location, there is an acceleration and deceleration of the bubble. In these locations, the bubble decelerates as the pinning occurs and it accelerates as it detaches from the surface. The acceleration occurs due to the instability between the roughness peaks which results in a rapid motion of the trailing edge toward the next peak of the surface roughness. These phenomena can be seen for all cases of pinning and motion of the bubble as it exits the pore.

4.4. Change in the Bubble's Pressure and Velocity While Passing through Circular Pore with 0.4 mm Roughness

The effect of the pore roughness identified by the change in the radius of curvature of a bubble passing through a circular pore with 0.4 mm roughness is shown in Figure 11a. A similar trend of the change in the radius of curvature detected for the case of 0.2 mm roughness. The number of the detected peaks of the change in curvature is lower due to the lower number of the pore roughness objects. The variation of the radius is higher due to the stronger interaction of the bubble and solid interface. The bubble interface shape changes from convex to concave which results in discontinuities in the instantaneous change of the radius of curvature.

For clarity of the discussion, the details of the stages of the change in the curvature highlighted by the blue box in Figure 11a, are represented in Figure 12a. The bubble passes through the different stages of deformation and these stages are numbered and displayed in Figure 12b. The bubble has a convex trailing interface before the pinning of the phase. There is a slight increase in curvature of the trailing edge at location (1). This is due to the pinning of the bubble that occurs at this condition leading to a higher curvature for the bubble's interface. As the bubble moves further into the pore, the bubble moves to the next peak of the pore roughness. The smaller cross-sectional area available for the bubble's trailing edge in location (2) leads to a decrease in curvature of the bubble which can be seen by the local minimum at $y^* \sim 1.9$. The bubbles interface becomes a flat surface at location (3) which leads to $R_T \to \infty$ at location $y^* \sim 2.25$ in Figures 11a and 12a. The driving force of the continuous phase moves the bubble forward leading to the change in curvature of the bubble to be concave as shown in location (4). This phenomenon can be also observed at different locations along the pore geometry as shown in locations (6), (8), (10) and (12).

The effect of pinning of the phase in this pore geometry on the instantaneous change in the pressure of the bubble at different locations is shown in Figure 11b. The overall trend of the change in the pressure is similar to the circular pore discussed in the previous section. A similar critical pressure is detected in this case as shown for the smooth surface as the bubble enters the pore. The phase pinning pressure, however, is different in this condition due to the multiple locations of pinning in the flow passage. The pressure of the pinning occurs at different locations as the bubble passes the pore throat resulting in a region with a variation in the pressure drop. At the location where the pinning occurs, a series of peaks are detected. The lowest pressure difference across the bubble occurs when the bubble has the smallest value of curvature of the trailing edge at location (6) and the largest pressure is detected for the location of phase pinning at the pore throat having the smallest negative curvature of the bubble at location (8) as shown in Figure 12a.

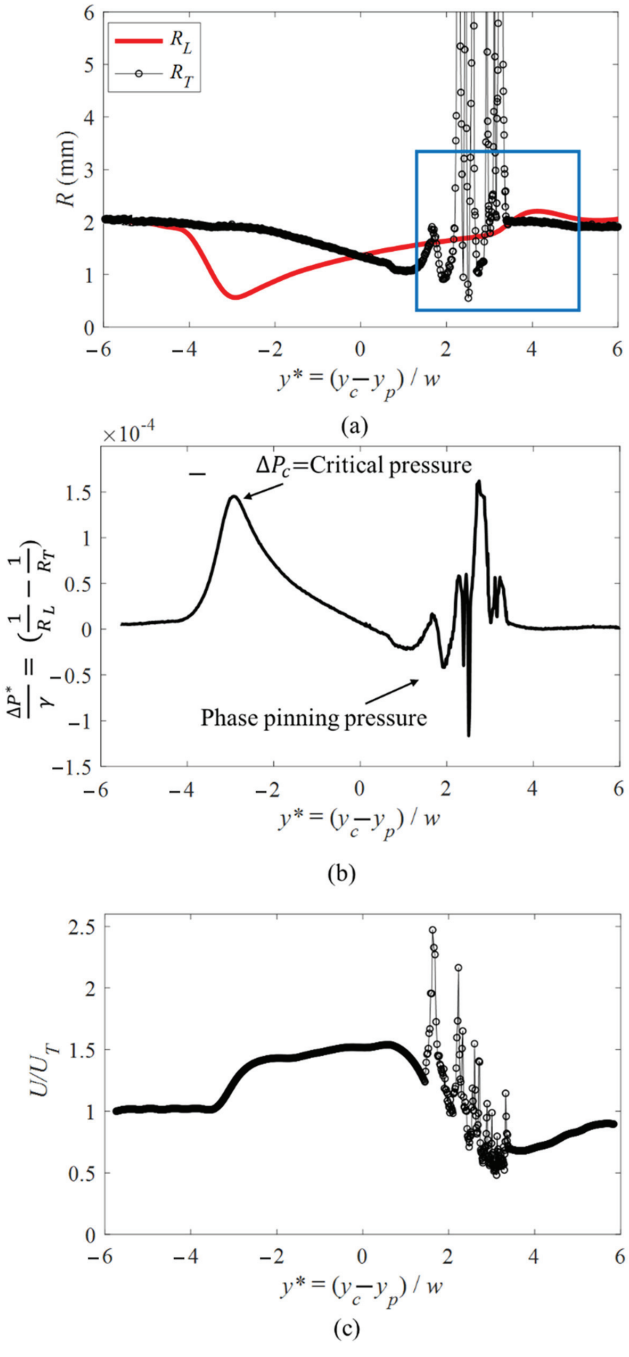

Figure 11. Plots of (**a**) change in the radii of curvature of leading and trailing edge of a bubble, (**b**) pressure along the bubble, and (**c**) velocity of the of the projected area of a bubble (R_b ~1.95 mm) passing through a circular pore with 0.4 mm roughness on the surface (Sample images of different conditions are shown in Figure 6III).

The effect of the phase pinning on the velocity the projected area of a bubble passing through the rough pore can be seen in Figure 11c. As shown in the case of 0.2 mm of roughness, at each pinning location, there is an acceleration and deceleration of the bubble. In these locations, the bubble decelerates as the pinning occurs and it accelerates as it detaches from the surface. The number of the peaks in this case (0.4 mm) is less than the smaller roughness (0.2 mm) due to a lower number of peaks along the pore interface. The velocity of the bubble increases to 1.5 of its terminal velocity for both cases of the pore roughness (0.2 and 0.4 mm). The increase in the velocity of the bubble at each peak of the surface roughness is higher for the case of 0.4 mm. This is due to the stronger phase pinning phenomena at these locations. These phenomena can be seen for all cases of the pinning and the motion of the bubble as it passes through the pore.

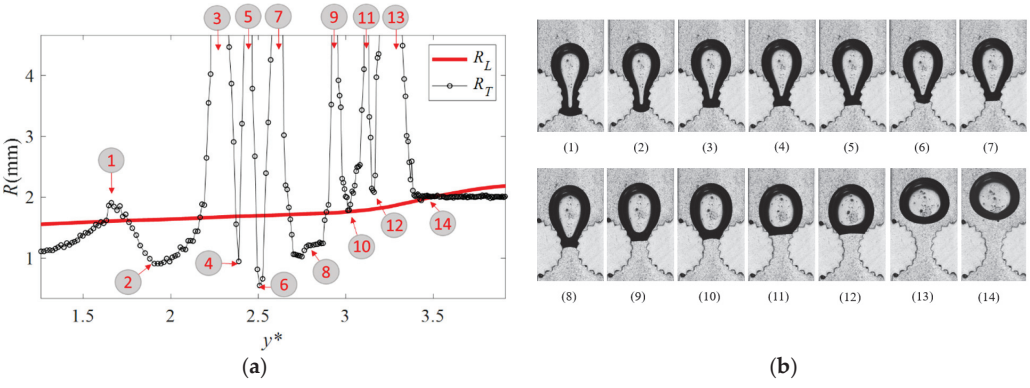

(**a**) (**b**)

Figure 12. (**a**) zoomed-in condition represented in Figure 10a and (**b**) stages of bubble pinning in a pore.

4.5. Change in the Bubble's Pressure and Velocity While Passing through a Sharp Pore

The variation in the radius of curvature of the leading and trailing edge of a bubble passing through a sharp pore is shown in Figure 13. The bubbles leading, and trailing edge have a similar trend as observed for the bubble flow in a circular pore. Only one phase pinning location can be observed as the bubble passes through the sharp geometry. Comparing the location of the pinning of the bubble in this case and the smooth round pore, shown in Figures 12a and 13a, the pinning in the case of the sharp pore occurs further into the pore (y^* ~ 4 for circular pore and y^* ~ 3 for the sharp pore). This is due to the difference in the structure of the pore throat. In a sharp pore, the bubble detaches from the solid geometry right after it passes through the pore throat. For the case of the circular pore, however, the bubble is in contact with the pore further in the axial direction due to the gradual change in the pore geometry.

The critical pressure and the pinning pressure of the sharp pore can also be seen in the peaks shown in Figure 13b. The phase pinning pressure in this condition is slightly larger than the one detected for a circular pore. This is because the pinning in the sharp pore occurs closer to the pore throat where the available cross-sectional area is smaller compared to the phase pinning locations of other pore structures. The smaller gap between the pore results in more deformation and a higher-pressure gradient. The effect of the change in the pressure on the velocity is shown in Figure 13c. A lower acceleration is observed in this case due to the difference in the available cross-sectional area at different locations along the pore.

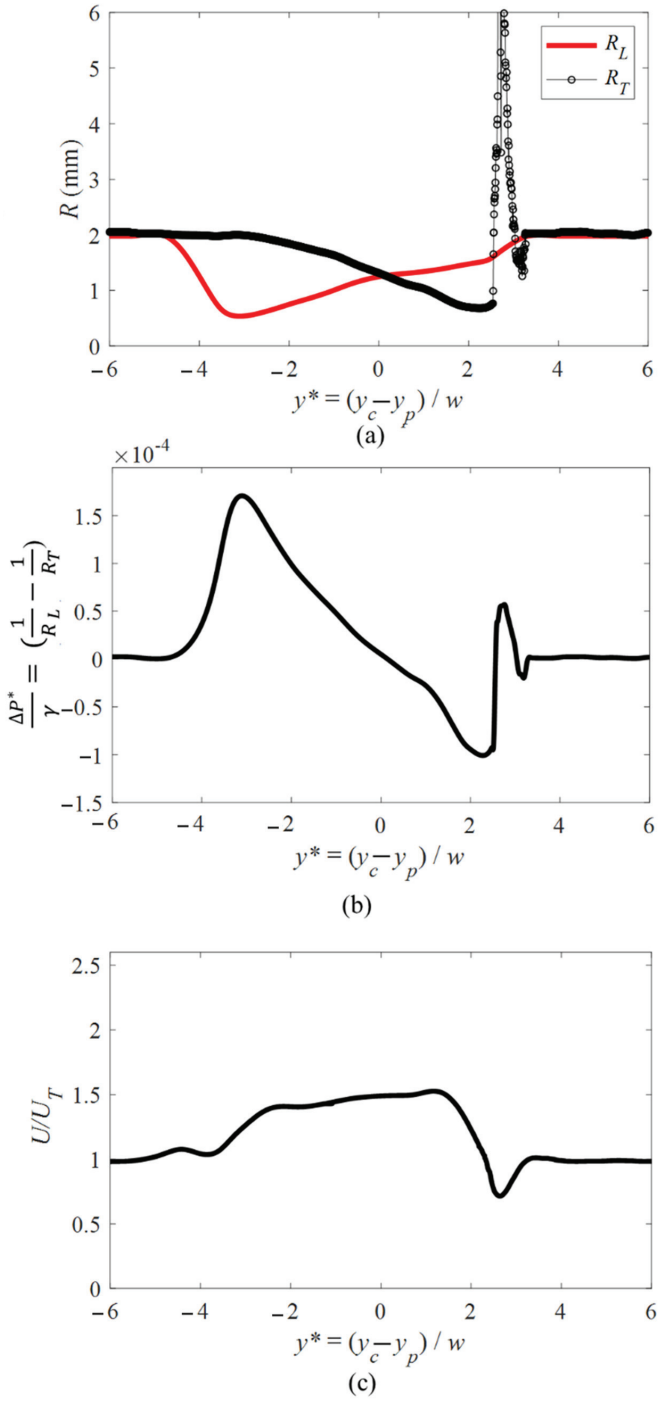

Figure 13. Plots of (**a**) change in the radii of curvature of leading and trailing edge of a bubble, (**b**) pressure along the bubble, and (**c**) velocity of the projected area of a bubble (R_b ~1.95 mm) passing through a sharp pore (Sample images of different conditions are shown in Figure 6IV).

4.6. Bubble's Transit Time in Different Pore Geometries

The variation of the transit time required for bubbles of different sizes passing through different pore geometries is represented in Figure 14. The transit time in this study is the measured time required for the bubble leading edge to enter the pore structure and the trailing edge to exit the pore structure determined from image analysis obtained using the optical setup. The overall trend of the change in the transit time at the same flow rate in the confined geometry is represented by the fitted line for each collected data set.

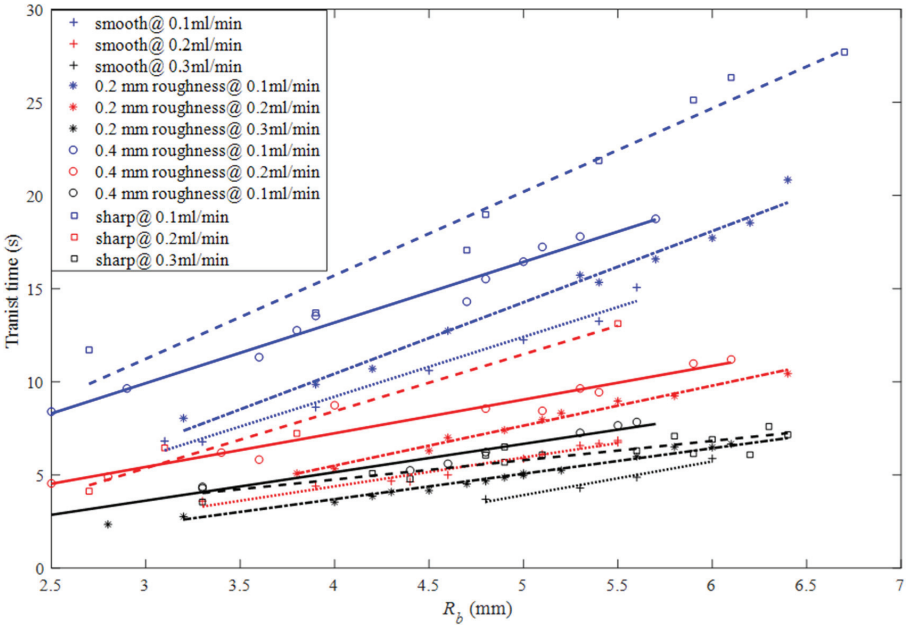

Figure 14. Plots of change in the transit time of bubble at different flow rates, size, and pore geometry.The flowrates are color-coded where black, red and blue corresponds to 0.1, 0.2 and 0.3 mm/min, respectively.

For all conditions, the bubble's transit time increases linearly as the size of the bubble increases. This is due to the higher Volume of the larger bubbles which results in lower mobility of the bubble in the pore geometry. From the figure, the highest transit time corresponds to the motion of a bubble carried with a lower flow rate of the continuous phase. The lower flow rate provides a lower driving force for the bubble passage which leads to a slower bubble motion in the pore geometry.

Figure 14 also shows that there is a significant difference between the transit times of bubbles moving through different geometries. The transit time for the bubble flow in the sharp pore is mostly the highest among the tested pore geometries. The higher required time for the bubble passage through pore space in this condition is due to the difference between the decreases in the available cross-sectional area to the flow. In the sharp pore, the available cross-sectional area decreases at a smaller rate compared to the round pore. The higher available cross-sectional area for the flow for each stage along the pore results in lower acceleration of the bubble and slower motion of the phase in this geometry. The lower acceleration of the bubble's velocity in the sharp pore can be observed by comparing the velocities reported in Figures 9 and 13.

At the same flow rate, the lowest transit time occurs in the case of a bubble flow in the smooth circular surface. This condition occurs since the only resistance, in this case, arises due to the critical pressure at the entrance and the phase pinning at the exit of the pore

geometry. The transit time increases as the roughness on the wall of the pore geometry increases. The increase in the transit time is due to the multiple phase pinning events that occur for the bubble passage after the pore throat. For the case of a bubble flow in the smooth circular pore, as shown in Figure 9, the bubble only pins on the exit of the channel and the reduction in the velocity occurs only in this location. For the bubble passing through the 0.4 mm roughness pore the pinning is a more severe result in the change in the direction of the curvature (concave to convex and vice versa). The change in the trailing interface results in more delay in the motion of the bubble.

5. Conclusions

The main goal of the current study was to determine the effect of pore geometry on the motion and mobilization of an isolated bubble passing through a pore. The effect of the pore structure was studied by the tracking of bubble deformation, pressure, the velocity of the of the projected area, and the required transit time for the phase passage. Four different pore geometries of a circular with a smooth surface, circular with 0.2 mm and 0.4 mm roughness, and a sharp pore were considered for this study. The evidence from this study suggests that the motion of the bubble passing through a pore space is highly affected by the geometry of the pore solid interface.

Investigation of the deformation of the bubble has shown that the different pore structures considered in this study all have a similar effect on the leading edge. However, significant differences were observed for the deformation of the bubble's trailing edge. For the smooth circular pore structure and sharp pore, only one phase pinning event was observed before the bubble detached from the pore surface. For a bubble passing through a rough pore, the bubble has many pinning events for each peak of the roughness after the pore throat. The number of pinning events increases by the number of roughness structures on the pore surface. The strength of the interaction also increases by the height of each peak of the pore roughness.

The results of the pressure change across the bubble showed that in addition to the critical pressure introduced by the entrance of the pore, a phase pinning pressure is also introduced during the phase passage in the pore. For all cases, a similar critical pressure at the entrance was observed. The pinning pressure was highly affected by the properties of the pore structure. The change in the pressure due to phase pinning was observed with a higher number of peaks and a wider range of pressure effects for pores having a rough surface structure. The applied pinning pressure at each pore roughness resulted in the positive pressure difference along the bubble and ultimately, deceleration of the phase motion.

This study has found that generally, the transit time of the bubble through the pore structure increases with an increase in the pore surface roughness and the size of the dispersed phase. A shorter transit time was observed for the case of the smooth pore due to the minor effect of the phase pinning at the exit of the pore. Phase pinning in the rough structures leads to the delayed passage of the bubble in these pore geometries.

This research extends our knowledge of the pore-scale interactions of pore structure and multi-phase flow on the mobilization of the pore. The values obtained for the pressure in this study is unique due to the presence of the confined walls of the flow channel. The results of the trend of the change in the pressure in this research support the bulk flow studies that a higher driving force is required for the mobilization of a trapped phase in a rough and unstructured pore geometries. The findings from this study suggest that the critical pressure for mobilization of trapped isolated phase in a pore geometry can be predicted by the study of the motion of an individual isolated phase. The current study was also able to detect the phase pinning introduced pressure which results in the delayed passage of multi-phase flows in the pore structure.

Author Contributions: Conceptualization, S.A. and D.S.N.; methodology, S.A.; software, S.A.; validation, S.A. and D.S.N.; formal analysis, S.A. and D.S.N.; investigation, S.A.; resources, S.A.; data curation, S.A.; writing—original draft preparation, S.A.; writing—review and editing, S.A. and D.S.N.; visualization, S.A.; supervision, S.A. and D.S.N.; project administration, D.S.N.; funding acquisition, D.S.N. All authors have read and agreed to the published version of the manuscript.

Funding: This research was funded from Natural Sciences and Engineering Research Council (NSERC) of Canada, the Alberta Innovates and the Canadian Foundation for Innovation (CFI).

Institutional Review Board Statement: Not applicable.

Informed Consent Statement: Not applicable.

Data Availability Statement: The data presented in this study are available on request from the corresponding author.

Conflicts of Interest: The authors declare no conflict of interest.

References

1. Huang, J.S.; Varadaraj, R. Colloid and interface science in the oil industry. *Curr. Opin. Colloid Interface Sci.* **1996**, *1*, 535–539. [CrossRef]
2. Soottitantawat, A.; Bigeard, F.; Yoshii, H.; Furuta, T.; Ohkawara, M.; Linko, P. Influence of emulsion and powder size on the stability of encapsulated D-limonene by spray drying. *Innov. Food Sci. Emerg. Technol.* **2005**, *6*, 107–114. [CrossRef]
3. Nakano, M. Places of emulsions in drug delivery. *Adv. Drug Deliv. Rev.* **2000**, *45*, 1–4. [CrossRef]
4. Chatzis, I.; Morrow, N.R.; Lim, H.T. Magnitude and Detailed Structure of Residual Oil Saturation. *Soc. Pet. Eng. J.* **1983**, *23*, 311–326. [CrossRef]
5. Geistlinger, H.; Zulfiqar, B. The Impact of Wettability and Surface Roughness on Fluid Displacement and Capillary Trapping in 2-D and 3-D Porous Media: 1. Wettability-Controlled Phase Transition of Trapping Efficiency in Glass Beads Packs. *Water Resour. Res.* **2020**, *56*, e2019WR026826. [CrossRef]
6. Geistlinger, H.; Ataei-Dadavi, I.; Mohammadian, S.; Vogel, H.J. The impact of pore structure and surface roughness on capillary trapping for 2-D and 3-D porous media: Comparison with percolation theory. *Water Resour. Res.* **2015**, *51*, 9094–9111. [CrossRef]
7. Johnson, P.C.; Johnson, R.L.; Bruce, C.L.; Leeson, A. Advances in in situ air sparging/biosparging. *Bioremediat. J.* **2001**, *5*, 251–266. [CrossRef]
8. Mohammadian, S.; Geistlinger, H.; Vogel, H.J. Quantification of Gas-Phase Trapping within the Capillary Fringe Using Computed Microtomography. *Vadose Zone J.* **2015**, *14*, 1–9. [CrossRef]
9. Wildenschild, D.; Sheppard, A.P. X-ray imaging and analysis techniques for quantifying pore-scale structure and processes in subsurface porous medium systems. *Adv. Water Resour.* **2013**, *51*, 217–246. [CrossRef]
10. Anbari, A.; Chien, H.T.; Datta, S.S.; Deng, W.; Weitz, D.A.; Fan, J. Microfluidic Model Porous Media: Fabrication and Applications. *Small* **2018**, *14*, 1703575. [CrossRef]
11. Zhang, Z.; Li, L.; Xie, W.; Wang, H. Experimental study of bubble formation process on the micro-orifice in mini channels. *Exp. Therm. Fluid Sci.* **2020**, *117*, 110144. [CrossRef]
12. Hu, R.; Lan, T.; Wei, G.J.; Chen, Y.F. Phase diagram of quasi-static immiscible displacement in disordered porous media. *J. Fluid Mech.* **2019**, *875*, 448–475. [CrossRef]
13. Cha, L.; Xie, C.; Feng, Q.; Balhoff, M. Geometric criteria for the snap-off of a non-wetting droplet in pore-throat channels with rectangular cross-sections. *Water Resour. Res.* **2021**, *57*, e2020WR029476. [CrossRef]
14. Zou, A. Effects of Grain-Size Distribution and Hysteresis on Soil-Water Characteristic Curve (SWCC). Ph.D. Thesis, Nanyang Technological University, Singapore, 2018.
15. Chen, H.; Yang, M.; Chen, K.; Zhang, C. Relative Permeability of Porous Media with Nonuniform Pores. *Geofluids* **2020**, *2020*, 5705424. [CrossRef]
16. Molnar, I.L.; Gerhard, J.I.; Willson, C.S.; O'Carroll, D.M. Wettability Effects on Primary Drainage Mechanisms and NAPL Distribution: A Pore-Scale Study. *Water Resour. Res.* **2020**, *56*, e2019WR025381. [CrossRef]
17. Mehmani, A.; Kelly, S.; Torres-Verdín, C.; Balhoff, M. Capillary Trapping Following Imbibition in Porous Media: Microfluidic Quantification of the Impact of Pore-Scale Surface Roughness. *Water Resour. Res.* **2019**, *55*, 9905–9925. [CrossRef]
18. Qiao, Z.; Wang, Z.; Zhang, C.; Yuan, S.; Zhu, Y.; Wang, J. PVAm–PIP/PS composite membrane with high performance for CO_2/N_2 separation. *AIChE J.* **2012**, *59*, 215–228. [CrossRef]
19. Jiang, H.; Guo, B.; Brusseau, M.L. Characterization of the micro-scale surface roughness effect on immiscible fluids and interfacial areas in porous media using the measurements of interfacial partitioning tracer tests. *Adv. Water Resour.* **2020**, *146*, 103789. [CrossRef]
20. Khishvand, M.; Akbarabadi, M.; Piri, M. Micro-scale experimental investigation of the effect of flow rate on trapping in sandstone and carbonate rock samples. *Adv. Water Resour.* **2016**, *94*, 379–399. [CrossRef]

21. Askari, R.; Taheri, S.; Hejazi, S.H. Thermal conductivity of granular porous media: A pore scale modeling approach. *AIP Adv.* **2015**, *5*, 097106. [CrossRef]
22. Yu, L.; Sang, Q.; Dong, M.; Yuan, Y. Effects of interfacial tension and droplet size on the plugging performance of oil-in-water emulsions in porous media. *Ind. Eng. Chem. Res.* **2017**, *56*, 329237–329246. [CrossRef]
23. Ansari, S.; Sabbagh, R.; Yusuf, Y.; Nobes, D.S. The role of emulsions in steam-assisted-gravity-drainage (SAGD) oil-production process: A review. *SPE J.* **2019**, *25*, 969–989. [CrossRef]
24. Amani, P.; Suzanne, H.; Victor, R.; Firouzi, M. Comparison of flow dynamics of air-water flows with foam flows in vertical pipes. *Exp. Therm. Fluid Sci.* **2020**, *119*, 110216. [CrossRef]
25. Ezeuko, C.; Wang, J.; Gates, I. Investigation of emulsion flow in SAGD and ES-SAGD. In Proceedings of the SPE Heavy Oil Conference, Calgary, AL, Canada, 12–14 June 2012; pp. 1–16.
26. Smith, W.O.; Crane, M.D. The Jamin effect in cylindrical tubes. *J. Am. Chem. Soc.* **1930**, *52*, 1345–1349. [CrossRef]
27. Seo, J.H.; Lele, S.K.; Tryggvason, G. Investigation, and modeling of bubble-bubble interaction effect in homogeneous bubbly flows. *Phys. Fluids* **2010**, *22*, 063302. [CrossRef]
28. Patel, T.; Patel, D.; Thakkar, N.; Lakdawala, A. A numerical study on bubble dynamics in sinusoidal channels. *Phys. Fluids* **2019**, *31*, 052103. [CrossRef]
29. Benet, E.; Vernerey, F.J. Mechanics and stability of vesicles and droplets in confined spaces. *Phys. Rev. E* **2016**, *94*, 062613. [CrossRef]
30. Kim, S.H.; Hyun, S.P.; Donggun, K.; Kim, M.H. Wetting characteristic of bubble on micro-pillar structured surface under a water pool. *Exp. Therm. Fluid Sci.* **2019**, *100*, 135–143. [CrossRef]
31. Vasiljevic, D.; Parojcic, J.; Primorac, M.; Vuleta, G. An investigation into the characteristics and drug release properties of multiple W/O/W emulsion systems containing low concentration of lipophilic polymeric emulsifier. *Int. J. Pharm.* **2006**, *309*, 171–177. [CrossRef]
32. Mittal, K.L. *Particles on Surfaces 1: Detection, Adhesion, and Removal*; Plenum Press: New York, NY, USA, 1988.
33. Ansari, S.; Yusuf, Y.; Sabbagh, R.; Soltani, H.; Kinsale, L.; Nobes, D.S. An imaging derivation of the pressure field of a multi-phase flow in a porous media using μ-SPIV. In Proceedings of the 19th International Symposium on the Application of Laser and Imaging Techniques to Fluid Mechanics, Lisbon, Portugal, 16–19 July 2018.
34. Gkotsis, P.K.; Evgenidis, S.P.; Karapantsios, T.D. Influence of Newtonian and non-Newtonian fluid behaviour on void fraction and bubble size for a gas-liquid flow of sub-millimeter bubbles at low void fractions. *Exp. Therm. Fluid Sci.* **2019**, *109*, 109912. [CrossRef]
35. Sattari, A.; Tasnim, N.; Hanafizadeh, P.; Hoorfar, M. Motion and deformation of migrating compound droplets in shear-thinning fluids in a microcapillary tube. *Phys. Fluids* **2021**, *33*, 053106. [CrossRef]
36. Tian, Z.; Youwei, C.; Xi, L.; Lijun, W. Bubble shape and rising velocity in viscous liquids at high temperature and pressure. *Exp. Therm. Fluid Sci.* **2019**, *102*, 528–538. [CrossRef]
37. Jamshidi, N.; Mostoufi, N. Investigating bubble dynamics in a bubble column containing shear thinning liquid using a dual-tip probe. *Exp. Therm. Fluid Sci.* **2018**, *94*, 34–48. [CrossRef]
38. Javadpour, F. Bubble breakup in porous media. *J. Can. Pet. Technol.* **2007**, *46*, 26–32. [CrossRef]
39. Azadi, R.; Nobes, D.S. On the three-dimensional features of a confined slug bubble in a flowing square capillary. *Phys. Fluids* **2021**, *33*, 033327. [CrossRef]
40. Ansari, S.; Nobes, D.S. Interaction of loosely packed bubbly flow passing through a pore space. *J. Vis.* **2020**, *23*, 649–660. [CrossRef]
41. Ansari, S.; Yusuf, Y.; Sabbagh, R.; Nobes, D.S. Determining the pressure distribution of a multi-phase flow through a pore space using velocity measurement and shape analysis. *Meas. Sci. Technol.* **2019**, *30*, 054004. [CrossRef]
42. Soltani, H.; Sabbagh, R.; Nobes, D.S. The passage of bubbles rising through a confining rectangular geometry. *Phys. Fluids* **2018**, *10*, 103302. [CrossRef]
43. Jin, B.J.; Kim, Y.W.; Lee, Y.; Yoo, J.Y. Droplet merging in a straight microchannel using droplet size or viscosity difference. *J. Micromech. Microeng.* **2010**, *20*, 035003. [CrossRef]
44. Wang, M.; Hung, Y.L.; Lin, F.H.; Lin, S.Y. Dynamic behaviors of droplet impact and spreading: A universal relationship study of dimensionless wetting diameter and droplet height. *Exp. Therm. Fluid Sci.* **2009**, *33*, 1112–1118. [CrossRef]
45. Sarioglu, A.F.; Aceto, N.; Kojic, N. A microfluidic device for label-free, physical capture of circulating tumor cell clusters. *Nat. Methods* **2015**, *12*, 685–691. [CrossRef]
46. Preira, P.; Grandne, V.; Forel, J.-M.; Gabriele, S.; Camara, M.; Theodoly, O. Passive circulating cell sorting by deformability using a microfluidic gradual filter. *Lab Chip* **2013**, *13*, 161–170. [CrossRef]
47. Mugele, F. On the shape of a droplet in a wedge: New insight from electrowetting. *Soft Matter* **2015**, *11*, 7717–7721.
48. Mohamed, H.; Murray, M.; Turner, J.N.; Caggana, M. Isolation of tumor cells using size and deformation. *J. Chromatogr. A* **2009**, *1216*, 8289–8295. [CrossRef]
49. Ansari, S.; Nobes, D.S. The effect of three-phase contact line pinning during the passage of an isolated bubble through a confining pore. *Phys. Fluids* **2021**, *33*, 053310. [CrossRef]
50. Benet, E.; Badran, A.; Pellegrino, J.; Vernerey, F. The porous media's effect on the permeation of elastic (soft) particles. *J. Membr. Sci.* **2017**, *535*, 10–19. [CrossRef]

51. Ansari, S.; Sabbagh, R.; Soltani, H.; Nobes, D.S. Flow visualization of a bubble penetration through porous media in SAGD process using μSPIV. In Proceedings of the 5th International Conference on Experimental Fluid Mechanics—ICEFM, Munich, Germany, 2–4 July 2018.
52. Jamin, M.J. Memoire sur l'equilibre et les mouvements de liquides dans corps poreux. *Compt. Rend. Acad. Sci.* **1860**, *50*, 172–176.
53. Ansari, S. Experimental Study of the Geometric Characteristics of Bubbles/Droplets Passing through a Pore Space. Ph.D. Thesis, University of Alberta, Edmonton, AL, Canada, 2021.
54. Raffel, J.; Ansari, S.; Nobes, D.S. An Experimental Investigation of Flow Phenomena in a Multistage Micro-Tesla Valve. *J. Fluids Eng.* **2021**, *11*, 111205. [CrossRef]
55. Ansari, S. Newtonian and Non-Newtonian Flows through Mini-Channels and Micro-Scale Orifices for SAGD Applications. Master's Thesis, University of Alberta, Edmonton, AL, Canada, 2016.
56. Ansari, S.; Rashid, M.A.I.; Waghmare, P.R.; Ma, Y.; Nobes, D. Newtonian, and non-Newtonian flows through micro scale orifices. In Proceedings of the 10th Pacific Symposium on Flow Visualization and Image Processing, Naples, Italy, 15–18 June 2015.
57. Sahasrabudhe, S.N.; Rodriguez-Martinez, V.; O'Meara, M.; Farkas, B.E. Density, viscosity, and surface tension of five vegetable oils at elevated temperatures: Measurement and modeling. *Int. J. Food Prop.* **2017**, *20*, 1965–1981. [CrossRef]
58. Segur, J.B.; Oderstar, H.E. Viscosity of glycerol and its aqueous solutions. *Ind. Eng. Chem.* **1951**, *43*, 2117–2120. [CrossRef]
59. Azadi, R.; Wong, J.; Nobes, D.S. Experimental and analytical investigation of meso-scale slug bubble dynamics in a square capillary channel. *Phys. Fluids* **2020**, *32*, 083304. [CrossRef]

fluids

MDPI

Article

CFD Investigation into the Effects of Surrounding Particle Location on the Drag Coefficient

David Dodds [1], Abd Alhamid R. Sarhan [1,2] and Jamal Naser [1,*]

[1] Department of Mechanical and Product Design Engineering, Swinburne University of Technology, Hawthorn, VIC 3122, Australia
[2] Department of Biomedical Engineering, The University of Melbourne, Carlton, VIC 3010, Australia
* Correspondence: jnaser@swin.edu.au

Abstract: In the simulation of dilute gas-solid flows such as those seen in many industrial applications, the Lagrangian Particle Tracking method is used to track packets of individual particles through a converged fluid field. In the tracking of these particles, the most dominant forces acting upon the particles are those of gravity and drag. In order to accurately predict particle motion, the determination of the aforementioned forces become of the upmost importance, and hence an improved drag force formula was developed to incorporate the effects of particle concentration and particle Reynolds number. The present CFD study examines the individual effects of particles located both perpendicular and parallel to the flow direction, as well as the effect of a particle entrain within an infinite matrix of evenly distributed particles. Results show that neighbouring particles perpendicular to the flow (Model 2) have an effect of increasing the drag force at close separation distances, but this becomes negligible between 5–10 particle diameters depending on particle Reynolds number (Re_p). When entrained in an infinite line of particles co-aligned with the flow (Model 1), the drag force is remarkably reduced at close separation distances and increases as the distance increases. The results of the infinite matrix of particles (Model 3) show that, although not apparent in the individual model, the effect of side particles is experienced many particle diameters downstream.

Keywords: CFD modelling; drag force; solid concentration; particle Reynolds number; gas-solid flow

Citation: Dodds, D.; Sarhan, A.A.R.; Naser, J. CFD Investigation into the Effects of Surrounding Particle Location on the Drag Coefficient. *Fluids* **2022**, *7*, 331. https://doi.org/10.3390/fluids7100331

Academic Editor: Mehrdad Massoudi

Received: 10 September 2022
Accepted: 13 October 2022
Published: 17 October 2022

1. Introduction

Dilute gas-solid flows are of considerable importance in many technical and industrial processes to efficiently transport solid particles that have a wide range of sizes (few μm to few mm) and density [1,2]. The application includes, but not limited to pneumatic conveying, fluidised beds, vertical risers, classifiers, cyclones, and flow mixing devices [3,4]. Pneumatic conveying, due to its many advantages such as simplicity and flexibility in operation, environmental compliance, and inherent safety, is widely used in the chemical, food processing, and cement industries and also in order to transport pulverised coal in thermal power plants [5]. This wide application has led to extensive research on pneumatic conveying of solids through the different pipe elements [6,7]. Despite its wide application, the design of the pipe network for pneumatic conveying is still a challenge because ostensibly small changes in the system or product frequently cause significant changes in the system performance or design [8]. Furthermore, during the flowing, these fine particles have not only the interactions with gas phase but also the collisions with each other and the wall of the pipes [9,10]. Therefore, the flow phenomena of gas–solid two-phase flows are very complex. Computational Fluid Dynamics (CFD) is usually used for modelling the flow in these systems for a number reasons ranging from the design stage to monitoring flows where experimental measurements are unavailable.

The CFD modelling relies heavily on a strong knowledge base of the fluid flow under consideration, and as such, the behaviour of particle motion is of the utmost importance

when trying to simulate gas particle flows [11]. Over the years, many researchers have looked into the CFD modelling of gas-particle flows and the degree of accuracy has greatly improved with advances in turbulence modelling and computing power [12–14]. In many applications, the importance of the drag force in accurately predicting particle motion cannot be understated [15,16]. When looking at gas driven flows, the drag force is responsible for the acceleration of the particles. In CFD simulations, especially using the Lagrangian framework [17], the most common approach to determine the drag force on a particle is using the standard drag coefficient curve, which is based on experimental studies of a sphere in unbounded fluid flow. The most commonly accepted approximation of this curve is given by the following equation [18]:

$$C_D = \frac{24}{\mathrm{Re}}\left(1 + 0.15\mathrm{Re}^{0.687}\right) \mathrm{Re} < 1000 \quad (1)$$

As it can be seen, the above equation is solely a function of the local particle Reynolds number, and as such, discounts other effects that may affect the drag on a particle. In a situation whereby particles are relatively spread out, this assumption can be correctly employed to accurately predict particle motion, but in many industrial flows, it is impossible to assume that the distribution will be such that particles will not interact and in turn will affect each other's motion.

A number of researchers have tried to measure the influence on the drag force of a particle in the presence of other particles. Liang, Hong and Fan [19] proved that altering the position of surrounding particles experienced drastic changes in drag coefficient. A configuration of three-coaligned particles led to a reduction of drag experienced by the centre particle compared with that of the leading particle at a separation distance of 2–3 d_p. Cheng and Papanicolaou [20] calculated the analytical force on an array of particles at low Reynolds numbers and volume fraction. The analytical results showed good comparison with the phenomenological results available at the time of this work. Kim, Elghobashi and Sirignano [21] solved the full Navier–Stokes equations for spherical particle motion at a range of Reynolds numbers and particle-to-fluid density ratios. The full Navier–Stokes solution showed considerable differences to some of the more commonly used particle motion formulas and resulted in the authors proposing their own new particle motion formula. Zhang and Fan [16] proposed a new semi analytical expression for the drag force of an interactive particle due to wake effect. This work was based on the experimental findings of Liang, Hong and Fan [19] looking at separation distances up to 7 particle diameters and particle Reynolds number ranging from 54–154. Zhang and Fan [22] used the above work as a basis to predict the rise of interactive bubbles in liquids. The work showed that the new drag model and the inclusion of both the added mass and basset force provided the best agreement with the available experimental data [23].

The work of Liang, Hong and Fan [19] looked at three particles co-aligned and at separation distances up to 7 particle diameters, which corresponds to a particle volume fraction of approximately 10^{-3}. In order to extend this work to investigate the effects at lower concentration values, 10^{-4}, which is common in many dilute phase industrial flows, a full CFD study of this work was undertaken. The aim of this study was to produce a new drag force relation that considered the influence of particle concentration as well as particle Reynolds number. The new relation needed to be a generic equation which relied on the particle concentration or particle volume fraction, α, because the Lagrangian particle tracking method tracks individual representative isolated particles without considering the position of surrounding particles. An assumption was made that because no particle position is actually known, the particles in any given cell are evenly distributed in a cubic formation, see Figure 1. Utilising this assumption, the volume fraction can be transformed into particles separated by a uniform distance in all directions.

$$\varepsilon = \frac{Volume\ of\ particles}{Volume\ of\ cell} = \frac{\frac{1}{6}\pi d^3}{L^3} = \frac{\pi d^3}{6L^3} = \frac{\pi d^3}{6\left(l/d\right)^3} = \frac{\pi}{6l^3} \quad (2)$$

where L is the distance between particle centres and l is the distance between particle centres as a ratio of particle diameter.

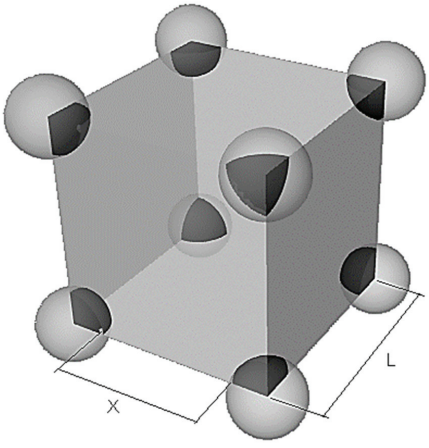

Figure 1. Uniform particle distribution.

2. Mathematical Models

This section covers the numerical methods used to solve the motion of both the continuous fluid and the dispersed particle motion. The continuous fluid phase is calculated by solving the governing equations. The dispersed phase is solved in the Lagrangian framework using Newton's law to describe individual representative particle motion. In present work, CFD technique is used as a tool to develop a new particle drag force equation that considered the influence of particle concentration (α) as well as particle Reynolds number. This paper used the CFX-5 package to replicate experimental work of Liang, Hong and Fan [19].

2.1. Governing Equations

A general form of the transport equation used in CFD model is shown in Equation (3). This equation describes the instantaneous transport of any variable quantity ϕ, which may be mass, momentum, heat, or a scalar quantity such as turbulent kinetic energy.

$$\rho \frac{\partial}{\partial t}(\phi) + \rho u_i \frac{\partial}{\partial x_i}(\phi) = \frac{\partial}{\partial x_i}\left(\Gamma \frac{\partial \phi}{\partial x_i}\right) + S \tag{3}$$

where ρ is the fluid density, x is the distance in the ith, u is the velocity in the ith, Γ is the diffusion coefficient of the variable ϕ and S is a source or sink term for the variable ϕ. For a fluid with constant density, the Navier–Stokes system of equations consist of the continuity Equation (4), derived from the principle of conservation of mass, and three equations derived from the principle of the conservation of momentum (5).

$$\frac{\partial \rho}{\partial t} + \frac{\partial}{\partial x_j}(\rho u_i) = 0 \tag{4}$$

$$\rho \frac{\partial u_i}{\partial t} + \rho u_j \frac{\partial}{\partial x_j}(u_i) = -\frac{\partial p}{\partial x_i} + \frac{\partial}{\partial x_j}(2\mu s_{ij}) \tag{5}$$

where S_{ij} is the strain tensor, defined as:

$$s_{ij} = \frac{1}{2}\left(\frac{\partial u_i}{\partial x_j} + \frac{\partial u_j}{\partial x_i}\right) \tag{6}$$

2.2. Turbulence Model

In the present study, the Reynolds Averaged Navier–Stokes (RANS) equation was used to describe turbulent flows. The RANS can be used with approximations based on knowledge of the properties of flow turbulence to give approximate time-averaged solutions to the Navier-Stokes equations. The RANS equation can be written in the following form:

$$\rho\frac{\partial U_i}{\partial t}+\rho\frac{\partial}{\partial x_j}(U_iU_j)=-\frac{\partial p}{\partial x_i}+\frac{\partial}{\partial x_j}\left(2\mu s_{ij}-\rho\overline{u_i'u_j'}\right) \tag{7}$$

which only differs from the laminar form by the term $\rho\overline{u_i'u_j'}$. The quantity is known as the Reynolds stress tensor and has six independent components. As the Reynolds stress tensor contains six unknown quantities combined with the unknown velocity and pressure terms, we now have 10 unknowns and only 4 equations (3 momentum and the continuity) to solve. In order to analytically solve these equations, a form of turbulence closure method is required. The turbulence model used to simulate the experimental results was the standard k-ε model [13]. A Reynolds stress turbulence model was also used in the simulation and compared for accuracy purposes only.

2.3. Particle Phase Model

The calculation of the particle motion comes directly from Newton's second law, which states:

$$m\frac{du}{dt}=F \tag{8}$$

where F is the force on the particle, and m is the mass of the particle. Although this F is made up of a few different forces, the major contributing factor during dilute phase flow is the drag force between the continuum and the dispersed phases.

2.3.1. Drag Force Model

The drag force generally takes the form:

$$F_D=\frac{1}{2}A_{CS}\rho C_D|V_{\mathrm{Rel}}|V_{\mathrm{Rel}} \tag{9}$$

where A_{CS} is the cross-sectional area perpendicular to the velocity direction, ρ is the density of the continuum medium, V_{Rel} is the relative velocity between the particle and the continuum phase and C_D is the coefficient of drag of the particle. The standard model by [24] employed by CFX-5 is given by:

$$C_D=\frac{24}{\mathrm{Re}}\left(1+0.15\mathrm{Re}^{0.687}\right) \tag{10}$$

were

$$\mathrm{Re}=\frac{\rho|V_{\mathrm{Rel}}|d}{\mu} \tag{11}$$

here d is the diameter of the particle, ρ is the fluid density and μ is the viscosity. This relation for the drag coefficient only relates the amount of drag to the relative velocity. For extremely dilute flows whereby the particles are well dispersed, this relation is adequate, but when the volume fraction of particles increases, the effects of neighbouring particles cannot be excluded. The following section covers the development of a new particle drag coefficient formula considering the effect of neighbouring particles on the drag force particles entrained in particle streams.

2.3.2. Turbulent Dispersion

The effect of the fluid turbulence on the particle motion is considered via the turbulent dispersion method. As the fluid flow is calculated as a time averaged steady-state flow, the velocity at any point can be quantified as a mean and fluctuating component of veloc-

ities. The fluctuating components of velocity are calculated using Gaussian probability distribution of zero mean and standard deviation of:

$$sd = \sqrt{\frac{2}{3}k} \tag{12}$$

where k is the kinetic energy of the fluid in a particular cell. This calculated fluctuating component combined with the time-averaged mean value at that point are used to predict particle motion in that immediate area.

2.3.3. Particle-Wall Collision Model

The standard particle-wall collision based of the work of Shuen, Solomon, Zhang and Faeth [25] included in CFX-5 consists of particle being reflected off the wall surface based on the coefficient of restitution. This coefficient is a direct measure of the amount of energy lost during the collision process and effectively reduces the normal velocity of the rebounding particle. The figure shows the relationship between the pre and post collision velocities, both parallel and normal to wall. To model particle wall collision a rough-wall collision model similar to that of Sommerfeld [26] was implemented. This model considers the effects of slight undulations in the wall surface. These slight undulations result in slightly modified impact angles by introducing a virtual wall as seen in Figure 2.

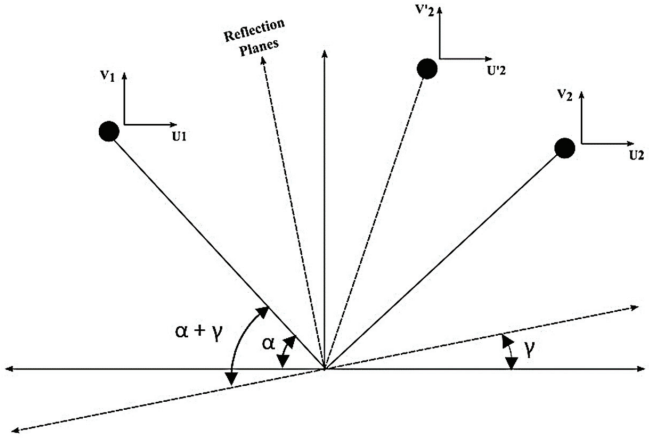

Figure 2. The effect of the virtual wall inclination on the post collision properties.

The calculation for post collision velocities is approached the same as normal wall, but the incoming velocities are adjusted to incorporate the slight impact angle change. The formulas to calculate the post-collision velocities for both sliding and non-sliding collisions are as follows:

Non-sliding collision

$$u_2 = \frac{5}{7}(u_1) \tag{13}$$

$$v_2 = -ev_1 \tag{14}$$

Sliding collision

$$u_2 = u_1 + \mu_d(1+e)v_1 \tag{15}$$

$$v_2 = -ev_1 \tag{16}$$

where u_1 and u_2 represents the corresponding velocities pre and post collision in the tangential direction with respect to the collision, v are the velocities normal to the wall, e

is the coefficient of restitution and μ is the coefficient of friction. A non-sliding collision occurs when the following condition is valid:

$$|u_1| \leq \frac{7}{2}\mu_o(1+e)v_1 \tag{17}$$

The equations for the standard model and improved are identical, but the incoming velocities for the improved model have been modified according the roughness angle based on the work of [26].

2.3.4. Particle-Particle Collision Model

The standard CFX-5 software [27] package does not account for particle-particle collision as part of the Lagrangian framework. As a consequence, the software needed to be modified to consider the effect of particle collisions through different flow systems. The modelling method implemented into the program is based on the model developed and refined by Sommerfeld [28]. The basis of this method is the creation of a fictitious particle that is used for the calculation of collision probability and if required the collision process.

As the Lagrangian particles are tracked individually through the flow domain, sampling the average particle velocities through a particular computational cell creates a fictitious particle. With the fictitious particle created, the collision probability of collisions occurring between the tracked and fictitious particles is calculated using a similar method for that of the kinetic theory of gases. The formula for the collision probability is as follows:

$$P_{coll} = \frac{\pi}{4}\left(D_{p,real} + D_{p,fict}\right)^2 \left|\vec{u}_{p,real} - \vec{u}_{p,fict}\right| n_p \Delta t, \tag{18}$$

where D is the diameter of the relevant particle, u the velocity of the relevant particle, n_p is the number of particles per unit volume and Δt is the time step. After the collision probability is calculated, this probability is compared with a random number (RN) that is generated. A collision is to be simulated if the generated RN is less than the $P_{coll.}$ When a collision is to be simulated, the location of collision point on the real particle is determined randomly and the resulting post collision velocities calculated using the follows formulas:

$$u_1' = u_1\left(1 - \frac{1+e}{1+{}^{m1}/_{m2}}\right) \tag{19}$$

where u_1 and u_1' are the pre and post collision velocities, respectively, in the tangential direction relative to the collision vector between particle center at the time of impact, e is the coefficient of restitution between the two particles, and m_1 and m_2 are the respective masses. In the normal direction, during the collision process, a particle may slide against the wall surface or depending on the friction between the faces, the particle may rotate in a non-sliding collision. The effects of the two sliding conditions are accounted for by:
non-sliding collision

$$v_1' = v_1\left(1 - \frac{{}^{2}/_{7}}{1+{}^{m_1}/_{m_2}}\right) \tag{20}$$

sliding collision

$$v_1' = v_1\left(1 - \mu(1+e)\frac{u_1}{v_1}\frac{1}{1+{}^{m_1}/_{m_2}}\right) \tag{21}$$

where e is the coefficient of restitution, μ is the coefficient of friction and m_1 and m_2 are the respective masses of the considered particles.

3. Numerical Simulation Overview

3.1. Description of the Simulated Cases

The experimental work of Liang, Hong and Fan [19] was used in the present work for numerical method. In their work, four different orientations were investigated. The

first considered the effect of varying angle with respect to the flow direction at given separation distance. The second configuration looked a three co-aligned particle in the flow direction. The third test case considered a central test particle surrounded by 6 equally spaced particles in hexagonal configuration. The final case looked at a central test particle surround by 8 particles in cubic orientation. As previously mentioned the three co-aligned particles work forms the basis of the following study whereby separation distances from 0.25 to 7 x/d were investigated where the results for 0–3 x/d were compared with the experimental data of [19]. The published results considered the flow conditions where the particle Reynolds number equalled 54. The set up consists for the CFD model replicates those dimensions seen in the experimental work, with a pipe diameter of 15.24 cm and a particle diameter of 1.58 cm. The particles are co-aligned along the centreline of the pipe. The present CFD geometry based on the [19] experiments and inlet velocity profile is given in Figure 3. Figure 4 shows a section through the mid-plane of the pipe highlighting the mesh densities used. The mesh for these simulations was unstructured for the bulk of the domain, but regions close to the pipe wall and particle surfaces were structured in nature. These are the areas of greater gradients of flow variables. Beyond the structured region, heavy unstructured refinement was enforced around the particle surfaces and along the centreline of the pipe as this are the regions of most interest and the areas where the greater velocity gradients occur. To obtain an acceptable accuracy with acceptable computational time, various grid independency tests were conducted with different mesh resolutions. The predicted results were verified to have been no significant impact of the grid resolution on the results. A time step of 0.01 s was used in the present model.

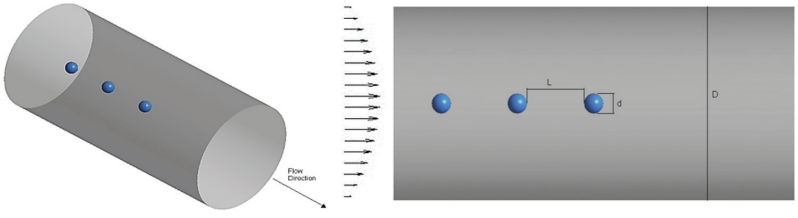

Figure 3. Present CFD geometry based on the work of Liang (1996) and inlet velocity.

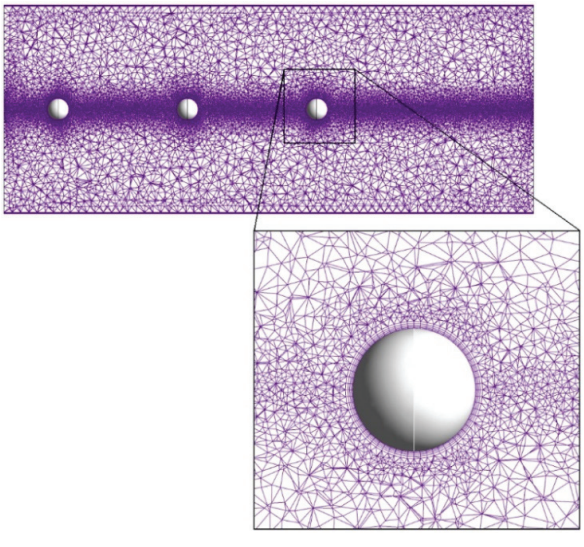

Figure 4. Mesh configuration for the present CFD geometry.

3.2. Boundary Conditions

To accurately replicate the experimental conditions of Liang, Hong and Fan [19], a fully developed laminar pipe flow condition is used at the inlet boundary:

$$u = u_0\left(1 - \frac{r^2}{R^2}\right) \tag{22}$$

Both the pipe wall and particle surfaces were set as no-slip boundary conditions with the velocity equal to zero. Outlet of the pipe was set to an opening type with a static pressure value equal to atmospheric pressure since it gives better convergence results. In present work the convergence criteria for all numerical simulations of all the residual were taken as 10^{-4} for each scaled residual component. A glycerine/water solution of approximately 82 wt% glycerine was used in this study. Fluid properties were set according to the values given in Table 1.

Table 1. Fluid properties for Liang (1996) experimental replication work.

ρ (kg/m^3)	μ (kg/m.s)	d_p (m)	D_{pipe} (m)	u_0 (m/s) at Re = 54
1206	0.057	0.015875	0.154	0.16

4. Results and Discussion

Figure 5 shows the good agreement between the experimental study of Liang, Hong and Fan [19] co aligned particle work and the present CFD validation work, where cd is the drag force coefficient on the test particle and cd0 is the drag force coefficient on an isolated particle. The CFD model was able to predict the drag force accurately on all three particles.

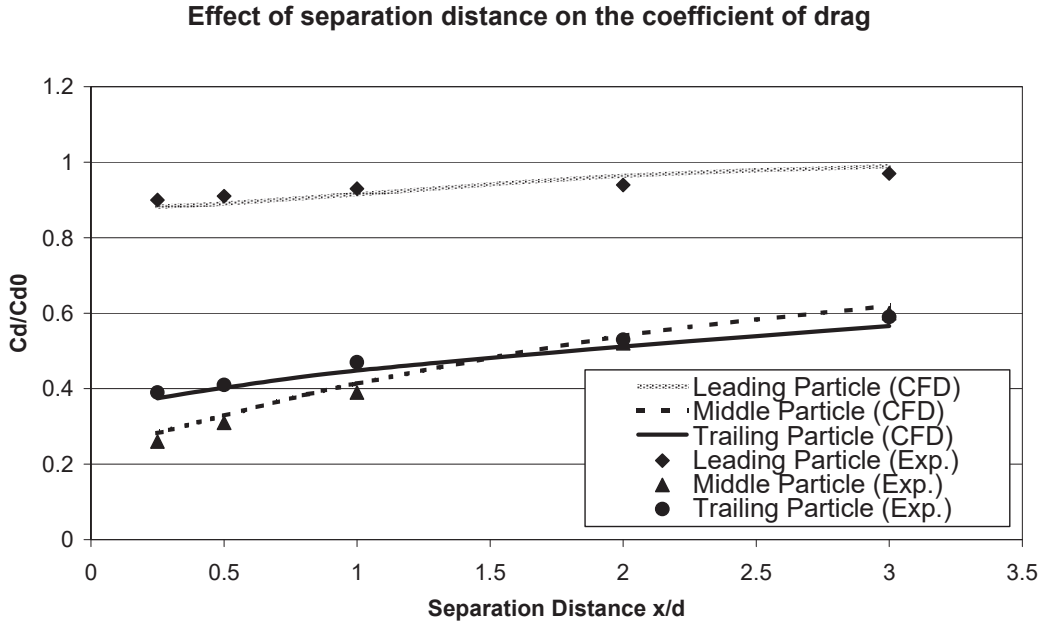

Figure 5. Validation of the Liang experiment for three co-aligned particles at Re = 54.

The results also accurately predicted the transition of drag force whereby the drag on the middle particle surpasses that of the trailing particle. Figure 6 shows the velocity contour plot of the present CFD study at a separation distance of 5 particle diameters and

a Reynolds number of 54. The leading particle is subjected to higher velocities than the trailing particles which in turn leads to the higher drag force.

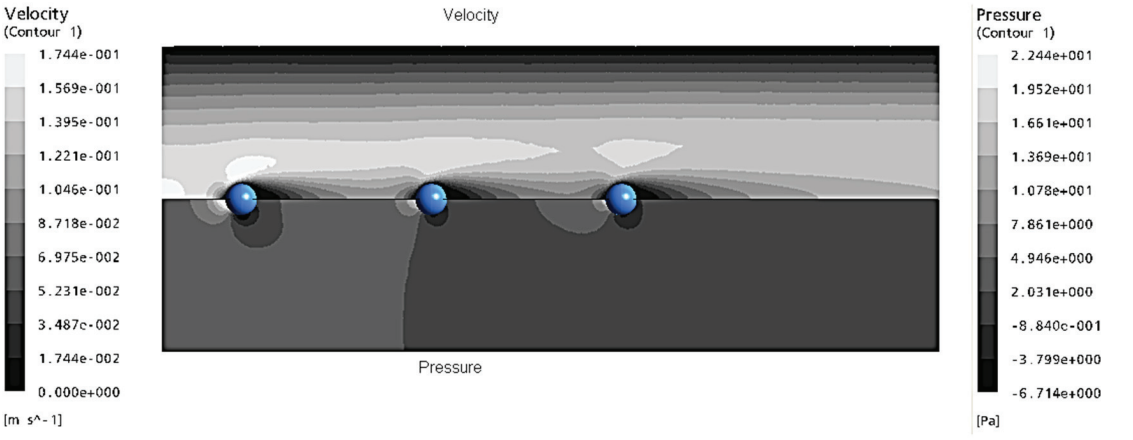

Figure 6. Velocity and pressure contours plot of Liang experiment at a separation distance of 5 particle diameters and Re = 54.

Figure 7 shows a close-up view of the recirculation area behind the three particles. The leading particle, due to the higher incoming velocity, has a larger recirculation area and results in higher drag forces. Due to the close agreement of the predicting ability of the CFD model, it is valid to assume an accurate extension of this work could be undertaken.

To fully help understand the phenomenon at work in the particle drag of clusters of particles, it is necessary to consider various cases. In the present work, three different cases were investigated:

- Model 1 investigates the drag force of an average particle within an infinite line of particles co aligned with the flow direction. This model will highlight the effects of inline wake characteristics.
- Model 2 considers a particle surrounded by an infinite plane of particles aligned perpendicular to the flow to investigate the influence of neighbouring particles.
- Model 3 investigates an infinite matrix of particles, which is a combination and extension of the previous two models.

The results of cases 1 and two are for comparative purposes only and necessary to fully understand the effect of position and location of particles on surrounding particles.

4.1. Particles Aligned with Flow (Model 1)

Model 1 looks at the case of infinite number particles co-aligned with the direction of flow (see, Figure 8a). This Model highlights the influence of particle wake on the drag force when aligned with the flow direction. The ranges of the simulations completed for this Model 1 include particle separation distances of 1 to 20 particle diameters and particle Reynolds numbers varying from 1 to 50.

In order to accurately model an infinite number of particles in flow direction, the inlet and outlet regions (see, Figure 8b), require a periodic boundary condition. The periodic boundary condition forces the quantities leaving the domain to be reintroduced into the domain through the inlet patch. The drag force created by the fluid moving passed the particles results in an energy loss due to friction between the shearing layers of fluid adjacent to the particle surface. The periodic boundary condition forms an endless loop of fluid that unless corrected will eventually stall. To overcome this phenomenon an equal amount of momentum is introduce evenly throughout the domain to ensure continuous flow.

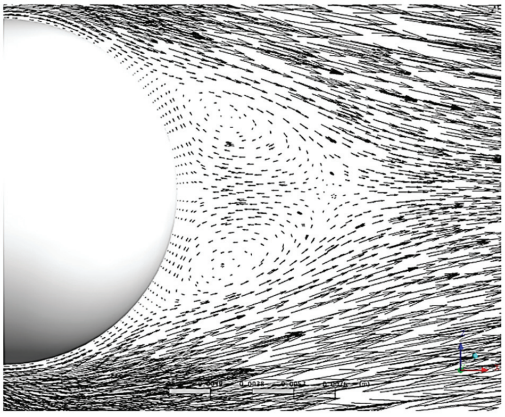

(a). Leading particle

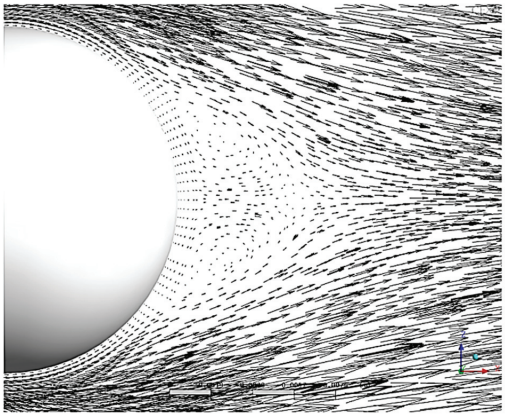

(b). Middle particle

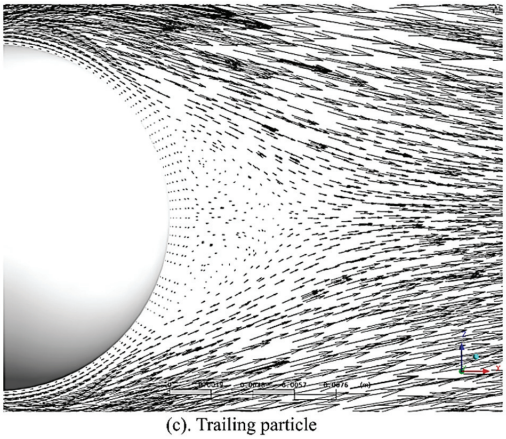

(c). Trailing particle

Figure 7. Velocity vector plot of (**a**). leading particle, (**b**). middle particle, (**c**). trailing particle at x/d = 5d and Re = 54.

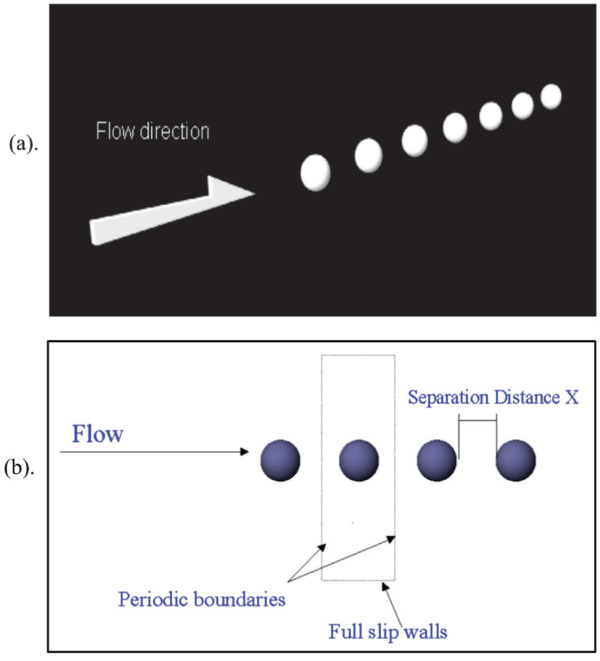

Figure 8. (**a**). Configuration for Model 1, (**b**). Model 1 boundary conditions.

To test the introduction of firstly the momentum introduction method and the periodic boundary condition, a pseudo-isolated particle was simulated (separation distance of 80 pd) at various Reynolds numbers and compared with commonly accepted relation for drag force of isolated particles ($F_D = \frac{1}{2} C_D \rho A V^2 \quad where\ C_D = \frac{24}{\mathrm{Re}}\left(1 + 0.15\,\mathrm{Re}^{0.687}\right)$). Figure 9 shows the close agreement between the theoretical value based on an isolated particle and the CFD simulations. In the cross-stream direction, the effects of the wall on the flow characteristics needed to be removed so a series of geometries were tested at varying distances to determine the minimum distance from the wall for the simulation. It was found the use of 20 d wall distance removed all wall effects from the flow. At a distance of 20 d, a symmetry boundary or free slip (shear stress = 0) was used. This kind of boundary condition removed the drag due to wall friction as is seen in pipe flows.

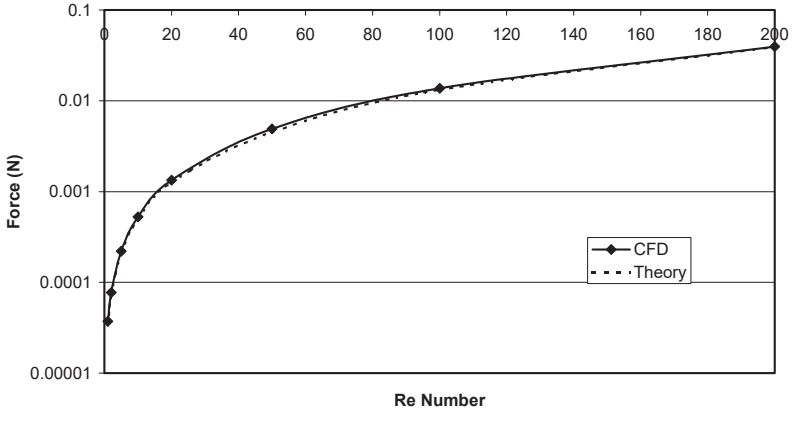

Figure 9. Validation of periodic boundary conditions.

Figure 10 shows the normalised drag force plot for Model 1, where f is the predicted drag force on the test particle and f0 is the corresponding drag force for an isolated particle. It can be noted that at very small separation distances, which represents high particle volume fractions, the reduction of drag is large for all Reynolds numbers. The larger the Reynolds numbers the greater the reduction in drag force. At a separation distance of 1 particle diameter and a Reynolds number of 50, the average particle drag force is approximately 18% of that of an isolated particle at the same Reynolds number. This is the phenomenon that is used by birds to fly great distance by sharing the drag force between the birds. The experimental work of Katz and Meneveau [29] experimentally studied the rise velocity of interactive bubbles and considered the relative between two identical bubble and several separation distances. The results suggest the relative velocity between the particles increased at smaller separation distances. This is consistent with the CFD predictions shown whereby a reduction in drag force would correspond to an increase velocity of the trailing bubble leading to greater relative velocity between to the two bubbles.

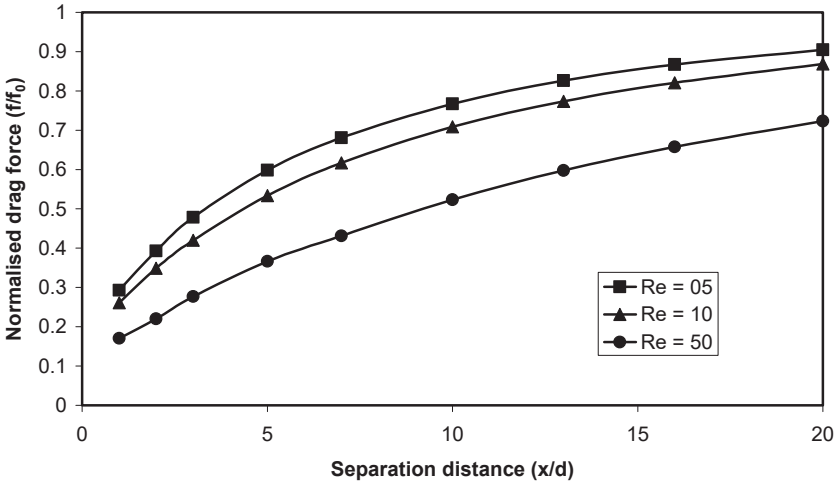

Figure 10. Normalised drag force of Model 1.

The velocity contours for some limited cases of Model 1 are shown in Figure 11. These plots highlight the reason the drag force at smaller separation distances. At 1 particle diameter separation distance, the wake from the previous particle engulfs the trailing particle leading to lower oncoming fluid flow velocity and consequentially lower drag force.

4.2. Particles Perpendicular to Flow (Model 2)

Model 2 investigates the effects of particles located perpendicular to the flow (see, Figure 12a). The range of separation distance for this case includes 1 to 20 particle diameters. Model 2 focussed on the influence of neighbouring particle perpendicular to the flow direction and as such the cross-sectional dimensions were important. The length of the geometry was set to double the separation distance of the particle to the side boundaries. The geometrical design yields little effect on the drag force with the outlet set at this ratio to the side boundaries. This case required an infinite plane of particles perpendicular to the flow to be simulated. This plane is the product of using symmetry boundaries again on the wall regions parallel with the flow, but with this case, the distance to the symmetry boundary will varying accordingly to the separation distance being modelled. (See Figure 12b).

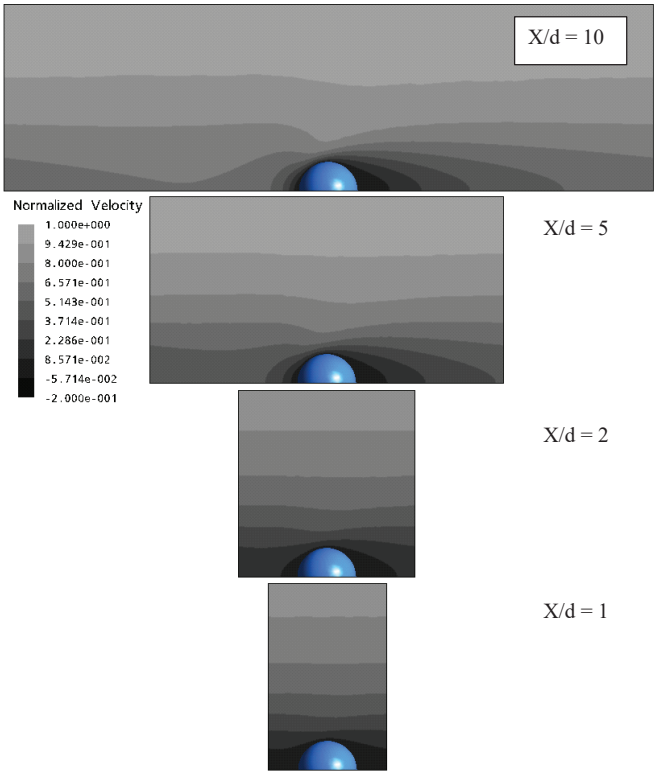

Figure 11. Velocity contour plots for separation distances x/d = 10, 5, 2 and 1 at Re= 50.

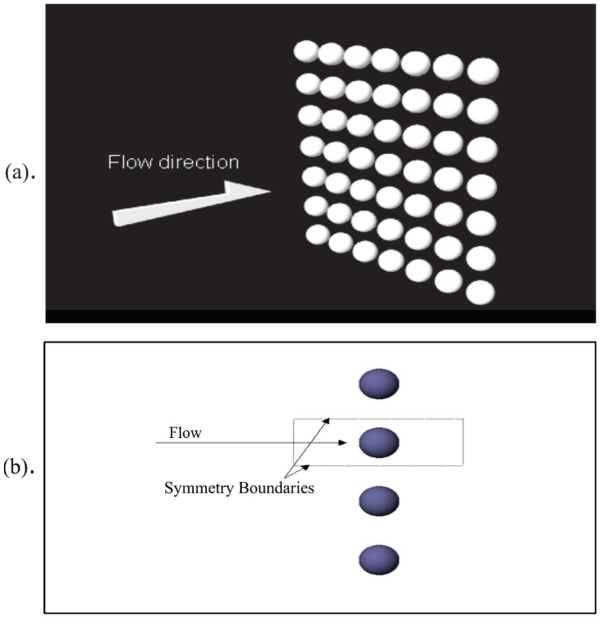

Figure 12. (**a**). Configuration for Model 2, (**b**). Model 2 boundary conditions.

Looking at the drag force results for Model 2 (see, Figure 13), the drag force on the test particle sharply increased compared to that of an isolated particle at the smallest separation distance whereas all the results showed a normalised drag force greater than unity with the greater separation distances showing very little difference from unity. The main reason the increase in drag force is due to the higher velocity experienced by the particle due to the fact that the cross section for the flow to move through decreases past the particle causing the velocity to increase to conserve continuity. This would explain why the results for the smallest geometry are so extreme because this is the case where the flow reduces the most. For example, the case of a separation distance of 1 particle diameter reduces the cross-sectional area past the particle by approximately 20%. Following along the same lines of thinking the smaller Reynolds number results provide greater force increases because the rate of change of drag coefficient and hence drag force with respect to Reynolds number is greater at lower numbers thereby leading to higher experienced drag force as the increase in seen velocity results in higher Reynolds numbers.

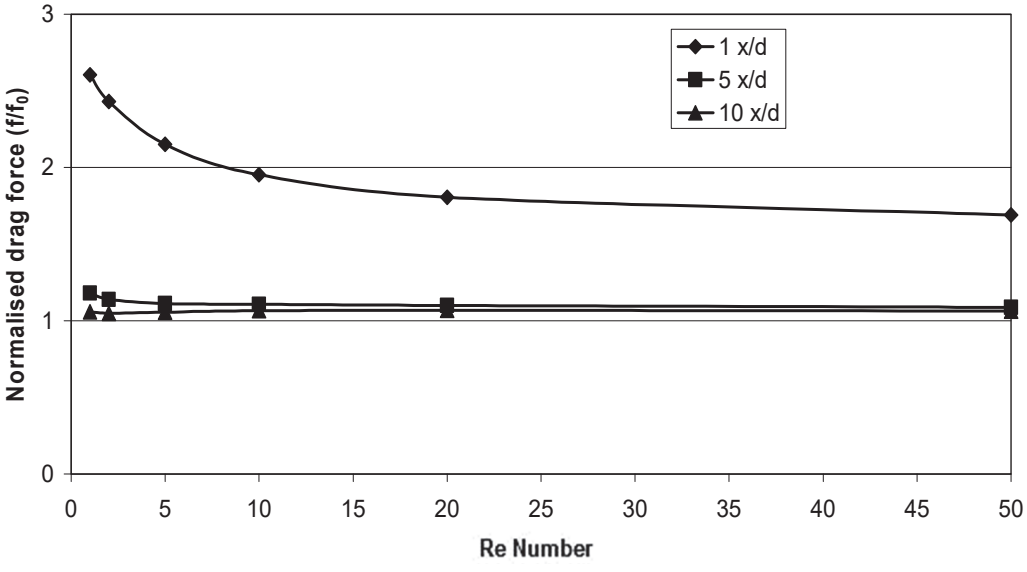

Figure 13. Normalised drag force of Model 2.

The increased drag force attributed to the squeezing of the flow or the 'nozzle' effect was also noted by Chen and Lu [30]. In their experimental work, the drag force on 2 and 3 particles positioned side-by-side in the oncoming flow were measured. Their results suggest that at smaller separation distances, the drag force increases, which they primary conclude is based on the nozzle effect, which causes a rise in local Reynolds numbers. Although there is some difference in the magnitude of force increase between the predicted CFD results and those of the experimental work (see, Figure 14), it is noticeable from their work, that the case of three particle yielded slightly higher drag force increase compared with those of the two-particle case. With this in mind, the infinite array of particles perpendicular to flow in these CFD predictions would naturally expect to produce higher drag forces due to introduction of additional particles.

The velocity contour plots of Figure 15 show how the smaller separation distance greatly increases the maximum normalized velocity. The case of separation distance of 10 x/d shows almost a constant normalized velocity of close to unity resulting in a drag force ratio of approximately the same magnitude. This highlights the importance of the "nozzle" effect on the drag force for the smaller geometries caused by close neighbouring particles.

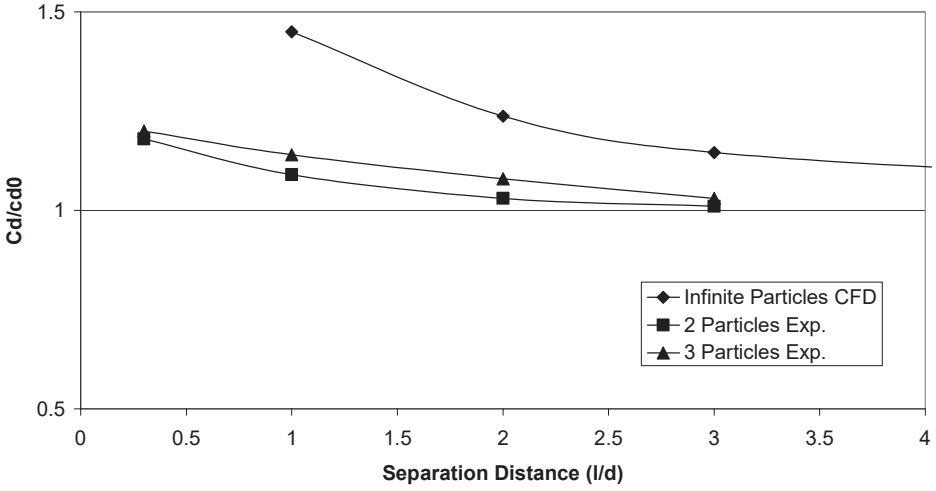

Figure 14. Comparison of CFD simulation results for Model 2 and available experimental data.

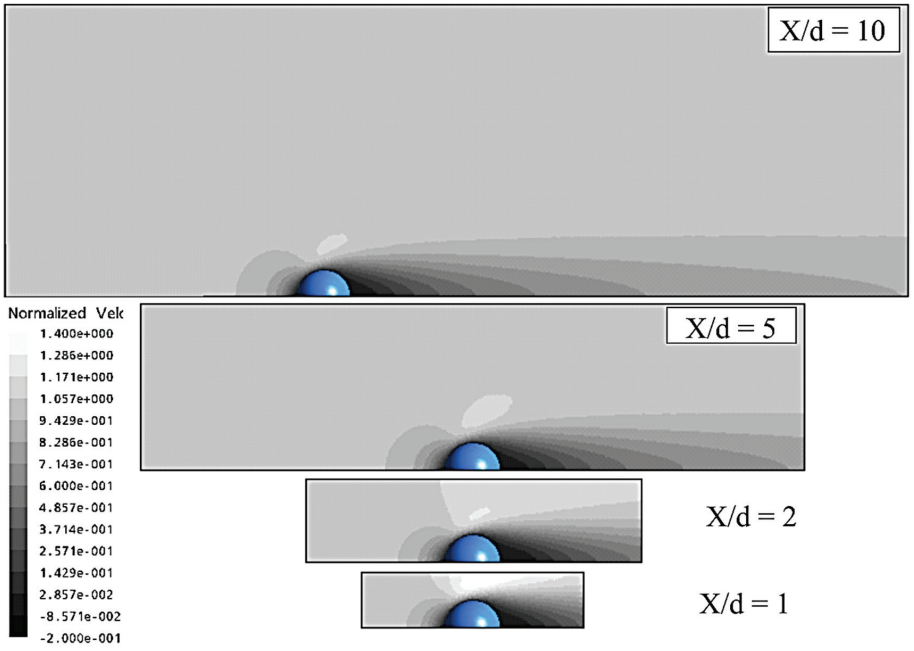

Figure 15. Velocity contour plots of Model 2 for separation distances x/d = 10, 5, 2 and 1 at Re = 50.

4.3. Infinite Matrix of Particles (Model 3)

The final model consisted of a combination of Models 1 and 2 to form an infinite matrix of particles from which a new drag force was developed (see, Figure 16a). The geometry for Model 3 consisted of a cubic shape of dimensions based on separation distance. As would be expected being a combination of Models 1 and 2, the combination of boundary conditions were also applied to this model. As in Model 1, the periodic boundary condition and introduced momentum were used in Model 3. From Model 2, the symmetry boundary conditions were used (see, Figure 16).

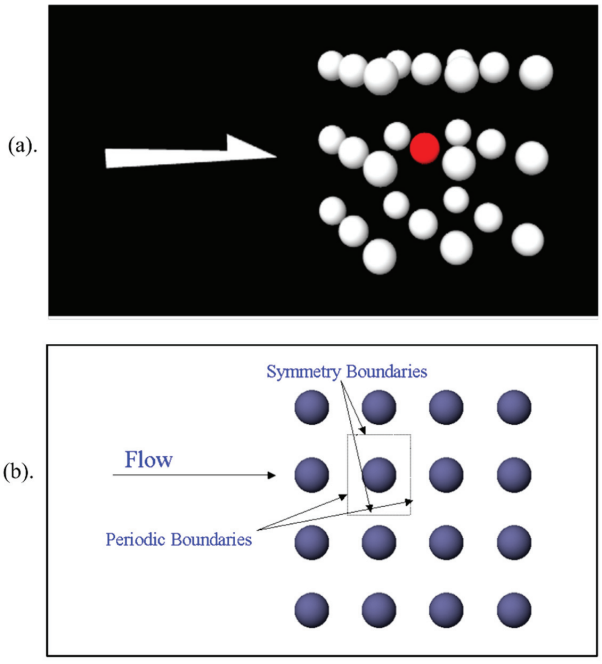

Figure 16. (**a**). Configuration for Model 3, (**b**). Model 3 boundary conditions.

Results for the drag force of Model 3 are seen in Figure 17. For all the cases, there was a sharp increase in drag force at the smaller separation distances similar to that noted for Model 2. This increase again is caused due the increase of perceived velocity seen at the particle due to the constriction in the flow due to the physical presence of the particle. This would also explain why the effect is less noticeable at the greater separation distances. Also of interest is that as the Reynolds number increases the constriction effect is dramatically reduced mainly in part to fact that as rate of change of drag coefficient with respect to Reynolds decreases dramatically at higher Re.

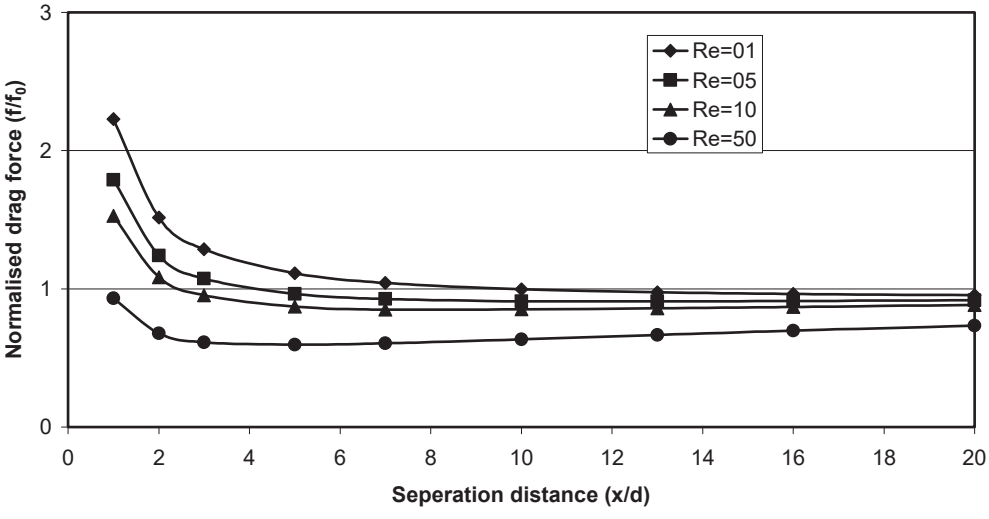

Figure 17. Normalised drag force of Model 3.

Figure 18 shows the velocity contour plots at various separation distances ranging from 10 to 1 x/d. At the smallest separation distance, it can be easily seen that the wake of the previous particle continues to the next, generally, this result in a reduction of drag force but due to the constriction effect previously discussed, the drag is higher. The constriction effect is highlighted in the contour's plots, as the normalised velocity of the smaller separation cases is higher than those of the 10 x/d case.

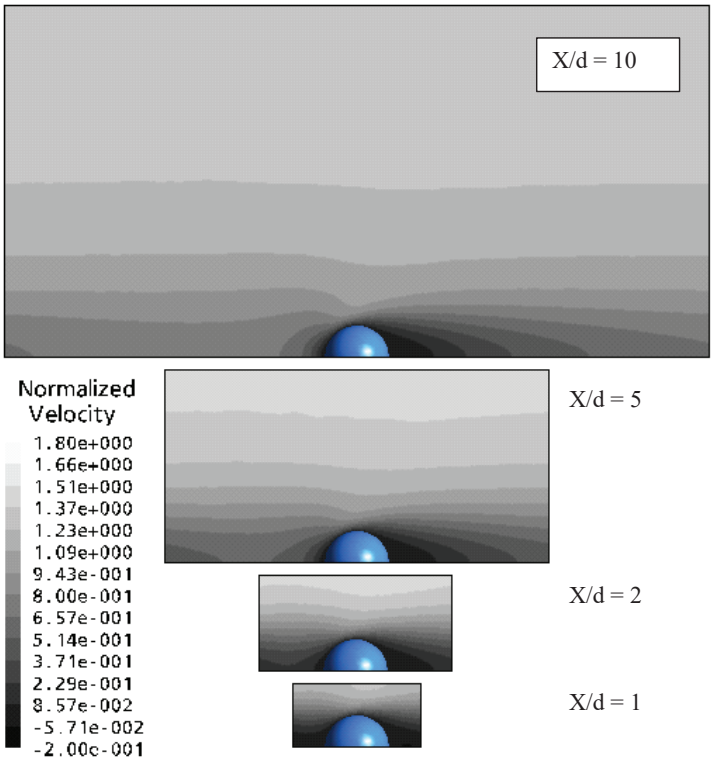

Figure 18. Velocity contour plots for Model 3 at Re = 50 and separation distances x/d = 10, 5, 2 and 1.

A series of comparison graphs of the three models are shown in Figure 19. The first graph shows that at low Reynolds numbers, the results for Model 3 and Model 2 are almost identical. This is due mainly to the constriction effect discussed early in the chapter. At a Reynolds number of 5 and above it is clear to see distinction between the models. Again, all the results show the sudden increase of drag at smaller separation distances due to the change of flow area, something that is not seen in Model 1 because the wall boundaries were set far enough away to minimise any area change to negligible proportions. For the higher Reynolds number cases it can be seen that apart from the sudden increase at smaller separation distance, as the particles spread, the results replicate the trends seen in Model 1 with the magnitudes of the drag force reduction slightly smaller as it approaches unity.

Figure 20 shows the differences between Model 1 and 3 under the same flow conditions. It can be seen that the wake length produce in Model 1 is greater than that produced by Model 3. The difference in the models is the effect produced by the introduction of neighbouring particles upstream. It is interesting to note that effect of Model 2 beyond 5 particle diameters of separation distance was seen to be negligible, further downstream these particles impact on the wake length shortening and consequential drag force increase. The normalised drag coefficients shown in Figure 21 reinforce the influence of neighbouring particles from Model 2 as there is a clear differential between Model 1 and 3.

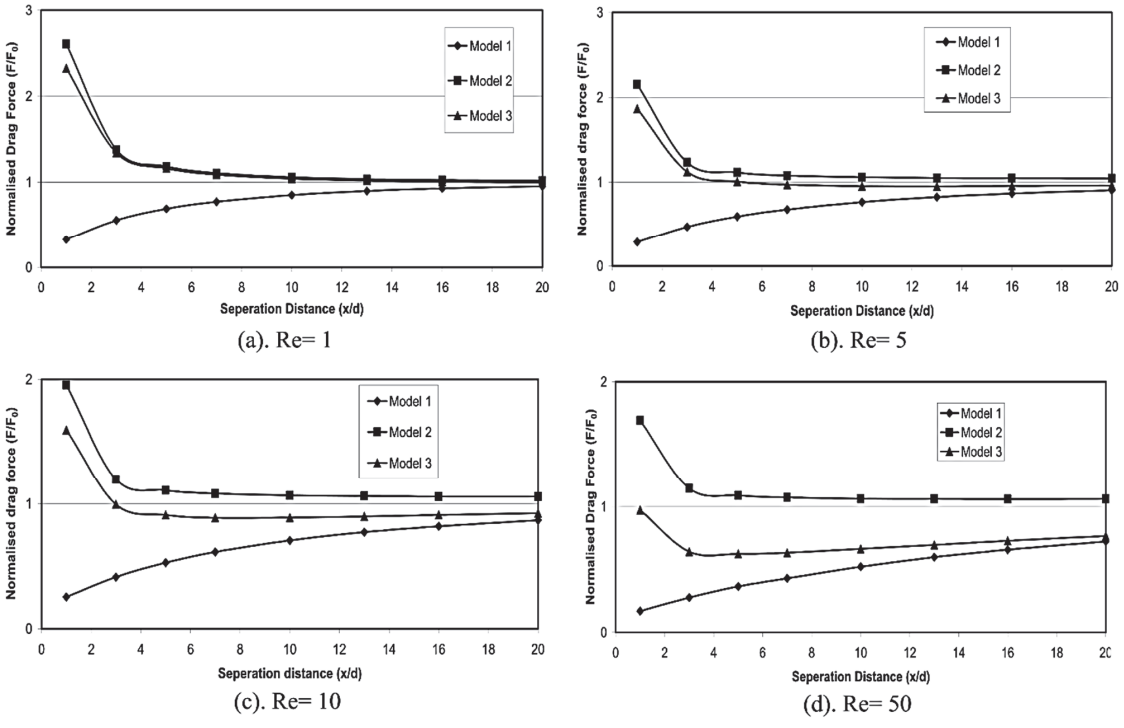

Figure 19. Comparison of the normalised drag force of different models at different Reynolds number.

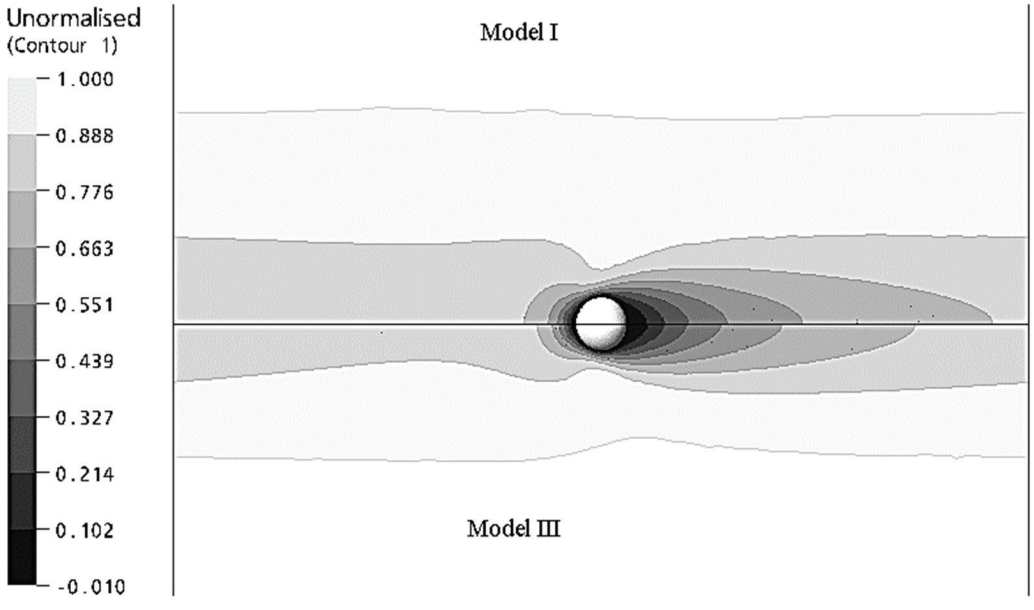

Figure 20. Comparison of Models 1 and 3 at separation distance x/d = 16 and Re = 50.

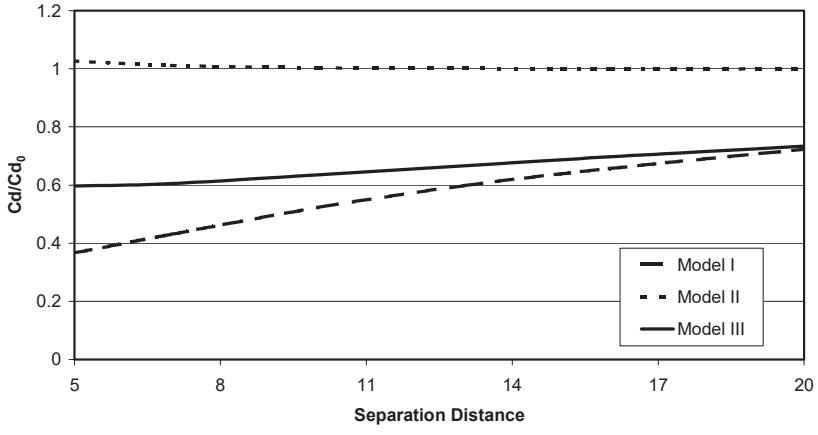

Figure 21. Comparison of normalised drag coefficients for the three different models at a Re = 5.

The fitment of an equation to predict the drag coefficient of a spherical considering both Reynolds number and particle concentration (α) is based on the results seen in Figure 22. The equation development is based on Reynolds number between 1 and 50 and separation distance of 5 to 20 x/d. The separation distance corresponds particle volume fractions of 10^{-2} and 5×10^{-5}. To generate an equation for the data obtained from the present CFD prediction in the previous sub sections, a least squares method was utilised. A generic form of the equation was generated as seen in Equation (9). The least squares regression program solved for the constant A, B, C and D.

$$C_D = \frac{24}{\mathrm{Re}}\left(1 + 0.15\mathrm{Re}^{0.687} + A\,\mathrm{Log}\left[\sqrt[3]{\frac{\pi}{6\alpha}}\right]^{B} + C[\mathrm{Log}(\mathrm{Re})]^{D}\right) \tag{23}$$

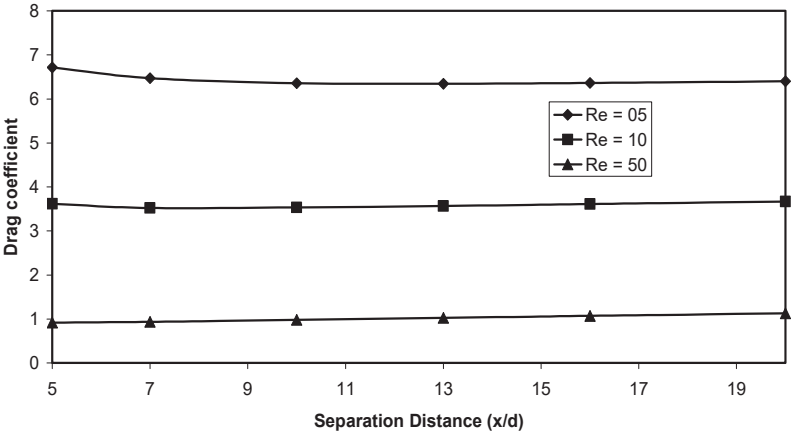

Figure 22. Drag coefficients for various Reynolds number of Model 3.

Substituting in the values from Table 2, the generic equation takes the form of Equation (9).

$$C_D = \frac{24}{\mathrm{Re}}\left(1 + 0.15\,\mathrm{Re}^{0.687} + 0.000353\left[\mathrm{Log}\left(\sqrt[3]{\frac{\pi}{6\alpha}}\right)\right]^{15.93} - 0.16[\mathrm{Log}(\mathrm{Re})]^{3.62}\right) \tag{24}$$

Table 2. Calculated constants for generic equation.

A	B	C	D	RMS Error
15.94	0.000353	−0.16	3.62	0.0439

The results were more accurately predicted for those particles whose sizes were closest to the average diameter. Of the three different particle size ranges, the medium particle with an average of 226 μm produced the best CFD predictions with almost perfect predictions. The cases of the larger and smaller particle sizes (342 μm and 136 μm respectively) while still showing improved predictions; they were not as prominent as the medium case. Several limitations to this newly developed drag model need to be acknowledged. Firstly, the particle concentration (α) range for this formula is considered to be adequate for the purpose of modelling dilute flows using the Lagrangian framework. In simulated flows where regions exceed the 0.01 volume fraction, limitations on the newly developed drag force, require the particle drag to be calculated using the standard drag model. This is not considered to be such a problem because at high particle concentrations (α) the particle motion is governed predominately by inter-particle collisions and less by drag force. Secondly, the limitation set on the particle Reynolds number is also considered to be adequate for the use in industrial type flows where the transport of small particles (less than 1 mm) is to be considered whereby generally the local particle Reynolds number would rarely exceed 50. In the case of larger particles producing the particle Reynolds numbers greater than 50 the new drag force will not be used, and the standard drag model would then be used. Finally, the present developed drag force formula has been calculated on a study of the relationship between the drag forces of mono-sized particles. Particles of differing diameter will obviously affect the resulting wake size and consequently the amount of drag reduction seen by trailing particles. A smaller particle (i.e., $d_p \geq 136$ μm) will not reduce the drag force as significantly on a larger particle (i.e., $d_p \leq 342$ μm) as would be expected if the situation were reversed. With this in mind, narrow particle size distributions are best suited for use with this formula, as the particles would be considered almost mono-sized. Any particles outside of this narrow band would be subject to incorrect reductions in drag force, particularly smaller particles, which may lead to variations from any validating experimental data. Although this limitation would exclude many applications if the new formula were to be used although the reductions in drag force may not be entirely accurate, it would still yield improvement over the standard drag force model.

5. Summary and Conclusions

The present work accurately reproduced the drag force results seen in the Liang, Hong and Fan [19] experimental study of three co-aligned particle at various separation distances. An extension of this work resulted in the CFD study of three models of varying particle configurations. Model 1 highlighted the important influence that particle wake has on the drag force of trailing particles. From this study, it was found that a trailing particle at small separation distances and a Reynolds number of 50 experience a reduction of up to 80% of drag force. Although not as prominent as this case all scenarios resulted in reduction of the seen drag force with this model. Model 2 considered the effect of neighbouring particle perpendicular to the flow. In all cases, the drag force increased due to a squeezing of the flow at the constriction, as expected this was much more prominent at the smaller separation distance. Most notably at a separation distance of 1 and a Reynolds number also 1 the drag force increased by over 250%. Beyond about 5 particle diameters this effect was almost negligible with drag approximating those of isolated particles at the same Reynolds numbers. For Model 3 for which the new drag equation was developed, at smaller separation distances its behaviour mimics that of Model 2 again because of the squeezing of flow. As the separation distance increased, the results followed more of the results seen for Model1. For both extremes, the increase or reduction of drag force were never as high

as the results seen the models whose behaviour it was following. As the application of a new drag force model is to be used primarily for Lagrangian particle tracking where dilute flows are of most interest the range of separation distance was reduced to 5 to 20 particle diameters. This firstly made the fitment of a curve to the data easier and more accurate and secondly the importance of the drag force in dense phase flow becomes secondary to those of particle-particle collisions above and beyond a volume fraction of 0.01, which represents 5 particle diameters of separation distance.

Author Contributions: D.D. and J.N. conceived of the presented idea. D.D. developed the theory and A.A.R.S. performed the computations. D.D. and A.A.R.S. verified the analytical methods. J.N. supervised the findings of this work. All authors have read and agreed to the published version of the manuscript.

Funding: This research received no external funding.

Institutional Review Board Statement: Not applicable.

Informed Consent Statement: Not applicable.

Data Availability Statement: Data available on request from the authors.

Conflicts of Interest: The authors have no conflict of interest to declare that are relevant to the content of this article.

Nomenclature

A	surface area of the particle
A_{CS}	cross-sectional area perpendicular to the velocity direction
C_D	coefficient of drag of the particle
D_p	particle diameter
e	Restitution coefficient
F	force on the particle
F_D	drag force
k	kinetic energy of the fluid in a particular cell
L	distance between particle centres
m_p	particle mass
n_p	number of particles per unit volume
P_{coll}	collision probability
Re_p	Particle Reynolds number
S_ϕ, $S_{P\phi}$	source terms
S_{ij}	strain tensor
u	velocity in the i^{th}
$U_{p,g}$	velocity of particle and gas respectively
V_{Rel}	relative velocity
x	distance in the i^{th}
Greek letters	
ρ	density of the continuum medium
ε	volume fraction
ϕ	variable quantity
Γ_ϕ	diffusion quantity
μ	Viscosity

References

1. Yan, F.; Luo, C.S.; Zhu, R.; Wang, Z.Y. Experimental and Numerical Study of a Horizontal-Vertical Gas-Solid Two-Phase System with Self-Excited Oscillatory Flow. *Adv. Powder Technol.* **2019**, *30*, 843–853. [CrossRef]
2. Senapati, S.K.; Dash, S.K. Dilute Gas-Particle Flow through Thin and Thick Orifice: A Computational Study through Two Fluid Model. *Part. Sci. Technol.* **2020**, *38*, 711–725. [CrossRef]
3. Liu, J.; BaKeDaShi, W.; Li, Z.; Xu, Y.; Ji, W.; Zhang, C.; Cui, G.; Zhang, R. Effect of Flow Velocity on Erosion–Corrosion of 90-Degree Horizontal Elbow. *Wear* **2017**, *376–377*, 516–525. [CrossRef]

4. Chinenye-Kanu, N.M.; Hossain, M.; Droubi, M.G.; Islam, S.Z. Numerical Investigation of Two-Phase Flow Induced Local Fluctuations and Interactions of Flow Properties Through Elbow. In Proceedings of the 1st International Conference on Numerical Modelling in Engineering, Ghent, Belgium, 28–29 August 2018; Abdel Wahab, M., Ed.; Springer: Singapore, 2019; pp. 124–141.
5. Ariyaratne, W.K.H.; Ratnayake, C.; Melaaen, M.C. CFD Modeling of Dilute Phase Pneumatic Conveying in a Horizontal Pipe Using Euler–Euler Approach. *Part. Sci. Technol.* **2018**, *37*, 1015–1023. [CrossRef]
6. Hu, D.F.; Huang, Z.L.; Sun, J.Y.; Wang, J.D.; Liao, Z.W.; Jiang, B.B.; Yang, J.; Yang, Y.R. Numerical Simulation of Gas-Liquid Flow through a 90° Duct Bend with a Gradual Contraction Pipe. *J. Zhejiang Univ.-SCIENCE A* **2017**, *18*, 212–224. [CrossRef]
7. Zhou, H.; Huang, Y.; Yang, Y.; Mo, G.; Li, J.; Cen, K. Experimental Measurements of Gas–Solid Flow and Splitting Mechanisms of a Coal Pipe Splitter with a Perpendicularly Arranged Upstream Elbow. *Particuology* **2016**, *25*, 143–150. [CrossRef]
8. Kumar Senapati, S.; Kumar Dash, S. Computation of Pressure Drop and Heat Transfer in Gas-Solid Suspension with Small Sized Particles in a Horizontal Pipe. *Part. Sci. Technol.* **2020**, *38*, 985–998. [CrossRef]
9. Zhao, H.; Zhao, Y. CFD–DEM Simulation of Pneumatic Conveying in a Horizontal Channel. *Int. J. Multiph. Flow* **2019**, *118*, 64–74. [CrossRef]
10. Jain, R.; Tschisgale, S.; Frohlich, J. A Collision Model for DNS with Ellipsoidal Particles in Viscous Fluid. *Int. J. Multiph. Flow* **2019**, *120*, 103087. [CrossRef]
11. Kaushal, D.R.; Thinglas, T.; Tomita, Y.; Kuchii, S.; Tsukamoto, H. CFD Modeling for Pipeline Flow of Fine Particles at High Concentration. *Int. J. Multiph. Flow* **2012**, *43*, 85–100. [CrossRef]
12. Tu, J.Y.; Fletcher, C.A.J. Numerical Computation of Turbulent Gas-Solid Particle Flow in a 90° Bend. *AIChE J.* **1995**, *41*, 2187–2197. [CrossRef]
13. Jones, W.P.; Launder, B.E. The Prediction of Laminarization with a Two-Equation Model of Turbulence. *Int. J. Heat Mass Transf.* **1972**, *15*, 301–314. [CrossRef]
14. Banakermani, M.R.; Naderan, H.; Saffar-Avval, M. An Investigation of Erosion Prediction for 15° to 90° Elbows by Numerical Simulation of Gas-Solid Flow. *Powder Technol.* **2018**, *334*, 9–26. [CrossRef]
15. Chen, Y.; Third, J.R.; Muller, C.R. A Drag Force Correlation for Approximately Cubic Particles Constructed from Identical Spheres. *Chem. Eng. Sci.* **2015**, *123*, 146–154. [CrossRef]
16. Zhang, J.; Fan, L.S. A semianalytical expression for the drag force of an interactive particle due to wake effect. *Ind. Eng. Chem. Res.* **2002**, *41*, 5094–5097. [CrossRef]
17. Shang, Z.; Lou, J.; Li, H. CFD of Dilute Gas–Solid Two-Phase Flow Using Lagrangian Algebraic Slip Mixture Model. *Powder Technol.* **2014**, *266*, 120–128. [CrossRef]
18. Miao, Z.; Kuang, S.B.; Zughbi, H.; Yu, A.B. CFD simulation of Dilute-Phase Pneumatic Conveying of Powders. *Powder Technol.* **2019**, *349*, 70–83. [CrossRef]
19. Liang, S.C.; Hong, T.; Fan, L.S. Effects of Particle Arrangements on the Drag Force of a Particle in the Intermediate Flow Regime. *Int. J. Multiph. Flow* **1996**, *22*, 285–306. [CrossRef]
20. Cheng, H.W.; Papanicolaou, G. Flow Past Periodic Arrays of Spheres at Low Reynolds Number. *J. Fluid Mech.* **1997**, *335*, 189–212. [CrossRef]
21. Kim, I.; Elghobashi, S.; Sirignano, W.A. On the Equation for Spherical-Particle Motion: Effect of Reynolds and Acceleration Numbers. *J. Fluid Mech.* **1998**, *367*, 221–253. [CrossRef]
22. Zhang, J.; Fan, L.S. On the Rise Velocity of an Interactive Bubble in Liquids. *Chem. Eng. J.* **2003**, *92*, 169–176. [CrossRef]
23. Dodds, D.; Naser, J. The Effect of Particle Concentration on the Coefficient of Drag of a Spherical Particle. In Proceedings of the 15th Australian Mechanics Conference, Sydney, Australia, 13–17 December 2004; pp. 13–17.
24. Clift, R.; Grace, J.R.; Weber, M.E. *Bubbles, Drops, and Particles*; Academic Press: Cambridge, MA, USA, 1978.
25. Shuen, J.S.; Solomon, A.S.P.; Zhang, Q.F.; Faeth, G.M. Structure of Particle-Laden Jets-Measurements and Predictions. *Aiaa J.* **1985**, *23*, 396–404. [CrossRef]
26. Sommerfeld, M. Modeling of Particle Wall Collisions in Confined Gas Particle Flows. *Int. J. Multiph. Flow* **1992**, *18*, 905–926. [CrossRef]
27. ANSYS, CFX-5, Canonsburg, USA. 2005. Available online: https://www.ansys.com/products/fluids/ansys-cfx (accessed on 10 September 2022).
28. Sommerfeld, M. Validation of a Stochastic Lagrangian Modelling Approach for Inter-Particle Collisions in Homogeneous Isotropic Turbulence. *Int. J. Multiph. Flow* **2001**, *27*, 1829–1858. [CrossRef]
29. Katz, J.; Meneveau, C. Wake-Induced Relative Motion of Bubbles Rising in Line. *Int. J. Multiph. Flow* **1996**, *22*, 239–258. [CrossRef]
30. Chen, R.C.; Lu, Y.N. The flow characteristics of an interactive particle at low Reynolds numbers. *Int. J. Multiphase Flow* **1999**, *25*, 1645–1655. [CrossRef]

fluids

MDPI

Article

The Influence of Mitral Valve Asymmetry for an Improved Choice of Valve Repair or Replacement

Dario Collia [1,*,†] and Gianni Pedrizzetti [1,2,†]

[1] Department of Engineering and Architecture, University of Trieste, 34127 Trieste, Italy
[2] Department of Biomedical Engineering, University of California, Irvine, CA 92617, USA
* Correspondence: dario.collia@dia.units.it
† These authors contributed equally to this work.

Abstract: The study of valve asymmetry represents an important avenue for modern cardiac surgery. The correct choice of leaflet reconstruction may indicate a new path in the quality and long-term survival of patients. A systematic investigation was performed with a total of 25 numerical simulations using a healthy ventricle and an ideal valve with varying degrees of valve asymmetry. An overall assessment is made in terms of vorticity, kinetic energy, dissipated energy, and hemodynamic forces. The results indicate that the optimal asymmetry to consider for a valve repair or prosthetic design is between 0.2 and 0.4 with an optimal point of about 0.3. Out of this range, the heart is subjected to an excessive workload, which can only worsen the patient's state of health.

Keywords: CFD; mitral valve; valvular asymmetry; cardiovascular flow

Citation: Collia, D.; Pedrizzetti, G. The Influence of Mitral Valve Asymmetry for an Improved Choice of Valve Repair or Replacement. *Fluids* **2022**, *7*, 293. https://doi.org/10.3390/fluids7090293

Academic Editor: Mehrdad Massoudi

Received: 12 August 2022
Accepted: 2 September 2022
Published: 5 September 2022

Publisher's Note: MDPI stays neutral with regard to jurisdictional claims in published maps and institutional affiliations.

1. Introduction

The function of the mitral valve (MV) is to allow and regulate the correct access of blood into the left ventricle (LV). The MV has a characteristic elliptical shape and is composed of an annulus and two leaflets, posterior and anterior, respectively. Its function is crucial for correct ventricular functioning as it directs the flow within it, ensuring correct mixing and redirection of blood towards the aorta in healthy conditions. On the other hand, in pathological conditions, the leaflets of the MV have prolapsed and a quantity of the blood is regurgitated into the atrium during the systole. Depending on the different types of mitral regurgitation (MR) [1], there are different therapeutic solutions; in particular, in the cases of severe MR, the therapy is usually a cardiac surgery for valve repair or, less frequently, valve replacement with a prosthesis. Over the years, different methods have been developed to treat this pathology. The first option was the substitution with a mechanical or biological prosthetic valve; this, however, brings along several complications [2,3]. To date, the recommended treatment for degenerative mitral valve disease is mitral valve repair (MVR), as opposed to valve replacement with a biological or mechanical valve, because surgical valve reconstruction is associated with improved event-free survival [4,5]. Surgical MVR is the gold-standard therapeutic procedure for patients with degenerative mitral valve regurgitation [4,6] and follows two fundamental principles: restoring a good surface of leaflet coaptation and correcting for annular dilatation [4,7]. Transcatheter solutions represent additional options that are currently recommended only in patients at risk [5,8,9]. Although the reparation is the gold standard, endovascular replacement is expected to increase with the improvement in and availability of endovascular prostheses. One important point to consider during the planning of valve repair or for the good design of a valve prosthesis is the identification of the appropriate range of valve asymmetry [10]. The present study uses the approach of direct numerical simulation (DNS) to provide indication of this range. Several techniques have been introduced in the literature to overcome the numerical difficulties due to the movement of the numerical domain, including the formulations of space-time finite elements, immersed boundary methods, the method of level sets,

the fictitious domain method, unfit finite elements and the arbitrary Lagrangian–Eulerian formulation (ALE) [11–14]. The numerical method, used in this work, was extensively employed in previous studies, and technical details are described in a dedicated methodological validation study [15], where the valvular dynamics were compared with that obtained with complete fluid–structure interaction [16]. In a previous study [10], the proper range of valve asymmetry is investigated in terms of false and effective regurgitation, as well as a thorough distribution of washout in healthy, pathological, and repaired cases with different levels of valve asymmetry. Therein, the physiological degree of asymmetry was found to be associated with small regurgitation and a proper ventricular wash-out for normal ventricles. This work follows up to provide a more comprehensive assessment and indication of the proper range of valve asymmetry to be used for a repair or prostheses design, and we extend the previous study and analyze the results from an energetic and mechanical point of view by investigating how valve asymmetry affects hemodynamic forces and the amount of kinetics energy produced and dissipated.

2. Materials and Methods

2.1. Geometries

A total of 25 numerical simulations were performed and analyzed using the same healthy LV for 25 MVs, each with a different degree of valve asymmetry. The time-varying geometry of a healthy LV has been extracted from 3D echocardiography; the moving borders were obtained by a semi-automatic procedure within a dedicated software (4D LV analysis, Tomtec Imaging Systems GmbH, Unterschleissheim, Germany). At every instant, the entire LV endocardial surface is described by its 3D coordinates, which are then interpolated on a structured mesh made of 768 points along the circumference and 384 points from the base to the apex. LV geometry during all phases of the heartbeat is described by the position vector $\mathbf{X}(\vartheta, s, t)$ of its endocardial surface, where the structured parametric coordinates (ϑ, s) run along the circumference and from base to apex, respectively, and t is time. The position vector marks the material points of the LV, and their velocity is obtained from temporal differentiation. The LV clinical parameters are: End Diastolic Volume (EDV) = 139 mL, End Systolic Volume (ESV) = 53 mL, Stroke Volume = 86 mL, Ejection Fraction (EF) = 62%, and E/A = 1.5.

A controllable geometry of the MV is obtained from an ideal model through a mathematical description introduced in a previous study [17]. The radius of the valve, $R = 1.5$ cm, is kept constant (to adapt to the LV geometry) and with the normal elliptical shape (a parameter that describes the ratio between the length of the flaps in the two perpendicular directions set at a value of $1/3$). The asymmetry of this valve is described by a dimensionless parameter ϵ that mimics the difference in length between the anterior and the posterior leaflets, normalized to their sum [17]. The asymmetry is modified starting from an extreme value $\epsilon = 0.6$ to the opposite extreme $\epsilon = -0.6$, where the lengths of the anterior and posterior leaflet are $(1 + \epsilon)R$ and $(1 - \epsilon)R$, respectively. The analysis varies with continuity, with 25 positions selected with increments $\Delta\epsilon = 0.05$ between the two extreme values. In Figure 1, we show the complete geometry (a) with the semi-open valve at an instant indicated in the volume rate curve (b) and two MVs with asymmetry configurations, which are $\epsilon = 0.6$ and $\epsilon = -0.6$ (c,d). The MV geometries are reorganized for convenience in terms of another pair of parametric coordinates (ϑ, s), where s ranges from zero at the annulus to 1 and the trailing edge ϑ is the azimuthal angle.

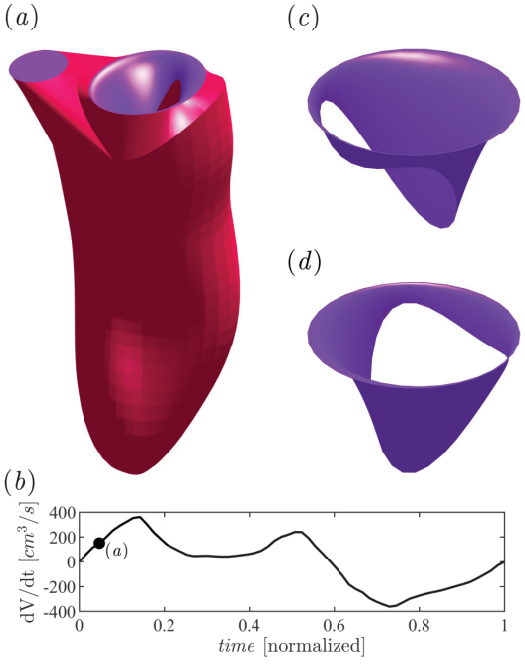

Figure 1. LV geometry (**a**) and its dV/dt curve (**b**). Ideal MV in semi-open configuration for $\epsilon = 0.6$ (**c**) and $\epsilon = -0.6$ (**d**), respectively.

The intermediate geometric configurations are reconstructed considering the two leaflets as moving independently of each other and each one associated with a degree of opening, say $\varphi_1(t)$ and $\varphi_2(t)$, for the anterior and posterior leaflets, respectively, that range from zero (closed leaflet) to $\frac{\pi}{2}$ (fully open). Therefore, the valve is mathematically described by its coordinates $\mathbf{X}_v(\vartheta, s, \varphi_1, \varphi_2)$. This parametric expression represents a two-dimensional set of all the possible valve configurations that are preliminarily calculated depending on two degrees of freedom (the opening degree of the two leaflets) between a fully closed configuration, $\mathbf{X}_v(\vartheta, s, 0, 0)$, when both angles are 0 and a fully open $\mathbf{X}_v(\vartheta, s, \frac{\pi}{2}, \frac{\pi}{2})$ when both angles are $\frac{\pi}{2}$. The dynamic equation of the leaflet-opening angles was obtained by the constraint that the motion of the leaflet surface must match the velocity of the fluid at the position of the same surface; a brief description is given below. A comprehensive description and verification of the computational method, including a comparison with a fluid–structure interaction model with a given set of tissue parameters, are reported elsewhere [15]. In synthesis, the valvular leaflets are assumed to move with the flow with no elastic resistance other than the constraint of remaining in the set of configurations described by the two degrees of freedom. Under this assumption, the leaflet dynamics are obtained by least-squares minimization of the difference, integrated over the valvular surface $\mathbf{A}_v$, between the fluid and the valve velocity component normal to the valvular surface. The result is a system of linear equations whose i^{th} term reads

$$\left[\int_{A_v}\left(\frac{\partial \mathbf{X}_v}{\partial \varphi_i}\cdot\boldsymbol{n}\right)\left(\frac{\partial \mathbf{X}_v}{\partial \varphi_j}\cdot\boldsymbol{n}\right)dA\right]\frac{d\varphi_j}{dt} = \int_{A_v}(\boldsymbol{v}\cdot\boldsymbol{n})\left(\frac{\partial \mathbf{X}_v}{\partial \varphi_i}\cdot\boldsymbol{n}\right)dA \quad (1)$$

where v is the fluid velocity and $\boldsymbol{n}$ the local normal to valvular surface. $i = 1, 2$, for the 2 degrees of freedom MV, and summation over $j = 1, 2$ is implicitly assumed. The dynamic

model described by system (1) represents an asymptotic limit of the loosest MV within the prescribed two-dimensional set of geometric configurations; as the model reproduces an asymptotic behavior, it does not require the introduction of mechanical parameters of the tissues that would otherwise be necessary for solving the momentum equation for the solid. On one hand, this is an advantage for applications where such properties are not available or cannot be measured; on the other, this model represents an approximation with respect to a complete calculation with fluid–structure interaction. This simplifies the solution that is aimed to reproduce the main properties of the LV fluid dynamics in the presence of a moving MV, assumed to have loose moving elements when the general properties of the valvular structure are not available. The absence of papillary muscles and chordae tendineae represent a limitation of the model. Here, the unidirectional valvular flow, avoiding the valve from opening towards the atrium, is ensured internally by the constraint on the degree of freedom that plays a surrogate function for the chordae tendinae. On the other hand, the presence of these anatomical structures inside the ventricle may influence the flow; however, the direct influence of these thin elements is expected to be marginal, and it was not evidenced in detailed analyses of blood flow recorded "in vivo" [18,19]. In this regard, this study has been extensively validated with an FSI model [15,16] and subsequently with a previous study [10] showing the homogeneity of the ideal MV with the real one and its movement. In the study by [20], it is shown how the presence of the chordae tendineae is not influential in the numerical simulation; the models with and without the cords showed similar results, and the essential thing is that the movement is faithfully reproduced, which was amply demonstrated for our cases [10,15,21–26]. A systematic analysis of the properties and limitations of such valvular modeling for flow simulation is reported in a dedicated methodological study [15]. The aortic valve, which is downstream of the LV flow fields, is modeled as a simple orifice with a surface that is either open or closed. This simple orifice model is represented by a surface that opens when two conditions apply: the MV is closed and the average normal velocity at the valve position is directed toward the aorta, and it is closed otherwise. In this way, it is not necessary to prescribe the open or closed state of the valve from global considerations because the exact start-to-end times of systole and diastole can be difficult to precisely define under pathological conditions. This AV model includes an explicit influence of the MV on the AV dynamics; on the other hand, the MV dynamics depends directly on the flow and by the fact that the AV is open or closed.

2.2. Fluid Dynamics

The numerical method is extensively described and validated in a dedicated methodological study [15], where the valvular dynamics are compared with those obtained by complete fluid–structure interaction [16]. In this section, we briefly recall the main points of the method used. The intraventricular fluid dynamics is evaluated by numerical solution of the Navier–Stokes and continuity equations

$$\frac{\partial \boldsymbol{v}}{\partial t} + \boldsymbol{v} \cdot \nabla \boldsymbol{v} = -\nabla p + \nu \nabla^2 \boldsymbol{v}, \tag{2}$$

$$\nabla \cdot \boldsymbol{v} = 0; \tag{3}$$

where $\boldsymbol{v}(t, \mathbf{x})$ is the velocity vector field, $p(t, \mathbf{x})$ is the kinematic pressure field and ν is the kinematic viscosity (assumed 0.04 cm^2/s). The solution is achieved by the immersed boundary method in a bi-periodic Cartesian domain as described in previous studies, e.g., [10,15,21,24,27]. Time advancement is achieved using a fractional step method as follows. Velocity is preliminarily advanced in time by the Navier–Stokes Equation (2) using a low-storage, third-order Runge–Kutta explicit scheme. Boundary conditions are set on the moving immersed boundaries that comprise the ventricle geometry and valve surface inside a bi-periodic domain with a grid made $128 \times 128 \times 160$ points and 8192 time steps per heartbeat. Then, the velocity is corrected by an irrotational field that projects the preliminary solution on a divergence-free vector field space.

2.3. Kinetic Energy and Dissipation Rate

The kinetic energy (KE) of the blood reflects a fundamental component of the work performed by the LV [28,29], and it is computed as follows

$$KE(t) = \frac{\rho}{2} \int_V v^2 \, dV, \tag{4}$$

where $V(t)$ is the ventricular volume, v the modulus of the velocity, and ρ the blood density. The KE dissipation rate

$$D(t) = \rho\nu \int_V S_{ij} \frac{\partial v_i}{\partial x_j} \, dV, \tag{5}$$

where S is the rate of deformation tensor and ν is the kinematic viscosity, provides a measure of the efficiency of blood flow and it is an indicator of ventricular function [25,30].

2.4. Vorticity and Vortex Formation Time

The formation of the vortex and its orientation inside the ventricle influence the correct course of the flow throughout the cardiac cycle until its expulsion [27,31]. The computation of the average vorticity inside the ventricle is

$$\overline{\omega} = \frac{1}{V} \int_V |\boldsymbol{\omega}| \, dV, \tag{6}$$

where $\boldsymbol{\omega}(t) = \nabla \times \boldsymbol{v}$ is the vorticity vector field. The vortex formation time (VFT) is an important parameter used for the evaluation of LV function [32]; this dimensionless parameter is computed as

$$VFT = \int_{T_E} D^{-1} \, v_{MVO} \, dt, \tag{7}$$

where v_{MVO} is the mean velocity across the MV orifice [10,21], D the average diameter, and T_E is the diastolic E-wave period. This parameter measures the quality of the vortex formation process and optimal LV filling. Recent studies [33] have shown that the optimal range is $3 \leq \text{VFT} \leq 4$, although a value up to 5 is also considered acceptable [34]. High values are associated with the breakdown of the forming vortex and turbulence, while lower values correspond to suboptimal propulsion [35].

2.5. Hemodynamic Forces

The forces exchanged between blood and the surrounding tissues have special relevance in ventricular function as they are found to have a role in modulating the response to morphogenesis in embryonic hearts [36], as well as to pathologies in adult hearts [37]. In particular, the hemodynamic force (HDF) is the global force exchanged that is made by the integral of the intraventricular pressure gradient and to a minor extent, of the viscous forces. HDF depends on the intraventricular flow and may help reveal a sub-optimal cardiac function when contraction or relaxation does not develop in association with a proper intraventricular pressure gradient. The HDF vector is obtained by the integral over the volume of the force density that is on the right side of (2) and can be computed by

$$\mathbf{F}(t) = \rho \int_{V(t)} \left[\frac{\partial \boldsymbol{v}}{\partial t} + \boldsymbol{v} \cdot \nabla \boldsymbol{v} \right] dV. \tag{8}$$

The volume integral in Equation (8) can also be rewritten, with the aid of the Gauss theorem, as a surface integral and evaluated from the dynamics of the endocardial boundary and the exchange of momentum across the mitral and aortic orifices [38]. This gives a formula equivalent to (8) that reads

$$\mathbf{F}(t) = \rho \int_{S(t)} \left[\boldsymbol{x} \left(\frac{\partial v}{\partial t} \cdot \boldsymbol{n} \right) + \boldsymbol{v}(\boldsymbol{v} \cdot \boldsymbol{n}) \right] dS, \tag{9}$$

where $S(t)$ is the closed surface bounding the volume, comprising both the tissue and the valvular orifices, and $\boldsymbol{n}$ is the outward unit normal vector. The second expression (8) is often simpler to compute numerically and is used here.

3. Results

Fluid Dynamics, Vortex Formation, and Energetic Analysis

Before discussing the results, in Figure 2, we show the dV/dt curve obtained from the LV geometry superimposed to the diastolic flow rate measured across the MV in the two limit cases: LV with MV ($\epsilon = 0.6$ and $\epsilon = -0.6$, respectively). The three curves are not distinguishable as they overlap almost exactly; this preliminary validation test is aimed to confirm the consistency of the numerical results and the equality of the amount of blood entering for all cases to verify that any variation is imputable to the MV asymmetry only.

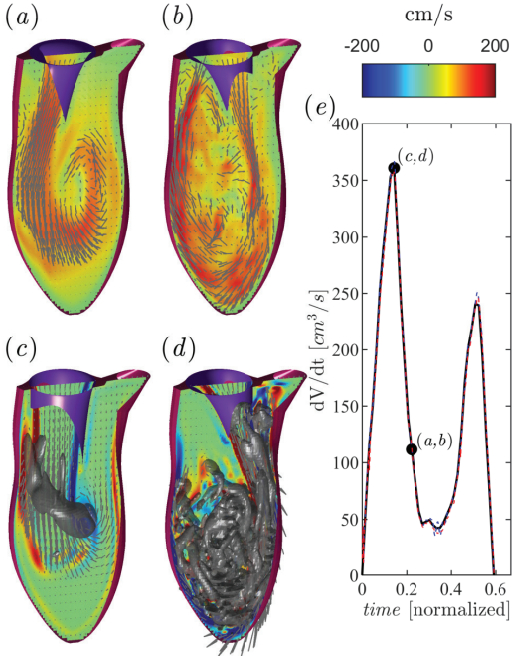

Figure 2. Velocity field of MV with (**a**) $\epsilon = 0.6$, (**b**) $\epsilon = -0.6$; flow field of MV with (**c**) $\epsilon = 0.6$, (**d**) $\epsilon = -0.6$ as indicated in the box of the dV/dt curve (**e**); the normal vorticity is shown in red to blue color from -200 units to 200 units (cm/s) equal to the inverse of the heartbeat period and the velocity vector (every 4 grid points) on a longitudinal plane crossing the center of MV of the aorta and the LV apex; the three-dimensional gray surfaces represent one isosurface of the λ_2 parameter.

In Figure 2a,b, we show the directionality of the diastolic flow inside the ventricle in the two limit cases ($\epsilon = 0.6$ and $\epsilon = -0.6$), and a more complete view of the intermediate points is shown in a previous study [10]. As seen in the previously mentioned study, a valve with positive asymmetry directs the flow to a physiological rotation with its extreme shape shown in Figure 2a; in the case of negative asymmetry, the direction of the flow is reversed and increases its velocity, which maintains the reversed flow direction during the entire filling phase. A very positive asymmetry highlights the predominance of the posterior leaflet with a very deviating flow toward the posterior wall; as we approach a more balanced direction between the two leaflets, the flow takes a more regular and physiological direction, while negative asymmetry reverses the flow direction and makes the valve behave as if it were reversed. This demonstrates qualitatively how the leaflet's asymmetry affects the direction of the flow. In Figure 2c we show the formation and direction of the vortex

ring in case with ϵ = 0.6. Compared with an ideal healthy case [10,15], the vortex is inclined and directed towards the left wall of the LV similarly to various pathological valve cases [10,21,23]. Instead, in Figure 2d, the flow is inverted ($\epsilon = -0.6$), the vortex breaks very early, and the vorticity increases due to the generation of turbulence inside the LV.

This point is supported by the result shown in Figure 3a reporting the $\overline{\omega}_{E_{peak}}$ values that are higher for $\epsilon-$ and decrease as the curve transits towards $\epsilon+$. This is also confirmed by the VFT values in Figure 3b. These results indicate how effectively an MV with $\epsilon-$ actually affects the ability of the LV to redirect flow to the systolic outlet. In fact, the VFT reaches more physical values when it approaches the direction of positive asymmetry, showing how good ventricular functionality corresponds to the correct distribution of the flow. Taking into account the values published in a previous work [22] and the existing literature [32–35], we identify an optimal range between ϵ = 0.15 and 0.6, considering that after ϵ = 0.4, fairly stationary values are found.

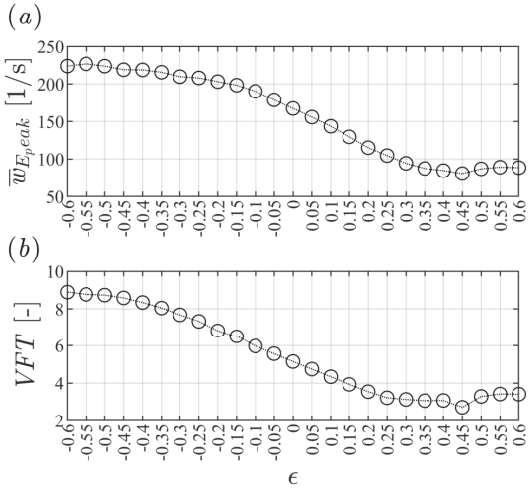

Figure 3. Graphical representation of (**a**) diastolic peak values of mean vorticity and (**b**) VFT values for different valve asymmetry.

The same behavior is found in terms of $KE_{E_{peak}}$, as shown in Figure 4a. The $KE_{E_{peak}}$ is higher for $\epsilon = -0.6$ and the distribution of these values for each level of valve asymmetry follows the same trend as in Figure 3. This production of KE is due to the higher mitral jet velocity in line with the orientation of the flow and the vorticity produced. When the valve asymmetry is reduced, the quantity of $KE_{E_{peak}}$ decreases until it returns to a more physiological value. Furthermore, in this case, there is an evident transition between positive and negative asymmetry. From the literature, it is easy to identify a normal range from the experimental observation performed with 4D Flow MR; this value is between 6 ± 0.6 for control cases [28] and 8.9 ± 1.1 for athletes [39]. The energy dissipation rate, $D_{E_{peak}}$, also follows the same trend and is in line with the existing values [22,40]; eventually from these results, the optimal values for valve asymmetry appear above ϵ = 0.2.

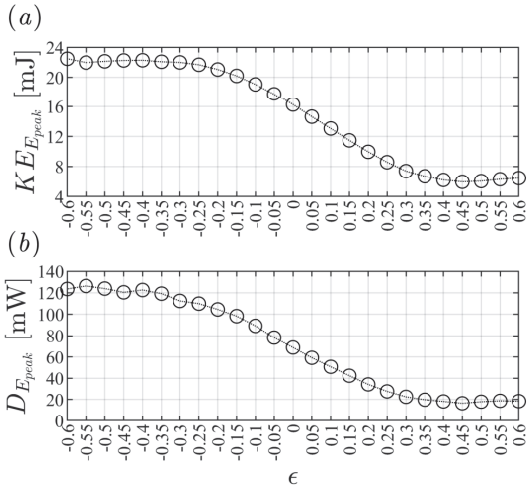

Figure 4. Graphical representation of (**a**) diastolic peak values of KE and (**b**) D for different valve asymmetry.

Figure 5a–c report the three components of the hemodynamic force during the E-wave curve. In panel (a), it can be seen how the sign of the x-component, Fx, where the x-axis is the lateral direction along the ideal line connecting the two valves, is largely affected by the asymmetry level until changing its sign. This is due to the different lengths and positions that the leaflets assume in different asymmetrical conditions. To confirm this, there is literature that describes the E-wave of the HDFs in the direction of x as positive [37,38,41–43], thus again marking the choice of $\epsilon-$ in a valve repair or design as non-physiologic. In the transverse direction, Fy values are similar and do not vary much; this is desirable since this direction is not directly affected by the valve movement. In the longitudinal direction, on the other hand, an increase in Fz can be noted in the $\epsilon-$ cases. This increase is not very high from the point of view of normality [44], but it may become relevant when it is a result of a valve repair or replacement. The $\epsilon+$ values are in line with the literature for healthy cases, while the $\epsilon-$ values are in line with the literature for healthy athletes and therefore require a trained heart [41,43]. A patient who undergoes cardiac surgery usually has a heart with very variable EF and dysfunctions dictated by valvular pathology. Repairing or replacing an MV with a non-physiological degree of valve asymmetry could induce higher stress to the ventricular tissues. This is important because the presence of the physiological components HDF support the correct redirection of blood from the MV towards the LV outflow tract, which does not occur in $\epsilon-$ cases. These results are summarized in Figure 5d–f, where the absolute values at peak systole are reported for different valve asymmetry. values This figure is useful for identifying the range and the optimal asymmetry value. In $|Fx_{E_{peak}}|$, there is a minimum point at $\epsilon = 0.3$, which corresponds to the asymmetry level that produces no lateral thrust, therefore, where the intraventricular pressure gradient is directed—on average—from the base to the apex. The transversal force $|Fy_{E_{peak}}|$ presents a variation in values that is minimal, irrelevant, and fairly constant for all $\epsilon+$ cases, while the longitudinal force, $|Fz_{E_{peak}}|$, displays a rapid decrease up to $\epsilon = 0.3$ and then moves into a stationary phase.

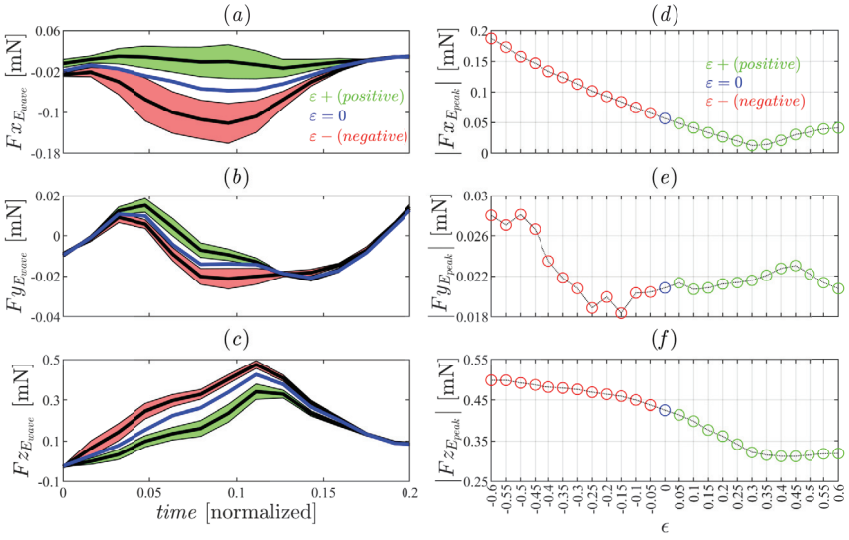

Figure 5. Graphical representation of HDF E-wave curve for different valve asymmetry of (**a**) Fx, (**b**) Fy and (**c**) Fz projections. Green color represent the *SD* of $\epsilon+$, blue line $\epsilon = 0$, red color the *SD* of $\epsilon-$ and black line the mean value for $\epsilon+$ and $\epsilon-$, respectively. Graphical representation of the HDF peak for different valve asymmetries of (**d**) $|Fx|$, (**e**) $|Fx|$ and (**f**) $|Fx|$ projections. Green represents $\epsilon+$, blue represents $\epsilon = 0$, and red represents $\epsilon-$.

4. Conclusions

The evaluation and determination of the proper valve asymmetry are crucial in cardiac surgery because a correct repair or a correct valve implant substantially increases the possibility of a long and better quality of life [45,46]. In a previous study on valve asymmetry [10], it was shown that an MV with negative asymmetry behaves like a turned MV. Those results show how the different asymmetrical positions of the leaflets and their length influence the flow direction inside the LV, affecting the amount of blood regurgitated in the atrium during systole in healthy, pathological, and repaired MV conditions. The ideal range is identified therein between $\epsilon = 0.2$ and $\epsilon = 0.4$ based on a global assessment of the ventricular washout. With this study, we extend the analysis including energetic and dynamic assessments using a different healthy LV. After verifying and confirming that the ventricular flow trend is equal to the previous study, we also verified the vortex formation and the vorticity generated in different situations of valve asymmetry. The results show how an $\epsilon-$ produces inverted flow and a vortex breaking early, generating high vorticity, which, associated with VFT, indicates the ventricular difficulty of directing the flow towards the systole, such that the ventricle is more stressed and fatigued. Consequently, high and non-physiological values of KE and D also confirm this and decrease with the reduction in ϵ until more natural values of $\epsilon+$ are obtained. The HDFs further highlighted this gap between $\epsilon-$ and $\epsilon+$ in an evident way in the Fx component, where the length and position of the two leaflets influence the orientation of the diastolic curve, making it non-physiological for $\epsilon-$ and positive for $\epsilon+$. In a more detailed way, the Fz component shows that the negative asymmetry values produce values similar to each other and comparable to an athlete's heart that does not find comfort, as occurs in patients who undergo these surgical practices in non-optimal conditions even with a preserved EF. The diastolic function of the LV plays an important role in cardiac physiology. Lusitropia, the ability of cardiac myocytes to relax, is affected by both biochemical events within the myocyte and biomechanical events in the LV [47]. An abnormal diastolic function has been recognized in many cardiovascular diseases and is associated with worse outcomes, including total mortality and hospitalizations for heart failure [48]. These results show

how $\epsilon-$ negatively influences diastolic function, indicating that MV repair or replacement in this direction has to be avoided. The optimal range of ϵ is between 0.2 and 0.4 with an optimum point of about 0.3. Despite the modeling limitations of the analysis, optimal values of asymmetry agree well with physiological values of asymmetry, as visible from the length of MV leaflets in healthy subjects [49]. The computational model used here should not be confused with an FSI model, primarily because it does include the elastic properties of the tissues that would be required to solve the momentum equation for the solid elements. Therefore, it describes an asymptotic behavior only and was designed to provide a relatively straightforward application of LV flow simulations in clinical conditions when the mechanical properties of tissue are not available or cannot be extrapolated. To reach this objective, the model includes a number of simplifications that correspond to a series of limitations that are described in a previous methodological article [15]. However, this model is already used and validated in the clinical setting for the evaluation of various physiological and pathological conditions [10,15,21–23,50]. Our results provide an indication before surgery, which can make it clearer to surgeons which type of valve asymmetry to use for a correct valve repair/replacement and above all what to expect in the case of a different solution. This could be a great help in preventing disastrous consequences and in directing the patient towards an optimal clinical condition. A limitation of this study is the lack of extension to cases with pathological LV; this is a deliberate choice to make a first complete valvular analysis. This evaluation will be extended to several LV cases in a subsequent study.

Author Contributions: D.C. and G.P. have made a substantial, direct and intellectual contribution to the work. All authors have read and agreed to the published version of the manuscript.

Funding: This research was funded by the Italian Ministry of Education, Universities and Research (MIUR); MIUR code: 2017A889FP_ 006; CUP code: J34I19001480001.

Institutional Review Board Statement: Not applicable.

Informed Consent Statement: The images of the human subjects were recorded at the Cardiovascular Department of the Azienda Sanitaria Universitaria Giuliano Isontina, Trieste. The geometries were provided in an anonymous form for the numerical study. All procedures involving human subjects have been performed in accordance with the Declaration of Helsinki and under the approval of the Ethics Committee of the University of Trieste (protocol no. 0025052).

Data Availability Statement: All data generated or analysed during this study are included in this published article.

Acknowledgments: The authors acknowledge the Research Project of National Interest PRIN 2017 "Fluid dynamics of hearts at risk of failure: towards methods for the prediction of disease progression".

Conflicts of Interest: The authors declare no conflict of interest.

References

1. Freed, A.; Levy, D.; Levine, R.A.; Larson, M.G.; Evans, J.C.; Fuller, D.L.; Lehman, B.; Benjamin, E.J. Prevalence and clinical outcome of mitral-valve prolapse. *N. Engl. J. Med.* **1999**, *341*, 1–7. [CrossRef]
2. Shapira, Y.; Vaturi, M.; Sagie, A. Hemolysis associated with prosthetic heart valves: A review. *Cardiol. Rev.* **2009**, *17*, 121–124. [CrossRef] [PubMed]
3. Cooper, K.C.; Wagner, R. Xenotransplantation. *Nonhum. Primates Biomed. Res.* **2012**, *1*, 391–402.
4. Adams, D.H.; Rosenhek, R.; Falk, V. Degenerative mitral valve regurgitation: Best practice revolution. *Eur. Heart J.* **2010**, *31*, 1958–1966. [CrossRef] [PubMed]
5. Elbey, M.A.; Dalan, L.P.; Attizzani, G.F. Value of MitraClip in reducing functional mitral regurgitation. *US Cardiol. Rev.* **2019**, *13*, 30. [CrossRef]
6. Castillo, J.G.; Anyanwu, A.C.; Fuster, V.; Adams, D.H. A near 100% repair rate for mitral valve prolapse is achievable in a reference center: Implications for future guidelines. *J. Thorac. Cardiovasc. Surg.* **2012**, *144*, 308–312. [CrossRef]
7. Carpentier, A. Cardiac valve surgery-the 'French correction'. *J. Thorac. Cardiovasc. Surg.* **1983**, *86*, 323–337. [CrossRef]
8. Colli, A.; Adams, D.H.; Fiocco, A.; Pradegan, N.; Longinotti, L.; Nadali, M.; Pandis, D.; Gerosa, G. Transapical NeoChord mitral valve repair. *Ann. Cardiothorac. Surg.* **2018**, *7*, 812–320. [CrossRef]

9. Stone, G.W.; Lindenfeld, J.A.; Abraham, W.T.; Kar, S.; Lim, D.S.; Mishell, J.M.; Whisenant, B.; Grayburn, P.A.; Rinaldi, M.; Kapadia, S.R.; et al. Transcatheter mitral-valve repair in patients with heart failure. *N. Engl. J. Med.* **2018**, *379*, 2307–2318. [CrossRef]
10. Collia, D. Mitral valve asymmetry in healthy, pathological, and repaired cases. *Phys. Fluids* **2021**, *22*, 077118. [CrossRef]
11. Danilov, A.; Lozovskiy, A.; Olshanskii, M.; Borgquist, R.; Vassilevski, Y. A finite element method for the Navier–Stokes equations in moving domain with application to hemodynamics of the left ventricle. *Russ. J. Numer. Anal. Math. Model.* **2017**, *32*, 225–236. [CrossRef]
12. Peskin, C.S. Numerical Analysis of Blood Flow in the Heart. *J. Comput. Phys.* **1977**, *25*, 220–252. [CrossRef]
13. Zakerzadeh, R.; Hsu, M.C.; Sacks, M.S. Computational methods for the aortic heart valve and its replacements. *Expert Rev. Med. Devices* **2017**, *14*, 849–866. [CrossRef] [PubMed]
14. Vassilevski, Y.; Liogky, A.; Salamatova, V. Application of Hyperelastic Nodal Force Method to Evaluation of Aortic Valve Cusps Coaptation: Thin Shell vs. Membrane Formulations. *Mathematics* **2021**, *9*, 1450. [CrossRef]
15. Collia, D.; Vukicevic, M.; Meschini, V.; Zovatto, L.; Pedrizzetti, G. Simplified mitral valve modeling for prospective clinical application of left ventricular fluid dynamics. *J. Comput. Phys.* **2019**, *398*, 108895. [CrossRef]
16. Meschini, V.; de Tullio, M.; Querzoli, G.; Verzicco, R. Flow structure in healthy and pathological left ventricles with natural and prosthetic mitral valves. *J. Fluid Mech.* **2018**, *834*, 271–307. [CrossRef]
17. Domenichini, F.; Pedrizzetti, G. Asymptotic Model of Fluid—Tissue Interaction for Mitral Valve Dynamics. *Cardiovasc. Eng. Technol.* **2015**, *6*, 95–104. [CrossRef]
18. Elbaz, M.S.M.; Calkoen, E.E.; Westenberg, J.J.M.; Lelieveldt, B.P.F.; Roest, A.A.W.; van der Geest, R.J. Vortex flow during early and late left ventricular filling in normal subjects: Quantitative characterization using retrospectively-gated 4D flow cardiovascular magnetic resonance and three-dimensional vortex core analysis. *J. Cardiovasc. Magn. Reson.* **2014**, *16*, 78. [CrossRef]
19. Arvidsson, P.M.; Kovács, S.J.; Töger, J.; Borgquist, R.; Heiberg, E.; Carlsson, M.; Arheden, H. Vortex ring behavior provides the epigenetic blueprint for the human heart. *Sci. Rep.* **2016**, *6*, 22021. [CrossRef]
20. Meschini, V.; de Tullio, M.D.; Verzicco, R. Effects of mitral chordae tendineae on the flow in the left heart ventricle. *Eur. Phys. J. E* **2018**, *41*, 27. [CrossRef]
21. Collia, D.; Zovatto, L.; Pedrizzetti, G. Analysis of mitral valve regurgitation by computational fluid dynamics. *APL Bioeng.* **2019**, *3*, 036105. [CrossRef] [PubMed]
22. Collia, D.; Zovatto, L.; Tonti, G.; Pedrizzetti, G. Comparative Analysis of Right Ventricle Fluid Dynamics. *Front. Bioeng. Biotech.* **2021**, *9*, 667408. [CrossRef] [PubMed]
23. Collia, D.; Pedrizzetti, G. Cardiac Fluid Dynamics in Prolapsed and Repaired Mitral Valve. In Proceedings of the XXIV AIMETA Conference 2019, Rome, Italy, 15–19 September 2019; Carcaterra, A., Paolone, A., Graziani, G., Eds.; Lecture Notes in Mechanical Engineering; Springer: Cham, Switzerland, 2020; pp. 857–867.
24. Pedrizzetti, G.; Canna, G.L.; Alfieri, O.; Tonti, G. The vortex an early predictor of cardiovascular outcome? *Nat. Rev. Cardiol.* **2008**, *11*, 545–553. [CrossRef] [PubMed]
25. Pedrizzetti, G.; Domenichini, F. Left ventricular fluid mechanics: The long way from theoretical models to clinical applications. *Ann. Biomed. Eng.* **2015**, *43*, 26–40. [CrossRef]
26. Celotto, C.; Zovatto, L.; Collia, D.; Pedrizzetti, G. Influence of mitral valve elasticity on flow development in the left ventricle. *J. Biomech.* **2019**, *75*, 110–118. [CrossRef]
27. Domenichini, F. On the consistency of the direct forcing method in the fractional step solution of the navier–stokes equations. *J. Comput. Phys.* **2008**, *227*, 6372–6384. [CrossRef]
28. Carlsson, M.; Heiberg, E.; Toger, J.; Arheden, H. Quantification of left and right ventricular kinetic energy using four-dimensional intracardiac magnetic resonance imaging flow measurement. *J. Heart Circ. Physiol.* **2011**, *302*, 893–900. [CrossRef]
29. Garg, P.; Crandon, S.; Swoboda, P.P.; Fent, G.J.; Foley, J.R.J.; Chew, P.G.; Brown, L.A.E.; Vijayan, S.; Hassell, M.E.C.J.; Nijveldt, R.; et al. Left ventricular blood flow kinetic energy after myocardial infarction—Insights from 4d flow cardiovascular magnetic resonance. *J. Cardiovasc. Magn. Res.* **2018**, *20*, 2344–2350. [CrossRef]
30. Hayashi, T.; Itatani, K.; Inuzuka, R.; Shimizu, N.; Shindo, T.; Hirata, Y.; Miyaji, K. Dissipative energy loss within the left ventricle detected by vector flow mapping in children: Normal values and effects of age and heart rate. *J. Cardiol.* **2015**, *66*, 403–410. [CrossRef]
31. Kilner, P.; Yang, G.; Wilkes, A.J.; Mohiaddin, R.; Firmin, D.; Yacoub, M. Asymmetric redirection of flow through the heart. *Nature* **2000**, *404*, 759–761. [CrossRef]
32. Kheradvar, A.; Rickers, C.; Morisawa, D.; Kim, M.; Hong, G.; Pedrizzetti, G. Diagnostic and prognostic significance of cardiovascular vortex formation. *J. Cardiol.* **2019**, *74*, 403–411. [CrossRef] [PubMed]
33. King, G.; Ngiam, N.; Clarke, J.; Wood, M.J.; Poh, K.K. Left ventricular vortex formation time in elite athletes. *Int. J. Cardiovasc. Imaging* **2019**, *35*, 307–311. [CrossRef]
34. Kheradvar, A.; Assadi, R.; Falahatpisheh, A.; Sengupta, P.P. Assessment of Transmitral Vortex Formation in Patients with Diastolic Dysfunction. *JASE* **2012**, *25*, 220–227. [CrossRef] [PubMed]
35. Mangual, J.O.; Kraigher-Krainer, E.; De Luca, A.; Toncelli, L.; Shah, A.; Solomon, S.; Galantic, G.; Domenichini, F.; Pedrizzetti, G. Comparative numerical study on left ventricular fluid dynamics after dilated cardiomyopathy. *J. Biomech.* **2013**, *46*, 1611–1617. [CrossRef] [PubMed]

36. Hove, J.R.; Köster, R.W.; Forouhar, A.S.; Acevedo-Bolton, G.; Fraser, S.E.; Gharib, M. Intracardiac fluid forces are an essential epigenetic factor for embryonic cardiogenesis. *Nature* **2003**, *421*, 172–177. [CrossRef]
37. Arvidsson, P.M.; Töger, J.; Carlsson, M.; Steding-Ehrenborg, K.; Pedrizzetti, G.; Heiberg, E.; Arheden, H. Left and right ventricular hemodynamic forces in healthy volunteers and elite athletes assessed with 4D flow magnetic resonance imaging. *Am. J. Physiol. Heart Circ. Physiol.* **2017**, *312*, H314–H328. [CrossRef]
38. Pedrizzetti, G. On the computation of hemodynamic forces in the heart chambers. *Am. J. Physiol. Heart Circ. Physiol.* **2019**, *95*, 109323. [CrossRef]
39. Steding-Ehrenborg, K.; Arvidsson, P.; Töger, J.; Rydberg, M.; Heiberg, E.; Carlsson, M. Determinants of kinetic energy of blood flow in the four-chambered heart in athletes and sedentary controls. *Am. J. Physiol. Heart Circ. Physiol.* **2016**, *310*, 113–122. [CrossRef]
40. Seo, J.; Mittal, R. Effect of diastolic flow patterns on the function of the left ventricle. *Phys. Fluids* **2013**, *25*, 110801. [CrossRef]
41. Pedrizzetti, G.; Arvidsson, M.; Töger, J.; Borgquist, R.; Domenichini, F.; Arheden, H.; Heiberg, E. On estimating intraventricular hemodynamic forces from endocardial dynamics: A comparative study with 4D flow MRI. *J. Biomech.* **2017**, *60*, 203–210. [CrossRef]
42. Arvidsson, P.M.; Töger, G.; Pedrizzetti, G.; Heiberg, E.; Borgquist, R.; Carlsson, M.; Arheden, H. Hemodynamic forces using four-dimensional flow MRI: an independent biomarker of cardiac function in heart failure with left ventricular dyssynchrony? *Am. J. Physiol. Heart Circ. Physiol.* **2018**, *315*, H1627–H1639. [CrossRef]
43. Vallelonga, F.; Airale, L.; Tonti, G.; Argulian, E.; Milan, A.; Narula, J.; Pedrizzetti, G. Introduction to Hemodynamic Forces Analysis: Moving Into the New Frontier of Cardiac Deformation Analysis. *J. Am. Heart Assoc.* **2013**, *10*, e023417. [CrossRef]
44. Faganello, G.; Collia, D.; Furlotti, S.; Pagura, L.; Zaccari, M.; Pedrizzetti, G.; Di Lenarda, A. A new integrated approach to cardiac mechanics: reference values for normal left ventricle. *Int. J. Cardiovasc. Imaging* **2020**, *36*, 2173–2185. [CrossRef]
45. Schnittman, S.R.; Itagaki, S.; Toyoda, N.; Adams, D.H.; Egorova, N.N.; Chikwe, J. Survival and long-term outcomes after mitral valve replacement in patients aged 18 to 50 years. *J. Thorac. Cardiovasc. Surg.* **2018**, *155*, 96–102. [CrossRef]
46. Chikwe, J.; Toyoda, N.; Anyanwu, A.C.; Itagaki, S.; Egorova, N.N.; Boateng, P.; El-Eshmawi, A.; Adams, D.H. Relation of Mitral Valve Surgery Volume to Repair Rate, Durability, and Survival. *J. Am. Coll. Cardiol.* **2018**, *69*, 2397–2406. [CrossRef]
47. Villars, P.S.; Hamlin, S.K.; Shaw, A.D.; Kanusky, J.T. Role of diastole in left ventricular function, I: Biochemical and biomechanical events. *Am. J. Crit. Care* **2004**, *13*, 394–403. [CrossRef]
48. Nagueh, S.F. Left Ventricular Diastolic Function: Understanding Pathophysiology, Diagnosis, and Prognosis with Echocardiography. *JACC Cardiovasc. Imaging* **2020**, *13*, 228–244. [CrossRef]
49. Oliveira, D.; Srinivasan, J.; Espino, D.; Buchan, K.; Dawson, D.; Shepherd, D. Geometric description for the anatomy of the mitral valve: A review. *J. Anat.* **2020**, *237*, 209–224. [CrossRef]
50. Pandis, D.; Anyanwu, A. Commentary: Four-dimensional left ventricular flow imaging after surgical valve reconstruction—Pretty pictures or marker of repair quality? *J. Thorac. Cardiovasc. Surg.* **2020**, *163*, 962–964. [CrossRef]

fluids

MDPI

Review

Dilational Rheology of Fluid/Fluid Interfaces: Foundations and Tools

Eduardo Guzmán [1,2,*], Armando Maestro [3,4,*], Carlo Carbone [1], Francisco Ortega [1,2] and Ramón G. Rubio [1]

[1] Departamento de Química Física, Facultad de Ciencias Químicas, Universidad Complutense de Madrid, Ciudad Universitaria s/n, 28040 Madrid, Spain
[2] Instituto Pluridisciplinar, Universidad Complutense de Madrid, Paseo Juan XXIII 1, 28040 Madrid, Spain
[3] Centro de Física de Materiales (CSIC, UPV/EHU), Paseo Manuel de Lardizabal 5, 20018 San Sebastián, Spain
[4] IKERBASQUE—Basque Foundation for Science, Plaza Euskadi 5, 48009 Bilbao, Spain
* Correspondence: eduardogs@quim.ucm.es (E.G.); armando.maestro@ehu.eus (A.M.); Tel.: +34-913944107 (E.G.); +34-943018935 (A.M.)

Abstract: Fluid/fluid interfaces are ubiquitous in science and technology, and hence, the understanding of their properties presents a paramount importance for developing a broad range of soft interface dominated materials, but also for the elucidation of different problems with biological and medical relevance. However, the highly dynamic character of fluid/fluid interfaces makes shedding light on fundamental features guiding the performance of the interfaces very complicated. Therefore, the study of fluid/fluid interfaces cannot be limited to an equilibrium perspective, as there exists an undeniable necessity to face the study of the deformation and flow of these systems under the application of mechanical stresses, i.e., their interfacial rheology. This is a multidisciplinary challenge that has been evolving fast in recent years, and there is currently available a broad range of experimental and theoretical methodologies providing accurate information of the response of fluid/fluid interfaces under the application of mechanical stresses, mainly dilational and shear. This review focused on providing an updated perspective on the study of the response of fluid/fluid interfaces to dilational stresses; to open up new avenues that enable the exploitation of interfacial dilational rheology and to shed light on different problems in the interest of science and technology.

Keywords: area; compression; dilation; expansion; interfaces; rheology; surface excess

Citation: Guzmán, E.; Maestro, A.; Carbone, C.; Ortega, F.; Rubio, R.G. Dilational Rheology of Fluid/Fluid Interfaces: Foundations and Tools. *Fluids* **2022**, *7*, 335. https://doi.org/10.3390/fluids7100335

Academic Editor: Mehrdad Massoudi

Received: 15 September 2022
Accepted: 17 October 2022
Published: 20 October 2022

1. Introduction

Complex fluid/fluid interfaces are ubiquitous, be it in nature, industry, or academia. For instance, they can be exploited to provide structure to different products, including foam and emulsion-based items. Moreover, they are present in a broad range of chemical processes, including liquid-liquid extraction, froth flotation, wastewater treatment, or tertiary oil recovery. On the other hand, fluid/fluid interfaces can be exploited as platforms for nanostructured material fabrication, or as models to elucidate problems with biological and medical relevance [1–5]. Therefore, it may be expected that most of the fluid/fluid interfaces with technological or scientific relevance involve systems operating under dynamic conditions, and hence, the understanding of the dynamic and mechanical properties of interfacial layers laden at fluid/fluid interfaces is of paramount importance for living systems, foods, personal care products, and the environment [6].

The rheological performance of fluid/fluid interfaces can be modulated almost at will, to design soft interface-dominated materials for specific applications [7,8]. This makes understanding the deformation and flow of fluid/fluid interfaces under the application of mechanical stresses, i.e., the rheological properties of the interface, a matter of key importance for science and technology [9,10]. For instance, the understanding and control of the rheological response of fluid/fluid interfaces plays a very important role in the control of emulsion stability [11,12], foamability and foam stability (resistance against drainage) [13],

lung surfactant performance [4,14], aerosol formation [15], tear film stability [16,17], encapsulation process [18], coffee ring formation [19], tertiary oil recovery [20], or remote sensing [21,22].

The description of the rheological response of 2D systems (or more correctly, quasi-2D systems), i.e., layers of surface-active compounds confined at fluid/fluid interfaces, is not always trivial. In fact, interfacial rheology relies on the confinement of the applied deformation within the xy plane, which requires to introduce specific modification to the classical rheological formalism used for the study of the mechanical response of bulk systems. This is of a paramount importance because, in most of the cases, the small thickness of fluid/fluid interfaces makes it difficult to decouple the pure interfacial rheological response from the contribution associated with the response of the adjacent bulk phases to the applied stress. Therefore, it is necessary to develop suitable experimental and theoretical methodologies enabling such decoupling [23,24]. This is significant because the combination of experimental and theoretical tools may significantly contribute to the impact of the stress boundary conditions on the behavior and breakup of thin films [25].

Despite the importance of the mechanical properties of fluid/fluid interfaces for many technological and scientific purposes, there is a broad range of features that yet remains unclear, and deserving of additional research effort. Therefore, this review is focused on providing an updated perspective of the current understanding of the performance of fluid/fluid interfaces under the application of dilational stresses. This is important because dilational rheology plays an essential role in a broad range of scientific and technological features, ranging from the formation and stability of foams to the respiratory cycle, and from tertiary oil recovery to demulsification processes [20,26–28]. However, the study of the performance of interfaces under dilational stresses is particularly challenging because it requires one to deconvolute the changes in thermodynamic properties associated with the changes in the interfacial concentration and the intrinsic compressional viscoelasticity, which is not always easy [29]. To effectively conduct a study of the dilational rheology of fluid/fluid interfaces, the first part of the review is focused on the description of the physical bases governing the response of fluid/fluid interfaces upon the application of different mechanical stresses. Then, the most fundamental aspects of the interfacial behavior under the application of a dilational stress are discussed. Afterward, a discussion of the available experimental and theoretical tools for studying the dilational rheology of fluid/fluid interfaces is included. Finally, the effect of the non-linear character of the dilational deformation on the rheological response of fluid/fluid interfaces is briefly discussed.

2. Interfacial Rheology: Foundations

The adsorption of soluble species to the interface of a bulk solution, or the direct deposition of insoluble surface-active species at the interface, leads to the formation of the so-called Gibb and Langmuir monolayers, respectively. The formation of an interfacial layer at the fluid/fluid interface leads to the decrease of the interfacial tension, γ, in relation to that corresponding to the bare interface, γ_0. However, the use of the interfacial tension only provides an equilibrium description of the true picture of the interface and, as previously mentioned, this is not enough in most practical applications of fluid/fluid interfaces. In fact, fluid/fluid interfaces with technological and scientific relevance are commonly subject to external mechanical perturbations that result in a modification of their size or shape [30]. The understanding of the response of fluid/fluid interfaces to mechanical processes is essential, because even the simplest deformation processes can yield to very complex responses, including multiple dynamic processes or deformation mixing different interfacial modes [31].

The interfacial response against perturbations that modify the size of the interface, without affecting its shape, can be defined in terms of the dilational elasticity and viscosity; whereas, the modification of the interfacial shape without varying the dimensions of the interface, i.e., at constant size, is described in terms of the shear elasticity and viscosity [30,32]. Moreover, under specific stress conditions, fluid/fluid interface can undergo out-of-plane

deformations. These out-of-plane deformation modes lead to a displacement of the whole monolayer, or parts of the monolayer, in relation to the equilibrium position of the interfacial plane (splaying or bending), resulting in the emergence of different phenomena, e.g., buckling of the monolayer, expulsion of material into the bulk, or the formation of multilayers [33]. These transverse out-of-plane deformations are restored under the action of interfacial-tension-driven forces, whereas in-plane modes (shear and dilation) are directly restored by interfacial tension gradients associated with the interfacial concentration [24,34]. The interfacial tension gradients can emerge due to different factors, including the interfacial convection of adsorbed species or the heterogeneity of the adsorbed layers. However, the origin of the interfacial tension gradients occurring during interfacial rheology experiments is found in the externally triggered modification of properties, e.g., interfacial concentration, directly affecting the interfacial tension. This drives the Marangoni flows trying to restore interfacial equilibrium [31]. Figure 1 shows a sketch representing the in-plane and out-of-plane deformation modes that can occur in fluid/fluid interfaces under the action of mechanical stresses.

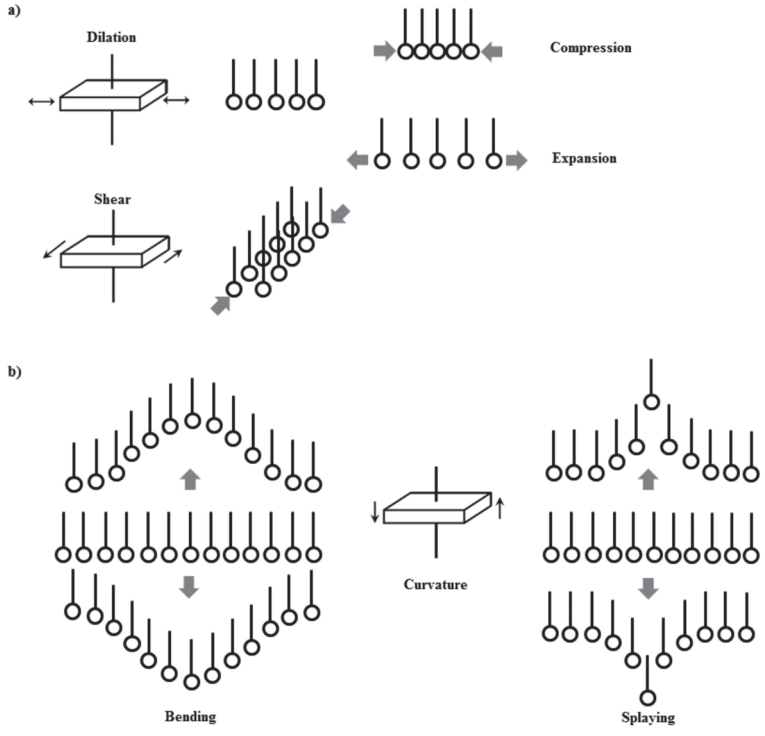

Figure 1. Sketch of different surface relaxation modes: (**a**) in-plane-modes (dilation and shear) and (**b**) out-of-plane modes (bending and splaying). Reprinted from Maestro and Guzmán [34], with permission under Open access CC BY 4.0 license, https://creativecommons.org/licenses/by/4.0/ (accessed 22 August 2022).

It should be noted that, in most of cases, the out-of-plane deformations can be rigorously modeled, whereas the in-plane modes have been commonly analyzed for long time using very simplified models that may be considered generalizations of the bulk behavior to the interface, which neglects some subtle aspects of the interfacial rheology, e.g., the existence of a finite dilational modulus, which is not considered in bulk models, designed for incompressible fluids or the role of the curvature modes [10,35]. Moreover, in most cases, the different rheological modes are coupled, and hence, the determination of the

real (storage modulus) and imaginary (loss modulus) components of the corresponding viscoelastic moduli is not always trivial. This can be understood considering that the origin on the interfacial property gradient can arise from different processes; e.g., interfacial tension gradients can be originated by a gradient of the interfacial concentration, or by the convective transport that generates a concentration gradient. This makes it difficult, in some cases, to independently obtain the different modes of the rheological response from a single experiment [31]. However, this coupling is of interest in specific cases, e.g., for obtaining dilational moduli from experiments involving capillary waves [36]. Moreover, the coupling between the interfacial response and the mechanical properties of the adjacent fluids or their structure may introduce additional problems for a proper evaluation of the viscoelastic moduli [23].

The rheological analysis of interfaces requires the use of a continuum mechanical approach. This assumes that bulk flows can be described in terms of the conservation equations for mass, momentum, and energy, and specific coupling conditions. This leads to the definition of the interface as a 2D dividing surface located between two adjacent fluid phases ("sharp interface" framework) [10]. Considering the above picture, it is possible to define the Cauchy interfacial stress tensor σ_s as a combination of two contributions: (i) the interfacial energy, which accounts for the energetic cost associated with the presence of a fluid interface of a fixed area, and provides information of any process changing the interfacial concentration and affecting the interfacial tension, and (ii) the Marangoni stresses emerging as a result of spatial interfacial tension gradients [9,10]. Thus, it is possible to define the interfacial stress tensor according to the following expression.

$$\sigma_s = \gamma(\Gamma,\ T)\delta_s + T_{ij}, \tag{1}$$

where δ_s is the surface unit tensor, and γ is the interfacial tension, which is a state variable depending on the interfacial concentration and temperature. The second contribution to the interfacial stress tensor is the anisotropic tensor or interfacial extra stress (T_{ij}), and accounts for the energy required to deform the interface [1,37]. The surface stress tensor can be considered as a 2D second-order symmetric and tangential tensor embedded in 3D space [9].

Considering a purely viscous fluid/fluid interface, it is possible to provide a definition of the anisotropic tensor in terms of the Boussinesq–Scriven model [9]:

$$T_v = [(\kappa_s - \eta_s)\nabla_s \cdot v]\delta_s + 2\eta_s D_s, \tag{2}$$

where κ_s and η_s are the interfacial dilational and shear viscosities, respectively. ∇_s is the interfacial gradient operator, v is the velocity vector on the interface, and D_s is the interfacial rate-of-deformation tension [38]. In general, the Boussinesq–Scriven model is used for defining the rheological properties of fluid/fluid interfaces due to the viscoelastic character of most fluid/fluid interfaces [39].

In the case of a purely elastic fluid/fluid interface, it is possible to define the anisotropic tensor by a linear elastic model, according to the following expression (only valid for infinitely small deformations) [10]:

$$T_e = [(E_s - G_s)\nabla_s \cdot u]\delta_s + 2G_s U_s, \tag{3}$$

with E_s and G_s being the interfacial dilational and shear elasticity, respectively; u the displacement vector on the interface; and U_s the interfacial infinitesimal strain tensor. It should be noted that bending stresses can also play a very important role under specific conditions, e.g., densely packed particle-laden fluid/fluid interfaces. However, for simplicity they are commonly not included [9].

The description of elastic interfaces against larger stresses requires the introduction of a finite strain tensor. This is possible by separating the dilational and shear contributions in an interfacial elastic stress described by the following expression [40]:

$$T_e = \frac{E_s}{\mathrm{Y}} \ln(\mathrm{Y})\delta_s + \frac{G_s}{\mathrm{Y}}\left(\frac{B_s}{\mathrm{Y}} - \frac{1}{2} tr\left(\frac{B_s}{\mathrm{Y}}\right)\delta_s\right), \tag{4}$$

where the deformations are defined by the left-Cauchy-Green interfacial strain tensor B_s, and Y is the relative area deformation, i.e., the ratio between the instantaneous interfacial area and the interfacial area in a reference state. The combination of the two limit cases, i.e., the Newtonian and the quasi-linear neo-Hookean, is essential for a realistic description of real fluid/fluid interfaces, where viscoelasticity is of a paramount importance [9].

3. Interfacial Dilational Rheology: General Aspects

The determination of the response of interfaces against dilation offers different experimental and theoretical challenges that are not present when the properties against shear stresses are evaluated. In fact, the application of isotropic dilational stresses to the interface, without any shear influence, is very difficult [9,41]. Moreover, the change in the interfacial area is associated with the change in the interfacial concentration of the surface-active molecules existing at the interface, which yields a change in the state variable, i.e., the interfacial tension. On the other hand, when soluble surface active molecules are concerned, the modification of the interfacial concentration may be accompanied by exchange processes involving the transference of molecules between the interface and the bulk, which introduces, in many cases, additional relaxation processes to the problem [9]. In fact, the ability of surface molecules and active soluble molecules to diffuse (diffusivity) from the adjacent fluid phases to the interface, and from the interface into the adjacent fluid phases as result of the modification of the interfacial area, can originate surface tension changes which are counteracted by the Marangoni flows, aimed toward re-establishing the interfacial equilibrium.

The application of an infinitesimal uniaxial mechanical perturbation to a fluid/fluid interface leads to a small change of the surface area, δA, which induces a time dependence modification of the interfacial pressure by a $\delta\Pi$ quantity (with Π being the interfacial pressure defined as $\Pi = \gamma - \gamma_{12}$, and γ_{12} the interfacial tension of a fluid/fluid interface loaded with surface active molecules). This change strongly emerges dependent on the timescale probed during the specific experiment, and can be approximated according to the following expression:

$$\delta\Pi(t) = \Pi(t) - \Pi_0 = \frac{\partial \Pi}{\partial t}\delta A = -E(t)u(t), \tag{5}$$

where $u(t)$ and $E(t)$ account for the temporal dependence of the compressional strain and dilational viscoelastic modulus, respectively, and $\Pi(t)$ and Π_0 account for the temporal evolution of the interfacial pressure and the initial interfacial pressure, respectively. Thus, it possible to define the time evolution of the viscoelastic dilational modulus in terms of the following expression:

$$E(t) = -A_0\left(\frac{\partial \Pi}{\partial A}\right)_T, \tag{6}$$

and that corresponding to the compressional strain as:

$$u(t) = \frac{\delta A}{A_0}. \tag{7}$$

From an experimental perspective, the dilational rheology measurements rely on the application of a time-dependent stress to the interface, and the evaluation of the time-dependent change of the interfacial tension. These type of measurements allow for the

evaluation of the ratio between the temporal evolution of the interfacial tension and the time-dependent stress, which is defined as the complex dilational viscoelastic modulus [42]:

$$E(\omega) = \frac{\mathcal{F}\{\Delta\gamma(t)\}}{\mathcal{F}\{\Delta \ln(A(t))\}}, \tag{8}$$

where $\mathcal{F}$ is the Fourier transform function, $\Delta\gamma(t)$ is the time evolution of the interfacial tension, $A(t)$ is the time evolution surface area, and ω is the angular frequency. The complex modulus can be split into its real (E_s) and imaginary components (E_v), which correspond to the storage and loss moduli, respectively [43,44]. Assuming an oscillatory deformation of small amplitude and a fixed frequency ω, it is possible to define the complex dilational viscoelastic modulus as complex magnitude according to the following expression:

$$E(\omega) = E_s(\omega) + iE_v(\omega) = E_s(\omega) + \mathrm{i}\omega\kappa_s, \tag{9}$$

with the loss moduli allowing one to calculate the dilational viscosity $\kappa_s = E_v/\omega$, and the storage modulus E_s defining the dilational elasticity. It should be stressed that the constitutive viscoelastic parameters $E_s(\omega)$ and $\omega\kappa_s$ are functions of ω. Therefore, they provide information about the time-dependent response of the system subject to small perturbations of the interfacial area, playing a central role in probing the interfacial dynamics of adsorbed films.

The definition of the viscoelastic interfacial dilational modulus accounts for a change in the applied stress as a result of the adsorption/desorption state of the molecules and the interfacial structure. Thus, interfacial area changes can promote different relaxation processes, with different characteristic timescales, that are associated with the different mechanisms involved in reestablishing the equilibrium state of the interface after the dilational deformation [45–47].

For fluid layers under equilibrium condition, or when the layers are disturbed following a quasi-static path ($\omega \to 0$), the interfacial dilation forces an instantaneous modification of the interfacial concentration ($\delta A/A = -\delta\Gamma/\Gamma$), and it is possible to define a limit value for the dynamic modulus at zero frequency. This is the so-called static modulus, which is given by the Gibbs elasticity ε_0, defined as:

$$E_s(\omega \to 0) \to \varepsilon_0 = \Gamma\left(\frac{\partial\Pi}{\partial\Gamma}\right)_{eq}, \tag{10}$$

Hence, this apparent elasticity can be considered a result of the deformation-induced change in the interfacial concentration ($\Gamma = 1/A$), which in turn modifies the interfacial tension. This magnitude can be obtained from the relative slope of the equilibrium isotherm [30]. According to the above discussion, it is possible to define a dilational viscosity at zero frequency in terms of the frequency independent Newtonian limit:

$$\kappa_s(\omega \to 0) = \kappa_0, \tag{11}$$

Figure 2 summarizes the typical material response expected for a viscoelastic layer undergoing a single relaxation process as a result of the dilational deformation.

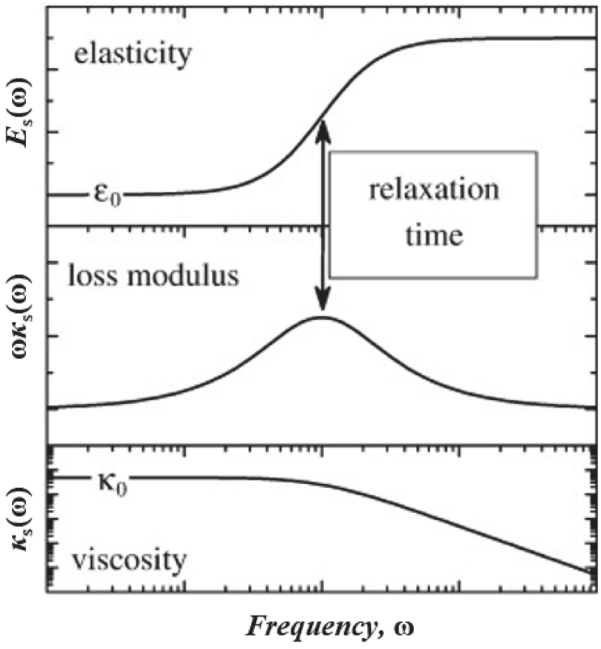

Figure 2. Sketch of the typical material response for a viscoelastic layer undergoing a single relaxation process upon the application of a dilational stress. Adapted from Mendoza et al. [30], with permission from Elsevier, Copyright (2014).

4. Rheological Tools for Evaluating the Response of Planar Fluid/Fluid Interfaces against Dilation

The last few years have been very fruitful in terms of the development of suitable tools to measure the response of planar fluid/fluid interfaces against dilational deformation [48,49]. Unfortunately, many of such tools provide information of the response against deformations within the linear response regime, which does not provide, in most cases, a suitable representation of some of the phenomena occurring in complex fluid/fluid interfaces, which are of technological and scientific interest [6,9]. However, these tools provide important information regarding the relaxation mechanism driving the re-equilibration of the interface upon dilational deformations. In fact, the experimental and theoretical tools of the interfacial dilational rheology provide information about the exchange mechanisms of material between the interface and the adjacent fluid phases, as well as the different reorientation and exchange process occurring between molecules confined within the interface [50–52]. This section focuses on the description of the most fundamental methodological features of the determination of the dilational response of planar fluid/fluid interfaces. However, it should be stressed that even the description of the mechanical response of curved interfaces is not discussed in this work. The understanding of the rheological response of curved interfaces has gained importance due to their recognized role in terms of its technological importance, including the stability of emulsions and foams, or coffee-ring formations upon the evaporation of liquid droplets deposited on solid substrates [19,53,54].

4.1. Experimental Tools

The characterization of the dilational response of interfacial layers requires careful selection of the most suitable technique, as well as appropriate experimental conditions. Several experimental techniques can be applied for evaluating the response of fluid/fluid interfaces to dilational stresses, offering different sensitivities and measurement ranges [50].

This section provides a brief overview of the types of experiments and experimental techniques that are currently available for studying fluid/fluid interfaces subjected to dilational deformations.

4.1.1. Experimental Techniques

This section includes a brief overview of the most common methodologies used for evaluating the dilational properties of fluid/fluid interfaces. A more detailed discussion about the experimental techniques used for this purpose may be found in references [9,50].

Drop/Bubble Shape Tensiometers

The use of drop/bubble shape tensiometers on the evaluation of the dilational viscoelasticity of fluid/fluid interfaces relies on the determination of the time evolution of the interfacial tension during harmonic changes of the area at a fixed frequency. This information can be extracted from an analysis of the changes occurring in the drop/bubble shape profile during the process, and is achieved by applying the Young–Laplace equation. This approach provides a framework to calculate the interfacial tension, by assuming that the contributions associated with shear are negligible. Therefore, the analysis of the drop/bubble shape profile can be only exploited for rheological simple interfaces characterized by an isotropic and constant stress along the whole interface.

$$(\kappa_1 + \kappa_2)\gamma = p - \rho g z, \tag{12}$$

where κ_1 and κ_2 are the curvature radius of the drop/bubble, p is the pressure difference across the interface, g is the gravitational acceleration, ρ the fluid density, and z the vertical coordinate. It is worth noting that the deformation of drops/bubbles cannot be always assumed as purely radial. Moreover, the drop/bubble requires an instantaneous mechanical equilibrium for a correct evaluation of the interfacial tension, which limits the applicability of drop/bubble shape tensiometers for the evaluation of the interfacial dilational modulus for deformation frequencies in the range 10^{-3}–0.2 Hz [55].

It is worth mentioning that the evaluation of the interfacial tension by applying Equation (12) is not always straightforward, especially because it is often difficult to obtain accurate values of the curvature radius. This can be commonly solved, considering that drops/bubbles undergo an axisymmetric deformation under the application of an external force. This condition is not fulfilled when densely coated drops and bubbles are considered [56,57].

In general, the use of drop/bubble shape tensiometers for evaluating the dilational properties assumes the existence of a single isotropic and constant tension for the entire interface. This allows for the application of the generalized Young–Laplace equation [58]:

$$\kappa_\Phi \sigma_\Phi + \kappa_s \sigma_s = p - \rho g z, \tag{13}$$

with κ_Φ and σ_Φ defining the principal curvature and stress in circumferential direction, respectively, whereas κ_s and σ_s account for the principal curvature and stress in meridional direction, respectively. The interfacial stresses are magnitudes that depend on the interfacial deformation; hence, its evaluation should be locally performed because the deformation may not be constant within the whole drop/bubble. On the other hand, when the deformations are non-isotropic, the principal interfacial stresses become equal [9].

Capillary Pressure Tensiometers

An alternative approach for evaluating the dilational rheological properties of fluid/fluid interfaces relies on the determination of the capillary pressure inside droplets or bubbles, together with their dimensions. In this case, the determination of the interfacial tension does not require a strong gravitational deformation of the drops/bubbles, which was necessary with conventional shape tensiometers [59]. This allows a reduction in the size of the drops/bubbles used (in the range 20–200 μm). Thus, it is possible to reduce cap-

illary and inertial relaxation times, enabling an extension of the probed frequencies up to 100 Hz [45]. Moreover, this approach reduces the role of the shear contributions on the deformation, making acceptable the isotropic assumption for the resolution of the Young–Laplace equation to determine the interfacial tension [9,10,60].

In recent years, methods using oscillating drops/bubbles have been further developed to extend the frequency range that can be probed. One of the most popular alternatives for this purpose is to design a device consisting of a closed cell, a pressure sensor, and a piezo translator, which monitors the time evolution of the capillary pressure during the experiments. Thus, it is possible to determine the rheological properties of fluid/fluid interfaces in the 0.5–450 Hz range. Moreover, this type of device allows for the measurement of the rheological properties of interfaces formed for two fluids with very similar densities [56,61].

Langmuir Troughs

The Langmuir trough is a common experimental setup used for studies dealing with the dilational properties of fluid/fluid interfaces [62,63]. It consists of two barriers, arranged parallel at opposite extremes of the trough, that can be used to compress or expand the area available for the interface under controlled conditions. During the compression/expansion of the interface, the interfacial tension is monitored by using a surface balance fitted with a contact probe; generally, a Wilhelmy plate. This reduces the interfacial stress for specific deformation conditions [4].

It is worth mentioning that the interfacial stress measured in the Langmuir trough, as a result of a uniaxial deformation, in many cases, includes both dilational and shear components [64]. Moreover, special care is required for interpreting the rheological properties of solid-like layers obtained using Langmuir troughs, because in many cases the deformation field cannot be defined as homogeneous, and hence, it depends on the specific geometric constraints of the used trough [40,65]. The inability to apply a purely isotropic stress, which leads to rheological responses containing dilational and shear contributions, is a very important problem when interfaces with a complex microstructure are analyzed. The application of anisotropic stresses to such complex systems results in a rheological response characterized by the change of the area and the shape under compression [10,40]. This can be solved by introducing several modifications to the Langmuir trough to ensure a purely dilational deformation of fluid/fluid interfaces [40].

The most useful design of Langmuir trough to ensure a pure dilational deformation of planar fluid/fluid interfaces is the proposed by Pepicelli et al. [40]. This relies on a radial trough which is isotropically deformed by an elastic band held by twelve "fingers". The interfacial pressure is determined by using a Wilhelmy rod, ensuring radial symmetry. This type of device allows for the application of isotropic deformation, avoiding any shear effect on the interfacial deformation [66].

Wave Damping

A traditional approach exploited for the evaluation of the mechanical response of fluid/fluid interfaces against high frequency dilational deformations relies on the study of the damping of capillary waves. These can be generated upon the application of mechanically, thermally, or electrically driven perturbations of the interface, when their propagation happens along the fluid/fluid interface. During their propagation, the waves are dampened by the action of surface forces that try to restore the flatness of the interface [22,67–71].

The study of the rheological properties by the evaluation of the dampening of surface waves allows the study of information of the dilational properties of fluid/fluid interfaces up to frequencies of about 100 kHz [72]. Information about dilation properties of fluid/fluid interfaces can be also obtained from the longitudinal wave dampening. These are propagated mainly by interfacial tension gradients, allowing one to probe the dilational rheology of fluid/fluid interfaces at lower values of deformation frequencies than when capillary waves are used [50,73–75].

Despite the broad range of frequencies (0.1–10^5 Hz) that can be probed by the evaluation of the damping of waves generated at fluid/fluid interfaces, and the contactless character of this type of technique, the interpretation of the data is not straightforward, which limits their applicability [72,76]. Recently, Slavchov et al. [68] reviewed the most fundamental aspects of capillary wave damping as a tool for evaluating the mechanical response of fluid/fluid interfaces and other of its potential applications. Moreover, they analyzed some recent theoretical developments on the use of capillary waves. Rajan [77] has recently solved the problems associated with the use of the damping of interfacial waves for the determination of the rheological properties of liquid/liquid interfaces, providing results of the interfacial elasticity and viscosity of water/oil interfaces.

The use of Faraday waves can be an alternative for studying the properties of fluid/fluid interfaces for systems with very low values of this property [78,79]. Henderson [80] used the analysis of Faraday waves to evaluate the mechanical response of interfaces with monolayers of different insoluble molecules, and found that the effectiveness of wave damping was enhanced as the interfacial packing of the interfacial film increased. Similar results were found for monolayers of wheat storage proteins [81].

4.1.2. Experimental Methods

The experimental methods used for studying the dilational rheological response of fluid/fluid interfaces rely on the mechanical perturbation of the interfacial area, and the measurement of the response.

Stress Relaxation Experiments

Relaxation experiments of fluid/fluid interfaces can be performed by applying a sudden perturbation of a controllable parameter defining the equilibrium state of a monolayer at a fluid/fluid interface, e.g., interfacial area, or interfacial concentration, among others. This type of perturbation takes the system to an out-equilibrium situation, and hence, the system undergoes a relaxation process to reestablish the equilibrium state [82]. Stress relaxation experiments can be performed using Langmuir troughs or drop/bubble shape tensiometers [83].

In a stress relaxation experiment, the time evolution of the interfacial tension $\gamma(t)$ or the interfacial pressure $\Pi(t)$ are recorded, after a sudden change (compression or expansion) of the interfacial area. This change of the interfacial area takes the interfacial pressure far from its equilibrium value, inducing a change of the interfacial pressure $\Delta\Pi$ that defines the interfacial stress. This acts as a restoring force which tries to recover the equilibrium state of the interface once the strain ceases [84].

Creep Experiments

Creep experiments are commonly performed by using Langmuir troughs. In this type of experiment, an equilibrated interface characterized by its equilibrium interfacial pressure Π_0 is suddenly compressed, i.e., as fast as possible, until it reaches a desired interfacial pressure value; then, the surface pressure is constantly maintained by changing the interfacial area. Thus, the excess of interfacial pressure is adjusted by considering the area relaxation process, allowing one to define the creep compliance as [85]:

$$J(t) = \frac{u(t)}{\sigma} = \frac{\frac{\delta A}{A_0}}{\Pi - \Pi_0}. \tag{14}$$

The creep compliance $J(t)$ is a phenomenological function, providing information on how the structure of the film resists the application of a controlled stress [85,86].

Oscillatory Area Experiments

Oscillatory area experiments rely on the application of a sinusoidal perturbation to the interface, at a constant frequency ω, which is a profile described as $u(t) = \delta A/A_0 =$

$(u_0/2)\exp(i\omega t)$. The deformation of drops or bubbles at low frequencies almost guarantees a pure dilational deformation of the interface. However, for planar films studied in Langmuir troughs, the in-plane shear components can appear coupled to the dilational ones in both the applied strain and the response stress, which makes it difficult to extract true information of the dilational viscoelastic moduli. This may also occur in relaxation and creep experiments. It should be noted that the shear contributions present for films at fluid/fluid interface values are smaller values than those obtained for the dilational contributions, and hence, it can be neglected in oscillatory area experiments [30,87].

If the deformation allows the monolayer response within the linear regime to be maintained, this will follow a sinusoidal function with the same frequency of the strain.

$$\Pi(t) = \Pi_0 - \sigma(t), \tag{15}$$

with $\sigma(t) = \frac{\sigma_0}{2}\exp(i\omega + \phi_\sigma)$. ϕ_σ introduces a phase factor that includes the contribution associated with any delay in the response, due to viscous contributions in the rheological response of the interface. From oscillatory area experiments, within the linear regime, it is possible to obtain the elastic modulus E_s and the dilational viscosity κ_s

$$E_s = Ecos\phi_\sigma, \tag{16}$$

and

$$\omega\kappa_s = Esin\phi_\sigma, \tag{17}$$

with $E = \frac{\sigma_0}{u_0}$.

Surface Waves Experiments

Interfacial rheology experiments using surface waves are possible following two different strategies. The first takes advantage of the waves originated as a result of the "natural" thermal fluctuations of the surface position, which can be explained in terms of the second law of thermodynamics. The second strategy is based on the production of "artificial" surface waves upon the application of external stimuli, e.g., electrical or mechanical perturbations. Independently of the nature of the used waves, the features of the fluctuations (amplitude, frequency, damping, etc.) can be related to the interfacial rheological properties of the probed systems [88–90]. In fact, any displacement of the fluid/fluid interface in relation to their flat level shape can be interpreted as an interfacial motion guided by an external force, and restored as result of the viscoelastic properties of the fluid phases and the interface itself [36,91].

One of the most common techniques based on the study of surface waves is the surface quasi-elastic light scattering (SQELS) technique, which relies on the light scattered by transverse surface waves. These provide a measurement of the dynamics associated with the thermal induced roughness of the interface [36,91,92]. Thus, it is possible to evaluate the interfacial dynamics under equilibrium conditions by observing the dynamics of thermal fluctuations around the equilibrium state. These fluctuations present a very small length scale (a few Angstrom), allowing one to probe the interfacial rheology in the linear regime. SQELS experiments can be based on the determination of the heterodyne autocorrelation function or the power spectrum of the scattered light $P(\omega)$.

$$P(q,\omega\ ) = \frac{k_B T}{\pi\omega}\left[\frac{i\omega\eta(m+q) + Eq^2}{D(q,\omega)}\right], \tag{18}$$

where k_B is the Boltzmann constant and η the subphase viscosity. q and m define the wave-vector and the diffraction order, respectively. E is the complex dilational modu-

lus (compression+shear), and $D(\omega)$ the surface wave dispersion relation defined by the following expression [36]:

$$D(q,\omega) = \left[Eq^2 + i\omega(m+q)\right]\left[\gamma q^2 + i\omega(m+q) - \frac{\rho\omega^2}{q}\right] - [i\omega\eta(q-m)]^2, \quad (19)$$

with $m = \sqrt{q^2 + \frac{i\omega}{\eta}}$. The dilational elasticity and viscosity can be determined by measuring $P(\omega)$ and the interfacial tension. SQELS allows probing of the dilational viscoelastic properties of interfaces in the frequency range 10^3–10^6 Hz [93].

A second example of experiments based on surface waves relies on the excitation of surface waves with higher amplitudes than those obtained in SQELS experiments (~1μm). This is possible under the application of an external physical stimulus, commonly mechanical or electrical, as an excitation force. In general, electrical stimuli are preferred to mechanical ones because they present a non-invasive character, allowing for an easier experimental design [30].

Electrically excited surface waves are so-called electrocapillary waves (ECW), and they can be evaluated by measuring the spatial profile of the generated waves by using spatially resolved laser reflectometry. Thus, it is possible to obtain a spatial profile that follows a damped wave function, defined as:

$$A = cos\left(\frac{2\pi x}{\lambda} + \phi\right)\exp(-\beta x), \quad (20)$$

where λ accounts for the capillary wavelength and β for the spatial damping constant of the capillary wave oscillations. ϕ defines a phase term obtained as a function of the excitation frequency. ECW experiments are required to perform measurements at different frequencies to obtain the group velocity, and to transform the results obtained from the space domain to the time domain. Then, by combining the frequency of the independently measured interfacial tension and the values of λ and β obtained in the fitting of the spatial profile of the damped wave, it is possible to calculate the interfacial dilational elasticity and viscosity by solving numerically the dispersion equation for each measured frequency (in the range 20–10^3 Hz) [30].

It should be noted that the above wave damping considers a sharp fluid/fluid interface, which is coated by a thin monomolecular film. However, the situation becomes more complicated when thick films are adsorbed at the fluid/fluid interface. A detailed discussion of the role of the interface thickness on the ability of fluid/fluid interfaces for dampening waves can be found in the literature [94–96].

4.2. Theoretical Models

The use of suitable theoretical models for analyzing the frequency dependence of the dilational viscoelastic properties of fluid/fluid interfaces can shed light on the relaxation mechanism involved in the reestablishment of the interfacial equilibrium after a dilational deformation [45,97]. The Lucassen-Van den Tempel model assumes that the adsorption-desorption equilibrium occurs freely, and no adsorption barriers are present; thus, the material exchange between the bulk and the interface is governed by diffusion [45,98,99]. This is only possible assuming that the formation of an interfacial layer of the interface requires the equilibrium between the interface and the species existing in the bulk, i.e., the formation of a soluble or Gibbs monolayers. Thus, it is possible to define the complex viscoelastic modulus according to the following relationship:

$$E = \frac{1 + \xi + i\xi}{1 + 2\xi + 2\xi^2}\varepsilon_0, \quad (21)$$

where $\xi = \sqrt{\frac{\omega_D}{\omega}}$, with $\omega_D = D\left(\frac{dc}{d\Gamma}\right)^2_{eq}$ being the characteristic frequency of the exchange process, D the diffusion coefficient, and c the bulk concentration. From the above definition, it is possible to assume two limits. In the first limit, $\omega \to \infty$ and $\omega_D \to 0$, which results in $E_s \to \varepsilon_0$ and $E_v \to \omega\kappa_s \to 0$, and the monolayer behaves as an insoluble one (Langmuir monolayer), i.e., there are no possibilities for material exchange between the interface and the adjacent fluid phases. The opposite situation occurs when $\omega \to 0$ and $\omega_D \to \infty$, which results in $E_s, \omega\kappa_s \to 0$, leading to a situation where the resistance to the compression is negligible, and the equilibrium between the bulk and the interface can occur during the compression process. For those cases in which the frequency assumes intermediate values, the condition $0 < E_s < \varepsilon_0$ and $\omega\kappa_s \neq 0$ is fulfilled.

The above model assumes that the interfacial concentration only changes as a result of the exchange of molecules between the fluid/fluid interface and the adjacent bulk phases (Gibb monolayers). However, this is not possible when insoluble layers are considered. In these cases, it can be only expected relaxation processes that are circumscribed to the fluid/fluid interface. This type of relaxation mechanism can also appear in soluble monolayers. There are several possible interfacial tension relaxation processes that can directly affect the interface upon a dilational deformation [100]. These correspond to the internal reorganization of the adsorption layer, which can occur according to different mechanisms, e.g., phase transitions, molecular reorientation, and molecular folding/unfolding [17,45,101–103].

The existence of a relaxation mechanism involving only the interface requires introducing a generic thermodynamic variable X, which gives a description of the advancement of the relaxation process. This new variable, combined with the interfacial tension and the interfacial concentration, permits a description of the state of the interface. Thus, it is possible to define a state equation for the interface according to the following expression:

$$\gamma = \gamma(\Gamma, X). \tag{22}$$

Assuming a relaxation process following a first order kinetics, it is possible to define the kinetic equation as:

$$\frac{dX}{dt} = -k\left(X - X_{eq}\right), \tag{23}$$

where k is the characteristic constant of the process and X_{eq} is the value of the thermodynamic variable under equilibrium conditions [45,104]. The above framework allows a description of the dependence of the viscoelastic modulus in terms of the frequency as:

$$E = \varepsilon_0 + \sum_{j=1}^{N}\left(\varepsilon_j - \varepsilon_{j-1}\right)\frac{1 + \mathrm{i}\lambda_j}{1 + \lambda_j^2}, \tag{24}$$

where $\lambda_j = \omega_j/\omega$ and ω_j provide information about the characteristic frequency of the j-th relaxation processes, and ε_j and ε_{j-1} are thermodynamic parameters related to the limit elasticities. For insoluble systems, ε_0 stands for the limit elasticity when the deformation tends to zero.

The frequency dependence of the imaginary part of the dilational viscoelastic modulus is characterized by peaks, with their maximum corresponding to the characteristic frequency of the involved relaxation processes. The maxima of the peaks in the imaginary part correspond to the inflection points in the real part curves. Figure 3 represents the frequency dependence of the real or imaginary parts of the dilational viscoelastic modulus for fluid/fluid interfaces presenting different relaxation processes.

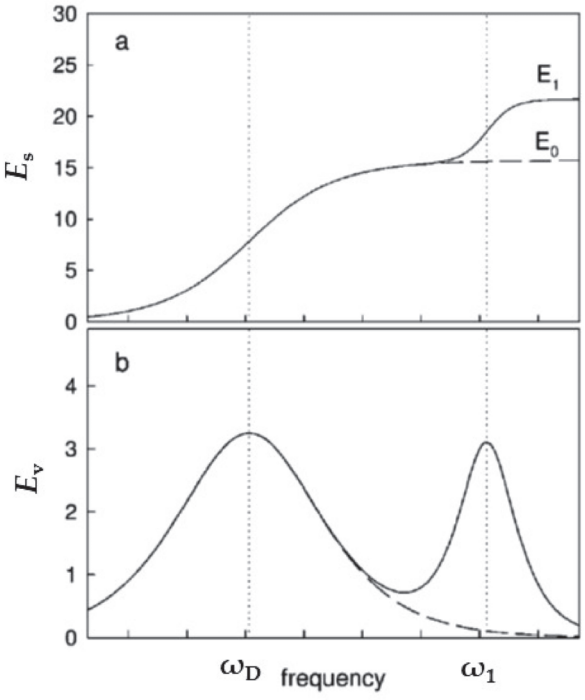

Figure 3. Sketch of the typical dependences of the (**a**) real and (**b**) imaginary parts of the viscoelastic modulus for fluid/fluid interfaces presenting different relaxation processes. The dashed lines correspond to a system presenting a relaxation process characterized by a relaxation process defined in terms of the Lucassen-van der Tempel model, and the continuous lines represent the typical behavior of a fluid/fluid interfaces where a relaxation process affecting only the interface is coupled to a Lucassen-van der Tempel-like relaxation. Reprinted from Liggieri et al. [104], with permission from Royal Society of Chemistry, Copyright (2011).

For systems presenting several relaxation processes, it is possible to superimpose them following a linear combination scheme to fabricate an expression for the frequency dependence of the dilational viscoelastic modulus containing an arbitrary number of processes [45,46,103,105].

5. Evaluation of the Mechanical Relaxation Spectrum from Dilational Rheology Experiments

One of the main challenges when dilational rheology experiments are performed is related to the evaluation of the mechanical response of fluid/fluid interfaces in a broad range of frequencies. Unfortunately, this requires a combination of techniques, which introduces two main issues: (i) the accessibility to the different techniques is not always easy; and (ii) some devices cannot be used for studying both soluble and insoluble interfacial layers. Figure 4 presents a summary of some of the experimental techniques accessible for evaluating the dilational response of fluid/fluid interfaces, as well as the frequency range in which they can be used.

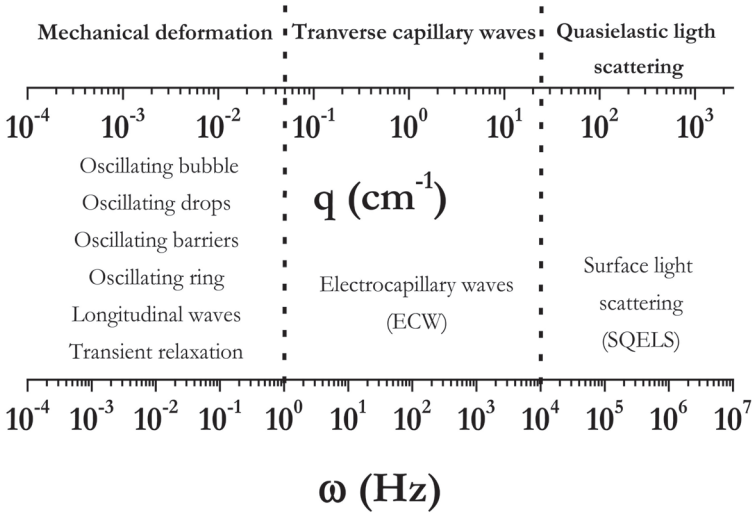

Figure 4. Summary of some of the most extended methodologies for evaluating the dilational response of fluid/fluid interface, together with the accessible frequency ranges for such techniques.

Presently, there has been only one study concerning the whole relaxation spectrum in the frequency range 10^{-3}–10^{3} Hz [104]. This required combining an oscillatory drop tensiometer, a capillary pressure tensiometer, and an electrocapillary wave instrument to access the whole frequency range. Moreover, there are several studies where the combination of different techniques has provided information about the mechanical relaxation spectrum, and information regarding the real and imaginary part of the viscoelastic modulus values from the whole frequency range is not available [106–108].

Assuming the difficulties associated with performing dilational rheology experiments in a broad frequency range, it is necessary to adapt classical approaches of conventional rheology to the study of fluid/fluid interfaces. One example of these approaches is to adapt the widely used time-temperature superposition principle for extending the range of frequencies accessible for the analysis of data [109]. The applicability of this type of superposition is limited to the thermo-rheologically simple, which are characterized by the presence of a single relaxation mechanism over the whole temperature and frequency range explored. Despite the proved effectiveness of the superposition principle for describing the bulk rheology of different systems, its application to the study of fluid/fluid interfaces is recent [52]. Bae et al. [52] proposed to describe dilational interfacial rheology by using a concentration-frequency superposition methodology. Thus, it was possible to expand the explored frequency range, even though the accessible data were acquired in a limited region. The concentration-frequency superposition can be defined in terms of the following set of expressions:

$$E_s\left(\omega, c^{ref}\right) = \beta_\varepsilon E_s[\alpha(c)\omega, c], \tag{25}$$

and

$$E_v(\omega,) = \beta_\varepsilon E_v[\alpha(c)\omega, c], \tag{26}$$

where $E_s\left(\omega, c^{ref}\right)$ and $E_v\left(\omega, c^{ref}\right)$ represent the dilational elastic and viscous moduli, respectively, as were obtained at the experimental frequency for a fixed value of the bulk concentration c^{ref} which is fixed at reference, and $E_s[\alpha(c)\omega, c]$ and $E_v[\alpha(c)\omega, c]$ correspond to the elastic and viscous moduli, respectively, at a certain bulk concentration c, in which the deformation frequency has been re-scaled by a shift factor α enabling the superposition of the real and imaginary parts of the viscoelastic dilational modulus. β_ε is a shifting factor for ensuring the perfect overlapping between the data. When $\beta_\varepsilon \to 0$, the frequency-

concentration superposition method provides information related to the concentration dependence of the rheological response, which provides the basis for enlarging the frequency window accessible for the experiments. Figure 5 shows, for the sake of example, the superposition of the curves corresponding to the dilational elasticity modulus and the loss tangent ($tan\delta = E_v/E_s$) for mixtures of chitosan and an anionic surfactant with increasing surfactant concentrations. The introduction of the shift factors to the rheological results allows for the establishment of master curves for the elastic modulus and the loss tangent.

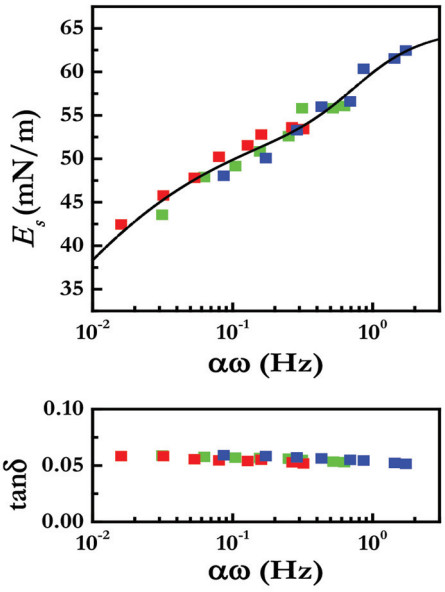

Figure 5. Re-scaled frequency dependences of the elastic modulus and loss tangent for chitosan-anionic surfactant mixtures with different surfactant concentrations (symbols of different color represents the set of data for solutions with different concentrations) and a fixed chitosan concentration of 2 g/L (pH 4.5 and ionic strength 120 mM NaCl). The symbols are the experimental results, and the solid lines represent the best fit of the experimental curves to a model, including a Lucassen-Van der Tempel-like relaxation process and a relaxation process affecting the interface. Adapted from Akanno et al. [51], with permission from Royal Society of Chemistry, Copyright (2020).

6. Non-Linear Dilational Interfacial Rheology

The above discussion has so far dealt with the dilational response of fluid/fluid interfaces to small amplitude deformations. However, the situation significantly changes when the amplitude of the deformation is large enough to push the response of interfacial films far from the linear regime. It should be noted that, in some systems, the onset in the region of a non-linear response is reached even with deformations of very small amplitude [110–112].

The analysis of the non-linear response in dilational rheology is not straightforward, mainly due to the difficulties associated with providing a suitable definition of the applied deformation [113]. This may be understood by considering axisymmetric drop shape analysis as an example. In many cases, this type of experiment relies on inhomogeneous deformation, which depends on the position [114]. This is a very critical issue because the stretching can be very different depending on the interface area, even though this is not considered in most cases for data analysis. Moreover, the interference of time-dependent and deformation-dependent rheological properties also complicates the analysis of non-linear behavior of fluid/fluid interfaces.

The study of the Lissajous curves is very useful for evaluating the properties of fluid/fluid interfaces under non-linear conditions. The asymmetry of the Lissajous plots results in four different contributions: two defining the extension part of the cycle (the dilational moduli at minimum E_s^{EM} and large E_s^{EL} extension), and two providing information of the compression part of the cycle (the dilational moduli at minimum E_s^{CM} and large E_s^{CL} compression) [113,115]. Figure 6 shows a schematic representation of the stress decomposition to obtain the four contributions.

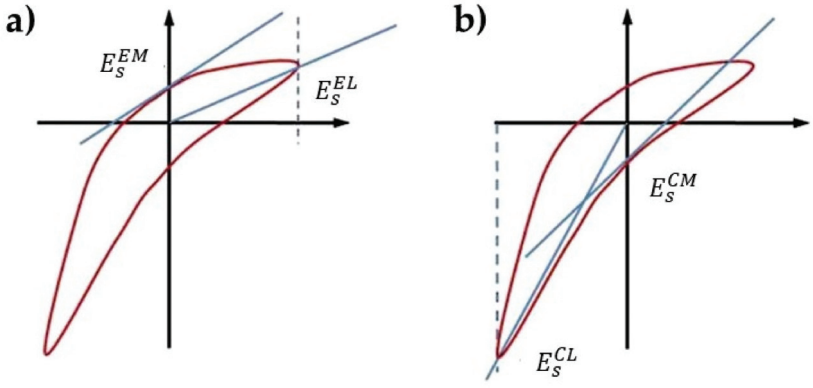

Figure 6. Definition of minimum and large-strain moduli. (**a**) Minimum and large deformation dilational moduli in extension. (**b**) Minimum and large deformation dilational moduli in compression. Adapted from Sagis and Fischer [113], with permission from Elsevier, Copyright (2014).

Using the abovementioned four contributions, it is possible to define two parameters defining the non-linearity; the first defining the compression part of the cycle:

$$S_c = \frac{E_s^{CL} - E_s^{CM}}{E_s^{CL}}, \tag{27}$$

and the second accounting for the extension part of the cycle:

$$S_E = \frac{E_s^{EL} - E_s^{EM}}{E_s^{EL}}. \tag{28}$$

The evaluation of the S factors as a function of the applied strain provides quantitative information on the non-linearity of the interface [113].

As an alternative to the graphical analysis in terms of a stress decomposition, the non-linear rheological response of interfaces can also be analyzed by representing the stress by using Fourier series, making use of the Fourier-transform rheology [111]. This relies on defining the stress response in terms of a Fourier expansion:

$$\sigma(t) = \sigma_0 \exp(\mathrm{i}\omega t) + \sigma_1 \exp(2\mathrm{i}\omega t) + \sigma_2 \exp(3\mathrm{i}\omega t) + \ldots, \tag{29}$$

where σ_0 defines the amplitude of the stress response defined with respect to the initial interfacial pressure, and σ_1, σ_2, etc., correspond to the amplitudes of the harmonic terms of the non-linear response. The use of Fourier transform rheology for modelling the non-linear dilational response of fluid/fluid interfaces presents an important limitation associated with the definition of the stress as an expansion around a zero-interface deformation rate, which can provide information only for systems with small deviations from the linearity. A very useful methodology for quantifying the non-linearity of the rheological response of

fluid/fluid interfaces is by introducing the concept of the Total Harmonic Distortion (THD), defined as [116]:

$$THD = \frac{\sqrt{\sum_{k>0} \sigma_k}}{\sigma_0}, \quad (30)$$

where σ_k corresponds to the amplitudes of the harmonic terms of the non-linear response. The above definition of the *THD* indicates that when this parameter assumes a null value, the systems present a linear rheological response, while larger values of this parameter show the emergence of a non-linear response of the fluid/fluid interface. Another alternative to decomposing the stress response in non-linear systems is the Volterra series [117].

7. Concluding Remarks

The study of the dilational properties of fluid/fluid interfaces has been extensively developed in recent years due to their recognized importance in different features of science and technology. In this review, an updated overview of the currently available theoretical and experimental strategies for evaluation of the dilational properties of fluid/fluid interfaces has been presented.

The more recently available knowledge on the interpretation of rheological data is based on constitutive models. However, a more detailed understanding of the rheological properties of fluid/fluid interfaces is required to introduce information about structural features, allowing the establishment of a link between the mechanical response of the interface and its structure. Therefore, it is necessary to advance the development of more suitable models, enabling a better description of the dilational rheology of fluid/fluid interfaces. Unfortunately, there are several challenges to overcome with regard to the evaluation of the mechanical performance of fluid/fluid interfaces, with the separation of the bulk effects and the response of the interface being one of the most important issues identified in the experimental and theoretical development of the study of the dilational rheology of fluid/fluid interfaces.

Author Contributions: The manuscript was written with the input at all authors. All authors have read and agreed to the published version of the manuscript.

Funding: This work was funded in part by MICINN under Grant PID2019-106557GB-C21 and by E.U. on the framework of the European Innovative Training Network—Marie Sklodowska-Curie Action Nano Paint (Grant Agreement 955612).

Institutional Review Board Statement: Not applicable.

Informed Consent Statement: Not Applicable.

Data Availability Statement: This manuscript has not contributed to the generation of any new data.

Conflicts of Interest: The authors declare no conflict of interest. The funders had no role in the design of the study; in the collection, analyses, or interpretation of data; in the writing of the manuscript; or in the decision to publish the results.

References

1. Forth, J.; Kim, P.Y.; Xie, G.; Liu, X.; Helms, B.A.; Russell, T.P. Building Reconfigurable Devices Using Complex Liquid–Fluid Interfaces. *Adv. Mater.* **2019**, *31*, 1806370. [CrossRef] [PubMed]
2. Guzmán, E. Current Perspective on the Study of Liquid–Fluid Interfaces: From Fundamentals to Innovative Applications. *Coatings* **2022**, *12*, 841. [CrossRef]
3. Guzmán, E.; Martínez-Pedrero, F.; Calero, C.; Maestro, A.; Ortega, F.; Rubio, R.G. A broad perspective to particle-laden fluid interfaces systems: From chemically homogeneous particles to active colloids. *Adv. Colloids Interface Sci.* **2022**, *302*, 102620. [CrossRef] [PubMed]
4. Guzmán, E. Fluid Films as Models for Understanding the Impact of Inhaled Particles in Lung Surfactant Layers. *Coatings* **2022**, *12*, 277. [CrossRef]
5. Guzmán, E.; Santini, E. Lung surfactant-particles at fluid interfaces for toxicity assessments. *Curr. Opin. Colloid Interface Sci.* **2019**, *39*, 24–39. [CrossRef]

6. Klein, C.O.; Theodoratou, A.; Rühs, P.A.; Jonas, U.; Loppinet, B.; Wilhelm, M.; Fischer, P.; Vermant, J.; Vlassopoulos, D. Interfacial Fourier transform shear rheometry of complex fluid interfaces. *Rheol. Acta* **2019**, *58*, 29–45. [CrossRef]
7. Masuda, T.; Takai, M. Design of biointerfaces composed of soft materials using controlled radical polymerizations. *J. Mater. Chem. B* **2022**, *10*, 1473–1485. [CrossRef]
8. Sagis, L.M.C.; Liu, B.; Li, Y.; Essers, J.; Yang, J.; Moghimikheirabadi, A.; Hinderink, E.; Berton-Carabin, C.; Schroen, K. Dynamic heterogeneity in complex interfaces of soft interface-dominated materials. *Sci. Rep.* **2019**, *9*, 2938. [CrossRef]
9. Jaensson, N.; Vermant, J. Tensiometry and rheology of complex interfaces. *Curr. Opin. Colloid Interface Sci.* **2018**, *37*, 136–150. [CrossRef]
10. Jaensson, N.O.; Anderson, P.D.; Vermant, J. Computational interfacial rheology. *J. Non-Newton. Fluid Mech.* **2021**, *290*, 104507. [CrossRef]
11. Wei, Y.; Xie, Y.; Cai, Z.; Guo, Y.; Zhang, H. Interfacial rheology, emulsifying property and emulsion stability of glyceryl monooleate-modified corn fiber gum. *Food Chem.* **2021**, *343*, 128416. [CrossRef]
12. Botti, T.C.; Hutin, A.; Quintella, E.; Carvalho, M.S. Effect of interfacial rheology on drop coalescence in water–oil emulsion. *Soft Matter* **2022**, *18*, 1423–1434. [CrossRef]
13. Wang, H.; Wei, X.; Du, Y.; Wang, D. Experimental investigation on the dilatational interfacial rheology of dust-suppressing foam and its effect on foam performance. *Process. Saf. Environ. Prot.* **2019**, *123*, 351–357. [CrossRef]
14. Thai, L.P.A.; Mousseau, F.; Oikonomou, E.K.; Berret, J.F. On the rheology of pulmonary surfactant: Effects of concentration and consequences for the surfactant replacement therapy. *Colloids Surf. B* **2019**, *178*, 337–345. [CrossRef]
15. Haslbeck, K.; Schwarz, K.; Hohlfeld, J.M.; Seume, J.R.; Koch, W. Submicron droplet formation in the human lung. *J. Aerosol Sci.* **2010**, *41*, 429–438. [CrossRef]
16. Svitova, T.F.; Lin, M.C. Tear lipids interfacial rheology: Effect of lysozyme and lens care solutions. *Optom. Vis. Sci.* **2010**, *87*, 10–20. [CrossRef]
17. Rubio, R.G.; Guzmán, E.; Ortega, F.; Liggieri, L. Monolayers of Cholesterol and Cholesteryl Stearate at the Water/Vapor Interface: A Physico-Chemical Study of Components of the Meibum Layer. *Colloids Interfaces* **2021**, *5*, 30. [CrossRef]
18. Zhang, H.; Lamnawar, K.; Maazouz, A. Fundamental studies of interfacial rheology at multilayered model polymers for coextrusion process. *AIP Conf. Proc.* **2015**, *1664*, 100008. [CrossRef]
19. Perrin, L.; Akanno, A.; Guzman, E.; Ortega, F.; Rubio, R.G. Pattern Formation upon Evaporation of Sessile Droplets of Polyelectrolyte/Surfactant Mixtures on Silicon Wafers. *Int. J. Mol. Sci.* **2021**, *22*, 7953. [CrossRef]
20. Sun, H.-Q.; Zhang, L.; Li, Z.-Q.; Zhang, L.; Luo, L.; Zhao, S. Interfacial dilational rheology related to enhance oil recovery. *Soft Matter* **2011**, *7*, 7601–7611. [CrossRef]
21. Gade, M.; Byfield, V.; Ermakov, S.; Lavrova, O.; Mitnik, L. Slicks as Indicators for Marine Processes. *Oceanography* **2013**, *26*, 138–149. [CrossRef]
22. Ermakov, S.A.; Khazanov, G.E. Resonance damping of gravity–capillary waves on water covered with a visco-elastic film of finite thickness: A reappraisal. *Phys. Fluids* **2022**, *34*, 092107. [CrossRef]
23. Sánchez-Puga, P.; Tajuelo, J.; Pastor, J.M.; Rubio, M.A. Flow field-based data analysis in interfacial shear rheometry. *Adv. Colloids Interface Sci.* **2021**, *288*, 102332. [CrossRef]
24. Guzmán, E.; Tajuelo, J.; Pastor, J.M.; Rubio, M.Á.; Ortega, F.; Rubio, R.G. Shear rheology of fluid interfaces: Closing the gap between macro- and micro-rheology. *Curr. Opin. Colloid Interface Sci.* **2018**, *37*, 33–48. [CrossRef]
25. Wong, W.-H.B.; Hulsen, M.A.; Anderson, P.D. A numerical model for the development of the morphology of disperse blends in complex flow. *Rheol. Acta* **2019**, *58*, 79–95. [CrossRef]
26. Nilsson, M.A.; Kulkarni, R.; Gerberich, L.; Hammond, R.; Singh, R.; Baumhoff, E.; Rothstein, J.P. Effect of fluid rheology on enhanced oil recovery in a microfluidic sandstone device. *J. Non-Newton. Fluid Mech.* **2013**, *202*, 112–119. [CrossRef]
27. Perez, P.L.; Zaragoza, J.N.; Patel, N.K.; Dion, M.A. Impact of Asphaltene Stabilizers on the Elasticity of a Crude Oil–Water Interface and Its Correlation to Demulsification under Desalting Conditions. *Energy Fuels* **2022**, *36*, 275–289. [CrossRef]
28. Guzmán, E.; Santini, E.; Ferrari, M.; Liggieri, L.; Ravera, F. Evaluating the Impact of Hydrophobic Silicon Dioxide in the Interfacial Properties of Lung Surfactant Films. *ACS Environ. Sci. Technol.* **2022**, *56*, 7308–7318. [CrossRef] [PubMed]
29. Nagel, M.; Tervoort, T.A.; Vermant, J. From drop-shape analysis to stress-fitting elastometry. *Adv. Colloids Interface Sci.* **2017**, *247*, 33–51. [CrossRef] [PubMed]
30. Mendoza, A.J.; Guzmán, E.; Martínez-Pedrero, F.; Ritacco, H.; Rubio, R.G.; Ortega, F.; Starov, V.M.; Miller, R. Particle laden fluid interfaces: Dynamics and interfacial rheology. *Adv. Colloids Interface Sci.* **2014**, *206*, 303–319. [CrossRef] [PubMed]
31. Manikantan, H.; Squires, T.M. Surfactant dynamics: Hidden variables controlling fluid flows. *J. Fluid Mech.* **2020**, *892*, P1. [CrossRef]
32. Krotov, V.V. Basics of Interfacial rheology. In *Interfacial Rheology*; Miller, R., Liggieri, L., Eds.; Brill: Leiden, The Netherlands, 2009; pp. 1–37.
33. Garbin, V. Collapse mechanisms and extreme deformation of particle-laden interfaces. *Curr. Opin. Colloid Interface Sci.* **2019**, *39*, 202–211. [CrossRef]
34. Maestro, A.; Guzmán, E. Colloids at Fluid Interfaces. *Processes* **2019**, *7*, 942. [CrossRef]
35. Nitschke, I.; Voigt, A. Observer-invariant time derivatives on moving surfaces. *J. Geom. Phys.* **2022**, *173*, 104428. [CrossRef]
36. Langevin, D. Light scattering by liquid surfaces, new developments. *Adv. Colloids Interface Sci.* **2021**, *289*, 102368. [CrossRef]

37. Fuller, G.G.; Vermant, J. Complex Fluid-Fluid Interfaces: Rheology and Structure. *Annu. Rev. Chem. Biomol. Eng.* **2012**, *3*, 519–543. [CrossRef]
38. Stone, H.A.; Leal, L.G. The effects of surfactants on drop deformation and breakup. *J. Fluid Mech.* **1990**, *220*, 161–186. [CrossRef]
39. De Kinkelder, E.; Sagis, L.; Aland, S. A numerical method for the simulation of viscoelastic fluid surfaces. *J. Comput. Phys.* **2021**, *440*, 110413. [CrossRef]
40. Pepicelli, M.; Verwijlen, T.; Tervoort, T.; Vermant, J. Characterization and modelling of Langmuir interfaces with finite elasticity. *Soft Matter* **2017**, *13*, 5977–5990. [CrossRef]
41. Sagis, L. Dynamic surface tension of complex fluid-fluid interfaces: A useful concept, or not? *Eur. Phys. J. Spec. Top.* **2013**, *222*, 39–46. [CrossRef]
42. Reichert, M.D.; Alvarez, N.J.; Brooks, C.F.; Grillet, A.M.; Mondy, L.A.; Anna, S.L.; Walker, L.M. The importance of experimental design on measurement of dynamic interfacial tension and interfacial rheology in diffusion-limited surfactant systems. *Colloids Surf. A* **2015**, *467*, 135–142. [CrossRef]
43. Miller, R.; Ferri, J.; Javadi, A.; Krägel, J.; Mucic, N.; Wüstneck, R. Rheology of interfacial layers. *Colloid Polym. Sci.* **2010**, *288*, 937–950. [CrossRef]
44. Karbaschi, M.; Lotfi, M.; Krägel, J.; Javadi, A.; Bastani, D.; Miller, R. Rheology of interfacial layers. *Curr. Opin. Colloid Interface Sci.* **2014**, *19*, 514–519. [CrossRef]
45. Ravera, F.; Ferrari, M.; Santini, E.; Liggieri, L. Influence of surface processes on the dilational visco-elasticity of surfactant solutions. *Adv. Colloids Interface Sci.* **2005**, *117*, 75–100. [CrossRef]
46. Guzmán, E.; Liggieri, L.; Santini, E.; Ferrari, M.; Ravera, F. Influence of silicananoparticles on dilational rheology of DPPC–palmitic acid Langmuir monolayers. *Soft Matter* **2012**, *8*, 3938–3948. [CrossRef]
47. Guzmán, E.; Liggieri, L.; Santini, E.; Ferrari, M.; Ravera, F. Mixed DPPC–cholesterol Langmuir monolayers in presence of hydrophilic silica nanoparticles. *Colloids Surf. B* **2015**, *105*, 284–293. [CrossRef]
48. Omari, Y.E.; Yousfi, M.; Duchet-Rumeau, J.; Maazouz, A. Recent Advances in the Interfacial Shear and Dilational Rheology of Polymer Systems: From Fundamentals to Applications. *Polymers* **2022**, *14*, 2844. [CrossRef]
49. Ravera, F.; Miller, R.; Zuo, Y.Y.; Noskov, B.A.; Bykov, A.G.; Kovalchuk, V.I.; Loglio, G.; Javadi, A.; Liggieri, L. Methods and models to investigate the physicochemical functionality of pulmonary surfactant. *Curr. Opin. Colloid Interface Sci.* **2021**, *55*, 101467. [CrossRef]
50. Firouzi, M.; Kovalchuk, V.I.; Loglio, G.; Miller, R. Salt effects on the dilational viscoelasticity of surfactant adsorption layers. *Curr. Opin. Colloid Interface Sci.* **2022**, *57*, 101538. [CrossRef]
51. Akanno, A.; Guzmán, E.; Ortega, F.; Rubio, R.G. Behavior of the water/vapor interface of chitosan solutions with an anionic surfactant: Effect of polymer–surfactant interactions. *Phys. Chem. Chem. Phys.* **2020**, *22*, 23360–23373. [CrossRef]
52. Bae, J.-E.; Jung, J.B.; Kim, K.; Lee, S.-M.; Kang, N.-G. A study on time-concentration superposition of dilatational modulus and foaming behavior of sodium alkyl sulfate. *J. Colloid Interface Sci.* **2019**, *55*, 704–716. [CrossRef]
53. Suja, V.C.; Rodríguez-Hakim, M.; Tajuelo, J.; Fuller, G.G. Single bubble and drop techniques for characterizing foams and emulsions. *Adv. Colloids Interface Sci.* **2020**, *286*, 102295. [CrossRef]
54. Akanno, A.; Perrin, L.; Guzmán, E.; Llamas, S.; Starov, V.M.; Ortega, F.; Rubio, R.G.; Velarde, M.G. Evaporation of Sessile Droplets of Polyelectrolyte/Surfactant Mixtures on Silicon Wafers. *Colloids Interfaces* **2021**, *5*, 12. [CrossRef]
55. Noskov, B.A. Dilational surface rheology of polymer and polymer/surfactant solutions. *Curr. Opin. Colloid Interface Sci.* **2010**, *15*, 229–236. [CrossRef]
56. Javadi, A.; Krägel, J.; Makievski, A.V.; Kovalchuk, V.I.; Kovalchuk, N.M.; Mucic, N.; Loglio, G.; Pandolfini, P.; Karbaschi, M.; Miller, R. Fast dynamic interfacial tension measurements and dilational rheology of interfacial layers by using the capillary pressure technique. *Colloids Surf. A* **2012**, *407*, 159–168. [CrossRef]
57. Saad, S.; Neumann, A. Axisymmetric drop shape analysis (ADSA): An outline. *Adv. Colloids Interface Sci.* **2016**, *238*, 62–87. [CrossRef]
58. Danov, K.; Stanimirova, R.; Kralchevsky, P.; Marinova, K.; Alexandrov, N.; Stoyanov, S.; Blijdenstein, T.; Pelan, E. Capillary meniscus dynamometry—method for determining the surface tension of drops and bubbles with isotropic and anisotropic surface stress distributions. *J. Colloid Interface Sci.* **2015**, *440*, 168–178. [CrossRef]
59. Ravera, F.; Loglio, G.; Kovalchuk, V.I. Interfacial dilational rheology by oscillating bubble/drop methods. *Curr. Opin. Colloid Interface Sci.* **2010**, *15*, 217–228. [CrossRef]
60. Kotula, A.P.; Anna, S.L. Regular perturbation analysis of small amplitude oscillatory dilatation of an interface in a capillary pressure tensiometer. *J. Rheol.* **2014**, *59*, 85–117. [CrossRef]
61. Kovalchuk, V.I.; Krägel, J.; Makievski, A.V.; Loglio, G.; Ravera, F.; Liggieri, L.; Miller, R. Frequency characteristics of amplitude and phase of oscillating bubble systems in a closed measuring cell. *J. Colloid Interface Sci.* **2002**, *252*, 433–442. [CrossRef]
62. Guzmán, E.; Santini, E.; Ferrari, M.; Liggieri, L.; Ravera, F. Evaluation of the impact of carbonaceous particles in the mechanical performance of lipid Langmuir monolayers. *Colloids Surf. A* **2022**, *634*, 127974. [CrossRef]
63. Guzmán, E.; Santini, E.; Ferrari, M.; Liggieri, L.; Ravera, F. Interaction of Particles with Langmuir Monolayers of 1,2-Dipalmitoyl-Sn-Glycero-3-Phosphocholine: A Matter of Chemistry? *Coatings* **2020**, *10*, 469. [CrossRef]
64. Petkov, J.; Gurkov, T.; Campbell, B.; Borwankar, R. Dilatational and shear elasticity of gel-like protein layers on air/water interface. *Langmuir* **2000**, *16*, 3703–3711. [CrossRef]

65. Vora, S.; Bognet, B.; Patanwala, H.; Young, C.; Chang, S.; Daux, V.; Ma, A. Global strain field mapping of a particle-laden interface using digital image correlation. *J. Colloid Interface Sci.* **2018**, *509*, 94–101. [CrossRef]
66. Alicke, A.; Simon, S.; Sjöblom, J.; Vermant, J. Assessing the interfacial activity of insoluble asphaltene layers: Interfacial rheology versus interfacial tension. *Langmuir* **2020**, *36*, 14942–14959. [CrossRef]
67. Duncan, J.H.; Waxman, A.M.; Tulin, M.P. The dynamics of waves at the interface between a viscoelastic coating and a fluid flow. *J. Fluid Mech.* **1985**, *158*, 177–197. [CrossRef]
68. Slavchov, R.I.; Peychev, B.; Ismail, A.S. Characterization of capillary waves: A review and a new optical method. *Phys. Fluids* **2021**, *33*, 101303. [CrossRef]
69. Sergievskaya, I.; Ermakov, S.; Lazareva, T.; Guo, J. Damping of surface waves due to crude oil/oil emulsion films on water. *Mar. Pollut. Bull.* **2019**, *146*, 206–214. [CrossRef]
70. Ermakov, S.A. Damping of gravity-capillary waves on water surface covered with a visco-elastic film of finite thickness. *Izv. Atmos. Ocean. Phys.* **2003**, *39*, 624–628.
71. Ermakov, S.A.; Kijashko, S.V. Laboratory study of the damping of parametric ripples due to surfactant films. In *Marine Surface Films. Chemical Characteristics, Influence on Air-Sea Interactions and Remote Sensing*; Gade, M., Hühnerfuss, H., Korenowski, G.M., Eds.; Springer: Berlin, Germany, 2006; pp. 113–128.
72. Langevin, D. Rheology of adsorbed surfactant monolayers at fluid surfaces. *Annu. Rev. Fluid Mech.* **2014**, *46*, 47–65. [CrossRef]
73. Liu, X.; Duncan, J.H.; Korenowski, G.M.; Kelly, J.S. A laboratory study of longitudinal waves in surfactant films in a water wave tank. *J. Geophys. Res. Oceans* **2007**, *122*, C06005. [CrossRef]
74. Rajan, G.K. Dissipation of interfacial Marangoni waves and their resonance with capillary-gravity waves. *Int. J. Eng. Sci.* **2020**, *154*, 103340. [CrossRef]
75. Rajan, G.K. Solutions of a comprehensive dispersion relation for waves at the elastic interface of two viscous fluids. *Eur. J. Mech. B Fluids* **2021**, *89*, 241–258. [CrossRef]
76. Derkach, S.R.; Krägel, J.; Miller, R. Methods of measuring rheological properties of interfacial layers (Experimental methods of 2D rheology). *Colloid J.* **2009**, *71*, 1–17. [CrossRef]
77. Rajan, G.K. Damping rate measurements and predictions for gravity waves in an air–oil–water system. *Phys. Fluids* **2022**, *34*, 022113. [CrossRef]
78. Lau, Y.M.; Westerweel, J.; Van De Water, W. Using Faraday Waves to Measure Interfacial Tension. *Langmuir* **2020**, *36*, 5872–5879. [CrossRef]
79. Kharbedia, M.; Caselli, N.; Herráez-Aguilar, D.; López-Menéndez, H.; Enciso, E.; Santiago, J.A.; Monroy, F. Moulding hydrodynamic 2D-crystals upon parametric Faraday waves in shear-functionalized water surfaces. *Nat. Commun.* **2021**, *12*, 1130. [CrossRef]
80. Henderson, D.M. Effects of surfactants on Faraday-wave dynamics. *J. Fluid Mech.* **1998**, *365*, 89–107. [CrossRef]
81. Henderson, D.M.; Larsson, K.; Rao, Y.K. A study of wheat storage protein monolayers by Faraday wave damping. *Langmuir* **1991**, *7*, 2731–2736. [CrossRef]
82. Monroy, F.; Ortega, F.; Rubio, R.G. Dilatational rheology of insoluble polymer monolayers: Poly(vinylacetate). *Phys. Rev. E* **1998**, *58*, 7629. [CrossRef]
83. Guzmán, E.; Ritacco, H.; Ortega, F.; Svitova, T.; Radke, C.J.; Rubio, R.G. Adsorption Kinetics and Mechanical Properties of Ultrathin Polyelectrolyte Multilayers: Liquid-Supported versus Solid-Supported Films. *J. Phys. Chem. B* **2009**, *113*, 7128–7137. [CrossRef]
84. Alexandrov, N.A.; Marinova, K.G.; Gurkov, T.D.; Danov, K.D.; Kralchevsky, P.A.; Stoyanov, S.D.; Blijdenstein, T.B.J.; Arnaudov, L.N.; Pelan, E.G. Interfacial layers from the protein HFBII hydrophobin: Dynamic surface tension, dilatational elasticity and relaxation times. *J. Colloid Interface Sci.* **2012**, *376*, 296–306. [CrossRef]
85. Hilles, H.; Monroy, F. Dilational creep compliance in Langmuir polymer films. *Soft Matter* **2011**, *7*, 7790–7796. [CrossRef]
86. Findley, W.N.; Lai, J.S.; Onaran, K. *Creep and Relaxation of Nonlinear Viscoelastic Materials*; Dover Publications, Inc.: New York, NY, USA, 1976.
87. Ravera, F.; Liggieri, L.; Loglio, G. Dilational rheology of adsorbed layers by oscillating drops and bubbles. In *Interfacial Rheology*; Miller, R., Liggieri, L., Eds.; Brill: Leiden, The Netherlands, 2009; pp. 138–173.
88. Lombardini, P.P.; Piazzese, F.; Cini, R. The Marangoni wave in ripples on an air-water interface covered by a spreading film. *Il Nuovo Cimento C* **1982**, *5*, 256–263. [CrossRef]
89. Ghia, P.L.; Trivero, P. On the vibration modes of the air-water interface in the presence of surface films. *Il Nuovo Cimento C* **1988**, *11*, 305–315. [CrossRef]
90. Fiscella, B.; Lombardini, P.P.; Trivero, P.; Cini, R. Ripple damping on water surface covered by a spreading film: Theory and experiment. *Il Nuovo Cimento C* **1985**, *8*, 491–500. [CrossRef]
91. Monroy, F.; Ortega, F.; Rubio, R.G.; Velarde, M.G. Surface rheology, equilibrium and dynamic features at interfaces, with emphasis on efficient tools for probing polymer dynamics at interfaces. *Adv. Colloids Interface Sci.* **2007**, *134–135*, 175–189. [CrossRef]
92. Cicuta, P.; Hopkinson, I. Recent developments of surface light scattering as a tool for optical-rheology of polymer monolayers. *Colloids Surf. A* **2004**, *233*, 97–107. [CrossRef]
93. Sutherland, G.; Halsne, T.; Rabault, J.; Jensen, A. The attenuation of monochromatic surface waves due to the presence of an inextensible cover. *Wave Motion* **2017**, *68*, 88–96. [CrossRef]

94. Jenkins, A.D.; Jacobs, S.J. Wave damping by a thin layer of viscous fluid. *J. Fluid Mech.* **1997**, *9*, 1256. [CrossRef]
95. Monroy, F. Surface hydrodynamics of viscoelastic fluids and soft solids: Surfing bulk rheology on capillary and Rayleigh waves. *Adv. Colloid Interface Sci.* **2017**, *247*, 4–22. [CrossRef]
96. Muñoz, M.G.; Monroy, F.; Hernández, P.; Ortega, F.; Rubio, R.G.; Langevin, D. Anomalous Damping of the Capillary Waves at the Air−Water Interface of a Soluble Triblock Copolymer. *Langmuir* **2003**, *19*, 2147–2154. [CrossRef]
97. Baidakov, V.G.; Protsenko, S.P.; Bryukhanov, V.M. Relaxation processes at liquid-gas interfaces in one- and two-component Lennard-Jones systems: Molecular dynamics simulation. *Fluid Ph. Equilibria* **2019**, *481*, 1–14. [CrossRef]
98. Lucassen, J.; Van Den Tempel, M. Dynamic measurements of dilational properties of a liquid interface. *Chem. Eng. Sci.* **1972**, *27*, 1283–1291. [CrossRef]
99. Van den Tempel, M.; Lucassen-Reynders, E. Relaxation processes at fluid interfaces. *Adv. Colloid Interface Sci.* **1983**, *18*, 281–301. [CrossRef]
100. Liggieri, L.; Miller, R. Interfacial rheology—The response of two-dimensional layers on external perturbations. *Curr. Opin. Colloid Interface Sci.* **2010**, *15*, 256–263. [CrossRef]
101. Muñoz-López, R.; Guzmán, E.; Velázquez, M.M.; Fernández-Peña, L.; Merchán, M.D.; Maestro, A.; Ortega, F.; Rubio, R.G. Influence of Carbon Nanosheets on the Behavior of 1,2-Dipalmitoyl-sn-glycerol-3-phosphocholine Langmuir Monolayers. *Processes* **2020**, *8*, 94. [CrossRef]
102. Guzmán, E.; Fernández-Peña, L.; Akanno, A.; Llamas, S.; Ortega, F.; Rubio, R.G. Two Different Scenarios for the Equilibration of Polycation—Anionic Solutions at Water–Vapor Interfaces. *Coatings* **2019**, *9*, 438. [CrossRef]
103. Llamas, S.; Guzmán, E.; Akanno, A.; Fernández-Peña, L.; Ortega, F.; Campbell, R.A.; Miller, R.; Rubio, R.G. Study of the Liquid/Vapor Interfacial Properties of Concentrated Polyelectrolyte–Surfactant Mixtures Using Surface Tensiometry and Neutron Reflectometry: Equilibrium, Adsorption Kinetics, and Dilational Rheology. *J. Phys. Chem. C* **2018**, *122*, 4419–4427. [CrossRef]
104. Liggieri, L.; Santini, E.; Guzmán, E.; Maestro, A.; Ravera, F. Wide-frequency dilational rheology investigation of mixed silica nanoparticle–CTAB interfacial layers. *Soft Matter* **2011**, *7*, 7699–7709. [CrossRef]
105. Akanno, A.; Guzmán, E.; Fernández-Peña, L.; Llamas, S.; Ortega, F.; Rubio, R.G. Equilibration of a Polycation–Anionic Surfactant Mixture at the Water/Vapor Interface. *Langmuir* **2018**, *34*, 7455–7464. [CrossRef] [PubMed]
106. Llamas, S.; Mendoza, A.J.; Guzmán, E.; Ortega, F.; Rubio, R.G. Salt effects on the air/solution interfacial properties of PEO-containing copolymers: Equilibrium, adsorption kinetics and surface rheological behavior. *J. Colloid Interface Sci.* **2013**, *400*, 49–58. [CrossRef] [PubMed]
107. Maestro, A.; Kotsmar, C.; Javadi, A.; Miller, R.; Ortega, F.; Rubio, R.G. Adsorption of β-Casein–Surfactant Mixed Layers at the Air–Water Interface Evaluated by Interfacial Rheology. *J. Phys. Chem. B* **2012**, *116*, 4898–4907. [CrossRef] [PubMed]
108. Maestro, A.; Ortega, F.; Rubio, R.G.; Rubio, M.A.; Krägel, J.; Miller, R. Rheology of poly(methyl methacrylate) Langmuir monolayers: Percolation transition to a soft glasslike system. *J. Chem. Phys.* **2011**, *134*, 104704. [CrossRef]
109. Riande, E.; Diaz-Calleja, R.; Prolongo, M.G.; Masegosa, R.; Salom, C. *Polymer Viscoelasticity: Stress and Strain in Practice*; CRC Press: Boca Raton, FL, USA, 2000.
110. Hilles, H.; Maestro, A.; Monroy, F.; Ortega, F.; Rubio, R.G. Polymer monolayers with a small viscoelastic linear regime: Equilibrium and rheology of poly(octadecyl acrylate) and poly(vinyl stearate). *J. Chem. Phys.* **2007**, *126*, 124904. [CrossRef]
111. Hilles, H.; Monroy, F.; Bonales, L.J.; Ortega, F.; Rubio, R.G. Fourier-transform rheology of polymer Langmuir monolayers: Analysis of the non-linear and plastic behaviors. *Adv. Colloid Interface Sci.* **2006**, *122*, 67–77. [CrossRef]
112. Guzmán, E.; Santini, E.; Ferrari, M.; Liggieri, L.; Ravera, F. Effect of the Incorporation of Nanosized Titanium Dioxide on the Interfacial Properties of 1,2-Dipalmitoyl-sn-glycerol-3-phosphocholine Langmuir Monolayers. *Langmuir* **2017**, *33*, 10715–10725. [CrossRef]
113. Sagis, L.M.C.; Fischer, P. Nonlinear rheology of complex fluid–fluid interfaces. *Curr. Opin. Colloid Interface Sci.* **2014**, *19*, 520–529. [CrossRef]
114. Ferri, J.K.; Fernandes, P.A.L.; McRuiza, J.T.; Gambinossi, F. Elastic nanomembrane metrology at fluid–fluid interfaces using axisymmetric drop shape analysis with anisotropic surface tensions: Deviations from Young–Laplace equation. *Soft Matter* **2012**, *8*, 10352–10359. [CrossRef]
115. Bykov, A.G.; Guzmán, E.; Rubio, R.G.; Krycki, M.M.; Milyaeva, O.Y.; Noskov, B.A. Influence of temperature on dynamic surface properties of spread DPPC monolayers in a broad range of surface pressures. *Chem. Phys. Lipids* **2019**, *225*, 104812. [CrossRef]
116. Loglio, G.; Pandolfini, P.; Miller, R.; Makievski, A.V.; Krägel, J.; Ravera, F.; Noskov, B.A. Perturbation–response relationship in liquid interfacial systems: Non-linearity assessment by frequency–domain analysis. *Colloids Surf. A* **2005**, *261*, 57–63. [CrossRef]
117. Bykov, A.G.; Liggieri, L.; Noskov, B.A.; Pandolfinib, P.; Ravera, F.; Loglio, G. Surface dilational rheological properties in the nonlinear domain. *Adv. Colloid Interface Sci.* **2015**, *222*, 110–118. [CrossRef]

MDPI
St. Alban-Anlage 66
4052 Basel
Switzerland
www.mdpi.com

Fluids Editorial Office
E-mail: fluids@mdpi.com
www.mdpi.com/journal/fluids

Academic Open
Access Publishing

mdpi.com

ISBN 978-3-7258-1292-9